Springer Proceedings in Physics 197

Leonid A. Bulavin
Alexander V. Chalyi *Editors*

Modern Problems of Molecular Physics

Selected Reviews from the 7th International Conference "Physics of Liquid Matter: Modern Problems", Kyiv, Ukraine, May 27–31, 2016

Springer

Springer Proceedings in Physics

Volume 197

The series Springer Proceedings in Physics, founded in 1984, is devoted to timely reports of state-of-the-art developments in physics and related sciences. Typically based on material presented at conferences, workshops and similar scientific meetings, volumes published in this series will constitute a comprehensive up-to-date source of reference on a field or subfield of relevance in contemporary physics. Proposals must include the following:

- name, place and date of the scientific meeting
- a link to the committees (local organization, international advisors etc.)
- scientific description of the meeting
- list of invited/plenary speakers
- an estimate of the planned proceedings book parameters (number of pages/ articles, requested number of bulk copies, submission deadline).

More information about this series at http://www.springer.com/series/361

Leonid A. Bulavin · Alexander V. Chalyi
Editors

Modern Problems of Molecular Physics

Selected Reviews from the 7th International Conference "Physics of Liquid Matter: Modern Problems", Kyiv, Ukraine, May 27–31, 2016

Springer

Editors
Leonid A. Bulavin
Department of Molecular Physics
Taras Shevchenko National University of Kyiv
Kyiv
Ukraine

Alexander V. Chalyi
Department of Medical and Biological Physics
Bogomolets National Medical University
Kyiv
Ukraine

ISSN 0930-8989 ISSN 1867-4941 (electronic)
Springer Proceedings in Physics
ISBN 978-3-319-61108-2 ISBN 978-3-319-61109-9 (eBook)
https://doi.org/10.1007/978-3-319-61109-9

Library of Congress Control Number: 2017958837

Printed on acid-free paper

This Springer imprint is published by Springer Nature
The registered company is Springer International Publishing AG
The registered company address is: Gewerbestrasse 11, 6330 Cham, Switzerland

Preface

Once upon a time, about 30 years ago, at the summer school on theoretical physics, lying on the beach of a gentle Black Sea in the sport camp of the Odessa University together with the well-known throughout the physical world scientists Valentin Pokrovsky and Alexander Patashinskii, who wrote a famous book "Fluctuation Theory of Phase Transitions" (Pergamon Press, Oxford, 1979), one of the editors (A.Ch.) of the Springer book "Modern Problems of Molecular Physics: Selected Reviews" heard from them such words: "Our great teacher Dau told us that there is nothing to consider the density of a liquid is different from the unit!".

Should we explain the meaning of this sacramental phrase for respected readers, which seems to be an "error" by the Nobel Prize Laureate Lev Landau? In fact, a genius physicist L. D. Landau did not make mistakes in his physical works. Indeed, the density of the most common in nature, simultaneously so unique and mysterious, liquid water is equal to 1 in grams per cubic centimeter under normal conditions at room temperature and at atmospheric pressure. Then, what is a reason to use the word "error" even in quotes? As is known, Landau did not consider the physics of the liquid state of matter was equally interesting and promising area for building a successful physical theory, as, say, the solid-state physics or the physics of elementary particles. There is a well-known statement: "Theoretical physics is the physics of limiting cases". In this sense, it is difficult to introduce small parameters for liquids, and the water density is not such a small parameter.

It is interesting to note that Landau made many of his outstanding work in Ukraine, being a Head of the Theoretical Physics Department at the Kharkov Institute of Physics and Technology. Here, in 1934 at the age of 26, he became a Doctor of Physical and Mathematical Sciences, and a year later received the title of Professor. Thus, the theoretical physics in Ukraine (and not only in Ukraine, and not only the theoretical physics) has received a tremendous impact for its further development, thanks to the Kharkov period of Landau scientific activities.

Unfortunately, the great physicist died very early-at the age of 60, in April 1968. One may say, paraphrasing one of our bards of that time: "60 is the time of achievements! 60 is the age of the tops!…60 seems like a lot, 60 is still not enough!".

We are sure that L. D. Landau, who received the Nobel Prize on physics in November 1962 for his outstanding work on superfluidity of quantum liquids, or more precisely, "for his pioneering theories for condensed matter, especially liquid helium", could make much more enlightening discoveries, including the field of classical liquids, did not be that fatal car accident on January 7, 1962.

In more than half a century since that time, the physics of liquids has leaped forward. It is sufficient to list the main directions of development of these advanced knowledge areas: nanophysics of liquid systems, medical applications of liquids; water and aqueous solutions in normal and metastable state; ionic and ionic-electronic liquids; magnetic liquid systems; phase transitions and critical phenomena; surface phenomena and liquids in confined geometry; quantum liquids; radiation physics of liquids; etc.

All these areas were presented at the 7th International Conference "Physics of Liquid Matter: Modern Problems" (PLMMP-2016) which was held during May 27–31, 2016, in Kyiv, Ukraine. The PLMMP-2016 International Conference was organized by the Taras Shevchenko National University of Kyiv and Bogolyubov Institute for Theoretical Physics of the National Academy of Sciences of Ukraine. The scientific program of the conference comprised invited lectures, oral presentations, and posters contributed by hundreds of scientists from many countries all over the world (Austria, Brazil, France, Germany, Great Britain, Hungary, Italy, Poland, Portugal, Romania, Russia, Slovakia, Turkey, Ukraine, and United States of America).

Of course, the realization of the PLMMP-2016 International Conference is an important event in the scientific life of Ukraine, whose role cannot be overestimated. After all, the state of science and education largely determines the economic independence of any country and its ability to provide adequate answers to the challenges of modern civilization processes.

The book "Modern Problems of Molecular Physics: Selected Reviews" represents the collection of selected plenary and invited lectures of the PLMMP-2016 Conference and is aimed at elucidation the most important and modern aspects of the molecular physics, condensed and soft matter physics. The unification of experimental, theoretical, and computational methods allow to receive significant results in such four directions: (a) *Liquid Systems with Nanoparticles*, (b) *Ionic and Ionic-Electronic Liquids*, (c) *Magnetic Liquid Systems*, and (d) *Phase Transitions and Critical Phenomena*. This book is written for the scientific researchers as well as for teachers, engineers, students, and all those readers interested in modern problems of the physical sciences.

On behalf of the Organizing Committee of the PLMMP-2016 Conference and editors of the book "Modern Problems of Molecular Physics: Selected Reviews", we would like to thank all the plenary and invited speakers as well as all the participants for their valuable contributions and brainstorming discussions, the International Advisory Board and Local Organizing Committee for assistance in

organizing and realization the scientific program of the PLMMP-2016 Conference, and the Springer International Publishing AG Switzerland for helping to organize the publication of the book “Modern Problems of Molecular Physics: Selected Reviews” in Springer Proceedings in Physics.

Kyiv, Ukraine

Leonid A. Bulavin
Alexander V. Chalyi

Contents

Contributors

L. Almasy Neutron Spectroscopy Department, Wigner Research Centre for Physics, Budapest, Hungary; State Key Laboratory Cultivation Base for Nonmetal Composites and Functional Materials, South-West University of Science and Technology, Mianyang, China

Sergey Artemenko Institute of Refrigeration, Cryotechnologies, and Eco-Power Engineering, Odessa National Academy of Food Technologies, Odessa, Ukraine

Viktor Artemyuk G.V. Kurdymov Institute for Metal Physics of the NAS of Ukraine, Kiev, Ukraine

M. V. Avdeev Frank Laboratory of Neutron Physics, Joint Institute for Nuclear Research, Dubna, Moscow Reg., Russia

Lucia Balejcikova Institute of Experimental Physics SAS, Košice, Slovakia

Leonid A. Bulavin Faculty of Physics, Taras Shevchenko National University of Kyiv, Kiev, Ukraine

Philip J. Camp School of Chemistry, University of Edinburgh, David Brewster Road, Edinburgh, Scotland; Institute of Natural Sciences and Mathematics, Ural Federal University, Ekaterinburg, Russia

Jean-Marie Catala Institut Charles Sadron (CNRS-UdS), Strasbourg, France

Vitaly V. Chaban Instituto de Ciência e Tecnologia, Universidade Federal de São Paulo, São José dos Campos, SP, Brazil

Alexander V. Chalyi Department of Medical and Biological Physics, Bogomolets National Medical University, Kiev, Ukraine

Oksana Dobush Institute for Condensed Matter Physics of the National Academy of Sciences of Ukraine, Lviv, Ukraine

Maxim Evstigneev Belgorod State University, Belgorod, Russia

A. V. Feoktystov Jülich Centre for Neutron Science (JCNS), Heinz Maier-Leibnitz Zentrum (MLZ), Garching, Germany

I. V. Gapon Frank Laboratory of Neutron Physics, Joint Institute for Nuclear Research, Dubna, Moscow Reg., Russia; Faculty of Physics, Taras Shevchenko National University of Kyiv, Kiev, Ukraine

V. M. Garamus Helmholtz-Zentrum Geesthacht: Centre for Materials and Coastal Research, Geesthacht, Germany

Veronika Gdovinova Institute of Experimental Physics SAS, Košice, Slovakia

Abdenacer Idrissi University of Lille, Science and Technology, LASIR (UMR CNRS A8516), Villeneuve d'Ascq Cedex, France

Giancarlo Jug Dipartimento di Scienza ed Alta Tecnologia and To.Sca.Lab, Università dell'Insubria, Como, Italy; INFN – Sezione di Pavia, Pavia, Italy

Oleg N. Kalugin Department of Inorganic Chemistry, V. N. Karazin Kharkiv National University, Kharkiv, Ukraine

Love Karbivska G.V. Kurdymov Institute for Metal Physics of the NAS of Ukraine, Kiev, Ukraine

Volodymyr Karbivskyy G.V. Kurdymov Institute for Metal Physics of the NAS of Ukraine, Kiev, Ukraine

Victoria Karnaukh Faculty of Engineering, Department of Food Engineering, Akdeniz University, Antalya, Turkey

Lukasz Konczak Jerzy Haber Institute of Catalysis and Surface Chemistry, Polish Academy of Sciences, Krakow, Poland

Martina Koneracka Institute of Experimental Physics SAS, Košice, Slovakia

Peter Kopcansky Institute of Experimental Physics SAS, Košice, Slovakia

Volodymyr A. Koverga University of Lille, Science and Technology, LASIR (UMR CNRS A8516), Villeneuve d'Ascq Cedex, France

Yuri Kozitsky Maria Curie-Skłodowska University, Lublin, Poland

Mykhailo Kozlovskii Institute for Condensed Matter Physics of the National Academy of Sciences of Ukraine, Lviv, Ukraine

Martina Kubovcikova Institute of Experimental Physics SAS, Košice, Slovakia

Nataliya Kutsevol National Taras Shevchenko University of Kyiv, Kiev, Ukraine

Olena Kyzyma Faculty of Physics, Taras Shevchenko National University of Kyiv, Kyiv, Ukraine; Joint Institute for Nuclear Research, Dubna, Moscow reg., Russia

Bogdan A. Marekha Normandie University, Caen, France

Vladimir V. Matveev St. Petersburg State University, Saint Petersburg, Russia

Victor Mazur Institute of Refrigeration, Cryotechnologies, and Eco-Power Engineering, Odessa National Academy of Food Technologies, Odessa, Ukraine

Matus Molcan Institute of Experimental Physics SAS, Košice, Slovakia

A. V. Nagornyi Frank Laboratory of Neutron Physics, Joint Institute for Nuclear Research, Joliot-Curie 6, 141980 Dubna, Moscow Reg., Russia; Faculty of Physics, Taras Shevchenko National University of Kyiv, Kiev, Ukraine

Tomasz Panczyk Jerzy Haber Institute of Catalysis and Surface Chemistry, Polish Academy of Sciences, Krakow, Poland

V. I. Petrenko Frank Laboratory of Neutron Physics, Joint Institute for Nuclear Research, Dubna, Moscow Reg., Russia; Faculty of Physics, Taras Shevchenko National University of Kyiv, Kiev, Ukraine

Yuriy Plevachuk Department of Metal Physics, Ivan Franko National University of Lviv, Lviv, Ukraine

Yuriy Prylutskyy ESC "Institute of Biology and Medicine", Department of Biophysics and Medical Informatics, Taras Shevchenko National University of Kyiv, Kyiv, Ukraine

Michal Rajnak Institute of Experimental Physics SAS, Košice, Slovakia; Faculty of Electrical Engineering and Informatics, Technical University of Košice, Košice, Slovakia

Michel Rawiso Institut Charles Sadron (CNRS-UdS), Strasbourg, France

Anastasiia V. Riabchunova Department of Inorganic Chemistry, V. N. Karazin Kharkiv National University, Kharkiv, Ukraine

Uwe Ritter Institute of Chemistry and Biotechnology, Technical University of Ilmenau, Ilmenau, Germany

Peter Scharff Institute of Chemistry and Biotechnology, Technical University of Ilmenau, Ilmenau, Germany

Vasyl Sklyarchuk Department of Metal Physics, Ivan Franko National University of Lviv, Lviv, Ukraine

Georgiy Smolyakov Institut Charles Sadron (CNRS-UdS), Strasbourg, France

Milan Timko Institute of Experimental Physics SAS, Košice, Slovakia

Natalia Tomasovicova Institute of Experimental Physics SAS, Košice, Slovakia

Konstantin V. Tyutyukin St. Petersburg State University, Saint Petersburg, Russia

L. Vekas Center for Fundamental and Advanced Technical Research, Romanian Academy-Timisoara Branch, Timisoara, Romania

Iuliia V. Voroshylova CIQ(UP)/REQUIMTE@LAQV, Departamento de Química e Bioquímica, Faculdade de Ciências, Universidade do Porto, Porto, Portugal

Pawel Wolski Jerzy Haber Institute of Catalysis and Surface Chemistry, Polish Academy of Sciences, Krakow, Poland

Andriy Yakymovych Department of Metal Physics, Ivan Franko National University of Lviv, Lviv, Ukraine; Department of Inorganic Chemistry—Functional Materials, Faculty of Chemistry, University of Vienna, Vienna, Austria

Vlasta Zavisova Institute of Experimental Physics SAS, Košice, Slovakia

Part I
Liquid Systems with Nanoparticles

Chapter 1
Self-Organization of Pristine C_{60} Fullerene and its Complexes with Chemotherapy Drugs in Aqueous Solution as Promising Anticancer Agents

Leonid A. Bulavin, Yuriy Prylutskyy, Olena Kyzyma, Maxim Evstigneev, Uwe Ritter and Peter Scharff

Abstract The self-organization of pristine C_{60} fullerene and its complexation with chemotherapy drugs (in particular, doxorubicin, cisplatin and landomycin A) in aqueous solution were reviewed as a possible key stage of the mechanism of the in vivo and in vitro biological synergy, observed when these drugs are administered along with C_{60} fullerene. The results of application of various physico-chemical methods have been analyzed enabling to get insight into the nature of forces

L. A. Bulavin · O. Kyzyma
Faculty of Physics, Taras Shevchenko National University of Kyiv,
Volodymyrska Str., 64, Kyiv 01601, Ukraine
e-mail: bulavin221@gmail.com

O. Kyzyma
e-mail: alyona_kizima@mail.ru

Y. Prylutskyy (✉)
ESC "Institute of Biology and Medicine", Department of Biophysics
and Medical Informatics, Taras Shevchenko National University of Kyiv,
Volodymyrska Str., 64, Kyiv 01601, Ukraine
e-mail: prylut@ukr.net

O. Kyzyma
Joint Institute for Nuclear Research, 6 Joliot-Curie Str., 141980 Dubna,
Moscow reg., Russia

M. Evstigneev
Belgorod State University, 85 Pobedy Str., 308015 Belgorod, Russia
e-mail: max_evstigneev@mail.ru

U. Ritter · P. Scharff
Institute of Chemistry and Biotechnology, Technical University of Ilmenau,
25 Weimarer Str., 98693 Ilmenau, Germany
e-mail: uwe.ritter@tu-ilmenau.de

P. Scharff
e-mail: peter.scharff@tu-ilmenau.de

L. A. Bulavin and A. V. Chalyi (eds.), *Modern Problems of Molecular Physics*,
Springer Proceedings in Physics 197, https://doi.org/10.1007/978-3-319-61109-9_1

stabilizing complexes of C_{60} fullerene with these drugs. A physico-chemical mechanism has been proposed allowing, at least in part, to explain the C_{60}-drug biological interaction.

1.1 Introduction

C_{60} fullerenes have been intensively investigated in the last decades mainly because of the vast range of their potential applications in biomedicine [1, 2]. Due to its nanometer size the pristine C_{60} fullerenes are able to interact with biomolecules and penetrate through the cell membrane [3–5]. They exhibit antioxidant properties and, being non-toxic (at low concentration at least) [6–10], exert specific health effects (e.g. suppress the growth of malignant tumors [11, 12]) and display biological synergy with antitumor drugs [13–15]. Although these molecules have extremely low water solubility, they form stable colloid solutions containing individual C_{60} fullerenes as well as C_{60} fullerene aggregates (clusters) in water, when subjected to extended mixing, sonication or solvent exchange [16, 17]. To understand behavior of C_{60} fullerene in the biological medium (at the levels of cell, tissue and organ) and its interaction with drugs, it is necessary to know exactly its concentration in water (dose effect), distribution in size and shape (size effect). Because the biomedical effects of the C_{60} fullerene nanoparticles directly depend on these properties [18, 19], their knowledge will enable understanding of 'which form of C_{60} fullerene is bioactive, namely a single molecule or its cluster?' and 'how this molecule interact with other drugs in biological media?'

In this chapter we shall briefly review the recent advances in physico-chemical characterization of pristine C_{60} fullerene and its interaction with antitumor drugs in aqueous solutions.

1.2 Self-Organization of C_{60} Fullerene Particles in Aqueous Solution

Investigations of the behavior of pristine C_{60} fullerene particles in aqueous solution have been undertaking since the end of 90-ies when the method of preparation of stable water colloid solutions had become routinely available [17, 20, 21]. By that time much had already been known on the properties of C_{60} fullerene in organic solvents, which had, in part, facilitated analogous studies in aqueous solutions.

To date, the C_{60} fullerene is considered as a colloidal particle due to the fact that its diameter equals to 10 Å. This conclusion originates from traditional point of view that the 10 Å border corresponds to the lower border of the colloidal range of dispersity, and the range of true solutions is under this limit [22]. Thus, aqueous solutions of any C_{60} fullerenes must feature properties of colloidal systems,

which contain associates of solvated C_{60} fullerenes of different size. Theoretical analysis of possible hydrated $(C_{60})_N$ clusters had shown, that the smallest stable C_{60} fullerene cluster (I_h symmetry group) consists of 13 C_{60} molecules [23, 24]. Its diameter is 3.36 nm (accounting for a molecular diameter of the water molecule), which is in excellent agreement with the scanning tunneling microscopy data [25]. More extended analysis revealed that cluster diameters regularly rise within the range from 3.4 to 36 nm, viz. 3.4, 7.1, 10.9, 14.5, 18.1, 21.8, 25.4, 28.8, 32.4, and 36.0 nm [25], i.e. each following particle is larger than the preceding one by 3.4–3.8 nm. Hence, it is considered that this row of C_{60} fullerene nanoparticles should be formed of hydrated $(C_{60})_{13}$ clusters. Thus, further investigation of the C_{60} fullerene aqueous solution (C_{60}FAS) had been split on characterization of the clusters' structure and morphology, and understanding the mechanism of cluster formation.

1.2.1 Characterization of the C_{60} Fullerene Aqueous Solution

A variety of physico-chemical methods has been applied in order to understand the specificity of C_{60} fullerene cluster formation. Characterization of C_{60} fullerene particles in aqueous solutions has been accomplished by means of UV-Vis spectroscopy [23, 24, 26–29], electron and tunneling microscopy [26, 30–35], atomic-force microscopy (AFM) [26, 36], zeta-potential [26, 32, 37, 38], dynamic light scattering (DLS) [26, 30, 32–34, 39], FTIR/Raman spectroscopy [27–29, 35, 36], small angle neutron scattering (SANS) [16, 29, 36, 40] and some other methods.

The most direct and readily accessible UV-Vis spectroscopy evidenced the existence of three most intense broad UV absorption bands with maxima at 208, 265 and 347 nm and generally resembles that in organic solvents (Fig. 1.1a) [26, 27]. The assignment of these bands to particular electron transitions, and the computation of the corresponding electronic parameters have been done [23]. The common feature of the UV-Vis spectra of C_{60}FAS is the light scattering, most evidently seen on dilution and affecting the value of the absorption.

The composition of C_{60}FAS was typically monitored using AFM and tunneling/electron microscopy techniques [26, 30–36]. The typical AFM picture is given in Fig. 1.1c; the similar pictures have been reported during the past 10 years by different research groups. The picture demonstrates randomly arranged individual C_{60} molecules with diameter ~0.7 nm and their bulk sphere-like aggregates with a height of 2–50 nm. Interestingly, some individual C_{60} fullerene aggregates with a height of ~100 nm were also reported in the probe microscopy images, indicating a polydisperse nature of C_{60}FAS, including either monomers or aggregates having diameters ranging from several to hundreds of nanometers.

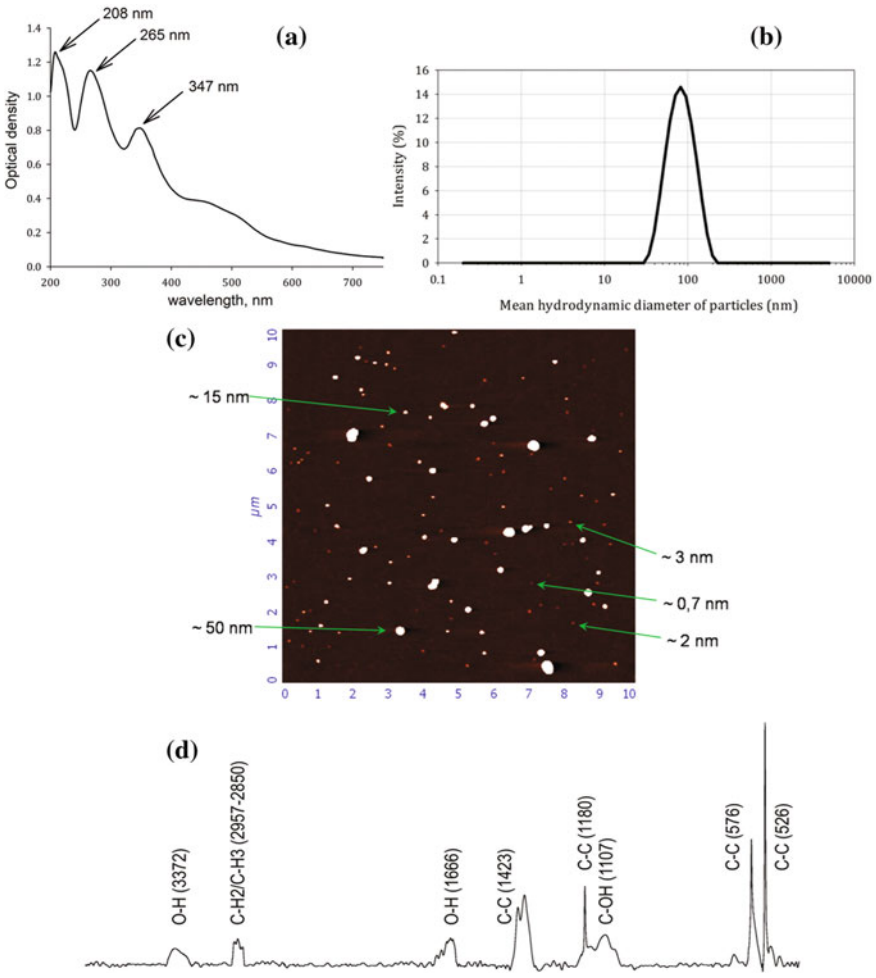

Fig. 1.1 Examples of experimental data measured for C_{60}FAS: UV-Vis spectrum (**a**), DLS spectrum (**b**), AFM image (**c**), IR spectrum (**d**). Redrawn from [26, 36, 54]

The results from microscopy images have also been confirmed by DLS and SANS data [16, 26, 29, 30, 32–34, 36, 39, 40]. The wide distribution of hydrodynamic dimensions of C_{60} fullerene particles by intensity with *z*-average ~70–120 nm (Fig. 1.1b) most directly evidences the polydispersity, independently supported by SANS. The gyration radii R_g = 15…20 nm calculated from the latter method well agrees with the dimensions of the particles seen in AFM. Importantly, the existence of 'slow' aggregation (in the scale of months) of C_{60} fullerenes, resulting in increase of R_g was reported in aqueous solution similar to

that established before in organic solvents [32, 33, 39, 41]. However, no significant alteration of the aggregate structures and properties of polydispersity were noted. Moreover, experimental data indicate that the structural and morphological features of polydisperse C_{60} fullerene aggregates present in aqueous solution remain essentially similar for different methods of C_{60}FAS preparation as well [36].

The magnitude of the zeta-potential, which is related to the stability of colloid dispersions, spans in relatively wide range from −9 mV up to −38 mV [21, 26, 37, 38] and evidences the presence of negative charge on the surface of C_{60} molecule in solution. A high negative charge of colloid clusters (or, more strictly, the electrostatic repulsion between the negatively charged clusters) plays significant role in the stabilization of C_{60}FAS (i.e. it disfavors the aggregation and makes the solution electrically stable).

The presence of negative charge on C_{60} fullerene surface is a generally accepted fact and is considered to be the key, but not the sole factor of C_{60} fullerene solubility in aqueous solution. The formation of the ordered, H-bonded and sphere-like hydrated shells around fullerene's surface, is another important issue extensively discussed over the past decade [27, 29, 30, 35, 36, 42–46]. However, recent FTIR spectroscopy data suggested that there is one more factor which should also be considered [35, 36]. The FTIR spectrum of C_{60}FAS (Fig. 1.1d) displays the typical pattern of peaks which could be expectedly assigned to C-C vibrational modes of C_{60} molecule. However, additional peaks were reported independent of the method of C_{60}FAS preparation and corresponded to C-O stretching. It strongly suggests that C_{60} fullerene cage is hydroxylated and hydroxyls forming alcohol functional groups exist in the structure of C_{60} fullerene in water. Hence the primary mechanism of C_{60} fullerene solubilization in water could be the attachment of the OH-groups to C_{60} fullerene carbons [35, 36] which explains why the lone C_{60} molecules and their clusters exist at equilibrium in solution for quite a long time. It also explains the irreversible character of the adsorption/desorption isotherms [30], the minimal extraction of C_{60} fullerene from water-colloid solutions by toluene [21], and the ability of C_{60} fullerenes from aqueous solution to hold water molecules even in vacuum [27]. The covalent attachment of the OH-groups does not exclude the possibility of electron transfer from water molecules to C_{60} fullerene enabling to explain the negative charge of C_{60} fullerene particles. It follows that the previous model of stabilization of hydrated C_{60} fullerene by water molecules joined together by H-bonding network [27, 29] needs to be revisited with mandatory account for the available results of molecular dynamics simulations of hydrated C_{60} fullerenes [43–46]. The latter reports weakening and breakage of the H-bonds between water molecules in immediate vicinity of the C_{60} fullerene surface and the overall dynamic character of the hydration shell around C_{60} fullerene particles in water.

1.2.2 Aggregation of the C_{60} Fullerenes in Aqueous Solution

So far the effect of cluster formation (or aggregation) has been extensively studied in terms of the kinetics of aggregation and the equilibrium distribution of C_{60} fullerene clusters [7, 16, 17, 21, 23–36, 39–41]. It has been recently established that the aggregates of pristine C_{60} fullerenes provide an excellent template for formation of highly ordered inclusion complexes with other molecules, resulting in amplified physico-chemical or biological properties [47, 48]. Apart from the basic physico-chemical interest to the aggregation process, it was recently found that the in vitro toxicity of C_{60} fullerene is correlated with its ability to undergo aggregation [49] and specifically the aggregated forms of C_{60} fullerene may effectively bind with biopolymers [50]. Therefore the C_{60} fullerene aggregation is considered now to be of general interest.

It has long been noted that under the dilution and simultaneous light mechanical shaking of C_{60}FAS, the large clusters can dissociate into the small ones, similar to that observed before in C_{60} fullerene benzene solution. It has also been established that the C_{60} fullerene solutions undergo 'fast' and 'slow' kinetics of cluster formation [23, 32, 33, 41]. The former is considered to be diffusion-limited and the latter is reaction-limited. Under first approximation the 'fast' mode occurs at typical diffusion timescale and thereby resembles equilibrium aggregation process well known for small molecules in solution [51]. It still remains relatively poorly investigated. The 'slow' mode occurs in the timescale of days and months, and has been extensively reviewed [41, 52]. Below we shall focus on thermodynamics of the equilibrium aggregation of C_{60} fullerene nanoparticles.

Surprisingly, determination of thermodynamical parameters of aggregation, such as equilibrium aggregation constant, or enthalpy/entropy/Gibbs free energy changes have been accomplished in just a few works [43, 44, 53–55]. Possible reasons for this include an incomplete understanding of the microscopic picture of C_{60} fullerene cluster formation in solution, and, as a consequence, difficulties in building a theoretical model of C_{60} fullerene aggregation. For example, a very complex interplay between the van der Waals, electrostatic and hydrophobic interactions on C_{60} fullerene aggregation, which presumably does not follow classical hydrophobic effect, was shown [42–44]. It points out that the overall thermodynamic picture of C_{60} fullerene aggregation in aqueous solution deviates from classical aggregation of small molecules, which makes this issue still a vacant niche for further research studies.

Presumably the first attempt to measure equilibrium C_{60} fullerene aggregation constant was accomplished in [54] by means of titrating the C_{60} fullerene aqueous solution and recording the intensity-averaged distributions of particles present in solution in DLS experiment. These data allow computing the mean hydrodynamic diameter, d_z (z-average), and translational diffusion coefficient, D, of light scattering particles. The corresponding experimental dependence of d_z on the C_{60} fullerene concentration, C_0 / r (where r is the dilution factor), is given in Fig. 1.2.

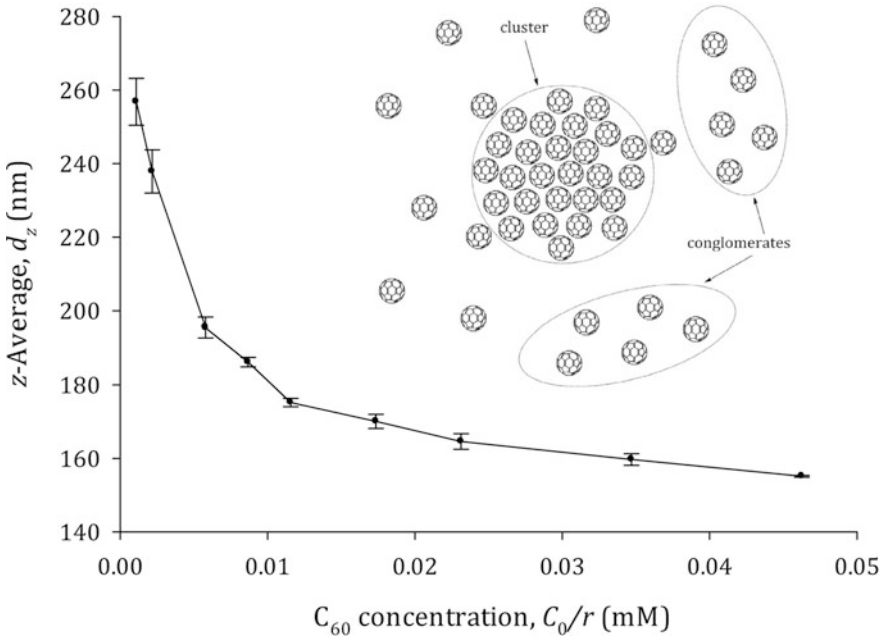

Fig. 1.2 Experimental dependence of z-average on C_{60} fullerene concentration. Redrawn from [54]

Currently the accepted position on the aggregation of small molecules in diluted aqueous solutions suggests that on increasing the concentration of the solute, the translational diffusion coefficient must decrease as a result of an increase in the aggregates' dimensions [56, 57]. Qualitatively, a similar view exists with respect to the aggregation of C_{60} fullerene as well, supported by theoretical computation of the dependence of D on C_{60} fullerene concentration in toluene [52]. However, the dependence $d_z(C_0/r)$ in Fig. 1.2 obtained using standard methods of C_{60}FAS preparation demonstrates the reverse behavior: increasing the solute concentration results in a decrease in the value of d_z. Unfortunately, direct comparison of these results with existing literature data is not possible, because these articles are restricted to dealing with measurements of D (or d_z) of C_{60} fullerene in solution at a single concentration point in each case (e.g. [32, 50]). However, analysis of literature data associated with small molecule aggregation suggests that on reaching micellar concentrations, the concentration dependence of the directly measured translational diffusion coefficient (e.g. by DLS or similar valid method) goes into reverse [58, 59]. This result is commonly interpreted in terms of the direct interaction of micelles with each other in solution due to non-covalent forces, an effect that has been known for some time [58, 59]. The micellar interaction acts as an addition to Brownian motion and, consequently, results in elevation of the diffusion coefficient on raising the solute concentration. Taking into account the polydisperse

nature of C_{60}FAS and the existence of C_{60} fullerene clusters with diameters in the magnitude range 10–100 nm, it was suggested that the reverse dependence of the $d_z(C_0/r)$ curve in Fig. 1.2 is a consequence of the interaction effect for $(C_{60})_n$ clusters [54]. Hence, the shape of the titration curve in Fig. 1.2 is governed by two opposite tendencies, viz. the aggregation leading to increase of d_z, and interaction of clusters leading to decrease of d_z.

Based on the DLS titration experiment a physical model of the C_{60} fullerene aggregation was suggested [54] (the so-called 'up-scaled model'). According to this model the aggregation occurs as a simultaneous binding of large number of small C_{60} fullerene particles or monomers (referred to as 'conglomerates', see Fig. 1.2) with large C_{60} fullerene clusters (nucleus of the cluster, considered not undergoing dissociation onto smaller ones). As a consequence of this process, the equilibrium distribution of C_{60} fullerene particles by dimension is formed, which can be quantified in terms of equilibrium aggregation constant K_F (or Gibbs free energy change, ΔG_F). The resultant equation enabling to calculate the experimental titration curve $d_z(C_0/r)$ in Fig. 1.2 is given as [54].

$$d_z = \frac{d_0}{1 + A' \frac{C'_{M0}}{r}} \cdot \frac{\left[1 + (B-1)BK_F C'_{R1}\right]^2 + B^3 K_F C'_{R1}}{\left(1 - BK_F C'_{R1}\right)^3 \sum_{i=0}^{\infty} (1+Bi)^{5/3} \left(BK_F C'_{R1}\right)^i}, \tag{1.1}$$

where

$$C'_{R1} = \frac{r + C'_{M0}BK_F + (C_0 - C'_{M0})K_F - \sqrt{\left(r + C'_{M0}BK_F + (C_0 - C'_{M0})K_F\right)^2 - 4rK_F(C_0 - C'_{M0})}}{2rBK_F},$$

C'_{M0}, A', K_F, B, d_0 are the search parameters, obtained by means of fitting the experimental curve in Fig. 1.2 with (1.1).

The reported value of the aggregation constant equals to $K_F = 56000\ \mathrm{M}^{-1}$ [54], well matching the theoretically calculated Gibbs free energy change in [53].

The titration experiment reviewed above and resulted in determination of K_F had been further complemented with estimation of enthalpy and entropy change associated with the aggregation process [55]. Direct calorimetric measurement of the heat effect on dilution and temperature dependence of z-average in DLS experiment had evidenced nearly zero enthalpy change. A final conclusion was made stating purely entropic character of the C_{60} fullerene aggregation. The main contribution to ΔG_F is considered to be due to hydrophobic interaction, i.e. liberation of water molecules weakly bound to C_{60} fullerene particles on cluster formation (i.e. those molecules belonging to distant hydration shells of the C_{60} fullerene particle). Importantly, in this process the first hydration shell surrounding C_{60} fullerenes remains essentially unchanged resulting in a contact distance between the surfaces of the interacting C_{60} fullerene particles larger than observed for typical aromatic-aromatic stacking (ca. 0.5 nm). Theoretical decomposition of ΔG_F onto

energetic contribution from various physical factors had shown that the net van der Waals and electrostatic terms appear to be relatively small due to the compensatory nature of the intermolecular interaction and the interaction with solvent on complex formation [54], additionally confirming the entropic nature of C_{60} fullerene aggregation in aqueous solution.

1.3 Self-Organization of C_{60} Fullerene-Antitumor Drug Mixtures

So far the possibility of modification of biological and/or physico-chemical properties of C_{60} fullerene or drug was mainly considered in terms of covalent conjugation of the drug molecules with C_{60} fullerene [47]. As a consequence, a series of C_{60}-drug conjugates were reported possessing improved properties [60, 61]. On the other hand, the presence in the structure of C_{60} molecule of aromatic surface composed of conjugated carbon rings suggests the possibility of its effective interactions via π-stacking with aromatic moieties of proteins, nucleic acid bases, aromatic vitamins, antibiotics and other compounds which may be present in a biosystem. Hence, the non-covalent complexation of C_{60} fullerenes with bio-receptors and aromatic drugs may contribute to some extent to the observed biological effects at the cellular and organism levels. Indirect justification of this hypothesis may come from the well-known fact that some cellular effects of the action of aromatic biologically active compounds may be interpreted in terms of their complexation in physiological medium [51]. During the past few years two sets of reports appeared evidencing a strong biological interaction in vitro and in vivo between C_{60} fullerene and the aromatic antitumor drugs, doxorubicin (Dox) [13–15, 62–64] and cisplatin (Cis) [65]. The peculiarity of this interaction was the following: (i) the most pronounced effect was observed during simultaneous administration of the drugs and C_{60} fullerene, (ii) the physico-chemical interaction of the drug with C_{60} fullerene is non-covalent, (iii) preliminary indices of the correlation of the in vitro biological effect with equilibrium constant of complexation of C_{60} fullerene with aromatic drug molecules were noted [64]. Thus the knowledge of how C_{60} molecules interact with aromatic drugs is important for understanding the mechanism of medico-biological action of C_{60} fullerenes.

Currently available data on the structure and thermodynamics of the interaction between C_{60} fullerenes and aromatic molecules are scarce and limited to systems mainly studied in non-polar solutions (see [66] and references therein) and several systems studied in aqueous solution [13, 62, 65–70]. Below we shall briefly review the main results of structural and thermodynamical analysis of the C_{60} fullerene interaction with Dox, Cis and novel angucycline antibiotic landomycin A (LA) [71] as the systems which have been most extensively investigated to date as compared to others.

1.3.1 C_{60} Fullerene Complexation with Doxorubicin

Antitumor antibiotic Dox belongs to the group of the most effective and extensively used drugs in chemotherapy of cancer. The principal limitation for its use is relatively high side toxicity, creating a long-standing challenge for generations of researchers attempting to minimize this drawback. As discussed above C_{60} fullerene was demonstrated to improve the medico-biological effect of Dox in vivo and in vitro making this drugs' combination of potential interest for clinical studies.

A range of various physico-chemical methods was applied in order to detect the complexation between C_{60} fullerene and antibiotic Dox [13, 62, 66, 68, 69]. In neutral solution conditions the Dox molecule bears positive charge, whereas the C_{60} fullerene is negatively charged.

The AFM investigation of the C_{60}-Dox mixture in low concentration range in non-salted aqueous solution evidenced the formation of new island-type structures (Fig. 1.3e), which were assigned to the complexes between the C_{60} and Dox molecules [68]. Similar situation was also reported in physiological solution, although in this case the interpretation of the results was strongly obscured by the presence of salt crystals [69]. The C_{60}-Dox interaction was also displayed by UV-Vis spectroscopy by hypochromic changes of the absorption maximum (Fig. 1.3a) with a slight bathochromic shift with increasing C_{60} fullerene concentration [13, 66, 68]. Quite expectedly the zeta-potential study of C_{60}-Dox mixture gave a pronounced positive shift of zeta-potential peak evidencing shielding of the C_{60} molecule negative charge and charging of these clusters by complexation of positively-charged Dox with C_{60} fullerene clusters [69]. The remarkable change in translational diffusional motion of Dox molecules on addition of C_{60} fullerene, monitored by diffusion-ordered NMR spectroscopy (DOSY), had also supported the existence of complexation (Fig. 1.3d) [68]. And, finally, the SANS data yielded the distribution function of pair distances, pointing out on the existence of at least two statistically different entities in solution, which are the C_{60} fullerene aggregates and the complexes between the C_{60} and Dox molecules (Fig. 1.3b) [62]. The qualitative experimental data were complemented by calculation of the most probable structure of the C_{60}-Dox complex, from which the maximal filling of the C_{60} fullerene surface by three Dox molecules was noted (Fig. 1.3c) [13, 66].

In contrast to the set of results reviewed above and concluded on the existence of complexation, an additional experimental dataset was reported, which had not directly supported this statement. First, at high C_{60} fullerene concentrations the UV-Vis hypochromic shift changes sign and becomes hypsochromic (Fig. 1.3a) [66]. The isothermal titration calorimetric measurements (ITC) had given nearly zero heat effect of C_{60} fullerene addition to Dox solution, and ^{1}H NMR titration curves had unexpectedly displayed very negligible changes inconsistent with the complexation hypothesis [68].

In addition, NMR DOSY titration curve for translational diffusion coefficient for Dox molecules exhibited reverse behavior (Fig. 1.3d) as compared to that initially

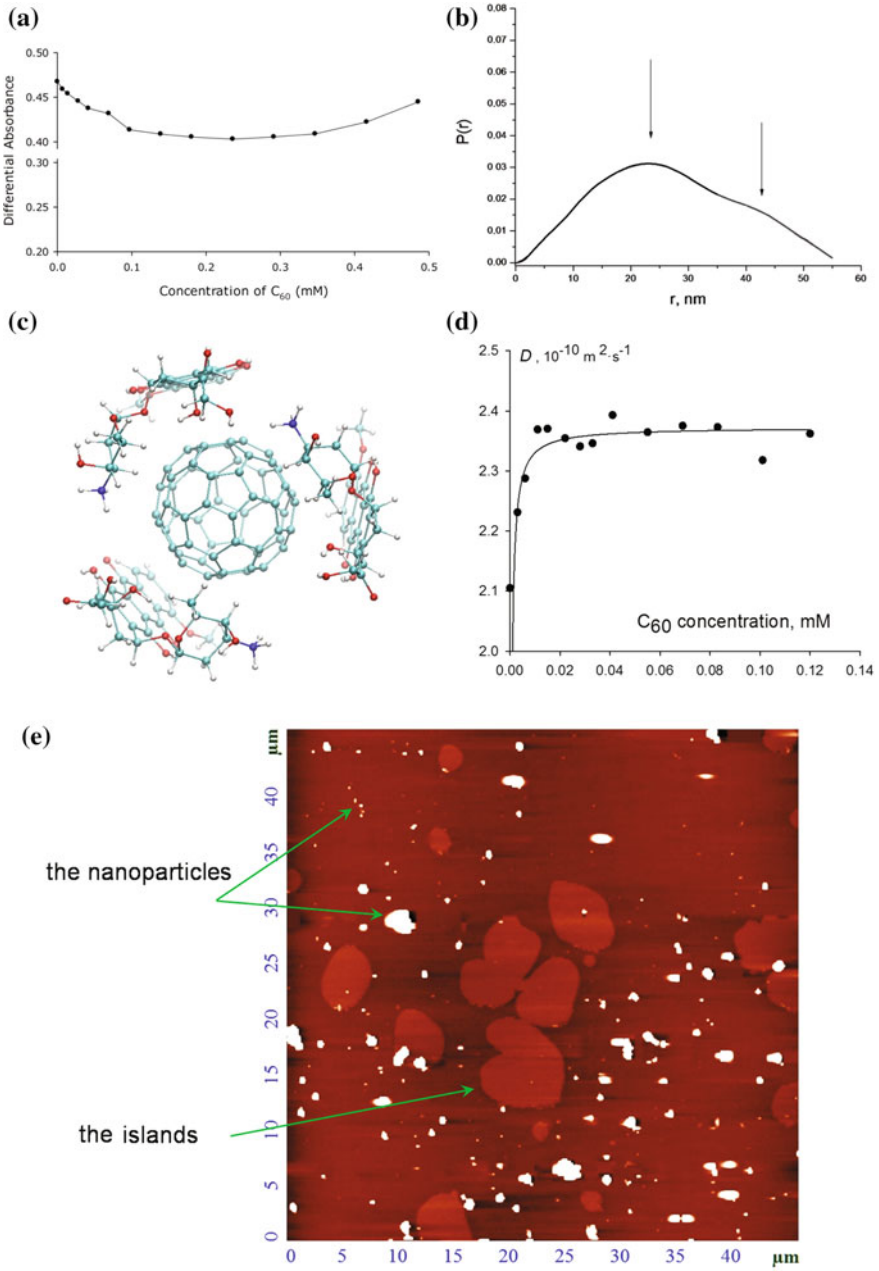

Fig. 1.3 Examples of experimental data measured for C_{60} fullerene-doxorubicin aqueous solution: UV-Vis titration curve (**a**), SANS pair distribution function (**b**), calculated C_{60}-Dox structure (**c**), DOSY translational diffusion coefficient (**d**), AFM image (**e**). Redrawn from [62, 66, 68]

expected (analogous to that discussed above for DLS titration experiment of C_{60} fullerene aqueous solution) [68].

The observed distinguishment of various physico-chemical methods, which directly evidence or demonstrate no signs of C_{60}-Dox complexation, received complete interpretation in [68]. The essence of this view is grounded on two main statements:

(i) the first hydration shell around the C_{60} fullerenes cannot be detached by Dox complexation, resulting in big distance (~0.5 Å) between the surfaces of Dox and C_{60} molecules in the complex. As a consequence, magnetic ^{1}H NMR shielding could be minimal (as evidenced in NMR experiment), and the enthalpic contribution from van der Waals and electrostatic forces could be damped (as evidenced in ITC experiment). Hence, the C_{60}-Dox complexation appears to be entropically-driven, i.e. mainly governed by hydrophobic force due to removal of water molecules from the second and higher-level hydration shells around C_{60} fullerene particles;

(ii) the binding of Dox molecules at moderate and high C_{60} fullerene concentrations mainly occurs by means of adsorption into large C_{60} fullerene clusters, resulting in the effect called 'ligand-induced C_{60} fullerene aggregation'. In brief, positively charged Dox molecules being absorbed by negatively-charged C_{60} fullerene clusters, induce additional cluster growth due to attenuated electrostatic repulsion between C_{60} molecules. It induces additional light scattering (as evidenced in UV-Vis experiment) and results in reverse self-diffusion behavior of Dox molecules (as evidenced in NMR DOSY experiment).

The physical model of C_{60}-Dox interaction outlined in these two statements enabled to build the thermodynamical model of their interaction and compute the corresponding equilibrium hetero-complexation constant, $K_L \approx 6000\ \mathrm{M}^{-1}$ [66]. This value was further used to correlate the relative in vitro biological effect of the action of C_{60}-Dox mixture on human buccal epithelium cells [64] and to compare the C_{60} fullerene hetero-complexation affinity to various drugs [66].

1.3.2 C_{60} Fullerene Complexation with Cisplatin

Aqueous soluble inorganic derivative of bi-valent platinum, i.e. cisplatin (Cis-[Pt(II)$(NH_3)_2Cl_2$]), is currently one of most extensively used chemotherapeutic drug for cancer treatment. Similar to Dox, the principal drawback of Cis is its side toxicity limiting its use in clinical practice. However, the success in improving the medico-biological effect of Dox by mixing it with C_{60} fullerene (see above) had inspired similar studies with C_{60}-Cis mixture, yielding positive outcome in vivo and in vitro [65].

Investigation of possible complexation between C_{60} fullerene and Cis has been carried out using generally similar protocol as that reviewed above for C_{60}-Dox interaction [70]. It should be noted that the direct complexation between C_{60} and Cis molecules should likely be relatively weak as compared with C_{60}-Dox system, because the π-stacking in the former case would be absent. Quite expectedly, the UV-Vis spectra (Fig. 1.4b) gave minor signs of interaction, and ITC demonstrated nearly zero heat effect. In contrast, SANS-derived pair distribution function (Fig. 1.4c) had evidenced the existence of two apparent statistically different entities in aqueous solution, one of which was assigned to the C_{60}-Cis complexes. This finding was partly supported by SEM and DLS studies (Fig. 1.4a, d). The latter investigation demonstrated apparent shift of the distribution of hydrodynamic radii of light scattering particles to higher numbers on addition of Cis to C_{60} fullerene aqueous solution. The ab initio structure of the C_{60}-Cis complex was shown to feature stable energy minimum.

In general, the revealed patterns of physico-chemical interaction of C_{60} fullerene with Cis have been found to resemble much the interaction of C_{60} molecule with antitumor antibiotic Dox, reviewed above. The complexation of Cis with C_{60} fullerene is entropic by origin and is totally driven by hydrophobic interactions. The binding of Cis occurs mainly into large C_{60} fullerene clusters via non-specific adsorption, although the existence of weak 1:1 C_{60}-Cis complexes could not be ruled out.

1.3.3 C_{60} Fullerene Complexation with Landomycin A

LA is a new antitumor antibiotic of angucycline group, possessing high antitumor activity against cancer cells of different origin, which induces early apoptosis in target cells [72–76].

The AFM image displaying the content of aqueous mixture of C_{60} fullerene with LA is given in Fig. 1.5a. The observed aggregates having the height of 2–25 nm may either be related to C_{60} fullerene and LA. The point nano-objects with the height of 0.6–1.8 nm may also be associated with C_{60} fullerene or LA molecules, or their complexes, which seem to be undistinguishable due to similarity of the LA and C_{60} fullerene dimensions.

In contrast to AFM results, the DLS data evidence apparent shift of the z-average on addition of LA to C_{60}FAS (Fig. 1.5b). However, the most interesting is the concomitant change in the shape of distribution of light scattering particles, which becomes narrower and shifts to larger dimensions. This observation means that LA solution affects the distribution of C_{60} fullerene clusters and indirectly points out on the possibility of interaction between the LA and C_{60} molecules. The magnitude of zeta-potential measured for C_{60}-LA mixture had shifted up to −10 mV from the initial value of −22.1 mV measured for C_{60}FAS additionally confirming the possibility of interaction. And, finally, the SANS experiment had also evidenced the changes in scattering signal in the C_{60}-LA mixture. As seen from Fig. 1.5c in small

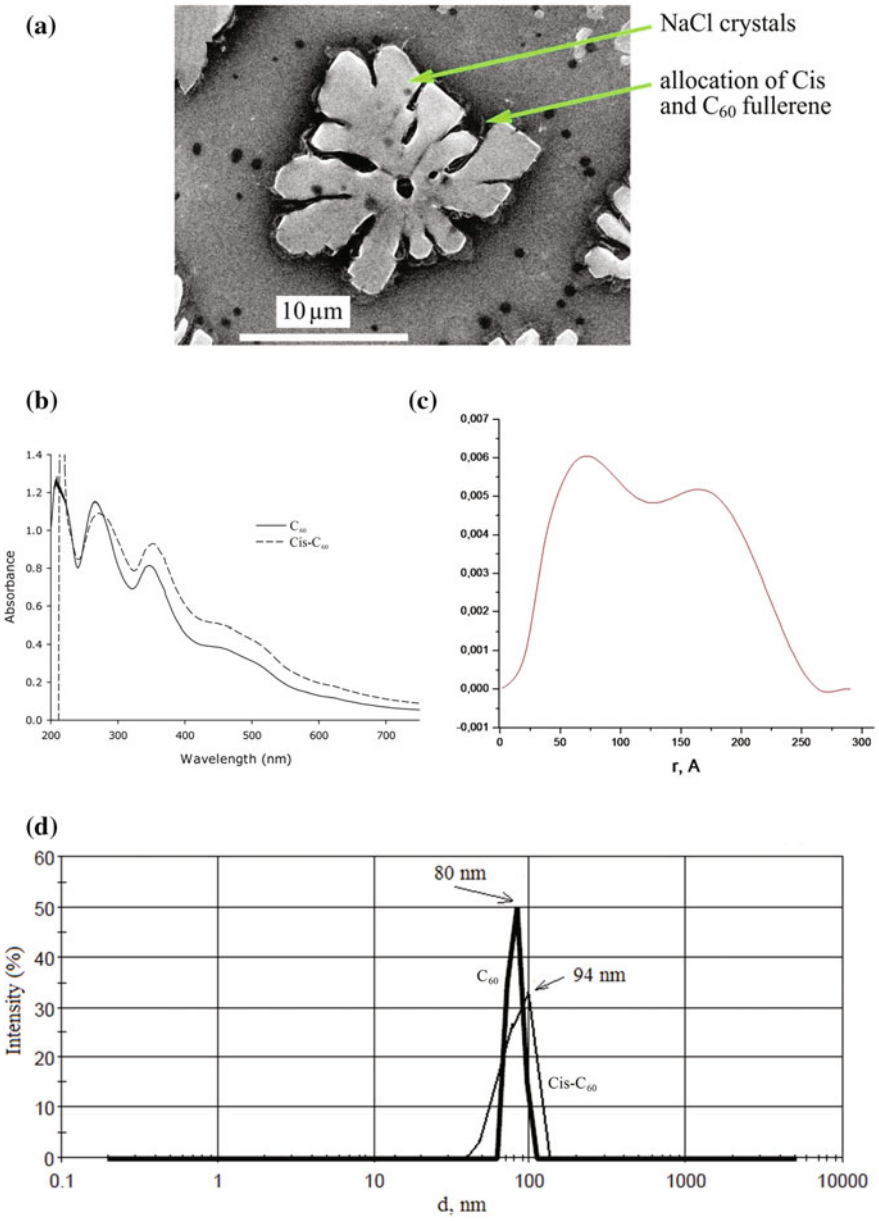

Fig. 1.4 Examples of experimental data measured for C_{60} fullerene-cisplatin aqueous solution: SEM image (**a**), UV-Vis spectrum (**b**), SANS pair distribution function (**c**), DLS spectrum (**d**). Redrawn from [70]

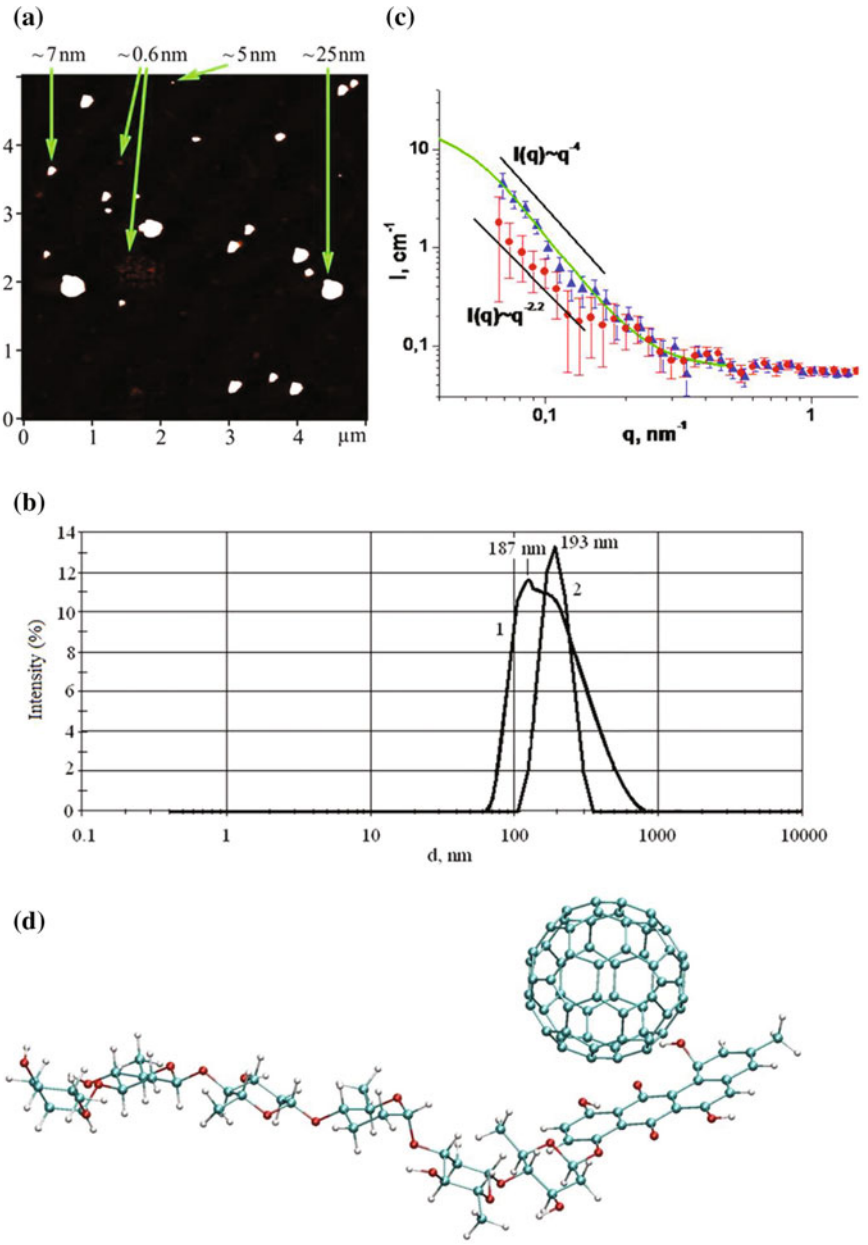

Fig. 1.5 Examples of experimental data measured for C_{60} fullerene-landomycin A aqueous solution: AFM image (**a**), DLS spectrum (**b**), SANS data (C_{60}FAS—triangle, C_{60}-LA mixture—circle) (**c**), calculated C_{60}-LA structure (**d**). Redrawn from [79]

q-region the behavior of scattering intensity changes from $I(q) \sim q^{-4}$ for C_{60}FAS to $I(q) \sim q^{-2.2}$ for the mixture with LA. Such alteration of the scattering curve suggests that compact spherical C_{60} fullerene clusters in aqueous solution are changed to fractal-type organization of the aggregates with mass fractal dimension, $D = 2.2$, in the C_{60} fullerene mixture with drug.

LA is an aromatic compound containing flat benz[a]anthraquinone chromophore. As a consequence the most probable arrangement of the molecules in 1:1 C_{60}-LA complex is the π-stacked structure outlined in Fig. 1.5d. The principal contribution to the stability of such complex is given by the interactions between the drug's chromophore and C_{60} fullerene surface, and the role of deoxyoligosaccharide chain seems to be minor.

1.4 Conclusions

The self-organization of C_{60} fullerene and its complexation with chemotherapy drugs (in particular, doxorubicin (Dox), cisplatin (Cis) and landomycin A (LA)) in aqueous solution were reviewed in this chapter as a possible key stage of the mechanism of the in vivo and in vitro biological synergy, observed when these drugs are administered along with C_{60} fullerene. Although the investigated drugs are very different in terms of chemical structure and properties, their thermodynamic patters of binding with C_{60} fullerene were found to be generally similar. Apart from certain specificities of binding, the complexation was found generally non-specific, entropic by origin and occurring mainly into large C_{60} fullerene clusters, governed by hydrophobic interactions. This physico-chemical mechanism may be further transferred onto biological system, viz. on simultaneous administration the hydrophobic C_{60} fullerene clusters incorporating Cis, Dox or LA molecules protect them from reactive environment when moving in biological fluid. Hence, these clusters may act as a delivery system and elevate the active concentration of the drug which induces biological effect. Such mechanism, at least in part, explains the biological synergy observed experimentally for C_{60}-Cis and C_{60}-Dox mixtures. Apparently, this is a speculative model which requires further investigation and may just be used as a starting hypothesis in further studies of C_{60}-drug biological interactions. On the other hand, the use of C_{60} fullerene as a potential delivery system is extensively discussed now in scientific literature (see for review [47]). The model thus suggested agrees well with the mechanism of entrapment of surface active compounds by C_{60} fullerene clusters [77], and may probably shed light on the mechanism of biological synergy observed on simultaneous administration of fullerenol with Dox [78], which has not received explanation so far.

Acknowledgements This work was, in part, supported by Russian Science Fund (project no. 14-14-00328) and STCU project N6256.

References

1. F. Cataldo, T. Da Ros (eds.), *Medicinal Chemistry and Pharmacological Potential of Fullerenes and Carbon Nanotubes. Series: Carbon Materials: Chemistry and Physics* (Springer, Netherlands, 2008)
2. P. Anilkumar, F. Lu, L. Cao et al., Fullerenes for applications in biology and medicine. Current Med. Chem. **18**, 2045 (2011)
3. V.V. Turov, V.F. Chehun, T.V. Krupskaya et al., Effect of small addition of C_{60} fullerenes on the hydrated properties of nanocomposites based on highly dispersed silica and DNA. Chem. Phys. Lett. **496**, 152 (2010)
4. S. Foley, C. Crowley, M. Smaihi et al., Cellular localisation of a water-soluble fullerene derivative. Biochem. Biophys. Res. Commun. **294**, 116 (2002)
5. S. Prylutska, R. Bilyy, M. Overchuk et al., Water-soluble pristine fullerenes C_{60} increase the specific conductivity and capacity of lipid model membrane and form the channels in cellular plasma membrane. J. Biomed. Nanotechnol. **8**, 522 (2012)
6. S.V. Prylutska, I.I. Grynyuk, O.P. Matyshevska et al., Anti-oxidant properties of C_{60} fullerenes in vitro. Fuller. Nanotub. Carbon Nanostruct. **16**, 698 (2008)
7. G. Andrievsky, V. Klochkov, L. Derevyanchenko, Is the C_{60} fullerene molecule toxic?! Fuller. Nanotub. Carbon Nanostruct. **13**, 363 (2005)
8. N. Levi, R. Hantgan, M. Lively et al., C_{60}-Fullerenes: detection of intracellular photoluminescence and lack of cytotoxic effects. J. Nanobiotechnol. **4**, 14 (2006)
9. S.V. Prylutska, O.P. Matyshevska, A.A. Golub et al., Study of C_{60} fullerenes and C_{60}-containing composites cytotoxicity in vitro. Mater. Sci. Eng. C **27**, 1121 (2007)
10. J. Kolosnjaj, H. Szwarc, F. Moussa, Toxicity studies of fullerenes and derivatives. Adv. Exp. Med. Biol. **620**, 168 (2007)
11. H.J. Johnston, G.R. Hutchison, F.M. Christensen et al., The biological mechanisms and physicochemical characteristics responsible for driving fullerene toxicity. Toxicol. Sci. **114**, 162 (2010)
12. S.V. Prylutska, A.P. Burlaka, Y.I. Prylutskyy et al., Pristine C_{60} fullerenes inhibit the rate of tumor growth and metastasis. Exp. Oncol. **33**, 162 (2011)
13. S.V. Prylutska, A.P. Burlaka, P.P. Klymenko et al., Using water-soluble C_{60} fullerenes in anticancer therapy. Cancer Nanotechnol. **2**, 105 (2011)
14. R.R. Panchuk, S.V. Prylutska, V.V. Chumak et al., Application of C_{60} fullerene-doxorubicin complex for tumor cell treatment *in vitro* and in vivo. J. Biomed. Nanotechnol. **11**, 1139 (2015)
15. S. Prylutska, L. Skivka, G. Didenko et al., Complex of C_{60} fullerene with doxorubicin as a promising agent in antitumor therapy. Nanoscale Res. Lett. **10**, 499 (2015)
16. S.V. Prylutska, V.F. Korolovych, Y.I. Prylutskyy et al., Tumor-inhibitory effect of C_{60} fullerene complex with doxorubicin. Nanomed. Nanobiol. **2**, 49 (2015)
17. M.V. Avdeev, A.A. Khokhryakov, T.V. Tropin et al., Structural features of molecular-colloidal solutions of C_{60} fullerenes in water by small-angle neutron scattering. Langmuir **20**, 4363 (2004)
18. N.O. Mchedlov-Petrossyan, Fullerenes in liquid media: an unsettling intrusion into the solution chemistry. Chem. Rev. **113**, 5149 (2013)
19. Yu. Rud, L. Buchatskyy, Y. Prylutskyy et al., Using C_{60} fullerenes for photodynamic inactivation of mosquito iridescent viruses. J. Enzym. Inhib. Med. Chem. **27**, 614 (2012)
20. Z. Chen, R. Mao, Y. Liu, Fullerenes for cancer diagnosis and therapy: preparation, biological and clinical perspectives. Curr. Drug Metab. **13**, 1035 (2012)
21. G.V. Andrievsky, M.V. Kosevich, O.H. Vovk et al., On the production of an aqueous colloidal solution of fullerenes. J. Chem. Soc., Chem. Commun. **12**, 1281 (1995)
22. S. Deguchi, R.G. Alargova, K. Tsujii, Stable dispersions of fullerenes, C_{60} and C_{70}, in water. Prep. Charact. Langmuir **17**, 6013 (2001)

23. H.R. Kruyt (ed.), Colloid Science. vol. 1 Non-reversible systems (Moscow, Russia, 1955), 538p. (Russ. Transl.)
24. Y.I. Prylutskyy, S.S. Durov, L.A. Bulavin et al., Structure and thermophysical properties of fullerene C_{60} aqueous solutions. Int. J. Thermophys. **22**, 943 (2001)
25. L. Bulavin, I. Adamenko, Y. Prylutskyy et al., Structure of fullerene C_{60} in aqueous solution. Phys. Chem. Chem. Phys. **2**, 1627 (2000)
26. G.V. Andrievsky, V.K. Klochkov, E.L. Karyakina et al., Studies of aqueous colloidal solutions of fullerene C_{60} by electron microscopy. Chem. Phys. Lett. **300**, 392 (1999)
27. U. Ritter, Y.I. Prylutskyy, M.P. Evstigneev et al., Structural features of highly stable reproducible C_{60} fullerene aqueous colloid solution probed by various techniques. Fuller. Nanotub. Carbon Nanostruct. **23**, 530 (2015)
28. Z. Meng, S.M. Hashmi, M. Elimelech, Aggregation rate and fractal dimension of fullerene nanoparticles via simultaneous multiangle static and dynamic light scattering measurement. J. Colloid Interface Sci. **392**, 27 (2013)
29. A.O. Khokhryakov, M.V. Avdeev, V.L. Aksenov, L.A. Bulavin, Structural organization of colloidal solution of fullerene C_{60} in water by data of small angle neutron scattering. J. Mol. Liq. **127**, 73 (2006)
30. Y.I. Prylutskyy, V.I. Petrenko, O.I. Ivankov et al., On the origin of C_{60} fullerene solubility in aqueous solution. Langmuir **30**, 39–67 (2014)
31. J. Labille, J. Brant, F. Villieras et al., Affinity of C_{60} fullerenes with water. Fuller. Nanotub. Carbon Nanostruct. **14**, 307 (2006)
32. K.L. Chen, M. Elimelech, Relating colloidal stability of fullerene (C_{60}) nanoparticles to nanoparticle charge and electrokinetic properties. Environ. Sci. Technol. **43**, 7270 (2009)
33. J. Brant, H. Lecoanet, M.R. Wiesner, Aggregation and deposition characteristics of fullerene nanoparticles in aqueous systems. J. Nanopart. Res. **7**, 545 (2005)
34. K.L. Chen, M. Elimelech, Aggregation and deposition kinetics of fullerene (C_{60}) nanoparticles. Langmuir **22**, 10994 (2006)
35. J.A. Brant, J. Labille, J.Y. Bottero, M.R. Wiesner, Characterizing the impact of preparation method on fullerene cluster structure and chemistry. Langmuir **22**, 3878 (2006)
36. G.V. Andrievsky, V.K. Klochkov, A.B. Bordyuh, G.I. Dovbeshko, Comparative analysis of two aqueous-colloidal solutions of C_{60} fullerene with help of FTIR reflectance and UV-Vis spectroscopy. Chem. Phys. Lett. **364**, 8 (2002)
37. V.N. Bezmelnitsyn, A.V. Eletskii, M.V. Okun, E.V. Stepanov, Diffusion of aggregated fullerenes in solution. Phys. Scripta **53**, 364 (1996)
38. M. Wierzbicki, E. Sawosz, M. Grodzik et al., Comparison of anti-angiogenic properties of pristine carbon nanoparticles. Nanoscale Res. Lett. **8**, 195 (2013)
39. J. Labille, A. Masion, F. Ziarelli et al., Hydration and dispersion of C_{60} in aqueous systems: the nature of water-fullerene interactions. Langmuir **25**, 11232 (2009)
40. Y. Prilutski, S. Durov, L. Bulavin et al., Study of structure of colloidal particles of fullerenes in water solution. Mol. Cryst. Liq. Cryst. **324**, 65 (1998)
41. P. Scharff, K. Risch, L. Carta-Abelmann et al., Structure of C_{60} fullerene in water: spectroscopic data. Carbon **42**, 1203 (2004)
42. N.O. Mchedlov-Petrossyan, V.K. Klochkov, G.V. Andrievsky, Colloidal dispersions of fullerene C_{60} in water: some properties and regularities of coagulation by electrolytes. J. Chem. Soc., Faraday Trans. **93**, 4343 (1997)
43. J.H. Walther, R.L. Jaffe, E.M. Kotsalis et al., Hydrophobic hydration of C_{60} and carbon nanotubes in water. Carbon **42**, 1185 (2004)
44. L. Li, D. Bedrov, G. Smith, A molecular-dynamics simulation study of solvent-induced repulsion between C_{60} fullerenes in water. J. Chem. Phys. **123**, 204504 (2005)
45. L. Li, D. Bedrov, G.D. Smith, Water-induced interactions between carbon Nanoparticles. J. Phys. Chem. B **110**, 10509 (2006)
46. C.I. Wang, C.C. Hua, S.A. Chen, Dynamic solvation shell and solubility of C_{60} in organic solvents. J. Phys. Chem. B **118**, 9964 (2014)

47. J. Choi, S.D. Snow, J.-H. Kim, S.S. Jang, Interaction of C_{60} with water: first-principles modeling and environmental implications. Environ. Sci. Technol. **49**, 1529 (2015)
48. A. Montellano, T. Da Ros, A. Bianco, M. Prato, Fullerene C_{60} as a multifunctional system for drug and gene delivery. Nanoscale **3**, 4035 (2011)
49. Z.-Q. Li, Y.-M. Zhang, D.-S. Guo et al., Supramolecular assembly with multiple preorganised π-electronic. Cages Chem. Eur. J. **19**, 96 (2013)
50. D.Y. Lyon, L.K. Adams, J.C. Falkner, P.J. Alvarez, Antibacterial activity of fullerene water suspensions: effects of preparation method and particle size. J. Environ. Sci. Tech. **40**, 4360 (2006)
51. M. Song, S. Liu, J. Yin, H. Wang, Interaction of human serum album and C_{60} aggregates in solution. Int. J. Mol. Sci. **12**, 4964 (2011)
52. M.P. Evstigneev, Hetero-association of aromatic molecules in aqueous solution. Int. Rev. Phys. Chem. **33**, 229 (2014)
53. V.N. Bezmel'nitsyn, A.V. Eletskii, M.V. Okun, Fullerenes in solutions. Phys. Usp. **41**, 1091 (1998)
54. X. Zhao, A. Striolo, P.T. Cummings, C_{60} binds to and deforms nucleotides. Biophys. J. **89**, 3856 (2005)
55. Y.I. Prylutskyy, A.S. Buchelnikov, D.P. Voronin et al., C_{60} fullerene aggregation in aqueous solution. Phys. Chem. Chem. Phys. **15**, 9351 (2013)
56. D.P. Voronin, A.S. Buchelnikov, V.V. Kostjukov et al., Evidence of entropically driven C_{60} fullerene aggregation in aqueous solution. J. Chem. Phys. **140**, 104909 (2014)
57. D. Hazafy, M.-V. Salvia, A. Mills et al., NMR analysis of Nile Blue (C. I. Basic Blue 12) and Thionine (C. I. 52000) in solution. Dyes Pigment. **88**, 315 (2011)
58. A.A.H. Santiago, A.S. Buchelnikov, M.A. Rubinson et al., Shape-independent model (SHIM) approach for studying aggregation by NMR diffusometry. J. Chem. Phys. **142**, 104202 (2015)
59. M. Corti, V. Degiorgio, Quasi-elastic light scattering study of intermicellar interactions in aqueous sodium dodecyl sulfate solutions. J. Phys. Chem. **85**, 711 (1981)
60. D. Attwood, R. Blundell, V. Mosquera, Light scattering studies on the association of phenothiazine drugs in aqueous solutions of low ionic strength. J. Colloid Interface Sci. **157**, 50 (1993)
61. F. Lu, S.A. Haque, S.-T. Yang et al., Aqueous compatible fullerene—doxorubicin conjugates. J. Phys. Chem. C **113**, 17768 (2009)
62. J.-H. Liu, L. Cao, P.G. Luo et al., Fullerene-conjugated doxorubicin in cells. Appl. Mater. Interfaces **2**, 1384 (2010)
63. Y. Prylutskyy, A. Borowik, G. Gołuński et al., Biophysical characterization of the complexation of C_{60} fullerene with doxorubicin in a prokaryotic model. Mat-wiss u Werkstofftech **47**, 92 (2016)
64. S. Prylutska, I. Grynyuk, O. Matyshevska et al., C_{60} fullerene as synergistic agent in tumor-inhibitory doxorubicin treatment. Drugs R&D **14**, 333 (2014)
65. G.B. Skamrova, I.V. Laponogov, A.S. Buchelnikov et al., Interceptor effect of C_{60} fullerene on the in vitro action of aromatic drug molecules. Eur. Biophys. J. **43**, 265 (2014)
66. S. Prylutska, R. Panchuk, G. Gołuński et al., C_{60} fullerene enhances anticancer activity and overcomes tumor cells drug resistance. Nano Res. **10**, 652 (2017)
67. M.P. Evstigneev, A.S. Buchelnikov, D.P. Voronin et al., Complexation of C_{60} fullerene with aromatic drugs. Chem. Phys. Chem. **14**, 568 (2013)
68. A.S. Buchelnikov, V.V. Kostyukov, M.P. Yevstigneev, Y.I. Prylutskyy, Mechanism of complexation of the phenothiazine dye methylene blue with fullerene C_{60}. Russ. J. Phys. Chem. A **87**, 662 (2013)
69. Y.I. Prylutskyy, M.P. Evstigneev, I.S. Pashkova et al., Characterization of C_{60} fullerene complexation with antibiotic doxorubicin. Phys. Chem. Chem Phys. **16**, 23164 (2014)
70. Y.I. Prylutskyy, M.P. Evstigneev, V.V. Cherepanov et al., Structural organization of C_{60} fullerene, doxorubicin and their complex in physiological solution as promising antitumor agents. J. Nanopart. Res. **17**, 45 (2015)

71. Y.I. Prylutskyy, V.V. Cherepanov, M.P. Evstigneev et al., Structural self-organization of C_{60} and cisplatin in physiological solution. Phys. Chem. Chem. Phys. **17**, 26084 (2015)
72. J. Rohr, C. Hertweck, Comprehensive Natural Products II—Chemistry and Biology, eds. L. Mander, H.-W. Liu (Elsevier, Oxford, 2010), pp. 227–303
73. B. Ostash, A. Korynevska, R. Stoika, V. Fedorenko, Chemistry and biology of landomycins, an expanding family of polyketide natural products. Mini. Rev. Med. Chem. **9**, 1040 (2009)
74. M.K. Kharel, P. Pahari, M.D. Shepherd et al., Angucyclines: biosynthesis, mode-of-action, new natural products, and synthesis. Nat. Prod. Rep. **29**, 264 (2012)
75. L.V. Lehka, R.R. Panchuk, W. Berger et al., The role of reactive oxygen species in tumor cells apoptosis induced by Landomycin A. Ukr. Biochem. J. **87**, 72 (2015)
76. X. Yang, B. Fu, B. Yu, Total synthesis of Landomycin A, a potent antitumor angucycline antibiotic. J. Am. Chem. Soc. **133**, 12433 (2011)
77. M. Dalavalle, M. Leonzio, M. Calvaresi, F. Zerbetto, Explaining fullerene dispersion by using micellar solutions. Chem. Phys. Chem. **15**, 2998 (2014)
78. R. Injac, M. Perse, M. Cerne et al., Protective effects of fullerenol $C_{60}(OH)_{24}$ against doxorubicin-induced cardiotoxicity and hepatotoxicity in rats with colorectal cancer. Biomaterials **30**, 1184 (2009)
79. Y.I. Prylutskyy, V.V. Cherepanov, V.V. Kostjukov et al., Study of the complexation between Landomycin A and C_{60} fullerene in aqueous solution. RSC Adv. **6**, 81231 (2016)

Chapter 2
Colloid Nanoparticles and Carbon Nanotubes. What Can We Learn About Their Biomedical Application From Molecular Dynamics Simulations?

Tomasz Panczyk, Lukasz Konczak and Pawel Wolski

Abstract The behavior of a multi-walled carbon nanotube functionalized by magnetic nanoparticles through triethylene glycol chains is studied using molecular dynamics simulations. Particular attention is paid to the effect of magnetic anisotropy of nanoparticles which significantly affects the behaviour of the system under external magnetic field. The magnetization reversal process is coupled with the standard atomistic molecular dynamics equations of motion by utilizing the Neel-Brown model. The overdamped Langevin dynamics is used for the description of the inertialess magnetization displacements. The key results obtained in this study concern: an energetic profile of the system accompanying transition of a magnetic nanoparticle from the vicinity of the nanotube tip to its sidewall, the range of the magnetic anisotropy constant in which the system performs structural rearrangements, and the release dynamics of cisplatin from the interior of the nanocontainer. Another analyzed architecture uses small gold nanoparticles linked with the nanotube by hydrazone bond containing fragments. Because hydrazone bonds hydrolyze at slightly acidic pH those gold nanoparticles become chemically disconnected from the CNT at such conditions. Thus, the previously encapsulated cisplatin molecules in the CNT inner cavity can be released only at acidic pH. Analysis of the above process at the molecular scale leads to the conclusion that the feasibility of such a mechanism can be canceled by strong dispersion forces existing between gold nanoparticles and CNT. However, the presence of cisplatin in the inner cavity of the carbon nanotube strongly reduces the range of dispersion interactions. The determined properties of the studied systems strongly suggest their application in the area of nanomedicine as drug targeting and delivery nanovehicles.

T. Panczyk (✉) · L. Konczak · P. Wolski
Jerzy Haber Institute of Catalysis and Surface Chemistry, Polish Academy of Sciences,
ul. Niezapominajek 8, 30-239 Krakow, Poland
e-mail: panczyk@vega.umcs.lublin.pl

L. A. Bulavin and A. V. Chalyi (eds.), *Modern Problems of Molecular Physics*,
Springer Proceedings in Physics 197, https://doi.org/10.1007/978-3-319-61109-9_2

2.1 Introduction

Carbon nanotubes (CNT) and magnetic nanoparticles (MNP) are considered as materials of great importance in medical diagnosis or as drug carriers. Normally, the studies are focused on their individual applications rather than on their composites. But CNT-MNP composites reveal even more interesting properties though their fabrication might be a challenge in some cases. MNPs are widely applied as contrast agents in magnetic resonance imaging (MRI); however, there are many other medical applications of MNPs like in vitro bioseparation, drug delivery or hyperthermia [1–3]. Similarly, CNTs are currently recognized as very promising drug carriers acting either as molecular cargoes or as parts of drug-CNT composties enhancing pharmacological activity of the drugs [4–9].

CNTs possess many intriguing features that make them attractive drug delivery carriers. It is well-known that they experience the enhanced permeability and retention (EPR) effect [10]. The EPR effect enables CNTs to transport chemotherapeutic agents preferentially to tumor sites. However, this is not a specific property of CNTs as any nanoparticulate drug delivery system also experiences the EPR effect. A very specific property of CNTs is their needle-like shape which facilitates transmembrane penetration and intracellular accumulation of drugs via the "nanoneedle" mechanism [11]. CNTs have also been shown to enter cells via energy-dependent endocytic pathways, [12] and display extraordinary ability for drug loading onto the surface or within the interior core of CNTs via both covalent and non-covalent interactions [13–16]. Finally, targeting molecules, such as folic acid, antibodies, and magnetic nanoparticles can be further incorporated onto the drug-loaded CNTs [17–20].

In our recent publications [21–23] many properties of carbon nanotubes functionalized by magnetic nanoparticles through triethylene glycol chains were carefully investigated. We discussed some key factors which provide the fundamental conditions for the creation of a functional nanocontainer (NC) being able to encapsulate drug molecules and perform drug release by applying an external magnetic field. However, successful fabrication of the magnetically triggered NC seems to be still a challenge because its proper function needs highly precise molecular structure.

Drug release from CNTs can be triggered in response to other chemical or physical factors. Particularly interesting seems to be the pH change from physiological 7.4 to an acidic one. It is well-known that tumor microenvironments reveal several specific properties which can be utilized for controlled drug release. The highly reducing environment of tumor cells, and pH reduction to ca. 5.5 due to lactic acid production caused by anaerobic glycolysis, were studied as triggering factors for the release of cisplatin from carbon nanotubes [24]. Irinotecan or doxorubicin were also studied as model drugs for acidic pH induced release of drugs from the inner cavities or surfaces of CNTs [5, 9, 25–27]. However, in the majority

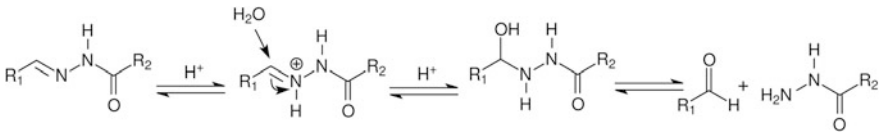

Fig. 2.1 Mechanism of hydrazone bond hydrolysis at acidic pH [28]

of cases the experimentally observed enhanced release of drugs at acidic pH is left without a deeper physical interpretation. For example, the pK_a of doxorubicin is ca. 8, so the observed enhanced release when the pH changes from 7.4 to 5.5 cannot be exclusively attributed to changes in the charge distribution or protonation of doxorubicin molecules.

In our theoretical studies of pH controlled drug delivery systems we applied a kind of reverse strategy. We constructed molecular architectures which have to be sensitive to pH in the discussed range. There are many chemical compounds which undergo structural transformations or even decomposition when pH drops from 7.4 to 5.5. One interesting example is hydrazone bond hydrolysis which occurs according to the scheme shown in Fig. 2.1 [28]. Thus, the application of hydrazone bonds fragments in the construction of pH sensitive drugs carriers is a very promising strategy since the hydrolysis phenomenon will occur precisely at tumor sites.

In this work we will discuss our observations concerning the system composed of a single-walled CNT and a gold nanoparticle functionalized by some chain molecules (linkers) containing hydrazone bond fragments [29]. To make a stable capped state of the CNT at neutral pH, the CNT tips were covalently linked with gold nanoparticles. However, the creation of the uncapped state upon hydrolysis of the hydrazone bonds turned out to be kinetically blocked. Therefore, theoretical analysis of such architecture on the molecular level helps to identify the most critical stages and point out which factors should be carefully optimized in order to make such a system fully functional.

2.2 Methods

The computational methodology utilized in this work is based on molecular dynamics simulations using the open source lammps code [30]. The detailed description of the force field, including magnetic interactions, and computational approaches in the case of the magnetically triggered nanocontainer, can be found in our previous work [22, 23, 31]. The details of computational methodology and the force field applied to the model of pH triggered detachment of gold nanoparticles from the CNT tips is available in our recent work [29].

2.3 Results and Discussion

2.3.1 Magnetically Triggered Nanocontainer

2.3.1.1 Construction of a Functional Architecture

Our numerous theoretical studies of the magnetically triggered nanocontainer performed so far, led to several conclusions concerning the molecular structure of the functional system. The mechanism of its action is based on simple physical premises; however, a few conditions must be satisfied. Let us start from schematic representation of the system under investigation.

Figure 2.2 shows the key elements of the magnetically triggered nanocontainer. They consist of: (i) carbon nanotube; it may either be single-walled or multi-walled. In the case of a single-walled nanotube, the nanocontainer operates at milder conditions, however, in such a case the upper limit of the diameter of the SWCNT must be accounted for. Stable SWCNTs can reach diameters not larger than 2 nm which, in view of other conditions, is too little for construction of functional nanocontainers. Multi-walled nanotubes can have larger diameters but at the same time the dispersion interactions between the nanotube and magnetic nanoparticle become stronger and this implies application of a very hard magnetic material for the magnetic nanoparticles. (ii) linker; it may be any chain-like molecule but its chemistry must allow for covalent linking either with nanotube or with the magnetic nanoparticle. Its length is important—it cannot be too long. In our studies we used triethylene glycol chains. (iii) magnetic nanoparticle; such nanoparticles posses a magnetization vector and an easy axis of magnetization. Depending on the choice of magnetic material, the displacement of the magnetization vector from the easy axis direction needs various amounts of energy delivered by an external magnetic field. We found that the higher value of the magnetic anisotropy constant of the nanoparticle, the quicker the response of the nanocontainer to the magnetic field. Therefore, hard magnetic materials are preferred. In our studies we used material properties of metallic cobalt, and we found that a nanoparticle of 10 nm diameter is

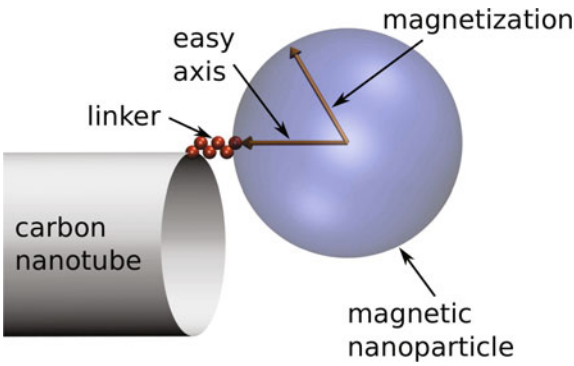

Fig. 2.2 Scheme of the magnetically triggered nanocontainer

enough to obtain a sufficiently high magnetic anisotropy energy. Because fine metallic nanoparticles can undergo fast degradation in aqueous media, we considered the presence of a protective layer on the surfaces of the magnetic nanoparticles. That layer, made from e.g. alumina, reduces to some extent the range of dispersion interactions between the nanoparticle and the nanotube, and it also produces an electric charge on the nanoparticle due to electric double layer formation. That extra charge affects the total interaction energy with the nanotube because the carbon atoms on the nanotube tips can be saturated by other hydrophilic groups such as amines or carboxylates.

2.3.1.2 Basic Properties at Normal Conditions

Due to the significant range of the dispersion interactions acting between the CNT and the MNPs (both are extended bodies), and the presence of linker between them, the normal state of the nanocontainer is with the MNP adjacent to the CNT tips. We call this state the capped one. The stability of this state depends on factors such as the size of the system, the chemical nature of the MNP surface and its surface charge, the presence of functional groups on the CNT tips, and, to some extent, the length and chemical nature of the linker. In the capped state the total energy of the nanocontainer reaches a minimum, E_c, as shown in Fig. 2.3. The depth of this minimum can be controlled by adjustment of the parameters mentioned above.

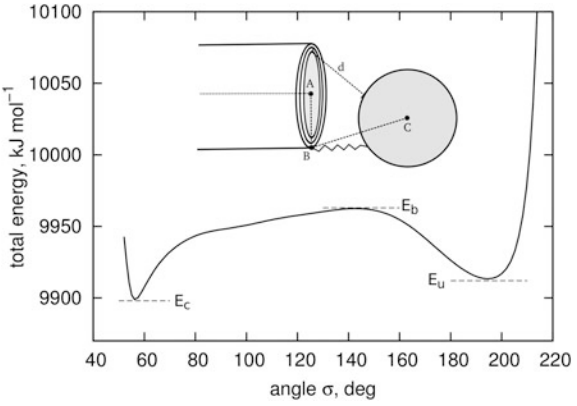

Fig. 2.3 Typical total energy profile of the nanocontainer associated with the transition of the magnetic nanoparticle from the nanotube tip to the sidewall (uncapping). E_c is the total energy minimum corresponding to the capped state, i.e. when the MNP adheres to the CNT tip, and E_u is the total energy minimum corresponding to the location of the MNP on the nanotube sidewall. E_b is the energy barrier separating these two minima. The total energy profile is plotted as a function of the angle σ which is defined by the coordinates of the points A, B and C shown in the inset. The section d is the distance between the surface of the MNP and carbon atoms located on the nanotube tip. It defines the degree of the uncapping

The preferred depth of the total energy minimum cannot be precisely determined but it should be "moderate". This is because the capped state should be stable at normal conditions, and so E_b–E_c should be greater than ca. 10 k_BT. Very strong interactions in the capped state are, however, not preferred because that state cannot be thermodynamically locked and irreversible.

Looking at Fig. 2.3 we notice that the total energy of the system increases with the increasing value of the angle σ (which, in turn is correlated with the slit size d), passes the maximum E_b, and ends up in the second minimum E_u. This second minimum corresponds to localization of the MNP on the nanotube sidewall, i.e. we can call this state the uncapped one. The depth of the energy well in the uncapped state can be controlled by adjustment of exactly the same parameters as in the capped state. However, in this case the structure (state) of the CNT sidewall is very important. For example, the presence of some functional groups on the sidewalls can affect the interaction energy mainly in the uncapped state with only minor influence on the stability of the capped state.

These two energy minima are separated by the energy barrier E_b. This parameter is crucial for the proper function of the nanocontainer. As mentioned, E_b controls the kinetic stability of both the capped and uncapped states. Thus, the key factor in the design of the functional nanocontainer is a suitable adjustment of the energy barrier E_b.

2.3.1.3 Interaction with the External Magnetic Field

If the nanocontainer in the capped state is exposed to an external magnetic field then the magnetizations of the MNPs experience Néel rotation. Thus, they rotate in order to align with the direction of the field but at the same time they displace from the easy axes directions. This leads to appearance of magnetic anisotropy energy U_a according to the formula:

$$U_a = K_a V \sin^2\theta \tag{2.1}$$

where K_a is the magnetic anisotropy constant of the material, V is volume of the magnetic core, and θ is the angle between magnetization vector and easy axis direction. The anisotropy energy creates a torque which drives the Brown rotation of the whole nanoparticle. However, at some point the linker between CNT and MNP hinders the Brown rotation. As a result, the MNP performs translation in order to minimize mismatch between the easy axis and magnetization directions. This translation leads finally to the uncapping of the nanotube.

Thus, the key factor responsible for the magnetically assisted uncapping of the nanocontainer is the magnetic anisotropy constant of the magnetic material. That parameter cannot be easily controlled as this is a material property. For example, the reported values of K_a for bulk metallic cobalt are 4.5×10^5 J m^{-3} and 2.5×10^5 J m^{-3} for hcp and fcc structures, respectively [32]. It is well known, however, that K_a is much larger for metal nanoparticles than for the bulk. For bulk samples, K_a is

primarily due to magnetocrystalline anisotropy whereas for nanoparticles the dominant contributions to the magnetic anisotropy arise from stresses, surface effects and the shape of the granules [33, 34]. Thus, for very small NPs consisting of about 30 Co atoms, the low-temperature value of K_a is 3×10^7 J m^{-3} i.e. two orders of magnitude larger than for bulk metal [34]. In other studies involving 40 Å cobalt NPs and temperatures about 600 K, it was found that $K_a = 6 \times 10^6$ J m^{-3} [35]. On the other hand, Respaud et. al. [32] found K_a in the range $0.83–1.0 \times 10^6$ J m^{-3} for ultrafine Co NPs (15 Å in diameter). As seen, the K_a value seems to be dependent on the NP sizes and probably also shape distribution and other factors that affect the values of K_a determined experimentally in different labs. Thus, it is difficult to predict a strict K_a value for a given case but knowing the above experimental values we can get a notion of the physically reasonable range of its values. The assumed diameter of magnetic cores in our model, 80 Å, is significantly larger than those the mentioned above, thus we might expect that actual K_a values for our cobalt NPs should be rather closer to 10^6 J m^{-3} than to 10^7 J m^{-3}. Obviously cobalt is neither the only nor the best material for the magnetic caps of the NC. Materials based on rare earth elements often exhibit enormously high saturation magnetization and magnetic anisotropy. For example, $SmCo_5$ exhibits K_a value as high as 1.3×10^7 J m^{-3} for bulk material [36]. It is likely that $SmCo_5$ nanoparticles would posses a K_a value about one order of magnitude larger. Therefore, such materials represent reasonable alternatives if Co NPs revealed a magnetic anisotropy too low for proper function of the NC.

Figure 2.4 shows an example of the magnetically triggered uncapping of a nanocontainer which is composed of magnetic nanoparticles with a K_a value representative of cobalt, i.e. 5×10^6 J m^{-3}. The strength of the external magnetic field was set to 4.7 T. This value produces the magnetic energy comparable to the anisotropy energy (2.1) and, as seen, it is enough to induce uncapping within times less than 10 ns. In Fig. 2.4 we also notice an important effect of the initial orientation of the nanocontainer with respect to the field direction. In some cases, when the orientation of the magnetization of a given nanoparticle is similar to the field direction, no uncapping occurs.

2.3.1.4 Spontaneous Recapping Without the External Magnetic Field

The uncapping transition involves overcoming an energy barrier, as mentioned in Sect. 2.3.1.2, and this can be done by exposing the system to an external magnetic field. The uncapped state is also separated by an energy barrier and that barrier can be significant. This means that the uncapping transition can be an irreversible process, however, this is not desirable. A functional nanocontainer should be able to spontaneously return to the capped state after some time. That property is necessary for drug loading prior to administration of the nanocontainer to the body.

As already mentioned, the energy barrier for the recapping transition can be controlled by modification of the nanotube sidewalls. We considered several methods, [23] however, the most promising seems to be covalent functionalization

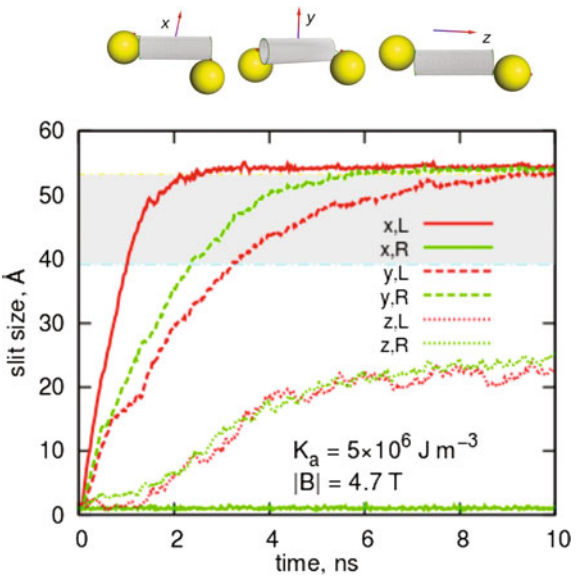

Fig. 2.4 Magnetically triggered uncapping of the nanocontainer after exposure to a 4.7 T external magnetic field. The initial configuration was the fully capped structure brought to equilibrium without the external magnetic field applied. The magnetizations of the MNPs were aligned with the directions of the easy axes. The symbols *x*, *y*, and *z* mean the direction of the applied field. Codes *L* (*left*) and *R* (*right*) are used for formaly distinguishing each end of the nanocontainer. The snapshots show the final configurations after 10 ns together with the indication of the magnetic field directions (arrows)

of the sidewall defect sites by other small functional groups. Table 2.1 shows selected results obtained by incorporation of amide groups on the sidewalls of triple-walled carbon nanotube.

As can be seen in Table 2.1, the energy barrier for the recapping of the bare triple-walled nanotube is about 72 kJ mol^{-1}. This is a relatively high (compared to k_BT) value and the recapping process will be very slow or it can even be kinetically blocked. It should be mentioned that MNPs are very heavy objects and their motion is orders of magnitude slower than atoms or molecules. Therefore, that value of the

Table 2.1 Energy barriers found for the nanocontainer composed of triple-walled carbon nanotube, amide functionalized triple-walled carbon nanotube, and additionally filled with cisplatin molecules

Nanotube	Energy barrier for uncapping, kJ mol^{-1}	Energy barrier for recapping, kJ mol^{-1}
Bare triple-walled	107.8	72.4
Amide functionalized	116.8	52.1
Amide functionalized and filled in cisplatin	145.7	47.27

energy barrier means that the MNP is locked in the uncapped state of the nanocontainer. However, when the sidewall of the nanotube is functionalized by amide groups, the energy barrier drops by 20 kJ mol^{-1}. Our estimation of the likelihood of the recapping transition, based on the transition state theory, leads to the conclusion that barriers lower than ca. 60 kJ mol^{-1} can be overcome spontaneously within a reasonable timescale [23]. Thus, the covalent functionalization by amide groups seems to be a method of choice in the construction of a fully functional nanocontainer.

The presence of drug molecules in the inner cavity of the nanotube also affects the energetic picture of the nanocontainer. However, the encapsulated cisplatin molecules modify mainly the energy barrier for the uncapping transition. Also, the amide groups localized on the sidewalls enhance the energy barrier of the uncapping. This is due to an extra energy component coming from polar amide groups (bearing partial electric charges) distributed circularly around the MNP at the capped state. The cisplatin molecules also provide an extra energy component due to their interactions with the MNP in the capped state. The question is why those amide groups lower the energy barrier to the uncapped state. The answer comes

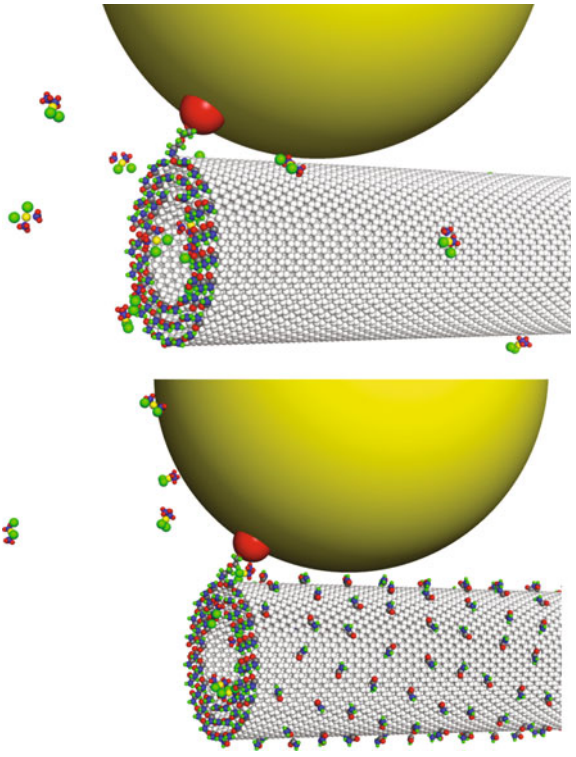

Fig. 2.5 Snapshots of the uncapped states of the nanocontainers composed of bare carbon nanotube (upper part) and amide functionalized nanotube (bottom part). In both cases, initially, the nanocontainers were filled in cisplatin molecules

from analysis of the system snapshots with and without the presence of amide groups. As can be seen in Fig. 2.5, the attached amide groups prevent the MNP from a very close contact with the nanotube sidewall. This, in turn, reduces the range of the dispersion interactions between these two bodies. Therefore, the amide groups, or actually any other groups localized on the nanotube sidewall, act as steric obstacles. The snapshots in Fig. 2.5 also show that cisplatin quickly escapes from the CNT interior upon formation of the uncapped state.

2.3.2 *Uncapping of Carbon Nanotube by Detachment of Colloid Nanoparticles*

2.3.2.1 Bonded Form at Neutral PH

According to the scheme shown in Fig. 2.1, the hydrazone bonds are stable at neutral pH. Thus, we constructed a model system in which a single-walled carbon nanotube is linked with a gold nanoparticles by N′-[(E)-(4-{2-[2-(2-sulfanylethoxy) ethoxy] ethoxy} phenyl) methylidene] formic hydrazide linkers. The system is shown in Fig. 2.6 and it is stable at neutral pH by definition. Therefore, we focused mainly on the stability of the unbonded form at acidic pH.

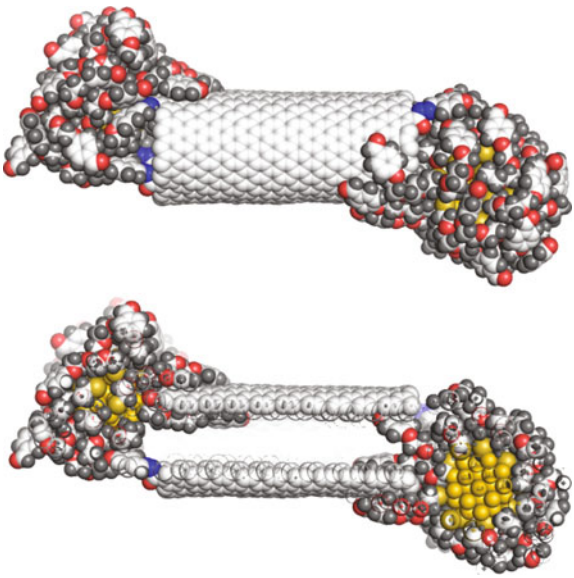

Fig. 2.6 Simulation snapshot of a CNT functionalized by gold nanoparticles at neutral pH using the linkers N′-[(E)-(4-{2-[2-(2-sulfanylethoxy) ethoxy] ethoxy} phenyl) methylidene] formic hydrazide. The bottom part shows the cross-section of the system

2.3.2.2 Detachment of Gold Nanoparticles Upon Hydrolysis of Hydrazone Bonds

At acidic pH the hydrazone bonds are cleaved and gold nanoparticles are chemically disconnected from the CNT. Thus, we should observe detachment of gold nanoparticles from the CNT tips and release of previously encapsulated drug molecules from the CNT inner space. However, our calculation results concerning such systems led to the conclusion that gold nanoparticles do not detach from the CNT. A closer analysis of the system structure showed that some linkers, attached to gold nanoparticles, were incorporated in the internal space of the CNT, as shown in the inset of Fig. 2.7.

The presence of linkers in the CNT interior is the main factor responsible for the lack of detachment of gold nanoparticles from the CNT tips because the dispersion interactions between the hydrophilic nanoparticles and the hydrophobic CNT in such a small system should not be large. The potential of mean force (pmf), determined from biased simulations, reaches about 250 kJ mol^{-1} for the process of enforced separation of these two species (Fig. 2.7). Therefore, we can conclude that spontaneous detachment of gold nanoparticles from the CNT is thermodynamically impossible in the considered conditions.

However, an analysis of the system when the CNT interior is filled with cisplatin molecules gives the energy barrier against detachment not bigger than 15 kJ mol^{-1} (Fig. 2.8). This is not a big value and the spontaneous detachment and release of cisplatin should occur in normal conditions without any extra energy bias. Such a strong difference between the solvent filled CNT (Fig. 2.7) and cisplatin filled CNT

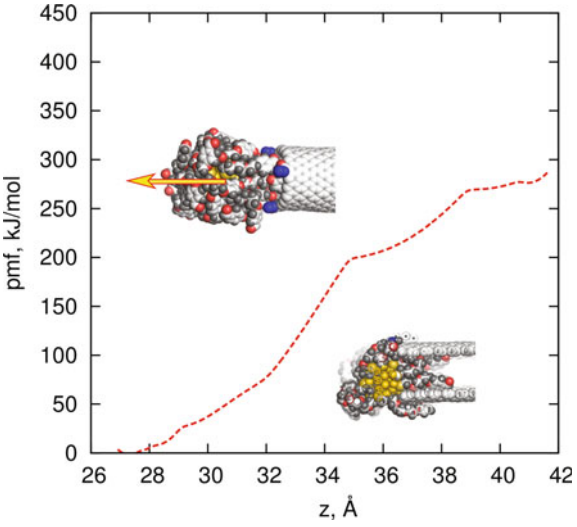

Fig. 2.7 Potential of mean force (pmf) determined while dragging the gold nanoparticle from the tip position to the bulk for the case when the interior of the nanotube is filled with solvent. The pmf was determined using the umbrella sampling method with weighted histogram analysis. The bottom snapshot shows a cross-section of the system in its initial position

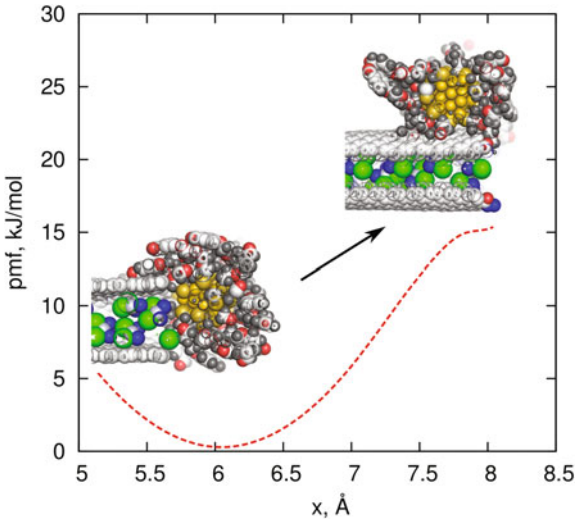

Fig. 2.8 Potential of mean force (pmf) determined while dragging the gold nanoparticle from the tip position to the sidewall for the case when the interior of the nanotube is filled with a mixture of cisplatin and solvent. The lefthand side snapshot shows the system structure in its initial position, while the righthand side shows the final position

(Fig. 2.8) is due to the lack of incorporation of linkers to the CNT interior in the latter case. Cisplatin forms a kind of condensed phase in the CNT internal space, and this prevents incorporation of linkers and reduces their anchoring effect.

2.4 Conclusions

Computer simulations are a valuable tool for predictions of how a particular molecular structure behaves under given conditions, and they can be used for the design of functional drug delivery systems. Magnetically controlled nanocontainers might be promising candidates as a drug targeting and delivery systems. They allow for high loadings of active component inside the nanotube and controllable release by means of an external magnetic field. However, they need a careful tuning of the molecular structure in order to obtain a proper energetic balance between the different states of the system. The presence of polar groups attached to the nanotube sidewalls makes the system fully functional, more hydrophilic, and reduces the risk of agglomeration of an ensemble of such systems into big clusters.

Hydrazone bond hydrolysis at slightly acidic pH is a promising factor for the construction of smart drug delivery systems. However, as shown in the analyzed system, there might appear some phenomena (difficult to predict in advance) which render the function impossible. In the particular case of capping the CNT by gold nanoparticles, we found that the incorporation of linkers in the CNT interior might lock the nanoparticles at the nanotube tips. Also, if bigger system sizes are considered, there might be a risk of locking the nanoparticles by dispersion interactions between the nanoparticles and the CNT.

Acknowledgements This work was supported by National Science Centre (NCN). Grant no. UMO-2012/07/E/ST4/00763.

References

1. S. Laurent, D. Forge, M. Port, A. Roch, C. Robic, L. Vander Elst, R.N. Muller, Magnetic iron oxide nanoparticles: synthesis, stabilization, vectorization, physicochemical characterizations, and biological applications. Chem. Rev. **108**, 2064–2110 (2008). https://doi.org/10.1021/cr068445e
2. M. Arruebo, R. Fernández-Pacheco, M.R. Ibarra, J. Santamaría, Magnetic nanoparticles for drug delivery. Nano Today. **2**, 22–32 (2007). https://doi.org/10.1016/S1748-0132(07)70084-1
3. K.A. Brown, C.C. Vassiliou, D. Issadore, J. Berezovsky, M.J. Cima, R.M. Westervelt, Scaling of transverse nuclear magnetic relaxation due to magnetic nanoparticle aggregation. J. Magn. Magn. Mater. **322**, 3122–3126 (2010). https://doi.org/10.1016/j.jmmm.2010.05.044
4. B.S. Wong, S.L. Yoong, A. Jagusiak, T. Panczyk, H.K. Ho, W.H. Ang, G. Pastorin, Carbon nanotubes for delivery of small molecule drugs. Adv. Drug Deliv. Rev. **65**, 1964–2015 (2013). https://doi.org/10.1016/j.addr.2013.08.005
5. H. Huang, Q. Yuan, J.S. Shah, R.D.K. Misra, A new family of folate-decorated and carbon nanotube-mediated drug delivery system: synthesis and drug delivery response. Adv. Drug Deliv. Rev. **63**, 1332–1339 (2011). https://doi.org/10.1016/j.addr.2011.04.001
6. D. Iannazzo, A. Piperno, A. Pistone, G. Grassi, S. Galvagno, Recent advances in carbon nanotubes as delivery systems for anticancer drugs. Curr. Med. Chem. **20**, 1333–1354 (2013). https://doi.org/10.2174/0929867311320110001
7. C.L. Lay, J. Liu, Y. Liu, Functionalized carbon nanotubes for anticancer drug delivery. Expert Rev. Med. Devices **8**, 561–566 (2011). https://doi.org/10.1586/erd.11.34
8. J. Li, S.Q. Yap, C.F. Chin, Q. Tian, S.L. Yoong, G. Pastorin, W.H. Ang, Platinum (iv) prodrugs entrapped within multiwalled carbon nanotubes: selective release by chemical reduction and hydrophobicity reversal. Chem. Sci. **3**, 2083 (2012). https://doi.org/10.1039/c2sc01086k
9. C. Tripisciano, M.H. Rümmeli, X. Chen, E. Borowiak-Palen, Multi-wall carbon nanotubes—a vehicle for targeted Irinotecan drug delivery. Phys. Status Solidi B **247**, 2673–2677 (2010). https://doi.org/10.1002/pssb.201000143
10. H. Maeda, Macromolecular therapeutics in cancer treatment: the EPR effect and beyond. J. Controlled Release **164**, 138–144 (2012). https://doi.org/10.1016/j.jconrel.2012.04.038
11. A. Bianco, K. Kostarelos, C.D. Partidos, M. Prato, Biomedical applications of functionalised carbon nanotubes. Chem. Commun. Camb. Engl. 571–577 (2005). https://doi.org/10.1039/b410943k
12. N.W.S. Kam, Z. Liu, H. Dai, Carbon nanotubes as intracellular transporters for proteins and dna: an investigation of the uptake mechanism and pathway. Angew. Chem. **118**, 591–595 (2006). https://doi.org/10.1002/ange.200503389
13. Z. Ali Mohammadi, S.F. Aghamiri, A. Zarrabi, M.R. Talaie, A comparative study on non-covalent functionalization of carbon nanotubes by chitosan and its derivatives for delivery of doxorubicin. Chem. Phys. Lett. **642**, 22–28 (2015). https://doi.org/10.1016/j.cplett.2015.10.075
14. M. Bassiouk, V.A. Basiuk, E.V. Basiuk, E. Álvarez-Zauco, M. Martínez-Herrera, A. Rojas-Aguilar, I. Puente-Lee, Noncovalent functionalization of single-walled carbon nanotubes with porphyrins. Appl. Surf. Sci. **275**, 168–177 (2013). https://doi.org/10.1016/j.apsusc.2012.12.167
15. H. Ismaili, F. Lagugné-Labarthet, M.S. Workentin, Covalently assembled gold nanoparticle-carbon nanotube hybrids via a photoinitiated carbene addition reaction. Chem. Mater. **23**, 1519–1525 (2011). https://doi.org/10.1021/cm103284g

16. Y.C. Jung, H. Muramatsu, T. Hayashi, J.H. Kim, Y.A. Kim, M. Endo, M.S. Dresselhaus, Covalent attachment of aromatic diisocyanate to the sidewalls of single- and double-walled carbon nanotubes. Eur. J. Inorg. Chem. **2010**, 4305–4308 (2010). https://doi.org/10.1002/ejic.201000507
17. A.R. Hilgenbrink, P.S. Low, Folate receptor-mediated drug targeting: from therapeutics to diagnostics. J. Pharm. Sci. **94**, 2135–2146 (2005). https://doi.org/10.1002/jps.20457
18. R. Li, R. Wu, L. Zhao, M. Wu, L. Yang, H. Zou, P-glycoprotein antibody functionalized carbon nanotube overcomes the multidrug resistance of human leukemia cells. acs nano **4**, 1399–1408 (2010). https://doi.org/10.1021/nn9011225
19. T. Panczyk, A. Jagusiak, G. Pastorin, W.H. Ang, J. Narkiewicz-Michalek, Molecular dynamics study of cisplatin release from carbon nanotubes capped by magnetic nanoparticles. J. Phys. Chem. C **117**, 17327–17336 (2013). https://doi.org/10.1021/jp405593u
20. F. Yang, C. Jin, D. Yang, Y. Jiang, J. Li, Y. Di, J. Hu, C. Wang, Q. Ni, D. Fu, Magnetic functionalised carbon nanotubes as drug vehicles for cancer lymph node metastasis treatment. Eur. J. Cancer **47**, 1873–1882 (2011). https://doi.org/10.1016/j.ejca.2011.03.018
21. T. Panczyk, T.P. Warzocha, Monte carlo study of the properties of a carbon nanotube functionalized by magnetic nanoparticles. J. Phys. Chem. C **113**, 19155–19160 (2009). https://doi.org/10.1021/jp9062065
22. T. Panczyk, M. Drach, P. Szabelski, A. Jagusiak, Magnetic anisotropy effects on the behavior of a carbon nanotube functionalized by magnetic nanoparticles under external magnetic fields. J. Phys. Chem. C **116**, 26091–26101 (2012). https://doi.org/10.1021/jp3101442
23. T. Panczyk, P. Wolski, L. Konczak, J. Narkiewicz-Michalek, Sidewall functionalization of carbon nanotubes as a method of controlling structural transformations of the magnetically triggered nanocontainer: a molecular dynamics study. J. Phys. Chem. C **119**, 8373–8381 (2015). https://doi.org/10.1021/acs.jpcc.5b01155
24. G. Pastorin, J. Li, S.L. Yoong, W.J. Goh, B.M.S. Czarny, Z. Yang, K. Poddar, M. Dykas, A. Patra, T. Thirumalai Venkatesan, C. Lee, T. Panczyk, In vitro controlled release of cisplatin from gold-carbon nanobottles via cleavable linkages. Int. J. Nanomedicine. 7425 (2015). https://doi.org/10.2147/IJN.S93810
25. Z. Ji, G. Lin, Q. Lu, L. Meng, X. Shen, L. Dong, C. Fu, X. Zhang, Targeted therapy of SMMC-7721 liver cancer in vitro and in vivo with carbon nanotubes based drug delivery system. J. Colloid Interface Sci. **365**, 143–149 (2012). https://doi.org/10.1016/j.jcis.2011.09.013
26. N.M. Dinan, F. Atyabi, M.-R. Rouini, M. Amini, A.-A. Golabchifar, R. Dinarvand, Doxorubicin loaded folate-targeted carbon nanotubes: Preparation, cellular internalization, in vitro cytotoxicity and disposition kinetic study in the isolated perfused rat liver. Mater. Sci. Eng., C **39**, 47–55 (2014). https://doi.org/10.1016/j.msec.2014.01.055
27. B. Anbarasan, S.V. Babu, K. Elango, B. Shriya, S. Ramaprabhu, pH responsive release of doxorubicin to the cancer cells by functionalized multi-walled carbon nanotubes. J. Nanosci. Nanotechnol. **15**, 4799–4805 (2015). https://doi.org/10.1166/jnn.2015.9817
28. J. Kalia, R.T. Raines, Hydrolytic stability of hydrazones and oximes. Angew. Chem. Int. Ed. **47**, 7523–7526 (2008). https://doi.org/10.1002/anie.200802651
29. T. Panczyk, L. Konczak, J. Narkiewicz-Michalek, G. Pastorin, Corking and uncorking carbon nanotubes by metal nanoparticles bearing ph-cleavable hydrazone linkers. theoretical analysis based on molecular dynamics simulations. J. Phys. Chem. C (2015). https://doi.org/10.1021/acs.jpcc.5b08383
30. S. Plimpton, Fast parallel algorithms for short-range molecular dynamics. J. Comput. Phys. **117**, 1–19 (1995). https://doi.org/10.1006/jcph.1995.1039
31. T. Panczyk, P. Szabelski, M. Drach, Implicit solvent model for effective molecular dynamics simulations of systems composed of colloid nanoparticles and carbon nanotubes. J. Colloid Interface Sci. **383**, 55–62 (2012). https://doi.org/10.1016/j.jcis.2012.06.035
32. M. Respaud, J.M. Broto, H. Rakoto, A.R. Fert, L. Thomas, B. Barbara, M. Verelst, E. Snoeck, P. Lecante, A. Mosset, J. Osuna, T.O. Ely, C. Amiens, B. Chaudret, Surface effects on the

magnetic properties of ultrafine cobalt particles. Phys. Rev. B. **57**, 2925–2935 (1998). https://doi.org/10.1103/PhysRevB.57.2925

33. A. Gavrin, C.L. Chien, Fabrication and magnetic properties of granular alloys. J. Appl. Phys. **67**, 938 (1990). https://doi.org/10.1063/1.346100
34. B.J. Hickey, M.A. Howson, D. Greig, N. Wiser, Enhanced magnetic anisotropy energy density for superparamagnetic particles of cobalt. Phys. Rev. B. **53**, 32–33 (1996). https://doi.org/10.1103/PhysRevB.53.32
35. S. Gubin, Y. Spichkin, Y. Koksharov, G.Y. Yurkov, A. Kozinkin, T. Nedoseikina, M. Korobov, A. Tishin, Magnetic and structural properties of Co nanoparticles in a polymeric matrix. J. Magn. Magn. Mater. **265**, 234–242 (2003). https://doi.org/10.1016/S0304-8853(03)00271-3
36. C.H. Chen, M.S. Walmer, M.H. Walmer, W. Gong, B.-M. Ma, The relationship of thermal expansion to magnetocrystalline anisotropy, spontaneous magnetization, and T[sub c] for permanent magnets. J. Appl. Phys. **85**, 5669 (1999). https://doi.org/10.1063/1.369835

Chapter 3
Phase Behavior of Liquids Embedded with Graphene Genealogic Tree Nanoparticles

Sergey Artemenko, Victoria Karnaukh and Victor Mazur

Abstract This work discusses the phase behavior of conventional liquids and their binary mixtures in the presence of graphene genealogic tree nanoparticles. An algorithm for evaluation of critical parameters shift after adding the nanoparticles to the pure liquid is applied to estimate critical point of nanofluid. It is argued that dimensionless thermodynamic surfaces of reference liquid and nanofluid with volume nanoparticle concentration less than 5% are coincided. A global phase diagram approach is proposed to evaluate a possible azeotropic states in binary mixtures after nanoparticles doping. The influence of graphene genealogic tree nanoparticles (carbon nanotubes—CNT, fullerenes—$C_{60,}$ and graphene flakes) on the liquid–liquid equilibria is discussed. The change in location of upper critical end point (UCEP) for liquid–liquid coexistence curve of the mixture of nitrobenzene and heptane and system of nitrobenzene, heptane and graphene genealogic tree nanoparticles is predicted.

3.1 Introduction

Nanofluids (NF) have received considerable attention due to their potential to enhance the thermal, chemical and physical properties of conventional working fluids [1, 2]. Knowledge the NF phase behavior is of immense interest to decode the

S. Artemenko · V. Mazur (✉)
Institute of Refrigeration, Cryotechnologies, and Eco-Power Engineering, Odessa National Academy of Food Technologies, 1/3, Dvoryanskaya Str, Odessa 65082, Ukraine
e-mail: victor.mazur@gmail.com

S. Artemenko
e-mail: sergey.artemenko@gmail.com

V. Karnaukh
Faculty of Engineering, Department of Food Engineering, Akdeniz University, Antalya 07058, Turkey
e-mail: kvita9@rambler.ru

L. A. Bulavin and A. V. Chalyi (eds.), *Modern Problems of Molecular Physics*, Springer Proceedings in Physics 197, https://doi.org/10.1007/978-3-319-61109-9_3

puzzle phenomena associated with novel and emergent nanotechnologies. Nevertheless, so far, there are neither experimental nor theoretical assessments in literature available evaluating the values of changes in the singularities for conventional liquids after nanoparticle doping. The results of this study present analyzes the phase behavior of liquids and binary mixtures embedded with graphene genealogic tree nanoparticles.

To predict the NF phase behavior we suggested that dimensionless thermodynamic surfaces of reference liquid and nanofluid with volume nanoparticle concentration less than 5% are coincided and we apply an algorithm for evaluation of critical parameters shift after nanoparticle adding for pure liquid in order to estimate critical point location of nanofluid. Shift of the carbon dioxide critical point in presence of the graphene genealogic tree nanoparticles (carbon nanotubes—CNT, fullerene—C_{60}, and graphene flakes) is evaluated. The critical temperature of the nanofluid varies insignificantly, while the critical density essentially depends on the density of nanoparticles.

Phase behavior of binary mixtures with nanoparticle presence is analyzed with global phase diagram technique as a most comprehensive system of mapping of the global equilibrium surface onto the surface of the critical parameters of components. This approach was selected to determine the possible types of phase equilibria in binary mixtures with nanofluids and provides some general ideas for universal phase diagrams visualization. Nanostructured materials change the singularity positions and consequently impact the phase behavior types of binary mixtures of nanoliquids due to the shift of critical points of the components.

To predict the azeotropy appearance in binary nanoliquids the global phase diagram for the one-fluid Redlich-Kwong equation of state model is used. An example of transition from the zeotropic R1234yf—R161 system to the most likely azeotropic state (the R1234yf—R161—graphene genealogic tree nanoparticles mixture) is considered here.

The impact of nanoparticles on the shift of three-phase equilibria in the II type of phase behaviour is provided for the nitrobenzene–heptane system. The changes in location of upper critical end point (UCEP) for liquid–liquid coexistence curve of nitrobenzene–heptane after adding graphene genealogic tree nanoparticles are predicted. NF phenomena look as a prospective pathway to create a new class of sustainable working fluids and bring such benefits like energy efficiency (e.g., improving heat transfer, reducing pumping power), lower operating costs, smaller/lighter systems (small heat exchangers) and cleaner environment (e.g., reducing heat transfer fluid inventory) [3, 4].

3.2 Impact of Nanoparticles on the Critical Point Shift

A critical point is the singular point of the pressure-density-temperature surface that designates conditions under which a liquid and its vapor phase can coexist. Knowledge of critical point (line) gives information about thermodynamic behavior

of pure substance (binary mixture). Nanoparticles change the intermolecular interactions between nanofluid components and shift the location of singularities. It is suggested the liquids with small impurities do not violate the corresponding state principle and the dimensionless thermodynamic surfaces of reference liquid and nanofluid coincide [5, 6].

The fundamental equations of state in reduced form [7, 8] are used to restore thermodynamic surface in vicinity of singular point. Compressibility factor (Z) of nanofluid in the range 0–5% volume concentrations φ of nanoparticles (np) was found via scaled reference fluid properties

$$Z = Z(\rho_{Cnf}/\rho,\ T/T_{Cnf}). \tag{3.1}$$

Critical parameters of nanofluid (ρ_{Cnf}, T_{Cnf}) were calculated from fundamental equation of state in vicinity of critical point. The density of nanofluid (nf) was determined via reference fluid density (rf) by standard approximation [9]:

$$\rho_{nf} = (1-\varphi)\rho_{rf} + \varphi\rho_{np} \tag{3.2}$$

To estimate the nanofluid critical parameters an algorithm from [5] was applied. From the fundamental EoS for reference liquid the p—ρ—T data in vicinity of critical point were generated to establish the fitting parameters in the power law equations [7]

$$\frac{\rho_\sigma}{\rho_c} - 1 = N_1\left(1 - \frac{T_\sigma}{T_c}\right) \pm N_2\left(1 - \frac{T_\sigma}{T_c}\right)^\beta \tag{3.3}$$

Here ρ_c and T_c are critical density and temperature; N_1, N_2, β are fitting parameters; ρ_σ and T_σ are density and temperature along saturation curve.

An (3.3) is valid both reference liquid and nanofluids only in the critical domain. The fitting parameters in (3.3) were restored from the ρ—T data for reference liquid and then used to estimate critical parameters of nanofluid. Reliability and accuracy of algorithm tested at limit $\varphi = 0$ to reproduce the critical points of reference liquids. The results of our calculations reproduce the EoS data from [7, 8] within experimental accuracy of density measurements for given substance.

Estimation of the CO_2 critical point change with different bulk density of nanoparticles: graphene genealogic tree (CNT—Fig. 3.1a, fullerenes—Fig. 3.1b, and graphene flakes—Fig. 3.1c).

The portrait of thermodynamic behavior near critical point for selected fluids was obtained via application of the fundamental equations of state [7, 8]. The variations of critical temperature and density after adding of different nanoparticles are provided in Table 3.1 and in Fig. 3.2. The growth of nanoparticle concentration leads to insignificant change of critical temperature for the nanoliquid CO_2 with graphene derivatives.

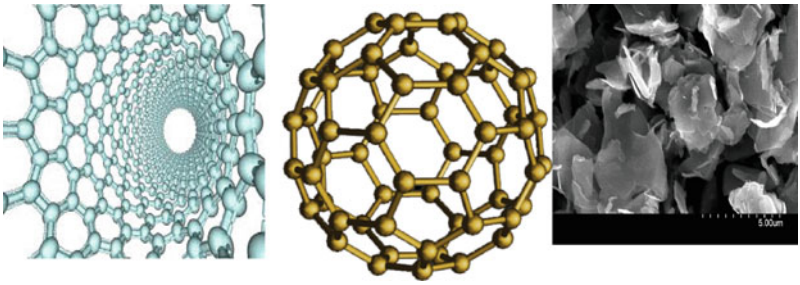

(a) $\rho_{CNT} = 1330$ kg/m^3 **(b)** $\rho_{C60} = 1650$ kg/m^3 **(c)** $\rho_G = 2230$ kg/m^3

Fig. 3.1 Graphene and its derivatives. (**a**) $\rho_{CNT} = 1330$ kg/m^3, (**b**) $\rho_{C60} = 1650$ kg/m^3, (**c**) $\rho_G = 2230$ kg/m^3

Table 3.1 Effect of graphene derivatives on the shift of critical temperature ($\Delta T_c = T_{cnf} - T_{cCO2}$) and density ($\Delta\ \rho_c = \rho_{cnf} - \rho_{cCO2}$)

Graphene derivatives	$\Delta\rho_c$, kg/m^3 at $\varphi = 1\%$	$\Delta\rho_c$, kg/m^3 at $\varphi = 5\%$	ΔTc, K at $\varphi = 1\%$	ΔTc, K at $\varphi = 5\%$
CNT	5.7	22.6	0.01	0.11
C_{60}	7.5	33.2	0.01	0.13
Graphene flakes	12.5	55.7	0.02	0.19

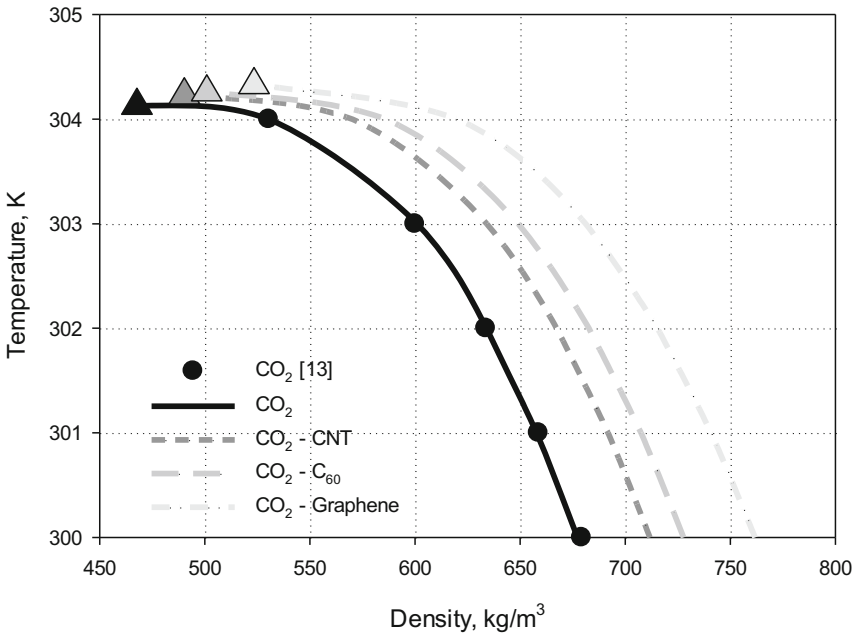

Fig. 3.2 Effect of graphene derivatives doping on position of the carbon dioxide critical point (triangles) and liquid–vapor transition

The change in the nanofluid critical density under the graphene derivatives impact is more significant and linearly dependent on the density of the implanted nanoparticles.

3.3 Azeotropy Phenomena in the Binary Nanoliquids

Global phase diagram is a convenient and effective tool to recognize azeotropy phenomena in binary mixtures. The limits of the critical azeotropy at $x_i \to 0$ or at $x_i \to 1$ is determined from azeotropy conditions

$$\mu_i^l = \mu_i^g, \quad i = 1, 2, \quad x_i^l = x_i^g \tag{3.3}$$

where μ_i and x_i are chemical potential and composition of ith component in the liquid (l) and gas (g) phases, correspondingly.

The system of thermodynamic equations defines a degenerated critical azeotrope line. Solution of this system gives the boundaries in global phase diagram between zeotropic (shaded region) and azeotropic [A (azeotropy), H (heteroazeotropy)] states in Fig. 3.3. For equal sized molecules ($Z_3 = 0$) the azeotropic borders are straight lines in the (Z_1, Z_2)-plane. To separate the azeotropic and zeotropic regions

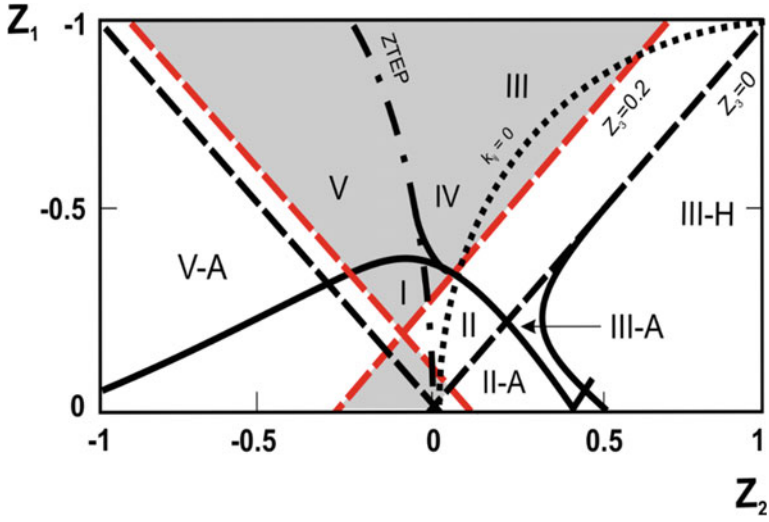

Fig. 3.3 Part of global phase diagram for the one-fluid Redlich-Kwong EoS model with different size molecules ($Z_3 = 0$, $Z_3 = 0.2$); Notations: ▬ tricritical line; ▬ ▬ azeotropic boundaries; ▪▪▪▪▪▪ the Lorentz-Berthelot combining rule; I–V types of phase behavior without azeotropic states; I-A–V-A types of phase behavior with azeotropic states; ZTEP is line of zero-temperature end points

on the global phase diagram the series of inequalities were developed. A corresponding relationship for the modified Redlich-Kwong EoS [10] was given in [11]:

$$Z_2 = \mp Z_1 - 0.67(1 \pm Z_1)\left(\frac{1 - Z_4}{1 \pm Z_3} - 1\right). \tag{3.4}$$

The dimensionless parameters of the Redlich-Kwong model were chosen according Deiters and Pegg [12]:

$$\begin{aligned} Z_1 &= \frac{d_{22} - d_{11}}{d_{22} + d_{11}}, \\ Z_2 &= \frac{d_{22} - 2d_{12} + d_{11}}{d_{22} + d_{11}}, \\ Z_3 &= \frac{b_{22} - b_{11}}{b_{22} + b_{11}}, \\ Z_4 &= \frac{b_{22} - 2b_{12} + b_{11}}{b_{22} + b_{11}} \end{aligned} \tag{3.5}$$

where

$$d_{ij} = \frac{T_{ij}^* b_{ij}}{b_{ii} b_{jj}}, \quad T_{ij}^* = \left(\frac{0.204\, a_{ij}}{R b_{ij}}\right)^{2/3}.$$

The adjustable binary interaction parameters k_{ij} and l_{ij} are determined in classical form via the Lorentz-Berthelot combining rules ($k_{ij} = l_{ij} = 0$):

$$a_{ij} = (1 - k_{ij})\sqrt{a_{ii}\, a_{jj}}, \quad b_{ij} = (1 - l_{ij})\frac{b_{ii} + b_{jj}}{2}. \tag{3.6}$$

The intersection of straight lines determines the occurrence of double azeotropy phenomenon [10].

As an example of nanoparticles impact on the phase behaviour of binary mixture, we considered the zeotropic system R1234yf—R161 with low global warming potential as a possible replacement of obsolete refrigerant R134a. On the global phase diagram a mixture of interest that belongs to the II type of phase behavior corresponds to the point with coordinates $Z_1 = -0.03$, $Z_2 = -0.05$. The EoS parameters for both low-boiling compound R1234yf and R161 were taken from [13]: $T_C = 367.85$ K, $\rho_C = 485.55$ kg m^{-3} and $T_C = 375.3$ K, $\rho_C = 301.81$ kg m^{-3}.

Global phase diagrams of binary fluids represent the boundaries between different types of phase behaviour in a dimensionless parameter space. In a real p—T—x space, two relatively similar components usually have an uninterrupted critical curve between the two critical points of the pure components. Here we consider phase behavior of the R1234yf—R161 zeotropic blend and R1234yf—R161—graphene genealogic tree nanoparticles as most likely azeotropic system that are recognized as low global warming potential (GWP) refrigerant to replace the R134a

refrigerant. The binary interaction parameters were fitted by the Lorentz-Berthelot combination rule ($k_{ij} = l_{ij} = 0$). The results of phase equilibria calculations for different temperatures in the pressure—composition diagrams demonstrate that the R1234yf doped with the CNT, C_{60}, and graphene nanoparticles, correspondingly increases the critical temperature of pure low-boiling component until 369 K. This shift conduces to transformation from zeotropic state to azeotropic state ($Z_1 = -0.03$, $Z_2 = +0.05$).

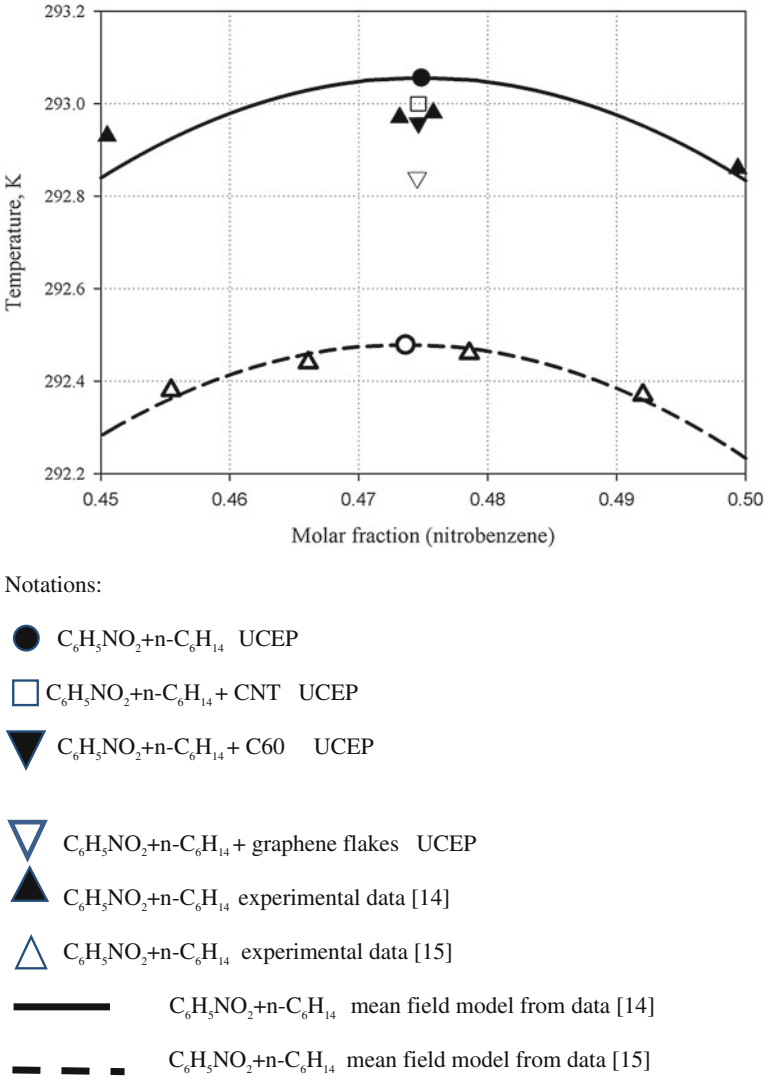

Fig. 3.4 Liquid–liquid coexistence curves and UCEP location of the binary fluids nitrobenzene–heptane and nitrobenzene–heptane–nanoparticles

3.4 Impact of Nanoparticles on the Shift of Liquid–Liquid Equilibria

A liquid-liquid critical point (LCCP) is the endpoint of a liquid-liquid phase transition line is observed in all types of phase behavior excluding I type. LCCP represents a critical point where two types of local structures coexist. Influence of nanoparticles of graphene genealogic tree on the liquid–liquid equilibria we have analyzed for the II type of phase behaviour the binary nitrobenzene–heptane blend. The both the Redlich-Kwong and any other mean field models cannot simultaneously describe experimental data near critical point and at low temperatures. The more exact description of experimental data from [14] and [15] in the near-critical region was preferred. Coefficients k_{ij} (l_{ij}) are 0.01824 (0.01392) for nitrobenzene–heptane and nitrobenzene–heptane–nanoparticles were determined. Deviations of mean field model from experimental data for binary mixtures of interest are provided in Fig. 3.4. The changes of coefficients k_{ij} and l_{ij} displace the liquid–liquid coexistence curve of binary mixture and location of upper critical end point (Fig. 3.4). Experimental data processing gives values of the upper critical end point (UCEP) for the liquid–liquid coexistence curve of the binary fluids nitrobenzene–heptane and nitrobenzene–heptane–nanoparticles: $T_{UCEP} = 293.0$ K, $x_{UCEP} = 0.519$ and $T_{UCEP} = 292.5$ K, $x_{UCEP} = 0.531$, correspondingly. The adding of graphene genealogic tree nanoparticles leads to intermediate values for UCEP (Fig. 3.4).

3.5 Conclusion

This study demonstrates existing relationships between the critical point shift in conventional liquids and phase equilibria phenomena in mixtures embedded with graphene genealogic tree nanoparticles. The results obtained represent very useful information for scientists and engineers working in the area of nanotechnology applications. The critical point shift for carbon dioxide with different types of nanoparticle doping: (CNT, C_{60}, and graphene flakes) is estimated. Global phase diagram concept is applied to restore possible phase diagrams as functions of critical density and temperature of mixture components.

It is proven the azeotropy phenomena can arise if nanoparticles added to zeotropic blends. As an example, transition from the zeotropic mixture R1234yf—R161 to the azeotropic mixture R1234yf—R161—nanoparticles pretended to be replacement the refrigerant R134a is discussed.

The shift of three phase (liquid–liquid–gas) equilibria for the II and III types of phase behavior is considered for the nitrobenzene ($C_6H_5NO_2$)—heptane (n-C_6H_{14}) system. The liquid–liquid coexistence curve is distorted under nanoparticles impact

of the graphene derivatives. The effect of nanoparticles leads to a decrease in the temperature of the upper critical end point as a function of the density of the nanoparticles. Maximum decreasing UCEP temperature is observed for graphene flakes doping.

References

1. R.L. Smith Jr., Z. Fang, Properties and phase equilibria of fluid mixtures as the basis for developing green chemical processes. Fluid Phase Equilib. **302**, 65–73 (2011)
2. C. King, D. Pendlebury, WEB of knowledge— "research fronts 2013" (2013), http://sciencewatch.com/sites/sw/files/sw-article/media/research-fronts-2013.pdf
3. S.A. Angayarkanni, J. Philip, Review on thermal properties of nanofluids: recent developments. Adv. Coll. Interface. Sci. **225**, 146–176 (2015)
4. Y. Prylutskyy, S. Durov, L. Bulavin, et al., Structure and thermophysical properties of fullerene C60 aqueous solutions. Int. J. Thermophys. **22**(3) (2001)
5. D. Nikitin, V. Mazur, Thermodynamic and phase behaviour of fluids embedded with nanostructured materials. Int. J. Therm. Sci. **62**, 44–49 (2012)
6. S. Artemenko, V. Mazur, O. Vasilieva, Thermodynamic and phase behavior of nanofluids, in *Proceedings in Physics,* (Springer, 2015), pp. 313–333
7. E. Lemmon, R. Span, Short fundamental equations of state for 20 industrial fluids. J. Chem. Eng. Data **51**, 785 (2006)
8. R. Span, W. Wagner, A new equation of state for carbon dioxide covering the fluid region from the triple-point temperature to 1100 K at pressures up to 800 Mpa. J. Phys. Chem. Ref. Data **25**(6), 1509 (1996)
9. J. Avsec, M. Oblak, The calculation of thermal conductivity, viscosity and thermodynamic properties for nanofluids on the basis of statistical nanomechanics. Int. J. Heat Mass Trans. **50** (21–22), 4331 (2007)
10. G. Soave, Equilibrium constants from a modified Redlich-Kwong equation of state. Chem. Eng. Sci. **27**, 1197–2003 (1972)
11. S. Artemenko, V. Mazur, Azeotropy in the natural and synthetic refrigerant mixtures. Int. J. Refrig **30**, 831–839 (2007)
12. U.K. Deiters, J.L. Pegg, Systematic investigation of the phase behavior of binary fluid mixtures. I. Calculations based on the Redlich-Kwong equation of state. J. Chem. Phys. **90**, 6632–6641 (1989)
13. E. Lemmon, M. Huber, M. McLinden, NIST reference fluid thermodynamic and transport properties—REFPROP. version 9.1. (NIST, Boulder, 2013)
14. P.V. Borzenkov, V.P. Zhelezny, The nanoparticles effect on the liquid–liquid phase equilibrium parameters. Part1. Refrig. Eng. Technol. **6**, 4–9 (2014)
15. J. Shelton, D. Balzarini, Coexistence curve of the binary fluid nitrobenzene–heptane. Can. J. Phys. **59**, 334 (1981)

Part II
Ionic and Ionic-Electronic Liquids

Chapter 4
Peculiarities of NMR Relaxation in Ionic Liquids: Difficulties in Interpretation and Novel Possibilities

Vladimir V. Matveev and Konstantin V. Tyutyukin

Abstract An applicability of ^{13}C and ^{1}H relaxation rates ($1/T_1$) to direct calculations of the characteristic reorientation time (τ_c) in imidazolium-based ionic liquids has been analyzed. It has shown that ^{13}C NMR relaxation technique can be applied to ionic liquids as successfully as it took place for other liquid systems and allows one to get τ_c values for each carbon directly. The corresponding ^{1}H data are affected by dipole-dipole interaction only at "higher temperature" range while at lower temperatures spin-diffusion process controls the proton relaxation. Both carbon and hydrogen $1/T_1$ dependences are suitable for calculation of τ_c and reveal equal numerical values for a number of functional groups of [emim]Ac at the proper temperature range. On the other hand, ^{1}H relaxation curves of some functional groups allow one to detect motions, unobservable in the carbon relaxation and, thereby, to extract more information concerning details of the dynamics of the $[amim]^+$ cations.

4.1 Introduction

For many decades, NMR T_1-relaxation has been used successfully to study a variety of fluid systems, including both pure liquids and various solutions, see e.g. [1–3] and references within. In the most cases one needs to obtain a temperature dependence of the $1/T_1$ with one or more maxima, and this dependence can be transformed to the temperature dependence of the characteristic reorientation time (τ_c) for each chemical/functional group of the system under investigation.

During 2 or 3 last decades a new class of liquid systems drew much attention, and the systems are known now as "Ionic Liquids" (*ILs, RTILs*). A lot of reviews were dedicated both to the unique properties of ionic liquids [4–6] and to results of an application of the NMR technique to ILs [7–13]. Keeping in mind these reviews the main purpose of this work was not a comprehensive survey of all the publi-

V. V. Matveev (✉) · K. V. Tyutyukin
St. Petersburg State University, 199034 Saint Petersburg, Russia
e-mail: v.matveev@spbu.ru; vmatveev@nmr.phys.spbu.ru

L. A. Bulavin and A. V. Chalyi (eds.), *Modern Problems of Molecular Physics*,
Springer Proceedings in Physics 197, https://doi.org/10.1007/978-3-319-61109-9_4

cations but a discussion of some trends in the application of NMR, especially of NMR relaxation, to understanding of structure and dynamics of ILs of various kinds with focusing on some differences/problems appearing during an evaluation of the NMR relaxation data in ILs. An accent has been made on critical analysis of common approach to the interpretation of ^{13}C T_1 relaxation data for imidazolium-based ILs because for these systems an erroneous interpretation is replicated for ca. last 15 years.

In view of the above only articles directly related to the designated task i.e., those connected to carbon or proton relaxation in ionic liquids of [amim]X kind, were cited in full (within the limits of our knowledge). Of the rest of the literature, only articles over the last 2–3 years were cited as well as some articles from previous years which were not included in the reviews listed above.

4.2 Basics of the Theory of NMR T_1 Relaxation

First, we would like to recall briefly the basics of NMR relaxation for fluid systems taking into consideration that similar information was already included in a number of recent reviews and textbooks. In particular for the case of ^{1}H and ^{13}C nuclei the dipole-dipole interaction is the main one which affects the relaxation rate [1–3].

For the theoretical description of T_1 frequency and/or temperature dependences the Bloembergen-Purcell-Pound theory (further BPP) is usually used. The BPP as well as the other NMR relaxation theories is based on the concept of spectral density function, $J(\omega, \mathbf{T})$. This function generally can be written using a set of relaxation times, τ_i, and their contributions, C_i; note that the sum of all C_i equals 1.

$$J(\omega, \mathbf{T}) = \sum_i \frac{C_i \tau_i(\mathbf{T})}{1 + (\omega \tau_i(\mathbf{T}))^2}, \tag{1}$$

Here ω is a cyclic resonant frequency ($2\pi\upsilon_0$) for the nucleus investigated.

In the case of dipole-dipole mechanism of relaxation with one correlation time τ_c this theory reduced to expressions (2) for ^{13}C and (3) for ^{1}H [1–3, 14–16].

$$\frac{1}{T_{1C}}(\omega_C, \mathbf{T}) = s_C^2 A_0 \left(\frac{6\tau_c(\mathbf{T})}{1 + (4.97\omega_C \tau_c(\mathbf{T}))^2} + \frac{\tau_c(\mathbf{T})}{1 + (2.97\omega_C \tau_c(\mathbf{T}))^2} + \frac{3\tau_c(\mathbf{T})}{1 + (\omega_C \tau_c(\mathbf{T}))^2} \right), \tag{2}$$

$$\frac{1}{T_{1H}}(\omega_H, \mathbf{T}) = s_H^2 A_0 \left(\frac{\tau_c(\mathbf{T})}{1 + (\omega_H \tau_c(\mathbf{T}))^2} + 4\frac{\tau_c(\mathbf{T})}{1 + (2\omega_H \tau_c(\mathbf{T}))^2} \right). \tag{3}$$

where ω_H and ω_C—cyclic resonant frequency ($2\pi\upsilon_0$) for ^{1}H and ^{13}C, respectively; s_c^2 and s_H^2 (≤ 1) are so called order parameters which will be discussed later; A_0 is a

constant which does not depend on temperature and frequency. For hydrogen and carbon nuclei this constant is given by expressions (3) and (4):

$$A_0(\mathrm{H}) = \frac{3}{10}\left(\gamma_{\mathrm{H}}^4 \hbar^2 / r_{HH}^6\right), \tag{4}$$

$$A_0(C) = \frac{3}{10}\left(\gamma_C^2 \gamma_H^2 \hbar^2 / r_{CH}^6\right), \tag{5}$$

where $\hbar$ is the reduced Plank constant ($h/2\pi$), r_{HH} is the distance between the interacting H-atoms, r_{CH} is a length of the C–H bond, γ_{H} and γ_{C} are magnetogyric ratios for ^{1}H and ^{13}C nuclei.

Formulas (2) and (3) describe a relaxation under interaction of two isolated nuclei. The theory considering interaction of several nuclei leads to quite complicated formulas however, it appears that rather good approximation turns out multiplication of the right part of the (2) and (3) by number of pair interactions of the nucleus with an environment (interacting couples), and this approach will be used in further calculations. Only the nearest neighbor spins were thus considered due to a strong dependence of the dipole-dipole interaction intensity on the distance (r^{-6}).

Expressions (2) and (3) describe a dependence of the relaxation rates on the correlation time (τ_c) and resonance frequency (ω_H or ω_C). There are several procedures in order to transform $1/T_1$ values to τ_c magnitudes. Let us discuss them in more detail.

The simplest way is to use the ratio $1/T_1 = constant * \tau_c$ which is valid at so-called "extreme narrowing" case, i.e. at $\tau_c\omega \ll 1$. This situation is common for systems with low viscosity and/or at not high working frequency, and it was used for a lot of pure liquids, liquid mixtures, and electrolyte solutions. However in the case of ionic liquids, due to much higher viscosity, this procedure is often insufficient and can even lead to absolutely wrong results.

Another known procedure is based on the use of the total temperature dependence. In this case an achievement of the $1/T_1$ maximum point is extremely essential, since at that point the τ_c magnitude can be directly calculated using (6) and (7):

$$\tau_c\omega_H = 0.616, \tag{6}$$

$$\tau_c\omega_C = 0.791, \tag{7}$$

for hydrogen and carbon, respectively [1–3, 14]. At the same time the y value at the point of maximum allows an independent determination of the constant (s^2A) in expressions (2) or (3) hence, a further calculation of τ_c at any temperature.

Experimentally specified dependences can be obtained by "scanning" of $1/T_1$ relaxation rates on temperature, and for their approximation one may use expressions (2) or (3) in common with standard Arrhenius dependence of the correlation time

$$\tau_c(\mathbf{T}) = \tau_0 \exp(E_a/R\mathbf{T}), \tag{8}$$

where E_a—is an activation energy for this type of movement, R—the gas constant, τ_0 (so-called "τ_c at zero **T**")—the parameter which isn't making clear physical sense. At approximations of experimental dependences A_0, E_a и τ_0 are commonly used as adjustable parameters.

The approach described above is rather effective and is widely used for the analysis of orientation mobility of various liquid systems including ionic liquids. A shortcoming of the approach is a postulation of the τ_c Arrhenius dependence with one energy of activation (5) for the whole temperature range studied while it is well known that for many liquid systems (some pure liquids, solutions and so forth) such approach is unfair.

At the same time it is obvious from (2) and (3) that $1/T_1$ experimental dependences can be directly counted in values of the correlation times, and, thereby, give valid τ_c dependences on temperature. In practice, however, there are a number of difficulties. First, the numerical values of A_0 are known with insufficient accuracy because of the strong dependence on the exact r_{HH} and r_{CH} distances values in a liquid or solution. Second, an introduction of the $s^2 \leq 1$ coefficient which takes into account possible contributions to the relaxation rates from other molecular movements in complex molecules is needed for some cases. In particular, according to (1), the $J(\omega, \boldsymbol{T})$ in (2) is a combination of various contributions with different τ_i values reflecting the nucleus reorientation. For two different correlation times e.g. τ_{c1} and τ_{c2}, (1) transforms to Woessner "anisotropic rotation" model [15, 16] or to Lipari-Szabo "model-free" approach [17]. Both models predict a function with two maxima but the experimental curves are often able to reflect only a part of the whole function because of temperature and/or frequency limits i.e., only one of two possible maxima is observed. Therefore the dependence might look like a curve with only maximum. However factors c_1 and/or c_2 in (1) and corresponding factors in (2) and (3) are unknown, may be sufficiently less than 1, and therefore a direct calculation of τ_c may lead to wrong τ_c values. In this regard rather wide circulation was received by a method of measuring of relaxation times in so-called "dispersive" area, i.e. in the area which is including $1/T_1$ maximum. It allows one to determine a τ_c value in the maximum point directly using ratios (6) and (7) and not to demand a preliminary knowledge of the A_0 (or s^2A_0). On the contrary, the last value can be independently determined from $1/T_1$ magnitude at the point of maximum.

Thus, the foregoing analysis revealed, that each of the existing procedures used for a conversion of relaxation rates to the correlation times (the characteristic times of the rotational reorientation) contains approximations that require the verification in each individual case. Nevertheless, the τ_c magnitudes obtained are well suited for characterization of the average ion mobility as a whole and of each functional group, for which a separate line exists in the NMR spectrum.

Experimental

Three pure ionic liquids: [bmim]PF_6, [bmim]BF_4, and [emim]Ac were received from Sigma-Aldrich and used without further purification. All NMR measurements were carried out using NMR AVANCE-400 spectrometer at resonance frequencies (f_0) 100 MHz for ^{13}C nuclei and 400 MHz for ^{1}H ones.

4.3 Carbon $1/T_1$ Temperature Dependences

Regular publications on measuring the relaxation rates in ionic liquids started to appear from the beginning of the 90s, and most of them are already reflected in the reviews and books over the years. It is useful to note that many of pure ILs, especially the imidazolium-based ones (see above), are very suitable for investigation by NMR relaxation due to their much higher viscosity comparing to conventional pure liquids and electrolyte solutions. As the result a lot of investigations were made using ^{13}C NMR, see reviews above. Some of the most recent works will be also cited at the end of the paper. The advantages of using the carbon resonance compared to hydrogen one look almost evident, since carbon is included in the cation skeleton and therefore directly reflects the cation mobility while the hydrogen relaxation can mask a relatively slow reorientation of the cation due to the additional rapid rotation of CH_n-groups.

Probably the first regular investigations of ^{13}C relaxation rates, $1/T_{1C}$ was made by Carper with coworkers in several imidazolium-based ILs [7, 18–22]. Indeed, these authors carried out measurements of temperature dependences of $1/T_1$ for ^{13}C nuclei in $[amim]^+$ cations, showed that these dependences correspond to the expected ones (2), and calculated numerical magnitudes of the reorientation times (τ_c) for each group in the investigated ILs. Up to now these papers are cited in practically all reviews (including e.g. a review of 2016 [13]) as the basic works in the topic. However a number of questions and/or problems appeared if one decided to penetrate deeper into the interpretation procedure. So we reanalyzed ones more both the data and the interpretation procedure of the Carper's group approach and would like to demonstrate below that some of the authors' key assumptions used in the τ_c calculation were wrong.

First, the authors reported about non-monotonic temperature dependence of the characteristic time (hereinafter correlation time, τ_c) for the imidazolium-ring carbons reorientation which appeared after direct calculations using (2), see Fig. 4.2 (Fig. 2 from [20]).

To try to explain and understand this non-physical dependence authors attributed the result to a strong influence of the chemical shift anisotropy (CSA) on ring carbons relaxation and suggested to use nuclear Overhauser effect (NOE) experiments in order to reach correct results, i.e. monotonic τ_c increasing with the decreasing of temperature. To agree with the procedure one should declare at least three assumptions that require an additional verification:

(i) Using (2) for direct transformation of $1/T_{1C}$ dependences to τ_c ones reveals wrong results namely, non-monotonic temperature dependences of τ_c;
(ii) A reason of (i) is a fact that $1/T_{1C}$ values are not of pure dipole-dipole origin but contain a sufficient contribution from CAS interaction, whereby the (2) ceases to be valid.
(iii) NOE experiments require for right transformation of experimental $1/T_{1C}$ values to τ_c ones.

Since the CSA contribution is proportional to the permanent magnetic field the assumption (ii) could be checked directly. Measuring the spin-lattice relaxation time (T_1) at two different magnetic fields [23] revealed undoubtedly an absence of the CSA contribution for any carbon of the $[amim]^+$ cation (the CSA contribution was found less than 2%). As the result, this led to a situation where well-known and successfully used NMR relaxation approach could not be applied to ionic liquids due to unknown reasons. The situation was unclear up to 2014 when the assumption (i) was rejected [14]. And let us discuss this procedure in more detail.

The authors [14] recalculated τ_c values by following the same procedure as in the works [7, 18–22] i.e. using the (2) for direct transformation a $1/T_1$ magnitude to the τ_c value. Initially non-monotonic τ_c dependences were obtained similar to those obtained earlier, see Fig. 4.2. However, a deeper analysis revealed an error in the calculations. Namely (2) has two real roots at each temperature and both roots are positive. Temperature dependences of the roots, i.e. of the calculated τ_c values, are shown in Fig. 3 from [14].

The root#1, marked by the dotted line, shows an increase of the molecular mobility under temperature *increasing*, i.e. corresponds to conventional models of molecular mobility. The second root, otherwise, shows an increase of the molecular mobility under temperature *decreasing*. It contradicts any existing theory and therefore this root doesn't make physical meaning. It is worth emphasizing that such situation is not a feature of only ionic liquids as similar solutions of the (1) with two roots will turn out for any fluid system where maximum in the $1/T_1$ temperature dependence is observed, e.g. in viscous liquids or concentrated electrolytes solutions.

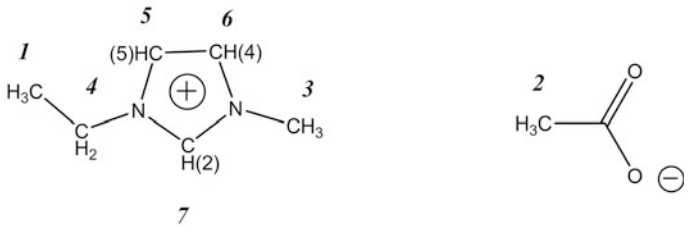

Fig. 4.1 Demonstrates a chemical structure of the $[emim]^+$ cation of the $[emim]CH_3COO$ ([emim]Ac) ionic liquid (IL) from the most common family of the imidazolium-based ILs. Numbering of lines in the Figure will be used further to describe the ^1H relaxation in [emim]Ac

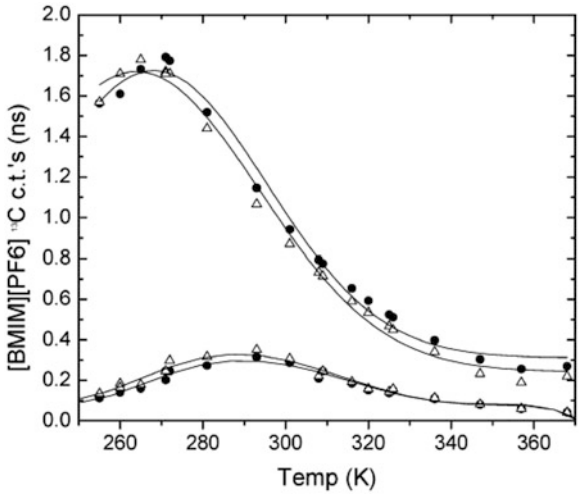

Fig. 4.2 From [20]. Corrected (upper curves) and initial (lower curves) correlation times (ns) for [BMIM][PF6] ionic liquid versus temperature. (bulls) Imidazolium ring C2 carbon; (open triangles) average of imidazolium ring C4 and C5 carbons. Reproduced with permission

Coming back to calculations in the [20], the authors used the smaller root magnitude at *all* temperatures as marked in Fig. 4.3 by the red line and thus calculated wrong values of the τ_c at lower temperatures. On the contrary, if one uses the root#1 in the whole temperature range, then calculations lead to conventional temperature dependence of τ_c for all spectral lines. Hence, $1/T_1$ data are enough for

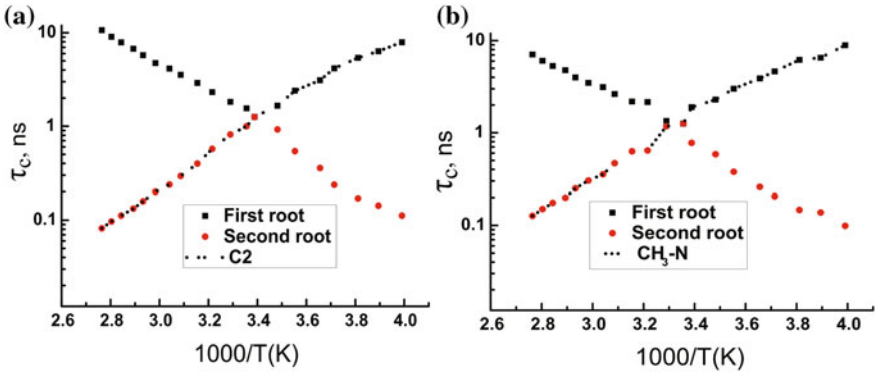

Fig. 4.3 From [14]. Roots of (2) for two carbons of the $[bmim]^+$ cation; left panel corresponds ring carbon C2, right panel—non-ring carbon CH_3–N. Correct correlation times correspond to the root marked by dot lines. More detail see in the text. Reproduced with permission

calculation of right τ_c magnitudes and no additional experimental measurements, such as NOE, required.

Hence, the results of [14] have shown that ^{13}C NMR relaxation technique can be applied to ionic liquids as successfully as it took place for other liquid systems.

On the other hand, it is reasonable to expect that NOE data in the same systems can provide additional information on the systems properties under the condition of accurate analysis. But this task is not still carried out.

4.3.1 *Comparison of the Behavior of Analogous Groups in the Studied ILs*

At the next step one may try to compare ^{13}C relaxation curves for the analogous groups in a few ILs namely, [bmim]PF_6, [bmim]BF_4, and [emim]Ac. For [bmim]PF_6 the curves were firstly obtained by Carper with coauthors [18–20]. Later other group [14] repeated the measurements and found that Carper's group experimental data had no errors and could be used without any correction. We carried out also additional measurements for [bmim]BF_4 and [emim]Ac ILs. To provide an overall picture of differences in T_1 relaxation, the comparison of $1/T_1$ temperature dependencies, is presented in Figs. 4.4 and 4.5 [24].

As follows from the Figures, each group reveals similar dependences in all three ILs, and the dependence corresponds to the expression (2), i.e. looks as a curve with one minimum. That is, the comparison of the carbon relaxation curves does not show a difference in the behavior of studied liquids. For [emim]Ac IL the carbon data allowed an observation of the anion as well. The $1/T_1$ curves of acetate carbons (Fig. 4.4) reveal similar shape, close T_{max} values but significantly different magnitudes of $1/T_1$. This set of the data allows one to assume that COO-carbon

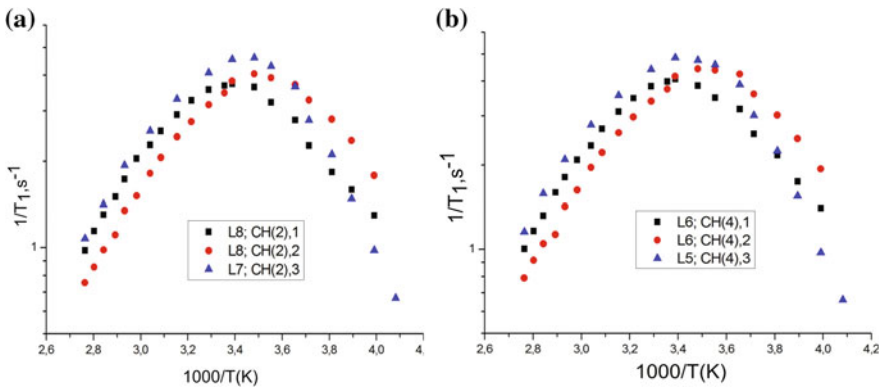

Fig. 4.4 Comparison of behavior of $1/T_1$ temperature dependencies for C2 (**a**) and C4 (**b**) ring carbons in three ILs: [bmim]PF_6, [bmim]BF_4, and [emim]Ac

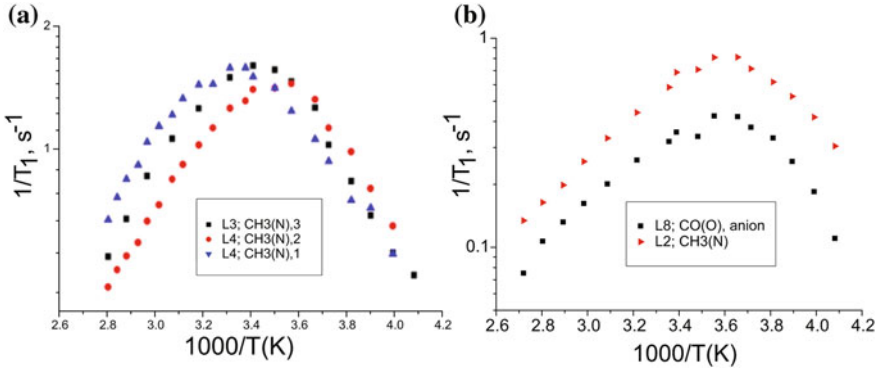

Fig. 4.5 Comparison of $1/T_1$ temperature dependencies for CH_3-N carbon in three ILs, [bmim]PF_6, [bmim]BF_4, and [emim]Ac (**a**) and for two carbons of the CH_3COO^- anion in [emim]Ac ionic liquid

relaxation is also affected by dipole-dipole interaction between a carbon atom and hydrogen ones while smaller $1/T_1$ values of the COO-carbon correspond to higher distances between this carbon atom and hydrogen ones in the anion CH_3-group.

Both carbons of the acetate anion have the maximum of relaxation rate at close temperatures (277.8 ± 3.5 K), relatively less than ring carbons. On one hand this is an evidence of the anion rotation (reorientation) as a whole so that the intramolecular (anisotropic) rotation of the methyl group does not make any significant contribution into the average correlation time of the methyl carbon. On the other hand a relatively high mobility of the anion may be a consequence of the incomplete association of the counter-ions. As a result, the correlation time which is determined from the position of the $1/T_1$ relaxation rate maximum represents the weighted average value between the reorientation time of ion pair and of the characteristic time of the faster process, rotation of the dissociated anion.

4.3.2 *Correlation Times and Activation Energies of Different Groups*

As noted above, a relative position of the maximum itself characterizes a mobility of the cation groups. Namely, a lower T_{max} corresponds to the higher mobility. However, it is possible a direct calculation of τ_c at each temperature using the corresponding $1/T_1$ at current **T** and the s^2A_0 value calculated at T_{max}. A more detailed procedure was described in [14], and the results are presented on the Table 4.1. In order to demonstrate an adequacy of the calculation procedure the calculated τ_c values for both carbons of the CH_3COO^- anion are shown in Fig. 4.6. As evident from the Figure the values are much closer despite a strong difference in

Table 4.1 Fitting parameters for ^{13}C data: Correlation times, activation energies and T_{max} positions of different groups in three ionic liquids

Group	E_a, kJ/mol	T_{max}, K	τ_c at 273 K, ns	Group	E_a, kJ/mol	T_{max}, K	τ_c at 273 K,[b] ns
CH_3-buthyl/ethyl	19.8/	–/	–/	CH(4)	28.3/	274/	1.26/
					37.0/	295/	2.9/
	17.9/	–/	–/		34.3	295	2.76
	19.3[a]	–	–				
CH_2-gamma	21.7/	257/	0.25/	CH(5)	28/	274/	1.26/
	23.8/	257/	0.56/		33.8/	295/	2.90/
	–	–	–		32.5	287	2.93
CH_2-beta	24.1/	250/	0.61/	CH(2)	28.5/	281/	1.52/
	26.1/	263/	0.82/		37.4/	295/	3.11/
	–	–	–		33.0	287	2.82
CH_3-N	28.0/	281/	1.54/	CH_3-acetate	26.3	274	1.26
	30.8/	298/	3.90/				
	32.3	295	2.97				
CH_2-alpha	26.7/	274/	1.26/	COO-acetate	24.0	281	1.46
	34.5/	295/	2.58/				
	33.8	287	1.95				

Comments to the table

[a][bmim]BF4/[bmim]PF6/[emim]Ac

[b]Arrhenius approximation does not hold at 273 K, so we present values of correlation times at 313 K for more correct comparison

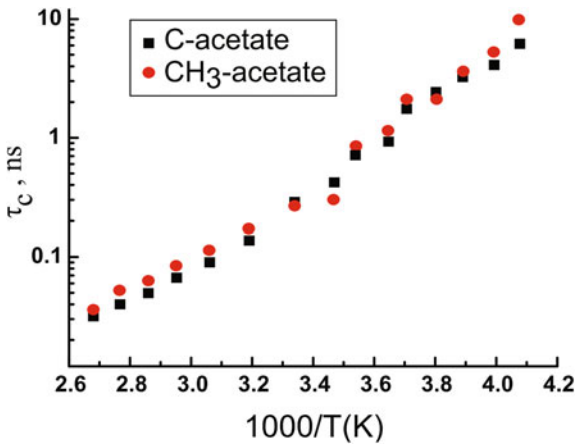

Fig. 4.6 Comparison of behavior of τ_c temperature dependencies for CH_3- and COO-carbons of the CH_3COO^- anion

the $1/T_1$ magnitudes, Fig. 4.5b. Thus it supports a conclusion about the anion reorientation as a **whole.**

The data from Table 4.1, i.e. ^{13}C correlation times reveal a few trends which are valid for all studied ILs. First, the τ_c values in the IL cations demonstrate similar

dependences on a group location: (i) correlation time values of butyl chain groups increase moving towards the imidazolium ring of [bmim]BF_4 and [bmim]PF_6 ILs, (ii) the longest correlation time for every IL is observed for CH_3-methyl group, (iii) CH-ring carbons, CH_2-N, and CH_3-N groups have close correlation times and thus characterize a mobility of the cation as a whole. Partly these trends were already observed and discussed in the literature.

4.4 Comparison of Information Obtained from ^{1}H and ^{13}C NMR Relaxation Data

As discussed above, the ^{13}C relaxation looks more suitable to test the cation reorientation. On the other hand ^{1}H measurements require much less spectrometer time and efforts. Therefore it was interesting to understand the limits up to which one can use ^{1}H data in order to characterize both the cation reorientation as a whole and the reorientation of each functional group. To check the idea we have also analyzed ^{1}H relaxation data for the same ILs.

4.4.1 General Comparison

First one can compare temperature dependences of the ^{13}C and ^{1}H relaxation rate. As it was already mentioned above the $1/T_1$ curves for all carbon nuclei correspond to the expected dependence (2) over the entire temperature range. For ^{1}H relaxation such kind of the dependence is observed only for the "high-temperature" part of the curves, and in the "low-temperature" area (below ca. 260 K) $1/T_{1H}$ values become practically independent of temperature and identical for all lines (see Fig. 4.7a and b).

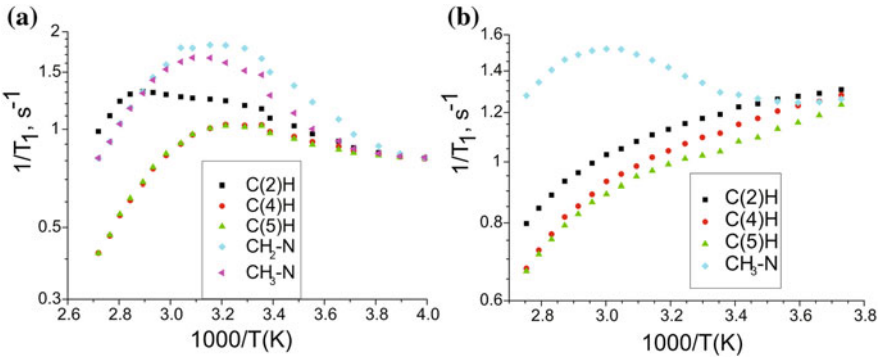

Fig. 4.7 Hydrogen $1/T_1$ temperature dependences for some groups of [emim]CH_3COO (**a**) and [bmim]PF_6 (**b**) ionic liquids

Such behavior was attributed to the spin-diffusion interaction which becomes the main mechanism of ^{1}H relaxation at low temperatures (under low molecular mobility), [25]; see also [26], where the same effect was observed for $1/T_{1C}$ but in much smaller measure.

Another apparent difference between carbon and proton relaxation manifests itself in a deviation of some proton curves from the (3). We will return to this effect later and now let us try to compare τ_c values obtained from ^{1}H and ^{13}C data using the groups with similar $1/T_{1C}$ and $1/T_{1H}$ shapes. And we would like to start from a number of functional groups of the [emim]Ac IL following [25].

4.4.2 Carbon-Hydrogen Comparison for [Emim]Ac

The ^{1}H NMR spectrum of the [emim]CH_3COO IL is well known, see e.g. [25], and lines numbering coincides numbers in Fig. 4.1 (above) i.e. follows the chemical shift (δ) increasing. There are 5 groups for which the $1/T_1$ maximum was observed both in ^{1}H and ^{13}C dependences namely: CH_3(N), CH_3(O), CH_2(N) and two groups of the imidazolium ring: C(4)H and C(5)H; correspond spectrum lines: 2–6. These proton $1/T_1$ dependences are similar to ^{13}C ones at least for the higher temperature range where ^{1}H relaxation affects by the dipole-dipole interaction, see also [25].

Calculations of τ_c values for ^{1}H were executed using the same procedure as for the carbon relaxation rates, see above. Two examples are shown in Fig. 4.8, pictures for other groups are similar [25].

As evident from the Fig. 4.8, the τ_c values calculated using ^{1}H and ^{13}C data coincide for ring groups as well as for aliphatic ones in the "high temperature" range. The same situation is valid for other functional groups mentioned above, see in more detail in [25], and this fact proves an adequacy of the used approach for the determination of characteristic times of the cation reorientation in the [emim]Ac

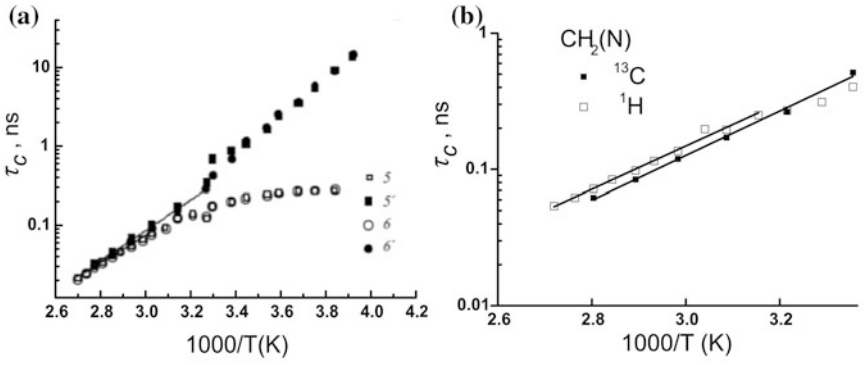

Fig. 4.8 Comparison of τ_c curves calculated from ^{13}C and ^{1}H data for ring C(4)H/CH(5)H (**a**) and CH_2-N (**b**) groups of the cation in the [emim]Ac ionic liquid

ionic liquid. It means in turn that proton $1/T_1$ data as well as ^{13}C ones are suitable for calculation of τ_c numerical values for a number of functional groups of [emim]Ac at the proper temperature range. This means also an identical nature of the orientation mobility process which controls the proton and carbon relaxation.

4.4.3 Comparison of ^{13}C and ^{1}H Relaxation Data for [Bmim]PF_6 and [Bmim]BF_4

Some $1/T_{1H}$ temperature dependences for [bmim]PF_6 IL are shown in Fig. 4.7b. For [bmim]BF_4 the dependences are very close in their shape to [bmim]PF_6 for each functional group differing only in numerical values and in the position of the maxima. However the ^{1}H curves of these two ILs do not show a close similarity in shape to corresponding ^{13}C curves though the main trends mentioned above remain.

Since the most of ^{1}H dependencies have more or less pronounced maximum one can try to calculate the correlation times using the same procedure as above. Once more the obtained τ_c are not equal to the corresponding ^{13}C data. In more detail a description of ^{1}H relaxation in the [bmim]PF_6 and [bmim]BF_4 ILs will be presented in [27].

4.4.4 ^{1}H and ^{13}C Difference

Now let us return to the difference in the behavior of ^{13}C and ^{1}H curves for some functional groups of the studied ILs. There are two examples below, (see Fig. 4.9).

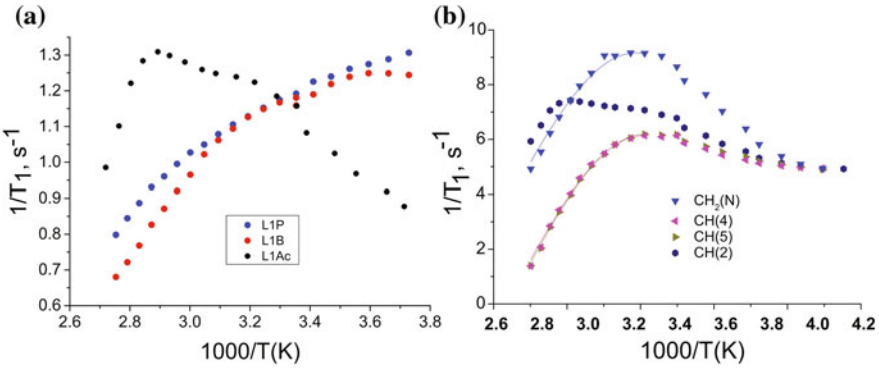

Fig. 4.9 Comparison of ^{1}H $1/T_1$ curves for C(2)H groups in three studied ionic liquids (**a**) and for some groups in [emim]CH_3COO (**b**)

One can observe a different temperature behavior of ^{1}H relaxation of the C(2)H ring hydrogen in [emim]CH_3COO from one side, and in [bmim]BF_4 or [bmim]PF_6 from another side (Fig. 4.9a). For the ILs with the BF_4^- and PF_6^- anions a behavior of the curves is similar and looks like an overlap of two or more broad unresolved lines, while in the case of the [emim]Ac a pronounced maximum is observed for C(4)H and C(5)H hydrogens (Fig. 4.9b). In addition, for the C(2) hydrogen one more maximum is clearly observable at higher temperature, and the maximum corresponds to the largest of the observed τ_c i.e. reflects the slowest cation reorientation.

Thus we have found that ^{1}H relaxation curves in some cases allowed one to detect motions, unobservable in the carbon relaxation and, thereby, to extract more information concerning details of a dynamics of the $[amim]^+$ cations. In particular, a different $1/T_1$ behavior for different anions leads to the hypothesis about different ways of the cation packaging in these systems. And it turned out that this assumption correlates well with the literature data on computer simulation of the same ionic liquids.

As the final point of our work a list of some most recent publications [28–47] which were published after Damodaran's review [13] is presented. We took into account the works where NMR—in any of its variants namely, spectra, relaxation, or diffusion—was used to study of ionic liquids. A very brief glance at the list as well as the recent reviews allows one to conclude that a sufficient part of the NMR publications during the recent years begins to be paid to the proton and inorganic ILs, to mixtures of an IL with other compounds, and to ILs in porous materials. Undoubtedly, it is due to the use of IL-based electrolytes in supercapacitors, ionic batteries etc. However the study of the basic physical and chemical properties of ILs of different kinds remains the essential aim of researchers.

Acknowledgements The NMR measurements have been partially carried out in the Center for Magnetic Resonance of Research Park of St. Petersburg State University.

References

1. A. Abragam, *Principles of Nuclear Magnetism* (Oxford University Press, Oxford, U.K., 1961)
2. G.C. Levy, D.J. Kerwood, *Encyclopedia of Nuclear Magnetic Resonance*, vol. 2 (Willey, New York, 1996)
3. Chizhik, V.I. et al., *Magnetic Resonance and Its Applications* (Springer, 2014). ISBN 978-3-319-05299-1
4. B. Kirchner, *Ionic Liquids*. Topics in current chemistry, vol. 290 (Springer, Berlin Heidelberg, 2010)
5. S.T. Handy, *Ionic Liquids—Classes and Properties* (InTech, 2011), http://www.intechopen.com/books/ionic-liquids-classes-and-properties (ISBN 978-953-307-634-8)
6. K. Ghandi, A review of ionic liquids their limits and applications. Green Sustain. Chem. **4**, 44–53 (2014)
7. J.H. Antony, D. Mertens et al., Pure Appl. Chem., **76**, 255–261 (2004)
8. R. Giernoth, *NMR Spectroscopy in Ionic Liquids* In Ionic Liquids, ed. by B. Kirchner. Topics in current chemistry, vol. 290, p. 263 (Springer, Berlin, Heidelberg, 2009)

9. V.P. Ananikov, Chem. Rev. **111**, 418–454 (2011)
10. K. Hayamizu, Ionic Liquids—Classes and Properties (Chapter 10), in *Translational and Rotational Motions for TFSA-Based Ionic Liquids Studied by NMR Spectroscopy*, ed. by S.T. Handy, vol. 344 (In Tech, 2011). ISBN 978-953-307-634-8
11. A.-L. Rollet, C. Bessada, Annu. Reports NMR Spectrosc. **78**, 149–207 (2013)
12. R. Giernoth, A. Bröhl et al., Interactions in ionic liquids probed by in situ NMR spectroscopy. J. Mol. Liq. **192**, 55–58 (2014)
13. K. Damodaran, Recent NMR studies of ionic liquids. Annu. Reports NMR Spectrosc. **88**, 215–244 (2016)
14. V.V. Matveev, D.A. Markelov et al., ^{13}C NMR relaxation and reorientation dynamics in imidazolium-based ionic liquids: revising interpretation. Phys. Chem. Chem. Phys. **16**, 10480–10484 (2014)
15. D.E. Woessner, J. Chem. Phys. **36**, 1–4 (1962)
16. D.E. Woessner, Brownian motion and correlation times. eMagRes (Wiley online library, 2007). https://doi.org/https://10.1002/9780470034590.emrstm0047
17. G. Lipari, A. Szabo, J. Am. Chem. Soc. **104**, 4546 (1982)
18. J.H. Antony, D. Mertens et al., ChemPhysChem **4**, 588–594 (2003)
19. W.R. Carper, P.G. Wahlbeck et al., Anal. Bioanal. Chem. **378**, 1548–1554 (2004)
20. W.R. Carper, P.G. Wahlbeck et al., J. Phys. Chem. A **108**, 6096–6099 (2004)
21. J.H. Antony, D. Mertens et al., J. Phys. Chem. A **109**, 6676–6682 (2005)
22. N.E. Heimer, J.S. Wilkes et al., J. Phys. Chem. A **110**, 868–874 (2006)
23. M. Imanari, H. Tsuchiya et al., Magn. Reson. Chem. **47**, 67–70 (2009)
24. E.V. Brui, ^{13}C NMR investigation of molecular mobility of ion groups in some ionic liquids, Master's thesis. Lappeenranta University of Technology, 2012
25. V.V. Matveev, D.A. Markelov et al., Molecular mobility of counterion functional groups in ionic liquid 1-ethyl-3-methylimidazolium acetate according to ^{1}H and ^{13}C NMR relaxation data. Russ. Chem. Bull. **62**(9), 1985–1990 (2013)
26. N.E. Heimer, R.E. Del Sesto et al., Magn. Reson. Chem. **42**, 71–75 (2004)
27. V.V. Matveev, D.A. Markelov et al., Magn. Reson. Chem., accepted
28. M. Shadeck, *Translational and Rotational Diffusion in Ionic Liquids Through NMR Spectroscopy* (The Pennsylvania State University, Thesis, 2015)
29. H. Abe, T. Takekiyo et al., Anomalous freezing of nano-confined water in room-temperature ionic liquid 1-Butyl-3-methylimidazolium nitrate. ChemPhysChem **17**, 1136–1142 (2016)
30. N. Gjineci, E. Boli et al., Separation of the ethanol/water azeotropic mixture using ionic liquids and deep eutectic solvents. Fluid Phase Equilib. **424**, 1–7 (2016)
31. K.S. Han, X. Wang et al., Distribution of 1-Butyl-3-methylimidazolium Bistrifluoromethyl-sulfonimide in mesoporous silica as a function of pore filling. J. Phys. Chem. C **117**, 15754–15762 (2013)
32. H. Abe, T. Takekiyo et al., Direct evidence of confined water in room-temperature ionic liquids by complementary use of small-angle x-ray and neutron scattering. J. Phys. Chem. Lett. **5**, 1175–1180 (2014)
33. T.Y. Wu, Y.-H. Wang et al., Influence of LiTFSI addition on conductivity, diffusion coefficient, spin—lattice relaxation times, and chemical shift of one-dimensional NMR spectroscopy in litfsi-doped dual-functionalized imidazolium-based ionic liquids. J. Chem. Eng. Data **60**, 471–483 (2015)
34. K. Hayamizu, S. Tsuzuki et al., Transport and electrochemical properties of three quaternary ammonium ionic liquids and lithium salts doping effects studied by NMR spectroscopy. J. Chem. Eng. Data **59**, 1944–1954 (2014)
35. C.I. Daniel, F. Vaca Chávez, C.A.M. Portugal, J.G. Crespo, P.J. Sebastião, ^{1}H NMR relaxation study of a magnetic ionic liquid as a potential contrast agent. J. Phys. Chem. B **119**, 11740–11747 (2015)
36. L.M. Varela, T. Méndez-Morales, Carrete et al., Solvation of molecular cosolvents and inorganic salts in ionic liquids: a review of molecular dynamics simulations. J. Mol. Liq. **210**, 178–188 (2015)

37. Y. Shimizu, Y. Wachi et al., NMR study on ion dynamics and phase behavior of a piperidinium-based room-temperature ionic liquid: 1-Butyl-1-methylpiperidinium Bis(fluorosulfonyl)amide. J. Phys. Chem. B, **120**(25), 5710–5719 (2016). https://doi.org/10.1021/acs.jpcb.6b04095
38. C.A. Rumble, A. Kaintz et al., Rotational dynamics in ionic liquids from NMR relaxation experiments and simulations: benzene and 1-Ethyl-3-methylimidazolium. J. Phys. Chem. B **120**, 9450–9467 (2016)
39. Bradley J. Butler, Donald S. Thomas et al., NMR spectroscopy to follow reaction progress in ionic liquids. Magn. Reson. Chem. (2014). https://doi.org/10.1002/mrc.4161
40. M.N. Garaga, M. Persson et al., Local coordination and dynamics of a protic ammonium based ionic liquid immobilized in nano-porous silica micro-particles probed by Raman and NMR spectroscopy. Soft Matter (2016). https://doi.org/10.1039/c5sm02736e
41. I. Seymour, D.S. Middlemiss et al., Characterizing oxygen local environments in paramagnetic battery materials via 17O NMR and DFT calculations. J. Am. Chem. Soc. **138**, 9405–9408 (2016)
42. S.K. Davidowski, F. Thompson et al., NMR characterization of ionicity and transport properties for a series of diethylmethylamine based protic ionic liquids. J. Phys. Chem. B **120**, 4279–4285 (2016)
43. Danuta Kruk, Milosz Wojciechowski et al., Dynamics of ionic liquids in bulk and in confinement by means of ^{1}H NMR relaxometry—BMIM-$OcSO_4$ in an SiO_2 matrix as an example. Phys. Chem. Chem. Phys. **18**, 23184 (2016)
44. Sachin Thawarkar, Nageshwar D. Khupse et al., Comparative investigation of the ionicity of aprotic and protic ionic liquids in molecular solvents by using conductometry and NMR spectroscopy. ChemPhysChem **17**, 1006–1017 (2016)
45. R. Nanda, Thermal dynamics of lithium salt mixtures of ionic liquid in water by PGSE NMR spectroscopy. RSC Adv. **6**, 36394 (2016)
46. T.-Y. Wua, S.-G. Sub et al., Diffusion coefficients, spin-lattice relaxation times, and chemical shift variations of NMR spectra in LiTFSI-doped ether- and allyl-functionalized dicationic ionic liquids. J. Taiwan Inst. Chem. Eng. **60**, 138–150 (2016)
47. X. Zhu, H. Zhang et al., Structural heterogeneities in solutions of triethylamine nitrate ionic liquid: ^{1}H NMR and LC model study. J. Solut. Chem. **45**, 359–370 (2016)

Chapter 5
Transport Properties and Ion Aggregation in Mixtures of Room Temperature Ionic Liquids with Aprotic Dipolar Solvents

Oleg N. Kalugin, Anastasiia V. Riabchunova, Iuliia V. Voroshylova, Vitaly V. Chaban, Bogdan A. Marekha, Volodymyr A. Koverga and Abdenacer Idrissi

Abstract The results of experimental (conductometry, NMR-diffusometry) and computational (MD simulations) studies on the binary mixtures of room-temperature imidazolium- and pyridinium-based ionic liquids (RTILs) with acetonitrile (AN), γ-butyrolactone (γ-BL) and propylene carbonate (PC) over the wide composition range are presented. The conductometric analysis was carried out in the RTILS mole fraction (χ(RTIL),) range between 0.0 and 0.5 in the temperature ranges from 278.15 to 328.15 K. Notably, all binary systems exhibit conductivity maximum at, χ(RTIL),

O. N. Kalugin (✉) · A. V. Riabchunova
Department of Inorganic Chemistry, V. N. Karazin Kharkiv National University, Svoboda sq., 4, Kharkiv 61022, Ukraine
e-mail: onkalugin@gmail.com

A. V. Riabchunova
e-mail: ryabchunova.anastasia@gmail.com

I. V. Voroshylova
CIQ(UP)/REQUIMTE@LAQV, Departamento de Química e Bioquímica, Faculdade de Ciências, Universidade do Porto, Rua do Campo Alegre, 4169-007 Porto, Portugal
e-mail: voroshylova@gmail.com

V. V. Chaban
Instituto de Ciência e Tecnologia, Universidade Federal de São Paulo, 12231-280 São José dos Campos, SP, Brazil
e-mail: vvchaban@gmail.com

B. A. Marekha
Normandie University, UNICAEN, CERMN, FR CNRRS 3038 INC3M, SF 4206 ICORE, Bd Becquerel, 14000 Caen, France
e-mail: bogdan.a.marekha@gmail.com

V. A. Koverga · A. Idrissi
University of Lille, Science and Technology, LASIR (UMR CNRS A8516), Bât. C5, Cité Scientifique, 59655 Villeneuve d'Ascq Cedex, France
e-mail: v.a.koverga@gmail.com

A. Idrissi
e-mail: nacer.idrissi@univ-lille1.fr

L. A. Bulavin and A. V. Chalyi (eds.), *Modern Problems of Molecular Physics*, Springer Proceedings in Physics 197, https://doi.org/10.1007/978-3-319-61109-9_5

between 0.1 and 0.2. This maximum slightly shifts towards smaller χ(RTIL), as counter-ion gets larger. Self-diffusion coefficients of solvent molecules and cations were obtained by means of ^{1}H-NMR-diffusometry in mixtures of 1-n-butyl-3-methylimidazolium bis(trifluoromethylsulfonyl)imide tetrafluoroborate, trifluoro methanesulfonate and hexafluorophosphate with PC, γ-BL and AN over the whole concentration range at 300 K. The relative diffusion coefficients of solvent molecules to cations as a function of composition were established to be depended on a solvent but not on the anion of RTIL. In all cases the relative diffusion coefficients demonstrate a plateau at $\chi(\text{RTIL}) < 0.2$ and then increase significantly for AN, moderately for γ-BL or negligibly for PC at higher RTIL content. Such behavior was attributed to the different solvation ability of the investigated solvents. In the mixtures with [BMIM][PF_6] anion diffusion coefficients derived from ^{31}P NMR were found to be higher than the corresponding values for cation in RTIL-depleted systems and lower in the RTIL-enriched systems. The inversion of relative ion diffusion is observed near the equimolar composition and being insensitive to the solvent. At this point a remarkable change in the diffusion mechanism of ion of RTIL is expected. Additionally, molecular dynamics simulations on the binary mixtures of 1-ethyl-3-methylimidazolium and 1-butyl-3-methylimidazolium tetrafluoroborates with AN were performed. The conductivity correlates with a composition of ion aggregates simplifying its predictability. Large amounts of AN stabilize ion pairs, although destroy greater ion aggregates. Based on the simulation results, we show that conductivity of the studied mixtures significantly depend on the ion aggregation.

5.1 Introduction

Room-temperature ionic liquids (RTILs) are salts with a melting point around or below ambient temperature usually containing bulky and asymmetric organic cations and small inorganic anions. RTILs exhibit a variety of peculiar features such as broad liquid temperature range, negligible vapor pressure, high thermal stability, non-flammability, excellent solvation ability and wide electrochemical window. RTILs have been successfully used in in variety of applications such as green solvents [1], in organic synthesis [2–6], extraction and separation processes [7–9], material processing and preparation [10–12], electrochemistry [13–15], gas [16, 17] and liquid [18] chromatography, gas capture applications [19, 20].

The viscosity of ionic liquids is 2–3 orders of magnitude higher than that of the ordinary molecular solvents, and this constitutes a major drawback for the use of RTIL in electrochemistry based devices. The high viscosity of RTILs arises from strong Coulombic interactions and, consequently, can be considered as their intrinsic property. Therefore, one could not expect to be able to modulate viscosity of RTILs substantially by changing the constituent ions without altering the properties of interest. Another possible way to modulate the RTIL viscosity is to increase the temperature, however, this effect (ca. by less than 50 K) only leads to the insignificant reduction of viscosity [21]. One of the efficient ways to modulate

the RTIL viscosity is to combine RTILs with conventional molecular solvents that not only leads to a reduction of viscosity but also extends their properties and, thus, application areas and operating conditions. Mixing RTILs and molecular liquids was found to cause a significant decrease of viscosity and a sharp increase of conductivity [22–25].

In contrast to the well-known non-aqueous electrolyte solutions, where salt concentrations rarely overcome 0.2–0.3 mol fraction limit, imidazolium-based RTILs are fully miscible with majority of the non-aqueous polar solvents. For example, for imidazolium- and pyrrolidinium- based ionic liquids it was established that they are fully miscible with aprotic solvents of moderate polarity commonly used in electrochemistry (e.g. PC, AN and γ-BL and others). AN, γ-BL and PC significantly differ in terms of their macrosopic polarity (dielectric constants at 298.15 K equal 35.96, [26] 41.7, [27] 64.96, [28] respectively), donicity (Gutmann's donor numbers at 298.15 K equal 14.1 [29], 18.0 [30] and 15.1 [29], respectively) and viscosity (298.15 K values are 0.339 [31], 1.76 [32] and 2.5120 mPa s [28], respectively) and, hence, can considerably change the physico-chemical properties of RTILs [33]. Mixing RTILs with electro-chemically stable dipolar aprotic solvents of optimal composition open a way for their application in electric double-layer capacitors and other electrochemical devices [34–38].

Among the large variety of RTILs, imidazolium- and pyridinium- based derivatives are probably the most intensively studied due to their unique properties [39]. This makes such RTILs promising electrolytes for applications in different electrochemical devices. Surprisingly, systematic studies of the transport properties of binary mixtures of RTILs with dipolar aprotic solvents are still scarce, despite the large practical interest to such systems. In this view, the rational application of the binary mixtures of RTILs with molecular solvents requires microscopic information about the key factors that define the composition dependence of their transport properties such as conductivity and diffusion.

A number of conductometric studies of the mixtures of RTILs with molecular solvent over the full concentration range is available in literature [22, 40–50]. Although many mixtures of RTILs with molecular solvents demonstrate maximum on concentration dependence of specific conductivity between 0.1 and 0.3 mol fractions of RTIL [22, 41, 43–47, 49], there is no clear explanation of this phenomenon so far.

Despite the importance of temperature influence on transport properties many recent investigations in dilute RTILs solutions present results only at 298 K [51–53].

The experimental studies of diffusion in mixtures of RTILs with polar molecular solvents are rather scarce. Currently, there is still lack of microscopic information on the microscopic structure and dynamics of ionic subsystem in the mixtures of RTILs with polar aprotic solvents.

Despite the broad set of experimental approaches targeted at the discovery of peculiarities of intermolecular interactions in binary systems of RTILs with molecular solvents, as mentioned above, most of them are indirect methods which

are typically challenging in interpretation. Modern methods of molecular modeling such as quantum chemical calculations joined with modern methods of analysis of electron density distribution as well as the methods of molecular dynamics simulation. [54, 55], can help to solve these problems and they also can complete the picture with information which is inaccessible from experiment.

In this chapter we present the results of conductometic, NMR-diffusometrical and MD simulation study on the binary mixtures of imidazolium- and pyridinium-based RTILs with AN, PC and γ-BL over the wide composition range.

The rest of the chapter is organized as follows. Section 5.2 presents the results of conductometric investigation of the binary mixtures of imidazolium- and pyridinium-based RTILs with acetonitrile (AN) at different temperatures in wide concentration range. The following RTILs have been studied: 1-ethyl-3-methylimidazolium tetrafluoroborate ([EMIM][BF_4]), 1-n-butyl-3-methylimidazolium bromide ([BMIM][Br]), 1-n-butyl-3-methylimidazolium tetrafluoroborate, [BMIM][BF_4], 1-n-butyl-3-methylimidazolium trifluoromethanesulfonate, [BMIM][TfO], 1-n-hexyl-3-methylimidazolium tetrafluoroborate, [HexMIM][BF_4] and 1-butyl-4-methylpyridinium tetrafluoroborate, [BMP][BF_4] in AN, at 278.15, 288.15, 298.15, 308.15, 318.15 and 328.15 K within the concentration range χ(RTIL) = 0.001 to 0.5.

In the Sect. 5.3 we present the results of a NMR-diffusometrical study on mixtures of 1-*n*-butyl-3-methylimidazolium based RTILs, namely trifluoromethanesulfonate [BMIM][TfO], tetrafluoroborate [BMIM][BF_4], bis(trifluoromethanesulfonyl)imide, [BMIM][TFSI] and hexafluorophosphate, [BMIM][PF_6] with AN, PC and γ-BL over the entire composition range.

Section 5.4 presents the results of Molecular Dynamics Simulations on the mixture of two common RTILs, [EMIM][BF_4] and [BMIM][BF_4], with AN over

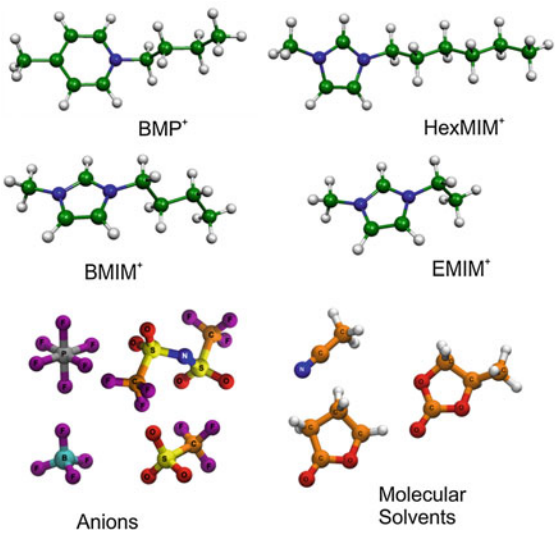

Fig. 5.1 Structures of the ions composing the studied RTILs [EMIM][BF_4], [BMIM][BF_4], [HexMIM][BF_4], [BMP][BF_4], [BMIM][Br], [BMIM][PF_6], [BMIM][Tf], [BMIM][TFSI] and the molecular solvents (AN, PC and γ-BL)

the entire range of compositions at 283–323 K. Our recent technique [56] exploiting uniformly scaled electrostatic charges is used to account for electronic polarization of RTILs. The available experimental densities and viscosities of the [EMIM][BF_4]/AN [23, 44] and [BMIM][BF_4]/AN [22, 23, 57, 58] are applied to validate our simulations.

Structures of the ions composing the studied ionic liquids [EMIM][BF_4], [BMIM][BF_4], [HexMIM][BF_4], [BMP][BF_4], [BMIM][Br], [BMIM][PF_6], [BMIM][Tf], [BMIM][TFSI] and the molecular solvents are shown in Fig. 5.1.

5.2 Conductometric Study of Binary Systems Based on RTILs and Acetonitrile

5.2.1 Experimental

All investigated here RTILs are commercially available and were purchased from Merck. The degree of purity of the received RTILs was >99%. To remove possible water impurity, RTILs were dried under high vacuum at elevated temperature (~373 K) in a rotary evaporator during ~24 h. No further purification was attempted before use. AN was purchased from Merck as well. The purification of the solvent (the degree of purity of the received AN was >99.8%) was performed according to the procedure, described elsewhere [59]. The success of purification was controlled by solvent specific conductivity, κ. At 298.15 K κ(AN) was $\sim 2 \times 10^{-8}$ S cm^{-1} which is in accordance with the available literature values [60].

In the present study each working solution was prepared separately, directly from RTIL sample, and measured immediately. To avoid the water ingress to the working solutions, the preparation of the solutions was executed in a glovebox, filled with dry and filtered nitrogen gas. Additionally, each flask with a prepared solution was sealed with laboratory film Parafilm M. A specially designed conductometric cell with three electrodes was used to measure electrical resistance of the solutions. Priorly to the experiment, the new cells were calibrated against the aqueous solutions of KCl according to the method, described in [61], and the constants' values (31.40–72.48 cm^{-1} at 298.15 K) were found to be sufficiently high for measurements of concentrated solutions. All the measurements were carried out in temperature controlled water bath (with accuracy of 0.01 K) LCR 821 ac bridge (uncertainty of the equipment is ~0.1%) was employed to measure electrical resistance at 1 kHz frequency.

The density of the RTIL-AN solutions, d_m, was calculated by the formula [23, 49]:

$$d_m = \varphi_0 d_0 + \varphi_{\mathrm{RTIL}} d_{\mathrm{RTIL}} \,, \tag{5.1}$$

where φ_0 and φ_{RTIL} are volume fractions of AN and RTIL, respectively. Pure RTILs densities were taken from literature [21, 23, 44, 49, 62–67]. Pure AN

density, d_0, was calculated by the following equation [60] at each experimental temperature:

$$d_0^{-1} = 1.24446 + 1.6458 \times 10^3 (T - 273.15) + 2.92 \times 10^6 (T - 273.15)^2. \quad (5.2)$$

5.2.2 Results and Discussion

Temperature dependence of specific conductance, κ, as a function of ionic liquid mole fraction, χ_{RTIL}, in RTIL-AN systems is presented in Fig. 5.2. Evidently, binary mixtures RTIL-AN demonstrate a common behavior of a concentrated electrolyte solutions: with the electrolyte concentration increase (from 0 to 0.1–0.2 mol%) the specific conductance in all studied system sharply rises, passes through a maximum, and decreases smoothly. As it can be seen the Fig. 5.2, the κ-χ_{RTIL} dependence in all studied RTIL-AN systems presents similar response on temperature increase, namely, the position of conductivity maximum shifts towards higher concentrations.

Noteworthy, the reported experimental conductivity data for [EMIM][BF_4]–AN, [BMIM][BF_4]–AN and [HexMIM][BF_4]–AN solutions at 298.15 K are in a complete agreement with those presented by Buchner et al. [44] (Fig. 5.3). However, there is a substantial difference with those reported by Zhu et al. [22]. In attempt to relate the extreme specific conductivity with the ion species in RTIL-based

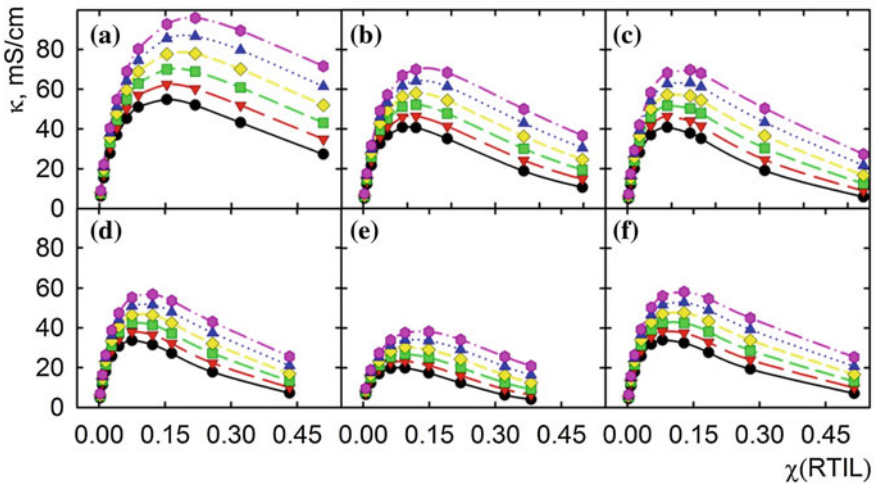

Fig. 5.2 Specific conductivity, κ, of [EMIM][BF_4] (**a**), [BMIM][BF_4] (**b**), [BMP][BF_4] (**c**), [HexMIM][BF_4] (**d**), [BMIM][Br] (**e**), [BMIM][Tf] (**f**), in mixture with AN as a function of the molar fraction of RTILs from $T = 278.15$ K (black circles) to $T = 328.15$ K (magenta hexagons) in steps of 10 K

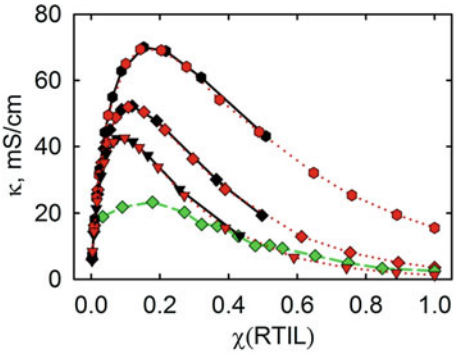

Fig. 5.3 Specific conductivity, κ, of [EMIM][BF_4] (hexagons), [BMIM][BF_4] (diamonds) and [HexMIM][BF_4] (triangles) as a function of molar fraction of RTIL, data from this work (black symbols, solid lines) in comparison with literature data, reported by Buchner et al. [44] (red symbols, dotted lines) and Zhu et al. [22] (green symbols, dashed line). All data are given at 298.15 K

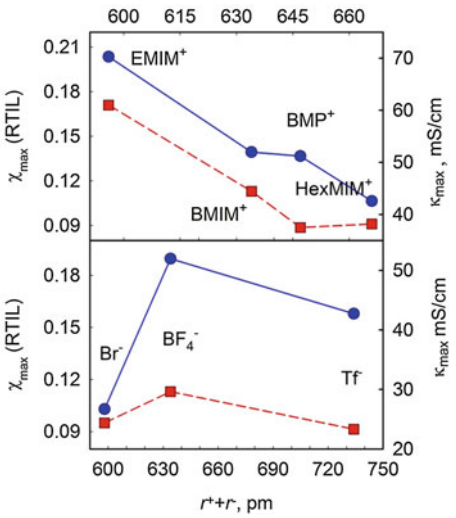

Fig. 5.4 Dependence of maximum specific conductivity, κ_{max}, (right axis, blue circles, solid lines) and the corresponding RTIL mole fraction, χ_{max}, (left axis, red squares, dashed lines) on the sum of ionic radii for RTILs with common anion, $[BF_4]^-$, (top plot) and common cation, $[BMIM]^+$, (bottom plot) in AN. All data are given at 298.15 K

mixtures, the dependences of maximum conductivity, κ_{max}, and the corresponding RTIL mole fraction, χ_{max}, on the sum of cation and anion radii at 298.15 K are presented in Fig. 5.4.

As it follows from Fig. 5.4, in solutions of RTIL with the same anion, $[BF_4]^-$, the κ_{max} decreases and the corresponding χ_{max} lowers upon the increase of cation radius and, consequently, size, in the sequence $[EMIM]^+ < [BMIM]^+ < [BMP]^+ < [HexMIM]^+$. In the case of solutions of RTILs with the same cation, $[BMIM]^+$, the same regularity can be observed for [BMIM][BF_4]–AN and [BMIM][Tf]–AN cases: with the increase of the anion radius from 232 pm (for $[BF_4]^-$) to 332 pm (for

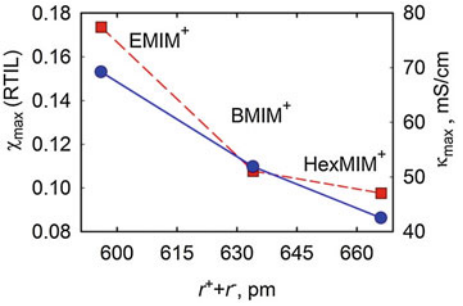

Fig. 5.5 Dependence of maximum specific conductivity, κ_{max}, (right axis, blue circles, solid lines) and the corresponding RTIL mole fraction, χ_{max}, (left axis, red squares, dashed lines) in RTILs—ethanol mixtures on the sum of ionic radii for RTILs with common anion, $[PF_6]^-$. All data are given at 298.15 K

$[Tf]^-$), both the κ_{max} and χ_{max} values diminish. Interestingly, the maximum values of specific conductivity and the corresponding concentration in [BMIM][Br]–AN system do not follow the above mentioned behavior, being smaller than in [BMIM] $[BF_4]$–AN mixture. This behavior of κ_{max} and χ_{max} in the case of [BMIM][Br]–AN solution can be understood by taking into account stronger interactions of anion and cation, as the data on diluted solutions suggest [68].

It was founded, that the same tendency is observed not only for AN, but also for alcohols. Figure 5.5 shows the concentration dependence of maximum specific conductivity and the corresponding mole fraction of ionic liquid for RTILs—ethanol systems [48].

Two of the most essential dynamic properties of any electrolyte solution—conductivity and viscosity—can be related by Walden's rule. The rule states, that the product of the viscosity of solution, η, and the molar conductivity, Λ, is a constant at a particular temperature:

$$\Lambda \cdot \eta = const. \tag{5.3}$$

On the one hand, the empiric formula, suggested by Seddon et al. in [69], can be used to estimate the viscosity in ionic liquid–molecular liquid mixtures (correlation coefficient of the equation is >0.98:

$$\eta = \eta_{RTIL} \cdot \exp(A \cdot \chi_s), \tag{5.4}$$

where η_{RTIL} is a viscosity of pure ionic liquid, χ_s is a mole fraction of molecular liquid and A is a constant, characteristic for each specific system. The A coefficient cannot be calculated theoretically, but can be found for some RTIL–ML mixtures in literature.

Alternatively, the viscosity of ionic liquid–molecular liquid mixture as a function of mole fraction of molecular liquid, χ_s, at a fixed temperature can be described as a linear dependence (correlation coefficient is >0.99) in the coordinates $\log\eta$ *versus* χ_s. Therefore, the viscosity in a binary mixture ionic liquid—solvent can be estimated starting with viscosity for pure RTIL and pure ML.

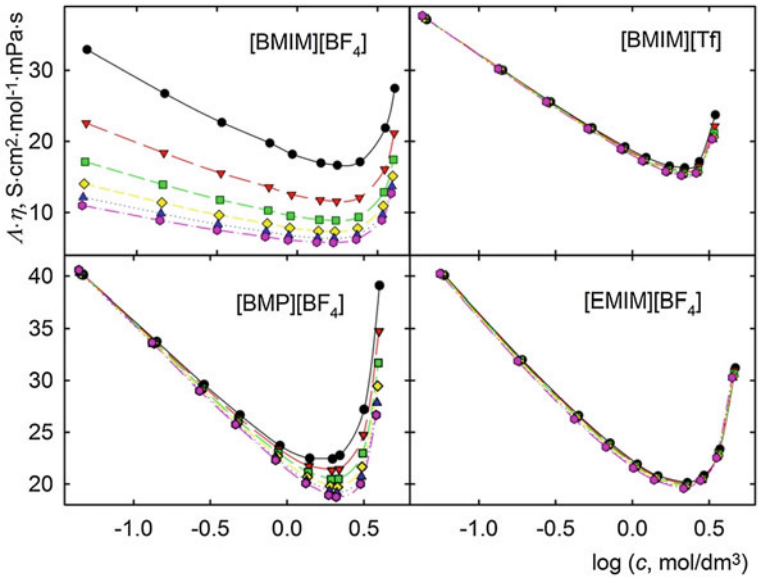

Fig. 5.6 Relation between $\Lambda \cdot \eta$ (Walden's product) and log$c$ (where c is the concentration of RTIL) in RTILs–AN binary system from $T = 278.15$ K (black circles) to $T = 328.15$ K (magenta hexagons) in step of 10 K

Vogel-Tamman-Fulcher (VTF) equation is a well-known formula to represent the viscosity in pure fluids, including RTILs [21, 62–65, 70]:

$$\eta_{\mathrm{RTIL}} = \eta_0 \cdot \exp(B/(T - T_0)), \tag{5.5}$$

where η_0, B, and T_0 are constants, characteristic for a particular fluid. They can be found in literature for a great deal of pure ionic liquids. Using literature parameters η_0, B, and T_0 [21, 62–64], and Eq. (5.5) the viscosities of four studied RTILs ([EMIM][BF_4], [BMIM][BF_4], [BMIM][Tf] and [BMP][BF_4]) at all experimental temperatures were determined. The viscosities of AN at each temperature were taken from the work by Barthel et al. [60]. Then, the viscosities of RTIL–AN mixtures were estimated from viscosities of pure fluids which, afterwards were employed to calculate Walden's product in studied systems.

The relation between RTIL–AN system's transport properties (viscosity and conductivity via Walden's product) and concentration in coordinates $\Lambda \cdot \eta$ versus log$c$ is represented on Fig. 5.6. As it can be observed, the $\Lambda \cdot \eta$ product value decreases linearly as the logarithm of the RTIL concentration increases, it goes over minimum and finally rises. All presented curves are analogous in form and dimension for all analyzed mixtures at all experimental temperatures. Curiously, the RTIL content in a mixture at minimum $\Lambda \cdot \eta$ value on $\Lambda \cdot \eta$ – log$c$(RTIL) curve coincides with the $\chi_{\max}$ mole fraction at maximum on $\kappa - \chi$(RTIL) dependence. For comparison purposes, Fig. 5.7 demonstrates the $\Lambda \cdot \eta$ – log$c$(RTIL) plots for

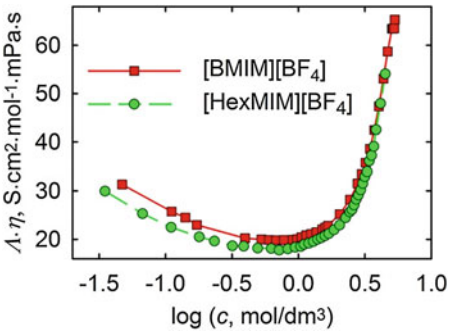

Fig. 5.7 Relation between $\Lambda \cdot \eta$ (Walden's product) and log$c$ (where c is concentration of RTIL) in solutions [BMIM][BF_4] and [HexMIM][BF_4] in ethanol at $T = 298.15$ K

Table 5.1 Distances between ions in quasi-crystal ($l_{\pm}$, nm) in binary mixtures RTIL–AN, sums of ion radii ($r_+ + r_-$, nm) for respective ionic liquids. Δr represents the discrepancy between $l_{\pm}$ and $r_+ + r_-$

RTIL	$l_{\pm}$	$r_+ + r_-$	Δr
[BMIM][Br]	0.783	0.598	0.185
[EMIM][BF_4]	0.695	0.596	0.099
[BMIM][BF_4]	0.805	0.634	0.171
[HexMIM][BF_4]	0.836	0.666	0.170
[BMIM][Tf]	0.800	0.734	0.066
[BMP][BF_4]	0.787	0.647	0.140

literature data [48] on on ionic liquid–alcohol mixtures. The curves act in matching manner to RTIL–AN systems, with the $\Lambda \cdot \eta$ – log$c$(RTIL) dependence passing through minimum.

Taking into account the mixture concentration both at minimum points on $\Lambda \cdot \eta$ – log$c$(RTIL) curves and at maximum points on $\kappa - \chi$(RTIL) curves, along with the large volumes of imidazolium and pyridinium cations, we presume, that the appearance of turning-points on these dependences is the reflection of the starting to contact ions in solution. When the system reaches this concentration, the viscosities rise drastically. One way to examine this hypothesis is to estimate the inter-particle distance, $l_{\pm}$, at the χ_{max} concentration by equation

$$l_{\pm} = (2 \cdot N_A \cdot c_{max})^{-1/3}, \tag{5.6}$$

treating a mixture at this concentration as a quasi-crystal [71]. The $l_{\pm}$ values for ionic liquids – acetonitrile mixtures, derived from (5.6), together with the sum of the cation and anion radii, $r_+ + r_-$, for each RTIL are listed in Table 5.1. $l_{\pm}$ and $r_+ + r_-$ values are of similar magnitude. As it can be seen from the Table 5.1, certain difference between these values is virtually invariable, except for two RTILs ([EMIM][BF_4] and [BMIM][Tf]), confirming the correctness of the above-mentioned suppose: the extremum on κ-χ_{RTIL} dependence in ionic liquid–molecular solvent systems occurs upon the start of direct contact between ions, which results in a fast rise of viscosity.

5.2.3 Summary

The results of electrical conductivity measurements of acetonitrile solutions of 6 room-temperature ionic liquids—[EMIM][BF_4], [HexMIM][BF_4], [BMIM][Br], [BMP][BF_4], [BMIM][BF_4], and [BMIM][Tf]—in a wide range of temperatures (278.15–328.15 K) and concentrations (up to 4.5 mol dm^{-3}) are presented.

It was found, that the occurrence of a turning-point on the dependence of electrical conductivity on the mole fraction of RTIL is a general characteristic of systems RTIL–AN. As temperature increases, the maximum of conductivity shifts to more concentrated region in all of the studied binary systems. Besides that, the conductivity maximum moves to less concentrated region with the rise of the counter-ion size. The systems with greater sum of ionic radii of a RTIL show smaller values of electrical conductivity in a turning-point at each measured temperature.

According to the presented data, the plots $\Lambda \cdot \eta$ – log$c$(RTIL) show linear behavior till the concentration of turning-point on the dependence of specific conductivity on the RTIL mole fraction. The comparison of inter-ionic distances in mixtures ionic liquid–molecular liquid with the sum of cation and anion of the respective RTIL allows to conclude, that substantial rise of the viscosity in the mixture and, consequently, the turning-points on the curves "Walden's product—RTIL molar concentration" and "specific conductivity—RTIL mole fraction" appears when the mixture reaches the state of liquid quasi-crystal with the RTIL ions being in direct contact. As follows from the reported study, the turning-point can be observed when the inter-ion distance ranges from 0.6 to 0.8 nm, depending on structural characteristics of ions of a given ionic liquid.

5.3 Translational Diffusion in Mixtures of Imidazolium RTILs with Polar Aprotic Molecular Solvents

5.3.1 Experimental

5.3.1.1 Materials

RTILs for the present investigation were purchased from Solvionic (France) with a purity of 99.5%. Water content was not higher than 500 ppm, whereas that of halides and methylimidazole did not exceed 10 ppm and 50 ppm, respectively, according to the supplier. The special attention was paid to the purity of the RTILs since even traces of some impurities can influence on such properties of RTILs as viscosity [69] and self-diffusion coefficients [72, 73].

In order to reduce the interfering effect of moisture, all RTILs before any manipulations were kept under vacuum ($p < 10^{-6}$ bar, 60 °C) during 4 h. PC ($\leq$20 ppm H_2O, 99.7%) and γ-BL (99.0%, $\leq$1000 ppm H_2O) were purchased

from Sigma-Aldrich, AN ($\leq$100 ppm H_2O, 99.9%, UV-IR grade) was supplied by Carl Roth (Germany). AN and γ-BL were additionally dried under the 4 Å molecular sieves.

All mixtures were prepared by weight in a glovebox filled with dry argon. Samples were sonicated for 30 min to enhance the mixing. Afterwards solutions were transferred to 5-mm o.d. NMR tubes (Wilmad-LabGlass) fitted with a coaxial insert containing D_2O as NMR-lock solvent and parafilmed. We employed a non-uniform concentration grid which is denser around the composition corresponding to conductivity maximum in these mixtures, i.e. χ(RTIL) ~ 0.15.

5.3.1.2 NMR Measurements

NMR measurements were performed on a Bruker Avance-II 400 spectrometer equipped with a 5-mm BBI probe with z-gradient. Sample temperature was kept constant around 300.0 K with accuracy ±0.1 K by using VT-2000 Bruker unit. The variable temperature unit was calibrated by means of the standard samples of 4% MeOH in MeOH-d_4 and 80% ethylene glycol in DMSO-d_6 [74]. Before measurements each sample was equilibrated in the probe's acquisition zone $\geq$15 min. The residual signal of the internal-lock solvent for ^1H and to external 85% H_3PO_4 for ^{31}P were used as references for correspondent chemical shifts. The measurements of diffusion coefficients were performed by applying the standard Bruker ledbpgp2s pulse sequence [75]. This pulse sequence allows one to avoid artifacts originated from thermal convection during sample rotation [76, 77]. The ledbpgp2s pulse sequence also satisfies recommendations by Annat et al. [78].

Gradients were additionally calibrated by well-known diffusion coefficient of residual HDO in D_2O [79]. Typical NMR-diffusion experiments employed 16 acquisition scans with a gradient pulse length (δ) of 1.2–5 ms and a diffusion delay (Δ) of 100–200 ms. These parameters were chosen to obtain ~95% attenuation of the signal at the highest gradient strength. The latter was varied in 16 steps up to ~50 G cm^{-1} in a way that its squared value changed in equal increments. Gradient pulses were of squared sine shape, gradient recovery and longitudinal eddy-current delays equaled to 0.2 and 5 ms, respectively. It was shown [77], that pulse length and relaxation delay do not seriously influence on reliability of the results [77]. Nevertheless, rough estimations of these parameters were performed for each sample. As these characteristic times were found to depend significantly on concentration they were optimized to ensure accurate results.

Selected samples were tested at different diffusion delays to ensure the absence of thermal convection effects [76].

The data was analyzed with the standard TopSpin T1/T2 relaxation utility by fitting the decay of the integral intensity of the corresponding signal to the Stejskal-Tanner equation [80] (5.7)

$$A = A_0 \exp\left(-\gamma^2 \delta^2 g^2 D \left(\Delta - \frac{\delta}{3} \right) \right) \tag{5.7}$$

which relates the attenuated signal amplitude, A, with its non-perturbed value, A_0, using the gyromagnetic ratio of the probe nucleus, γ, gradient strength, g, gradient pulse length, δ, diffusion delay time, Δ, and self-diffusion coefficient of the diffusing particle, D.

Comparing our results with literature data for the pure RTILs and molecular liquids (AN, γ-BL and PC) (Table 5.2) demonstrates rather good agreement.

5.3.2 Results and Discussion

5.3.2.1 Absolute Self-diffusion Coefficients

The concentration dependence of self-diffusion coefficients in the ion-molecular systems can be treated by using different approaches [81]. At present, there is no any theory would be able to predict and explain diffusivities of the components in liquid mixtures and electrolyte solutions over a broad range of composition.

Figure 5.8 demonstrates a typical behavior of the self-diffusion coefficients of all species (cations, anions and solvent molecules) as a function of the molar fraction of RTIL, χ(RTIL). An inspection of the whole set of the experimental data allows to identify the following general trends. First, in all the studied systems the self-diffusion coefficients of cations and anions of RTILs and AN, γ-BL and PC molecules follow an exponential on χ(RTIL) scale. Due to this fact the concentration dependence of the experimental logarithmic diffusion coefficients can be reproduced with high accuracy by the third-order polynomial:

$$\log D = \sum_{i=0}^{3} a_i \chi^i(\text{RTIL}) \tag{5.8}$$

A comparison of two transport properties, diffusion and viscosity, leads to the conclusion that the observed decrease in self-diffusion coefficients of the binary mixture components with increasing χ(RTIL) could be attributed to the exponential viscosity increase [23, 69].

Secondly, for all the compositions solvent molecules move several times faster as compare with ions. Cations and anions in their turn reveal the similar mobilities. Such behavior is typically considered as an indication of high correlations in ionic mobilities due to strong electrostatic interaction [82, 83]. And finally, it interesting to underline that the diffusion coefficients of all the components of the studied systems vary over 1.6–2 orders of magnitude with χ(RTIL).

The comparison of our data with literature results of Liang et al. [81] and Hsu et al. [84] demonstrates a good coincidence not only for the absolute values of the

Table 5.2 Experimental self-diffusion coefficients, D (10^{-9} m^2 s^{-1}), of the pure components at 300 K (this work) and the literature data obtained by using NMR technique[a]

Experiment		Literature	
Component	This work	Value	Temperature, K
AN	5.1	4.85[b]	298.15
		4.31[c]	298.2 K, high-pressure diaphragm cell with trace $[^{14}C]H_3CN$
		4.37[d]	298.15
		4.34[e]	298.15, open-end capillary
γ-BL	0.83	0.83[f]	303.15
		0.9[g]	303.15
		0.83[h]	295
PC	0.62	0.55[f]	303.15
		0.58[g]	303.15
		0.57[i]	298.15
		0.49[j]	298.15
		0.52[k]	298.15
$[BMIM]^+$/ $[Tf]^-$	0.018/–	0.019/0.014[l]	300
$[BMIM]^+$/ $[PF_6]^-$	0.0078/ 0.0066	0.0080/ 0.0059[l]	300
		0.0071/ 0.0054[m]	300
$[BMIM]^+$/ $[BF_4]^-$	0.017/–	0.016/0.015[l]	300
		0.0158/ 0.0146[m]	300
		0.01301/ 0.01292[n]	300
		0.016/–[b]	298.15
$[BMIM]^+$/ $[TFSI]^-$	0.036/–	0.0299/ 0.0238[l]	300
		0.0282/ 0.0216[m]	300

[a]Experimental details are given along with temperature. [b][219]. [c][220]. [d][221]. [e][85]. [f][86]. Estimated from digitized graph. [g][222]. [h][223]. [i][224]. [j][225]. [k][226]. [l]Interpolated using equations from [21]. [m][227]. [n][228]

diffusion coefficients for cations and solvent molecules (Fig. 5.8), but also for their relative values (Fig. 5.9, Sect. 5.3.2.2).

Another interesting issue concerns the influence of ion aggregation on the self-diffusion coefficients of the constituting ions, D_+ and D_-, of RTILs [83]. It was shown, that in diluted solutions (χ(RTIL) < 0.1) of [HexMIM][TFSI] in the solvent with low dielectric constant ($CDCl_3$) the mobilities of cations and anions are rather

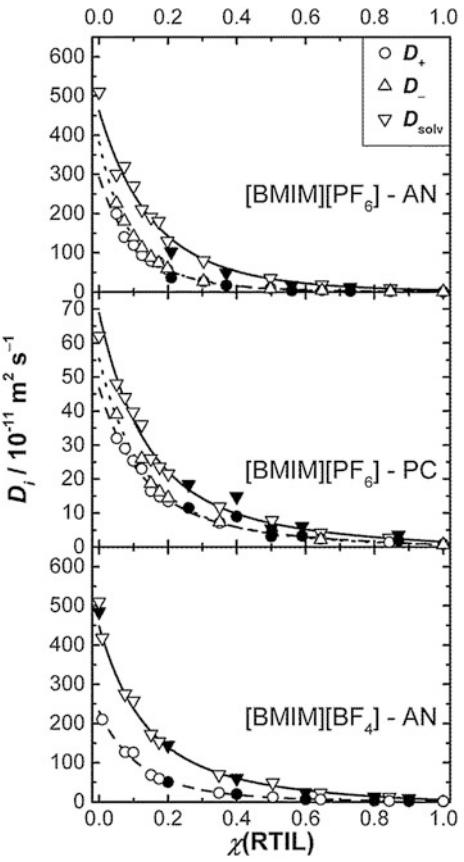

Fig. 5.8 Dependence of the experimental self-diffusion coefficients of the cations (D_+), anions (D_-) and solvent molecules (D_{solv}) on RTIL molar fraction in mixtures [BMIM][PF_6]–AN (*top*), [BMIM][PF_6]–PC (*middle*) [BMIM][BF_4] AN (*bottom*). Lines represent are fits of experimental data to (5.8). Filled symbols depict the data of Hsu et al. (*top* and *middle*) [84] and Liang et al. (*bottom*) [81]

correlated and demonstrate a mutual rapid growth at very high dilutions whereas viscosity of the system decrease but not so considerably. In the opposite case of the solvent with moderate value of dielectric constant (DMSO-d_6) it was established independent diffusion of the cation and anion with a constant value of the respective diffusion coefficients as a function of temperature and concentration. Such observations allow one to suppose an existence of a set ion aggregation from ion pairs to big ion clusters in the binary mixtures of RTILS with molecular solvents.

5.3.2.2 Relative Self-diffusion Coefficients Solvent-Cation as a Function of Mixture Composition

The concept of proportionality between ionic (mainly Li^+-based) and solvent diffusion coefficient was used an indication of the validity of the Stokes-Einstein relation, i.e. that particle diffusion is only modulated by macroscopic viscosity changes [85–90]. This approach is based on the observed proportionality between

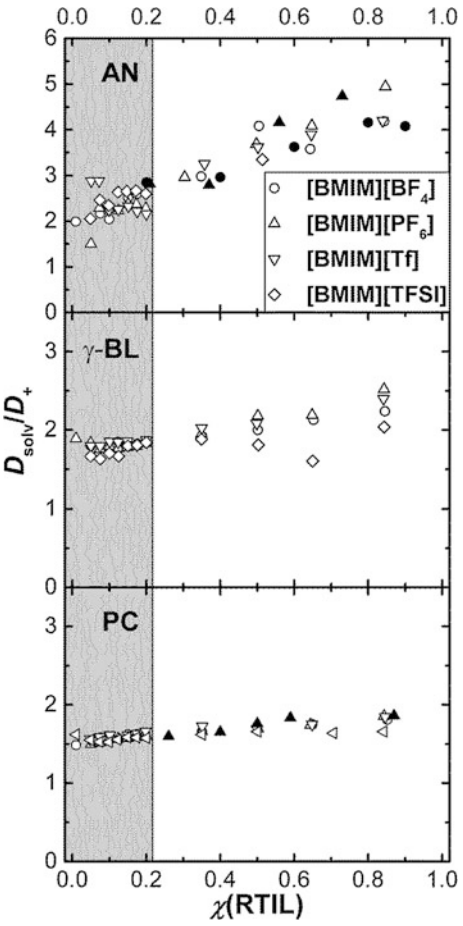

Fig. 5.9 The relative self-diffusion coefficients (D_{solv}/D_+) of as a function of RTIL molar fraction (open symbols). Filled triangles reflect results of Hsu et al. [84], while the filled circles are from Liang et al. [81]. The plateau region at $\chi(\text{RTIL}) < 0.2$ is highlighted in gray

the diffusion coefficients of neat solvents and their fluidity ($= \eta^{-1}$). Viscosity, in its turn, is believed to increase with concentration due to enhanced ion-molecular interactions. Any deviation from this relation was interpreted as a signature of the ionic association phenomena. Practically, the plot the ratio of the diffusion coefficient of solvent molecules over that of ions as a function of concentration is needed. It was expected that specific changes in ion-molecular and interionic interactions, if present, would cause an offset from a constant value. According to the Stokes-Einstein relation the ratio should be defined by the inverse ratio of the hydrodynamic radii of the diffusing species.

This methodology of analyzing the diffusion coefficient introduced by Hayamizu et al. [85–90] has been used for several diffusion studies of aqueous mixtures of RTILs [91, 92] over a broad range of concentrations. An improvement of this approach was proposed by Hsu et al. [84] in their study of [BMIM][PF_6] mixed with various non-aqueous solvents. Indeed, the authors of this paper introduced the

so-called 'aggregation index', defined as the diffusion ratio solvent-ion divided by the reciprocal of the corresponding radii ratio. The latter was estimated from quantum-mechanical calculations. It was shown that upon dilution and/or heating of RTIL the aggregation index decreases but never reaches the limiting value of unity. Furthermore, upon dilution and/or heating a weak tendency to ionic association was observed in PC and DMSO, while AN solvent has weak effect on the self-association. On the other hand, from the slope of the corresponding concentration trends an opposite conclusion can be reached: The steepest change in aggregation index was found for AN, whereas for PC it varied only slightly. As a consequence, when the mixture composition is varied, the structural changes are more pronounced in AN-based systems than those containing PC.

It should be mentioned the applicability of the Stokes-Einstein relation to RTIL-based systems is controversial [93–95] (vide infra) as well as the concept of hydrodynamic radius for such non-spherical particles as RTIL ions, which can also bear some degree of conformational flexibility. We then will stick here to the diffusion ratios of Hayamizu and disregard the aggregation index proposed by Hsu.

Figure 5.9 depicts the solvent-cation diffusion ratios as a function of mixture composition. Despite the expected significant influence of anions on the dynamic properties studied due to the substantial diversity of anion size, shape, symmetry and charge distribution, this figure shows that within experimental certainty the ratio is practically independent of the anion for all three employed solvents. This can be an indication of, either, negligible or, less probable, non-negligible but indistinguishable influence of different anions on the solvation pattern of the cations which is indirectly probed by the ratio of corresponding diffusion coefficients. We think first that this result may be challenged using other more accurate techniques that probe the probable differences in ion pairing tendencies of the studied RTILs. Second, in all three employed solvents the ratio scatters around some solvent-specific constant value at low RTIL content (χ(RTIL) < 0.2) before rising with increasing RTIL concentration. Such concentration dependence is a signature of ionic aggregation at higher concentrations. However, at low concentration range, the major factors determining particle diffusivities, namely their hydrodynamic size, mode of interaction with the microenvironment and microviscosity of the surrounding medium, either do not change or change simultaneously for cations and solvent molecules. Third, the rise at high RTIL concentrations is high, less significant and almost negligible in AN, γ-BL and PC, respectively. Indeed, for AN, at χ(RTIL) ≈ 0.85 solvent molecules diffuse 4–5 times faster than cations, compared to $D_{solv}/D_+ = 2.5$ at χ(RTIL) < 0.2.

The low concentration behavior can be rationalized by considering the relative sizes of the solvent molecules and neat solvent properties. Indeed, AN is the smallest molecule which results in higher value of the corresponding plateau value at χ(RTIL) < 0.2 while γ-BL and PC have somewhat bigger molecules and, hence, lower D_{solv}/D_+ plateau values. Also AN is the least polar and least donating solvent among the studied set, which suggests that its interaction with RTILs is more easily weakened with increasing RTIL concentration when compared to the cases of γ-BL and PC. Our observations are perfectly in line with those of Hsu et al. for [BMIM]

[PF_6]-based systems [84]. The fact that relative diffusion coefficients from different investigations agree better than the corresponding absolute values probably stems from probe calibration errors [96].

Originally, the Stokes-Einstein (SE) relation was derived under the assumption of a large sphere moving in a structureless continuum whose molecules are negligible in size with respect to the diffusing particle. It relates (5.9) the self-diffusion coefficient, D, of a particle to its hydrodynamic radius, r, a factor, A, determining the hydrodynamic boundary conditions (stick, slip or intermediate), and the medium viscosity, η.

$$D = kT/A\pi\eta r. \tag{5.9}$$

Accurate absolute values of the hydrodynamic radii of diffusing species can be estimated from data obtained by NMR experiments only if the gradient calibration of the probe was properly performed and the SE relation holds its relevance [97]. In mixtures of molecular solvents with RTILs, generally the SE relation is not satisfied. Indeed, usually unrealistically low values of the hydrodynamic radii of individual ions are found no matter how the boundary condition is set [81, 93–95]. This is associated with the fact that the representative diffusing species are of comparable sizes. In order to check the applicability of (5.9) to the studied mixtures, we are faced with the problem that the values of the hydrodynamic factor, A, are known for this mixture and it cannot be excluded that A (5.9) varies with composition due to possible changes of diffusion mechanism, solution structure, and/or boundary condition. As a consequence, we plot in Fig. 5.10, for a representative [BMIM][TFSI]-PC system, the effective Stokes radius $(Ar)_i = kT(D_i\eta\pi)^{-1}$ for cations and solvent molecules as a function of RTIL mole fraction. This representation is based on experimentally accessible quantities only. Viscosities were interpolated from experimental data by fitting logarithmic excess viscosities to a Riedlich-Kister type. Moreover, Fig. 5.10 provides strong evidence that for the studied system (other mixtures show very similar behavior) viscosity grows faster than particle diffusivities decrease when the RTIL concentration is increased. According to theory, the A factor in (5.9) equals four for slip [98] and six [99] for stick hydrodynamic boundary conditions. Taking this into account, reasonable values of the

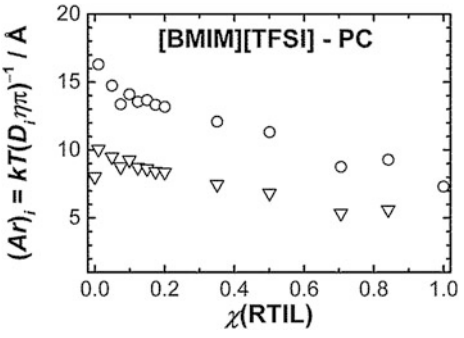

Fig. 5.10 Estimated effective Stokes radii, Ar, for cations (black circles) and solvent molecules (blue down triangles) in [BMIM][TFSI]-PC mixture as a function of RTIL mole fraction

hydrodynamic radii of cations and solvent molecules can only be expected at very low RTIL content. Indeed, the estimated values from quantum-chemical calculations of molecular volumes are 3.65 Å for $[BMIM]^+$ cation and 2.52, 2.95, and 3.06 Å for AN, γ-BL, and PC molecules, respectively. Moreover, predicted effective radii of the ion pairs range from ca. 4.0 to 4.5 Å suggesting that it is rather individual cations than the ion pairs which are the representative diffusing entities containing cation at these mole fractions. The inadequacy of the SE relation in concentrated mixtures of RTILs with molecular solvents is demonstrated by the fact that at higher concentrations the apparent hydrodynamic sizes progressively decrease down to unphysical values <2 Å. We consider this as strong evidence for and a clear indication of severe changes in solution microstructure and associated dynamics. In [BMIM][BF_4]/[PF_6]–PEG [100] and in [RMIM][$MeSO_3$]–H_2O mixtures [101, 102], Such a monotonic decrease of effective radii with IL concentration was also observed. This was interpreted as an increase in the size of non-polar domains formed by cation aggregates induced by the added solvent [101, 102]. The results of the Stokes-Einstein analysis of the observed ionic diffusivities on [EMIM][TFSI] dissolved in organic solvents of different polarity at very high dilutions (χ(RTIL) < 0.005) were interpreted in terms of weighted averages of dissociated and ion-paired species. For the least polar employed solvent ($CDCl_3$) the authors even detected a second set of resonances that was attributed to large ionic aggregates with aggregation numbers reaching 10–20 [103].

5.3.2.3 Relative Self-diffusion Coefficients as a Function of Mixture Composition

For mixtures with [BMIM][PF_6] RTIL we also measured anion diffusion by following ^{31}P nuclei. The apparent anion self-diffusion coefficients D_- were employed to study the corresponding diffusivity ratios presented in Fig. 5.11.

Surprisingly, solvent/anion ratio does not reveal a plateau at low RTIL content and rise more steeply (data not show) than the solvent/cation ratio. As a result, one observes an inversion of self-diffusion coefficients of cations and anions, so at

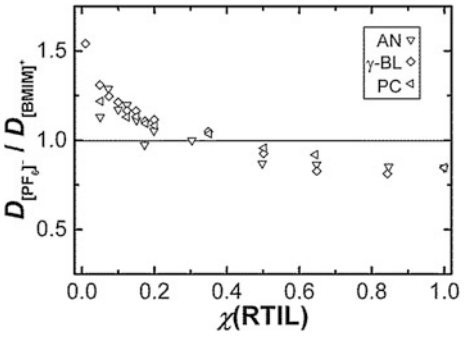

Fig. 5.11 Ratio of diffusion coefficients for counterions in [BMIM][PF_6] based mixtures as a function of RTIL content

χ(RTIL) < 0.5 cations diffuse slower as compare with anions, while in RTIL-rich mixtures and in pure RTILs $[BMIM]^+$ diffuse faster than $[PF_6]^-$ anions. Noteworthy, the observed trend seems to be solvent-independent.

This particular behavior was first noticed by Hsu et al. [84, 104]. Indeed, the surprisingly low translational mobility of the smaller anions in neat RTILs can be accelerated to a greater extent than that of the more voluminous cations by temperature increase and/or dilution with ordinary molecular liquid. That is to say, upon certain degree of dilution/heating the inversion of the counterion diffusivity has to occur. Based on numerous observations, mostly on the systems containing [BMIM][PF_6] [84] it was proposed and developed later on [104] the concept of hyper-anion predominance. The main idea is that in neat RTILs and in RTIL-rich mixtures there are not only neutral ion aggregates, but also some charged aggregated species, so called hyper-ions. In other words, charged species are mostly negatively charged. Therefore, the aggregates bearing positive charge are expected to be smaller in size (up to isolated cations) than the negatively charged ones. Given that the characteristic time-scale of NMR-diffusometry is on the order of tens to hundreds of ms, the apparent self-diffusion coefficient is a weighted average of the coexisting diffusing species. Thus, according to the hyper-anion predominance hypothesis, anions are mostly found in bigger aggregates, which move slower as compare with the smaller cation-enriched species. When diluted and/or heated the aggregates get more and more disrupted and eventually simple ions become the species which represent the diffusion phenomenon.

One can also find in the literature [83, 101] an alternative explanation of the "strangeness" of counterion diffusion inversion of RTILs. For example, Stark et al., who studied [RMIM][$MeSO_3$]–H_2O mixtures, [83, 101] used the concept of fast oscillating hydrophobic local subregions existing in pure RTILs and in RTIL-rich mixtures. These domains are thought to be formed by the nonpolar parts of the cations and to follow micellar-like organization. The authors supposed that at the same leap rate for cation and anions, the former ones have to pass bigger length between neighboring aggregates than the latter ones, that diffuse in the space between the aggregates. This could account for the higher values of cation self-diffusion coefficients.

In our opinion any hypothesis concerning the details of ion diffusivity in the mixtures of RTILs with molecular solvents should be based on the well established mechanism of the particle diffusion in such complex systems. We believe that this problem can be solved by applying an additional combination of the contemporary experimental and molecular modelling techniques such as quasi-elastic neutron scattering and molecular dynamics simulation. For example, Urahata and Ribeiro [105] by means of MD simulation have shown that for [RMIM][Hal] and [RMIM][PF_6] cation diffusivity is anisotropic, it is enhanced in the perpendicular direction with respect to the imidazolium ring plane. Similar, but a slightly different results showing diffusion anisotropy of cation in neat [BMIM][TFSI] RTIL were described by Liu and Maginn [106] However, such results can be adopted with some precaution since as it was shown [25, 107] mutual polarization of cation and anion in RTILs can influence significantly on dynamic properties of RTIL-based systems.

5.3.3 Summary

We present the results of NMR-diffusometry study on mixtures of [BMIM][TFSI], [BMIM][Tf], [BMIM][BF_4] and [BMIM][PF_6], with molecular solvents PC, AN and γ-BL over the whole concentration range at 300 K. Diffusion coefficients of all the components, namely cations, anions and solvent molecules gradually decrease with addition of RTIL, approximately following the exponential viscosity increase. In each solvent the ratio (D_{solv}/D_+) is almost insensitive to the anion. These relative diffusion coefficients do not change with increase of RTIL content up to $\chi(\text{RTIL}) < 0.2$, and increase slightly especially in case of AN We attribute this difference to rather weak cation solvation in AN over the whole concentration range. The established changes in the estimated hydrodynamic radii allow one to suppose a considerable change in solution microstructure and dynamics for the studied combinations of RTILs with molecular solvents. For the binary mixtures with [BMIM][PF_6] a inversion of ionic diffusion coefficients is observed about $\chi(\text{RTIL}) \approx 0.5$. At low RTIL concentration cations diffuse slower than anions in full accordance with their relative radii, whereas at high RTIL content and in pure RTILs cations diffusion is faster. Our results on inversion of cation/anion diffusion coefficients in the binary mixtures of RTILs with molecular solvents can be considered as a confirmation of some universal behavior such systems.

5.4 Molecular Dynamics Simulations of the Mixture of Imidazolium Ionic Liquids with Acetonitrile

5.4.1 State of the Field

Molecular dynamics (MD) simulations—including classical MD, [55, 108–116] ab initio MD, [117–125] semiempirical MD, [126–143] reactive MD, [144–151] and coarse-grained MD [152–158]—constitute currently the most successful group of methods in computational chemistry. In particular, MD is vigorously used to characterize one- and more-component liquid-matter systems [159–165]. The MD methods are based on real-time propagating Newtonian equations of motion in accordance with immediate forces acting on every interaction site of the simulated physical or chemical system. Microscopic quantities recorded during MD simulations in a certain thermodynamic ensemble are directly related to macroscopic (physicochemical) properties of the system. The simulated MD system shall meet the macroscopic limit, also known as the thermodynamic limit, i.e. the MD system must be sufficiently large, so that its volume increases strictly proportionally to the number of added identical particles (atoms, molecules, ions). With the above criterion met, the thermal motion of particles in the simulated MD system is identical to that of the real-world macroscopic system. Any observed discrepancies should be attributed to the insufficiently accurate interaction potentials, the main sources of

such inaccuracies being two-body-interaction simplification, electronic polarization effects, and quantum effects, provided the latter were omitted in the model Hamiltonian.

The computational power of modern supercomputing facilities is enough to routinely apply the classical MD method to nearly any system of physicochemical relevance. The MD systems, consisting of up to 10 000 interaction sites, can be sampled over the microsecond time scale. This opportunity excessively covers the needs to obtain thermodynamic, structure, and transport properties of even highly viscous systems. It has recently become possible to observe crystallization phenomena in real-time, whereas their conventional time scale is well above the nanosecond range. Free energy simulations using steered (external force) implementations of MD, umbrella-potential-like enhanced sampling, and gradual solute-solvent decoupling techniques are successfully employed to obtain solvation thermodynamics and describe the mean-force barriers for non-spontaneous processes.

Equilibrium MD delivers the following properties: (1) energy of vaporization, [166] (2) cohesion energy, [166] (3) arbitrary pairwise interaction energies in the many-body system, [167] (3) mass density, [168] (4) dielectric constant, [169] (5) saturated vapor pressure, [170, 171] (6) surface tension, [168] (7) radial distribution functional functions; [172] (8) coordination numbers; [172] (9) distribution of valence and non-valence angles in molecules at given temperature and pressure; [172] (10) distribution of molecular dipole moments; (11) self-diffusion coefficients; [107] (12) shear viscosity; [107] (13) electrical (specific) conductivity; [107] (14) life time of hydrogen bonds; [173] (15) orientation relaxation times; (16) thermal conductivity; [174] (17) vibration spectra; (18) excess molar quantities in the few-component systems; [25] (19) boiling point; [175] (20) critical point [176]. Most of the enumerated properties belong to physical chemistry in the sense that they can be obtained from the direct physical experiments. The other properties are inherent to microscopic simulations, e.g. interaction energies between specific moieties and certain relaxation times, which cannot be derived experimentally, but can drive further molecular design via precise understanding of each moiety's impact. The wealth of available properties makes it possible to use the MD method alone at the property prediction stage, leaving other methods (conductometry, NMR, etc.) for calibration and verification of the developed models. Provided the methodologies are established and routine user contributions are automated, MD is also more affordable both in terms of human-hours and core-hours, as compared to other methods.

Development or refinement of the interaction potential (model Hamiltonian, force field) is central to accuracy of the MD results [56, 177–180]. While quantum effects and sporadic chemical reactions are rarely important to obtain reliable macroscopic properties (except simulations of specific substances at specific conditions), electronic polarization plays a crucial role in many condensed-matter systems. Comprehensive efforts [181–189] have been made to introduce electronic polarization effects into classical Hamiltonians without the need to involve electronic-structure calculations, which may be costly at the thermodynamic limit.

The interaction parameters can be obtained from experimental data (e.g. covalent and van der Waals radii of atoms and ions), by manual tuning of the coefficients to reproduce benchmark properties (e.g. density and shear viscosity), and from ab initio calculations. The latter can, in principle, be used alone, as they provide all necessary quantities, such as bond length, valence angles, dihedrals, the corresponding force constants of stretching and bending, binding energies between the selected fragments. As exemplified for a wide range of ionic compounds and condensed phases, [56, 179, 180] this force field derivation approach, when used with conventional chemical wisdom, provides satisfactory to excellent results even for complicated molecular and ionic structures. Post-Hartree-Fock electronic-structure methods provide very reliable gas-phase properties, but fail to account for environmental effects with the same accuracy [190–193]. Implicit-solvation models are normally insufficiently accurate beyond benchmarking cases [194]. Furthermore, their relative errors are increased by orders of magnitude in the relatively large classical MD systems. All electronic-structure methods have problems in reproducing long-range interactions [195–198]. As a result, mass densities obtained from the constant-temperature constant-pressure density functional theory-based MD simulations are rarely accurate. Our unpublished results identified up to 20% discrepancies in densities of common molecular liquids using a few popular pure functionals and very high energy cut-off plane-wave basis sets.

Mixtures of ionic and molecular liquids represent strongly coupled condensed-matter systems [199–202]. In most cases, the mixtures are liquid and highly viscous at ambient conditions. An interplay of electrostatic and van der Waals interactions determines aggregation state and transport properties of the ion-molecular mixtures. Long-range interactions, beyond 1.5 nm of the interatomic distance, contribute up to 50% of cohesion energy. Hydrogen bonding is an important factor, which influences local structure around the cations. Furthermore, hydrogen bonding makes a key contribution to the miscibility of RTILs and polar molecular co-solvents, both protic and aprotic.

In the following, we demonstrate a full cycle of applying classical MD simulations to a few chosen systems involving imidazolium-based RTILs and acetonitrile. Electrochemically relevant properties are highlighted. Their importance for rational electrolyte design and reliability of prediction are commented on. We conclude with critically outlining the role of classical MD in understanding the RTIL + ML mixtures and performing robust electrolyte design.

5.4.2 Force Field Derivation

Periodic-box Car-Parrinello density functional theory-based MD simulations [203] were used to find the free energy minimum nuclear configurations of 1-ethyl-3-methylimidazolium tetrafluoroborate [EMIM][BF_4] and 1-butyl-3-methylimidazolium tetrafluoroborate [BMIM][BF_4]. The Car-Parrinello method [203] allows to avoid electronic-structure calculations at every time-step by

assigning an electron fictitious mass and simulating their motion as that of classical entities. In some cases, this method is more computationally efficient, as compared to Born-Oppenheimer MD. The BLYP exchange-correlation functional [204, 205] was used. The plane wave basis set was used with a conventional kinetic energy cut-off determined from the converged total energy and force. Due to a significant computational cost of the electronic-structure calculations, the system size was set to 8–12 ion pairs. The systems were simulated at 300, 350, and 400 K during 10 ps with a propagation time-step of 0.1 fs. After the systems were equilibrated, electrostatic charges on the cation and the anion were determined every 1000 time-steps and subsequently processed statistically. Temperature was found to exhibit a fairly marginal effect on the distribution of electrostatic charges. The average electrostatic charges were assigned in the developed force field. Since dispersion attraction is only negligibly sensitive to cation-anion coupling, the van der Waals (Lennard-Jones-12,6) coefficients were taken from the AMBER force field without modification. The hydrocarbon side chains of the imidazolium-based cations are assumed to be non-polarizable. More detailed description of the employed procedure, along with its pros and cons, is described elsewhere [56]. AN was simulated as a six-site fixed-charge model with harmonic stretching potentials, as devised by Nikitin and Lyubartsev [206]. The Lorentz-Berthelot rules were used to describe Lennard–Jones–12,6 interactions between AN and imidazolium-based RTILs.

5.4.3 Methodology

A unified methodology can be adapted for all binary mixtures of RTILs and MLs to simplify point-by-point comparison. The settings and algorithms proposed below can be safely applied to other RTIL containing MD systems. The entire composition ranges of the [EMIM][BF_4]/AN and [BMIM][BF_4]/AN mixtures were investigated. The MD systems contained 2070-9000 interaction sites, corresponding to 300 ion pairs of [EMIM][BF_4] and [BMIM][BF_4], some of which were substituted by AN molecules to prepare mixtures (5–90 mol%). Preliminary test simulations indicated that such system sizes constitute an optimal choice for the investigated set of physical chemical and microscopic properties. The mixtures were simulated at 283, 298, and 323 K under 1.0 bar. In this way, standard conditions, as well as slightly decreased and slightly increased temperatures, were included. The fluctuations of temperature around the designated value were maintained by the velocity rescaling thermostat (relaxation time 100 fs) [207]. The fluctuations of pressure around its constant value were maintained by the Parrinello-Rahman barostat (relaxation time 1000 fs, compressibility constant 4.5×10^{-5} bar^{-1}) [208]. The integration time-step of 1.0 fs was used, whereas every system was sampled during 50 000 ps after equilibration. In general, the integration time-step can be increased up to 2.0 fs, provided that all lengths of the carbon–hydrogen covalent bonds are constrained [209, 210]. The Cartesian coordinates were saved every 20 fs. All interactions were treated as two-body ones. The electrostatic forces were computed

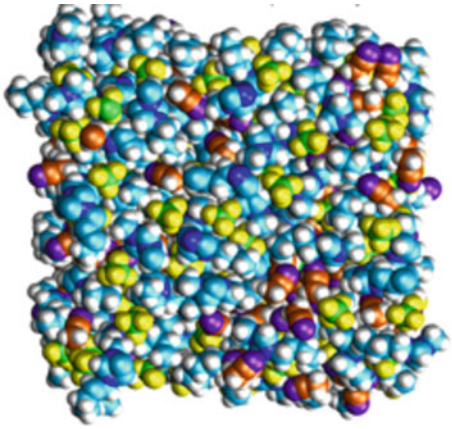

Fig. 5.12 An immediate ion-molecular configuration of the [BMIM][BF_4] + AN equimolar mixture after the free energy minimum at 298 K and 1 bar was reached. Visual Molecular Dynamics software, version 1.8, [216] was used to prepare this artwork

directly (using the Coulomb law for point charges) for the atom-atom separations below 1.5 nm. At longer distances, the Particle Mesh Ewald method in the reciprocal space [211] was used. The Lennard-Jones-12,6 forces were slightly modified between 1.2 and 1.3 nm to completely disappear at 1.3 nm. The list of neighboring atoms was updated every 10 time-steps within the radius of 1.5 nm. Figure 5.12 depicts periodic a simulation box of the RTIL + ML mixture.

Physicochemical and microscopic properties. To illustrate robustness of the established methodology, we computed and discussed a relatively small set of properties, which are most important to perform a thoughtful electrolyte design: (1) specific conductivity, (2) shear viscosity, (3) self-diffusion coefficients, (4) mass density, (5) cluster size distributions.

Ionic conductivity was computed from the linear slope of mean-square displacements of the collective translational dipole moment. The method is sometimes referred to as Einstein-Helfand and requires continuous movement of atoms, i.e. post-simulation removal of periodic boundary conditions. Shear viscosity was computed from the autocorrelation function of the off-diagonal elements of the pressure tensor. This method converges slowly, but allows to use equilibrium MD simulations, instead of explicitly simulating energy dissipation. Self-diffusion coefficient of every molecular and ionic species was computed from the slope of mean–squared displacements of atoms versus time. Mass density was computed from the thermal motion induced fluctuations of the MD system volume in the course of MD simulation. Ionic clusters were identified using the single-linkage method, in which the key distance is 0.50 (0.51) nm measured between the C-2 atom of the cation and the boron atom of the anion. This criterion was derived from the position of the first minimum in the radial distribution function for the respective interaction sites.

Computer codes. GROMACS 4 was used to carry out classical MD simulations [212–215]. VMD was used to observe ion-molecular trajectories and prepare molecular artwork [216]. PACKMOL was used to generate initial energy-efficient

ion-molecular configurations [217]. The scheduled MD simulations do not require high degrees of paralellization. We used 4–12 cores per simulation, depending on the number of interaction centers, with the domain decomposition scheme to efficiently distribute computation of immediate forces on-the-fly.

5.4.4 Discussion of MD Simulation Results

Predicting, which binary mixture exhibits the highest specific conductivity (Fig. 5.13) without experiments and simulations, is the most challenging and important task in the context of designing an electrolyte. Knowing the most conductive composition is essential for designing best performing electrolytes. While mobility of the individual ions (Figs. 5.14 and 5.15) increases with an addition of more molecular co-solvent, due to shear viscosity decrease (Fig. 5.16), the number of charge carriers in the solution decreases simultaneously. Thus, the conductivity maximum should be expected at some finite concentration. Ionic conductivity of [EMIM][BF_4] increases by up to three times upon dilution. In turn, specific conductivity of [BMIM][BF_4] increases by up to 13 times. Nonetheless, the absolute value κ([EMIM][BF_4]/AN) remains higher at all investigated temperatures. The increase of κ([EMIM][BF_4]/AN) is less steep, therefore, a range of binary compositions can be suitable for but AN impacts it very favorably. The ion motion is

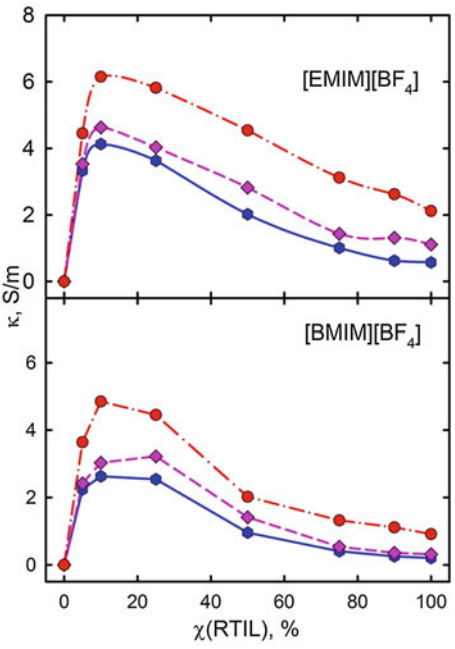

Fig. 5.13 Specific conductivity of the [EMIM][BF_4]/AN and [BMIM][BF_4]/AN mixtures computed at 283 K (blue hexagons), 298 K (magenta diamonds), and 323 K (red circles) versus molar fraction of RTILs. Note the location of the conductivity maximum

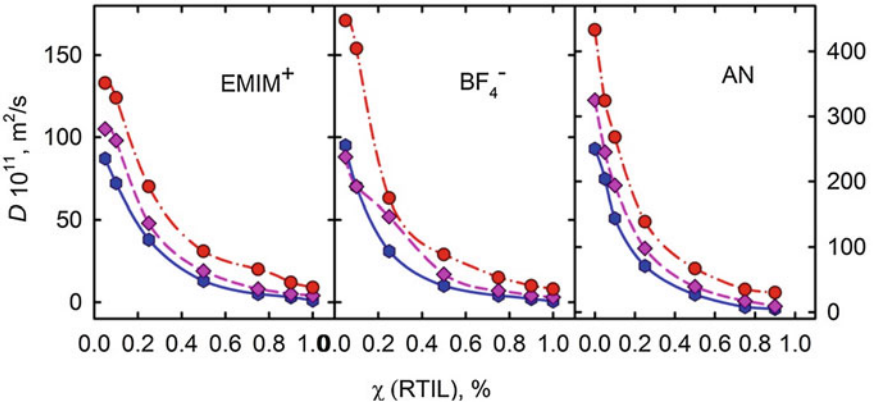

Fig. 5.14 Self-diffusion coefficients, D, of cation ($EMIM^+$), anion (BF_4^-) and solvent molecules (AN) of the [EMIM][BF_4]/AN mixtures computed at 283 K (blue hexagons), 298 K (magenta diamonds), and 323 K (red circles) versus molar fraction of RTILs

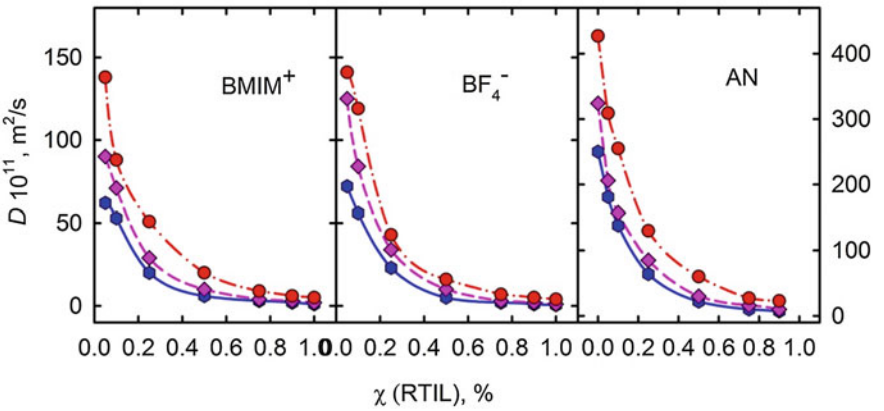

Fig. 5.15 Self-diffusion coefficients, D, of cation ($BMIM^+$), anion (BF_4^-) and solvent molecules (AN) of the [BMIM][BF_4]/AN mixtures computed at 283 K (blue hexagons), 298 K (magenta diamonds), and 323 K (red circles) versus molar fraction of RTILs

driven by AN, e.g. at χ (RTIL) < 10%, the ion diffusion coefficients in [EMIM][BF_4]/AN is approximately 1.1 times larger, as compared to [BMIM][BF_4]/AN. Mobility of co-solvent molecules is of crucial importance to achieve higher conductivities of the resulting electrolytes. We observed a strong correlation of specific conductivity with temperature. Whereas κ([EMIM][BF_4]/AN) increases by three times upon dilution at 323 K, it increases as much as by 7 times at 283 K. Compare, κ([BMIM][BF_4]/AN) increases by 13 times at 283 K. We conclude that addition of AN is crucially important for low-temperature electrolytes.

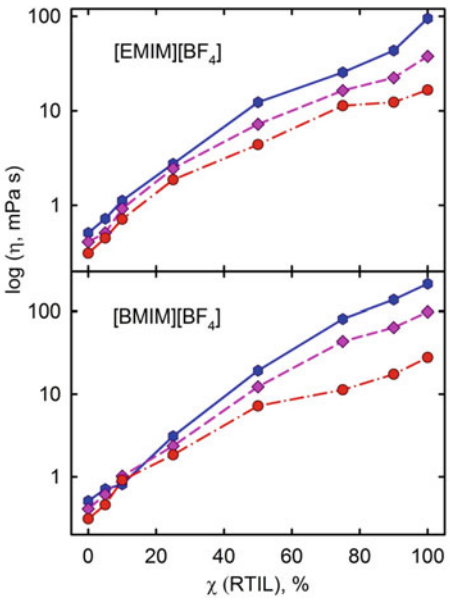

Fig. 5.16 Shear viscosity of the [EMIM][BF_4]/AN and [BMIM][BF_4]/AN mixtures computed at 283 K (red circles), 298 K (green squares), and 323 K (blue triangles) versus molar fraction of RTILs

Self-diffusion (Figs. 5.14 and 5.15) in the mixture and shear viscosity (Fig. 5.16) are connected directly by the Einstein-Stokes relationship ($D \sim \eta^{-1}$), provided that particles can be described as spheres. While the sphericity criterion is not completely fulfilled either for AN or for imidazolium-based RTILs, the trend is still observed. The ratio of cationic and anionic diffusion coefficients changes drastically as RTIL fraction gradually decreases. In the RTIL-rich mixtures, the anionic diffusion is 60–70% of the cationic diffusion, even though the imidazolium-based cations are a way more bulky, as compared to the spherical tetrafluoroborate anion. In turn, the anionic diffusion increases somewhat faster with temperature. As the molar fraction of AN increases, anionic diffusion becomes faster than the cationic one. This is easy to understand by considering the following factors. While the content of AN molecules is negligible, the cation and the anion create large ionic clusters (see below). Their structure is determined by the pairwise interaction between the fluorine atoms of the anion and the C(2)-H atom of the imidazole ring. The anions are bound to the cations, resulting in their slow self-diffusion (Figs. 5.14 and 5.15) and high viscosity (Fig. 5.16). Upon gradual addition of AN, the anions get substituted by the co–solvent molecules. The ion clusters dissolve and the anionic self-diffusion becomes much faster at lower RTIL fractions (Figs. 5.14 and 5.15). Interestingly, a drastic acceleration of the tetrafluoroborate anion nearly coincides with the location of the specific conductivity maximum.

Shear viscosity depends on temperature and fraction of RTILs crucially (Fig. 5.16). At higher fractions of RTILs, dependence on temperature is stronger. Compare η([BMIM][BF_4], 283 K) = 137 cP to η([BMIM][BF_4], 323 K) = 17 cP at χ(RTIL) = 90%. Viscosities of the [EMIM][BF_4]/AN mixtures are systematically

smaller, as compared to [BMIM][BF_4]/AN. The RTIL-rich mixtures are quite viscous and marginally conductive, therefore, small additions of AN are not practical. At higher AN fractions, χ(RTIL) < 25%, viscosity is decreased by an order of magnitude. As stated above, the transport properties of the AN-rich mixtures are controlled by AN. This is possible thanks to strong ion-molecular interactions and excellent miscibility of AN with imidazolium-based RTILs. The simulated viscosities appear in good to excellent agreement with the experimental data [21, 22, 57]. An alternative possibility to obtain shear viscosity and conjugated transport properties is simulating at a few elevated temperatures and extrapolating of the fitted (parametrized) Vogel-Tamman-Fulcher equation. As demonstrated using a few imidazolium-based RTILs, this method allows to save computational time quite significantly [218].

Density (Fig. 5.17) can be used to check an accuracy of the force field, since this property can be simulated very quickly. On another hand, experimental determination of density is also inexpensive, reliable, and straightforward. Point-by-point comparison reveals a very good agreement with literature results [23, 44]. E.g. simulated ρ([BMIM][BF_4]/AN) = 1094 kg m^{-3} in the equimolar mixture, compares perfectly to previously reported experimental value, 1102 kg m^{-3}. ρ([EMIM][BF_4]/AN, 50 mol%) = 1137 kg m^{-3} is quite close to the experimental value of 1167 kg m^{-3}. Mixtures of [BMIM][BF_4] are somewhat less dense, since a longer hydrocarbon side chain decreases density. This trend is also valid for pure RTILs. The densities of [EMIM][BF_4]/AN and [BMIM][BF_4]/AN are equal at χ(RTIL) = 25%.

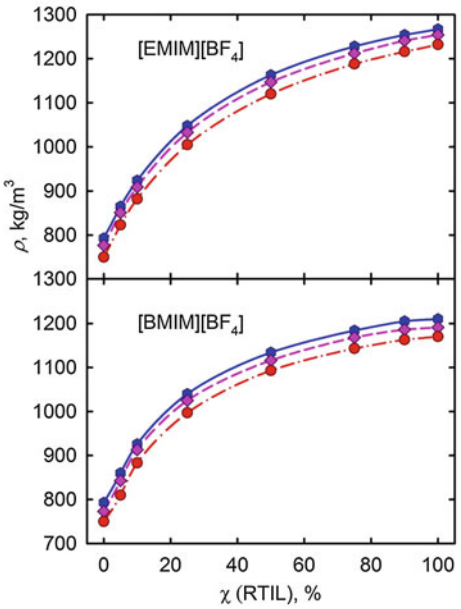

Fig. 5.17 The density of [EMIM][BF_4]/AN and [BMIM][BF_4]/AN mixtures computed at 283 K (blue hexagons), 298 K (magenta diamonds), and 323 K (red circles) versus molar fraction of RTILs

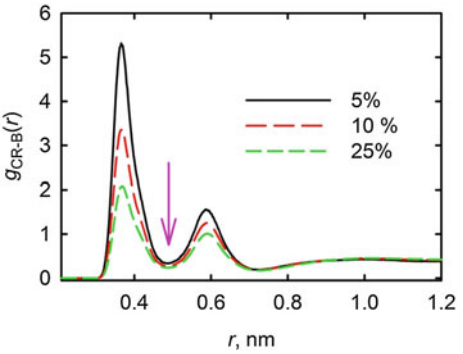

Fig. 5.18 Radial distribution functions, $g_{CR\text{-}B}(r)$, computed between the cation and the anion in the [EMIM][BF_4]/AN mixtures for a few AN-rich systems. The legend shows molar fractions of RTILs. Arrow indicates the position of the first minimum used as the single-linkage threshold for ion aggregates formation

Table 5.3 The average cluster sizes of [EMIM][BF_4] and [BMIM][BF_4] formed in AN at 283, 298, and 323 K

χ(RTIL),%	[EMIM][BF_4]			[BMIM][BF_4]		
	283 K	298 K	323 K	283 K	298 K	323 K
5	1.6	1.7	1.6	1.6	1.7	1.7
10	2.2	2.2	2.2	2.2	2.2	2.2
25	5.7	5.1	5.1	5.0	4.9	4.4
50	45	42	35	21	19	16

Formation of ion pairs and larger clusters deteriorate specific conductivity by decreasing translational mobility of charge carriers. Therefore, distribution of ion clusters and their lifetimes are essential to predict and explain location of the specific conductivity maximum in the binary mixtures.

The single-linkage threshold was set according to the first minimum position in radial distribution function $g_{CR\text{-}B}(r)$, where CR is the Carbon atom of imidazolium ring connected to the most positive Hydrogen atom, and B is Boron atom of BF_4^- anion (Fig. 5.18). The position of minimum is independent on molar fraction and marginally dependent on the imidazolium-based cation, 0.5 nm for [EMIM][BF_4] and 0.512 nm for [BMIM][BF_4], respectively. The choice of the atom pair and the threshold is somewhat arbitrary in the systems, in which more than one dominant intermolecular interaction exist. Selecting a maximum position as a threshold is also acceptable; in that case only strongly bound clusters would be detected, whereas the percentage of large ion clusters would be significantly lowered.

Tables 5.3 and 5.4 summarize the results of cluster analysis in terms of average cluster size and probabilities to form clusters of given size, respectively. Ion structures formed by [EMIM][BF_4] and [BMIM][BF_4] are similar. The size of the largest ion cluster is in direct proportion to the RTIL molar fraction. The preferential cluster is an ion pair. Its existence is most probable in the AN-rich mixtures. Significant percentages of the lone ions exist at χ(RTIL) = 5–10%, irrespective of

Table 5.4 Probabilities of formation of the [EMIM][BF_4] and [BMIM][BF_4] ion clusters of given size in the equimolar [EMIM][BF_4]/AN and [BMIM][BF_4]/AN mixtures at 323 K

Cluster size, (number of ions)	Probability, %		Cluster size, (number of ions)	Probability, %	
	[EMIM][BF_4]	[BMIM][BF_4]		[EMIM][BF_4]	[BMIM][BF_4]
1–10	42	55	91–100	2.4	0.5
11–20	14	19	101–110	2.0	0.3
21–30	8.4	9.8	111–120	1.8	0.2
31–40	6.0	5.8	121–130	1.5	0.1
41–50	4.7	3.5	131–140	1.1	0.1
51–60	4.0	2.4	141–150	1.1	0.1
61–70	3.5	1.6	151–160	0.8	0.0
71–80	2.7	1.0	161–170	0.7	0.0
81–90	2.6	0.8	171–240	1.0	0.0

the imidazolium-based cation. Note that the amount of lone ions is comparable to amount of ion pairs at χ(RTIL) = 25–50%. We conclude that ion pairs are insufficiently stable in the AN-rich mixtures. Relatively low stabilities of the following ion pairs—[EMIM] + [BF_4] and [BMIM] + [BF_4]—are responsible for the formation of a large variety of ion clusters (Table 5.4). The average sizes of the ion clusters are 1.7, 2.2, 5.1, 42 for 5, 10, 25, 50% of [EMIM][BF_4] at 298 K. It is clearly seen that clusters become larger as χ(RTIL) increases. A sharp elevation is seen from χ(RTIL) = 25% to χ(RTIL) = 50%. A similar ion cluster size distribution is observed in the [BMIM][BF_4]/AN mixtures (Table 5.3).

An average ion cluster size in [BMIM][BF_4]/AN is twice smaller than that in [EMIM][BF_4]/AN in the AN-rich mixtures. Unlike [EMIM] and [BF_4], [BMIM] and [BF_4] maintain larger percentages of smaller clusters. The largest detected cluster comprises 240 (in [EMIM][BF_4]/AN) and 170 (in [BMIM][BF_4]/AN) ions. Even though the probabilities of such clusters formation are negligible (less than 0.01%), the difference is quite significant. This difference reveals a substantial effect of the longer hydrocarbon side chain in [BMIM][BF_4].

To recapitulate, an average aggregate size is directly proportional to AN molar fraction. As χ (AN) increases, total number of charge carriers (ions of RTIL) decreases. The location of the specific conductivity maximum results from an interplay of these properties. Position of the conductivity maximum coincides with the largest χ(RTIL) at which percentage of lone ions starts to exceed percentage of ion pairs. Our results suggest that lone ions contribute most to specific conductivity of the system. Ionic clusters and their size distributions can be used to predict and correlate shear viscosity in mixtures, as highlighted recently using another family of RTILs as an example [209].

5.4.5 Summary

Molecular dynamics, and in particular classical molecular dynamics, represents a powerful and affordable research technique for ionic liquids and their binary mixtures with molecular liquids. Determination of the valid model Hamiltonian is most essential to guarantee high quality of the predicted properties. Development of unified force field derivation algorithms is of high value for the progress of the field. The cost of most physicochemically relevant classical MD simulations is covered by the available supercomputing resources.

In this work, we exemplified a successful and robust application of classical MD to characterize the [EMIM][BF_4]/AN and [BMIM][BF_4]/AN mixtures over their entire composition ranges. We identified location of the specific conductivity maximum, being the most important data for an electrolyte design, and explained it by two competing factors using viscosity and self-diffusion data. We showed that maximum conductivity correlates with ionic clustering and can be, therefore, hypothesized using an average structure of the ion-molecular system. Classical MD readily provides most physicochemical properties, except electrochemical window, needed to rate one- and more-component electrolytes according to their suitability for a certain electrochemical application.

Acknowledgements O.N.K. and A.V.R. acknowledge the Grants #0115U000483 and #0116U000834 of Ministry of Education and Science of Ukraine. V.V.C. acknowledges CAPES. This work was preformed using computational facilities of the joint computational cluster of SSI "Institute for Single Crystals" and Institute for Scintillation Materials of National Academy of Science of Ukraine incorporated into Ukrainian National Grid.

References

1. R.D. Rogers, K.R. Seddon (eds.), *Ionic liquids as Green Solvents. Progress and Prospects* (American Chemical Society, Washington DC, 2003)
2. M.A.P. Martins, C.P. Frizzo, D.N. Moreira, N. Zanatta, H.G. Bonacorso, Ionic liquids in heterocyclic synthesis. Chem. Rev. **108**(6), 2015–2050 (2008)
3. T. Welton, P. Wasserscheid (eds.), *Ionic Liquids in Synthesis*, 2nd edn. (VCH-Wiley Weinheim, Germany, 2007)
4. J. Dupont, R.F. de Souza, P.A.Z. Suarez, Ionic liquid (molten salt) phase organometallic catalysis. Chem. Rev. **102**(10), 3667–3692 (2002)
5. V.I. Pârvulescu, C. Hardacre, Catalysis in ionic liquids. Chem. Rev. **107**(6), 2615–2665 (2007)
6. M. Haumann, A. Riisager, Hydroformylation in room temperature ionic liquids (RTILs): catalyst and process developments. Chem. Rev. **108**(4), 1474–1497 (2008)
7. J.-f. Liu, Jiang G.-b., Liu J.-f., J.Å. Jönsson, Application of ionic liquids in analytical chemistry. Trends Anal. Chem. **24**(1), 20–27 (2005)
8. J.L. Anderson, D.W. Armstrong, G.-T. Wei, Ionic liquids in analytical chemistry. Anal. Chem. **78**(9), 2892–2902 (2006)
9. Y.C. Pei, J.J. Wang, X.P. Xuan, J. Fan, M. Fan, Factors affecting ionic liquids based removal of anionic dyes from water. Environ. Sci. Technol. **41**(14), 5090–5095 (2007)

10. Z. Li, Z. Liu, J. Zhang, B. Han, J. Du, Y. Gao et al., Synthesis of single-crystal gold nanosheets of large size in ionic liquids. J. Chem. Phys. B **109**(30), 14445–14448 (2005)
11. E.R. Cooper, C.D. Andrews, P.S. Wheatley, P.B. Webb, P. Wormald, R.E. Morris, Ionic liquids and eutectic mixtures as solvent and template in synthesis of zeolite analogues. Nature **430**, 1012–1016 (2004)
12. K. Ding, Z. Miao, Z. Liu, Z. Zhang, B. Han, G. An et al., Facile synthesis of high quality TiO_2 nanocrystals in ionic liquid via a microwave-assisted process. J. Am. Chem. Soc. **129** (20), 6362–6363 (2007)
13. M. Galiński, A. Lewandowski, I. Stępniak, Ionic liquids as electrolytes. Electrochim. Acta **51**(26), 5567–5580 (2006)
14. P. Hapiot, C. Lagrost, Electrochemical reactivity in room-temperature ionic liquids. Chem. Rev. **108**(7), 2238–2264 (2008)
15. B. Garcia, S. Lavallée, G. Perron, C. Michot, M. Armand, Room temperature molten salts as lithium battery electrolyte. Electrochim. Acta **49**(26), 4583–4588 (2004)
16. J.L. Anderson, J. Ding, T. Welton, D.W. Armstrong, Characterizing ionic liquids on the basis of multiple solvation interactions. J. Am. Chem. Soc. **124**(47), 14247–14254 (2002)
17. A. Heintz, D.V. Kulikov, S.P. Verevkin, Thermodynamic properties of mixtures containing ionic liquids. 2. Activity coefficients at infinite dilution of hydrocarbons and polar solutes in 1-methyl-3-ethyl-imidazolium bis(trifluoromethyl-sulfonyl) amide and in 1,2-dimethyl-3-ethyl-imidazolium bis(trifluoromethyl-sulfonyl) amide using gas−liquid chromatography. J. Chem. Eng. Data **47**(4), 894–899 (2002)
18. X. Xiaohua, Z. Liang, L. Xia, J. Shengxiang, Ionic liquids as additives in high performance liquid chromatography: analysis of amines and the interaction mechanism of ionic liquids. Anal. Chim. Acta **519**(2), 207–211 (2004)
19. E.D. Bates, R.D. Mayton, I. Ntai, H. James, J. Davis, CO_2 capture by a task-specific ionic liquid. J. Am. Chem. Soc. **124**(6), 926–927 (2002)
20. J. Zhang, S. Zhang, K. Dong, Y. Zhang, Y. Shen, X. Lv, Supported absorption of CO_2 by tetrabutylphosphonium amino acid ionic liquids. Chem. A Eur. J. **12**(15), 4021–4026 (2006)
21. H. Tokuda, K. Hayamizu, K. Ishii, M.A.B.H. Susan, M. Watanabe, Physicochemical properties and structures of room temperature ionic liquids. 1. Variation of anionic species. J. Phys. Chem. B **108**(42), 16593–16600 (2004)
22. A.L. Zhu, J.J. Wang, L.J. Han, M.H. Fan, Measurements and correlation of viscosities and conductivities for the mixtures of imidazolium ionic liquids with molecular solutes. Chem. Eng. J. **147**(1), 27–35 (2009)
23. J.J. Wang, Y. Tian, Y. Zhao, K. Zhuo, A volumetric and viscosity study for the mixtures of 1-n-butyl-3-methylimidazolium tetrafluoroborate ionic liquid with acetonitrile, dichloromethane, 2-butanone and N,N-dimethylformamide. Green Chem. **5**(5), 618–622 (2003)
24. E. Rilo, J. Vila, J. Pico, S. García-Garabal, L. Segade, L.M. Varela et al., Electrical conductivity and viscosity of aqueous binary mixtures of 1-alkyl-3-methyl imidazolium tetrafluoroborate at four temperatures. J. Chem. Eng. Data **55**(2), 639–644 (2010)
25. V.V. Chaban, I.V. Voroshylova, O.N. Kalugin, O.V. Prezhdo, Acetonitrile boosts conductivity of imidazolium ionic liquids. J. Phys. Chem. B. **116**(26), 7719–7727 (2012)
26. J. Barthel, K. Bachhuber, R. Buchner, J.B. Gill, M. Kleebauer, Dielectric spectra of some common solvents in the microwave region. Dipolar aprotic solvents and amides. Chem. Phys. Lett. **167**(1–2), 62–66 (1990)
27. C. Mialkowski, A. Chagnes, B. Carré, D. Lemordant, P. Willmann, Excess thermodynamic properties of binary liquid mixtures containing dimethylcarbonate and γ-butyrolactone. J. Chem. Thermodyn. **34**(11), 1847–1856 (2002)
28. J. Barthel, R. Neueder, H. Roch, Density, relative permittivity, and viscosity of propylene carbonate + dimethoxyethane mixtures from 25 °C to 125 °C. J. Chem. Eng. Data **45**(6), 1007–1011 (2000)
29. C. Reichardt, T. Welton, *Solvents and Solvent Effects in Organic Chemistry*, Fourth, Updated and Enlarged Edition (Wiley-VCH Verlag GmbH & Co. KGaA, Weinheim, 2011) 718 p.

30. J. Wu, Z. Lan, J. Lin, M. Huang, S. Hao, L. Fang, Influence of solvent on the poly (acrylic acid)-oligo-(ethylene glycol) polymer gel electrolyte and the performance of quasi-solid-state dye-sensitized solar cells. Electrochim. Acta **52**(24), 7128–7135 (2007)
31. M.T. Zafarani-Moattar, R. Majdan-Cegincara, Viscosity, density, speed of sound, and refractive index of binary mixtures of organic solvent + ionic liquid, 1-butyl-3-methylimidazolium hexafluorophosphate at 298.15 K. J. Chem. Eng. Data **52** (6), 2359–2364 (2007)
32. S. Aparicio, R. Alcalde, Characterization of two lactones in liquid phase: an experimental and computational approach. Phys. Chem. Chem. Phys. **11**(30), 6455–6467 (2009)
33. E. Couadou, J. Jacquemin, H. Galiano, C. Hardacre, M. Anouti, A comparative study on the thermophysical properties for two bis[(trifluoromethyl)sulfonyl]imide-based ionic liquids containing the trimethyl-sulfonium or the trimethyl-ammonium cation in molecular solvents. J. Phys. Chem. B **117**(5), 1389–1402 (2013)
34. H. Wang, S. Liu, K. Huang, X. Yin, Y. Liu, S. Peng, $BMIMBF_4$ ionic liquid mixtures electrolyte for Li-ion batteries. Int. J. Electrochem. Sci. **7**(2), 1688–1698 (2012)
35. E. Coadou, L. Timperman, J. Jacquemin, H. Galiano, C. Hardacre, M. Anouti, Comparative study on performances of trimethyl-sulfonium and trimethyl-ammonium based ionic liquids in molecular solvents as electrolyte for electrochemical double layer capacitors. J. Phys. Chem. C **117**(20), 10315–10325 (2013)
36. Q. Zhu, Y. Song, X. Zhu, X. Wang, Ionic liquid-based electrolytes for capacitor applications. J. Electroanal. Chem. **601**(1–2), 229–236 (2007)
37. A. Chagnes, H. Allouchi, B. Carre, D. Lemordant, Thermal analysis of γ-butyrolactone+1 butyl-3-methyl-imidazolium ionic liquids mixtures. Solid State Ionics **176**(15–16), 1419–1427 (2005)
38. A. Chagnes, M. Diaw, B. Carré, P. Willmann, D. Lemordant, Imidazolium-organic solvent mixtures as electrolytes for lithium batteries. J. Power Sources **145**(1), 82–88 (2005)
39. H. Ohno, *Electrochemical Aspects of Ionic Liquids* (Wiley-intercsience, Hoboken, New Jersey, 2005)
40. W. Li, Z. Zhang, J. Zhang, B. Han, B. Wang, M. Hou et al., Micropolarity and aggregation behavior in ionic liquid + organic solvent solutions. Fluid Phase Equilib. **248**, 211–216 (2006)
41. M. Diaw, A. Chagnes, B. Carr´e, P. Willmann, D. Lemordant, Mixed ionic liquid as electrolyte for lithium batteries. J. Power Sources **146**, 682–684 (2005)
42. W.J. Li, B.X. Han, R.T. Tao, Z.F. Zhang, J.L. Zhang, Measurement and correlation of the ionic conductivity of ionic liquid-molecular solvent solutions. Chin. J. Chem. **25**(9), 1349–1356 (2007)
43. J.N.C. Lopes, M.F.C. Gomes, P. Husson, A.A.H. Padua, L.P.N. Rebelo, S. Sarraute et al., Polarity, viscosity, and ionic conductivity of liquid mixtures containing C(4)C(1)im Ntf(2) and a molecular component. J. Phys. Chem. B. **115**(19), 6088–6099 (2011)
44. A. Stoppa, J. Hunger, R. Buchner, Conductivities of binary mixtures of ionic liquids with polar solvents. J. Chem. Eng. Data **54**(2), 472–479 (2009)
45. C. Comminges, R. Barhdadi, M. Laurent, M. Troupel, Determination of viscosity, ionic conductivity, and diffusion coefficients in some binary systems: ionic liquids plus molecular solvents. J. Chem. Eng. Data **51**(2), 680–685 (2006)
46. Y. Francois, K. Zhang, A. Varenne, P. Gareil, New integrated measurement protocol using capillary electrophoresis instrumentation for the determination of viscosity, conductivity and absorbance of ionic liquid–molecular solvent mixtures. Anal. Chim. Acta **562**, 164–170 (2006)
47. R. Zarrougui, M. Dhahbi, D. Lemordant, Effect of temperature and composition on the transport and thermodynamic properties of binary mixtures of ionic liquid N-Butyl-N-methylpyrrolidinium bis(trifluoromethanesulfonyl)imide and propylene carbonate. J. Solution Chem. **39**, 921–942 (2010)

48. E. Rilo, J. Vila, M. Garcı´a, L.M. Varela, O. Cabeza, Viscosity and electrical conductivity of binary mixtures of CnMIM-BF4 with ethanol at 288 K, 298 K, 308 K, and 318 K. J. Chem. Eng. Data **55**, 5156–5163 (2010)
49. W. Liu, L. Cheng, Y. Zhang, H. Wang, M. Yu, The physical properties of aqueous solution of room-temperature ionic liquids based on imidazolium: database and evaluation. J. Mol. Liq. **140**, 68–72 (2008)
50. H. Xu, D. Zhao, P. Xu, F. Liu, G. Gao, Conductivity and viscosity of 1-allyl-3-methyl-imidazolium chloride + water and + ethanol from 293.15 K to 333.15 K. J. Chem. Eng. Data **50**, 133–135 (2005)
51. M. Bester-Rogac, J. Hunger, A. Stoppa, R. Buchner, Molar conductivities and association constants of 1-butyl-3-methylimidazolium chloride and 1-butyl-3-methylimidazolium tetrafluoroborate in methanol and DMSO. J. Chem. Eng. Data **55**, 1799–1803 (2010)
52. H. Wang, J. Wang, S. Zhang, Y. Pei, K. Zhuo, Ionic association of the ionic liquids [C4mim][BF4], [C4mim][PF6], and [Cnmim]Br in molecular solvents. ChemPhysChem **10**, 2516–2523 (2009)
53. M. Bester-Rogac, A. Stoppa, J. Hunger, G. Hefter, R. Buchner, Association of ionic liquids in solution: a combined dielectric and conductivity study of bmim Cl in water and in acetonitrile. Phys. Chem. Chem. Phys. **13**(39), 17588–17598 (2011)
54. B. Kirchner, Ionic liquids from theoretical investigations, in *Ionic Liquids*, vol. 210 (Springer, Berlin, 2010), pp. 213–262
55. S. Zahn, M. Brehm, M. Brüssel, O. Hollóczki, M. Kohagen, S. Lehmann et al., Understanding ionic liquids from theoretical methods. J. Mol. Liq. **192**, 71–76 (2014)
56. V.V. Chaban, I.V. Voroshylova, O.N. Kalugin, A new force field model for the simulation of transport properties of imidazolium-based ionic liquids. Phys. Chem. Chem. Phys. **13**(17), 7910–7920 (2011)
57. W. Li, Z. Zhang, B. Han, S. Hu, Y. Xie, G. Yang, Effect of water and organic solvents on the ionic dissociation of ionic liquids. J. Phys. Chem. B **111**(23), 6452–6456 (2007)
58. Y. Huo, S. Xia, P. Ma, Densities of Ionic Liquids, 1-butyl-3-methylimidazolium hexafluorophosphate and 1-butyl-3-methylimidazolium tetrafluoroborate, with benzene, acetonitrile, and 1-propanol at T = (293.15 to 343.15) K. J. Chem. Eng. Data **52**(5), 2077–2082 (2007)
59. A. Weissberger, E.S. Proskauer, J.A. Riddick, E.E. Toops, *Organic Solvents: Physical Properties and Methods of Purification* (Inostrannaya Literatura, Moscow, 1958)
60. J. Barthel, R. Wachter, H.-J. Gores, *Modern Aspects of Electrochemistry* (Plenum Press, New York, 1979), pp. 1–80
61. J. Barthel, F. Feuerlein, R. Neueder, R. Wachter, Calibration of conductance cells at various temperatures. J. Solution Chem. **9**(3), 209–219 (1980)
62. A. Noda, K. Hayamizu, M. Watanabe, Pulsed-gradient spin-echo 1H and 19F NMR ionic diffusion coefficient, viscosity, and ionic conductivity of non-chloroaluminate room-temperature ionic liquids. J. Chem. Phys. B **105**, 4603–4610 (2001)
63. L.G. Sánchez, J.R. Espel, F. Onink, G.W. Meindersma, ABd Haan, Density, viscosity, and surface tension of synthesis grade imidazolium, pyridinium, and pyrrolidinium based room temperature ionic liquids. J. Chem. Eng. Data **54**, 2803–2812 (2009)
64. K.R. Harris, M. Kanakubo, L.A. Woolf, Temperature and pressure dependence of the viscosity of the ionic liquid 1-butyl-3-methylimidazolium tetrafluoroborate: viscosity and density relationships in ionic liquids. J. Chem. Eng. Data **52**(6), 2425–2430 (2007)
65. D. Tomida, A. Kumagai, K. Qiao, C. Yokoyama, Viscosity of [bmim][PF6] and [bmim][BF4] at high pressure. Int. J. Thermophys. **27**(1), 39–47 (2006)
66. A. Heintz, D. Klasen, J.K. Lehmann, Excess molar volumes and viscosities of binary mixtures of methanol and the ionic liquid 4-methyl-N-butylpyridinium tetrafluoroborate at 25, 40, and 50 °C. J. Solution Chem. **31**(6), 467–476 (2002)
67. M.T. Zafarani-Moattar, H. Shekaari, Apparent molar volume and isentropic compressibility of ionic liquid 1-butyl-3-methylimidazolium bromide in water, methanol, and ethanol at T = (298.15 to 318.15) K. J. Chem. Thermodyn. **37**(10), 1029–1035 (2005)

68. O.N. Kalugin, I.V. Voroshylova, A.V. Riabchunova, E.V. Lukinova, V.V. Chaban, Conductometric study of binary systems based on ionic liquids and acetonitrile in a wide concentration range. Electrochim. Acta **105**, 188–199 (2013)
69. K.R. Seddon, A. Stark, M.-J. Torres, Influence of chloride, water, and organic solvents on the physical properties of ionic liquids. Pure Appl. Chem. **72**(12), 2275–2287 (2000)
70. J. Jacquemin, P. Husson, A.A.H. Padua, V. Majer, Density and viscosity of several pure and water-saturated ionic liquids. Green Chem. **8**(2), 172–180 (2006)
71. O.N. Kalugin, I.V. Voroshylova, A.V. Ryabchunova, E.V. Lukinova, V.V. Chaban, Electrical conductivity in binary systems based on acetonitrile and imidazolium ionic liquids. Quest. Chem. Chem. Technol. **4**(1), 220–222 (2011)
72. T. Umecky, M. Kanakubo, Y. Ikushima, Self-diffusion coefficients of 1-butyl-3-methylimidazolium hexafluorophosphate with pulsed-field gradient spin-echo NMR technique. Fluid Phase Equilib. **228–229**, 329–333 (2005)
73. T. Umecky, T. Takamuku, T. Matsumoto, E. Kawai, M. Takagi, T. Funazukuri, Effects of dissolved water on Li^+ solvation in 1-ethyl-3-methylimidazolium bis(trifluoromethanesulfonyl)amide ionic liquid studied by NMR. J. Phys. Chem. B **117**(50), 16219–16226 (2013)
74. L. Yangzhong, NMR Temperature Calibration, http://www.staff.ustc.edu.cn/~liuyz/methods/NMR_VT_calibration.htm. Accessed 30 Jan 2014
75. D.H. Wu, A.D. Chen, C.S. Johnson, An improved diffusion-ordered spectroscopy experiment incorporating bipolar-gradient pulses. J. Magn. Reson. Ser. A **115**(2), 260–264 (1995)
76. N. Esturau, F. Sánchez-Ferrando, J.A. Gavin, C. Roumestand, M.-A. Delsuc, T. Parella, The use of sample rotation for minimizing convection effects in self-diffusion NMR measurements. J. Magn. Reson. **153**(1), 48–55 (2001)
77. S. Augé, B. Amblard-Blondel, M.-A. Delsuc, Investigation of the diffusion measurement using PFG and test of robustness against experimental conditions and parameters. J Chim. Phys. **96**(9/10), 1559–1565 (1999)
78. G. Annat, D.R. MacFarlane, M. Forsyth, Transport properties in ionic liquids and ionic liquid mixtures: the challenges of NMR pulsed field gradient diffusion measurements. J. Phys. Chem. B **111**(30), 9018–9024 (2007)
79. L.G. Longsworth, The mutual diffusion of light and heavy water. J. Phys. Chem. **64**(12), 1914–1917 (1960)
80. J.E. Tanner, E.O. Stejskal, Restricted self-diffusion of protons in colloidal systems by the pulsed-gradient, spin-echo method. J. Chem. Phys. **49**(4), 1768–1777 (1968)
81. M. Liang, X.-X. Zhang, A. Kaintz, N.P. Ernsting, M. Maroncelli, Solvation dynamics in a prototypical ionic liquid + dipolar aprotic liquid mixture: 1-butyl-3-methylimidazolium tetrafluoroborate + acetonitrile. J. Phys. Chem. B **118**(5), 1340–1352 (2014)
82. A.-L. Rollet, P. Porion, M. Vaultier, I. Billard, M. Deschamps, C. Bessada et al., Anomalous diffusion of water in [BMIM][TFSI] room-temperature ionic liquid. J. Phys. Chem. B **111**(41), 11888–11891 (2007)
83. N.T. Scharf, A. Stark, M.M. Hoffmann, Ion pairing and dynamics of the ionic liquid 1-hexyl-3-methylimidazolium bis(trifluoromethylsulfonyl)amide ($[C_6mim][NTf_2]$) in the low dielectric solvent chloroform. J. Phys. Chem. B **116**(37), 11488–11497 (2012)
84. W.-Y. Hsu, C.-C. Tai, W.-L. Su, C.-H. Chang, S.-P. Wang, I.W. Sun, A criterion for proper cosolvents used for ionic liquids: the lewis acidic and basic dual nature of propylene carbonate. Inorg. Chim. Acta **361**(5), 1281–1290 (2008)
85. Y. Aihara, K. Sugimoto, W.S. Price, K. Hayamizu, Ionic conduction and self-diffusion near infinitesimal concentration in lithium salt-organic solvent electrolytes. J Chem Phys. **113**(5), 1981–1991 (2000)
86. K. Hayamizu, Y. Aihara, S. Arai, Garcia. pulse-gradient spin-echo ^1H, ^7Li, and ^{19}F NMR diffusion and ionic conductivity measurements of 14 organic electrolytes containing $LiN(SO_2CF_3)_2$. J. Phys. Chem. B **103**(3), 519–524 (1999)
87. K. Hayamizu, Temperature dependence of self-diffusion coefficients of ions and solvents in ethylene carbonate, propylene carbonate, and diethyl carbonate single solutions and ethylene

carbonate + diethyl carbonate binary solutions of $LiPF_6$ studied by NMR. J. Chem. Eng. Data **57**(7), 2012–2017 (2012)
88. K. Hayamizu, A. Matsuo, J. Arai, A divalent lithium salt $Li_2B_{12}F_{12}$ dissolved in propylene carbonate studied by NMR methods. J. Electrochem. Soc. **156**(9), A744–A750 (2009)
89. K. Hayamizu, Y. Aihara, Ion and solvent diffusion and ion conduction of PC-DEC and PC-DME binary solvent electrolytes of $LiN(SO_2CF_3)_2$. Electrochim. Acta **49**(20), 3397–3402 (2004)
90. Y. Aihara, T. Bando, H. Nakagawa, H. Yoshida, K. Hayamizu, E. Akiba et al., Ion transport properties of six lithium salts dissolved in γ-butyrolactone studied by self-diffusion and ionic conductivity measurements. J. Electrochem. Soc. **151**(1), A119–A122 (2004)
91. J. Hou, Z. Zhang, L.A. Madsen, Cation/anion associations in ionic liquids modulated by hydration and ionic medium. J. Phys. Chem. B **2**
92. C.A. Hall, K.A. Le, C. Rudaz, A. Radhi, C.S. Lovell, R.A. Damion et al., Macroscopic and microscopic study of 1-ethyl-3-methyl-imidazolium acetate-water mixtures. J. Phys. Chem. B **116**(42), 12810–12818 (2012)
93. T.M. Alam, D.R. Dreyer, C.W. Bielawski, R.S. Ruoff, Combined measurement of translational and rotational diffusion in quaternary acyclic ammonium and cyclic pyrrolidinium ionic liquids. J. Phys. Chem. B **117**(6), 1967–1977 (2013)
94. K. Hayamizu, S. Tsuzuki, S. Seki, Y. Umebayashi, Multinuclear NMR studies on translational and rotational motion for two ionic liquids composed of BF_4 anion. J. Phys. Chem. B **116**(36), 11284–11291 (2012)
95. A.W. Taylor, P. Licence, A.P. Abbott, Non-classical diffusion in ionic liquids. Phys. Chem. Chem. Phys. **13**(21), 10147–10154 (2011)
96. J. Durand, F. Fernández, C. Barrière, E. Teuma, K. Gómez, G. González et al., DOSY technique applied to palladium nanoparticles in ionic liquids. Magn. Reson. Chem. **46**(8), 739–743 (2008)
97. A. Macchioni, G. Ciancaleoni, C. Zuccaccia, D. Zuccaccia, Determining accurate molecular sizes in solution through NMR diffusion spectroscopy. Chem. Soc. Rev. **37**(3), 479 (2008)
98. E. McLaughlin, Viscosity and self-diffusion in liquids. Trans. Faraday Soc. **55**, 28–38 (1959)
99. A. Einstein, *Investigations on the Theory of the Brownian Movement,* ed. by R. Furth (Dover Publications, New York, 1956), 144 p.
100. T.-Y. Wu, H.-C. Wang, S.-G. Su, S.-T. Gung, M.-W. Lin, C.-b. Lin, Characterization of ionic conductivity, viscosity, density, and self-diffusion coefficient for binary mixtures of polyethyleneglycol (or polyethyleneimine) organic solvent with room temperature ionic liquid $BMIBF_4$ (or $BMIPF_6$). J. Taiwan Inst. Chem. Eng. **41**(3), 315–325 (2010)
101. A. Stark, A.W. Zidell, M.M. Hoffmann, Is the ionic liquid 1-ethyl-3-methylimidazolium methanesulfonate [emim][$MeSO_3$] capable of rigidly binding water? J. Mol. Liq. **160**(3), 166–179 (2011)
102. A. Stark, A.W. Zidell, J.W. Russo, M.M. Hoffmann, Composition dependent physicochemical property data for the binary system water and the ionic liquid 1-butyl-3-methylimidazolium methanesulfonate ([C_4mim][$MeSO_3$]). J. Chem. Eng. Data **57**(12), 3330–3339 (2012)
103. N. Scharf, A. Stark, M. Hoffmann, Calorimetric study on the ion pairing and aggregation of 1-ethyl-3-methylimidazolium *bis*(trifluoromethylsulfonyl)amide ([C_2mim][NTf_2]) and related ionic liquids in the low-dielectric constant solvent chloroform. J. Solution Chem. **42**(10), 2034–2056 (2013)
104. W.-T. Chen, W.-Y. Hsu, M.-Y. Lin, C.-C. Tai, S.-P. Wang, I.W. Sun, Isolated BMI^+ cations are more than isolated PF_6^- anions in the room temperature 1-butyl-3-methylimidazolium hexafluorophosphate (BMI-PF_6) ionic liquid. J. Chin. Chem. Soc. **57**(6), 1293–1298 (2010)
105. S.M. Urahata, M.C.C. Ribeiro, Single particle dynamics in ionic liquids of 1-alkyl-3-methylimidazolium cations. J. Chem. Phys. **122**(2), 024511 1-9 (2005)
106. H. Liu, E. Maginn, A molecular dynamics investigation of the structural and dynamic properties of the ionic liquid 1-n-butyl-3-methylimidazolium bis(trifluoromethanesulfonyl) imide. J. Chem. Phys. **135**(12), 124507 1-16 (2011)

107. V. Chaban, Polarizability versus mobility: atomistic force field for ionic liquids. Phys. Chem. Chem. Phys. **13**(35), 16055–16062 (2011)
108. M.P. Allen, D.J. Tildesley, *Computer Simulations of Liquids* (Clarendon Press, Oxford, 1987)
109. R.C. Rapaport, *The Art of Molecular Dynamics Simulation* (Cambridge University Press, Cambridge, 1995)
110. V.C. Weiss, Liquid-vapor equilibrium and critical parameters of the ionic liquid 1-butyl-3-methylimidazolium hexafluorophosphate from molecular dynamics simulations. J. Mol. Liq. **209**, 745–752 (2015)
111. L.M. Varela, T. Mendez-Morales, J. Carrete, V. Gomez-Gonzalez, B. Docampo-Alvarez, L. J. Gallego et al., Solvation of molecular cosolvents and inorganic salts in ionic liquids: a review of molecular dynamics simulations. J. Mol. Liq. **210**, 178–188 (2015)
112. K. Goossens, K. Lava, C.W. Bielawski, K. Binnemans, Ionic liquid crystals: versatile materials. Chem. Rev. **116**(8), 4643–4807 (2016)
113. K. Dong, S.J. Zhang, J.J. Wang, Understanding the hydrogen bonds in ionic liquids and their roles in properties and reactions. Chem. Commun. **52**(41), 6744–6764 (2016)
114. B. Kirchner, F. Malberg, D.S. Firaha, O. Holloczki, Ion pairing in ionic liquids. J. Phys.-Condens. Matter **27**(46) (2015)
115. T.C. Mu, B.X. Han, Structures and thermodynamic properties of ionic liquids. Struct. Bond. **151**, 107–139 (2014)
116. H. Shirota, H. Fukazawa, T. Fujisawa, J.F. Wishart, Heavy atom substitution effects in non-aromatic ionic liquids: ultrafast dynamics and physical properties. J. Phys. Chem. B **114** (29), 9400–9412 (2010)
117. J.B. Haskins, C.W. Bauschlicher, J.W. Lawson, Ab initio simulations and electronic structure of lithium-doped ionic liquids: structure, transport, and electrochemical stability. J. Phys. Chem. B **119**(46), 14705–14719 (2015)
118. V.V. Chaban, O.V. Prezhdo, Electron solvation in liquid ammonia: lithium, sodium, magnesium, and calcium as electron sources. J. Phys. Chem. B **120**(9), 2500–2506 (2016)
119. A.C. Benniston, A. Harriman, Charge on the move: how electron-transfer dynamics depend on molecular conformation. Chem. Soc. Rev. **35**(2), 169–179 (2006)
120. V.V. Chaban, O.V. Prezhdo, Ab initio molecular dynamics of dimerization and clustering in alkali metal vapors. J. Phys. Chem. A **120**(25), 4302–4306 (2016)
121. V.V. Chaban, O.V. Prezhdo, Ionic vapor composition in critical and supercritical states of strongly interacting ionic compounds. J. Phys. Chem. B **120**, 4302–4309 (2016)
122. O. Acevedo, Simulating chemical reactions in ionic liquids using QM/MM methodology. J. Phys. Chem. A **118**(50), 11653–11666 (2014)
123. V.V. Chaban, O.V. Prezhdo, Nonadditivity of temperature dependent interactions in inorganic ionic clusters. J. Phys. Chem. C **119**(16), 8974–8979 (2015)
124. J.L. Gao, D.G. Truhlar, Y.J. Wang, M.J.M. Mazack, P. Loffler, M.R. Provorse et al., Explicit polarization: a quantum mechanical framework for developing next generation force fields. Acc. Chem. Res. **47**(9), 2837–2845 (2014)
125. V.V. Chaban, O.V. Prezhdo, Polarization versus temperature in pyridinium ionic liquids. J. Phys. Chem. B **118**(48), 13940–13945 (2014)
126. J.J.P. Stewart, Optimization of parameters for semiempirical methods V: modification of NDDO approximations and application to 70 elements. J. Mol. Model. **13**(12), 1173–1213 (2007)
127. N.A. Andreeva, V.V. Chaban, Global minimum search via annealing: nanoscale gold clusters. Chem. Phys. Lett. **622**, 75–79 (2015)
128. V. Chaban, Competitive solvation of (bis)(trifluoromethanesulfonyl)imide anion by acetonitrile and water. Chem. Phys. Lett. **613**, 90–94 (2014)
129. A.S. Aquino, F.L. Bernard, J.V. Borges, L. Mafra, F. Dalla Vecchia, M.O. Vieira et al., Rationalizing the role of the anion in CO2 capture and conversion using imidazolium-based ionic liquid modified mesoporous silica. Rsc Adv. **5**(79), 64220–64227 (2015)

130. J.J.P. Stewart, Application of the PM6 method to modeling the solid state. J. Mol. Model. **14** (6), 499–535 (2008)
131. V. Chaban, Solvation of the fluorine containing anions and their lithium salts in propylene carbonate and dimethoxyethane. J. Mol. Model. **21**(7), 172 (2015)
132. V. Chaban, Solvation of lithium ion in dimethoxyethane and propylene carbonate. Chem. Phys. Lett. **631**, 1–5 (2015)
133. V. Chaban, Hydrogen fluoride capture by imidazolium acetate ionic liquid. Chem. Phys. Lett. **625**, 110–115 (2015)
134. J.J.P. Stewart, Application of the PM6 method to modeling proteins. J. Mol. Model. **15**(7), 765–805 (2009)
135. N.A. Andreeva, V.V. Chaban, Electrostatic charge confinement using bulky tetraoctylammonium cation and four anions. Chem. Phys. Lett. **649**, 44–47 (2016)
136. J.J.P. Stewart, Optimization of parameters for semiempirical methods VI: more modifications to the NDDO approximations and re-optimization of parameters. J. Mol. Model. **19**(1), 1–32 (2013)
137. V. Chaban, Competitive solvation of the imidazolium cation by water and methanol. Chem. Phys. Lett. **623**, 76–81 (2015)
138. V. Chaban, Annealing relaxation of ultrasmall gold nanostructures. Chem. Phys. Lett. **618**, 46–50 (2015)
139. V. Chaban, The thiocyanate anion is a primary driver of carbon dioxide capture by ionic liquids. Chem. Phys. Lett. **618**, 89–93 (2015)
140. F.L. Bernard, F.D. Vecchia, M.F. Rojas, R. Ligabue, M.O. Vieira, E.M. Costa et al., Anticorrosion protection by amine-ionic liquid mixtures: experiments and simulations. J. Chem. Eng. Data **61**(5), 1803–1810 (2016)
141. V.V. Chaban, N.A. Andreeva, Solvation of the morpholinium cation in acetonitrile. Effect of an anion. J. Mol. Model. **22**(1), 26 (2016)
142. V.V. Chaban, N.A. Andreeva, Sodium-ion electrolytes based on ionic liquids: a role of cation-anion hydrogen bonding. J. Mol. Model. **22**(8), 172 (2016)
143. V.V. Chaban, O.V. Prezhdo, Boron doping of graphene-pushing the limit. Nanoscale **8**(34), 15521–15528 (2016)
144. M.R. Weismiller, C.E. Junkermeier, M.F. Russo, M.R. Salazar, D. Bedrov, A.C.T. van Duin, ReaxFF molecular dynamics simulations of intermediate species in dicyanamide anion and nitric acid hypergolic combustion. Model. Simul. Mater. Sci. **23**(7) (2015)
145. E.E. Fileti, V.V. Chaban, O.V. Prezhdo, Exploding nitromethane in silico, in real time. J. Phys. Chem. Lett. **5**(19), 3415–3420 (2014)
146. V.V. Chaban, E.E. Fileti, O.V. Prezhdo, Buckybomb: reactive molecular dynamics simulation. J. Phys. Chem. Lett. **6**(5), 913–917 (2015)
147. V.V. Chaban, O.V. Prezhdo, Pressure-driven opening of carbon nanotubes. Nanoscale **8**(11), 6014–6020 (2016)
148. B. Zhang, A.C.T. van Duin, J.K. Johnson, Development of a ReaxFF reactive force field for tetrabutylphosphonium glycinate/CO2 mixtures. J. Phys. Chem. B **118**(41), 12008–12016 (2014)
149. V.V. Chaban, O.V. Prezhdo, Haber process made efficient by hydroxylated graphene: ab initio thermochemistry and reactive molecular dynamics. J. Phys. Chem. Lett. **7**(13), 2622–2626 (2016)
150. O. Bohm, S. Pfadenhauer, R. Leitsmann, P. Planitz, E. Schreiner, M. Schreiber, ReaxFF(+)-a new reactive force field method for the accurate description of ionic systems and its application to the hydrolyzation of aluminosilicates. J. Phys. Chem. C **120**(20), 10849–10856 (2016)
151. M.F. Russo, D. Bedrov, A.C.T. van Duin, Molecular dynamics investigation of hypergolic ionic liquids via the ReaxFF reactive force field. Abstr. Pap. Am. Chem. S **244** (2012)
152. M. Salanne, Simulations of room temperature ionic liquids: from polarizable to coarse-grained force fields. Phys. Chem. Chem. Phys. **17**(22), 14270–14279 (2015)

153. V.V. Chaban, H. Khandelia, Distribution of neutral lipids in the lipid droplet core. J. Phys. Chem. B **118**(38), 11145–11151 (2014)
154. C. Merlet, M. Salanne, B. Rotenberg, New coarse-grained models of imidazolium ionic liquids for bulk and interfacial molecular simulations. J. Phys. Chem. C **116**(14), 7687–7693 (2012)
155. H.A. Karimi-Varzaneh, F. Muller-Plathe, S. Balasubramanian, P. Carbone, Studying long-time dynamics of imidazolium-based ionic liquids with a systematically coarse-grained model. Phys. Chem. Chem. Phys. **12**(18), 4714–4724 (2010)
156. D. Roy, M. Maroncelli, An improved four-site ionic liquid model. J. Phys. Chem. B **114**(39), 12629–12631 (2010)
157. V.V. Chaban, H. Khandelia, Lipid structure in triolein lipid droplets. J. Phys. Chem. B **118** (35), 10335–10340 (2014)
158. Z.P. Liu, X.P. Wu, W.C. Wang, A novel united-atom force field for imidazolium-based ionic liquids. Phys. Chem. Chem. Phys. **8**(9), 1096–1104 (2006)
159. E. Bodo, L. Gontrani, R. Caminiti, N.V. Plechkova, K.R. Seddon, A. Triolo, Structural properties of 1-alkyl-3-methylimidazolium bis{(trifluoromethyl)sulfonyl}amide ionic liquids: X-ray diffraction data and molecular dynamics simulations. J. Phys. Chem. B **114**(49), 16398–16407 (2010)
160. F.J. Deive, A. Rodriguez, A.B. Pereiro, K. Shimizu, P.A.S. Forte, C.C. Romao et al., Phase equilibria of haloalkanes dissolved in ethylsulfate- or ethylsulfonate-based ionic liquids. J. Phys. Chem. B **114**(21), 7329–7337 (2010)
161. C. Hardacre, J.D. Holbrey, C.L. Mullan, M. Nieuwenhuyzen, T.G.A. Youngs, D.T. Bowron et al., Solid and liquid charge-transfer complex formation between 1-methylnaphthalene and 1-alkyl-cyanopyridinium bis{(trifluoromethyl)sulfonyl}imide ionic liquids. Phys. Chem. Chem. Phys. **12**(8), 1842–1853 (2010)
162. S. Aparicio, M. Atilhan, Mixed ionic liquids: the case of pyridinium-based fluids. J. Phys. Chem. B **116**(8), 2526–2537 (2012)
163. M. Brussel, M. Brehm, A.S. Pensado, F. Malberg, M. Ramzan, A. Stark et al., On the ideality of binary mixtures of ionic liquids. Phys. Chem. Chem. Phys. **14**(38), 13204–13215 (2012)
164. L. Deng, R. Shi, Y.T. Wang, Z.C. Ou-Yang, Hydrogen-bond rich ionic liquids with hydroxyl cationic tails. Chem. Phys. Lett. **560**, 32–36 (2013)
165. V.V. Chaban, E.E. Fileti, Mixtures of amino-acid based ionic liquids and water. J. Mol. Model. **21**(9), 236 (2015)
166. V.V. Chaban, The tricyanomethanide anion favors low viscosity of the pure ionic liquid and its aqueous mixtures. Phys. Chem. Chem. Phys. **17**(47), 31839–31849 (2015)
167. V.V. Chaban, E.E. Fileti, Free energy of solvation of carbon nanotubes in pyridinium-based ionic liquids. Phys. Chem. Chem. Phys. **18**(30), 20357–20362 (2016)
168. V.V. Chaban, Acetone as a polar cosolvent for pyridinium-based ionic liquids. Rsc Adv. **6** (11), 8906–8912 (2016)
169. V.V. Chaban, Force field development and simulations of senior dialkyl sulfoxides. Phys. Chem. Chem. Phys. **18**(15), 10507–10515 (2016)
170. V.V. Chaban, O.V. Prezhdo, Water phase diagram is significantly altered by imidazolium ionic liquid. J. Phys. Chem. Lett. **5**(10), 1623–1627 (2014)
171. V.V. Chaban, O.V. Prezhdo, Ionic vapor: what does it consist of? J. Phys. Chem. Lett. **3**(12), 1657–1662 (2012)
172. T. Malaspina, E. Fileti, V.V. Chaban, Peculiar aqueous solubility trend in cucurbiturils unraveled by atomistic simulations. J. Phys. Chem. B **120**(30), 7511–7516 (2016)
173. V.V. Chaban, A. Arruda, E.E. Fileti, Polypeptide A9K at nanoscale carbon: a simulation study. Phys. Chem. Chem. Phys. **17**(39), 26386–26393 (2015)
174. V.V. Chaban, E.E. Fileti, Atomically precise understanding of nanofluids: nanodiamonds and carbon nanotubes in ionic liquids. Phys. Chem. Chem. Phys. **18**(38), 26865–26872 (2016)

175. V.V. Chaban, O.V. Prezhdo, How toxic are ionic liquid/acetonitrile mixtures? J. Phys. Chem. Lett. **2**(19), 2499–2503 (2011)
176. V.V. Chaban, O.V. Prezhdo, Water boiling inside carbon nanotubes: toward efficient drug release. ACS Nano **5**(7), 5647–5655 (2011)
177. I.V. Voroshylova, V.V. Chaban, Atomistic force field for pyridinium-based ionic liquids: reliable transport properties. J. Phys. Chem. B **118**(36), 10716–10724 (2014)
178. V.V. Chaban, I.V. Voroshylova, Systematic refinement of Canongia Lopes-Padua force field for pyrrolidinium-based ionic liquids. J. Phys. Chem. B **119**(20), 6242–6249 (2015)
179. V.V. Chaban, O.V. Prezhdo, A new force field model of 1-butyl-3-methylimidazolium tetrafluoroborate ionic liquid and acetonitrile mixtures. Phys. Chem. Chem. Phys. **13**(43), 19345–19354 (2011)
180. V.V. Chaban, I.V. Voroshylova, O.N. Kalugin, The phenomenological account for electronic polarization in ionic liquid. ECS Trans. **33**(28), 43–55 (2011)
181. O. Borodin, Polarizable force field development and molecular dynamics simulations of ionic liquids. J. Phys. Chem. B **113**(33), 11463–11478 (2009)
182. O. Borodin, W. Gorecki, G.D. Smith, M. Armand, Molecular dynamics simulation and pulsed-field gradient NMR studies of bis(fluorosulfonyl)imide (FSI) and bis [(trifluoromethyl)sulfonyl]imide (TFSI)-based ionic liquids. J. Phys. Chem. B **114**(20), 6786–6798 (2010)
183. J.B. Hooper, O. Borodin, Molecular dynamics simulations of N,N,N, N-tetramethylammonium dicyanamide plastic crystal and liquid using a polarizable force field. Phys. Chem. Chem. Phys. **12**(18), 4635–4643 (2010)
184. X.J. Zhong, Z.P. Liu, D.P. Cao, Improved classical united-atom force field for imidazolium-based ionic liquids: tetrafluoroborate, hexafluorophosphate, methylsulfate, trifluoromethylsulfonate, acetate, trifluoroacetate, and bis(trifluoromethylsulfonyl)amide. J. Phys. Chem. B **115**(33), 10027–10040 (2011)
185. L.X. Dang, T.M. Chang, Molecular mechanism of gas adsorption into ionic liquids: a molecular dynamics study. J. Phys. Chem. Lett. **3**(2), 175–181 (2012)
186. A. Mondal, S. Balasubramanian, Quantitative prediction of physical properties of imidazolium based room temperature ionic liquids through determination of condensed phase site charges: a refined force field. J. Phys. Chem. B **118**(12), 3409–3422 (2014)
187. O.N. Starovoytov, H. Torabifard, G.A. Cisneros, Development of AMOEBA force field for 1,3-dimethylimidazolium based ionic liquids. J. Phys. Chem. B **118**(25), 7156–7166 (2014)
188. E. Choi, J.G. McDaniel, J.R. Schmidt, A. Yethiraj, First-principles, physically motivated force field for the ionic liquid [BMIM][BF4]. J. Phys. Chem. Lett. **5**(15), 2670–2674 (2014)
189. J.G. McDaniel, E. Choi, C.Y. Son, J.R. Schmidt, A. Yethiraj, Conformational and dynamic properties of poly(ethylene oxide) in an ionic liquid: development and implementation of a first-principles force field. J. Phys. Chem. B **120**(1), 231–243 (2016)
190. L.A. Curtiss, K. Raghavachari, P.C. Redfern, V. Rassolov, J.A. Pople, Gaussian-3 (G3) theory for molecules containing first and second-row atoms. J. Chem. Phys. **109**(18), 7764–7776 (1998)
191. L.A. Curtiss, P.C. Redfern, K. Raghavachari, V. Rassolov, J.A. Pople, Gaussian-3 theory using reduced Moller-Plesset order. J. Chem. Phys. **110**(10), 4703–4709 (1999)
192. L.A. Curtiss, P.C. Redfern, K. Raghavachari, Gaussian-4 theory. J. Chem. Phys. **126**(8), 084108 (2007)
193. M. Head-Gordon, J.A. Pople, M.J. Frisch, MP2 energy evaluation by direct methods. Chem. Phys. Lett. **153**(6), 503–506 (1988)
194. A.V. Marenich, C.J. Cramer, D.G. Truhlar, Universal solvation model based on solute electron density and on a continuum model of the solvent defined by the bulk dielectric constant and atomic surface tensions. J. Phys. Chem. B **113**(18), 6378–6396 (2009)
195. S. Grimme, J. Antony, S. Ehrlich, H. Krieg, A consistent and accurate ab initio parametrization of density functional dispersion correction (DFT-D) for the 94 elements H-Pu. J. Chem. Phys. **132**(15), 154104 (2010)

196. S. Grimme, W. Hujo, B. Kirchner, Performance of dispersion-corrected density functional theory for the interactions in ionic liquids. Phys. Chem. Chem. Phys. **14**(14), 4875–4883 (2012)
197. E.E. Zvereva, S. Grimme, S.A. Katsyuba, V.V. Ermolaev, D.A. Arkhipova, N. Yan et al., Solvation and stabilization of palladium nanoparticles in phosphonium-based ionic liquids: a combined infrared spectroscopic and density functional theory study. Phys. Chem. Chem. Phys. **16**(38), 20672–20680 (2014)
198. K. Regeta, C. Bannwarth, S. Grimme, M. Allan, Free electrons and ionic liquids: study of excited states by means of electron-energy loss spectroscopy and the density functional theory multireference configuration interaction method. Phys. Chem. Chem. Phys. **17**(24), 15771–15780 (2015)
199. V.V. Chaban, O.V. Prezhdo, Ionic and molecular liquids: working together for robust engineering. J. Phys. Chem. Lett. **4**(9), 1423–1431 (2013)
200. K. Fumino, R. Ludwig, Analyzing the interaction energies between cation and anion in ionic liquids: the subtle balance between Coulomb forces and hydrogen bonding. J. Mol. Liq. **192**, 94–102 (2014)
201. X.J. Wang, Y.L. Chi, T.C. Mu, A review on the transport properties of ionic liquids. J. Mol. Liq. **193**, 262–266 (2014)
202. K.R. Harris, Scaling the transport properties of molecular and ionic liquids. J. Mol. Liq. **222**, 520–534 (2016)
203. R. Car, M. Parrinello, Unified approach for molecular-dynamics and density-functional theory. Phys. Rev. Lett. **55**(22), 2471–2474 (1985)
204. A.D. Becke, Density-functional exchange-energy approximation with correct asymptotic-behavior. Phys. Rev. A **38**(6), 3098–3100 (1988). English
205. C.T. Lee, W.T. Yang, R.G. Parr, Development of the Colle-Salvetti correlation-energy formula into a functional of the electron-density. Phys. Rev. B **37**(2), 785–789 (1988)
206. A.M. Nikitin, A.P. Lyubartsev, New six-site acetonitrile model for simulations of liquid acetonitrile and its aqueous mixtures. J. Comput. Chem. **28**(12), 2020–2026 (2007)
207. G. Bussi, D. Donadio, M. Parrinello, Canonical sampling through velocity rescaling. J. Chem. Phys. **126**(1), 014101 (2007)
208. M. Parrinello, A. Rahman, Polymorphic transitions in single crystals: a new molecular dynamics method. J. Appl. Phys. **52**, 7182–7192 (1981)
209. V.V. Chaban, E.E. Fileti, Ionic clusters vs shear viscosity in aqueous amino acid ionic liquids. J. Phys. Chem. B **119**(9), 3824–3828 (2015)
210. G. Chevrot, E.E. Fileti, V.V. Chaban, Enhanced stability of the model mini-protein in amino acid ionic liquids and their aqueous solutions. J. Comput. Chem. **36**(27), 2044–2051 (2015)
211. T. Darden, D. York, L. Pedersen, Particle mesh Ewald: an N · log(N) method for Ewald sums in large systems. J. Chem. Phys. **98**, 10089–10099 (1993)
212. H.J.C. Berendsen, D. van der Spoel, R. van Drunen, GROMACS—a message-passing parallel molecular-dynamics implementation. Comput. Phys. Commun. **91**, 43–56 (1995)
213. E. Lindahl, B. Hess, D. van der Spoel, GROMACS 3.0: a package for molecular simulation and trajectory analysis. J. Mol. Model. **7**, 306–317 (2001). PubMed PMID: ISI:000171053900002
214. D. Van der Spoel, E. Lindahl, B. Hess, G. Groenhof, A.E. Mark, H.J.C. Berendsen, GROMACS: fast, flexible, and free. J. Comput. Chem. **26**(16), 1701–1718 (2005)
215. S. Pronk, S. Pall, R. Schulz, P. Larsson, P. Bjelkmar, R. Apostolov et al., GROMACS 4.5: a high-throughput and highly parallel open source molecular simulation toolkit. Bioinformatics **29**(7), 845–854 (2013)
216. W. Humphrey, A. Dalke, K. Schulten, VMD: visual molecular dynamics. J. Mol. Graph. **14**(1), 33–38 (1996)
217. L. Martinez, R. Andrade, E.G. Birgin, J.M. Martinez, PACKMOL: a package for building initial configurations for molecular dynamics simulations. J. Comput. Chem. **30**(13), 2157–2164 (2009)

218. V.V. Chaban, O.V. Prezhdo, Computationally efficient prediction of ionic liquid properties. J. Phys. Chem. Lett. **5**(11), 1973–1977 (2014)
219. R.L. Hurle, L.A. Woolf, Self-diffusion in liquid acetonitrile under pressure. J. Chem. Soc. Faraday Trans. 1 **78**(7), 2233–2238 (1982)
220. M. Holz, X.-a. Mao, D. Seiferling, A. Sacco, Experimental study of dynamic isotope effects in molecular liquids: detection of translation-rotation coupling. J. Chem. Phys. **104**(2), 669–679 (1996)
221. E. Hawlicka, R. Grabowski, Solvation of ions in acetonitrile-methanol solutions of sodium iodide. Ber. Bunsenges. Phys. Chem. **94**(4), 486–489 (1990)
222. K. Hayamizu, Y. Aihara, S. Arai, W.S. Price, Diffusion, conductivity and DSC studies of a polymer gel electrolyte composed of cross-linked PEO, γ-butyrolactone and $LiBF_4$. Solid State Ionics **107**(1–2), 1–12 (1998)
223. M. Takeuchi, Y. Kameda, Y. Umebayashi, S. Ogawa, T. Sonoda, S.-i. Ishiguro et al., Ion-ion interactions of LiPF6 and LiBF4 in propylene carbonate solutions. J. Mol. Liq. **148**(2–3), 99–108 (2009)
224. K. Kondo, M. Sano, A. Hiwara, T. Omi, M. Fujita, A. Kuwae et al., Conductivity and solvation of Li^+ ions of $LiPF_6$ in propylene carbonate solutions. J. Phys. Chem. B **104**(20), 5040–5044 (2000)
225. H. Tsunekawa, A. Narumi, M. Sano, A. Hiwara, M. Fujita, H. Yokoyama, Solvation and ion association studies of $LiBF_4$−propylenecarbonate and $LiBF_4$−propylenecarbonate−trimethyl phosphate solutions. J. Phys. Chem. B **107**(39), 10962–10966 (2003)
226. D. Nama, P. Kumar, P. Pregosin, T. Geldbach, P. Dyson, ^1H, ^{19}F-HOESY and PGSE diffusion studies on ionic liquids: the effect of co-solvent on structure. Inorg. Chim. Acta **359**(6), 1907–1911 (2006)
227. T.-Y. Wu, H.-C. Wang, S.-G. Su, S.-T. Gung, M.-W. Lin, C.-B. Lin, Aggregation influence of polyethyleneglycol organic solvents with ionic liquids $BMIMBF_4$ and $BMIMPF_6$. J. Chin. Chem. Soc. **57**(1), 44–55 (2010)
228. E. Hawlicka, Self-diffusion in multicomponent liquid systems. Chem. Soc. Rev. **24**(5), 367–377 (1995)

Chapter 6
Microsegregation in Ion-Electron Liquids: Molten Metals and Alloys

Yuriy Plevachuk, Vasyl Sklyarchuk and Andriy Yakymovych

Abstract A number of experimental studies of different physical and chemical properties and microstructure analysis revealed structure transformations in liquid metal alloys during solidification, especially near melting temperature (T_m). A complicated microstructure behavior was found in metal systems with different type of interatomic interactions (eutectics, monotectics and systems with intermetallic compounds in the solid state). Furthermore, pure liquid metals and semimetals have also indicated microstructure changes in the temperature region near the melting points. Several models describing such microstructure transformation are based on microsegregation processes resulting in the formation of microregions with different arrangement in the liquid matrix. F. Sommer proposed the association model to describe temperature and concentration dependencies of thermodynamic properties (enthalpies of mixing chemical activity etc.). According to this model chemical short-range ordered atom regions exist in the alloys with strong chemical interaction between atoms. Another approach is the quasieutectic model proposed by E. Kalashnikov which suggests the quasieutectic or statistical and intermediate atom distribution in the liquid state near T_m. Based on structure-sensitive properties a complex analysis of the microstructural changes during solidification in some eutectic and near eutectic alloys was carried out. The above mentioned models were used to perform quantitative estimation of the formed microregions with atomic concentration different from the statistical distribution. Based on the obtained results the overall picture of microsegregation

Y. Plevachuk (✉) · V. Sklyarchuk · A. Yakymovych
Department of Metal Physics, Ivan Franko National University of Lviv,
Kyrylo & Mephodiy str., 8, Lviv 79005, Ukraine
e-mail: plevachuk@mail.lviv.ua

V. Sklyarchuk
e-mail: sklyarchuk@ukr.net

A. Yakymovych
e-mail: andriy.yakymovych@univie.ac.at

A. Yakymovych
Department of Inorganic Chemistry—Functional Materials, Faculty of Chemistry,
University of Vienna, Althanstr. 14, 1090 Vienna, Austria

L. A. Bulavin and A. V. Chalyi (eds.), *Modern Problems of Molecular Physics*,
Springer Proceedings in Physics 197, https://doi.org/10.1007/978-3-319-61109-9_6

processes in the liquid metals and metal alloys regardless of the preferred type of interatomic interactions has been obtained.

6.1 Introduction

In contrast to investigations of different processes during solidification of metal alloys [1, 2], their behavior during melting is less studied. The two-phase melting-solidification region, where solid and liquid phases have the same chemical potentials, is marked on the phase diagram by the lines of solidus and liquidus.

Transition from the liquid to the solid state under equilibrium conditions can take place only in case of very slow cooling. Because the cooling which is accompanied by diffusion mass transfer cannot be endless, solidification is non-equilibrium. As a result, a composition of the formed solid solution is non-uniform.

Strictly speaking, melting and solidification of metal alloys are not the reversible processes. In contrast to a pure metal, where melting is accompanied by destruction of the crystalline lattice, transition to the liquid state in the alloy, which is a system of several components, is followed by solving of more refractory elements in the liquid. Under such circumstances, the melting continues in a certain temperature range. Existence of the refractory fractions together with gravitational liquation is the cause of overheating of the alloy.

In order to reflect on the phase diagrams these peculiarities of phase transformations, it was proposed to mark them by additional lines of metastability, which run under the liquidus line [3]. The lines of metastability are extensions of the lines of the liquidus below the eutectic point and indicate an equilibrium between a nucleus and a liquid in a certain interval of concentration.

Up to now, the works dedicated to undercooling without temperature gradients followed by solidification are rather scarce. The solidification temperatures, corresponding to the so-called specific points, which are located below the eutectic temperature, were also defined only in few binary alloys.

In the present study such specific points were determined for the binary system Pb–Bi using the data of electrical conductivity measurements. It should be noted that a correlation between the viscosity and electrophysical properties, such as electrical conductivity and thermoelectric power, was shown both for metal liquid alloys [4–6] and ionic liquid alloys [7–9]. Therefore, viscosity investigations will bring confirmation about possible transition of the liquid from the equilibrium to the metastable state. It should be noted that several theoretical studied devoted to calculations of structure transformations and changes of thermophysical properties near to and at the critical temperature for various materials [10–12], were published recently and became a basis for analysis of experimental measurements [13–15].

Based on the obtained results of electrical conductivity and viscosity measurements of Pb–Sn, Pb–Bi, Pb–Au, Pb–Mg, In–Bi and In–Sb eutectic systems, the

microheterogeneous structure in the melting-solidification region and microsegregation processes in the liquid alloys were studied.

6.2 Experimental Details

Temperature dependence of the electrical conductivity was measured by the four-point contact method. The cylindrical boron nitride crucibles were used for the molten samples. The later were produced from pure elements, which had been melted and evacuated inside the sealed quartz ampoules. The composition of the sample was accurate within 0.02 wt. %. In order to keep a constant chemical composition of the sample the measurements were carried out in neutral atmosphere of argon under pressure of about 10 MPa.

In order to avoid a direct contact between the melt and the thermocouples, the intermediate graphite electrodes for potential and current measurements were inserted into a wall of the crucible. Each electrode was connected with a WRe-5/20 thermocouple for temperature measurements, while one of two dissimilar conductors of the thermocouple was used for the measurement of electrical conductivity. The total error of the measurements of electrical conductivity did not exceed 2%. The experimental facility and the details of this method were reported in [16].

The dynamic viscosity was measured using the oscillating-cup viscometer [17]. The modified Roscoe equation was used for calculation of the viscosity from the data of the period of oscillations and the logarithmic decrement of the damped oscillations. The measurements were carried out in the atmosphere of helium, the excess pressure did not exceed 0.03 MPa. Each sample whose weight was about 30 g was weighed before and after the measurements, and the weight loss did not exceed 0.02 wt. %. The samples were measured in the cylindrical graphite crucibles with a diameter of 14 mm. A homogeneous temperature field inside the furnace (up to 0.3 K) has been maintained in the temperature interval of the measurements. The temperature was determined by the WRe5/20 thermocouple, located below the crucible. The total error of the viscosity measurements did not exceed 3%.

In addition, the viscosity of In–Bi and In–Sb systems was calculated using the hard sphere model [18]:

$$\eta = \frac{2.408 \times 10^{-8} \cdot \mu^{\frac{1}{3}}}{1 - 1.8702 \cdot \mu} \cdot \frac{(MT)^{\frac{1}{2}}}{V^{\frac{2}{3}}} \tag{6.1}$$

where η is a coefficient of the dynamic viscosity of a liquid, μ is the packing coefficient, M is the molar mass, V is the molar volume.

6.3 Association Model for Liquid Alloys

The association model proposed in [19–21] and successfully applied to different systems, has been considered in the present study for confirmation of fluctuations of concentration in In–Bi and In–Sb binary alloys. For this purpose, the mole fractions of two types of chemical complexes InBi and In_2Bi for the Bi–In system, and InSb and In_3Sb for In–Sb system in the liquid state were calculated using the association model.

We assume that a binary A–B liquid alloy consists of a pseudo quaternary mixture of n_{A1} and n_{B1} mol of $A1$ and $B1$ atoms of pure elements, and of n_{AiBj} and n_{AiBk} moles of two types of chemical complexes, $AiBj$ and $AiBk$, respectively. So, a number of moles, n, is as follows:

$$\begin{aligned} n &= n_{A1} + n_{B1} + n_{AiBj} + n_{AlBk}, \\ n_A &= n_{A1} + in_{AiBj} + ln_{AlBk}, \\ n_B &= n_{B1} + jn_{AiBj} + kn_{AlBk}, \end{aligned} \tag{6.2}$$

The absolute concentrations were obtained as $x_A = n_A/N$ and $x_B = n_B/N$ for 1 mol of a binary alloy (N = 1). The similar equations are valid for the concentrations of the particles in the liquid:

$$\begin{aligned} x_{A1} &= \frac{n_{A1}}{n_{A1} + n_{B1} + n_{AiBj} + n_{AlBk}}, \\ x_{B1} &= \frac{n_{B1}}{n_{A1} + n_{B1} + n_{AiBj} + n_{AlBk}}, \\ x_{AiBj} &= \frac{n_{AiBj}}{n_{A1} + n_{B1} + n_{AiBj} + n_{AlBk}}, \\ x_{AlBk} &= \frac{n_{AlBk}}{n_{A1} + n_{B1} + n_{AiBj} + n_{AlBk}}. \end{aligned} \tag{6.3}$$

The chemical potentials μ_n of the assumed species ν ($\nu = A1, B1, AiBj$ and $AlBk$) were

$$\begin{aligned} \mu_{A1} &= \mu^0_{A1} + RT \ln x_{A1} = \mu^0_A + RT \ln x_A \gamma_A \\ , \mu_{B1} &= \mu^0_{B1} + RT \ln x_{B1} = \mu^0_B + RT \ln x_B \gamma_B \end{aligned}$$

where R is the gas constant, T is the absolute temperature and γ_A, γ_B are the coefficients of activity. From this one can calculate:

$$\gamma_A = \frac{x_{A1}}{x_A} \exp\left(\frac{\mu^0_{A1} - \mu_{A1}}{RT}\right),$$

$$\gamma_B = \frac{x_{B1}}{x_B} \exp\left(\frac{\mu_{B1}^0 - \mu_{B1}}{RT}\right),$$

For calculation of the mole fractions of the associates in liquid In–Bi and In–Sb alloys the activity coefficients of pure components were taken from Hultgren et al. [22].

The concentration–concentration structure factor in long wave length limit or concentration fluctuations $S_{cc}(0)$ is one of the widely used parameters to analyse the degree of order in the liquid alloy [23, 24]. The following expression for viscosity, η, can be used to calculate $S_{cc}(0)$:

$$\begin{aligned} \eta &= \eta_0 \phi, \\ \phi &= \frac{c_1 c_2}{S_{cc}(0)}, \\ S_{cc}(0) &= c_1 c_2 \frac{\eta_0}{\eta}, \\ \eta_0 &= \sum_i c_i \eta_i, \end{aligned} \tag{6.4}$$

where η_i and c_i are the viscosity and the concentration of the component i.

The concentration fluctuation is also thermodynamically related to the molar enthalpy of mixing, H_M:

$$S_{cc}(0) = \frac{c_1 c_2}{1 - \frac{H_M}{RT}}. \tag{6.5}$$

Considering the ordering energy is equal to zero, Eq. (6.4) can be expressed as

$$S_{cc}(0) = (0)_{id} = (1 - c) \tag{6.6}$$

The mixing behaviour of liquid alloys can be deduced from the deviation of $S_{cc}(0)$ from the ideal value, $S_{cc}(0)_{id}$. Condition $S_{cc}(0) < S_{cc}(0)_{id}$ corresponds to unlike atoms pairing as nearest neighbours and condition $S_{cc}(0) > S_{cc}(0)_{id}$ corresponds to like atoms pairing in the first coordination shell.

6.4 Melting and Solidification

The physical properties of the lead-bismuth system attracts attention of scientists because the Pb–Bi alloys of the eutectic and near-eutectic compositions are considered as advanced materials for the liquid metal spallation neutron source as well as the liquid metal coolants for the new generation of critical and subcritical nuclear

reactors [25]. A number of works are dedicated to investigations of different properties of this system, but only several papers described behavior of electrical properties in the liquid state [26, 27]. Moreover, the processes of melting and solidification in the Pb–Bi alloys of the eutectic and near-eutectic compositions were studied insufficiently.

Therefore, several alloys of the composition close on both sides to the eutectic one, $Pb_{44}Bi_{56}$, were selected for studies of the electrical conductivity behavior. Dependence of the electrical conductivity on temperature for these eutectic, hypoeutectic and hypereutectic alloys is shown in Figs. 6.1, 6.2 and 6.3.

It is seen that the electrical conductivity curves, $\sigma(T)$, of the $Pb_{40}Bi_{60}$ alloy corresponding to the melting and solidification did not coincide and formed a hysteresis (Fig. 6.1a). An interval of solidification lies between 444 and 411 K.

It has been revealed that after several thermocyclings, completion of melting as well as beginning of the solidification were shifted for dozens of degrees towards higher temperature values compared to the corresponding points of the liquidus line reported in the handbook of binary alloy phase diagrams [28]. Note that for some samples the temperature shift is almost 40 K. As seen from Fig. 6.1, a first kink on the heating curve appeared at about 402 K, corresponding to beginning of melting. A second kink, which is observed at 432 K, can indicate that the liquid phase reached its critical concentration. A gradual increase of the temperature coefficient of conductivity $d\sigma/dT$ takes place with further heating. At 464 K the sample became completely molten, and further heating is accompanied by gradual decrease of the electrical conductivity. It is seen in Fig. 6.1b that the electrical conductivity of $Pb_{43}Bi_{57}$ alloy behaves similarly.

Temperature dependence of the electrical conductivity of the $Pb_{44}Bi_{56}$ alloy, corresponding to the eutectic composition, is presented in Fig. 6.2a. Heating of the

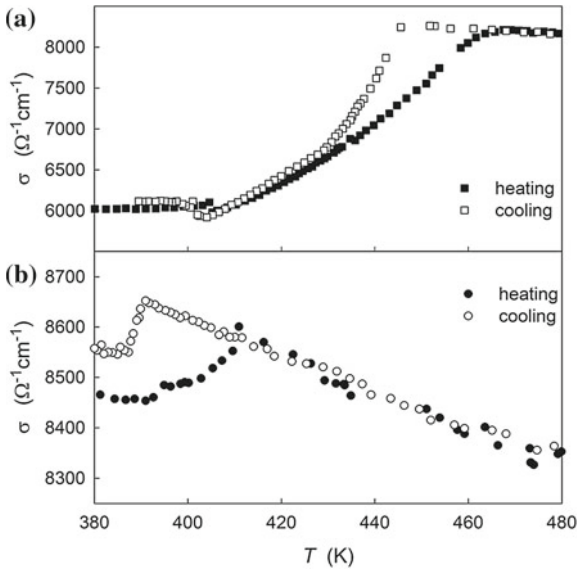

Fig. 6.1 Temperature dependence of the electrical conductivity of $Pb_{40}Bi_{60}$ (**a**) and $Pb_{43}Bi_{57}$ (**b**) liquid alloys [42]

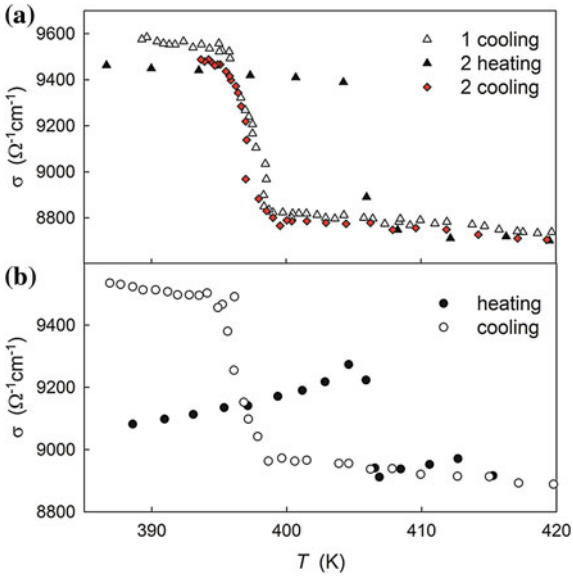

Fig. 6.2 Temperature dependence of the electrical conductivity of $Pb_{44}Bi_{56}$ (**a**) and $Pb_{45}Bi_{55}$ (**b**) liquid alloys [42]

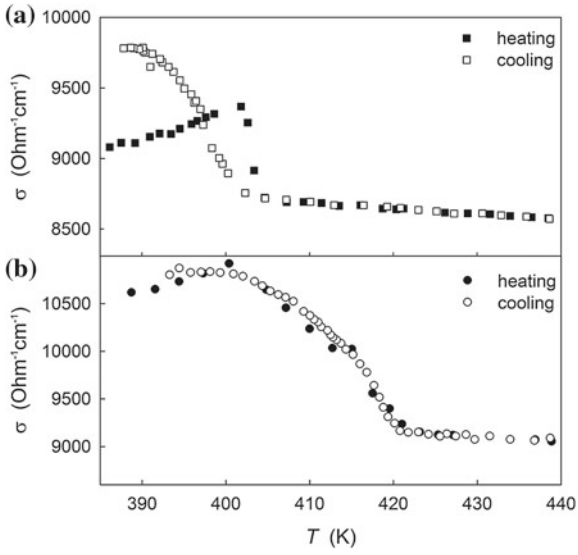

Fig. 6.3 Temperature dependence of the electrical conductivity of $Pb_{46}Bi_{54}$ (**a**) and $Pb_{50}Bi_{50}$ (**b**) liquid alloys [42]

solid sample is accompanied by a gradual decrease of conductivity. Reaching the melting temperature T_m, a drastic fall on the $\sigma(T)$ curve is observed. In the liquid state the electrical conductivity decreases gradually with heating.

Similar to the $Pb_{40}Bi_{60}$ and $Pb_{43}Bi_{57}$ alloys, each subsequent melting-solidification cycle resulted in displacement of the melting temperature (from 4 to 5 K) towards more high values. The interval of solidification, which

started at the eutectic point according to the phase diagram [28], did not exceed 4–5 K.

Two samples where a content of lead was slightly higher than in the eutectic composition, namely $Pb_{45}Bi_{55}$, $Pb_{46}Bi_{54}$ and $Pb_{50}Bi_{50}$, were chosen in order to investigate the hypereutectic region of this system. As seen from Fig. 6.3a, the $\sigma(T)$ dependence of the $Pb_{45}Bi_{55}$ liquid alloy is similar to electrical conductivity behavior of the $Pb_{44}Bi_{56}$ alloy.

A temperature hysteresis in the region of melting and solidification has been observed in liquid $Pb_{46}Bi_{54}$ alloy. The range of solidification in this composition extended from 402 to 390 K. Comparing behavior of the electrical conductivity in these alloys we suggest that the processes of solidification in the eutectic and near eutectic liquid alloys are very similar.

Investigation of the more distant alloy composition $Pb_{50}Bi_{50}$ revealed that the temperature values of liquidus (423 K) and solidus (400 K) did not change after thermocycling and remained the same in course of melting and solidification. Temperature dependence of electrical conductivity of the $Pb_{50}Bi_{50}$ alloy is very similar to the conductivity behavior of lead.

Based on a deep analysis of the obtained results of the electrical conductivity, we propose a model, which allows to supplement the phase diagram of the binary system in the region of the eutectic composition with regard to the metastable area. According to this model, two additional lines, the so-called "metastable" liquidus lines *M*1 and *M*2 can exist below the liquidus lines *L*1 and *L*2 (see Fig. 6.4).

Four curves, namely, *L*1, *M*1, *L*2 and *M*2 have four points of the intersection. The point *E* corresponding to the eutectic composition is at the intersection of the curves *L*1 and *L*2, point P1 is at the intersection of the curves *L*1 and *M*2, point *P*2 is at the intersection of the curves *L*2 and *M*1 and point *P*3 is at the intersection of the curves *M*1 and *M*2.

Depending on the initial alloy composition, different ways of the eutectic transformation are possible. Let us assume that the composition marked by *X*1 corresponds to the liquid alloy $Pb_{50}Bi_{50}$. Solidification of this alloy with

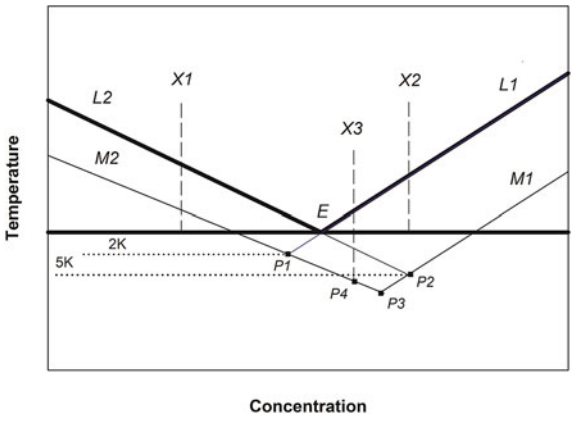

Fig. 6.4 Region of the metastable equilibrium near the eutectic composition of the binary alloy. *X*3 points to the hypothetic composition of the melt for the *P*4 construction [42]

undercooling along *M*2 results in precipitation of the solid alloy Pb–Bi, which composition is determined by the line of solidus. A liquid part of the alloy changes simultaneously its composition during cooling along *L*2 until the eutectic point *E*.

It has been suggested in [6] that there can be two possible solidification mechanisms. In case when the precipitated particles of the solid phase of the alloy are the nuclei of crystallization for another phase, the eutectic transformation takes place exactly at the point of eutectic *E*. Otherwise, these particles are not the centers of solidification, and precipitation continues upon cooling, passing *E*. In this case, the composition of the liquid phase changes along the extension of the line *L*2 up to crossing of the curves *L*2 and *M*1, *P*2. At the temperature corresponding to P2 particles of the second Bi-rich phase precipitate, pointing to the eutectic transformation.

The alloys of compositions located at another side of the eutectic point, e.g., $Pb_{40}Bi_{60}$, marked by *X*2, solidify very similar. Depending on impact of the first precipitates on the second liquid phase the eutectic transformation can start either in *E* or in *P*1. For the alloy composition, pointed by *P*3, the eutectic transformation runs without any initial nucleation. In this case the undercooling below *E* is negligible.

Solidification of the melt with a composition between *P*3 and *P*4 runs in a following way. Precipitations of the primary nuclei take place at temperatures determined by *M*2, the composition of the liquid phase changes gradually at constant temperature towards the increase of the second component content. The eutectic transformation takes place when a content of the second phase reaches *M*1.

Depending on velocity of the solidification, a region of the undercooling can change. In case of higher velocity, solidification will start at lower temperatures, so, the metastable" liquidus lines *M*1 and *M*2, as well as the *P*1, *P*2, *P*3 and *P*4 points, will be shifted. It means that the onset of the eutectic transformations can be at different temperatures and concentrations.

Additional confirmation of the metastable *M*-lines has been received from the electrical conductivity data for $Pb_{43}Bi_{57}$ alloy, located between *E* and *P*3 (see Fig. 6.4). As locations of *E*, *P*3, *P*4 cannot be determined very precisely, moreover, they are very close to each other, the alloy of this composition can be found between *P*4 and *P*3, but also between *P*3 and *P*2. The $Pb_{43}Bi_{57}$ melt begins to solidify at 391 K, which is 7 K lower than the eutectic temperature, and the corresponding point is located on the extension of *M*2. The eutectic transformation will begin when the composition of the liquid reaches *M*1. In course of heating $Pb_{43}Bi_{57}$, the temperature of liquidus (410 K) is higher than a value found from *L*1. It is suggested that a metastable solidification takes place, leading to precipitation of more refractory phases.

Thus, it was found that the very first particles, which start to precipitate, are not always the nuclei for appearance of the second phase in the melt. The data of temperature dependence of the electrical conductivity revealed that undercooling of the alloy compositions slightly different from the eutectic composition and hence the eutectic transformation at different temperatures, take place.

In case of the melt enriched by Pb, this transformation occurs at 5 K under *E* and is very similar to transformation in the alloy of the eutectic composition $Pb_{44}Bi_{56}$. At the same time, the eutectic transformation in the Bi-rich liquid alloy can occur at 2 K below *E*. We suppose that the points on the σ(T) where dσ/dT change can be interpreted as a kind of figurative points of a critical nucleation. These points can form the line of the critical nucleation in the region between the lines *L* and *M*, but in order to construct such a line, further investigations and more data are needed.

6.5 Microsegregation

Some anomalous behavior of the binary and ternary eutectic alloys is not limited to the melting-solidification area but is observed also at higher temperatures in the liquid state. Such peculiarities were recently revealed in a number of the Pb-based eutectic systems, like Pb–Sn, Bi–Pb–Sn, Bi–Pb, Au–Pb, Mg–Pb. Note that these systems are of permanent interest because they are widely applied as solder materials (Pb–Sn, Bi–Pb–Sn) or liquid–metal coolants in nuclear power stations (Bi–Pb, Au–Pb, Mg–Pb) [29, 30].

Investigation of the eutectic area of these systems revealed unpredictable behavior of their structure sensitive physical properties. The obtained results revealed that the metallic melts can undergo several structural transformations during heating beginning from their initial microheterogeneous state remaining after melting up to the homogeneous state od a true solution [31].

It was described recently that a regular solution becomes thermodynamically unstable as it approaches a temperature of eutectic T_e. (see [32] and references therein). The regions of stability and instability are divided by the binodal and spinodal lines. According to theoretical predictions, a maximum temperature of instability cannot exceed $2T_e$.

Reaching this temperature value during cooling, a regular solution loses stability and becomes metastable. Next transition to the irregular state can be conditioned by fluctuation processes or under the influence of external fields. Below the spinodal line a system becomes labile for the regular solution area, and no structure changes occur upon further cooling.

Different eutectic systems revealed anomalies (hysteresis, curve divergence) of some structure-sensitive properties, like density, internal friction or electrical resistivity, during temperature changes [31, 33–35]. One explanation is connected with the structure transformation of the local short-range order, which is accompanied by a break of the previous bonds and formation of new bonds or more disordered liquid at higher temperatures [35]. It is assumed that similar rearrangement of the structure results in gradual properties changes, like, e.g., in liquid tellurium [36] where transformation of structure is considerable [37]. This assumption was confirmed by results of the electrical conductivity and viscosity measurements, carried out for several Pb-based eutectic systems. The binary alloys of the eutectic compositions $Pb_{26.1}Sn_{73.9}$, $Pb_{44}Bi_{56}$, $Pb_{83}Mg_{17}$, $Pb_{50}Bi_{50}$, $Pb_{83}Mg_{17}$

and the ternary eutectic $Bi_{46}Pb_{29}Sn_{25}$ (all at. %) were chosen for the studies. Furthermore, existence of an inhomogeneous structure in complex eutectic melts such as In–Bi and In–Sb whose one component is a chemical compound, was examined based on the results of the viscosity.

Viscosity of liquid $Pb_{26.1}Sn_{73.9}$ and $Pb_{44}Bi_{56}$ eutectics is presented in Figs. 6.5 and 6.6. The viscosity decreases exponentially with upon heating. As in some earlier investigations [38, 39], the viscosity curves η(T) seem to be smooth.

But when we consider the curves "dη/d*T*—temperature", we can see oscillations within a certain temperature interval (see insets of Figs. 6.5 and 6.6). The oscillations are evident when we compare these curves with the curves from the Arrhenius equation (in dη/d*T*—T coordinates):

$$\eta = \eta_0 \exp(Q/RT) \tag{6.7}$$

where η_0 is a constant; Q is the activation energy of viscous flow and R is the ideal gas constant (see insets of Figs. 6.5 and 6.6). The parameters $\eta_0 = 0.6$ mPas and $Q = 5.915$ kJ · mol^{-1} for $Pb_{44}Bi_{56}$ and $\eta_0 = 0.55$ mPas and $Q = 5.912$ kJ · mol^{-1} for $Pb_{26.1}Sn_{73.9}$ were obtained from the experimental data $\ln(\eta_0) = f(1/T)$. It should be noted that similar oscillations were described earlier [33]. It is suggested that the oscillations are connected with the metastable quasieutectic structure remaining in some temperature range in the liquid state.

As reported in [31], such a quasieutectic structure remaining above the liquidus line may be a microemultion (microsuspension) of dispersed small particles, which are enriched in one component and distributed in a liquid matrix of a second component. As the densities of the components are different, a precipitation of the particles occurs. But this precipitation cannot be complete because of the Brownian motion. As a result, the uneven distribution of particles is set with height of the melt.

The conductivity of all the melts investigated decreases with heating (Figs. 6.7–6.12). The σ(*T*) results for the eutectics $Pb_{26.1}Sn_{73.9}$ and $Pb_{83}Mg_{17}$ agree with data

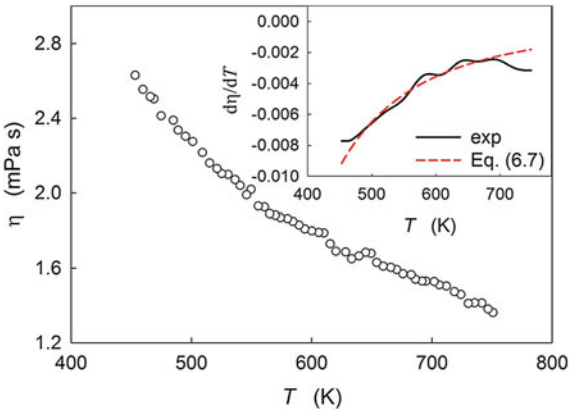

Fig. 6.5 Temperature dependence of the viscosity of $Pb_{26.1}Sn_{73.9}$ liquid alloy [5]

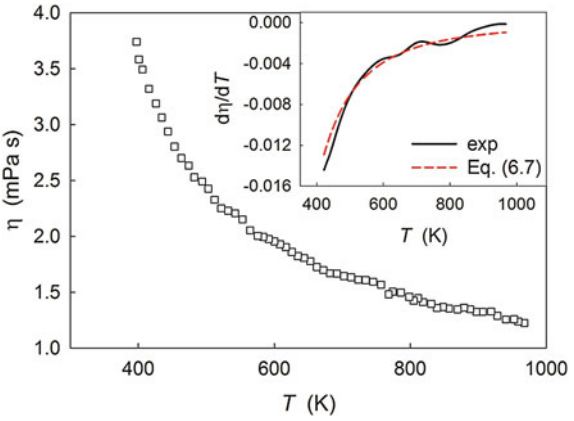

Fig. 6.6 Temperature dependence of the viscosity of $Pb_{44}Bi_{56}$ liquid alloy [5]

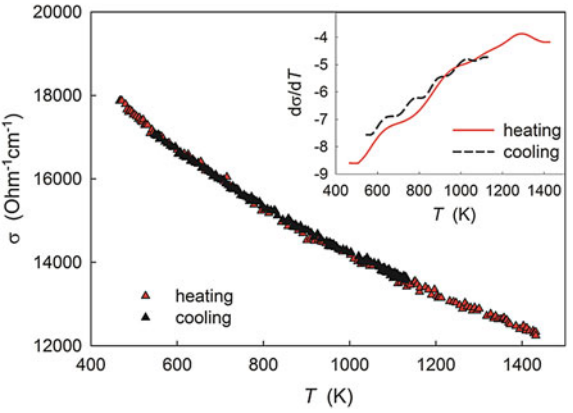

Fig. 6.7 Temperature dependence of the electrical conductivity of the $Pb_{26.1}Sn_{73.9}$ liquid alloy [5]

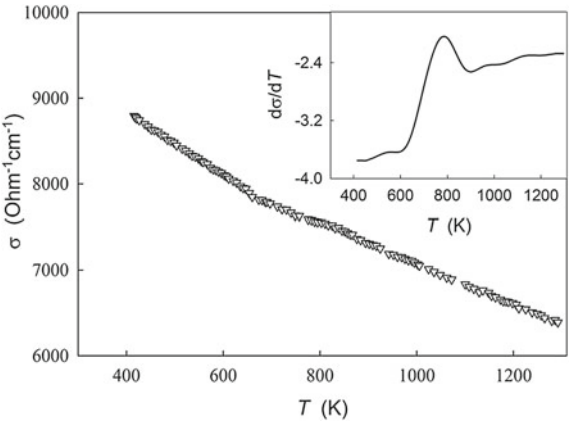

Fig. 6.8 Temperature dependence of the electrical conductivity of the $Pb_{44}Bi_{56}$ liquid alloy [5]

published in [4] for a limited temperature interval in the liquid state T_m + (100–200 K), as well as in [40]. Nevertheless, extending the temperature range and looking thoroughly into the electrical conductivity behavior, we observed some singularities on the σ(T) dependencies, contrary to our expectation. As in case of viscosity, the deviations from the smooth lines are more visible on the dσ/dT = f (T) dependencies (see results in Figs. 6.7 and 6.12). The temperature range of significant dσ/dT changes is peculiar for each system and composition, namely, from 600 to 1000 K for the $Pb_{26.1}Sn_{73.9}$ (Fig. 6.7), from 600 to 900 K for $Pb_{44}Bi_{56}$ (Fig. 6.8), from 550 to 950 K for the $Bi_{46}Pb_{29}Sn_{25}$ eutectic (Fig. 6.9), from 750 to 1020 K for $Pb_{83}Mg_{17}$ (Fig. 6.10), from 550 to 1000 K for the $Pb_{50}Bi_{50}$ melt (Fig. 6.11) and from 580 to 950 K for the $Pb_{85}Au_{15}$ (Fig. 6.12).

A hysteresis in the course of heating-cooling processes was observed for the $Pb_{26.1}Sn_{73.9}$ and also for $Pb_{50}Bi_{50}$ near-eutectic liquid alloys. In case of $Pb_{50}Bi_{50}$ the hysteresis is more evident. It should be noted that the electrical conductivity of

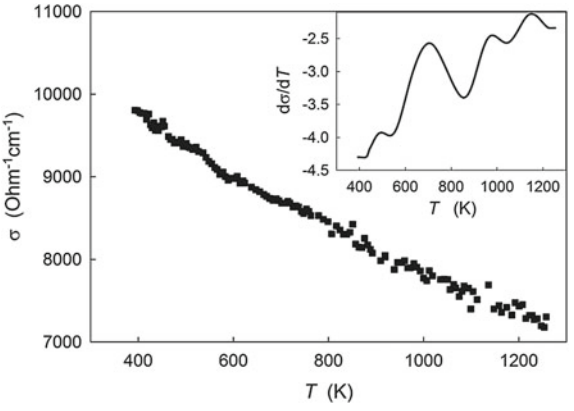

Fig. 6.9 Temperature dependence of the electrical conductivity of the $Bi_{46}Pb_{29}Sn_{25}$ liquid alloy [5]

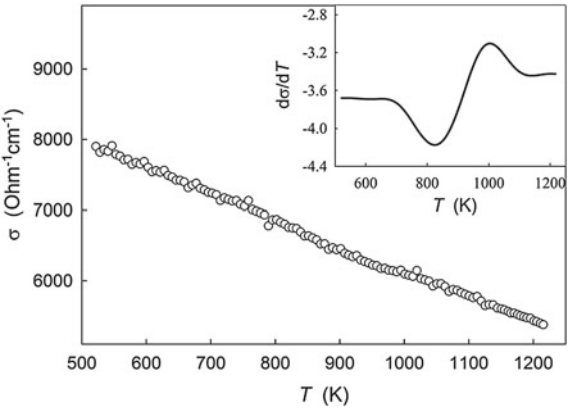

Fig. 6.10 Temperature dependence of the electrical conductivity of the $Pb_{83}Mg_{17}$ liquid alloy [5]

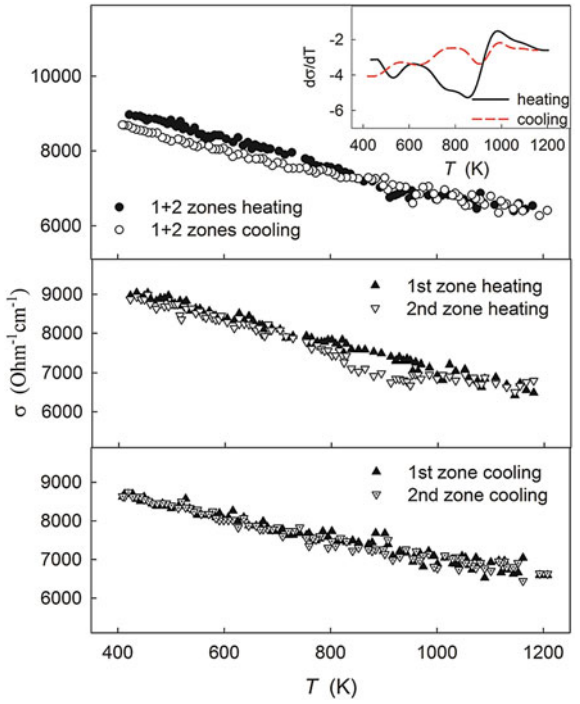

Fig. 6.11 Temperature dependence of the electrical conductivity of the liquid $Pb_{50}Bi_{50}$ alloy [5]

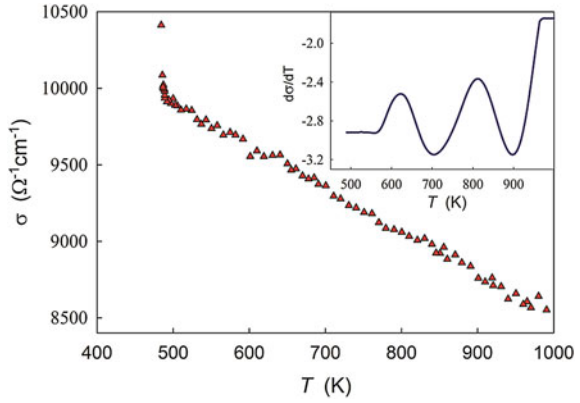

Fig. 6.12 Temperature dependence of the electrical conductivity of the $Pb_{85}Au_{15}$ liquid alloy [6]

the $Pb_{50}Bi_{50}$ melt presented in Fig. 6.11 was determined throughout the height of the sample. These measurements were performed in order to examine a supposed inhomogeneous particle distribution throughout the sample. The sample in the vertical crucible has been divided by potential electrodes into two imaginary zones. As seen from Fig. 6.11, a difference between the electrical conductivity values for the upper and lower zones upon heating between 750 and 1000 K confirmed that structural units are inhomogeneous distributed in the melt throughout the height. Beginning from about 1000 K this difference disappeared and was not observed in

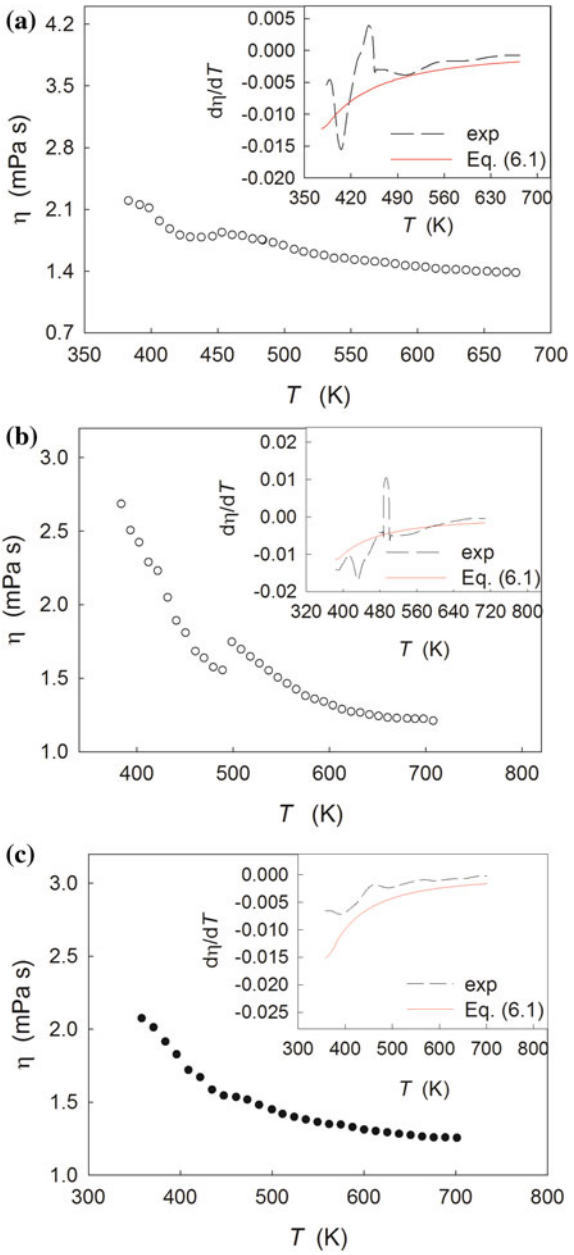

Fig. 6.13 Temperature dependence of the viscosity of liquid $In_{87}Bi_{13}$ (**a**), $In_{66}Bi_{34}$ (**b**) and $In_{77}Bi_{23}$ (**c**) alloys [43]

course of cooling. The revealed peculiarities confirm a permanent rearrangement of the melt structure.

The temperature dependencies of viscosity for In–Bi and In–Sb liquid alloys are presented in Figs. 6.13 and 6.14. The viscosity decreases exponentially with

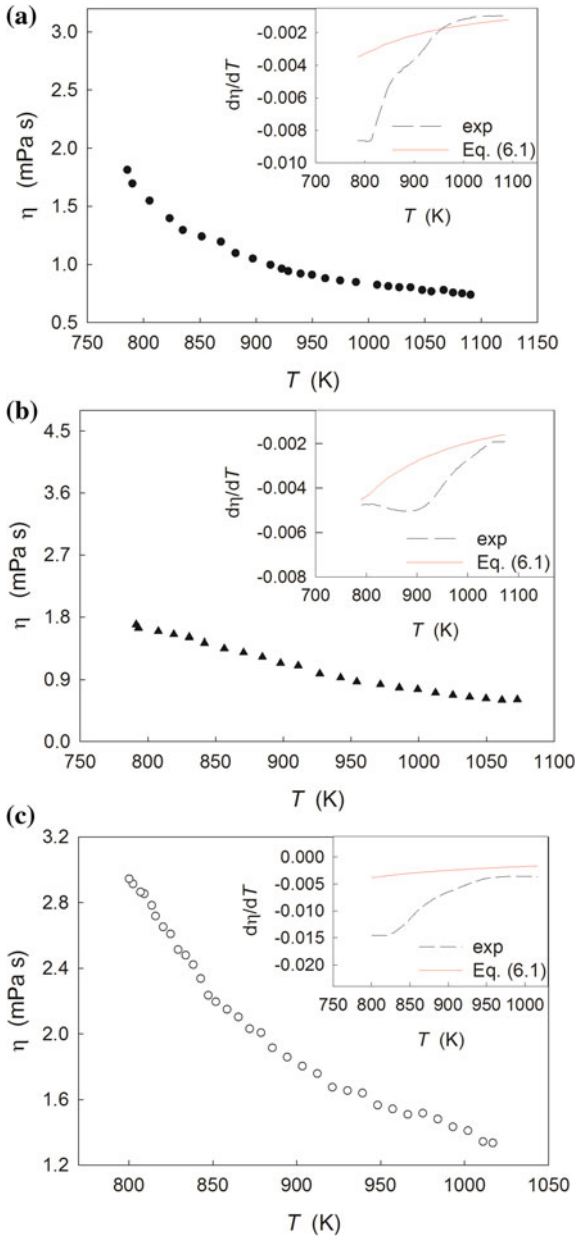

Fig. 6.14 Temperature dependence of the viscosity of liquid $In_{60}Sb_{40}$ (**a**), $In_{40}Sb_{60}$ (**b**) and $In_{50}Sb_{50}$ (**c**) alloys [43]

increasing temperature. Viscosity of In–Bi system revealed a deviation from the Arrhenius-like dependence with a local maximum at temperature about 450 K for the $In_{87}Bi_{13}$ alloy (Fig. 6.13a) and 500 K for the $In_{66}Bi_{34}$ alloy (Fig. 6.13b). For the eutectic melt a deviation from the exponential curve is less as compared to others

alloys (Fig. 6.13c). An analysis of $d\eta/dT$ (at the upper right hand corner) revealed that the hard sphere model can be applied only in the high temperature region. The experimental $d\eta/dT$ data for the melts with a content of In between 87 and 66 at. % revealed large oscillations up to 500 K.

The experimental viscosity data of liquid In–Sb alloys showed the most rapid decrease in values for the alloy containing 40 at. % Sb (Fig. 6.14). According to the phase diagram of the In–Sb system, the liquidus curve in the region of the equiatomic concentration is rather flat, assuming significant changes of concentration in the liquid during solidification because of different concentrations of the solid and liquid phases. It is suggested that the component redistribution begins in the liquid phase before solidification. These suggestions are in a good agreement with presented $d\eta/dT = f(T)$ dependencies in Fig. 6.14. A negligible viscosity decrease in the liquid InSb alloy can be explained by significant InSb–like chemical ordering whereby the contents of In and Sb are close in the liquid and solid states. A part of the chemically ordered InSb atomic groups dissociates during melting afterwards.

According to the model reported in [32], eutectic systems in the liquid state have regions of different thermodynamic stability. Similar to systems with a miscibility gap in the liquid state, these regions are determined by the lines of bimodal (B) and spinodal (S) (Fig. 6.13). But in contrast to the immiscible systems, they do not reveal evident phase separation. In the eutectic systems these regions can be considered as anomalous fluctuations of concentration, which manifest themselves as a deviation of physical characteristics from the predicted behavior. In this case we can speak about a peculiar kind of micro segregation.

After melting a sample is still chemically heterogeneous, and its quasieutectic structure remains. A gradient of concentration is set throughout the sample height. We assume that reversible changes in sample composition as well as of the particle sizes are possible in some interval where temperature dependence of electrical conductivity is linear, i.e., a slope of $d\sigma/dT$ is constant. The particles and a matrix are in the metastable equilibrium. At temperature, where a kink on the $\sigma(T)$ curve or a sharp $d\sigma/dT$ increase occur, the particle dissolution starts. Because of the interfacial tension the process slows down, therefore a melt can remain in the microheterogeneous state even at high temperatures.

A method allowing to determine the area of the of microheterogeneous stability in the liquid eutectic alloys was described in [32]. This method used suggestions reported in [41] and is based on extrapolation of the curves of the limited solubility of the components in the solid state to the over liquidus region. According to [32], the line of spinodal is a border line for stability of the homogeneous melt and has a maximum, corresponding to the temperature $2T_e$.

But the electrical conductivity data for investigated liquid alloys show that this value can be exceeded. The absence of kinks on the "conductivity-temperature" curves and a weak dependence of $d\sigma/dT$ on temperature suggest higher characteristic values then $2T_e$ for each system (Table 6.1).

The $2T_e$ value for the $Pb_{26.1}Sn_{73.9}$ eutectic is about 916 K; 796 K for the $Pb_{44}Bi_{56}$, and approx. 738 K for the $Bi_{46}Pb_{29}Sn_{25}$. According to experimental results, the temperatures corresponding to transition to the stable state were

Table 6.1 Characteristic temperatures and intervals of anomalous behavior of the electrical conductivity for investigated melts

Alloy	T_e, (K)	Range of anomalies (K)	$2T_e$, (K)	Transition to the stable state (K)
$Pb_{73.9}Sn_{26.1}$	456	600–1000	912	1350
$Pb_{44}Bi_{56}$	398	600–900	796	900
$Pb_{50}Bi_{50}$	423 (T_L)	550–1000	846 ($2T_L$)	1025
$Bi_{46}Pb_{29}Sn_{25}$	96	550–950	738	1150
$Pb_{83}Mg_{17}$	522	750–1020	1044	1130
$Bi_{43}Sn_{57}$	412		824	580
$Pb_{85}Au_{15}$	971	580–960	971	1000

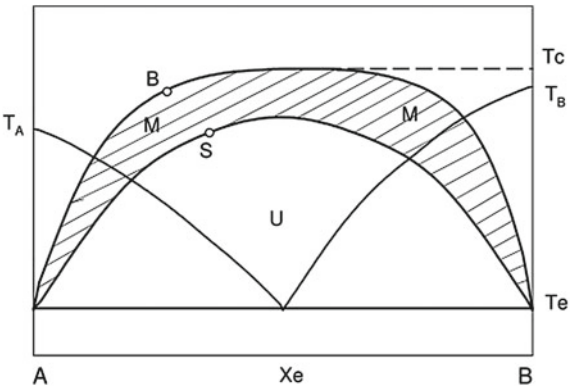

Fig. 6.15 Areas of thermodynamic stability in the eutectic system. M indicate a metastable state, U indicate a unstable state [5]

determined as 1350 K for $Pb_{26.1}Sn_{73.9}$, 900 K for $Pb_{44}Bi_{56}$, and 1150 K for the $Bi_{46}Pb_{29}Sn_{25}$.

It is suggested that the binodal line (B) constrains the region of the metastable (M) quasieutectic structure of the melt but not of the unstable structure (U) (Fig. 6.15). Location of the bimodal line is considerably higher than positions of the curves of the limited solubility, which are extrapolated to the liquid phase. It is possible that the lower points of the binodal coincide with the points located at the crossing of these curves and the eutectic horizontal. A fast transition through the temperature range between the curve of limiting solubility and the liquidus inhibits homogenisation of the solid phase, and some heterogeneities remain in the melt. Further increase of temperature results in rapprochement of compositions of the particle and the surrounding melt. These compositions become the same at the maximum point of the binodal and the metastable state of the microemulsion further is not be possible. But it is supposed that similar state can remain for a long time under the non-equilibrium conditions also at higher temperatures.

6.6 Fluctuations of Concentration and Mole Fractions of Associates

The composition dependence of the concentration fluctuations, $S_{cc}(0)$, was calculated for liquid In–Bi and In–Sb alloys using experimental results of the viscosity, $S_{cc}^{\eta}(0)$, and literature data of the molar enthalpy of mixing, $S_{cc}^{\Delta H}(0)$. The obtained results were compared with ideal values, $S_{cc}(0)_{id} = \sum_i c_i$. As shown in Figs. 6.16 and 6.17, the calculated values of the concentration fluctuations indicate a tendency to preferred interactions between unlike kind atoms, which leads to microheterogeneous structure and concentration fluctuations both in structure units with a short-range order and in the matrix with a random distribution of atoms.

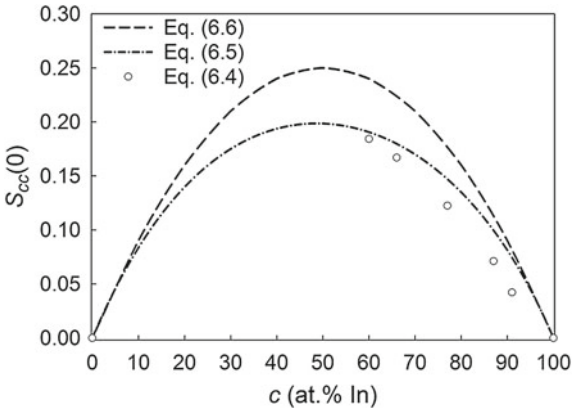

Fig. 6.16 Concentration fluctuations of liquid In–Bi alloys at 900 K [45]

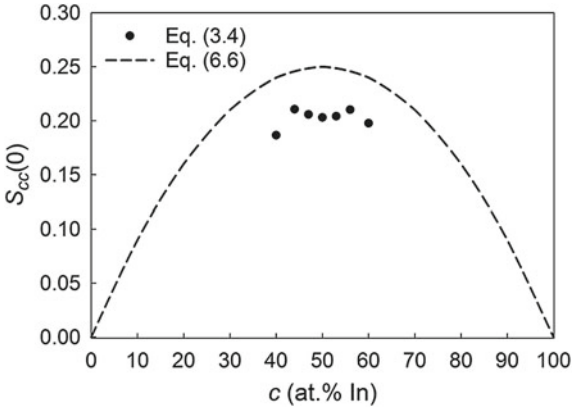

Fig. 6.17 Concentration fluctuations of liquid In–Sb alloys at 900 K [45]

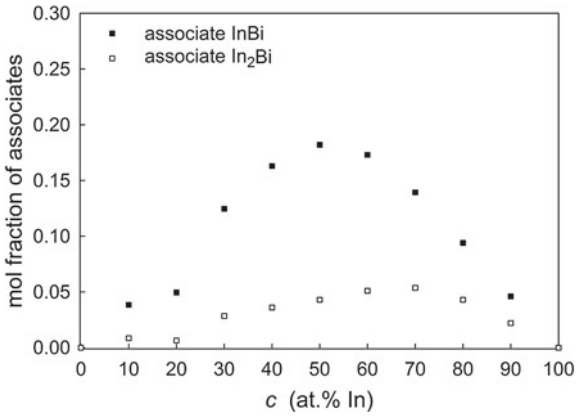

Fig. 6.18 mol fraction of InBi and In_2Bi associates in liquid In–Bi alloys at 900 K [44]

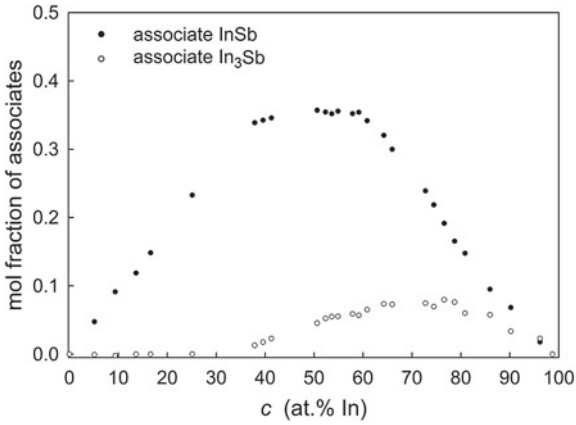

Fig. 6.19 mol fraction of InSb and In_3Sb associates in liquid In–Sb alloys at 900 K [43]

To confirm the fluctuations of concentration, the mole fractions of the associates InBi and In_2Bi as well as InSb and In_3Sb in the liquid state for In–Bi and In–Sb systems, respectively, were calculated using the association model (Figs. 6.18 and 6.19).

In order to explain the viscosity results for liquid In–Bi and In–Sb systems it was suggested that the alloys of these rather complicated eutectic systems, where one of the components is In_2Bi or InSb chemical compounds, respectively, consist in the liquid state of two structural units, namely, the self-associated pure elements and the chemically ordered In_2Bi- and InSb-like atomic groups. The changes of the structure and the composition with temperature are accompanied by concentration fluctuations in these systems.

6.7 Conclusions

Unusual behavior of structure-sensitive properties of the eutectic systems in a melting-solidification range confirmed that melting and solidification of metal alloys are not the reversible processes. In contrast to a pure metal, where melting is accompanied by destruction of the crystalline lattice, transition to the liquid state in the alloy, which is a system of several components, is followed by solving of more refractory elements in the liquid. Under such circumstances, the melting continues in a certain temperature range. The undercooling of the melts with compositions shifted oppositely with respect to the eutectic one occurs at different temperatures.

The anomalies of structure-sensitive properties in the eutectic melts confirmed an existence of the areas in the liquid state with different thermodynamic stability. These areas can be considered as anomalous fluctuations of concentration, which manifest themselves as a deviation of physical characteristics from the predicted behavior. The influence of heat treatment of the molten metallic alloy on the structure and properties of a final material within the specific working temperature range becomes significant in this connection.

References

1. D.E. Gray, *American Institute of Physics Handbook*, 3rd edn., ed. by B.H. Billings, D.E. Gray (McGraw-Hill, New York, 1972)
2. W. Kurz, D.J. Fisher, *Fundamentals of Solidification*, 3rd edn. (Trans Tech, Publications, Aedermannsdorf, Switzerland, 1981)
3. S.S. Kutateladze, V.E. Nakoryakov, *Phase Transitions in Pure Metals and Binary Alloys* (Akad. Nauk SSSR, Sibirskoe otd-nie, In-t teplofiziki, Novosibisk, 1980)
4. Y. Plevachuk, V. Sklyarchuk, A. Yakymovych, B. Willers, S. Eckert, J. Alloy. Comp. **394**, 63 (2005)
5. Y. Plevachuk, V. Sklyarchuk, A. Yakymovych, G. Gerbeth, J. Non-Cryst, Solids **354**, 4443 (2008)
6. Y. Plevachuk, V. Sklyarchuk, A. Yakymovych, S. Eckert, G. Gerbeth, J. Nucl. Mater. **434**, 291 (2013)
7. L. Bulavin, Y. Plevachuk, V. Sklyarchuk, I. Shtablavyy, N. Faidiuk, R. Savchuk, J. Nucl. Mater. **433**, 329 (2013)
8. L. Bulavin, Y. Plevachuk, V. Sklyarchuk, A. Omelchuk, N. Faidiuk, R. Savchuk, I. Shtablavyy, V. Vus, A. Yakymovych, Nucl. Eng. Des. **270**, 60 (2014)
9. L. Bulavin, V. Sokol'skii, O. Roik, V. Kazimirov, Y. Plevachuk, V. Sklyarchuk, N. Faidiuk, Phys. Chem. Liq. **54**, 717 (2016)
10. A.V. Chalyi, L.A. Bulavin, V.F. Chekhun, K.A. Chalyy, L.M. Chernenko, A.M. Vasilev, E. V. Zaitseva, G.V. Khrapijchyk, A.V. Siverin, M.V. Kovalenko, Condens. Matter Phys. **16**(2), 23008:1–12 (2013)
11. K.A. Chalyi, L.A. Bulavin, A.V. Chalyi, J. Phys. Stud. **9**(1), 66 (2005)
12. A.V. Chalyi, A.G. Lebed, *Non-Homogeneous Liquids Near the Critical Point and the Boundary of Stability and Theory of Percolation and Superconductivity of Ceramics* (Harwood Academic Publications, London, 1993)
13. L.A. Bulavin, A.V. Chalyi, O.I. Bilous, J. Mol. Liq. (2017)

14. A.V. Chalyi, *Physics of Liquid Matter: Modern Problems, Springer Proceedings in Physics*, ed. by L. Bulavin and A. G. Lebed (Springer, 2014), p. 31
15. Y. Plevachulk, V. Sklyarchuk, O. Alekhin, L. Bulavin, J. Mol. Liq. **127**, 33 (2006)
16. Yu. Plevachulk, V. Sklyarchuk, Meas. Sci. Technol. **12**(1), 23 (2001)
17. A. Yakymovych, V. Sklyarchuk, S. Mudry, J. Phys. Stud. **12**(1), **1601**(5) (2008)
18. O.I. Ostrovskii, V.A. Grygorian, A.F. Vishkarev, *Properties of Metal Alloys* (Mettalurgiya, Moscow, 1988)
19. F. Sommer, G. Duddek, B. Predel, Z. Metallkd. **69**(9), 587 (1978)
20. F. Sommer, Z. Metallkd. **73**(2), 77 (1982)
21. F. Sommer, Z. Metallkd. **73**(2), 72 (1982)
22. R.R. Hultgren, *Selected Values of the Thermodynamic Properties of Binary Alloys* (American Society for Metals, Metals Park, Ohio, 1973)
23. R.N. Singh, F. Sommer, Z. Metallkd. **83**(7), 533 (1992)
24. R.N. Singh, S.K. Yu, F. Sommer, J. Non-Cryst, Solids **156**, 407 (1993)
25. Y. Orlov, P. Martynov, V. Gulevski, *Issues of Lead Coolant Technology*, ed. by I.A.E. Agency (International Atomic Energy Agency, Vienna, Austria, 2001), pp. 95–98
26. A. Roll, T.K. Biswas, Z. Metallkd. **55**(12), 794 (1964)
27. G.T. Dyos, T. Farrell, *Electrical Resistivity Handbook* (Peter Peregrinus Ltd., London, 1992)
28. T.B. Massalski, *Binary Alloy Phase Diagrams* (Second edition ASM International, Materials Park, Ohio, USA, 1990)
29. I.A.E. Agency, *Power Reactors and Sub-critical Blanket Systems with Lead and Lead–Bismuth as Coolant and/or Target Material* (International Atomic Energy Agency, Vienna, Austria, 2003)
30. V.I. Subbotin, M.N. Arnol'dov, F.A. Kozlov, A.L. Shimkevich, At. Energy **92**(1), 29 (2002)
31. U. Dahlborg, M. Calvo-Dahlborg, P.S. Popel, V.E. Sidorov, Eur. Phys. J. B **14**(4), 639 (2000)
32. E.V. Kalashnikov, Tech. Phys. **42**(4), 330 (1997)
33. F.Q. Zu, Z.G. Zhu, B. Zhang, Y. Feng, J.P. Shui, J. Phys, Condens. Mat. **13**(50), 11435 (2001)
34. X.F. Li, F.Q. Zu, H.F. Ding, J. Yu, L.J. Liu, Q. Li, Y. Xi, Phys. B **358**(1–4), 126 (2005)
35. Y. Xi, F.Q. Zu, X.F. Li, J. Yu, L.J. Liu, Q. Li, Z.H. Chen, Phys. Lett. A **329**(3), 221 (2004)
36. V.M. Sklyarchuk, Yu.O. Plevachuk, Semiconductors **38**(12), 1365 (2004)
37. T. Yamaguchi, H. Ohtani, F. Yonezawa, J. Non-Cryst, Solids **250**, 437 (1999)
38. H.J. Fischer, A. Phillips, J. Metals **9**, 1060 (1954)
39. F. Herwig, M. Wobst, Wiss. Z. der TU Chemnitz. **4**, 391 (1991)
40. Yu. Plevachuk, V. Sklyarchuk, Z. Metallkd. **92**(6), 600 (2001)
41. I.A.I. Frenkel, *Kinetic Theory of Liquids*. *The International Series of Monographs on Physics* (Clarendon Press, Oxford, 1946)
42. V. Sklyarchuk, Yu. Plevachuk, G. Gerbeth, S. Eckert, J. Phys. Conf. Ser. **79**, 12019 (2007)
43. A. Yakymovych, V. Sklyarchuk, Yu. Plevachuk, S. Mudry, Rev. Adv. Mater. Sci. **23**(2), 213 (2010)
44. A. Yakymovych, S. Mudry, C. Luef, H. Ipser, Chem. Met. Alloys **1**(2), 159 (2008)
45. A. Yakymovych, S. Mudry, *Antimony: Characteristics, Compounds and Applications*, ed. by M. Razeghi (Nova Science Publisher, Evanston 2012) pp. 63–91

Chapter 7
Influence of the Nature of Counterions and Solvent on the Structure of PSS Solutions

Georgiy Smolyakov, Jean-Marie Catala, Nataliya Kutsevol and Michel Rawiso

Abstract We have studied by Small Angle X-ray Scattering (SAXS) semidilute solutions of the acid H^+- and salt Na^+-forms of polystyrene sulfonate (PSS) in water and organic solvents: DMSO and ethanol. The solutions in water were prepared without and with specific added low-molecular-weight electrolytes: NaCl, 1-ethyl-3-methylimidazolium tosylate and tosylic acid, or p-toluenesulfonic acid. We have shown that the Na^+–H^+ counterion exchange influences the effective charge fraction of the PSS macroions and hence their average conformation in water. However, the added low-molecular-weight electrolytes have none distinct effect on the SAXS profile of the acid form polystyrene sulfonate (PSSH) aqueous solutions. We conclude that, contrarily to the valence, the chemical nature of low-molecular-weight cations does not determine their condensation on macroanions. By using different solvents we can change the polyelectrolyte behavior, or structure. In particular for PSS, the replacement of water by the organic solvents DMSO and ethanol led to the appearance of a solvophobic effect.

G. Smolyakov · J.-M. Catala · M. Rawiso (✉)
Institut Charles Sadron (CNRS-UdS), 23 Rue du Loess,
BP 84047, 67034 Strasbourg, Cedex 2, France
e-mail: michel.rawiso@ics-cnrs.unistra.fr

N. Kutsevol
National Taras Shevchenko University of Kyiv, Volodymyrska 60,
Kiev 01601, Ukraine

L. A. Bulavin and A. V. Chalyi (eds.), *Modern Problems of Molecular Physics*,
Springer Proceedings in Physics 197, https://doi.org/10.1007/978-3-319-61109-9_7

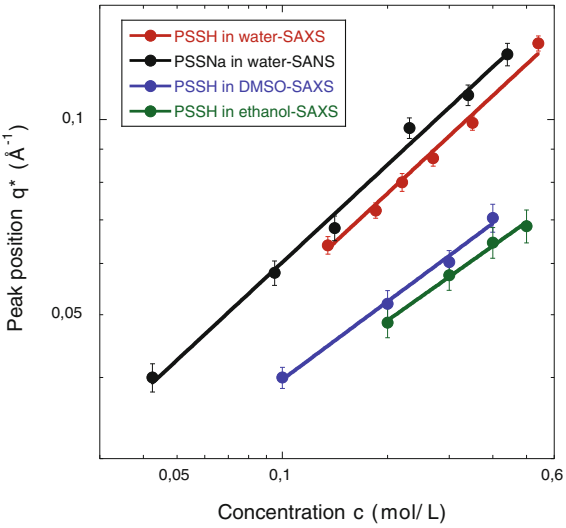

7.1 Introduction

Strong polyelectrolytes (PE) exist in water and polar organic solvents in dissociated form, i.e. macroions plus counterions [1–8]. When dissolved in a good solvent (solvophilic PE), their properties are more complex than those of neutral macromolecules mainly because electrostatic interactions are long-ranged (possibly screened by adding salts or Low-Molecular-Weight Electrolytes, LMWE). In a poor solvent (solvophobic PE), the complexity results from the competition between the long-range electrostatic repulsions and the short-range attractions associated with the poor solubility. In both cases, other degrees of freedom are brought by counterions that also play a crucial role with respect to interactions. Increasing attention has been paid to these charged polymers in aqueous solutions. However, the understanding of their properties is far from complete.

Various fundamental issues have been yet addressed in the science field of PE. Some of them remain the focus of an active research [9]. Among them, there is the problem of the interactions between macroions and counterions and the resulting counterion distribution. Specifically, it is well known that different small counter- and co-ions may result in different overall behaviors of PE, even when their valences are the same [10]. Although several aspects of ion-specific interactions have been understood, [11] we are still far from a satisfactorily simple model to explain the experimental data.

In the high coupling limit, counterions are only partially condensed on macroions, so the latter are charged. The effective charge fraction of macroions can be determined by different methods, among which are viscosimetry, osmotic pressure

measurements, electrophoresis, NMR etc. [12]. Small Angle X-ray Scattering (SAXS) can be used for this purpose as well [13]. The effective charge fraction leads to mutual electrostatic repulsions between macroions and correlations in their monomer positions in solution. Such correlations can be investigated by the small angle scattering methods, providing typical scattering profile $I(q)$ versus q (where $I(q)$ is the scattered intensity; q, the modulus of the scattering vector depending on the wavelength of the X-ray incident beam λ and the scattering angle θ, $q = (4\pi/\lambda) * sin(\theta/2)$). In this profile, the correlations cause the appearance of a broad maximum, the so-called polyelectrolyte peak, for some scattering vector q^* [14–17]. In particular, the shift with concentration of this polyelectrolyte peak is a signature of the various concentration regimes. In the framework of the isotropic model, we have for highly charged polyelectrolytes in good solvent: $q^* \sim c^{1/3}$, in the dilute regime; $q^* \sim c^{1/2}$, in the semidilute regime [4, 8]. By adding some low-molecular-weight electrolyte (LMWE), the electrostatic repulsions between macroions are screened and the polyelectrolyte peak as well is eliminated [18–20].

Polystyrene sulfonate (PSS), or poly(styrene-4-sulfonic acid), is a classical example of a strong polyelectrolyte. Water solutions of its salt forms with different metal and organic cations were studied by SAXS before [21]. Both LMWE-free solutions and the ones with different added LMWE were considered. The monovalent counterions involved in most of previous studies, were able only to display usual electrostatic interactions with macroions. Thus, the counterion condensation could be described according to the Manning-Oosawa approach [22, 23]. But this is not always the case [24]. On the other hand, as was observed by Hofmeister, each counterion could have own effect on polyelectrolyte behavior in a solution due to specific interactions with macroions [25]. Such interactions depend on the nature of counterions and can play a significant role.

This study aims at investigating the structure of PSS aqueous solutions without and with added LMWE, in which the macroion-counterion total interaction has several contributions. In addition to the usual electrostatic interaction, some specific interactions can be present. The latter can include H-bonding, dipole-dipole, aromatic π-π and aliphatic van der Waals contributions [26]. To achieve that, we have first used PSS in acid form (further PSS means the acid form, if another is not pointed) with protons as counterions. H^+ is very small and therefore has a very high charge density. Also, it does not contain electrons. This allows it to come very close to electronegative atoms and even penetrate in their electronic layers, thus increasing the electrostatic interaction, as well as providing H-bonding. For aqueous solutions in the presence of added LMWE, we used NaCl and two other specific LMWE:

- Tosylic acid (H-Tos), or p-Toluenesulfonic acid.
- 1-ethyl-3-methylimidazolium tosylate (EMIM-Tos), an organic low-melting salt (ionic liquid) (Fig. 7.1).

This organic salt in the liquid state has cations $EMIM^+$, theoretically able to display all above-mentioned types of interaction with PSS-units.

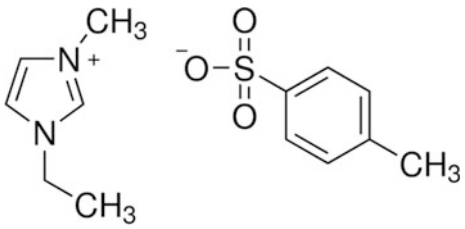

Fig. 7.1 Chemical structure of the EMIM-Tos ionic liquid

As we have a third component in our systems, the solvent, the interaction of counterions with it also should be taken into account [27]. Changing the nature of counterions, the PSS effective charge could be modified in this indirect way too.

To study the influence of different counterions on the position of the polyelectrolyte peak, q^*, we have compared the scattering behaviors of PSS with Na^+ and H^+ counterions in LMWE-free aqueous solutions, and specifically studied the c-dependence of q^* for the acid form. On the other hand, for aqueous solutions with added LMWE, we explored the efficiency of different LMWE to eliminate the polyelectrolyte peak.

Organic solvents could have significant potential with respect to polyelectrolytes, although a number of publications in this area remains rather limited [1, 28, 29]. Along their usual advantages, making them commonly used in different fields of chemistry, they are rather various. Thus, one can choose a solvent with suitable polarity and particular chemical structure to influence its interaction with a given polyelectrolyte and the structure of the latter in the solution.

PSS in organic solvents were not yet well studied due to insolubility of the most its salts in this type of solvents. Nevertheless, we should pay particular attention to the article [30]. The authors consider Na^+-salt form of partially sulfonated polystyrene in DMSO. They prove, that this polyelectrolyte does not display solvophobic effects in this organic solvent, like it does in water. But, they couldn't achieve the complete solubilization of the related Na^+-salt form of the fully sulfonated PSS in DMSO.

We have found that the acid form of fully sulfonated PSS is soluble in some organic solvents, which are polar and able to form hydrogen bonds. DMSO and ethanol are among them. PSS solutions in DMSO and ethanol were investigated at different concentrations in order to study the c-dependence of q^* and conclude about the PSS solvophilic or solvophobic character in these solvents.

7.2 Materials and Methods

Two PSS linear polyelectrolytes were obtained by sulfonation of their parent polystyrene (PS) neutral polymers. Thus, PS chains with a narrow molecular weight distribution were sulfonated according to the Makowski et al. procedure [31–34]. After neutralization with sodium hydroxide (NaOH), allowing to break sulfone

Table 7.1 Characteristics of PSS samples

Sample	M_w (g/mol)	$I = M_w/M_n$	c* (mol/L)
PSS1	$1.43*10^5$	1.06	$2.4*10^{-3}$
PSS2	$3.4*10^4$	1.09	$4.4*10^{-2}$

bridges, NaPSS polyelectrolytes were purified by extended dialysis against pure water. A titration with hydrogen chloride (HCl) was then carried out to obtain the PSS acid form. After a second dialysis against pure water and freeze-drying, PSS in white powder form was obtained. This powder was kept away from light under argon.

Size Exclusion Chromatography (SEC) analyzed PSS samples. Their critical overlap concentrations in salt-free aqueous solutions, c^*, were then evaluated from the degree of polymerization N-dependence of c^* ($c^* \sim N^{-2}$ scaling law) reported in reference [35]. The degrees of polymerization were deduced from the weight average molecular weights, M_W, obtained by SEC. The main characteristics are summarized in Table 7.1.

The degree of sulfonation, determined by NMR as well as elemental analysis, was higher than 95% for both PSS samples.

PSS2 was considered only for the PSS solutions in ethanol. For all other solvents, PSS1 was used. Actually, the difference in M_w-values has none importance, as we have always worked in the semidilute regime ($c > c^*$) where q^* does not depend on M_w. For simplicity we will call further both samples PSS.

NMR controlled the purity of the polyelectrolytes. From thermal gravimetric analysis (TGA), the weight fraction of water content in the PSS powder appeared equal to 15 wt%. But, PSS quickly absorbs the water from air until 22 wt% of H_2O. So prior to weight the PSS powder in order to prepare any solution, we waited 30 min to saturate it by water. The water content in PSS powder was then taken into account to evaluate the correct concentration of PSS in related solutions.

NaCl, H-Tos and EMIM-Tos LMWE, as well as DMSO and ethanol were purchased from Sigma-Aldrich.

SAXS experiments were carried out by using a diffractometer developed by Molecular Metrology, INC (Elexience in France). This diffractometer operates with a pinhole collimation of the beam and a two-dimensional gas-filled multiwire detector. A monochromatic ($\lambda = 1.54$ Å with $\Delta\lambda/\lambda < 4\%$) and focused X-ray beam is obtained through a multilayer optic designed and fabricated by Osmic, Inc. The size of the incident beam on the sample was 200 µm. The sample-detector distance was set at 1.5 m. This configuration allows performing measurements in the q-range $0.02 < q < 0.16$ Å^{-1}. The solutions were held in calibrated mica cells of 1 mm thickness from Teflon Kel-F, avoiding multiple scattering. The scattering data were treated according to a standard procedure for isotropic small angle X-ray scattering. The corrections of the geometrical factors and the detector cells efficiency were carried out with the use of a ^{55}Fe source. After radial averaging, the spectra were corrected for electronic noise of the detector, empty cell, absorption and sample thickness. A silver Behenate sample allowed the q-calibration, while the

Table 7.2 X-ray contrast lengths, K, and contrasts, K^2

	PSS^-/H_2O	Na^+, 5 H_2O/H_2O	$EMIM^+/H_2O$	PSS^-/DMSO	PSS^-/ethanol
K (10^{-12} cm)	9.40	5.46	−1.15	8.20	12.86
K^2 (10^{-24} cm^2)	88.34	29.82	1.33	67.17	165.32

normalization to the unit incident flux was performed using Lupolen, or water, as standard sample. Finally, the scattering of the solvent was subtracted to obtain the scattered intensities, $I(q)$ (cm^{-1}), associated with polyelectrolytes.

The contrast length and contrast values of the various elementary scatterer–solvent pairs, which are useful in this SAXS study, are listed in Table 7.2.

7.3 Results and Discussion

Influence of the nature of counterions on the effective charge fraction of PSS macroions in aqueous solutions.

For LMWE-free semidilute aqueous solutions of hydrophilic polyelectrolytes, we have from the scaling approach in the framework of the isotropic model [4, 8, 36]:

$$q^* = 2\pi f_{eff}^{2/7} (l_B/b)^{1/7} (bc)^{1/2} \tag{7.1}$$

f_{eff} is the effective charge fraction of the macroions; l_B, the Bjerrum length, 7.14 Å in water at room temperature; b, the monomer size or contour length, 2.56 Å for PSS; c, the PE concentration (mol/L).

Thus, q^* scales like $q^* \sim f_{eff}^{2/7}$. In its turn f_{eff} depends on the counterion condensation. In order to see the difference between counterions, we have studied LMWE-free aqueous solutions of PSS in acid and salt forms. The first form has protons as counterions, which have the smallest size, or ionic radius, and the highest charge density among all cations. In the second form, we have cations of the typical alkali metal, sodium (Na^+). The SAXS profiles of the related solutions for $c = 0.22$ M are shown in Fig. 7.2.

The profiles are distinct and specifically exhibit a polyelectrolyte peak at distinct positions. Thus, $q^*_{\text{acid}} < q^*_{\text{salt}}$, in agreement with some previous SANS results [37]. Actually, q^* should decrease from acid to salt form of PSS due to the effect of the form factor on the position of q^* measured from the total scattering function [38]. Since for the acid form we measure the macroion partial scattering function only, and for the salt one both macroion and counterion partial scattering functions are measured, q^*_{acid} must be higher, than q^*_{salt}. This is not the case, so the difference in q^* cannot be attributed to any effect of the form factor. Moreover, in this q-range there is no longer influence of large heterogeneities, i.e. the upturns that take place at smaller q-values. So, the difference in q^* for acid and salt forms of PSS can only result from the change in the effective charge fraction f_{eff} of respective

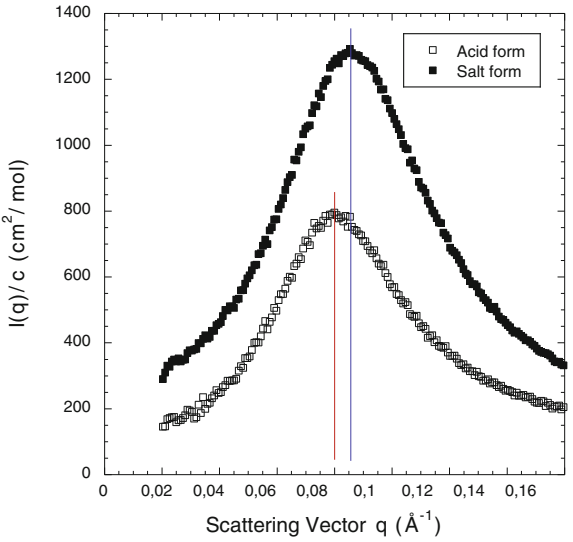

Fig. 7.2 SAXS profiles of c = 0.22 M LMWE-free aqueous solutions of PSS with H^+ (acid form) and Na^+ (salt form) counterions. The scattered intensities, $I(q)$, are normalized to the polyelectrolyte concentration, c

macroions. Indeed, l_B as well as c are identical for both acid and salt forms of PSS. Therefore, observed q^*-shift should be related to the difference in the effective charge fraction of PSS macroions. We have $(f_{eff})_{acid} < (f_{eff})_{salt}$ and this is due to a stronger tendency of H^+ counterions to condense in comparison with Na^+ ones, which should be primarily due to a stronger interaction with PSS anion units.

The significant change in the amplitude of the scattered intensity from the acid form of PSS to the salt one results from the fact that the scattered intensity for the acid form is mainly related to the macroion partial scattering function:

$$I(q) \approx K_m^2 S_{mm}(q) \tag{7.2}$$

whereas the one for the salt form involves the macroion and counterion partial scattering functions as well as a possible cross term:

$$I(q) = K_m^2 S_{mm}(q) + K_c^2 S_{cc}(q) + 2K_m K_c S_{mc}(q) \tag{7.3}$$

In these equations m refers to macroions (monomers of macroions); c, to counterions; K_m and K_c, to their respective contrast lengths (Table 7.2).

Thus, the condensed Na^+ counterions are responsible for the large increase in the scattered intensity from the PSSNa solution described by (7.3) with respect to that from the PSSH solution rather described by (7.2). Moreover, we note that the scattered intensity from the PSSNa solution decreases more strongly than the one from the PSSH solution at high q-values (q > 0.13 $Å^{-1}$). That is related to the form factor of the condensed Na^+ counterions.

For hydrophilic macroions, $q^* \sim c^{1/2}$, [15, 36] but the counterion contribution to the scattered intensity can change this apparent c-dependence for polyelectrolyte solutions [38].

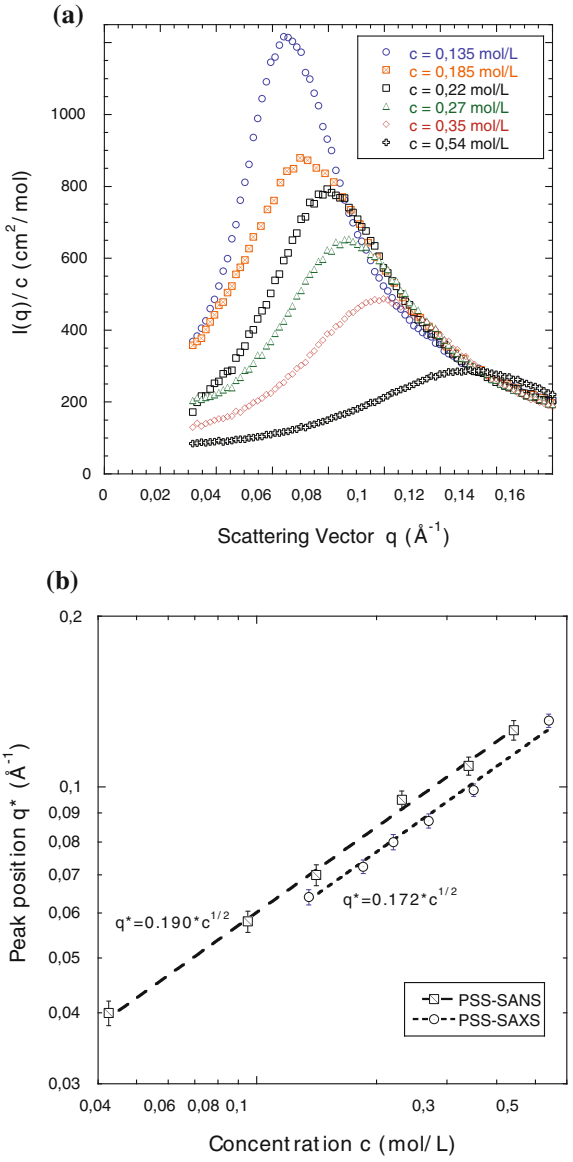

Fig. 7.3 LMWE-free aqueous solutions of PSS at different concentrations. **a** SAXS profiles. The scattered intensities, $I(q)$, are normalized to the polyelectrolyte concentration, c. **b** c-dependence of q^* in comparison with that for the salt forms of PSS_D in SANS (in both cases, only the PSS macroion scattering function $S_{mm}(q)$ is considered)

In order to study the influence of protons on the total scattering function, we have explored the change in the scattering function and specifically in the position of the polyelectrolyte peak q^* according to the concentration c for the acid form of PSS. The scattering profiles are shown in Fig. 7.3a.

The results demonstrate, that for LMWE-free PSS solutions in water q^* scales like $c^{1/2}$, as well as in the case of the salt form (with Na^+ or $N(CH_3)_4^+$ counterions)

of deuterated PSS (PSS_D) in H_2O through small-angle neutron scattering (SANS) [16, 38] (Fig. 7.3b). So, protons don't really contribute to the total scattering function, and that should be explained by their unique feature: absence of electron. Thus, they don't scatter X-rays, and don't really change the molar volume (and the scattering length density) of macroion units, when condensed. In SANS experiment for above described system, the contribution of Na^+- and $N^+(CH_3)_4$-counterions to the total scattering function is negligible too, and we are only concerned with the macroion scattering function (7.2).

The values of f_{eff} for PSS in acid and salt forms were determined from c-dependence of q^*. We have $(f_{eff})_{acid} = 0.27$ and $(f_{eff})_{salt} = 0.36$, respectively. So, there is a decrease in f_{eff} for the stronger condensed counterions.

The aqueous solutions of PSS in presence of different low-molecular-weight electrolytes were also studied. Three monovalent LMWE were considered: EMIM-Tos, H-Tos and NaCl. The corresponding scattering profiles measured for $c_{PSS} = c_{LMWE} = 0.22$ M are shown in Fig. 7.4. They are compared with the LMWE-free aqueous solutions of PSS at the same concentration. The SAXS profiles of the PSS solutions in the presence of added LMWE do no longer display any polyelectrolyte peak and are superimposed inside the small experimental uncertainties (SAXS measurements and concentrations). Thus, the nature of the added monovalent LMWE does not play a role, leading to none particular effect. Indeed, the $EMIM^+$ and Na^+ cations don't replace the H^+ condensed counterions and the effective charge fraction of the PSS macroions does not change. Correlatively, the ionic strength of the solutions is the same whatever the nature of the added monovalent LMWE.

Another observation from these SAXS profiles is that the latter are completely superimposed at the highest explored q-values, where the intermolecular

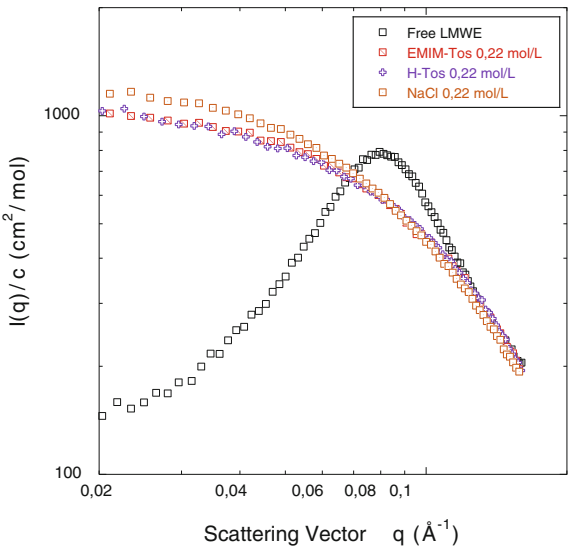

Fig. 7.4 SAXS profiles of the aqueous solutions of PSS in the absence and presence of three different LMWE; $c = c_{PSS} = 0.22$ M and $c_{LMWE} = 0$ and 0.22 M. The scattered intensities, $I(q)$ are normalized to the polyelectrolyte concentration, c

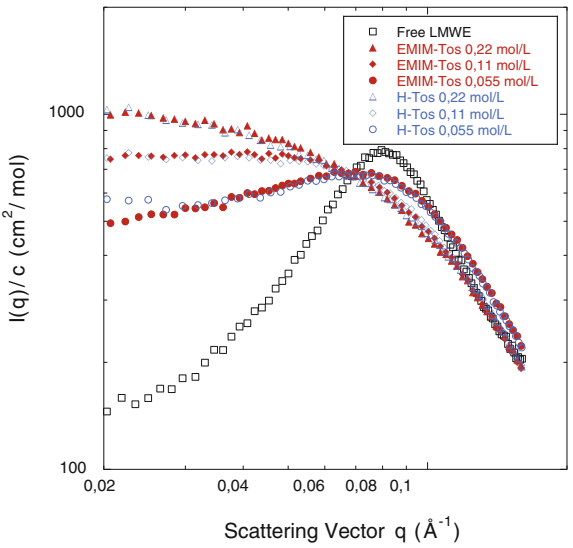

Fig. 7.5 SAXS profiles of the aqueous solutions of PSS in the presence of two different LMWE at distinct concentrations; $c = c_{PSS} = 0.22$ M; $c_{EMIM\text{-}Tos} = 0.22$ M, 0.11 M, 0.055 M; $c_{H\text{-}Tos} = 0.22$ M, 0.11 M, 0.055 M. The scattered intensities, $I(q)$, are normalized to the polyelectrolyte concentration, c

correlations are negligible. So, there is no more difference in the contrast length that could suggest any condensation of the $EMIM^+$ and Na^+ counterions.

To make more detailed comparison of the most interesting LMWE, EMIM-Tos and H-Tos, we have investigated the LMWE-concentration dependence of the scattered intensity. The results are presented in Fig. 7.5.

Again there is none significant differences in between the SAXS profiles associated with the same LMWE-concentration inside the experimental uncertainties. Thus, the $EMIM^+$ cations don't lead to any higher degree of condensation, associated with a smaller ionic strength of the solutions, than the H^+ ones. Yet, we could expect a stronger tendency of the $EMIM^+$ cations to condensate due to a higher interaction with the PSS macroion units, resulting from several contributions. Indeed, the complex chemical structures of both $EMIM^+$ counterions and PSS macroion units were chosen in a way to achieve an efficient interaction. Moreover, the $EMIM^+$ cations are partially hydrophobic, so their interaction with water should be weaker, causing a higher degree of counterion condensation.

From these experiments we conclude that the chemical nature of the monovalent low-molecular-weight cations don't play a role in their condensation onto macroanions.

Influence of the solvent nature on the structure of LME-free PSS solutions.

The nature of the solvent is another important factor, which can influence the PE behavior, or structure, in solution.

As was mentioned, for solvophilic macroions we have $q^* \sim c^{1/2}$. The exponent of this scaling law is therefore $n = ½$. But, provided some solvophobic effects appear, experiments show $n < ½$ [28, 30, 32, 33, 39, 40].

We have carried out a study of q^* versus c for PSS solutions in two classical organic solvents, DMSO and ethanol (EtOH). In this way, we could determine the

real q^*-values for PSS in these solvents and characterize the PSS behavior, or structure, in these solvents. Some other solvents were tested to achieve PSS solubility in them. In particular the next ones were taken for this purpose: acetone, acetonitrile, ethyl acetate, toluene. But, none of them solubilized PSS.

Solutions of PSS in DMSO at four different concentrations in the semidilute regime were studied by SAXS. Due to a presence of the relatively heavy S atom in high content in the solvent, the absorption of X-rays was quite high. Thus, to obtain a scattering profile with a sufficiently good statistics, a long time of scanning was required. The scattering curves are shown in Fig. 7.6a, and the resulting q^* versus c dependence is presented in Fig. 7.6b.

Similarly, PSS solutions at four different concentrations were studied in ethanol. The SAXS profiles of these solutions are in Fig. 7.6a and the related q^* versus c dependence in Fig. 7.6b.

An interesting point related to the PSS solutions in ethanol is a quick disappearance of upturns at small q-values. Thus, we can perform SAXS measurements for these solutions without waiting a long time after their preparation and explore more easily the region of small q-values, which is no longer disturbed by upturns. The reason of this phenomenon could be a lower viscosity of the PSS solutions in ethanol in comparison with the corresponding ones in water and DMSO.

From q^* versus c dependences the values of the exponent n were obtained. $n = 0.40$ in DMSO and $n = 0.38$ in ethanol. For both solvents considered, $n < ½$. Thus, PSS has a partially solvophobic character in these organic solvents.

In Fig. 7.7 we summarize the q^* versus c dependences determined from the studied systems for convenient comparison. Except the real systems two other ones are considered, which are PSS solutions in hypothetical solvents S1 and S2. For these solvents we have the next conditions: $\varepsilon_{S1} = \varepsilon_{DMSO}$, $\varepsilon_{S2} = \varepsilon_{ethanol}$, and in both S1 and S2 PSS behaves like a solvophilic polyelectrolyte. So going from water to S1 and S2 we only change the q^* values through the solvent polarity, maintaining the same type of PSS behavior, or solvophilic character. In this case, using (7.1) and taking into account that $f_{eff} = b/l_b$, we have:

$$q^* = (b/l_b)^{2/7}(l_B/b)^{1/7}(bc)^{1/2}$$

and thus $q^* = (b/l_b)^{1/7}(bc)^{1/2}$
Using $l_B = e^2/4\pi\varepsilon o\varepsilon kT$, we obtain:

$$q^* = (4\pi\varepsilon o\varepsilon kT/e^2)^{1/2} b^{9/14} c^{1/2} \tag{7.4}$$

So, we have $q^* \sim \varepsilon^{1/7}$. Thus, varying ε of the solvent, we obtained q^* versus c dependences for PSS in S1 and S2. As one can see, the q^*-values in these solvents are much higher than the ones in DMSO and ethanol.

From this comparison we demonstrate the solvophobic character of PSS in DMSO and ethanol. The solvophobic effect leads not only to a decrease in the exponent of the scaling law $q^* \sim c^{1/2}$, but to a decrease in the q^*-values as well.

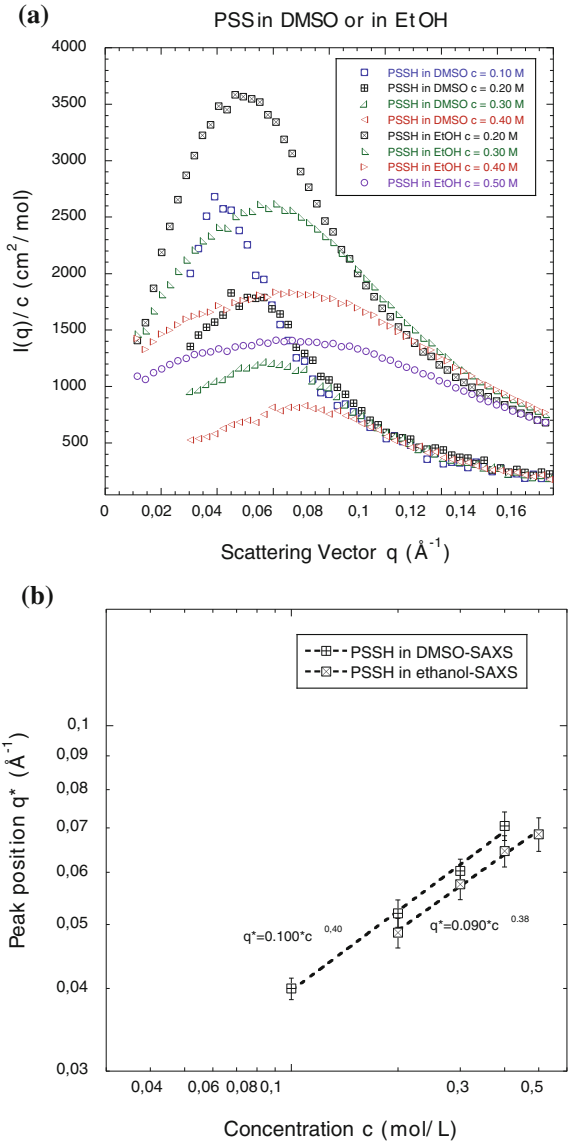

Fig. 7.6 **a** SAXS profiles of LMWE-free aqueous solutions of PSS at different concentrations in two distinct solvents: DMSO and EtOH (ethanol). The scattered intensities, $I(q)$, are normalized to the polyelectrolyte concentration, c. **b** Corresponding q^* versus c dependences

So, DMSO and ethanol solubilize the acid form of fully sulfonated PSS, but the behavior of the latter in these solvents is rather solvophobic, showing $n < ½$. q^*-values of PSS in DMSO and ethanol are strongly reduced with respect to the ones in the aqueous solutions. That is due to the lower polarity of the used organic solvents and to the solvophobic effect as well.

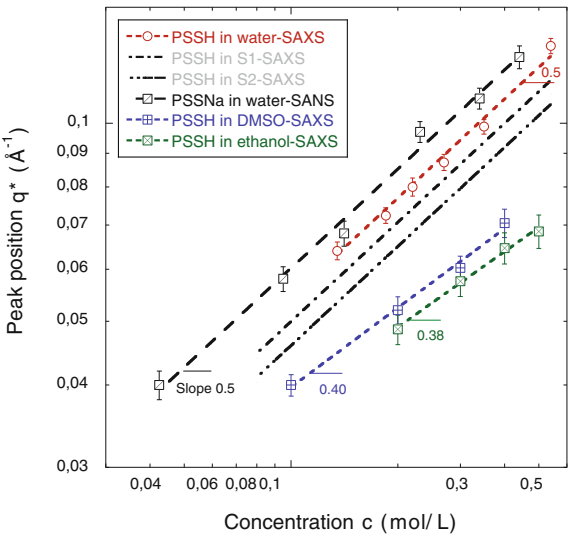

Fig. 7.7 Comparison of the q^* versus c dependences for all the studied systems. Protonated solvents were used in all cases

7.4 Conclusions

The present work gives new insight about the influence of counterions and solvent natures on the average structure of polyelectrolytes in semidilute solutions.

It was shown, that PSS in acid form has a lower effective charge and therefore a less extended average conformation with respect to the salt form with Na^+ counterions. This should be due to much smaller size and higher charge density of the H^+ counterions, which promote a stronger interaction with PSS macroanions and a higher degree of counterion condensation. This acid form of PSS shows a $q^* \sim c^{1/2}$ scaling law, which is attributed to the hydrophilic character of the PSS macroions and an almost full invisibility of condensed protons in SAXS measurements and thus a negligible contribution to the SAXS total scattering function of the partial one associated with counterions, $S_{cc}(q)$. In the case of added monovalent LMWE, the latter have none effect depending on the nature of the LMW cations. Whatever the LMWE, EMIM-Tos, H-Tos or NaCl, the counterion condensation is the same. The special position of $EMIM^+$ with respect to inorganic cations is due to its ability to display different types of interaction with the PSS units (H-bonding, dipole-dipole, aromatic π-π and aliphatic van der Waals interactions) and to its partially hydrophobic character. Detailed comparison of the influence of EMIM-Tos and H-Tos on polyelectrolyte average conformation showed that, at all c_{LMWE} investigated, there is no drastic change. So, the specific nature of the monovalent cations and their interactions with macroion units and the solvent don't really play a role.

Concerning the solvent nature, we have shown that using organic solvents DMSO and ethanol instead of water we observe solvophobic effects in PSS behavior, or structure, in the solutions. The n-values in the $q^* \sim c^n$ dependences were $n < ½$ for both DMSO and ethanol, and the q^*-values were much lower than

in the aqueous solutions. The changes in the q^*-values don't follow universal electrostatic relations, as PSS behaves in different manner in organic and aqueous solutions.

Acknowledgements We thank J. -P. Lamps from the Institut Charles Sadron for his help in PSS synthesis and purification. We are also grateful to A. Rameau for the PSS characterization by SEC and to J. Combet for fruitful discussions.

References

1. M. Hara (ed.), *Polyelectrolytes: Science and Technology* (Marcel Dekker, New York, 1993)
2. K.S. Schmitz, *Macroions in Solution and Colloidal Suspensions* (VCH, New York, 1993)
3. S. Förster, M. Schmidt, Adv. Polym. Sci. **120**, 51 (1995)
4. J.-L. Barrat, J.-F. Joanny, Adv. Chem. Phys. **94**, 1 (1996)
5. S. Jousset, H. Bellissent, J.-C. Galin, Macromolecules **31**, 4520 (1998)
6. T. Radeva (ed.), *Physical Chemistry of Polyelectrolytes* (Marcel Dekker, New York, 2001)
7. C. Holm, P. Kekicheff, R. Podgornik (eds.) in *Electrostatic Effects in Soft Matter and Biophysics*, vol. 46. NATO Science Series II-Mathematics, Physics and Chemistry (Kluwer Academic Press, Dordrecht, 2001)
8. A.V. Dobrynin, M. Rubinstein, Prog. Polym. Sci. **30**, 1049 (2005)
9. G.A. Papoian, M. Rubinstein, Soft Matter **8**, 9265 (2012)
10. W. Kunz, J. Henle, B. Ninham, Curr. Opin. Colloid Interface Sci. **9**, 19 (2004)
11. W. Kunz, *Specific Ion Effects* (World Scientific Publishing Company, 2009)
12. N. Anik, M. Airiau, M.-P. Labeau, C.-T. Vuong, J. Reboul, P. Lacroix-Desmazes, C. Gérardin, H. Cottet, Macromolecules **42**, 2767 (2009)
13. W. Essafi, F. Lafuma, C. Williams, Eur. Phys. J. B **9**, 261 (1999)
14. J.-P. Cotton, M. Moan,. J. Phys. Lett. **37**, L-75 (1976)
15. P.-G. de Gennes, P. Pincus, R.M. Velasco, F. Brochard, J. Phys. (France) **37**, 1461 (1976)
16. M. Nierlich, C.E. Williams, F. Boué, J.-P. Cotton, M. Daoud, B. Famoux, G. Jannink, C. Picot, M. Moan, C. Wolff, M. Rinaudo, P.-G. de Gennes, J. Phys. (France) **40**, 701 (1979)
17. K. Kaji, H. Urakawa, T. Kanaya, R.J. Kitamaru, J. Phys. (France) **49**, 993 (1988)
18. M. Olvera de la Cruz, L. Belloni, M. Delsanti, J.-P. Dalbiez, O. Spalla, M. Drifford, J. Chem. Phys. **103**, 5781 (1995)
19. K. Yoshikawa, M. Takahashi, V.V. Vasilevskaya, A.R. Khokhlov, Phys. Rev. Lett. **76**, 3029 (1996)
20. K. Nishida, K. Kaji, T. Kanaya, T. Shibano, Macromolecules **35**, 4084 (2002)
21. I. Sabbagh, Thesis, Université, Paris VII (1997); I. Sabbagh, M. Delsanti, P. Lesieur, Eur. Phys. J. B **12**, 253 (1999); I. Sabbagh, M. Delsanti, Eur. Phys. J. E **1**, 75 (2000)
22. G. S. Manning, J. Chem. Phys. **51**, 924, 934 (1969); Annu. Rev. Phys. Chem. **23**, 117 (1972); Ber. Bunsen-Ges. Phys. Chem. **100**, 909 (1996)
23. F. Oosawa, Biopolymers **6**, 134 (1968)
24. M. Muthukumar, J. Chem. Phys. **120**, 9343 (2004)
25. F. Hofmeister, Arch. Exp. Pathol. Pharmakol. **24**, 247 (1888)
26. J.N. Israelachvili, *Intermolecular and Surface Forces*, 3rd edn. (Elsevier Inc, 2011)
27. A. Alexander-Katz, L. Leibler, Soft Matter **5**, 2198 (2009)
28. T.A. Waigh, R. Ober, C.E. Williams, J.-C. Galin, Macromolecules **34**, 1973 (2001)
29. P. Aldebert, G. Gebel, B. Loppinet, N. Nakamura, Polymer **36**, 431 (1995)
30. W. Essafi, M.-N. Spiteri, C. E. Williams, F. Boue, Macromolecules **42**, 9568 (2009)
31. H.S. Makowski, R.D. Lundberg, G.S. Singhal, US Patent 3870841 to Exxon Research and Engineering Company, 1975

32. W. Essafi, F. Lafuma, C.E. Williams, Macroion characterization from dilute solutions to complex fluids, in *ACS Symposium Series*, vol. 548, ed. by K.S. Schmitz, Chapt. 21, 1994
33. M. Heinrich, Thesis, Université Louis Pasteur de Strasbourg, 1998
34. D. Baigl, T. Seery, C.E. Williams, Macromolecules **36**, 6878 (2003)
35. D.C. Boris, R.H. Colby, Macromolecules **31**, 5746 (1998)
36. A.V. Dobrynin, R.H. Colby, M. Rubinstein, Macromolecules **28**, 1859 (1995)
37. Y. Zhang, J.F. Douglas, E.J. Ermi, E.J. Amis, J. Chem. Phys. **114**, 3299 (2001)
38. J. Combet, F. Isel, M. Rawiso, F. Boué, Macromolecules **38**, 7456 (2005)
39. W. Essafi, F. Lafuma, C.E. Williams, J. Phys. II **5**, 1269 (1995)
40. W. Essafi, Thesis, Université Paris VI, 1996

Part III
Magnetic Liquid Systems

Chapter 8
Magnetic Fluids and Their Complex Systems

Peter Kopcansky, Milan Timko, Martina Koneracka, Vlasta Zavisova, Martina Kubovcikova, Matus Molcan, Lucia Balejcikova, Natalia Tomasovicova, Michal Rajnak and Veronika Gdovinova

Abstract The presented chapter provides an overview of selected magnetic nanoparticle systems (magnetic fluids, magnetosomes, magnetoferritin and liquid crystals doped with magnetic particles) as the unique materials with potential utilization in the field of biological and biomedical applications as well as in the field of technology. The main idea for magnetic nanoparticles incorporating is the improvement of material properties and to achieve better conditions for a wide range of scientific disciplines such as magnetic hyperthermia, drug delivery, magneto-optics, power engineering and others.

P. Kopcansky (✉) · M. Timko · M. Koneracka · V. Zavisova · M. Kubovcikova
M. Molcan · L. Balejcikova · N. Tomasovicova · M. Rajnak · V. Gdovinova
Institute of Experimental Physics SAS, Watsonova 47, 040 01 Košice, Slovakia
e-mail: kopcan@saske.sk

M. Timko
e-mail: timko@saske.sk

M. Koneracka
e-mail: konerack@saske.sk

V. Zavisova
e-mail: zavisova@saske.sk

M. Kubovcikova
e-mail: kubovcikova@saske.sk

M. Molcan
e-mail: molcan@saske.sk

L. Balejcikova
e-mail: balejcikova@saske.sk

N. Tomasovicova
e-mail: nhudak@saske.sk

M. Rajnak
e-mail: rajnak@saske.sk; michal.rajnak@tuke.sk

V. Gdovinova
e-mail: gdovinova@saske.sk

L. A. Bulavin and A. V. Chalyi (eds.), *Modern Problems of Molecular Physics*,
Springer Proceedings in Physics 197, https://doi.org/10.1007/978-3-319-61109-9_8

8.1 Introduction

Although magnetic nanoparticles (MNPs) have been studied for a few decades, they are still the object of an unceasing scientific interest. Their unique size and other physicochemical properties offer new opportunities and innovation possibilities in the design in a wide range of systems with improved specific properties. Amongst the magnetic nanoparticles used in a variety of applications, iron oxides particles—magnetite and maghemite are the most common [1]. These MNPs can act as precursors for synthesis of magnetic fluids (MFs) or can be used in other magnetic complex systems. The applications of various magnetic CSs in medicine and technology are today not just at the stage of visions. Nowadays, they are known the first real in vivo medical experiments and technical applications. Dr. A. Jordan has shown improvements in survival times of patients by using aminosilane-coated magnetite nanoparticles in drug delivery with subsequent hyperthermic treatment [2]. Among technological applications, dynamic sealing, heat dissipation, damping and many others can be mentioned [3]. In this chapter, different MNPs systems studies in the context of their biomedical and technical application are presented.

8.2 Magnetic Particle Systems for Bio-applications

8.2.1 MFs—Preparation, Functionalization, Characterization and Nanoencapsulation

8.2.1.1 Preparation of MFs

A big effort is addressed to develop MNPs for biotechnologies and medicine, especially for targeted drug delivery. For this purpose, the minimum toxicity, bio-compatibility and stability of MNPs in biological fluids is critical. In this section we shall look at magnetite nanoparticles (MNPs) that were precipitated from water solution of ferric and ferrous salts using ammonium hydroxide, washed by magnetic decantation, and then sodium oleate (SO) was applied as a surfactant in order to prevent MNPs agglomeration. The routine physicochemical characterization of the prepared MFs was carried out by the standard methods, such as magnetic measurements, scanning electron microscopy (SEM), dynamic light scattering (DLS) and infrared spectroscopy (FTIR). The FTIR spectra showed chemical bond linking SO molecules to MNPs. Superparamagnetic behavior of MNPs was proved

M. Rajnak
Faculty of Electrical Engineering and Informatics, Technical University of Košice, Letná 9, 04200 Košice, Slovakia

by magnetic measurements. Knowing the particle size is considered to be one of the basic preconditions if it is to be used effectively in biomedicine, which made us focus on study of particle-size distribution of MNPs. Four different methods were used to specify the value of size and size distribution of the MNPs: SEM, DLS, Differential Centrifugal Sedimentation (DCS) and magnetic measurements. SEM analysis revealed approximately spherical MNPs with a mean diameter of 67 nm and with a relatively narrow size distribution. DLS analysis confirmed monodispersed MFs with hydrodynamic diameter of 75 nm. The size distribution determined by DCS using sedimentation velocity analysis resulted in a mean diameter of 69 nm. The magnetic core diameter calculated from magnetization curve was 10.4 nm [4]. The surface and porous properties of magnetite, as an additional method for the particle size determination, were studied by the method of physical adsorption of nitrogen performed by NOVA 1200 apparatus (Quantachrome, USA) at 77 K. Before the measurement, the sample was activated in vacuum at 150 °C during the 21 h. The experimental data were processed by the BET (Brunauer, Emmett, Teller) isotherm in the range of relative pressure 0.05–0.2 p/p_0 to obtain the value of specific surface area. The total pore volume V_a value was evaluated from the maximum adsorption at relative pressure close to the saturation pressure. The pore size distribution was calculated using the BJH (Barret, Joyner, Hallenda) method from the desorption isotherm.

The measured adsorption/desorption isotherm is presented in Fig. 8.1a. The hysteresis loop between the adsorption and desorption branch is analogous to type H1, according to the IUPAC report [5], typical for materials showing a tendency towards agglomerate formation. In general, the hysteresis loop is associated with the presence of mesopores (pores with diameter in the range 2–50 nm) in the studied structure.

Considering the synthetic magnetite is non-porous material, the obtained loop related with the gas adsorption into the interparticle space in agglomerates. For the case of spherical, non-porous magnetic particles, the BET surface area is related to the $D_{BET} = 6000/\rho \cdot S_{BET}$, in which S_{BET} is specific surface area in m^2/g and ρ is a theoretical density in g/cm^3 [6]. Good correlation between the mean particle size from the BET surface area measurement and the average particle size from the

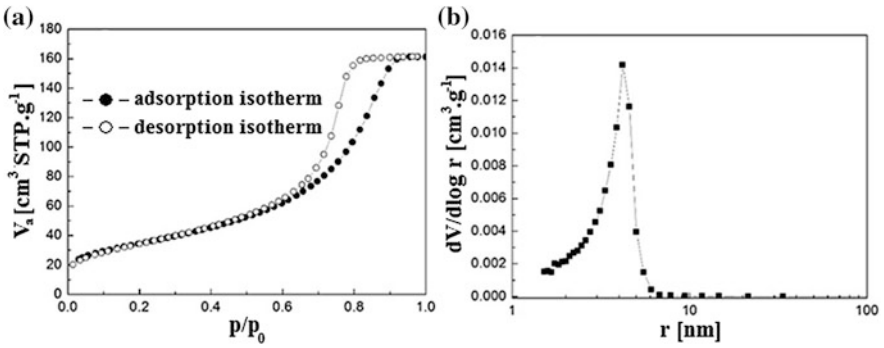

Fig. 8.1 **a** The adsorption and desorption isotherm of synthetic magnetite. **b** The pore size distribution curve of synthetic magnetite

Table 8.1 Physico-chemical parameters of SO coated magnetic particles

D_{HYDR} (nm)			PDI	D_{MAG}	S_{BET}	D_{BET}	I_S	$C(Fe_3O_4)$	IEP	ξ
DLS	DCS	SEM	–	(nm)	(m^2/g)	(nm)	(emu/g)	(mg/mL)	–	(mV)
75.6	69.4	67	0.135	10.4	124.7	11	28.1	35	3.21	−42

magnetic measurements was found. Furthermore, the pore size distribution curve of the magnetite is quite narrow showing the Gaussian character, Fig. 8.1b, pointed at the presence of pores with diameter in the range from 2 to 10 nm. This fact is in agreement with the results obtained from the adsorption and desorption isotherms analyzing. The calculated average pore diameter was 8.2 nm, what also indirectly corresponded with the average particle size obtained from magnetic measurement. The agglomerated particles of 10 nm in average could create the mesopore structure with such distribution. All obtained results are summarized in Table 8.1.

The number of characterization techniques was being successfully used to determine the particle size of pure magnetite as well as SO coated magnetite. The obtained results are in good consistency and indicate that the prepared MF fulfils the conditions for an applicable drug delivery system and can create the bases for the biocompatible magnetic fluid preparation.

8.2.1.2 Functionalized Magnetic Nanoparticles

Magnetic carriers suitable for clinical applications need to be biocompatible, meaning that they should not be toxic to the patient. However, after nanoparticles' injection into the bloodstream, they are rapidly coated by plasma proteins. The occurring process called opsonization is decisive for response of the body's defence system, the reticuloendothelial system (RES). As a result, for the in vivo application of nanoparticles a surface modification is to consider as to ensure the formation of non-toxic, biocompatible nanoparticles stable to the RES. Amongst the accessible biocompatible materials, three that we shall discuss here are polyethylene glycol (PEG), bovine serum albumin (BSA) and poly-L-lysine (PLL).

PEG is a hydrophilic polymer, able to restrain protein adsorption and, hence, delay or suppress the opsonization process, thus permitting a longer circulation time [7]. Polyethylene glycol with the average molecular weights of 400, 1000, 6000 and 20 000 g/mol (referred to as PEG400, PEG1000, PEG6000 and PEG20000) was selected to enhance the biocompatibility of the synthesized magnetic fluids. The modified samples were characterized by SEM and DLS to confirm the spherical shape and the size of nanoparticles. The hydrodynamic diameter was increased after PEG-modification of the samples. Moreover, the optimal weight ratio PEG/Fe_3O_4 needed for surface modification of magnetite nanoparticles (MNPs) was found out by differential scanning calorimetry (DSC), and zeta potential measurements. The weight ratio, at which maximum of PEG was adsorbed on magnetite nanoparticles,

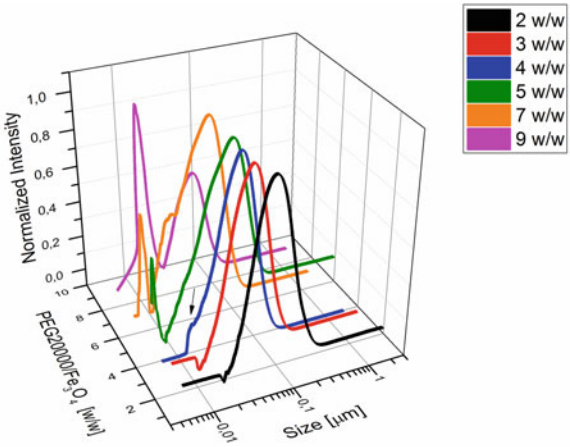

Fig. 8.2 Particle size distributions of MFPEG20000 with different PEG amount measured by DCS

was determined to be about 4.4 for the MFPEG1000 system, 2.8 for MFPEG6000 and 3.4 for MFPEG20000.

The results agree well with DCS measurements outcomes (see Fig. 8.2) [8, 9]. The existence of peak at weight ratio PEG/Fe_3O_4 = 4 can be related to presence of free PEG molecules. The next our aim was to study the biocompatibility of unmodified and PEG-modified magnetic particles through the fluorescence intensity measurements after protein adsorption. The nonspecific protein adsorption test exhibited that the longer polymer chain had higher effect in avoiding protein adsorption. This feature of the PEG-modified magnetic nanoparticles will be a benefit for the further in vivo studies [10]. In paper [11], in vitro cytotoxicity of MFPEG1000 with M_w(PEG) = 1000 g/mol) was investigated. The impact of MFPEG1000 on B16 mouse melanoma cells growth during 3-day exposition time was evaluated at three concentrations of Fe_3O_4 in MFPEG1000: 106, 4.2 and 2.1 mg/ml—and compared with the control B16 cells. After 24 h of treatment at lower concentrations small inhibition was observed, but 48 h later the lower concentrations have not affected the cell growth. The reduced inhibition after 48 h at the conc. 106 mg/ml was temporary, after 72 h at conc. 106 mg/ml of Fe_3O_4 in MFPEG growth inhibition of ca. 50% was reached.

Preparation and characterization of magnetic fluids with embodied bovine serum albumin (MFBSA) as potential treatment for amyloid related diseases is reported in [12]. BSA was suggested because it is the most common serum protein. Serum albumin has a significant function in the transport of a large number of organic molecules and drugs, which may be delivered to the appropriate cellular targets. Prepared nanoparticles could be potential drugs for controlling or curing of various diseases if requirements of biocompatibility, biodegradability and safety issues are fulfilled. In the mentioned work we have prepared 18 MFBSA samples with defined w/w BSA/Fe_3O_4 ratios ranging from 0.005 to 15.0 with a constant magnetite amount (30 mg/ml). Characterizations of all prepared samples were carried out using routine techniques such as TEM, SQUID magnetometer and DLS.

Fourier-transform infrared spectroscopy (FTIR) and DSC were used to ascertain the adsorption of BSA on magnetic particles with the stabilizing surfactant. As a wide range of diseases, including Alzheimer's and Parkinson's diseases, diabetes type II, and others are attributed to the existence of amyloid aggregates in different parts of the body, in paper [13] the interference of insulin amyloid fibrils with albumin modified magnetic fluids (MFBSAs) was studied. The destroying ability of MFBSAs to amyloid fibrils in vitro was proved. It was observed that the depolymerizating action of MFBSAs was affected by nanoparticle properties (hydrodynamic diameter, zeta potential and isoelectric point) influenced by the BSA content in MFBSAs. As the most active MFBSAs with lower BSA/Fe_3O_4 ratios (from 0.005 to 0.1) were identified with about 90% depolymerizing effectiveness. We assume that these outcomes could be a starting point for the future application of the active MFBSAs as therapeutic agents targeting insulin amyloidosis.

Cancer is a leading cause of death in many countries, accounting for 8.2 million deaths in 2012. In our work [14] we were concentrated on detection and targeting of tumor cells using an antibody coupled to MNPs. For this purpose we have prepared poly-L-lysine modified magnetic nanoparticles (MFPLL) for their further use as substrates for binding specific antibodies that are able to detect cancer cells. Biocompatible poly-L-lysine (PLL) is a positively charged amino acid *polymer*, which is in fact a synthetic polymer with wide use in pharmaceutical industry and, its sub-products, monomeric amino acid lysine units are characterized by no toxicity, no antigenity, good biocompatibility and biodegradability. Several MFPLL samples with different PLL/Fe_3O_4 weight ratio were prepared and tested to find out the optimal PLL/Fe_3O_4 weight ratio. The optimal value PLL/Fe_3O_4 (weight ratio) of 1.0, based on both zeta potential and DLS measurements, was in agreement with the outcome of UV/VIS measurements. Besides morphology and particle size characterization, the samples were studied in term of magnetic properties by MPMS magnetometer. In addition, AC susceptibility measurements as a complementary technique for particle size determination were used. From the relaxation peak of the imaginary component of the complex susceptibility hydrodynamic size of the nanoparticles could be derived and calculated. The relaxation time for Brownian rotation is given by $\tau_B = 3\eta V/(k_B T)$, where η is the carrier medium viscosity, k_B is the Boltzmann constant, T is the temperature and V is the hydrodynamic particle volume, which is typically larger than the magnetic volume Vm considering the adhesion of surfactant and carrier liquid molecules. For that purpose, AC susceptibility versus frequency dependences at different temperature were measured (Fig. 8.3).

The maximum of χ occurs at frequency f leading to relaxation time $\tau_B = 1/(2\pi f)$ (Fig. 8.4b). Using equation for Brownian relaxation time, corresponding hydrodynamic diameters were calculated. The acquired values are summarized in Table 8.2.

An additional measurement using DynoMag (Imego AB, Sweden) was carried out, where the frequency dependence of complex susceptibility at ambient temperature was measured in the extent from 1 Hz to 250 kHz. A peak at 493.7 Hz was observed which gives the hydrodynamic diameter value of 101 nm (Fig. 8.4).

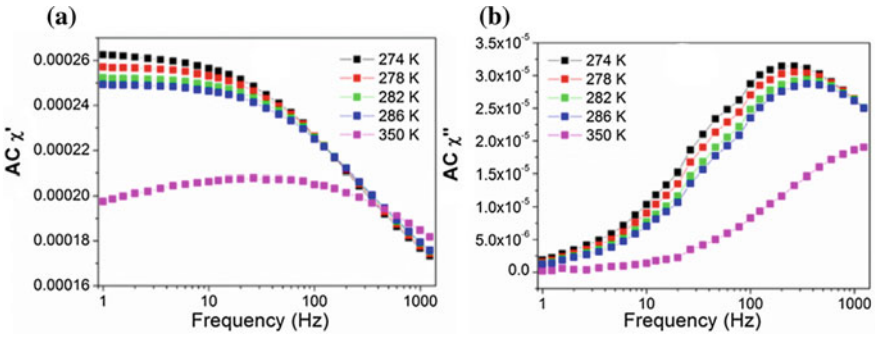

Fig. 8.3 AC susceptibility dependence on frequency of the sample MFPLL3 measured at different temperature

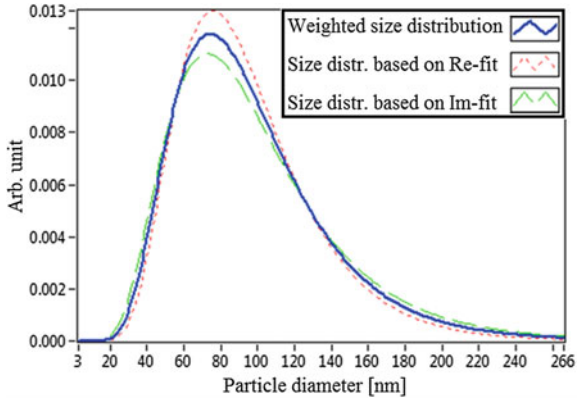

Fig. 8.4 Particle size distribution of amino modified MFPLL5

Table 8.2 Hydrodynamic diameter of MFPLL NPs calculated from AC susceptibility relaxation peak

Frequency (Hz)	Temperature (K)	D_{HYDR} (nm)
235	274	98.3
284	278	96.6
340	282	95.0
350	286	97.9
1250	350	102.7

Due to confirm amino binding on the magnetic nanoparticle surface, TGA a DSC analysis was carried out by NETZSCH STA F1 *Jupiter* thermal analyzer to study the thermal properties of the samples. The thermal measurements were performed simultaneously in both the differential scanning calorimetric (DSC) mode and the thermogravimetric (TG) mode. The measurements were performed in air with a dynamic heating rate 10 °C/min from 35 °C up to 560 °C. Aluminum crucibles were used during measurements and correction baselines were applied for

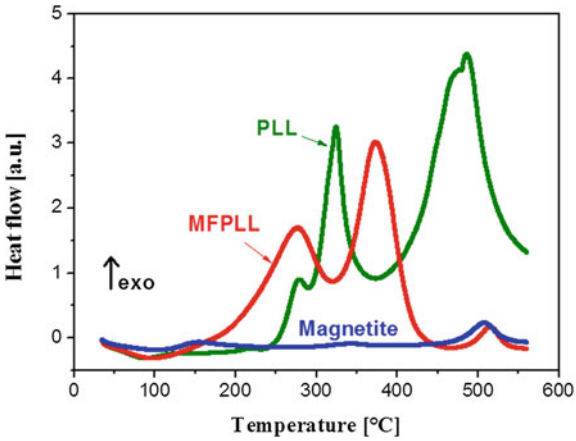

Fig. 8.5 DCS of naked magnetic nanoparticles, pure PLL and amino modified magnetic nanoparticles

correct measurements. Before measurements the samples were pressed into the pellets for better contact with the crucibles.

DSC curves of naked magnetite, pure PLL and amino modified magnetic nanoparticles are shown in Fig. 8.5. Magnetite (Fe_3O_4) being heated in air oxidizes to maghemite (γ-Fe_2O_3) and transforms to hematite (α-Fe_2O_3) showed exothermic peaks with maxima at 150 and 507 °C [15]. Most of PLL decomposition occurs at 260–590 °C. The first two exothermic peaks occurred at about 278 and 324 °C are related to decarboxylation and deamination processes [16], and double peak at ca. 486 °C belongs to decomposition of polymer backbone chain. In the DCS curve of magnetic particles coated by PLL it can be seen that decomposition temperature ranges are broadened and shifted compared to pure PLL that could be explained by presence of amino shell on nanoparticles surfaces [15]. Maghemite transformation to hematite is indicated by very similar peak to naked iron oxide peak with maxima about 514 °C. As the shell thickens, the transformation takes place in a relatively higher temperature range. Shift of PLL coated nanoparticles peak compared to naked nanoparticles indicate influence of PLL binding on the nanoparticles surface.

8.2.1.3 Nanoencapsulation

Polymeric nanoparticles have been investigated as drug delivery systems in the fields of pharmaceutics and medicine due to the compatibility with tissues and cells, subcellular size and other beneficial properties. During the last two decades several methods to synthesize polymeric nanoparticles have been developed and classified according to the mechanism of nanoparticles' formation.

The utilization of biodegradable and biocompatible poly(D,L-lactide) (PLA) and poly(D,L-lactic-*co*-glycolic acid) (PLGA) polymers as a capsulation material for drugs is described below. PLA and PLGA are extensively used in the biomedical industry and their monomeric units are normally found in the human organism [17, 18].

As drugs, anticancer drug taxol and antihypertensive drug aliskiren were chosen for encapsulation. The taxol (TAX) was chosen due to its therapeutic effects against various cancers (e.g. ovarian, breast, lung cancer) [19]. Hypertension (high blood pressure) became a global public health issue consequently leading to various complications. Aliskiren (ALIS) is a renin inhibitor used to treat hypertension by blood pressure lowering. However, the therapy efficacy is limited by the rather low bioavailability of ALIS [20]. One of the alternatives leading to increased ALIS bioavailability, decreased degradation and consequently to enhanced effect of ALIS on kidney activity is its nanoencapsulation. Spherical shaped magnetic nanospheres with encapsulated drugs (Fig. 8.6a) prepared by a modified nanoprecipitation technique were fully characterized [21].

Biodistribution of taxol loaded magnetic polymer nanospheres was investigated in the plasma, selected organs (liver, lung, spleen, kidney, heart) and the target tissue (placed in magnet pole during the treatment) [22]. The organ of the highest TAX content after intravenous administration was the liver. The following organs of high affinity were the spleen and the kidney (Fig. 8.6b). Several compositions of NPs with different magnetite/drug ratio for tumor treatment efficiency were tested. More effective seemed administering the composition with higher magnetite/drug weight ratio than in the sample with the smaller ratio this can be attributed to the fact that the samples with higher magnetite content were trapped more effectively in the target site (tumor) by the applied field. The tumor was damaged in both cases.

The effect of ALIS encapsulated into PLA nanospheres on systolic blood pressure male spontaneously hypertensive rats (SHR) aged 12 weeks was described in paper [23]. Blood pressure was measured on the tail artery by plethysmography technique. At the end of experiment (after 3 weeks), systolic blood pressure in non-encapsulated ALIS group was remarkably lower (178.7 ± 1.8 mmHg) than in the controls (203.4 ± 4 mmHg). Encapsulated ALIS, however, decreased blood

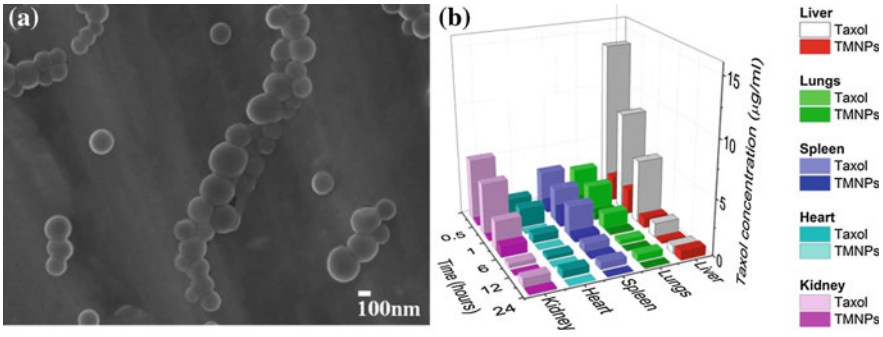

Fig. 8.6 **a** SEM image of taxol loaded magnetic nanospheres, **b** Time dependent distribution and comparison of TAX and TMNPs (TAX:PLGA:Fe_3O_4 10:100:50) in organs (content per one gram) after iv administration and use of an external magnetic field for 30 min

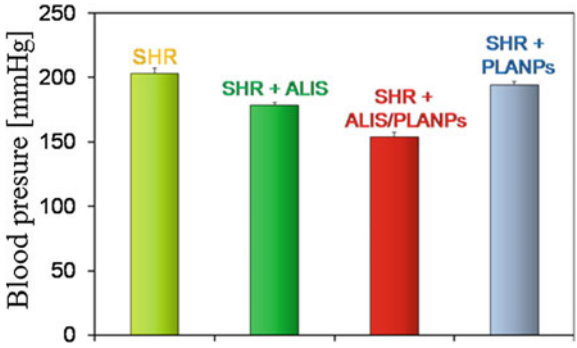

Fig. 8.7 Blood pressure of spontaneously hypertensive rats (SHR) after 3 weeks of ALIS therapy

pressure even more significantly and from the first week of the treatment (160 ± 5 mmHg vs. 203.4 ± 4 mmHg in the control rats) (see Fig. 8.7).

8.2.2 Magnetoferritin

8.2.2.1 The Overview and Physico-chemical Characterization of Magnetoferritin

In 1991, a novel synthetic route based on the formation of inorganic phases in a protein structure as a reaction cage was described. It was shown that the empty cavity of the iron-storage protein, ferritin, entitled apoferritin, could be used as a reaction medium for in vitro chemical synthesis of iron sulphide particles, manganese and uranium oxo-species of the controlled nanosize [24].

Apoferritin is a globular, water soluble protein, composed of 24 subunits that are assembled into a hollow structure with an external diameter of 10–12 nm and internal of 8–10 nm [25]. On the apoferritin surface, protein channels with a diameter of ~0.4 nm for binding and release of iron ions (8 × 3 fold hydrophilic, polar), and for electron transfer (6 × 4 multiple hydrophobic, non-polar) are placed [25]. The molecular weight of apoferritin is ~481 200 kDa and this value depends on the type of organism and tissue, from which apoferritin was isolated. Physiological apoferritin has ability to store inside the cavity up to 4500 iron atoms arranged in a crystal grid according to the specific needs of the organism, forming the ferritin biomacromolecule [26]. This flexible and dynamic structure [27], stable at temperatures up to 80 °C [28], is capable by natural autocatalytic activity [29] not only to control the flow of iron ions, but also other metals (e.g. Co^{2+}, Mn^{2+}, Fe^{2+}), molecules, and small chelate ligands, to form ferritin derivatives, such as Magnetoferritin [30–32].

The first synthesis of magnetoferritin was described by Meldrum and co-workers in 1992. Transmission electron microscopy and electron diffraction analysis indicated the presence of 6-nm spherical single crystals of the ferrimagnetic iron oxide,

magnetite (Fe_3O_4), surrounded by apoferritin shell [33]. Figure 8.8 shows the model of magnetoferritin structure. Two years later, J. W. M. Bulte et al. studied magnetic properties of magnetoferritin using SQUID magnetometer. Iron oxide nanoparticles in the inorganic core have shown superparamagnetic behavior without precise chemical characterization of the core composition [34]. Magnetite and its oxidation product, maghemite, are ferrimagnetic iron oxides [35] with similar values of saturation magnetization at room temperature: M_S (Fe_3O_4) = 90 A m^2 kg^{-1} and M_S (γ-Fe_2O_3) = 83.5 A m^2 kg^{-1}, therefore it is not possible to distinguish them directly by any magnetometric method [36]. The main difference between magnetite and maghemite is related with a characteristic first order phase transition known as Verwey transition at $T_v \sim 120$ K. Below this temperature a change in the crystal symmetry of magnetite and a decrease in electrical conductivity are observed. Verwey transition can be investigated by various methods, such as electron, neutron or photon diffraction, to determine the periodic arrangement of the magnetite crystal or to determine different isotopes of iron using e.g. nuclear magnetic resonance or Mössbauer spectroscopy [37]. For these reasons in the next work the presence of magnetite and higher amount of maghemite in magnetoferritin were detected using Mössbauer spectroscopy in the applied magnetic field with intensity of 9 T and temperature 4.2 K [38, 39]. In the study of Wong et al. magnetoferritin was synthetized by a chemical procedure using a regulated volume of oxidant, trimethylamine N-oxide, in deaerated solutions, at temperature 65 °C and pH 8.6. The modified chemical process enabled to synthesize magnetoferritin with various amount of iron atoms per one apoferritin biomacromolecule (loading factor, LF). Clusters of magnetoferritin with LF > 1000 and increasing of magnetic nanoparticles diameter with LF were observed using transmission electron microscopy. Superparamagnetic behavior of magnetoferritin was confirmed using SQUID magnetometer [40]. The temperature effect of dipolar interaction of agglomerated and well-separated magnetoferritin was investigated and the results well agreed with theoretical models [41]. In 2008 Kasyutich et al. prepared purified 3D ordered crystals of magnetoferritin with micro-sized scale about 10–100 μm using crystallization technology of proteins. 3D arrays of magnetic nanoparticles were characterized using magnetic and Raman spectroscopy [42, 43]. Detailed investigation of magnetoferritin nanoparticles with size ranging from 1.6 to 6 nm in colloidal solution using atomic force microscopy, transmission electron microscopy, X-ray diffraction, by Martínez-Pérez et al. have shown that the outer size of magnetoferritin decreased probably associated with conformational changes affected by iron oxides core formation. The magnetic response of the maghemite cores has been investigated by a combination of AC susceptibility, DC magnetization and Mössbauer spectroscopy [44].

8.2.2.2 Magneto-optical Study of Magnetoferritin

The magneto-optical investigation of superparamagnetic nanoparticles in MFer would allow distinguishing various iron oxides (maghemite γ-Fe_2O_3, magnetite

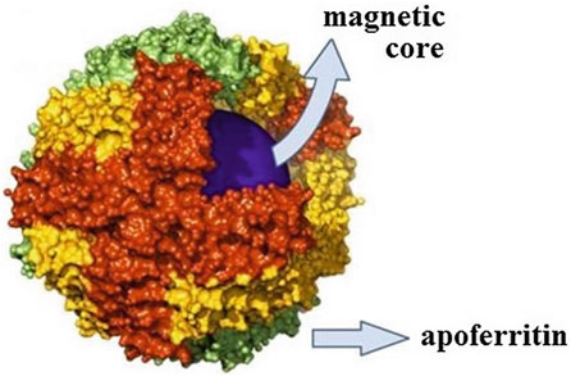

Fig. 8.8 The model of magnetoferritin structure. Reprinted by permission from Macmillan Publishers Ltd: [Nature Nanotechnology] (*M. A. Kostiainen,* et al. *Nat. Nanotechnol. 8, pp. 52–56.*), copyright (2013)

Fe_3O_4). Sensitive and non-invasive Cotton-Mouton and Faraday effects were chosen for MFer colloidal solution investigation without special chemical modification of MFer [45].

Magneto-optical Cotton-Mouton effect is related with optical anisotropy of superparamagnetic nanoparticles and with the orientation of their magnetic moments in an applied magnetic field. After transition of electromagnetic radiation through the sample, the rotation of the plane of light polarization will change the angle θ that is proportional to the birefringence Δn according to the equation:

$$\theta = \frac{\pi d}{\lambda} \Delta n \tag{8.1}$$

where d is the light pathway and λ is the wavelength of the used light. The magnetically induced optical linear birefringence, Δn, is defined as the difference of indices light quarries in a direction parallel and perpendicular to the direction of the vector of the magnetic field intensity: $\Delta n = n_{\parallel} - n_{\perp}$ [46].

Magnetically induced optical linear birefringence Δn was measured for colloidal dispersion of MFer and compared with Δn of commercial ferritin at λ 632,8 nm. Dependence of reduced (specific) magnetically induced linear birefringence (i.e. Δn, reduced by known iron concentration $\Delta n/c^{Fe}$) on the square of applied magnetic field intensity H^2 for diluted studied samples are shown in the Fig. 8.9 [47, 48]. Measurements have indicated visible differences in magneto-optical behavior of aqueous dispersion of MFer in comparison with ferritin. Obtained Cotton-Mouton constant K^{CM}, characteristic for given material, was calculated from experimental data at low region of magnetic field below 200 Oe. The K^{CM} value for MFer was about 4 orders of magnitude higher than for ferritin that was related to the presence of various kind of iron core inside both biomacromolecules. An important finding of this study was direct observation of the saturation measurements of $\Delta n/c^{Fe}$, which allows identification of magnetic core of the unknown sample of ferritin and its biogenic or synthetic derivatives [47, 48].

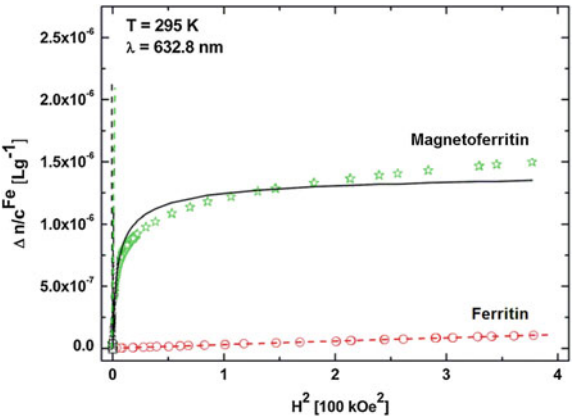

Fig. 8.9 The graph of the $\Delta n/c^{Fe}$ dependence on H^2. Reprinted from [48], Copyright (2011), with permission from Elsevier

This magneto-optical effect and calculated K^{CM} constants could be used in the future biomedical applications to identify and clarify the heterogeneous structure of the pathological brain ferritin, which contains also magnetite in patients with neurodegenerative diseases [48].

The orientation of magnetic moments of superparamagnetic nanoparticles in an applied magnetic field is the reason for the next magneto-optical effect, Faraday's effect. The rotation of the plane of light polarization will change the angle θ_F (Faraday rotation angle) whose size depends on the intensity of the external magnetic field, the light pathway, and used light wavelength, λ [49]. The main difference between Cotton-Mouton and Faraday effects consists in the direction of the vector of a linearly polarized light beam that passes through the sample against the vector of applied magnetic field intensity (Cotton-Mouton effect—perpendicular and Faradays effect—parallel direction) [50].

The dependence of the Faraday rotation on magnetic field has shown superparamagnetic behavior of magnetoferritin, described by Langevin function with log-normal distribution of nanoparticles sizes allowing to obtain the diameter of the cores. The Verdet constant calculated by approximation of experimental data at defined wavelength could be suitable parameter to distinguish various iron cores in unknown samples. The dependence of the Verdet constant on the light wavelength could be after standardization in generally used for the quantitative determination of the iron oxidation state in various nanoparticles with a specific size. The spectral functions of the Faraday rotation on the wavelength enabled to distinguish native ferritin and magnetoferritin cores, which can be a useful method for the detection of magnetite or for the diagnosis of various diseases, that are associated with magnetite formation in vivo in pathological tissues of the body [51].

8.2.2.3 Small-Angle Scattering Study of Magnetoferritin

Next studies were focused mainly on the structural characterization of magnetoferritin by small-angle scattering of neutrons (SANS) and X-rays (SAXS) on inhomogeneities in solution. The main reason for using these methods is the good resolution of several nanoscale sized objects, possibility of structural modeling, to get information about the size, shape of the partially or completely disordered systems, intermolecular interactions, (un)folding, conformational changes in macromolecules and determination ab initio models. The basic difference between SAXS and SANS is that photons are scattered from electron shell and neutrons from atom nuclei. In the case of SANS method there is a big difference between the neutron scattering length for hydrogen and deuterium that can be used for the variation of contrast by substitution of the light and heavy water in solvent [52–54].

The first results using structural sensitive SANS method have shown significant difference between scattering curves of MFer and apoferritin. Superparamagnetic cores in MFer with size distribution of about 5 nm affect the protein shell structure. The hydrodynamic diameter obtained using dynamic light scattering (DLS) for MFer was larger than for apoferritin that indicates colloidal polydispersity [55, 56]. Therefore, further investigation was focused on the structural study of MFer, varying in LF. SAXS curves of MFer with low LF of 160 in comparison with pure apoferritin have looked differently. Constructed pair-distance distribution functions (PDD) curves, by applying of the Indirect Fourier Transformation (IFT), were used for the ab initio modeling, where it was observed partially destroying MFer structure most probably caused by iron binding or magnetic core presence (Fig. 8.10) [57].

Other SAXS curves and PDD analysis have shown increasing aggregation with the LF of MFer. Comparisons of radius of gyration obtained using the Guinier approximation from the SANS and SAXS data and hydrodynamic diameter obtained by DLS, have shown that the MFer size increases with increasing LF and a strong aggregation occurs at LF over 600 [57].

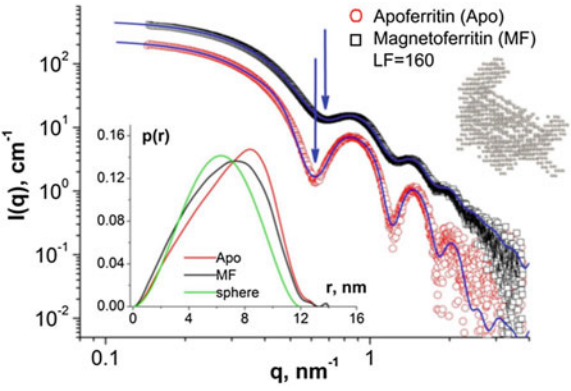

Fig. 8.10 Scattering curves, PDD and ab initio analysis of apoferritin and magnetoferritin. Reprinted from [57]. Copyright (2014), with permission from Elsevier

Further, MFer samples with different LF were studied using SANS contrast variation method, with varying of light and heavy components in solution. By fitting of linear Guinier plots from SANS data, the values radius of gyration and intensity were obtained subsequently.

The scattering lengths densities for various ratios of light and heavy water were calculated and obtained corresponding intensities were plotted versus the volume fraction of heavy water in the sample solutions. Minimum of the plotted parabola corresponded to the match point, in which the contrast is the lowest. This point was shifted with increasing LF. Nonzero intensity in the match point means structural polydispersity with increasing LF. In this study it was found that a high ratio between the amounts of magnetic component in the core and a protein could be explained by the partial destroying of the MFer shell [57, 58].

The recent study using SAXS was aimed the effect of MFer on the structure of lysozyme amyloid aggregates (LAA). It was shown that MFer affect the LAA structure that indicated destructed activity of MFer superparamagnetic nanoparticles. These results were supported by the fluorescence spectrophotometry measurements. MFer has ability to reduce the average size of lysozyme amyloid aggregates [59].

8.2.2.4 Potential Applications of Magnetoferritin

The first synthesis of magnetoferritin opened the door for its extensive studies. It was shown, that well-defined diameter of magnetoferritin nanoparticles, biological origin, superparamagnetic behavior and colloidal stability yield considerable potential of magnetoferritin for applications in various field of sciences, but especially in biomedicine and cell biology [33, 60]. The potential use of magnetoferritin in various bio-applications increase thanks to the ability of magnetoferritin to change its structural properties under defined physico-chemical conditions. The structure of magnetoferritin can be modified by different chemical substances [61], surfactants, signal molecules, drugs or antibodies [62, 63], consequent in protein shell change, so that the biomacromolecule can be fully folded, partially opened or completely disrupted.

Structural modifications of the internal or external MFer surface at defined physico-chemical conditions depending on the properties of specific substance or binding mechanism induce various potential applications of MFer, such as a standard for diagnosis of various diseases [47, 48, 51], in cell separation [63], magnetic resonance imaging of tissues [34, 64], as a contrast agent for cell labeling [65], in, nanocatalytical chemistry [66], or in targeted transport of anticancer drugs. The binding of drug and dyes to MFer structure could enable visualization of damaged tissues or targeted transport right to the pathological area of the organism with minimization of the drug secondary effects on healthy organs and tissues [67]. Recently it was shown, that MFer is able to resolve hydrogen peroxide to oxygen and water in the presence of the substrate, N,N-diethyl-p-phenylenediamine sulfate,

which after the reaction changed the color. Such peroxidase-like activity of magnetoferritin was more significant in the case of increasing loading factor [66].

8.2.3 Magnetosome Chains Magnetic Systems

Magnetosomes are intracellular organelles in magnetotactic bacteria (MTB) that allow them to sense and align themselves along a magnetic field. MTBs usually mineralize either iron oxide magnetosomes, which contain crystals of magnetite (Fe_3O_4), or iron sulfide magnetosomes, which contain crystals of greigite (Fe_3S_4). A crystal type depends on bacteria's form. Crystals are connected into chain-like structures via biological membrane (which consists of lipid bilayer membrane and specific soluble and transmembrane proteins) [68–73]. In magnetosome suspensions were observed magneto-optical birefringence and dichroism effects. It makes them appropriate materials for magneto-optic studies [74–76]. Anyway, the biocompatible character and magnetic properties of magnetosomes make them promising materials in bio-applications in medicine, especially in the field of magnetic hyperthermia [77–79].

8.2.3.1 Magnetosomes Preparation and Characterization Methods

Bacterial magnetosomes were produced by the biomineralization of MTB Magnetospirillum strain AMB-1. Bacteria synthesize magnetite—Fe_3O_4 nanoparticles. The detailed description of the cultivation process of the bacteria is given in our previous contribution [70].

The magnetosome isolation from the bacteria consists of a series of cycles of sonication, centrifugation and magnetic decantation. The importance of individual steps is as follows: sonication of culture media containing bacteria was performed because of disruption of the organic body of bacteria, which is connected with the release of magnetosome chains into the liquid medium. Centrifugation was performed for the purpose of deposition of the released magnetosome chains at the bottom of the plastic container as a result of centrifugal force. The specimen was taken out of the centrifuge and the decantation of unsettled nanoscopic magnetic parts of the sample at the bottom of the container was done. By decanting of the magnetic component of the sample (magnetosome chains) at the bottom of the container was allowed to pipet off an excess amount of non-magnetic fluid with remnants of the bodies of the bacteria. This process can also be described as a process of purification of the sample. The isolation parameters were as follows: (1) sonication (5 min), (2) centrifugation at 18,000 rpm for 30 min, (3) magnetic decantation on permanent magnets FeNdB (200 mT)—2 h. The non-magnetic part of the magnetosomes was pipetted away and the black residue (magnetosomes) in the centrifuge vial was diluted with HEPES—EDTA (first 2 cycles), followed by

washing with HEPES—NaCl (3rd cycle) and finally washing with 10 mM HEPES (10 times due to sample purification).

With a view to raise yield of the synthesis process our commonly used culture medium (NP) was modified by increasing of FQ and WVS quantity.

To achieve single magnetosomes the isolated magnetosome bounded in chains (M) were ultracentrifuged at 100 000 rpm for 4 h at 4 °C (UM) and ultracentrifuged at 100 000 rpm for 3 h and sonicated at power of 120 W for 3 h (SM), respectively.

The magnetosomes morphology and size were determined from scanning electron microscopy (SEM), transmission electron microscopy (TEM) and atomic force microscopy (AFM). More details about microscopy investigate are described in [80].

Magnetization characteristic of the prepared magnetosomes suspension were measured by SQUID magnetometer (Quantum Design) at room temperature.

The calorimetric properties of magnetosome suspensions within HEPES buffer were obtained by measuring of temperature increasing in the alternating magnetic field. Magnetic fields of various intensities at given frequency were generated with the help of solenoid with opened ferromagnetic core. The glass vial with the analyzed suspension was inserted into the gap of this ferromagnetic core. (Four different systems—the double-layer solenoid, Helmholtz coils, the inductor with C-shaped ferromagnetic core and the system of rotating magnetic field, generating of magnetic field are detailed described in our paper [81].) The amplitude determination of magnetic field strength was carried out by voltage measurement induced in the one turn placed in magnetic gap. Changes in temperature were recorded by thermometer with fiber optic sensor (FISO Technologies Inc. with accuracy ±0.1 K).

8.2.3.2 Selected Properties of Magnetosome Suspensions

Analysis of magnetosomes' suspension prepared by using different conditions during synthesis is described in papers [77, 82]. Typical electron micrographs of magnetosomes obtained by SEM technique for prepared samples NP, FQ and WVS are shown in Fig. 8.11. To compare the different preparation conditions the size distributions of magnetosomes (from 100 particles) according to SEM pictures was done.

The mean diameter of isolated magnetosomes with our commonly used culture medium (NP) was 47 nm. The mean diameter of the samples with modified culture medium was shifted to the higher values 52 nm and 58 nm for WVS and FQ, respectively.

The magnetization measurements at 293 K showed superparamagnetic behavior of NP magnetosomes suspension. Small increase in hysteresis (ferromagnetic behavior) was observed for sample WVS (H_C = 6.5 Oe) and FQ (H_C = 20 Oe). This can be caused by high shape anisotropy, resulting in non-zero coercivity of samples with higher mean diameter. The higher H_C value reveals stronger magnetic

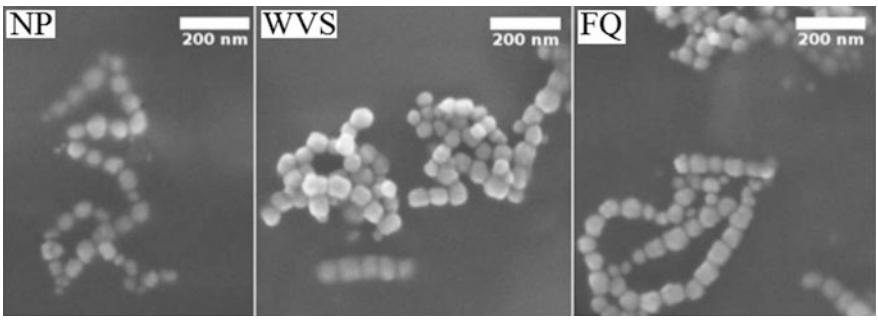

Fig. 8.11 Scanning electron micrograph of magnetosomes NP, WVS and FQ

correlations between particles of magnetite chains. The magnetization data are showed in Table 8.3. (The curves are presented in our work [82].)

Detailed analysis of sonicated and ultracentrifuged magnetosomes was done in our paper [83]. Figure 8.12 shows electron micrographs of three magnetosome samples: (I) standard magnetosomes sample, i.e. long-chain magnetosomes, (II) after centrifugation (100 000 rpm, 8 h), and (III) after centrifugation (100 000 rpm, 12 h) and sonication (120 W, 3 h).

Sample I illustrates typical magnetosomes morphology (long chains). As a result of centrifugation the magnetosomes' chains (sample II) were shorter in comparison with sample I. Individual, single magnetosomes are also present, but sporadic. Sample III showed reduced long chains number (see inset), but also small groups of a few magnetosomes and increased number of individual magnetosomes. This result demonstrates that the applied separation force was greatly enhanced after sonication.

The M–H hysteresis curves (Fig. 8.13) at room temperature indicate a ferromagnetic character of all samples with the same saturation magnetization $M_S = 2.1$ emu g^{-1} and coercive field 41 Oe, 12 Oe and 7 Oe for samples M, UM and SM, respectively. These outcomes correspond to the results from microscopy measurements.

Hyperthermic experiments were done at a frequency of $f = 508$ kHz versus the AC—field amplitude in the range 0–5 kA m^{-1}. The field dependences of one of the

Table 8.3 The mean diameter of magnetosomes d, coercive force H_C and saturation magnetization M_S of magnetosomes suspensions prepared at various conditions

	NP	WVS	FQ
d (nm)	47	52	58
H_C (Oe)	0	6.5	20
M_S (emu/g)	0.2	0.21	0.23

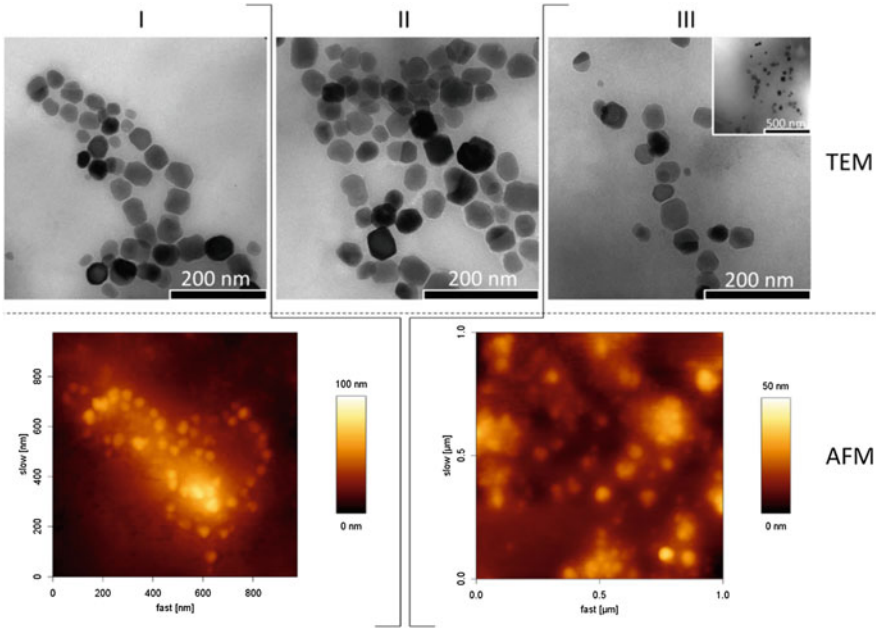

Fig. 8.12 TEM and AFM pictures of magnetosomes: I (M), II (UM) and III (SM)

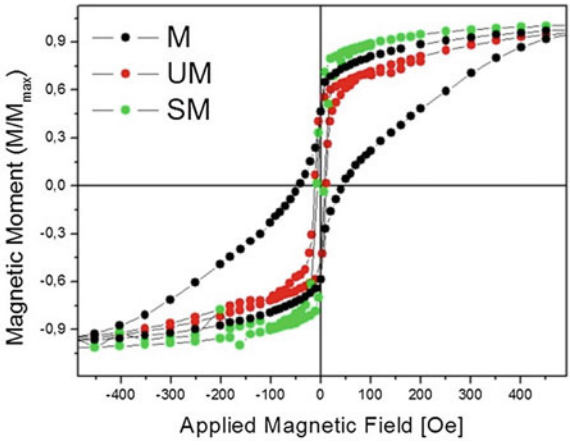

Fig. 8.13 Hysteresis loops for standard isolated magnetosomes sample (M), ultracentrifuged magnetosomes sample (UM) and sonicated magnetosomes sample (SM)

most important parameter of hyperthermia—the SAR ("**S**pecific **A**bsorption **R**ate") values are plotted in Fig. 8.14a).

Specific Absorption Rate is defined as the amount of heat released by a weight unit of the material per time unit during exposure to an oscillating magnetic field. This parameter is quite dependent on magnetic field frequency and intensity as well as on nanoparticle size, shape, material, agglomeration rate and dispersion media

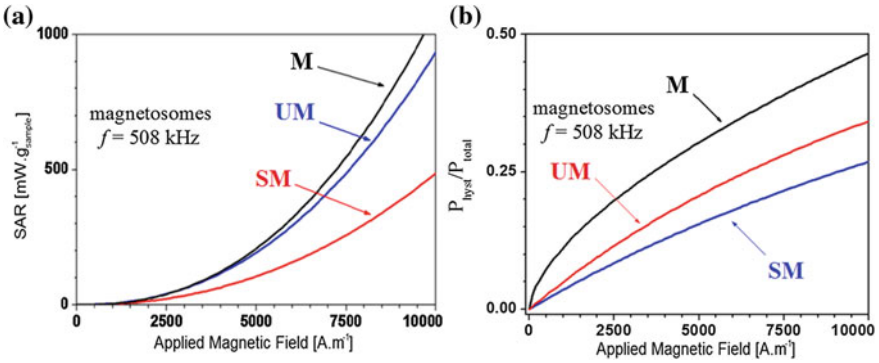

Fig. 8.14 **a** SAR dependence on the applied magnetic field. The curves represent standard isolated magnetosomes sample (M), ultracentrifuged magnetosomes sample (UM) and sonicated magnetosomes sample. **b** Proportion of hysteresis processes to total losses

[84]. It is important to have these values for the material as high as possible. The slope of the curve informs about the dynamics of temperature rise of the sample and it also informs about the power release in a unit of volume at a given magnetic field strength. The dynamics of the increase was more visible in samples M and UM, so the heating is more effective in the samples with unbroken chains and higher coercivity, where hysteresis losses contribute much more significantly (Fig. 8.14b). On the other hand, in sonicated samples, which have a significant presence of individual magnetosomes, the dominant mechanisms of heating are relaxation processes; hysteresis does not contribute too much. The SAR values at 10 kA m^{-1} and 508 kHz were 1083, 934 and 463 mW/g_{sample} for the M, UM and SM samples of magnetosomes, respectively. When we recalculate the SAR values per 1 g of magnetite (according equation: $SAR = ((\rho_S C_P)/m)^*(\Delta T/\Delta t)$ [77], where ρ_S is density of the sample, C_P is the specific heat capacity, m is the mass of magnetite per unit volume of the colloid and $\Delta T/\Delta t$ is heating rate at 10 kA/m) we get the values in the range 1278–594 W/$g_{magnetite}$.

The magneto-optical properties of magnetosomes were analyzed and described in the work [70]. Magnetically induced linear and circular anisotropy determined the significant role of chains in the orientational mechanism of these magnetic dipoles. Numerical adjustments of the linear anisotropy curves using a classical Langevin orientation model gave the average number of magnetosomes per chain, about 12. Magnetic and magneto-optical experiments exhibited the large sensitivity of magnetosomes to the magnetic field. This high sensitivity is interesting for optical applications due to very low field required to achieve the effect, which can make the technologic application in devices easier.

8.3 Magnetic Particle Systems for Technical Applications

8.3.1 Dielectric and Structural Properties of Transformer Oil-Based MFs

Transformer oils have been used as insulating and cooling medium for almost over a century in electrical power equipment, such as transformers and inductors [85, 86]. However, the development of future high voltage network and smart grid has given rise to high demands on the performance and reliability of the insulating and cooling material [87]. In recent years, transformer oil-based MFs (TOFF) have attracted much attention for their great improvement of heat transfer efficiency [88–93]. Taking into account the general "6 °C rule", which expresses that the rate of the insulation aging doubles approximately every 6 °C increase in temperature [94, 95], these MFs constitute an efficient and reliable cooling medium for future power transformers. Moreover, it has been found that TOFF can exhibit higher electrical breakdown field strength as compared to pure transformer oils [96]. This paradoxical finding is still not fully understood and great effort has been made to study dielectric properties of the innovative insulator in view of using various transformer oils, magnetic nanoparticles and surfactants. Here, we review some selected dielectric and structural properties of TOFF reported in recent years including our latest research results.

8.3.1.1 Dielectric Breakdown

TOFF have commonly been synthesized according to the basic procedure starting with the co-precipitation of magnetite (Fe_3O_4) nanoparticles from a solution of Fe^{2+} and Fe^{3+} ions with a suitable base (e.g. NH_4OH) [97, 98]. The co-precipitated nanoparticles are sterically stabilized with a single oleic acid layer chemisorbed on the particle surfaces. Purified nanoparticles are finally dispersed in transformer oil in a specified particle volume fraction Φ_V, which is a crucial parameter determining the resulting dielectric properties of TOFF. It is well known that the relative permittivity ε_r of TOFF is strongly dependent on the particle volume fraction. This fact can be expressed by Maxwell-Garnet formula, which is commonly used when describing the relative permittivity of a mixed dielectric, as highlighted in [99]:

$$\frac{\varepsilon_r - \varepsilon_{r1}}{\varepsilon_r + 2\varepsilon_{r1}} = \Phi_V \frac{\varepsilon_{r2} - \varepsilon_{r1}}{\varepsilon_{r2} + 2\varepsilon_{r1}} \tag{8.2}$$

where ε_{r1} and ε_{r2} are the relative permittivities of the transformer oil and nanoparticles, respectively. Segal et al. [96] presented for the first time that the electrical breakdown field strength of TOFF containing magnetite nanoparticles is comparable or in some cases superior to the pure carrier liquid—transformer oil. Particularly, the electrical tests of magnetite TOFF showed that for positive

streamers the breakdown voltage of the TOFF was almost twice increased as compared to the pure oil during the lightning impulse tests. This result was radical because it suggested that the addition of substantial particulate contamination in the transformer oil, albeit in the form of magnetite nanoparticles, can result in an improvement of the oil's insulating characteristics. After the first report, many researchers experimentally confirmed this paradoxical effect in TOFF based on various transformer oils and magnetic nanoparticles [100–104]. Recently, three times higher breakdown voltage was reported for a TOFF with particle volume fraction from 0.08 to 0.39% as compared to its base transformer oil [103]. Interestingly, besides the higher breakdown field strength, the velocity of positive streamers propagation was found to be reduced by the presence of the nanoparticles by 46% [96]. This important result proves that the presence of the magnetic nanoparticles results in the inhibition of the processes leading to the electrical breakdown in the oil. In other words, a slower streamer takes more time to short the gap between electrodes leading to the breakdown. Consequently, this gives a longer time period to extinguish the applied impulse voltage.

In an effort to explain the increased breakdown field strength, Hwang et al. [105] analyzed the effect of nanoparticle charging by free electrons from ionization, which usually form a streamer leading to the breakdown [106]. The proposed model shows that if the particle polarization is fast enough relative to the timescales of the streamer propagation, the presence of the particles in the oil will significantly modify the related electrodynamics. As it was shown, the relaxation time constant of the magnetite in transformer oil is $\tau_{r(Fe_3O_4)} = 7.47 \times 10^{-14}$ s, which is very short as compared to the microsecond time scales typically involved in the streamer propagation [105]. It was therefore assumed that the short relaxation time of magnetite nanoparticles allows charging of the particle surfaces due to the free electrons from the field ionization. Furthermore, for a magnetite TOFF, the extremely fast particle polarization causes the electric field lines to converge upon the relaxed nanoparticles. Then, the free charge carriers in the TOFF move along the electric field lines. Because the electrons move much faster than positive ions, the nanoparticles trap electrons faster than positive ions. Consequently, the nanoparticles become charged as the electrons redistribute uniformly on the equipotential surface. Thus, the process of electron charging of the nanoparticles converts the highly mobile electrons from field ionization to slow negatively charged nanoparticles. The effective mobility reduction factor was found to be approximately 1×10^5 [105]. Thus, the electron trapping is the possible cause of the reported [96] decrease in the streamer velocity and subsequent electrical breakdown field strength increase. This theoretical model was considered in several experimental studies on transformer oil-based MFs [103, 107–109].

8.3.1.2 Frequency Dependent Dielectric Response

Taking into account the aforementioned model, the particle mobility seems to play a key role in the streamer formation in a FOFF. Furthermore, such a theoretical consideration has stimulated experimental investigation of magnetic particle interactions with an external electric field. It is intuitive that any structural changes of the TOFF induced by electric forces can have a remarkable impact on a space charge migration, and finally on the streamer formation at high electric field intensities. Recently, within this context, strong indications of the electric field induced magnetic particle aggregation in a TOFF were obtained by the method of dielectric spectroscopy [110]. This method relies on the frequency dependent complex impedance and permittivity of a sample under test. Thus, various electrical polarization and corresponding relaxation processes can by revealed and identified [111].

The deduction of electric field induced aggregation of magnetic nanoparticles in a TOFF was based on the analysis of a pronounced low frequency relaxation process and its dependence on external electric field intensity. In Fig. 8.15, one can see the spectrum of the dissipation factor $(\tan \delta)$ of a thin TOFF layer (1.6 μm) determined as a ration of the complex permittivity components. After excluding the Maxwell-Wagner type of relaxation [112–115], the relaxation maximum was assigned to the interfacial polarization of free space charge in the TOFF, which can form a quasi-electric double layer (EDL) on the surface of the particles. Then, following the Schwarz model of EDL polarization [116], the counterions are free to move laterally on the particle surface. After application of an external electric field, the system becomes polarized due to the displacement of the counterions relative to the particle. This polarization process can account for the observed low frequency dielectric behavior. The corresponding relaxation time is given by the following term:

$$\tau = \frac{R^2}{2u_0 k_B T} \exp\left(\frac{E_a}{k_B T}\right) \tag{8.3}$$

where R is the radius of the particle, T is the absolute temperature, k_B is the Boltzmann constant, and u_0 is the charge mobility in a free solution, and E_a is the activation energy of the motion along the surface. Hence, one can assume that the considered particle aggregation should be reflected in the change of the low frequency relaxation time. This idea was demonstrated by measuring dielectric spectrum of a TOFF confined between two parallel plate electrodes [110]. Especially, the DC electric field induced particle aggregate formation can be detected by applying the DC bias voltage dependent dielectric spectroscopy. For that purpose, the tan δ spectra have been obtained with the applied DC bias voltage of different values. The measurements were performed at a constant electrode separation distance ($d = 1.6$ μm) with the effective value of the testing AC voltage of 32 mV. In order to reveal the induced aggregate behavior, a hysteresis-like measurement sequence was applied. After the application of DC bias voltage of 1 V, the

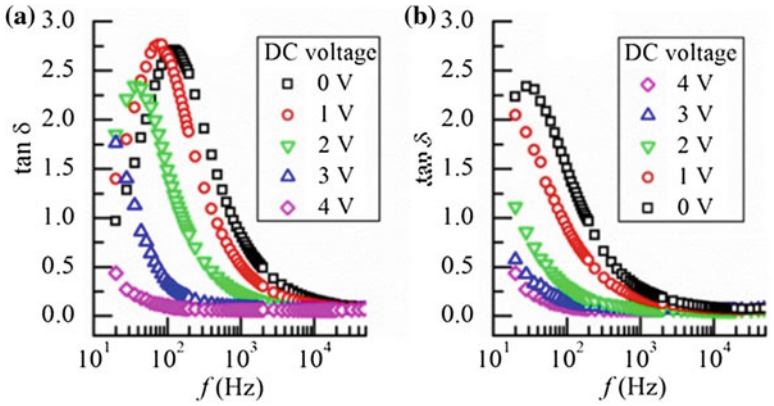

Fig. 8.15 The dependence of the tan δ spectrum on the applied DC bias voltage. The measurements were conducted one after the other with the following sequence: from 0 V up to 4 V (**a**), from 4 V down to 0 V (**b**). The investigated transformer oil-based MF with magnetic volume fraction $\Phi_V = 6.6\%$ was measured in a capacitor cell with electrode separation distance d = 1.6 μm and the applied test signal level of 32 mV (20 kV/m). The intensity of DC electric field was 0.625 MV/m, 1.25 MV/m, 1.875 MV/m, and 2.5 MV/m corresponding to the applied DC bias voltages of 1 V, 2 V, 3 V, and 4 V, respectively

relaxation maximum was slightly increased and shifted to lower frequencies (Fig. 8.15a). This was attributed to the initial formation of particle aggregates driven by the applied DC electric field. However, when the DC field was gradually increasing, the relaxation maximum was shifting to lower frequencies, whereas its amplitude was greatly decreasing. This is the consequence of the dominant polarization force of the DC electric field. In this case, the strong DC electric field induces the dipoles in the particles, giving rise to the induced particle dipole-dipole interactions. At the same time, this field polarizes and keeps the counter-ions on the opposite aggregate sides so strongly that their ability to respond the AC field decreases markedly. Thereby the DC electric field raises an energy barrier on the polarization axis, so reducing both mobility and the moving range of the counter-ions, what is reflected in the lower frequency position of the loss peak and its decreased amplitude, respectively. From the reverse measurements (Fig. 8.15b), one can notice a certain kind of remanence in the induced aggregate size when the relaxation time and the amplitude of the loss peak achieve the initial values with the noticeable lag. A greater degree of that lag is observed in the frequency position of the relaxation maxima, while their re-increase in amplitude seems to have a faster response to the decreasing DC voltage. It was proposed that the former is associated with the aggregate structure inertia when the total attractive forces (induced electric dipolar forces, magnetic forces, van der Walls interactions) are still able to resist the disrupting thermal energy effect. The latter is associated with the decreasing energy barrier, whereby the counter-ions surrounding the aggregate acquire greater freedom in response to the AC electric field. The above described behavior accounts for the fact that the relaxation maxima do not match at zero DC bias voltages.

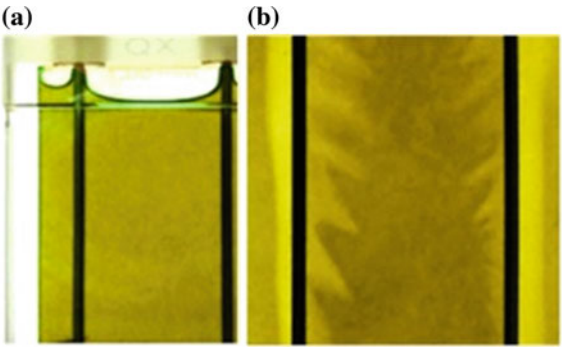

Fig. 8.16 TOFF appearance in zero electric field (**a**). Electrohydrodynamically driven pattern in the sample exposed to the DC electric field of 5 kV/cm (**b**). The electrode separation distance is set to 1 cm. The photographs are artificially colorized to enhance the contrast [117]

8.3.1.3 Direct Observation of MF Structural Changes in an Electric Field

In order to confirm the electric field induced particle aggregation and structural changes deduced from the dielectric spectroscopy results, other experimental methods were necessary to apply. One of the most solid evidence of the electric field and the consequent electrohydrodynamics influence on a bulk TOFF structure was obtained by a simple visual observation under suitable experimental conditions [117].

In Fig. 8.16, one can see photographs of a diluted TOFF sample ($\Phi_V = 0.05\%$) in a glass cuvette exposed to 0 and 5 kV/cm (DC). The initial application of the electric field resulted in a slow electrohydrodynamic flow and a separated cloud formation between the electrodes. A final shade of the cloud was achieved in approximately 2 min. After that, the cloud distortion followed with the spike-like structure formation from the cloud borders, pointing towards the field gradient (Fig. 8.16b). The created pattern behaved rather dynamically, as the spikes varied in length, width, and position. The initial cloud formation was associated with the migration of the space charges (including residual unwashed ions) towards the electrodes, which engenders weak fluid flow. As the ions accumulate in the field gradient onto the electrodes, the particles are pushed from that region by the electrohydrodynamic forces, leading to the cloud-like formation. The sample with such a separated cloud then exhibits the permittivity and conductivity gradients, and the further action of the DC field exerts an anisotropic electrostatic body force on the transition layer between the cloud and its surrounding. The action of that force thus sets the cloud in motion and distorts its shape in the direction of the applied field.

The distortion begins in the upper part and the spikes direct rather upwards, as a result of the applied field geometry [117]. It was therefore concluded that the observed phenomenon derives from the bulk motion induced by electrical body forces lodged in the cloud, not forces on individual particles, as bulk motion of colloids cannot be explained solely by dipole-dipole interactions between particles [118]. Furthermore, the pattern dynamics is driven by the interaction of the

electrostatic body force and the ionic current. As the former stretches the cloud borders towards the electrodes, the latter keeps pushing them out from the electrodes. Consequently, the irregular motion of the formed spikes can be observed. This motion quits immediately when the field is interrupted and diminishes due to the action of thermal energy. The pattern formation effect was equally observed in the cuvette positioned both, horizontally and vertically, so any gravity effect on the pattern shape has been excluded. It was found that the induced pattern formation does not depend on the voltage polarity and it is a reversible phenomenon.

The related nanoscopic structural changes of the TOFF in the glass cuvette were investigated by Small Angle Neutron Scattering (SANS), too [117]. SANS technique is successfully used for structural characterization of different types of MFs [119, 120]. In the reported work [117] the experiment focused on the measurement of the neutron scattering intensity I as a function of the momentum transfer modulus q in dependence on the electric field intensity. It was found that the scattered intensity in the small q region remarkably increases with the increasing electric field. This effect has been considered as a direct evidence of the particle aggregates in the TOFF induced by the electrohydrodynamics and polarization forces between the particles. Again, the dielectric contrast between the magnetic particles and the oil molecules plays the crucial role, leading to the induced electric dipole-dipole interactions and the subsequent aggregation. It was estimated that the mean aggregate size is greater than 300 nm, as determined from the minimal q covered in the experiment by $D \sim 2\pi/q$. Further analysis of the scattering profiles revealed that only a small (below 1%) fraction of all particles composes the aggregates. Finally, the neutron scattering from the TOFF in zero electric field yielded an isotropic 2D pattern corresponding to the quasi-spherical nanoparticles. On the other hand, in the applied DC electric field, 2D scattering patterns showed anisotropy corresponding to the elongated shape of the formed aggregates oriented along the electric field.

8.3.2 *Ferronematics—In Search for Liquid Crystalline Magnetic Field Sensors*

Liquid crystal (LC) materials exhibit remarkable properties placing them between isotropic liquids and crystals. The discovery that is widely recognized as the birth of liquid crystal science is attributed to Friedrich Reinitzer. In 1888 he observed a curious behavior of cholesterol benzoate that had “two melting points”, where the intermediate phase between them was later named as liquid crystalline phase [121]. The combination of liquids’ fluidity with the direction dependent electric and optical properties of crystalline solids makes LCs attractive for use in various commercial exploitations. Anisotropy in mechanical, electrical and magnetic properties permits LCs to be easily oriented, realigned, or deformed by electric or magnetic field, by heating, or by mechanical stresses. These materials have attracted great attention for many practical applications in LC display industry, in photonics

and magneto-optics, in nano- and biosensing. The search for new materials with exotic properties and for new technologies continues, in order to comply with the needs of these, and other novel applications.

LCs may be divided into two classes: lyotropic and thermotropic. Lyotropic LCs usually have two or more components (e.g., amphiphilic molecules in a solvent) that exhibit liquid-crystalline phase in certain concentration and temperature ranges. Thermotropic LCs are compounds whose liquid crystalline properties are induced purely by temperature variation. They possess one or more mesophases at temperatures between their melting point, below which the material is a crystalline solid, and the"clearing point", above which the material is an isotropic liquid. The properties of such conventional liquid phase are characterized by the molecules that are randomly oriented. Since their discovery, many LC phases have been identified [122]. One of the mesophases is the nematic phase, in which molecules are aligned parallel to each other. Molecules have no positional order and their tendency is to point in the same direction (along the director $\boldsymbol{n}$). One of the most important discoveries in the control of LCs by electric or magnetic fields was the threshold behavior in the reorientational response of LCs. The effect was described by Fréedericksz and named after him as "Fréedericksz transition" [123]. It laid the foundation for LC applications in modern technology.

The dielectric anisotropy ε_a of LCs is relatively large, and driving voltage of a few volts is sufficient to control the orientational response. Although LC can be controlled by a magnetic field, the magnetic sensitivity is rather low (the anisotropy of the diamagnetic susceptibility χ_a is of the order of 10^{-7}). It usually requires very high magnetic induction strength, of the order of Tesla to trigger the reorientation in LCs [122]. Brochard and de Gennes proposed a method which would increase the magnetic sensitivity of LCs. In 1970 they presented the first theory of ferromagnetic nanoparticles colloids in nematic LCs—"ferronematics" (FNs) [124]. The most important feature of FNs is an effective coupling between the magnetic particles (MPs) (their magnetic moment m) and the LC matrix (the director n). This coupling ensures that the effect of magnetic field will be transferred into the nematic host. The theory of Brochard and de Gennes [124] predicted a rigid anchoring with $\boldsymbol{m} \parallel \boldsymbol{n}$. Based on the estimations given in [124], first lyotropic [125, 126] and then thermotropic FNs have been studied [127]. Later experiments on thermotropic FNs have indicated that besides the predicted $\boldsymbol{m} \parallel \boldsymbol{n}$ condition, the case of $\boldsymbol{m} \perp \boldsymbol{n}$ is also possible. Based on the theory and experiments, Burylov and Raikher modified the theoretical description of FNs [128–130]. They considered a finite anchoring energy W between nematic molecules and the magnetic particles and defined the parameter ω as the combination of anchoring energy with elastic energy of the LC ($\omega = Wd/K$, where d is the size of the MPs and K represents orientational-elastic Frank energy). The parameter ω defines the type of anchoring of nematic molecules on MPs surfaces. For rigid anchoring $\omega \gg 1$, while the soft anchoring is defined by $\omega \leq 1$. The latter type of anchoring allows both boundary conditions $\boldsymbol{m} \perp \boldsymbol{n}$ and $\boldsymbol{m} \parallel \boldsymbol{n}$. In our former study a linear magnetodielectric response of dielectric permittivity versus magnetic field has been observed in these systems at low magnetic fields [131].

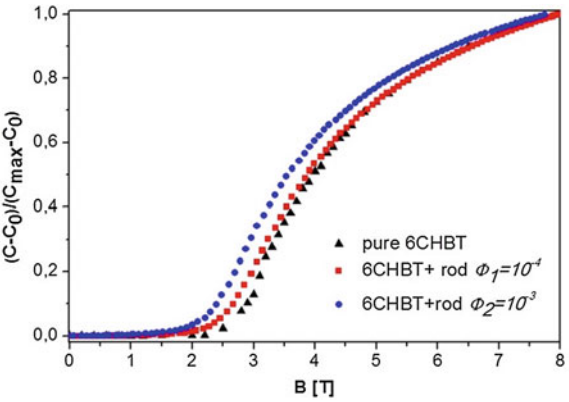

Fig. 8.17 Dependence of the dimensionless reduced capacitance of the liquid crystal 6CHBT and 6CHBT doped with rod-like particles of different magnetic particles' volume concentrations on the external magnetic field

Concerning FNs we have studied structural transitions in FNs based on different LCs [132–134], magnetic field induced phase transitions from isotropic to nematic phase [135], the response of these materials to low magnetic field [131] as well as that by applying a weak dc bias magnetic field to the FNs in isotropic phase it is possible to increase the ac magnetic susceptibility [136]. Increased response of FNs to applied magnetic fields by studying their dielectric and optical responses, as well as enhanced their shift of the transition temperature under the application of magnetic field could definitely trigger future experimental and theoretical research in the field of magnetically active composite materials.

In work [137] the magnetic Fréedericksz transition under the application of magnetic field was studied in FNs based on the nematic LC 6CHBT that was doped with rod-like MPs of volume concentration $\phi_1 = 10^{-4}$ and $\phi_2 = 10^{-3}$. Structural changes were observed by measurements of dielectric permittivity where the influence of the concentration of the MPs on the magnetic response of these FNs was studied. Figure 8.17 shows the magnetic Fréedericksz transition of undoped 6CHBT and in FNs doped with the rod-like MPs of different volume concentrations. It was observed that the volume concentration of the MNPs as well as the particle's size influenced the threshold of the magnetic Fréedericksz transition and the dielectric response to low magnetic fields (far below the Fréedericksz transition). The obtained critical value of the magnetic field for undoped 6CHBT is 2.63 T. The reduction of critical magnetic field strength becomes larger if the concentration of the MPs in FNs was increased.

Doping of LCs with small amount of MPs causes the decrease or increase of the threshold of the magnetic Fréedericksz transition [132, 133, 138–140]. It depends on the anisotropy of diamagnetic susceptibility χ_a of the nematic liquid crystal and also on initial mutual orientation of the nematic director n and the magnetic moment m of the MPs. Podoliak et al. [141] and Buluy et al. [142] have studied both experimental and theoretical the optical response of suspensions of ferromagnetic nanoparticles in nematic LCs on the magnetic field (which finally leads to a Fréedericksz transition). The authors have measured an additional, linear response

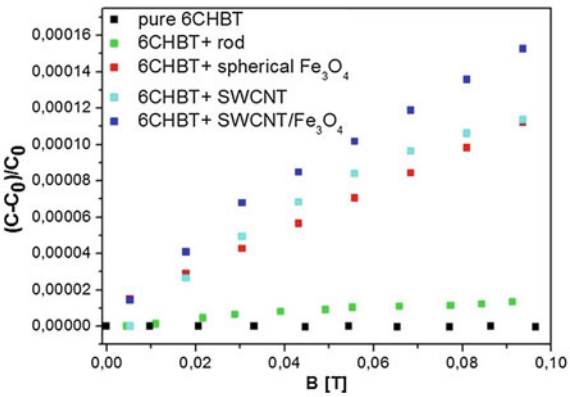

Fig. 8.18 Dependence of relative capacitance variation on the external magnetic field for undoped 6CHBT and 6CHBT doped with rod-like nanoparticles, spherical Fe_3O_4 nanoparticles, SWCNT and SWCNT/Fe_3O_4

in FNs at low magnetic fields, far below the threshold of Fréedericksz transition. These results inspired us to perform the experimental study of the dielectric permittivity response to low external magnetic fields (below 0.1 T). Our results in study of composite systems based on LC 6CHBT doped with spherical, rod-like MPs, single-wall carbon nanotubes (SWCNT), and SWCNT functionalized with Fe_3O_4 nanoparticles have shown, that it is possible to increase the sensitivity of LCs on the magnetic field not only in the high magnetic field region (order of several Tesla) but also in the low-magnetic field region [131]. The volume concentrations of MPs were $\phi_1 = 10^{-4}$ and $\phi_2 = 10^{-3}$. Magnetic Fréedericksz transition of undoped 6CHBT starts at 2.63 T. Due to doping, the Fréedericksz threshold is shifted to lower values, but it is still higher than 2 T.

Figure 8.18 shows the variation of the relative capacitance of the 6CHBT LC and 6CHBT doped with various types of nanoparticles with volume concentration $\phi = 10^{-4}$ as a function of the magnetic induction B in the low magnetic field range (up to 0.1 T). It provides a clear evidence for a linear magnetic field dependence of the capacitance in the region of low magnetic field. The FN suspensions may show well measurable response in capacitance to the applied magnetic field, even much below the magnetic Fréedericksz threshold independently of the type of the nanoparticles. The higher sensitivity of these materials on low magnetic fields is important for practical applications of FNs for example as sensors of magnetic field.

8.4 Conclusion

MNPs are undoubtedly interesting target of investigation due to their special properties and promising application potential. In this chapter we shortly reviewed the results of some studies implying magnetite nanoparticles (prepared by synthetic or biological route) in biomedical application stressing the biocompatibility as an important issue. Also in reviewed technical applications MNPs contributed to

improvement of transformer oil dielectric properties or to higher sensitivity of liquid crystals to external magnetic field. The results of conducted experiments are encouraging for future outlook in this field of science.

Acknowledgements This work was supported by Slovak Scientific Grant Agency VEGA (projects No. 0141 and 0045), by the Slovak Research and Development Agency under the contract No. APVV 0171-10, 15-0453, 14-0120, 14-0932, by the European Structural Funds in the frame of the projects ITMS 26220120033, COST NANOUPTAKE CA15119 and COST Radiomag TD1402.

References

1. S. Laurent, D. Forge, M. Port, A. Roch, C. Robic, L. Vander Elst, R.N. Muller, Chem. Rev. **108**, 2064 (2008)
2. D. Ortega, Q.A. Pankhurst, Nanosci. Nanostruct. Chem. **1**, 1 (2014)
3. C. Scherer, A.M.F. Neto, Brazillian J. Phys. **35**, 718 (2005)
4. M. Kubovčíková, I. Antal, J. Kováč, V. Závišová, M. Koneracká, P. Kopčanský, Acta Phys. Pol. A **126**, 268 (2014)
5. K.S.W. Sing, Pure Appl. Chem. **57**, 603 (1985)
6. P. Bowen, J. Dispers. Sci. Technol. **23**, 631 (2002)
7. S. Zalipsky, C. Gilon, A. Zilkha, Eur. Polym. J. **19**, 1177 (1983)
8. A. Jurikova, K. Csach, J. Miskuf, M. Koneracka, V. Zavisova, M. Kubovcikova, P. Kopcansky, M. Muckova, IEEE Trans. Magn. **49**, 236 (2013)
9. A. Józefczak, T. Hornowski, A. Skumiel, M. Łabowski, M. Timko, P. Kopčanský, M. Koneracká, A. Szlaferek, W. Kowalski, J. Magn. Magn. Mater. **321**, 1505 (2009)
10. M. Kubovčikova, I. Antal, M. Koneracka, V. Závišová, A. Jurikova, K. Siposova, Z. Gazova, J. Kovač, M. Kovarik, D. Kupka, P. Kopčanský, Magnetohydrodynamics **49**, 282 (2013)
11. V. Závišová, M. Koneracká, M. Múčková, J. Lazová, A. Juríková, G. Lancz, N. Tomašovičová, M. Timko, J. Kováč, I. Vávra, M. Fabián, A.V. Feoktystov, V.M. Garamus, M.V. Avdeev, P. Kopčanský, J. Magn. Magn. Mater. **323**, 1408 (2011)
12. M. Koneracká, A. Antošová, V. Závišová, Z. Gažová, G. Lancz, A. Juríková, N. Tomašovčová, J. Kováč, M. Fabián, P. Kopčanský, Phys. Procedia **9**, 254 (2010)
13. K. Siposova, M. Kubovcikova, Z. Bednarikova, M. Koneracka, V. Zavisova, A. Antosova, P. Kopcansky, Z. Daxnerova, Z. Gazova, Nanotechnology **23**, 55101 (2012)
14. I. Khmara, M. Koneracka, M. Kubovcikova, V. Zavisova, I. Antal, K. Csach, P. Kopcansky, I. Vidlickova, L. Csaderova, S. Pastorekova, M. Zatovicova, J. Magn. Magn. Mater. **427**, 114 (2017)
15. M. Mandal, S. Kundu, S.K. Ghosh, S. Panigrahi, T.K. Sau, S.M. Yusuf, T. Pal, J. Colloid Interface Sci. **286**, 187 (2005)
16. F. Rodante, G. Marrosu, Thermochim. Acta **171**, 15 (1990)
17. F. Danhier, E. Ansorena, J.M. Silva, R. Coco, A. Le Breton, V. Préat, J. Control. Release **161**, 505 (2012)
18. W. Amass, A. Amass, B. Tighe, Polym. Int. **47**, 89 (1998)
19. C. Fonseca, S. Simões, R. Gaspar, J. Control. Release **83**, 273 (2002)
20. F. Waldmeier, U. Glaenzel, B. Wirz, L. Oberer, D. Schmid, M. Seiberling, J. Valencia, G.-J. Riviere, P. End, S. Vaidyanathan, Drug Metab. Dispos. **35** (2007)
21. V. Závišová, M. Koneracká, M. Múčková, P. Kopčanský, N. Tomašovičová, G. Lancz, M. Timko, B. Pätoprstá, P. Bartoš, M. Fabián, J. Magn. Magn. Mater. **321**, 1613 (2009)

22. M. Kubovcikova, M. Koneracka, V. Zavisova, M. Muckova, M. Timko, L. Schmidtova, P. Bartos, P. Kopcansky, IEEE Trans. Magn. **49**, 353 (2013)
23. I. Antal, M. Kubovcikova, V. Zavisova, M. Koneracka, O. Pechanova, A. Barta, M. Cebova, V. Antal, P. Diko, M. Zduriencikova, M. Pudlak, P. Kopcansky, J. Magn. Magn. Mater. **380**, 280 (2015)
24. F.C. Meldrum, V.J. Wade, D.L. Nimmo, B.R. Heywood, S. Mann, Nature **349**, 684 (1991)
25. U. Testa, *Proteins of Iron Metabolism* (CRC Press, 2002)
26. S.H. Banyard, D.K. Stammers, P.M. Harrison, Nature **271**, 282 (1978)
27. X. Liu, E.C. Theil, Acc. Chem. Res. **38**, 167 (2005)
28. S. Stefanini, S. Cavallo, C.-Q. Wang, P. Tataseo, P. Vecchini, A. Giartosio, E. Chiancone, Arch. Biochem. Biophys. **325**, 58 (1996)
29. I.G. Macara, T.G. Hoy, P.M. Harrison, Biochem. J. **135** (1973)
30. N. Gálvez, B. Fernandez, E. Valero, P. Sánchez, R. Cuesta, J.M. Domínguez-Vera, Comptes Rendus Chim. **11**, 1207 (2008)
31. T. Douglas, V.T. Stark, Inorg. Chem. **39**, 1828 (2000)
32. F.C. Meldrum, T. Douglas, S. Levi, P. Arosio, S. Mann, J. Inorg. Biochem. **58**, 59 (1995)
33. F.C. Meldrum, B.R. Heywood, S. Mann, Science **257**, 522 (1992)
34. J.W. Bulte, T. Douglas, S. Mann, R.B. Frankel, B.M. Moskowitz, R.A. Brooks, C.D. Baumgarner, J. Vymazal, J.A. Frank, Invest. Radiol. **29**(Suppl 2), S214 (1994)
35. R.M. Cornell, U. Schwertmann, John Wiley & Sons, *The Iron Oxides: Structure, Properties, Reactions, Occurrences, and Uses* (Wiley-VCH, 2003)
36. B. D. Cullity and C. D. Graham, *Introduction to Magnetic Materials* (Wiley, 2011)
37. J. García, G. Subías, J. Phys.: Condens. Matter **16**, R145 (2004)
38. D.P.E. Dickson, S.A. Walton, S. Mann, K. Wong, Nanostruct. Mater. **9**, 595 (1997)
39. Q.A. Pankhurst, S. Betteridge, D.P.E. Dickson, T. Douglas, S. Mann, R.B. Frankel, Hyperfine Interact. **91**, 847 (1994)
40. K. Wong, T. Douglas, S. Gider, D. Awschalom, S. Mann, Chem. Mater. **10**, 279 (1998)
41. P. Southern, A.P. Robinson, O.I. Kasyutich, B. Warne, A. Bewick, W. Schwarzacher, J. Phys.: Condens. Matter **19**, 456204 (2007)
42. O. Kasyutich, A. Sarua, W. Schwarzacher, J. Phys. D Appl. Phys. **41**, 134022 (2008)
43. O. Kasyutich, D. Tatchev, A. Hoell, F. Ogrin, C. Dewhurst, W. Schwarzacher, J. Appl. Phys. **105**, 07B528 (2009)
44. M.J. Martínez-Pérez, R. de Miguel, C. Carbonera, M. Martínez-Júlvez, A. Lostao, C. Piquer, C. Gómez-Moreno, J. Bartolomé, F. Luis, Nanotechnology **21**, 465707 (2010)
45. J.F. Dillon, J. Magn. Magn. Mater. **31–34**, 1 (1983)
46. J. Ferre, G.A. Gehring, Reports. Prog. Phys. **47**, 513 (1984)
47. M. Koralewski, M. Pochylski, Z. Mitróová, L. Melníková, J. Kováč, M. Timko, P. Kopčanský, Acta Phys. Pol. A **121**, 1237 (2012)
48. M. Koralewski, M. Pochylski, Z. Mitróová, M. Timko, P. Kopčanský, L. Melníková, J. Magn. Magn. Mater. **323**, 2413 (2011)
49. P.N. Argyres, Phys. Rev. **97**, 334 (1955)
50. P.S. Pershan, J. Appl. Phys. **38**, 1482 (1967)
51. M. Koralewski, J.W. Kłos, M. Baranowski, Z. Mitróová, P. Kopčanský, L. Melníková, M. Okuda, W. Schwarzacher, Nanotechnology **23**, 355704 (2012)
52. M.V. Avdeev, J. Appl. Crystallogr. **40**, 56 (2007)
53. M.V. Avdeev, V.L. Aksenov, Phys. Usp. **53**, 971 (2011)
54. D.I. Svergun, M.H.J. Koch, Rep. Prog. Phys. **66**, 1735 (2003)
55. L. Melnikova, Z. Mitroova, M. Timko, K.J. Kovač, M. Koralewski, M. Pochylski, M.V. Avdeev, V.I. Petrenko, V.M. Garamus, L. Almasy, P. Kopčanský, Magnetohydrodynamics **49**, 293 (2013)
56. L. Melníková, Z. Mitróová, M. Timko, J. Kováč, M.V. Avdeev, V.I. Petrenko, V.M. Garamus, L. Almásy, P. Kopčanský, Mendeleev Commun. **24**, 80 (2014)
57. L. Melníková, V.I. Petrenko, M.V. Avdeev, V.M. Garamus, L. Almásy, O.I. Ivankov, L.A. Bulavin, Z. Mitróová, P. Kopčanský, Colloids Surf. B Biointerfaces **123**, 82 (2014)

58. L. Melnikova, V.I. Petrenko, M.V. Avdeev, O.I. Ivankov, L.A. Bulavin, V.M. Garamus, L. Almásy, Z. Mitroova, P. Kopcansky, J. Magn. Magn. Mater. **377**, 77 (2015)
59. P. Kopcansky, K. Siposova, L. Melnikova, Z. Bednarikova, M. Timko, Z. Mitroova, A. Antosova, V.M. Garamus, V.I. Petrenko, M.V. Avdeev, Z. Gazova, J. Magn. Magn. Mater. **377**, 267 (2015)
60. E.C. Theil, R.K. Behera, T. Tosha, Coord. Chem. Rev. **257**, 579 (2013)
61. I. Urban, N.M. Ratcliffe, J.R. Duffield, G.R. Elder, D. Patton, Chem. Commun. **46**, 4583 (2010)
62. P.K. Dehal, C.F. Livingston, C.G. Dunn, R. Buick, R. Luxton, D.J. Pritchard, Biotechnol. J. **5**, 596 (2010)
63. M. Zborowski, C.B. Fuh, R. Green, N.J. Baldwin, S. Reddy, T. Douglas, S. Mann, J. J. Chalmers, Cytometry **24**, 251 (1996)
64. V. Clavijo Jordan, M.R. Caplan, K.M. Bennett, Magn. Reson. Med. **64**, 1260 (2010)
65. M. Uchida, M. Terashima, C.H. Cunningham, Y. Suzuki, D.A. Willits, A.F. Willis, P.C. Yang, P.S. Tsao, M.V. McConnell, M.J. Young, T. Douglas, Magn. Reson. Med. **60**, 1073 (2008)
66. L. Melnikova, K. Pospiskova, Z. Mitroova, P. Kopcansky, I. Safarik, Microchim. Acta **181**, 295 (2014)
67. K. Fan, C. Cao, Y. Pan, D. Lu, D. Yang, J. Feng, L. Song, M. Liang, X. Yan, Nat. Nanotechnol. **7**, 459 (2012)
68. T. Prozorov, D.A. Bazylinski, S.K. Mallapragada, R. Prozorov, Mater. Sci. Eng. R Rep. **74**, 133 (2013)
69. L. Yan, S. Zhang, P. Chen, H. Liu, H. Yin, H. Li, Microbiol. Res. **167**, 507 (2012)
70. A. Dzarova, F. Royer, M. Timko, D. Jamon, P. Kopcansky, J. Kovac, F. Choueikani, H. Gojzewski, J.J. Rousseau, J. Magn. Magn. Mater. **323**, 1453 (2011)
71. A. Dzarova, F. Royer, D. Jamon, P. Kopcansky, F. Choueikani, H. Gojzewski, J. J. Rousseau, M. Timko, J. Magn. Magn. Mater. **323**, 1364 (2011)
72. A. Józefczak, M. Molčan, Z. Rozynek, T. Hornowski, A. Skumiel, M. Timko, J. Tóthová, P. Kopčanský, B. Leszczyński, Acta Phys. Pol., A **127**, 629 (2015)
73. A. Józefczak, A. Hashim, M. Molcan, T. Hornowski, A. Skumiel, M. Rajnak, P. Kopčanský, M. Timko, Magnetohydrodynamics **49**, 411 (2013)
74. D. Jamon, F. Donatini, A. Siblini, F. Royer, R. Perzynski, V. Cabuil, S. Neveu, J. Magn. Magn. Mater. **321**, 1148 (2009)
75. F. Royer, D. Jamon, J.J. Rousseau, V. Cabuil, D. Zins, H. Roux, C. Bovier, Eur. Phys. J. Appl. Phys. **22**, 83 (2003)
76. E. Hasmonay, E. Dubois, J.-C. Bacri, R. Perzynski, Y.L. Raikher, V.I. Stepanov, Eur. Phys. J. B **5**, 859 (1998)
77. M. Timko, M. Molcan, A. Hashim, A. Skumiel, M. Muller, H. Gojzewski, A. Jozefczak, J. Kovac, M. Rajnak, M. Makowski, P. Kopcansky, I.E.E.E. Trans, Magn. **49**, 250 (2013)
78. R. Hergt, R. Hiergeist, M. Zeisberger, D. Schüler, U. Heyen, I. Hilger, W.A. Kaiser, J. Magn. Magn. Mater. **293**, 80 (2005)
79. M. Molcan, H. Gojzewski, A. Skumiel, S. Dutz, J. Kovac, M. Kubovcikova, P. Kopcansky, L. Vekas, M. Timko, J. Phys. D Appl. Phys. **49**, 365002 (2016)
80. H. Gojzewski, M. Makowski, A. Hashim, P. Kopcansky, Z. Tomori, M. Timko, Scanning **34**, 159 (2012)
81. A. Skumiel, B. Leszczyński, M. Molcan, M. Timko, J. Magn. Magn. Mater. **420**, 177 (2016)
82. A. Hashim, M. Molcan, J. Kovac, Z. Varchulova, H. Gojzewski, M. Makowski, P. Kopcansky, Z. Tomori, M. Timko, Acta Phys. Pol., A **121**, 1250 (2012)
83. M. Molcan, A. Hashim, J. Kovac, M. Rajnak, P. Kopcansky, M. Makowski, H. Gojzewski, M. Molokac, L. Hvizdak, M. Timko, Acta Phys. Pol. A **126**, 198 (2014)
84. E. Garaio, J.M. Collantes, J.A. Garcia, F. Plazaola, S. Mornet, F. Couillaud, O. Sandre, J. Magn. Magn. Mater. **368**, 432 (2014)
85. J.-P. Crine, *Electrical Insulation Oils* (ASTM International, 100 Barr Harbor Drive, PO Box C700, West Conshohocken, PA 19428-2959, 1988), pp. 59-59–22

86. E. Kuffel, W.S. Zaengl, J. Kuffel, *High Voltage Engineering: Fundamentals* (Butterworth-Heinemann/Newnes, 2000)
87. M. Rafiq, Y.Z. Lv, Y. Zhou, K.B. Ma, W. Wang, C.R. Li, Q. Wang, Renew. Sustain. Energy Rev. **52**, 308 (2015)
88. I. Nkurikiyimfura, Y. Wang, Z. Pan, Renew. Sustain. Energy Rev. **21**, 548 (2013)
89. A. Lange, Phys. Fluids **14**, 2059 (2002)
90. H. Rahman, S.A. Suslov, J. Fluid Mech. **764**, 316 (2015)
91. D. Zablockis, V. Frishfelds, E. Blums, J. Phys.: Condens. Matter **20**, 204134 (2008)
92. S. Shuchi, K. Sakatani, H. Yamaguchi, J. Magn. Magn. Mater. **289**, 257 (2005)
93. A. Mukhopadhyay, R. Ganguly, S. Sen, I.K. Puri, Int. J. Heat Mass Transf. **48**, 3485 (2005)
94. V.M. Montsinger, Trans. Am. Inst. Electr. Eng. **49**, 776 (1930)
95. C.F. Yang, Adv. Mater. Res. **614–615**, 1109 (2012)
96. V. Segal, A. Hjortsberg, A. Rabinovich, D. Nattrass, K. Raj, in *Conference on Record of the 1998 IEEE International Symposium on Electrical Insulation (Cat. No.98CH36239)* (IEEE, n.d.), pp. 619–622
97. L. Vékás, D. Bica, M.V. Avdeev, China Particuol. **5**, 43 (2007)
98. A.-H. Lu, E.L. Salabas, F. Schüth, Angew. Chemie Int. Ed. **46**, 1222 (2007)
99. J. Miao, M. Dong, M. Ren, X. Wu, L. Shen, H. Wang, J. Appl. Phys. **113**, 204103 (2013)
100. F. Herchl, K. Marton, L. Tomčo, P. Kopčanský, M. Timko, M. Koneracká, I. Kolcunová, J. Phys.: Condens. Matter **20**, 204110 (2008)
101. J. Kudelcik, P. Bury, P. Kopcansky, M. Timko, Phys. Procedia **9**, 78 (2010)
102. P. Kopčanský, M. Koneracká, M. Timko, I. Potočová, K. Marton, L. Tomčo, Czechoslov. J. Phys. **54**, 659 (2004)
103. J.-C. Lee, H.-S. Seo, Y.-J. Kim, Int. J. Therm. Sci. **62**, 29 (2012)
104. T.-H. Tsai, P.-H. Chen, D.-S. Lee, C.-T. Yang, Nanoscale Res. Lett. **6**, 264 (2011)
105. J.G. Hwang, M. Zahn, F.M. O'Sullivan, L.A.A. Pettersson, O. Hjortstam, R. Liu, J. Appl. Phys. **107**, 14310 (2010)
106. J.C. Devins, S.J. Rzad, R.J. Schwabe, J. Appl. Phys. **52**, 4531 (1981)
107. J.-C. Lee, W.-H. Lee, S.-H. Lee, S. Lee, Mater. Res. Bull. **47**, 2984 (2012)
108. M. Chiesa, S.K. Das, Colloids Surf. A Physicochem. Eng. Asp. **335**, 88 (2009)
109. Y. Du, Y. Lv, C. Li, M. Chen, J. Zhou, X. Li, Y. Zhou, Y. Tu, J. Appl. Phys. **110**, 104104 (2011)
110. M. Rajnak, J. Kurimsky, B. Dolnik, P. Kopcansky, N. Tomasovicova, E.A. Taculescu-Moaca, M. Timko, Phys. Rev. E **90**, 32310 (2014)
111. A. Schönhals, F. Kremer, in *Broadband Dielectric Spectroscopy* (Springer Berlin Heidelberg, Berlin, Heidelberg, 2003), pp. 1–33
112. M.M. Rădulescu, J. Magn. Magn. Mater. **85**, 144 (1990)
113. I. Malaescu, C.N. Marin, J. Magn. Magn. Mater. **252**, 68 (2002)
114. I. Malaescu, C.N. Marin, J. Colloid Interface Sci. **251**, 73 (2002)
115. M. Rajnak, J. Kurimsky, B. Dolnik, K. Marton, L. Tomco, A. Taculescu, L. Vekas, J. Kovac, I. Vavra, J. Tothova, P. Kopcansky, M. Timko, J. Appl. Phys. **114**, 34313 (2013)
116. C. Grosse, V.N. Shilov, Colloids Surf. A Physicochem. Eng. Asp. **140**, 199 (1998)
117. M. Rajnak, V.I. Petrenko, M.V. Avdeev, O.I. Ivankov, A. Feoktystov, B. Dolnik, J. Kurimsky, P. Kopcansky, M. Timko, Appl. Phys. Lett. **107**, 73108 (2015)
118. M. Trau, S. Sankaran, D.A. Saville, I.A. Aksay, Nature **374**, 437 (1995)
119. V.I. Petrenko, M.V. Avdeev, V.M. Garamus, L.A. Bulavin, V.L. Aksenov, L. Rosta, Colloids Surf. A Physicochem. Eng. Asp. **369**, 160 (2010)
120. V.I. Petrenko, V.L. Aksenov, M.V. Avdeev, L.A. Bulavin, L. Rosta, L. Vekas, V.M. Garamus, R. Willumeit, Phys. Solid State **52**, 974 (2010)
121. F. Reinitzer, Monatshefte Für Chemie - Chem. Mon. **9**, 421 (1888)
122. P.G. de. Gennes, J. Prost, *The Physics of Liquid Crystals* (Clarendon Press, 1993)
123. V. Fréedericksz, V. Zolina, Trans. Faraday Soc. **29**, 919 (1933)
124. F. Brochard, P.G. de Gennes, J. Phys. **31**, 691 (1970)
125. L. Liebert, A. Martinet, J. Phys. Lett. **40**, 363 (1979)

126. A.M. Figueiredo Neto, L. Liebert, A.M. Levelut, J. Phys. **45**, 1505 (1984)
127. S.-H. Chen, N.M. Amer, Phys. Rev. Lett. **51**, 2298 (1983)
128. S.V. Burylov, Y.L. Raikher, Phys. Lett. A **149**, 279 (1990)
129. S.V. Burylov, Y.L. Raikher, J. Magn. Magn. Mater. **122**, 62 (1993)
130. S.V. Burylov, Y.L. Raikher, Mol. Cryst. Liq. Cryst. Sci. Technol. Sect. A. Mol. Cryst. Liq. Cryst. **258**, 107 (1995)
131. N. Tomašovičová, M. Timko, Z. Mitróová, M. Koneracká, M. Rajňak, N. Éber, T. Tóth-Katona, X. Chaud, J. Jadzyn, P. Kopčanský, Phys. Rev. E **87**, 14501 (2013)
132. P. Kopčanský, N. Tomašovičová, M. Koneracká, V. Závišová, M. Timko, A. Džarová, A. Šprincová, N. Éber, K. Fodor-Csorba, T. Tóth-Katona, A. Vajda, J. Jadzyn, Phys. Rev. E **78**, 11702 (2008)
133. P. Kopčanský, N. Tomašovičová, M. Koneracká, M. Timko, V. Závišová, N. Éber, K. Fodor-Csorba, T. Tóth-Katona, A. Vajda, J. Jadzyn, E. Beaugnon, X. Chaud, J. Magn. Magn. Mater. **322**, 3696 (2010)
134. Z. Mitróová, N. Tomašovičová, M. Timko, M. Koneracká, J. Kováč, J. Jadzyn, I. Vávra, N. Éber, T. Tóth-Katona, E. Beaugnon, X. Chaud, P. Kopčanský, New J. Chem. **35**, 1260 (2011)
135. P. Kopcansky, N. Tomasovicova, M. Koneracka, V. Zavisova, M. Timko, M. Hnatic, N. Eber, T. Toth-Katona, J. Jadzyn, J. Honkonen, E. Beaugnon, X. Chaud, IEEE Trans. Magn. **47**, 4409 (2011)
136. N. Tomašovičová, J. Kováč, Y. Raikher, N. Éber, T. Tóth-Katona, V. Gdovinová, J. Jadżyn, R. Pinčák, P. Kopčanský, Soft Matter **12**, 5780 (2016)
137. N. Tomašovičová, M. Timko, V. Závišová, A. Hashim, J. Jadzyn, X. Chaud, E. Beaugnon, P. Kopčanský, Magnetohydrodynamics **48**, 407 (2012)
138. N. Tomašovičová, M. Koneracká, P. Kopčanský, M. Timko, V. Závišová, J. Jadzyn, Phase Transitions **79**, 595 (2006)
139. E. Petrescu, E.-R. Bena, J. Magn. Magn. Mater. **321**, 2757 (2009)
140. L.J. Martínez-Miranda, L.K. Kurihara, J. Appl. Phys. **105**, 84305 (2009)
141. N. Podoliak, O. Buchnev, O. Buluy, G. D'Alessandro, M. Kaczmarek, Y. Reznikov, T. J. Sluckin, Soft Matter **7**, 4742 (2011)
142. O. Buluy, S. Nepijko, V. Reshetnyak, E. Ouskova, V. Zadorozhnii, A. Leonhardt, M. Ritschel, G. Schönhense, Y. Reznikov, Soft Matter **7**, 644 (2011)

Chapter 9
Structure, Dynamics, and Thermodynamics of Ferrofluids

Philip J. Camp

Abstract A survey of recent work on the structure, dynamics, and thermodynamics of ferrofluids is given. The emphasis is on new theoretical descriptions and computer simulations of simple models of colloidal ferromagnetic nanoparticles, but some favourable comparisons with experiments are shown to justify the choices of models. The survey summarises combined theoretical and computational studies of field-induced microstructure in ferrofluids, magnetisation curves, static and dynamic initial magnetic susceptibilities, thermodynamic properties, and sedimentation profiles.

9.1 Introduction

Ferrofluids contain colloidal magnetic nanoparticles, e.g. of magnetite (Fe_3O_4), stabilised with simple surfactants like oleic acid or oleylamine, and dispersed in a non-magnetic liquid like decalin or kerosene. Ferrofluids are technologically important, finding application as heat-conduction and damping media, liquid sealants, lubricants, and gas-fluidised beds [1]. In biomedicine, water-based magnetic liquids are used in tumour detection and destruction, targeted drug delivery, and magnetic resonance imaging [2, 3]. Ferrofluids are also 'simple' model polar liquids, in which magnetic dipole-dipole and dipole-field interactions play dominant roles [4]. The short-range interactions can be tuned in the normal way with steric stabilisers, and in the case of aqueous ferrofluids, added salt.

At PLMMP 2005 in Kyiv, I had the good fortune of meeting Alexey Ivanov, Ekaterina Elfimova, and Sofia Kantorovich from the Ural Federal University (formerly the Ural State University) in Ekaterinburg, Russia. In the following decade,

P. J. Camp (✉)
School of Chemistry, University of Edinburgh, David Brewster Road, Edinburgh EH9 3FJ, Scotland
e-mail: philip.camp@ed.ac.uk

P. J. Camp
Institute of Natural Sciences and Mathematics, Ural Federal University, 51 Lenin Avenue, Ekaterinburg 620000, Russia

L. A. Bulavin and A. V. Chalyi (eds.), *Modern Problems of Molecular Physics*,
Springer Proceedings in Physics 197, https://doi.org/10.1007/978-3-319-61109-9_9

the Ekaterinburg and Edinburgh teams have developed a broad range of theoretical and simulation techniques to describe ferrofluids, all based on rather simple coarse-grained models (Sect. 9.2). On the theoretical side, new statistical mechanical approaches have been established, such as the modified mean-field theory of the magnetic response, and the logarithmic free-energy theory of the thermodynamic properties. On the simulation side, Monte Carlo and molecular dynamics techniques have been developed to test the theoretical predictions. In this contribution, a selective summary of recent results will be presented, with emphasis on understanding experimental measurements. Examples will include field-induced microstructure (Sect. 9.3), the magnetisation curve (Sect. 9.4), initial and dynamic magnetic susceptibilities (Sect. 9.5), thermodynamic properties with and without applied fields (Sect. 9.6), and sedimentation profiles in monodisperse and polydisperse ferrofluids (Sect. 9.7).

9.2 Simple Models of Ferrofluids

A schematic diagram of a spherical colloidal ferromagnetic particle is shown in Fig. 9.1. The magnetic core diameter is x, and assuming that the particle is homogeneously magnetised, the magnetic dipole moment is $\mu = \pi M_{\rm s} x^3/6$ where $M_{\rm s}$ is the saturation magnetisation, usually taken to be the bulk value. The particle is sterically stabilised with a layer of surfactant molecules of thickness δ, such that the effective particle diameter is $\sigma = x + 2\delta$. The particles are immersed in a simple liquid characterised by regular parameters such as the density and the viscosity η. For small single-domain ferromagnetic particles, the dipole moment has two equally probable orientations in opposite directions along the magnetisation easy axis, and the associated switching between these two directions is called Néel relaxation. The time scale for this relaxation is $\tau_{\rm N} = \tau_0 \exp(KV/k_{\rm B}T)$ where $\tau_0 \sim 10^{-9}$ s, K is the anisotropy constant (a material parameter), and $V = \pi x^3/6$ is the magnetic core volume. For larger particles, $\tau_{\rm N}$ exceeds the timescale for Brownian rotation $\tau_{\rm B} = 3V\eta/k_{\rm B}T$, and so the dipole moment changes direction mainly by particle rotation. For magnetite in kerosene at room temperature ($T = 293$ K) the crossover between the Néel

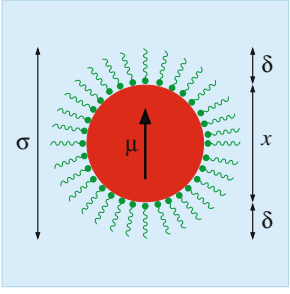

Fig. 9.1 Schematic diagram of a sterically stabilised ferromagnetic nanoparticle with magnetic core diameter x (shown in red), steric layer thickness δ (shown in green), and effective hard-core diameter $\sigma = x + 2\delta$

and Brownian regimes is at about 10 nm, and for 16 nm particles, $\tau_N \sim 1$ s and $\tau_B \sim 10^{-6}$ s [1].

The magnetic field at any point outside of a homogeneously magnetised sphere is identical to that produced by a central point dipole [5], and the magnetic interaction between two such spheres is identical to the interaction between two point dipoles (see [6] for a pedagogical derivation). The magnetic dipole-dipole interaction energy is

$$u_d(\boldsymbol{r}, \boldsymbol{\mu}_i, \boldsymbol{\mu}_j) = \frac{\mu_0}{4\pi}\left[\frac{(\boldsymbol{\mu}_i \cdot \boldsymbol{\mu}_j)}{rij^3} - \frac{3(\boldsymbol{\mu}_i \cdot \boldsymbol{rij})(\boldsymbol{\mu}_j \cdot \boldsymbol{rij})}{rij^5}\right] \tag{9.1}$$

where $\boldsymbol{r}$ is the separation vector, $\boldsymbol{\mu}_i$ is the dipole moment on particle i, and μ_0 is the vacuum magnetic permeability. There are various choices of short-range potential. The simplest choice is the hard-sphere (HS) potential, given by

$$u_{HS}(r) = \begin{cases} \infty & r < \sigma \\ 0 & r \geq \sigma \end{cases} \tag{9.2}$$

where $r = |\boldsymbol{r}|$. Another popular choice is the Lennard-Jones (LJ) potential

$$u_{LJ}(r) = 4\epsilon\left[\left(\frac{\sigma}{r}\right)^{12} - \left(\frac{\sigma}{r}\right)^{6}\right] \tag{9.3}$$

which contains an attractive component. The combination of the dipolar and LJ potentials is called the Stockmayer model [7]. A convenient, purely repulsive potential for molecular dynamics simulations is the Weeks-Chandler-Andersen (WCA) potential

$$u_{WCA}(r) = \begin{cases} u_{LJ}(r) - u_{LJ}(r_c) & r < 2^{1/6}\sigma \\ 0 & r \geq 2^{1/6}\sigma \end{cases} \tag{9.4}$$

which is effectively the LJ potential cut and shifted at its minimum. All of these short-range potentials are characterised by the effective particle diameter σ. This allows various physically meaningful parameters to be defined. The dipolar coupling constant is given by

$$\lambda = \frac{\mu_0}{4\pi}\left(\frac{\mu^2}{k_B T \sigma^3}\right) \tag{9.5}$$

and it characterises the strength of the dipole-dipole interactions as compared to the thermal energy $k_B T$. For magnetite nanoparticles with $x = 10$ nm and $M_s = 4.8 \times 10^5$ A m^{-1}, the dipole moment is $\mu = 2.5 \times 10^{-19}$ A m^2. Assuming a typical value of $\delta = 2$ nm for the thickness of the non-magnetic steric layer (e.g., oleic acid) the hard-core diameter is $\sigma = 14$ nm, and at room temperature ($T = 293$ K) the dipolar coupling constant is $\lambda \simeq 0.6$. The concentration of a ferrofluid is $\rho = N/V$, where N is the number of particles and V is the volume. In reduced units, this is expressed as

$$\rho^* = \rho\sigma^3. \tag{9.6}$$

A more intuitive measure is the volume fraction, given by

$$\varphi = \frac{\pi \rho^*}{6}. \tag{9.7}$$

For real ferrofluids, $\varphi \sim 0.1$, although concentrations of up to $\varphi \sim 0.5$ are possible in highly polydisperse samples. Ferrofluids are useful precisely because their properties can be switched with the application of magnetic fields. The strength of the particle-field interaction is measured by the Langevin parameter

$$\alpha = \frac{\mu_0 \mu H}{k_\mathrm{B} T} \tag{9.8}$$

where H is the external magnetic field strength. For the 10 nm magnetite nanoparticles considered above, $\alpha = 1$ corresponds to an external magnetic field $H \simeq 1.3 \times 10^4$ A m^{-1}.

9.3 Ferrofluid Microstructure

The lowest-energy arrangement of a pair of dipolar spheres is the nose-to-tail parallel ($\rightarrow\rightarrow$) configuration. The ground-state configuration of four or more dipolar spheres is a ring [8]. At low temperatures, chains are common structural motifs because they also have very low energy, but higher entropy than rings. It is also possible to observe branching points, where a particle is connected to three or four near neighbours [9, 10]. All of these structures have been observed in experiment and in simulations. Experimentally, ferrofluid structure can be observed using cryogenic transmission electron microscopy [11–14]. In simulations at low temperature ($\lambda \geq 4$) chains are dominant at moderate concentrations [15–17], while rings are the most common structural motif at very low concentrations [18]. At higher concentrations, clusters give way to 'normal' dense-liquid structures. It is also thought that spontaneously magnetised fluid domains can form at low temperatures and high concentrations [19–24].

Ferrofluids undergo field-induced structuring, with chain-like clusters aligning and growing in the field direction. In recent work, the growth of chain-like orientational correlations was studied using theory and Monte Carlo computer simulations [25, 26]. The theoretical approach is based on a virial expansion of the pair distribution function

$$g(r, \theta) = \sum_{k=0}^{\infty} \sum_{l=0}^{\infty} \varphi^k \lambda^l \beta_{kl}(r, \theta) \tag{9.9}$$

where the coefficients β_{kl} are functions of the interparticle separation r, and the angle of the separation vector $\boldsymbol{r}$ with the applied magnetic field $\boldsymbol{H}$, i.e., $\boldsymbol{r} \cdot \boldsymbol{H} = rH \cos\theta$. Figure 9.2a, c shows typical results for $g(r, \theta)$ in a monodisperse fluid of dipolar

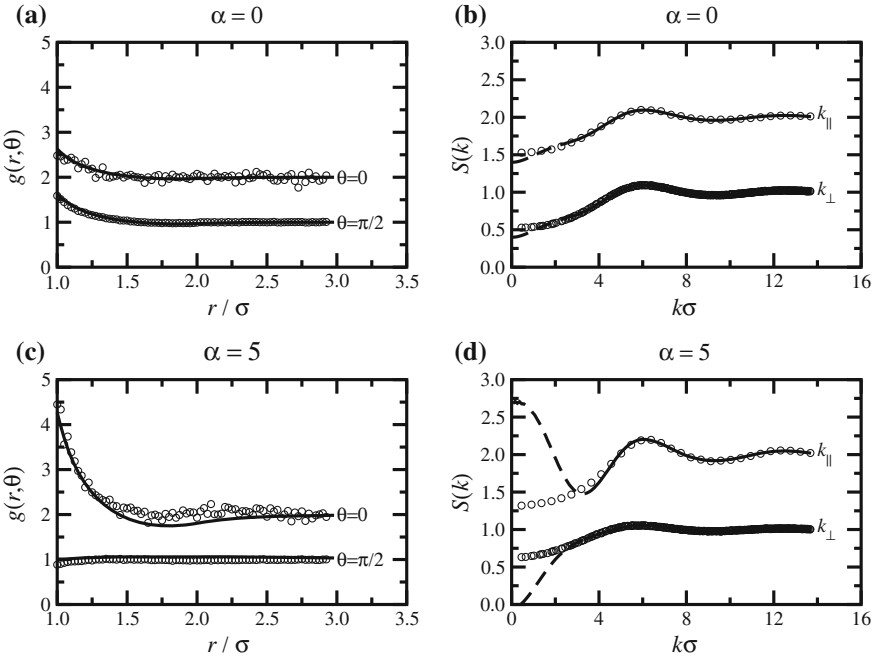

Fig. 9.2 Pair distribution function $g(r, \theta)$ (**a**) and (**c**) and structure factor $S(\boldsymbol{k})$ (**b**) and (**d**) for a monodisperse fluid of dipolar hard spheres with $\lambda = 1$, $\varphi = 0.1$, and $\alpha = 0$ (**a**) and (**b**) and 5 (**c**) and (**d**). The results for $\theta = 0$ and $k_{\parallel}$ are shifted up by one unit for clarity

hard spheres with $\lambda = 1$, $\varphi = 0.1$, and $\alpha = 0$ and 5 [25]. ($\alpha = 5$ corresponds to a ferrofluid magnetisation of about 80% of the saturation value—see Sect. 9.4.) Note that $g(r, \theta) = 0$ for $r < \sigma$. The theoretical curves correspond to a truncation of 9.9, keeping only the terms β_{00} (the hard-sphere pair distribution function from Percus-Yevick theory [27]), β_{01}, β_{02}, β_{11}, and β_{12}. Hence, only terms of orders up to φ and λ^2 are retained. The truncation in φ means that only the effects of a third particle on the pair distribution function are considered. The results show the growth in positional correlations in the direction parallel to the field (chain-like ordering) while in the perpendicular direction, there is a decrease in structure due to there being no lateral ordering of chain-like clusters. In neutron-scattering experiments it is possible to detect field-induced ordering by measuring the structure factor $S(\boldsymbol{k})$ at wavevectors $\boldsymbol{k}$ both parallel and perpendicular to the field direction [28–32]. $g(r, \theta)$ and $S(\boldsymbol{k})$ are related by a Fourier transform, and Fig. 9.2b, d shows comparisons of the structure factor of the same ferrofluid from theory and simulation. Since the theory is truncated at the three-body level, correlations beyond $r \geq 2\sigma$ will not be described very accurately, and hence the theoretical structure factor will be inaccurate for $k\sigma \leq \pi$. These portions of $S(k)$ are shown as dashed lines. This limitation notwithstanding, the increase in structure parallel to the field, and the decrease in structure perpen-

dicular to the field, are described quite faithfully in the region of the primary peak ($k\sigma \simeq 2\pi$) by the simple virial expansion. This type of analysis has also been applied to the more complex situation of a bidisperse ferrofluid, in describing all of the pair distribution functions and structure factors connecting small and large dipolar particles [26].

9.4 Magnetisation Curve

The magnetisation curve $M(H)$ is a very important property of a ferrofluid. Associated with that is the initial susceptibility, which will be considered separately in Sect. 9.5. The magnetisation curves of condensed matter have been studied for more than 100 years, beginning with Langevin's theory of non-interacting particles [33] which gives

$$M_{\mathrm{L}}(H) = \left(\frac{N\mu}{V}\right)\left(\coth\alpha - \frac{1}{\alpha}\right). \tag{9.10}$$

As mentioned above in Sect. 9.3, when $\alpha = 5$, $M_{\mathrm{L}}(H) \simeq 0.8\,N\mu/V$. For real ferrofluids, the non-interacting particle picture is inaccurate, particularly in weak fields, where the particle-particle interactions are at least as important as the particle-field interactions. There are many schemes for taking account of the interparticle interactions, including Weiss mean-field theory [34, 35], integral equations [36, 37], thermodynamic perturbation theory [38, 39], so-called modified mean-field theories [40, 41], Mayer cluster expansions [42–44], and density functional theory [45–47]. One of the most successful theories is the second-order modified mean-field (MMF2) theory, which is based on an expansion of the pair correlation function in terms of φ and λ, and its connection through the Yvon-Born-Green hierarchy [27] with the one-particle density, from which the magnetisation can be computed. The key result is that the magnetisation curve can be expressed by a Langevin-type expression but with an effective field H_{eff} modified by the contributions from the other particles.

$$M(H) = M_{\mathrm{L}}(H_{\mathrm{eff}}) \tag{9.11}$$

The effective field is of course given by an expansion, which at the MMF2 level is

$$H_{\mathrm{eff}} = H + \frac{1}{3}M_{\mathrm{L}}(H) + \frac{1}{144}M_{\mathrm{L}}(H)\frac{\mathrm{d}M_{\mathrm{L}}(H)}{\mathrm{d}H} + \ldots \tag{9.12}$$

The MMF2 has been tested critically against both experimental and simulation data for polydisperse ferrofluids [48, 49]. The particle-size distribution $p(x)$ is generally unknown, but the accuracy of the theory can be assessed by fitting the distribution to experimental data, and then checking the theory against essentially exact simulations with the fitted particle-size distribution. Crucially, experimental data are available for ferrofluids prepared at various concentrations by dilution of the same

high-concentration stock suspension. This means that, at the very least, an accurate theory should give the same particle-size distribution at each concentration. The particle-size distribution is conveniently expressed in terms of a Γ-distribution with only two parameters, a and x_0:

$$p(x) = \frac{x^a \exp(-x/x_0)}{x_0^{a+1}\Gamma(a+1)}. \tag{9.13}$$

Interestingly, of all of the approaches mentioned above, only the MMF2 theory gives the same fitted parameters over all concentrations. For the particular ferrofluid under consideration [48, 49], $a = 4.95$ and $x_0 = 1.23$ nm, with a mean magnetic-core diameter of $(a+1)x_0 = 7.32$ nm, and polydispersity $\sqrt{\langle x^2\rangle - \langle x\rangle^2}/\langle x\rangle = 0.41$. The quality of the fits is illustrated in Fig. 9.3, which shows $M(H)$ for ferrofluid samples with saturation magnetisations $M(\infty) = 5.0$, 7.8, 11.2, 16.9, 25.3, 37.8, and 57.0 kA m^{-1} (in order of increasing particle concentration). The agreement between theory, experiment, and simulation is excellent in all cases, and over the full range of magnetic field.

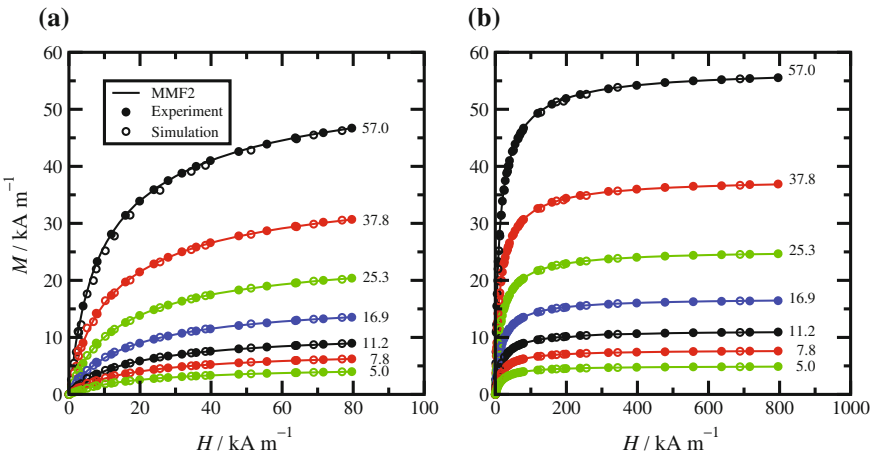

Fig. 9.3 Magnetisation curves for a polydisperse ferrofluid from theory (lines), experiment (filled points), and simulation (unfilled points): **a** low-field behaviour $H = 0$–80 kA m^{-1}; **b** full magnetisation curve $H = 0$–800 kA m^{-1}. The curves are labelled with the saturation magnetisation $M(\infty)$ in units of kA m^{-1}

9.5 Magnetic Susceptibility

9.5.1 Static Susceptibility

The initial magnetic susceptibility is an important material parameter, and is defined by

$$\chi = \left(\frac{\partial M}{\partial H}\right)_{H=0}. \tag{9.14}$$

The Langevin susceptibility $\chi_{\rm L}$ is easily determined from the corresponding magnetisation curve in 9.10:

$$\chi_{\rm L} = \frac{N\mu_0\mu^2}{3Vk_{\rm B}T} = \frac{4\pi\rho^*\lambda}{3} = 8\varphi\lambda. \tag{9.15}$$

As with the magnetisation curve, this is going to be a very poor approximation for any real ferrofluid. The MMF theories provide a framework for introducing interparticle interactions. At the MMF2 level, the expression for the initial susceptibility is [41]

$$\chi = \chi_{\rm L}\left(1 + \frac{1}{3}\chi_{\rm L} + \frac{1}{144}\chi_{\rm L}^2\right) \tag{9.16}$$

while at the MMF1 level, the last term in brackets is omitted. Since $\chi_{\rm L} \propto \varphi\lambda$, it is clear that the MMF theories correspond to retaining only those terms of order $\varphi\lambda$, $(\varphi\lambda)^2$, and $(\varphi\lambda)^3$. In principle, additional terms of different orders should be included. For example, the first correction to the MMF1-level term gives

$$\chi = \chi_{\rm L}\left[1 + \frac{1}{3}\chi_{\rm L}\left(1 + \frac{A}{25}\lambda^2\right) + \frac{1}{144}\chi_{\rm L}^2\right] \tag{9.17}$$

where A is a parameter depending only on the short-range potential and the temperature. For hard spheres, $A = 1$, while for the WCA potential at a temperature $k_{\rm B}T/\epsilon = 1$, $A = 0.943$ [41]. Equation 9.17 now contains terms of order $\varphi^2\lambda^4$, and hence will be referred to as MMF2 + $\varphi^2\lambda^4$. Figure 9.4a shows the magnetic susceptibility of a monodisperse fluid of dipolar WCA particles at temperature $k_{\rm B}T/\epsilon = 1$ [50]. The points are from Brownian dynamics simulations under two sets of conditions: $\lambda = 1$ and at various concentrations; and $\varphi = 0.105$ and with various dipolar coupling constants. The data are shown on the same scale by plotting χ as a function of the Langevin susceptibility $\chi_{\rm L}$ given in 9.15. Several theoretical curves are shown: the Langevin model; the MMF1 theory; the MMF2 theory; the MMF2 + $\varphi^2\lambda^4$ theory at fixed $\lambda = 1$; and the MMF2 + $\varphi^2\lambda^4$ theory with $\lambda = \chi_{\rm L}/8\varphi$ and $\varphi = 0.105$. The results show that the MMF1 theory and the MMF2 theory are very similar, and in good agreement with the simulation results with $\lambda = 1$ over the whole range of $\chi_{\rm L}$ and hence φ. The MMF1 and MMF2 theories are not as accurate with $\varphi = 0.105$ and with large values of λ, but by including the extra term of order $\varphi^2\lambda^4$ in 9.17, the

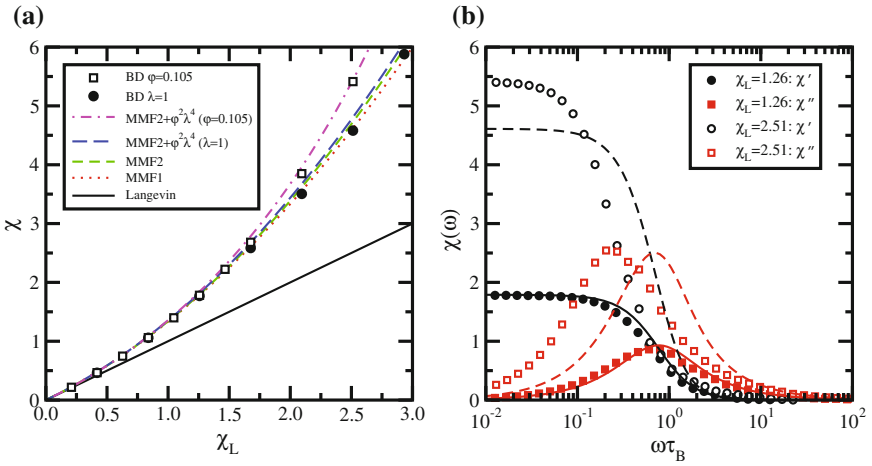

Fig. 9.4 **a** Initial magnetic susceptibility χ for a monodisperse fluid of dipolar WCA particles at $k_B T/\epsilon = 1$. The filled circles and unfilled squares are from Brownian dynamics simulations with $\lambda = 1$ (and various concentrations) and at $\varphi = 0.105$ (with various dipolar coupling constants), respectively. The lines represent various theories—see text. **b** Magnetic susceptibility spectra $\chi(\omega)$ for dipolar WCA particles at $\varphi = 0.105$ and with $\lambda = 1.5$ ($\chi_L = 1.26$) (filled points and solid lines), and at $\varphi = 0.105$ and with $\lambda = 3.0$ ($\chi_L = 2.51$) (unfilled points and dashed lines). The real and imaginary parts from simulations are shown as black circles and red squares, respectively, and the corresponding theoretical predictions are shown in black and red lines, respectively

agreement is greatly improved. These theories have been applied successfully to the description of real polydisperse ferrofluids [48, 49, 51], and extended to treat dense materials with record-breaking initial susceptibilities approaching 100 [52, 53]. An unusual situation occurs in low-concentration ferrofluids at very low temperature, where ring formation leads to flux closure and hence a dramatic drop in χ; this situation can be described using a cluster model [54].

A few comments are in order to put the current results in to context with well-known results for electrically polar liquids [27, 55]. The electrical analogue of the static susceptibility χ is $(\varepsilon - 1)$, where ε is the static dielectric constant. The dielectric constant of a spherical sample surrounded by a continuum with dielectric constant ε' is given by [56, 57]

$$\frac{(\varepsilon - 1)(2\varepsilon' + 1)}{(\varepsilon + 2\varepsilon')} = 3yg_K \tag{9.18}$$

where $y = \rho\mu^2/9\varepsilon_0 k_B T$, ε_0 is the vacuum permittivity, and $g_K = \langle M^2 \rangle / N\mu^2$ is the Kirkwood factor. g_K is determined by the correlations between particles, and is equal to

$$g_K = 1 + \int \mathrm{d}\boldsymbol{r} \int \mathrm{d}\boldsymbol{e}_1 \int \mathrm{d}\boldsymbol{e}_2 h(\boldsymbol{r}, \boldsymbol{e}_1, \boldsymbol{e}_2)(\boldsymbol{e}_1 \cdot \boldsymbol{e}_2) \tag{9.19}$$

where $\boldsymbol{\mu}_i = \mu \boldsymbol{e}_i$, $\boldsymbol{e}_i$ is the unit orientation vector for particle i, and $h(\boldsymbol{r}, \boldsymbol{e}_1, \boldsymbol{e}_2)$ is the pair correlation function. The dielectric constant should not depend on the sample geometry and surroundings, which implies that both $g_{\rm K}$ and h depend on sample details [27]. It is interesting to note the various predictions of 9.18 in the absence of any orientational correlations between particles ($g_{\rm K} = 1$), and with the magnetic equivalent of y being $\frac{1}{3}\chi_{\rm L}$. If $\varepsilon' = 1$ (vacuum surroundings) then 9.18 gives, in the magnetic picture, $\chi/(\chi + 3) = \frac{1}{3}\chi_{\rm L}$, and hence $\chi = \chi_{\rm L}/(1 - \frac{1}{3}\chi_{\rm L}) = \chi_{\rm L}(1 + \frac{1}{3}\chi_{\rm L} + \frac{1}{9}\chi_{\rm L}^2 + \ldots)$. The first and second terms in brackets are exact, while the third is merely of the correct sign. This is the Weiss (or Debye) mean-field model in which the effective field experienced by the particles is $H_{\rm eff} = H + \frac{1}{3}M$, with M determined self-consistently from the Langevin formula (9.11) [34, 35]. The theory also predicts a divergence in χ at $\chi_{\rm L} = 3$, signalling a spontaneous transition to a ferromagnetic state which has not been observed experimentally. In the Onsager-Kirkwood model $\varepsilon' = \varepsilon$ [58, 59] and hence the magnetic equivalent is $\chi(2\chi + 3)/(\chi + 1) = 3\chi_{\rm L}$. This gives for the susceptibility $\chi = \chi_{\rm L}(1 + \frac{1}{3}\chi_{\rm L}^2 - \frac{1}{9}\chi_{\rm L}^2 + \ldots)$; the third term in the brackets is of the wrong sign [60]. Finally, when $\varepsilon' = \infty$, the result is simply $\chi = \chi_{\rm L}$. Nonetheless, this last case provides the most convenient expression for χ given the appropriate virial expansion of h and hence $g_{\rm K}$ [61–64], and it also corresponds directly to the conducting boundary conditions that are most often used in computer simulations. This discussion shows that there are many ways to approach the calculation of χ, and that the results are often complicated and substantially different for a given level of approximation. The conclusion is that the MMF2 approach—and extensions of it—provides a convenient and accurate means of describing the static susceptibility of real ferrofluids based only on knowledge of $\chi_{\rm L}$.

9.5.2 Dynamic Susceptibility

The dynamic initial magnetic susceptibility—or magnetic susceptibility spectrum $\chi(\omega)$—is important for determining the dissipation of heat in ferrofluids subject to AC magnetic fields. The power dissipation is proportional to the square of the imaginary (or out-of-phase) part of the spectrum, $\chi''(\omega)$ [65]. This physical effect is utilised in hyperthermia treatments of tumours [2, 3, 66–68]. In the Brownian relaxation regime (as opposed to the Néel relaxation regime described in Sect. 9.2) the orientational dynamics of a single isolated dipolar particle are described by the Fokker-Planck equation [69, 70]

$$\frac{1}{D_{\rm r}}\frac{\partial W}{\partial t} = \frac{1}{\sin\theta}\frac{\partial}{\partial\theta}\left[\sin\theta\left(\frac{\partial W}{\partial\theta} + \frac{W}{k_{\rm B}T}\frac{\partial U}{\partial\theta}\right)\right] \tag{9.20}$$

where $D_{\rm r} = k_{\rm B}T/\pi\eta\sigma^3$ is the rotational diffusion coefficient, $W(\theta, t)$ is the one-particle probability density of the orientation of the dipole moment, and θ is the angle between the dipole moment and the applied AC field. The dipole-field interaction energy is

$$\frac{U}{k_{\mathrm{B}}T} = -\frac{\mu_0[\boldsymbol{\mu}\cdot\boldsymbol{H}(t)]}{k_{\mathrm{B}}T} = -\alpha(\cos\theta)e^{-i\omega t}. \tag{9.21}$$

The Fokker-Planck equation is easily solved in the weak-field case ($\alpha \to 0$, corresponding to the initial or linear-response regime) to give W, from which the magnetisation response $\boldsymbol{M}(t)$ can be determined. The proportionality between $\boldsymbol{M}(t)$ and $\boldsymbol{H}(t)$ is the frequency-dependent initial susceptibility $\chi(\omega)$. For a single isolated particle, the real part $[\chi'(\omega)]$ and imaginary part $[\chi''(\omega)]$ are given by the familiar Debye expressions

$$\chi'_{\mathrm{D}}(\omega) = \frac{\chi_{\mathrm{L}}}{1+(\omega\tau_{\mathrm{B}})^2} \tag{9.22}$$

$$\chi''_{\mathrm{D}}(\omega) = \frac{\chi_{\mathrm{L}}\omega\tau_{\mathrm{B}}}{1+(\omega\tau_{\mathrm{B}})^2} \tag{9.23}$$

where $\tau_{\mathrm{B}} = 1/2D_{\mathrm{r}}$ is the Brownian rotation time. To take account of interactions between particles, a similar approach to that outlined in Sect. 9.4 is taken. The effective magnetic field felt by a single particle is the sum of the applied external field and the contribution from all of the other particles. At the MMF1 level, this effective field gives an interaction energy equal to [71]

$$\frac{U}{k_{\mathrm{B}}T} = -\frac{\mu_0[\boldsymbol{\mu}\cdot\boldsymbol{H}_{\mathrm{eff}}(t)]}{k_{\mathrm{B}}T} = -\alpha(\cos\theta)e^{-i\omega t}\left[1+\frac{1}{3}\chi_{\mathrm{D}}(\omega)\right]. \tag{9.24}$$

Substituting this interaction energy in to the Fokker-Planck equation gives the result

$$\chi'(\omega) = \chi'_{\mathrm{D}}(\omega) + \frac{1}{3}\left\{\left[\chi'_{\mathrm{D}}(\omega)\right]^2 - \left[\chi''_{\mathrm{D}}(\omega)\right]^2\right\} \tag{9.25}$$

$$\chi''(\omega) = \chi''_{\mathrm{D}}(\omega)\left[1+\frac{2}{3}\chi'_{\mathrm{D}}(\omega)\right]. \tag{9.26}$$

Figure 9.4b shows magnetic susceptibility spectra for dipolar WCA particles at $k_{\mathrm{B}}T/\epsilon = 1$ and fixed concentration $\varphi = 0.105$, from Brownian dynamics simulations and the dynamical MMF1 theory [50, 72]. Two sets of data are shown: one with $\lambda = 1.5$ (or $\chi_{\mathrm{L}} = 1.26$) which is in the regime where the MMF1-level theory for the zero-frequency susceptibility $\chi'(0)$ is accurate; and the other with $\lambda = 3.0$ (or $\chi_{\mathrm{L}} = 2.51$) which is beyond the regime where MMF1 theory is expected to work. Firstly, the simulation results show that the peak frequency decreases with increasing dipolar interaction strength. This is due to the growth of chain-like correlations between particles, and the associated 'slowing down' of the rotational motion of small clusters. Secondly, the simulation results with $\chi_{\mathrm{L}} = 1.26$ are rather well described by the dynamical MMF1 theory, which gets right both the zero-frequency susceptibility $\chi'(0)$ and the position of the peak in $\chi''(\omega)$. Finally, there are substantial deviations between simulation and theory in the strong-interaction case ($\chi_{\mathrm{L}} = 2.51$) due to the truncation of the effective-field term in 9.24. In principle,

there should be additional terms akin to those in 9.12 and 9.17. This is an ongoing problem. As tested against experimental data for real, polydisperse ferrofluids, the dynamical MMF1 theory does rather well [71, 73].

9.6 Thermodynamic Functions

9.6.1 Free Energy and Equation of State

The thermodynamic properties of colloidal suspensions are of huge interest and importance. Central to all equilibrium thermodynamics is the Helmholtz free energy F. If F is known as a function of concentration and temperature, then all other thermodynamic functions can be determined using standard relations. It can also be used to examine inhomogeneous systems, within the bounds of the local-density approximation: see Sect. 9.7 for examples. There are many ways of estimating F, but a recently proposed route has proven to be particularly simple and effective—the so-called logarithmic free-energy theory. The standard virial expansion of F is [27]

$$F = F_{\rm id} + Nk_{\rm B}T \sum_{n=1}^{\infty} \frac{1}{n} B_{n+1} \varphi^n \tag{9.27}$$

where B_n is the nth virial coefficient. For dipolar particles, and accounting for the possibility of applying an external magnetic field, the expressions for the second and third virial coefficients are as follows [74].

$$B_2 = -\frac{1}{2} \int {\rm d}\boldsymbol{r}_{12} \langle f_{12} \rangle \tag{9.28}$$

$$B_3 = -\frac{1}{3} \int {\rm d}\boldsymbol{r}_{12} \int {\rm d}\boldsymbol{r}_{13} \langle f_{12} f_{23} f_{13} \rangle + \int {\rm d}\boldsymbol{r}_{12} \int {\rm d}\boldsymbol{r}_{13} \left[\langle f_{12} \rangle \langle f_{13} \rangle - \langle f_{12} f_{13} \rangle \right] \tag{9.29}$$

$f_{ij} = [\exp(-u_{ij}/k_{\rm B}T) - 1]$ is the Mayer f-function between particles i and j, where u_{ij} is the total pair potential. The angled brackets denote an orientational average weighted by the Boltzmann factor involving the particle-field interaction energies for each of the particles, e.g.,

$$\langle f_{12} \rangle = \left(\frac{\alpha}{4\pi \sinh \alpha} \right)^2 \int {\rm d}\boldsymbol{e}_1 \int {\rm d}\boldsymbol{e}_2 f_{12} \exp\left(\alpha \cos\theta_1 + \alpha \cos\theta_2 \right) \tag{9.30}$$

where θ is the angle between $\boldsymbol{e}$ and the applied field. The expression for B_2 is standard, but the expression for B_3 contains an extra (second) term which is not often included in textbook derivations. If the external field is zero or infinity (meaning

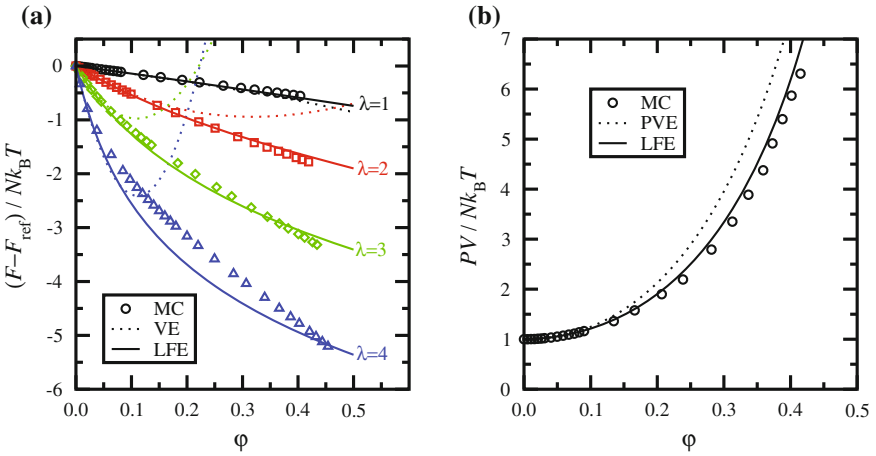

Fig. 9.5 **a** The difference in Helmholtz free energy between that of the dipolar hard-sphere model with dipolar coupling constant λ and that of the hard-sphere model ($\lambda = 0$). The points are from Monte Carlo simulations (MC), the dotted lines are from the original virial expansion (VE), and the solid lines are from the logarithmic free-energy theory (LFE). **b** The compressibility factor PV/Nk_BT for the dipolar hard-sphere model in an applied field, with $\lambda = 1$ and $\alpha = 5$. The points are from Monte Carlo simulations (MC), the dotted line is from the perturbed virial expansion (PVE), and the solid line is from the logarithmic free-energy theory (LFE)

$\alpha = 0, \infty$) then the 'fluctuation' term in square brackets disappears. But for all other finite field strengths, this term is non-zero, and typically represents about 10% of the total value of B_3. From the theoretical point of view, the calculation of virial coefficients is arduous. In the case of dipolar particles in zero field, it is possible to determine B_2 and B_3 rather accurately as expansions in powers of λ, up to about $\lambda \simeq 4$ [75]. In the presence of a field, these expansions involve additional complicated functions of α, and the range is currently limited to $\lambda \leq 2$. The validity and range of application of these expansions have been tested using numerical data from Mayer-sampling Monte Carlo calculations [74, 75].

The virial expansion is slow to converge, if at all. Given that higher order virial coefficients are rarely available, one way of extending the virial-expansion approach is to write a so-called perturbed virial expansion in the form

$$F = F_{\text{ref}} + Nk_BT \sum_{n=1}^{\infty} \frac{1}{n} \Delta B_{n+1} \varphi^n \tag{9.31}$$

where F_{ref} is the free energy of a well-characterised reference system such as the hard-sphere fluid, and ΔB_n is the difference in virial coefficients between the system of interest and the reference system. This follows closely an idea by Nezbeda and co-workers who wrote a similar expression for the pressure [76–78]. Going one step further, remembering that F is proportional to the logarithm of the partition function,

the logarithm can be 'put back in' by writing [74, 75]

$$F = F_{\rm ref} - Nk_{\rm B}T \ln\left(1 + \sum_{n=1}^{\infty} \frac{1}{n} I_{n+1} \varphi^n\right) \tag{9.32}$$

where the coefficients I_n must reproduce the perturbed virial expansion as a Maclaurin series in φ. The first two coefficients are $I_2 = -\Delta B_2$ and $I_3 = -\Delta B_3 + \Delta B_2^2$. The benefit of this logarithmic free-energy expression is that an expansion of the logarithm generates terms of all orders in φ, and so higher-order terms in the virial expansion are generated, albeit approximately. For the dipolar hard-sphere model, 9.27, 9.31, and 9.32 have been tested critically against the results of Monte Carlo simulations [75]. Figure 9.5a shows a comparison between the simulation results and the predictions of the virial expansion and the logarithmic free-energy theory with B_2, B_3, and B_4 represented as polynomial expansions. Results are shown over a broad range of concentration $0 \leq \varphi \leq 0.5$, and with dipolar coupling constants $\lambda = 1$–4. With $\lambda = 1$–3, the logarithmic free-energy theory is in excellent agreement with simulation results. The original virial expansion is only accurate at very low concentrations. With $\lambda = 4$, neither of the theories is particularly good, although this is at the onset of the chaining regime (see Sect. 9.3) and so any theory limited to two-, three-, or four-particle correlations is always going to struggle. The same methodology can be applied to systems in the presence of a field. Figure 9.5b shows the compressibility factor $PV/Nk_{\rm B}T$, with the pressure given by $P = -(\partial F/\partial V)_T$. The predictions of the perturbed virial expansion and the logarithmic free-energy theory are compared to the results from Monte Carlo simulations with $\lambda = 1$ and $\alpha = 5$ [74]. The same expressions for the second and third virial coefficients are used in the two theories. The agreement with simulation clearly shows the substantial benefit of the logarithmic formulation.

The logarithmic free-energy approach has been applied successfully to osmotic equations of state measured in ultracentrifugation experiments [75, 79, 80] and to the Stockmayer fluid [81]. Since the virial coefficients and the free energy are known as functions of the applied field, it is possible to determine the magnetisation curves, although the approach is not as good as the MMF2 theory [74]. The thermodynamic theory has also been used to great effect in the analysis of sedimentation profiles; this is discussed in Sect. 9.7.

9.6.2 Phase Diagram

The phase diagram of strongly interacting dipolar particles is a vast topic in its own right. In 1970 de Gennes and Pincus predicted that the phase diagram of purely dipolar particles (with no additional attractive interactions) would be very similar to that of a simple atomic fluid [82]. The argument put forward was that the leading-order term in the orientationally averaged potential of mean force is attractive and propor-

tional to $1/r^6$. In combination with a simple short-range repulsive interaction, this would indeed give rise to distinct liquid and vapour phases. A more detailed analysis suggests that the vapour-liquid critical point should belong to the Ising universality class [83]. All standard approaches to the vapour-liquid transition—thermodynamic perturbation theory, integral equations, logarithmic free-energy theory, etc.—predict a vapour-liquid critical point in the region of $\lambda = 3$–4. As discussed in Sect. 9.3, this is roughly where particle clustering begins. It appears from computer simulations that cluster formation does indeed interfere with phase separation, either through chaining [84, 85] or ring formation [86]. In either scenario, computer simulations are somewhat limited, in that the system sizes currently accessible are not very large as compared to the likely density-density correlation lengths between clusters. If there were a condensation transition of chains or rings driven by weak cluster-cluster interactions, then simulations of relatively small systems would not be able to accommodate the density fluctuations associated with a nearby critical point. From the practical point of view, a transition can be brought in to existence with very small perturbations to the system, e.g., contributions from higher multipole moments [87], added non-polar particles [88], and very weak additional isotropic interactions [89–91]. To sum up, on the basis of computer simulation results, it would appear that there is no vapour-liquid phase transition driven purely by dipolar interactions. Theories can always be constructed that mirror the current simulation results [9, 92, 93], but it remains an open theoretical challenge to prove that a dipole-driven transition does not exist, or if it does exist, then to predict under what physical conditions it can be observed.

9.7 Sedimentation

In this final section, the influence of thermodynamics on structure will be examined in the context of sedimentation profiles. Under certain conditions that are usually met in normal colloidal suspensions [94–96], analytical (ultra) centrifugation experiments provide a direct link between the concentration profile and the osmotic equation of state, and hence the thermodynamics. As mentioned in Sect. 9.6, such experiments on ferrofluids have provided equations of state that could be compared directly with theory and simulation [79, 80]. The key relation linking the gradient diffusion and sedimentation of particles in suspension is

$$-G = \frac{1}{k_{\mathrm{B}}T}\left(\frac{\partial\mu}{\partial\varphi}\right)\frac{\mathrm{d}\varphi}{\mathrm{d}z} \tag{9.33}$$

where G^{-1} is the usual gravitational length (a function of the particle size, the particle and liquid mass densities, and the temperature), z is in the direction of increasing gravitational potential, and $\mu = (\partial F/\partial N)$ is the chemical potential (not to be confused with the dipole moment). This expression—corresponding to the local-density

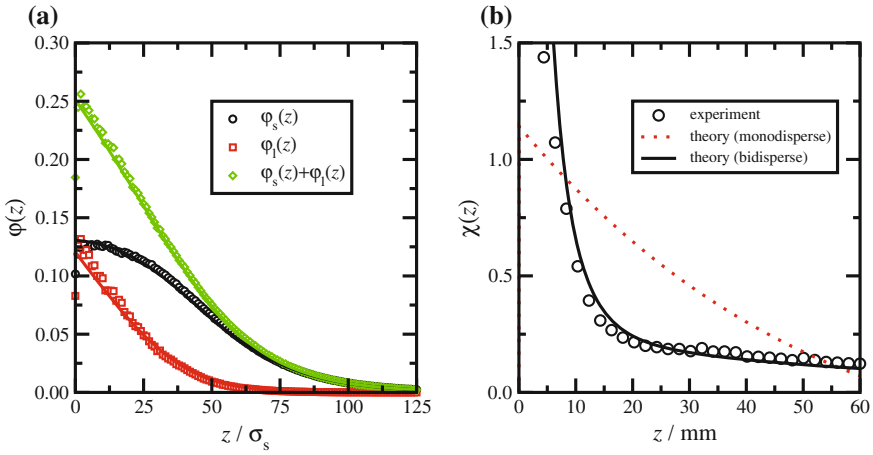

Fig. 9.6 **a** Volume-fraction profiles for small particles $\varphi_s(z)$ and large particles $\varphi_l(z)$, and the total volume-fraction profile $\varphi_s(z) + \varphi_l(z)$, in a bidisperse dipolar hard-sphere model—see text for parameters. The points are from Monte Carlo simulations and the lines are from theory. **b** Local susceptibility profile in a 60 mm section of a real polydisperse ferrofluid (points) with theoretical fits using a monodisperse model (dotted red line) and a bidisperse model (solid black line)

approximation—is only reliable if the gravitational length is large compared to the particle size, so that particle layering is absent. From the theoretical standpoint, the chemical potential can be obtained from the logarithmic free-energy theory from Sect. 9.6, and then 9.33 can be integrated to yield the concentration profile $\varphi(z)$. Experimentally, the concentration profile in ferrofluids can be measured using either the optical transmission [79, 80] or the local susceptibility [97]; in the latter case, $\varphi(z)$ can be obtained from $\chi(z)$ using a relation such as 9.16.

In recent work, the theoretical approach was validated against precise Monte Carlo simulation results, and applied to the analysis of experimental measurements [98]. Figure 9.6a shows a comparison of concentration profiles in a bidisperse ferrofluid consisting of a mixture of 'small' (s) particles with diameter σ_s, dipolar coupling constant $\lambda_s = 1$, and gravitational length $G_s^{-1} = 20\sigma_s$, and 'large' (l) particles with $\sigma_l = 1.25\sigma_s$, $\lambda_l = 1.95$, and $G_l^{-1} = 10.2\sigma_s$. The surface concentrations were $n_s\sigma_s^2 = 13.4$ and $n_l\sigma_s^2 = 2.9$, respectively. Equation 9.33 can easily be extended to mixtures of particles, and using a suitably generalised logarithmic free-energy theory with B_2 and B_3 as inputs, the predicted concentration profiles are in excellent agreement with those measured in simulations. Figure 9.6b shows the initial magnetic susceptibility profile for a real polydisperse ferrofluid, along with best fits with either a monodisperse or bidisperse model for the fluid. The fit parameters are the magnetic-core diameters and the relative concentrations of small and large particles; the overall content of magnetic material is fixed. The link between $\varphi(z)$ and $\chi(z)$ is made at the MMF2 level. It is easy to explain why the bidisperse model gives the correct sharp rise in $\chi(z)$ near the bottom of the profile. Figure 9.6a shows that large particles are localised near the bottom of the sample, and the large particles

have larger susceptibility by virtue of the larger dipole moment. Hence, the total susceptibility profile in a bidisperse system shows a sharper drop with increasing height than does a monodisperse system. In general, it is rather difficult to determine the particle-size distribution $p(x)$ without making some assumptions about the precise mathematical form, but even a two-component model is sufficient to capture the major effects of polydispersity [26, 99, 100].

9.8 Conclusions

In this contribution, a very brief and necessarily selective survey is made of theoretical and computational work on the structural, magnetic, thermodynamic, and sedimentation properties of ferrofluids carried out as a collaboration between groups in Edinburgh and Ekaterinburg. In all cases, statistical-mechanical theory is combined with simple models of colloidal magnetic nanoparticles to give insights on the links between microscopic and macroscopic properties of fluids governed by strong dipole-dipole interactions. For well-defined models, simulations provide critical and well-controlled tests of theory. Favourable comparisons with experiments show that the models adopted provide faithful descriptions of reality.

Not only are the theoretical results applicable to ferrofluids, but with suitable extensions, they could apply to a broader class of molecular materials with electric dipole moments. The theoretical methods can also be applied to suspensions of magnetic particles with non-spherical magnetic cores and/or anisotropic interactions [101], and this is a rapidly growing area in the field of magnetic fluids. Magnetic particles with rod-like [102], ellipsoidal [103], and even cubic [104] shapes can all be synthesised. The effective interactions between these types of particles are substantially different from those given by 9.1–9.4, and are not so easily expressed. Nonetheless, computational studies on elongated magnetic particles [101] and magnetic cubes [105] predict highly non-trivial ground-state structures. Anisotropy in the short-range interactions can alter the ground-state conformations of particles at or close to contact. For example, elongating the hard core of a particle parallel to the dipole direction disfavours the nose-to-tail parallel conformation of two particles, and favours the side-by-side antiparallel ($\uparrow\downarrow$) arrangement [106]. Anisotropy can also be induced in spherical particles, where the distribution of magnetic material is non-uniform: examples include capped colloids [107] and magnetic Janus particles [108]. Clearly, there are many possibilities for making functional magnetic fluids, and there is plenty of work ahead to understand these fascinating materials.

Acknowledgements First and foremost, I would like to acknowledge the collaboration and friendship of the Ekaterinburg group, and in particular, Professors Alexey Ivanov, Ekaterina Elfimova, and Sofia Kantorovich. Their energy, enthusiasm, and expertise are boundless, and I'm fortunate to participate in their scientific programmes. Much of the work summarised herein was carried out—or at least initiated—during collaborative visits to Edinburgh and Ekaterinburg. Many of those visits were supported by the Ural Federal University, and their continued support of this work is gratefully acknowledged.

References

1. R.E. Rosensweig, *Ferrohydrodynamics* (Dover Publications Inc, New York, 1998)
2. Q.A. Pankhurst, J. Connolly, S.K. Jones, J. Dobson, J. Phys. D Appl. Phys. **36**, R167 (2003)
3. Q.A. Pankhurst, N.T.K. Thanh, S.K. Jones, J. Dobson, J. Phys. D Appl. Phys. **42**, 224001 (2009)
4. P.I.C. Teixeira, J.M. Tavares, M.M. Telo da Gama, J. Phys. Condens. Matter **12**, R411 (2000)
5. J.D. Jackson, *Classical Electrodynamics*, 3rd edn. (Wiley, New York, 1999)
6. B.F. Edwards, D.M. Riffe, J.Y. Ji, W.A. Booth, Am. J. Phys. **85**, 130 (2017)
7. W.H. Stockmayer, J. Chem. Phys. **9**, 398 (1941)
8. I. Jacobs, C. Bean, Phys. Rev. **100**, 1060 (1955)
9. T. Tlusty, S.A. Safran, Science **290**, 1328 (2000)
10. A. Zilman, T. Tlusty, S.A. Safran, J. Phys. Condens. Matter **15**, S57 (2003)
11. K. Butter, P.H.H. Bomans, P.M. Frederik, G.J. Vroege, A.P. Philipse, Nat. Mater. **2**, 88 (2003)
12. K. Butter, P.H. Bomans, P.M. Frederik, G.J. Vroege, A.P. Philipse, J. Phys. Condens. Matter **15**, S1451 (2003)
13. M. Klokkenburg, R.P.A. Dullens, W.K. Kegel, B.H. Erné, A.P. Philipse, Phys. Rev. Lett. **96**, 037203 (2006)
14. M. Klokkenburg, B.H. Erné, J.D. Meeldijk, A. Wiedenmann, A.V. Petushkov, R.P.A. Dullens, A.P. Philipse, Phys. Rev. Lett. **97**, 185702 (2006)
15. J.J. Weis, D. Levesque, Phys. Rev. Lett. **71**, 2729 (1993)
16. D. Levesque, J.J. Weis, Phys. Rev. E **49**, 5131 (1994)
17. P.J. Camp, G.N. Patey, Phys. Rev. E **62**, 5403 (2000)
18. L. Rovigatti, J. Russo, F. Sciortino, Soft Matter **8**, 6310 (2012)
19. D. Wei, G.N. Patey, Phys. Rev. Lett. **68**, 2043 (1992)
20. D. Wei, G.N. Patey, Phys. Rev. A **46**, 7783 (1992)
21. J.J. Weis, D. Levesque, Phys. Rev. E **48**, 3728 (1993)
22. J.J. Weis, J. Chem. Phys. **123**, 044503 (2005)
23. J.J. Weis, D. Levesque, J. Chem. Phys. **125**, 034504 (2006)
24. M.A. Pounds, P.A. Madden, J. Chem. Phys. **126**, 104506 (2007)
25. E.A. Elfimova, A.O. Ivanov, P.J. Camp, J. Chem. Phys. **136**, 194502 (2012)
26. Yu.E. Nekhoroshkova, O.A. Goldina, P.J. Camp, E.A. Elfimova, A.O. Ivanov, J. Exp. Theor. Phys. **118**, 442 (2014)
27. J.P. Hansen, I.R. McDonald, *Theory of Simple Liquids*, 3rd edn. (Academic Press, London, 2006)
28. D.J. Cebula, S.W. Charles, J. Popplewell, Colloid. Polym. Sci. **259**, 395 (1981)
29. F. Gazeau, E. Dubois, J.C. Bacri, F. Boué, A. Cebers, R. Perzynski, Phys. Rev. E **65**, 031403 (2002)
30. G. Mériguet, F. Cousin, E. Dubois, F. Boué, A. Cebers, B. Farago, R. Perzynski, J. Phys. Chem. B **110**, 4378 (2006)
31. J. Wagner, B. Fischer, T. Autenrieth, J. Chem. Phys. **124**, 114901 (2006)
32. A. Wiedenmann, U. Keiderling, M. Meissner, D. Wallacher, R. Gähler, R.P. May, S. Preévost, M. Klokkenburg, B.H. Erné, J. Kohlbrecher, Phys. Rev. B **77**, 184417 (2008)
33. P. Langevin, J. Phys. Theor. Appl. **4**, 678 (1905)
34. P. Weiss, J. Phys. Theor. Appl. **6**, 661 (1907)
35. A. Tsebers, Magnetohydrodynamics **18**, 137 (1982)
36. M.S. Wertheim, J. Chem. Phys. **55**, 4291 (1971)
37. K.I. Morozov, A.V. Lebedev, J. Mag. Mag. Mater. **85**, 51 (1990)
38. Yu.A. Buyevich, A.O. Ivanov, Physica A **190**, 276 (1992)
39. A.O. Ivanov, Magnetohydrodynamics **28**, 353 (1992)
40. A.F. Pshenichnikov, V.V. Mekhonoshin, A.V. Lebedev, J. Mag. Mag. Mater. **161**, 94 (1996)
41. A.O. Ivanov, O.B. Kuznetsova, Phys. Rev. E **64**, 041405 (2001)
42. B. Huke, M. Lücke, Phys. Rev. E **62**, 6875 (2000)

43. B. Huke, M. Lücke, Phys. Rev. E **67**, 051403 (2003)
44. B. Huke, M. Lücke, Rep. Prog. Phys. **67**, 1731 (2004)
45. I. Szalai, S. Dietrich, J. Phys.: Condens. Matter **20**, 204122 (2008)
46. I. Szalai, S. Dietrich, J. Phys. Condens. Matter **23**, 326004 (2011)
47. I. Szalai, S. Nagy, S. Dietrich, J. Phys. Condens. Matter **25**, 465108 (2013)
48. A.O. Ivanov, S.S. Kantorovich, E.N. Reznikov, C. Holm, A.F. Pshenichnikov, A.V. Lebedev, A. Chremos, P.J. Camp, Phys. Rev. E **75**, 061405 (2007)
49. A.O. Ivanov, S.S. Kantorovich, E.N. Reznikov, C. Holm, A.F. Pshenichnikov, A.V. Lebedev, A. Chremos, P.J. Camp, Magnetohydrodynamics **43**, 393 (2007)
50. J.O. Sindt, P.J. Camp, S.S. Kantorovich, E.A. Elfimova, A.O. Ivanov, Phys. Rev. E **93**, 063117 (2016)
51. P.J. Camp, E.A. Elfimova, A.O. Ivanov, J. Phys. Condens. Matter **26**, 456002 (2014)
52. O.A. Goldina, A.V. Lebedev, A.O. Ivanov, E.A. Elfimova, Magnetohydrodynamics **52**, 35 (2016)
53. A.Y. Solovyova, O.A. Goldina, A.O. Ivanov, A.V. Lebedev, E.A. Elfimova, J. Chem. Phys. **145**, 084909 (2016)
54. S. Kantorovich, A.O. Ivanov, L. Rovigatti, J.M. Tavares, F. Sciortino, Phys. Rev. Lett. **110**, 148306 (2013)
55. H. Fröhlich, *Theory of Dielectrics: Dielectric Constant and Dielectric Loss*, 2nd edn. (Clarendon Press, Oxford, 1987)
56. U.M. Titulaer, J.M. Deutch, J. Chem. Phys. **60**, 1502 (1974)
57. S.W. de Leeuw, J.W. Perram, E.R. Smith, Proc. R. Soc. Lond. A **373**, 27 (1980)
58. L. Onsager, J. Am. Chem. Soc. **58**, 1486 (1936)
59. J.G. Kirkwood, J. Chem. Phys. **7**, 911 (1939)
60. D.W. Jepsen, J. Chem. Phys. **44**, 774 (1966)
61. A.D. Buckingham, C.G. Joslin, Mol. Phys. **40**, 1513 (1980)
62. C.G. Joslin, Mol. Phys. **42**, 1507 (1981)
63. C. Joslin, S. Goldman, Mol. Phys. **79**, 499 (1993)
64. K.I. Morozov, J. Chem. Phys. **126**, 194506 (2007)
65. R.E. Rosensweig, J. Magn. Magn. Mater. **252**, 370 (2002)
66. R. Hergt, R. Hiergeist, I. Hilger, W. Kaiser, Y. Lapatnikov, S. Margel, U. Richter, J. Magn. Magn. Mater. **270**, 345 (2004)
67. F. Sonvico, S. Mornet, S. Vasseur, C. Dubernet, D. Jaillard, J. Degrouard, J. Hoebeke, E. Duguet, P. Colombo, P. Couvreur, Bioconjug. Chem. **16**, 1181 (2005)
68. J.P. Fortin, C. Wilhelm, J. Servais, C. Ménager, J.C. Bacri, F. Gazeau, J. Am. Chem. Soc. **129**, 2628 (2007)
69. W.F. Brown Jr., J. Appl. Phys. **34**, 1319 (1963)
70. W.F. Brown Jr., I.E.E.E. Trans, Magn. **15**, 1196 (1979)
71. A.O. Ivanov, V.S. Zverev, S.S. Kantorovich, Soft Matter **12**, 3507 (2016)
72. A.O. Ivanov, S.S. Kantorovich, E.A. Elfimova, V.S. Zverev, J.O. Sindt, P.J. Camp, J. Mag. Magn. Mater. **431**, 141 (2017)
73. A.O. Ivanov, S.S. Kantorovich, V.S. Zverev, E.A. Elfimova, A.V. Lebedev, A.F. Pshenichnikov, Phys. Chem. Chem. Phys. **18**, 18342 (2016)
74. E.A. Elfimova, A.O. Ivanov, P.J. Camp, Phys. Rev. E **88**, 042310 (2013)
75. E.A. Elfimova, A.O. Ivanov, P.J. Camp, Phys. Rev. E **86**, 021126 (2012)
76. K. Aim, I. Nezbeda, Fluid Phase Equil. **12**, 235 (1983)
77. I. Nezbeda, W.R. Smith, Fluid Ph. Equilib. **216**, 183 (2004)
78. J. Krejči, I. Nezbeda, Fluid Ph. Equilib. **314**, 156 (2012)
79. B. Luigjes, D.M.E. Thies-Weesie, A.P. Philipse, B.H. Erné, J. Phys. Condens. Matter **24**, 245103 (2012)
80. B. Luigjes, D.M.E. Thies-Weesie, B.H. Erné, A.P. Philipse, J. Phys. Condens. Matter **24**, 245104 (2012)
81. E.A. Elfimova, A.O. Ivanov, J.O. Sindt, P.J. Camp, Mol. Phys. **113**, 3717 (2015)
82. P.G. de Gennes, P.A. Pincus, Phys. Kondens. Materie **11**, 189 (1970)

83. G. Stell, Phys. Rev. Lett. **32**, 286 (1974)
84. M.E. van Leeuwen, B. Smit, Phys. Rev. Lett. **71**, 3991 (1993)
85. J.O. Sindt, P.J. Camp, J. Chem. Phys. **143**, 024501 (2015)
86. L. Rovigatti, J. Russo, F. Sciortino, Phys. Rev. Lett. **107**, 237801 (2011)
87. G. Ganzenmüller, P.J. Camp, J. Chem. Phys. **127**, 154504 (2007)
88. N.G. Almarza, E. Lomba, C. Martín, A. Gallardo, J. Chem. Phys. **129**, 234504 (2008)
89. A.O. Ivanov, S.S. Kantorovich, P.J. Camp, Phys. Rev. E **77**, 013501 (2008)
90. Y.V. Kalyuzhnyi, I.A. Protsykevytch, G. Ganzenmüller, P.J. Camp, Europhys. Lett. **84**, 26001 (2008)
91. G. Ganzenmüller, G.N. Patey, P.J. Camp, Mol. Phys. **107**, 403 (2009)
92. R.P. Sear, Phys. Rev. Lett. **76**, 2310 (1996)
93. R. van Roij, Phys. Rev. Lett. **76**, 3348 (1996)
94. R. Piazza, S. Buzzaccaro, E. Secchi, A. Parola, Soft Matter **8**, 7112 (2012)
95. R. Piazza, S. Buzzaccaro, E. Secchi, J. Phys. Condens. Matter **24**, 284109 (2012)
96. R. Piazza, Rep. Prog. Phys. **77**, 056602 (2014)
97. A.F. Pshenichnikov, Instrum. Exp. Tech. **50**, 509 (2007)
98. E.A. Elfimova, A.O. Ivanov, E.V. Lakhtina, A.F. Pshenichnikov, P.J. Camp, Soft Matter **12**, 4103 (2016)
99. A.O. Ivanov, S.S. Kantorovich, Phys. Rev. E **70**, 021401 (2004)
100. E. Novak, E. Minina, E. Pyanzina, S. Kantorovich, A. Ivanov, J. Chem. Phys. **139**, 224905 (2013)
101. S. Kantorovich, E. Pyanzina, F. Sciortino, Soft Matter **9**, 6594 (2013)
102. T. Klein, A. Laptev, A. Günther, P. Bender, A. Tschöpe, R. Birringer, J. Appl. Phys. **106**, 114301 (2009)
103. S. Sacanna, L. Rossi, B.W.M. Kuipers, A.P. Philipse, Langmuir **22**, 1822 (2006)
104. L. Rossi, S. Sacanna, W.T.M. Irvine, P.M. Chaikin, D.J. Pine, A.P. Philipse, Soft Matter **7**, 4139 (2011)
105. J.G. Donaldson, S.S. Kantorovich, Nanoscale **7**, 3217 (2015)
106. S.C. McGrother, G. Jackson, Phys. Rev. Lett. **76**, 4183 (1996)
107. L. Baraban, D. Makarov, M. Albrecht, N. Rivier, P. Leiderer, A. Erbe, Phys. Rev. E **77**, 031407 (2008)
108. N. Zhao, M. Gao, Adv. Mater. **21**, 184 (2009)

Chapter 10
Magnetic Fluids: Structural Aspects by Scattering Techniques

V. I. Petrenko, A. V. Nagornyi, I. V. Gapon, L. Vekas, V. M. Garamus, L. Almasy, A. V. Feoktystov and M. V. Avdeev

Abstract The understanding of stabilization mechanisms for ferrofluids (which are presented as fine dispersions of magnetic nanoparticles coated with surfactants) is an important favorable circumstance in the synthesis of highly stable magnetic colloids with specific properties. The presented work reviews principal results that were obtained in thorough investigations of ferrofluid's stability regarding changes in the structure at nanoscale under various conditions, including the determination and analysis of the agglomeration regimes in biocompatible ferrofluids for biomedical applications. The structural features of the ferrocolloids and concomitant surfactant solutions were revealed and further analyzed principally relying on

V. I. Petrenko (✉) · A. V. Nagornyi · I. V. Gapon · M. V. Avdeev
Frank Laboratory of Neutron Physics, Joint Institute for Nuclear Research, Joliot-Curie 6, 141980 Dubna, Moscow Reg., Russia
e-mail: vip@nf.jinr.ru

V. I. Petrenko · A. V. Nagornyi · I. V. Gapon
Faculty of Physics, Taras Shevchenko National University of Kyiv, Kiev, Ukraine

L. Vekas
Center for Fundamental and Advanced Technical Research, Romanian Academy-Timisoara Branch, Timisoara, Romania

V. M. Garamus
Helmholtz-Zentrum Geesthacht: Centre for Materials and Coastal Research, Geesthacht, Germany

L. Almasy
Neutron Spectroscopy Department, Wigner Research Centre for Physics, Budapest, Hungary

L. Almasy
State Key Laboratory Cultivation Base for Nonmetal Composites and Functional Materials, South-West University of Science and Technology, Mianyang, China

A. V. Feoktystov
Jülich Centre for Neutron Science (JCNS), Heinz Maier-Leibnitz Zentrum (MLZ), Garching, Germany

L. A. Bulavin and A. V. Chalyi (eds.), *Modern Problems of Molecular Physics*, Springer Proceedings in Physics 197, https://doi.org/10.1007/978-3-319-61109-9_10

the data of Small-Angle Neutron Scattering (SANS). Thereby, for magnetic fluids prepared on the basis of nonpolar liquids (benzene, decalin) with magnetite nanoparticles covered by a single-layer shell of monocarboxylic acids, the studying of the effect of surfactant excess showed a tendency to a significant enhancement of the effective attraction between free (non-adsorbed) acid molecules. This explains the sharp and sudden loss of a ferrofluid's stability that occurs because of the liquid crystal transition when exceeding some critical concentration of an acid. This transition depends strongly on an interparticle solvent-acid interaction and peculiarity of the different critical concentrations is for different solvents. For an aqueous ferrofluid (nanomagnetite stabilized with a double-layered shell of sodium oleate (SO)) that is used as a precursor for a biocompatible modification with polyethylene glycol (PEG), the fraction of micelles of non-adsorbed surfactant and its change under modification were found by SANS. The comparison with another kinds of water-based ferrocolloids showed the different rate of surfactant adsorption on magnetite particles surface depending on the surfactant type. The aggregate reorganization and its growth in the ferrofluid after 'PEGylation' were observed. In order to illuminate the possible influence of the micelle formation with free surfactants on this process in the presence of polymer, the SANS study was performed on mixed SO/PEG aqueous solutions. SANS results revealed drastic morphological and interacting changes of micelles due to addition of PEG. In particular, it was concluded the screening of the micelle interaction due to the formation of an effective PEG shell around micelles at high (about 10 vol%) concentration of the polymer.

10.1 Introduction

Ferrofluids or magnetic fluids (MFs) are colloidal solutions of magnetic nanoparticles which size is about 10 nm. Such size provides sedimentation stability of the solution and also ensures single-domain state of magnetic nanoparticles which determines its superparamagnetic behavior. The main feature of MFs is combination of normal liquid behavior with a possibility of magnetic control of their flow. Structural investigations of ferrofluids are of current interest from fundamental as well as from practical points of view [1–3]. Magnetic fluids must be stabilized to avoid an aggregation between the nanoparticles due to strong attraction including the van der Waals and 'dipole–dipole' magnetic interactions. Surfactant layers which are adsorbed on the surface of magnetic nanoparticles are often used as steric stabilizator to increase minimal possible distance between magnetic nanoparticles and thus decreasing attraction.

In spite of a colloidal nature of ferrofluids, their property of preserving structural stability from an aggregation is an indispensable condition for possibility of the application. It is well known, a colloidal stability is achieved reaching the balance between different internal interactions, attractive or repulsive type, and thermal motion. This statement can be clearly explained addressing to the terms of the

energy balance, if the energy barrier, which can be determined accounting all interaction in the system, is exceeded by average thermal energy, the aggregation and sedimentation will dominate over the segregation into single particles. So, the stability can be considered as a measure of the ability of magnetic nanoparticles to be maintained in suspended state in the bulk of fluid for a long period of time. One of the most interesting properties of the surfactants lies in their ability to turn the stability of colloids. As was shown [4], it is possible to reach different stability regimes using the same colloidal dispersions just by changing the surfactant concentration. Independently of the sign of both the surfactant and the surface, the destabilization of the system consistently takes place above certain surfactant concentration due to a depletion effect from non-adsorbed micelles [4].

In spite of the fact that a coverage of ferrofluid technical application has become very extensive since long time, here is not yet any easy way to disperse the magnetic nanoparticles in a highly polar carrier, like water, while avoiding agglomeration [5]. A strong interaction of surfactants with water is still the main problem, this effect is competitive with the adsorption processes on the magnetic nanoparticles surface. At present, several ways to stabilize water-based ferrocolloids are known, but in the case of the biological media or even bio-mimicking media, there is not any possibility now to prevent agglomeration completely. Electrostatic and steric as well as combined stabilization layers can develop. It has been demonstrated that neither steric nor electrostatic effects alone can provide sufficient stability under physiological conditions [6]. In biomedical context, an agglomeration has side effects related to the difficult elimination of magnetic nanoparticles from organisms, such as the possible appearance of blood clots, as well as the reduction in the therapeutic efficiency. In view of the foregoing, any knowledge about the features of the agglomeration process in magnetic fluids is a crucial point for their development in biomedical applications. In this regard, the important goal is a reliable diagnostics of agglomeration and determination of the aggregation regimes and their control in biocompatible magnetic fluids.

Very often, due to analytical or technological reasons, the magnetic colloids need to be diluted. The question arises to what extent the colloidal stability is affected by the dilution process. Thus, the effect of dilution on the stability of a toluene-based ferrofluid containing cobalt particles has been studied [7]. Prior to dilution the colloid was found to have permanent sustainability from sedimentation under gravity, and only a small amount of aggregation was induced applying an uniform magnetic field. On dilution the ferrofluid was observed to lose the stability by reason of the assembling of particles into large aggregates. This problem was also investigated for magnetic colloids with particular compositions and dilution ratios [8]. The loss of colloidal stability was experimentally observed during dilution by increasing the content of polar carrier in magnetic colloids stabilized with double layer surfactants. The explanation for this behavior is the osmotically driven loss of the magnetic nanoparticles' hydrophilicity, due to the depletion of the outer surfactant layer.

In MFs based on low-polarity solvents, the presence of just single layers of surfactants leads to an increase in the average distance between nanoparticles and,

correspondingly, the weakening of magnetic 'dipole–dipole' attraction. Under these conditions, aggregation stability of the MF is determined to a great extent by the interaction between surfactant and solvent; therefore, one of the most important factors affecting on ferrocolloid stability is the concentration of surfactant molecules in the solution. In practice, there is an optimal ratio of the contents of magnetic nanoparticles and surfactant, a deviation from which violates stability of the MF [2, 9–11]. Thus, for example, an improvement of the stability of the colloidal solution at 14% oleic acid volume content, and deterioration at 20% was observed [12] and it was supposed that above some value an excess of oleic acid is not necessary. Therefore, this excess of oleic acid will disturb the chemical equilibrium between the surface of the particles and the liquid medium and apparently induces stripping of acid molecules from the surface of nanoparticles, which, in turn, deteriorates the stability of the magnetic fluid. Schematically such effect can be shown in Fig. 10.1. If the number of stabilizer (surfactant) molecules is insufficient, the stability deteriorates because these molecules cannot completely cover the surface of magnetic nanoparticles. In the case of surfactant excess, the mechanism of stability deterioration is not so obvious. It should be noted, this is an overall

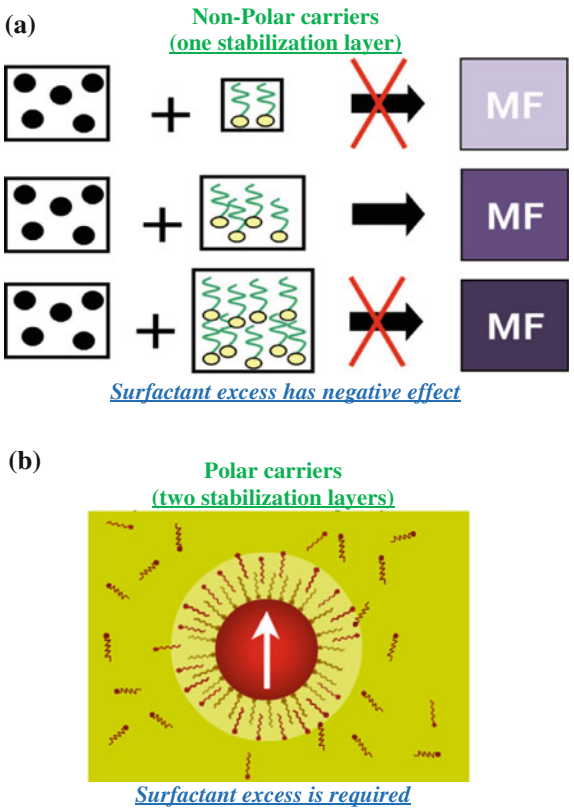

Fig. 10.1 Surfactant content in magnetic fluids with sterical stabilization: **a** non-polar MF; **b** polar ferrofluids

problem for colloidal solutions [4, 13–15]. Thus, according to [16] when sodium dodecylsulfate (SDS) concentration is close to or is above the critical micelles concentration (*cmc*), the TiO_2 nanoparticles sediment most slowly and without any agglomeration. At higher micelle concentration, SDS micelle depletion forces are very strong, causing fast flocculation, without coagulation. Then sedimentation occurs much faster. Also the sedimentation stability was found to increase with SDS concentration, *cSDS*, up to the *cmc*, as expected. For $cmc < cSDS < c^*$, where c^* is an experimentally determined concentration, the stability is unaffected by the presence of the SDS micelles. For $cSDS > c^*$, the dispersion stability against sedimentation becomes worse, rapidly changing with an increase in *cSDS* [16]. Also the effect of surfactant type and concentration on the final particle size and size distributions of Thiol-ene polymer particles was demonstrated [17]. Key parameters that are examined include the variation of surfactant concentration and the variation of surfactant kinds (anionic, cationic, and nonionic surfactants) and structural analogs. The chemical structure and concentration of the surfactants influenced the final particle size and size distribution of particles obtained. In general, smaller particles are obtained with higher concentrations of stabilizing agent, especially for ionic surfactant species [17]. At low hydrophobic nanoparticles concentrations in ionic surfactant solutions, the transition from the intermediate to the stable region, that is, the disappearance of the precipitate occurs at a constant surfactant concentration. This concentration is introduced as the "critical dispersion concentration" (*cdc*), this being the lowest required concentration of a surfactant that is necessary to disperse the hydrophobic particles. The existence of a system-specific critical *cdc/cmc* ratio, beyond which stable dispersions cannot be obtained, is proposed, which explains the disability of short-chain surfactants to disperse colloids [18]. Nanoparticles coated with self-assembled dodecyltrimethylammonium bromide shells are shown to undergo colloidal destabilization at higher temperatures [19]. This is caused by two different mechanisms depending on the surfactant concentration. Increasing the surfactant concentration increases the number of micelles, an increasing surfactant concentration results in a decrease of the breakdown temperature for the system studied. Also it was shown that stabilization of single wall carbon nanotubes is controlled by the concentration of surfactant and NaCl [20]. Phase separation occurs above 3.5 wt% SDS; in TX-100/SDS mixtures that threshold is lower. The mixed system has a good dispersant efficiency, although depletion occurs at lower concentrations.

It is obvious, that in polar MFs excess of surfactant is necessary to form second layer but again some optimal ratio between surfactant and magnetic particles exists. The formation of the first layer often involves chemical bonds on the active sites of the particle surface (e.g. Fe–OH on magnetite). The second layer forms via hydrophobic interaction. Again, like in non-polar MFs, the question of ferrofluids stability as well as optimal value of surfactant concentration arises and is actively discussed in literature. The adsorption of different organic acids and their effect on the pH-dependent colloidal stability and salt tolerance of magnetite nanoparticles were studied [21] and it was found that the organic acids can destabilize magnetite dispersions, while their high loading masks the original surface properties of

magnetite and improves colloidal stability and salt tolerance of dispersions. Wei Huang and co-workers have studied the stability of ionic liquid-based MFs, and the results showed that stable MF could not be obtained using bare particles, while the oleate-coated magnetite nanoparticles with volume fractions of 6.5% in ionic liquid displayed excellent stability [22].

Small-angle neutron scattering (SANS) is one of the most powerful and efficient methods of nanostructural investigation of various liquid nanosystems and in particular ferrofluids [23–25]. During SANS experiment a widening of the neutron beam passed through the sample is analyzed in terms of the differential scattering cross-section per sample volume (scattering intensity $I(q)$) as a function of scattering vector module $q = (4\pi/\lambda)\sin(\theta/2)$, where λ is the incident neutron wavelength and θ is the scattering angle. This dependence is quite sensitive to structural features of the studied system at the scale of 1–100 nm. Indeed, sizes of particles in magnetic liquids are mostly in this dimensional range. SANS investigations including specific techniques (contrast variation, scattering of polarized neutrons) give information about particle structure (size, polydispersity, stabilizing shell thickness, composition of particle`s core and shell, solvent rate penetration in surfactant layer, micelles structure), magnetic structure (magnetic size and composition), particle interaction (interparticle potential, magnetic moment correlation, phase separation) and cluster formation (aggregation and chain formation). The main task of SANS is obtaining of scattering length density (SLD) profile, which is defined as a sum of the coherent scattering length of all atoms in molecule divided by volume and usually represented in units of 10^{10} cm^{-2}. As an example, SLD profile for magnetic nanoparticles in sterically stabilized ferrofluids is presented on Fig. 10.2.

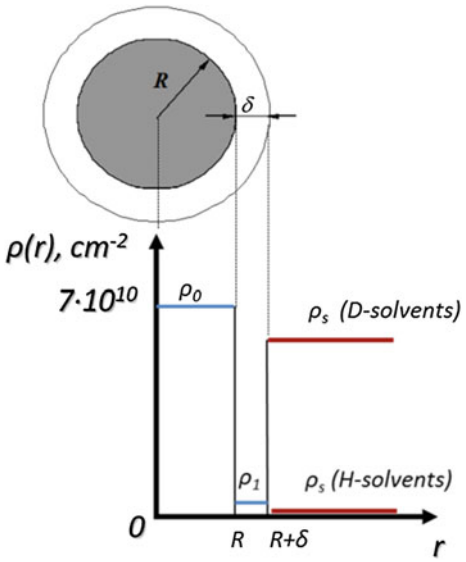

Fig. 10.2 Coherent scattering length density profile for magnetic nanoparticle in ferrofluids stabilized by surfactant in the frame of the 'core-shell' model (magnetic core and surfactants shell)

10.2 Structure and Stability of Non-polar Ferrofluids by SANS

Structural changes in MFs with different surfactant excesses were successfully investigated by small-angle neutron scattering (SANS) in systems based on low-polarity solvents (benzene and decahydronaphthalene), where nanomagnetite (obtained by co-precipitation reaction) was coated by monocarboxylic acids with different alkyl chain lengths and degrees of saturation (unsaturated oleic acid (OA), C18; saturated myristic acid (MA), C14) [10, 26–28]. The main observed changes were related to the interaction between free surfactants (monocarboxylic acids), which differed to a great extent from the interaction between surfactant molecules in pure solutions without magnetic particles [29]. The structure of complex (magnetite plus surfactant) particles and interaction between them did not change much up to 15 vol% excess of surfactant. With a further increase in the excess concentration above some critical value, the stability sharply deteriorated, which manifested itself in the coagulation of complex particles and precipitation of agglomerates. Also the possibility of expanding the range of surfactant stabilizers for MFs was analyzed recently [30]. Specifically, we were interested in the effect of their excess above optimal concentration on the stability of low polarity MFs. The main purpose was to reveal (using SANS) the structural changes caused by surfactants addition to initial highly stable solutions of magnetite nanoparticles coated by single adsorption layers of saturated monocarboxylic acids with hydrocarbon chains of different lengths (palmitic acid (PA), C16, and lauric acid (LA), C12) in decahydronaphthalene. The stabilization of MFs using these acids, along with saturated myristic acid [31], also provides highly stable concentrated systems; however, their stabilization efficiency is somewhat lower. Stabilization efficiency of a surfactant is relative fraction of magnetic nanoparticles, which are stabilized in a solution under the identical synthesis conditions and the same quantity of added surfactants during process of co-precipitation of magnetite with subsequent magnetic decantation (application of inhomogeneous magnetic field in order to initiate agglomeration and precipitation of non-stabilized magnetite). Thus, to obtain the desired concentration of magnetic particles in the final system with a less efficient surfactant, one must use a larger number of re-dispersion cycles with magnetic decantation of initially deposited magnetite in the surfactant-containing mixture. In the case with myristic acid, the stabilized size of magnetic nanoparticles in MFs with PA and LA is smaller than that obtained with the commonly used oleic acid [31]. In the SANS experiments usually deuterated solvents are used to provide a maximum neutron contrast with acid molecules and increase the signal-to-noise ratio by reducing the incoherent background from hydrogen.

In the SANS studies of effect of surfactant excess on structure and stability of non-polar ferrofluids [27, 28] experimental SANS curves for the diluted magnetic fluid without surfactant excess are initially analyzed by the model for non-interacting polydisperse particles with “core–shell” structure [32–34]. To confirm the appropriateness of the used model, similar MFs on non-deuterated

solvents are also studied, where the contrast between the stabilization shell and the solvent is minimal; therefore, scattering preferentially corresponds to the magnetite component. Parameters of the size distribution function for particles $Dn(r)$ (the characteristic radius and the width of the standard deviation) and the thickness of the surfactant shell δ are found when approximating the data for the MF samples without the acid excess, and they were further fixed upon fitting the experimental curves for the ferrofluids samples with the presence of free (excess) surfactant. Then these parameters were fixed when fitting the experimental curves for the MF samples with acid excess, and a term describing the scattering from free surfactant was introduced. Because of the small volume of acid molecules (in comparison with MF particles), this term had the form of the Guinier formula. When analyzing the scattering from MF particles, it was necessary to correct contrast taking into account the presence of free surfactant caused by the surfactant excess in the MF. It was found that the presence of free surfactant molecules in the non-polar MF not only contributes to scattering in a form of the Guinier term, but substantially decreases the average neutrons scattering length density of the fluid medium.

The concentration dependences of the radius of gyration and forward scattering intensity for surfactant molecules in a pure non-polar solvent and in the non-polar MF with surfactant excess are plotted and compared to conclude about interaction between surfactant molecules. It was shown previously [35] that the concentration dependence of forward scattering intensity ('intensity in zero angle') can be written in a form:

$$I(0)/\Phi \approx C(1+\Phi B), \tag{10.1}$$

where Φ is the volume fraction of molecules in the solvent; C is the constant associated with the volume of the particles and scattering length density of the solvent and particles; and B is the dimensionless analog of the second virial coefficient in the pair interaction potential.

$$B = v^{-1} \int (\mathrm{g(r)} - 1)\mathrm{dV}, \tag{10.2}$$

where v is the volume which is occupied by the particle in the liquid medium, $g(r)$ is the radial distribution function (or pair correlation function). The sign of parameter B indicates the character of interaction, namely, attraction if $B > 0$ and repulsion if $B < 0$. For example, for the hard sphere potential (only repulsion), $B = -8$ [35]. A similar expression for the concentration dependence of the observed radius of gyration has the form:

$$R_g^2 \approx \left(R_{g0}^2 + \Phi B P^2\right)/(1+\Phi B), \tag{10.3}$$

where R_{g0} is the actual radius of gyration of the molecule and P^2 is the squared distance, on which two particles in the solution correlate.

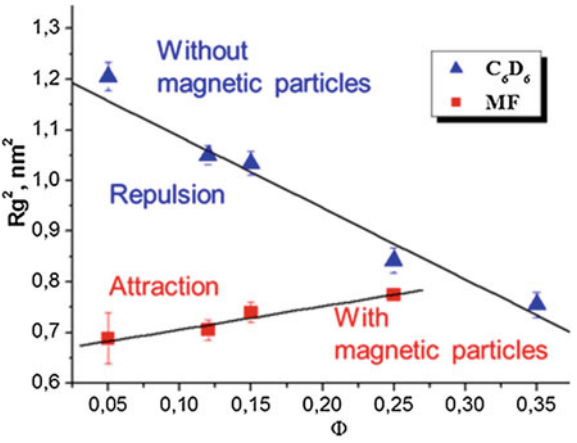

Fig. 10.3 Behavior of gyration radius for surfactants molecule in pure solvent and in ferrofluids depending on the volume fraction of the surfactant excess, Φ

The values of the dimensionless analog of the second virial coefficient B in the pure solution and in the MF are derived and also compared with calculation for the hard sphere potential. From such analysis, it was concluded that the attraction forces play an essential role in the pair interaction potential between the rod-like surfactant molecules. The additional repulsion was observed between the acid molecules in the MF, which is indicated by a decrease in the dimensionless second virial coefficient (Fig. 10.3). This observation can be associated with the so-called depletion attraction [36], when the effective attraction appears in the system due to the exclusion of relative small surfactant molecules from the space between relatively large magnetic particles. Previously similar data on the small-angle neutron scattering by the magnetite–oleic acid–benzene magnetic fluid with 1% content of the magnetic material and various OA excesses were presented in [10]. The character of interaction between the acid molecules, namely, in the presence of magnetic particles in benzene, a slight increase in the visible radius of gyration with an increase in the surfactant excess is observed, which indicates the dominance of the attraction between the OA molecules in the system. The value of the dimensionless second virial coefficient $B = -1.2$ for the OA molecules in the benzene based MF is much larger than for this system in decalin [27, 32], where $B = -2.2$. This indicates the larger contribution of attraction between the OA molecules in the benzene based MF compared with the decalin based MF. We can conclude that the aggregation stability of the decalin based MF in the presence of the surfactant excess is slightly higher than for the benzene based MF. This conclusion is also confirmed in practice since an abrupt violation in stability with the appearance of the precipitate was observed for the magnetite–oleic acid–benzene system with the volume fraction of the OA excess more than 25%, while this effect is unobservable in the case of the decalin based MF.

The structural parameters of various components of the non-polar (decalin or benzene) based MF with the surfactant excess (oleic acid) are found from the SANS data. It is shown that the structural variations in this case are related predominantly

to the character of interaction of free surfactant molecules in the MF volume. An increase in the attraction between the surfactant molecules in the presence of the MF particles is substantially smaller in decalin compared with the similar benzene based MF. This correlates with the fact that in contrast to benzene, the decalin based MF remains stable against aggregation in the concentration range of the OA excess up to 25 vol%. Thus, from the viewpoint of the MF microstructure, it is shown that the solvent–surfactant interaction plays a substantial role in the stabilization of these systems with an excess of surfactant.

It should be noted that the above mentioned algorithm of SANS data analysis for non-polar MFs with surfactant excess [10, 26–28] turned out to be invalid to obtain adequate approximating curves within the modified model of non-interacting spherical particles in the presence of free surfactant (lauric and palmitic acids). The reason is the existence of small (but sufficient to violate the model) structural instability of MF, which manifests itself in the formation of aggregates even at very small surfactant excess. Both parameters increase upon an initial excess of LA and PA; this increase is more pronounced in the samples stabilized by PA. Parameter of forward scattering intensity, $I(0)$, decreases with an increase in the free-surfactant fraction (Fig. 10.4a). This is explained by the decrease in the contrast of complex particles (magnetite/monocarboxylic acid) caused by the growth of the concentration of hydrogen-containing acids molecules in the solvent. Parameter R_g continues to rise with LA and PA excess in MFs, which indicates the growth of aggregation (Fig. 10.4b). One can notice an almost constant value of R_g parameter at the excess of OA or MA in ferrofluids (Fig. 10.4b) which is an indication of aggregation stability of MFs. Comparing the behavior of R_g for MFs stabilized by different acids, one can conclude that, in contrast to the fluids stabilized by oleic and myristic acids, the systems stabilized by LA and PA exhibit a much lower structural stability in the presence of surfactant excess. Thus, a clear correlation is observed between the stabilizing efficiency of the used acids and the MF stability in the presence of surfactant excess: the more efficiently a surfactant stabilizes magnetic particles in a fluid, the more stable the MF is under surfactant excess.

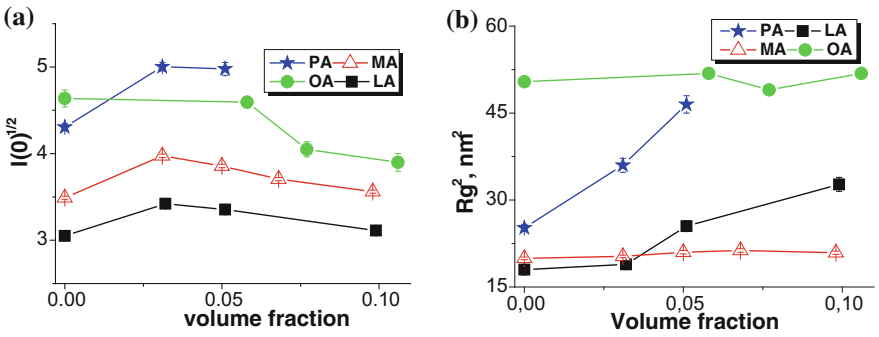

Fig. 10.4 Behavior of Guinier parameters (forward scattering intensity (**a**) and gyration radius (**b**)) versus volume fraction of surfactant excess for non-polar MFs stabilized by PA (blue stars), MA (red triangle), OA (green circle) and LA (black square)

The effect revealed can be explained by the presence of two competing contributions to the stabilizing efficiency of monocarboxylic acids. It is known [9] that the main parameter determining the steric repulsion of magnetic nanoparticles in MF is the thickness of surfactant shell, which is proportional to the alkyl chain length. In this context, the chain length in LA (C12) is insufficient to provide stabilization of this kind. An additional factor affecting the repulsion between particles is the elastic properties of the shell (i.e., the ability of the shells of MF particles penetrate each other and be deformed under contact) [37, 38]. The extended anisotropic structure of saturated-acid molecules leads to a peculiar organization of surfactant on the magnetite surface, which deteriorates the elastic properties of the shell and weakens repulsion. This effect manifests itself during stabilization by PA (C16); it is in agreement with the fact that the lowest efficiency of stabilizing magnetic nanoparticles in MFs is observed for stearic acid with a chain length of C18 (among other saturated monocarboxylic acids). Thus, MF stabilized by myristic acid (having an intermediate chain length, C14) remains most stable under surfactant excess. In this context, its behavior is close to that of MFs stabilized by unsaturated oleic acid, which exhibits the highest stabilizing efficiency.

The colloidal stability of ferrofluids is related with or even determined by the behavior of stabilizer's molecules in bulk solvents [27, 29, 39–41]. Thus, in most cases as a first stage of the synthesis, the medium, where magnetic nanoparticles are created, is supplemented by admixing concentrated solutions of fatty acids. Already at this stage the aggregation of fatty acids themselves can affect the final stability of magnetic fluids. SANS makes it possible to reveal such aggregation and follow the transition from the isotropic solution to liquid crystalline state with the growth in the solute concentration, as it is shown in Fig. 10.5 for organic solutions of saturated mono-carboxylic acids with stiff linear structure [42]. It is obtained that the critical concentration of this transition is inversely proportional to the length of surfactant molecules. Such aggregation leads to decreasing of the number of free surfactant required for adsorption and further stabilization of magnetic nanoparticles, thus affecting the final stability of the magnetic fluid and explaining why longer saturated fatty acids are worse stabilizers as compared to shorter ones. After SANS analysis of the interaction of acid molecules one comes to conclusion that the discussed transition goes easier in the presence of magnetic particles.

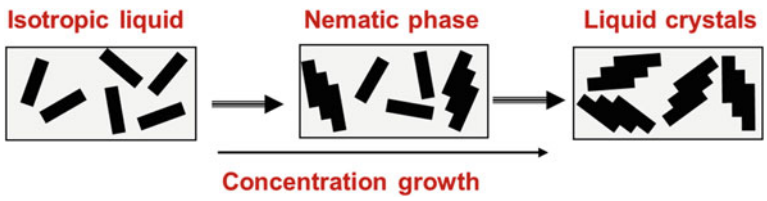

Fig. 10.5 Formation of the liquid crystalline phase in bulk organic solutions of mono-carboxylic acids with the growth of the volume fraction of the acids in solutions

The microstructure of the diluted organic solutions of saturated mono-carboxylic (myristic and stearic) acids was described in a self-consistent way by using the combination of IR-spectroscopy (information about preferable dimerization), molecular dynamics (MD) simulations (information about solvent organization at the solute-solvent interface) and SANS analysis (information about effective sizes of the acid molecules in solutions as a result of isomerization) [41, 43]. The data of the IR-spectroscopy and MD simulations are used in the modeling of the SANS curves from diluted solutions [43–49]. Aside from the scale characteristics of the acid molecules like apparent length and cross-sectional radius, an interpretation of the SANS data involves an extra parameter—the incoherent neutron scattering that was also found from approximation.

The combination of MD simulations and SANS method is very productive for investigation of the solutes with specific symmetry. The strongly anisotropic shape of fatty acid molecules makes it possible to consider the solute-solvent interface in the corresponding system of cylindrical coordinates and to model the scattering in terms of the radial scattering length distribution with a resolution far below 1 nm. It has been found that the structure of the radial solvation shell is sensitive to the size of the solvent molecules, which is expected when the cross-sectional diameter of the solute (here ~0.4–0.5 nm) is comparable with the characteristic size of the solvent molecule. For decalin (characteristic size ~1 nm) the modulation and its influence on the small-angle scattering are stronger than those for benzene (characteristic size ~0.7 nm). At the same time, it has been proved that for both solvents no more than two coordination layers of the solvation shell contribute to the scattering. The size parameters of the acids found by the proposed approach characterize well the isomerization of the dissolved molecules. The more extended structure of a decalin molecule as compared to that of a benzene molecule has been shown to be responsible for stronger solvent modulations at the interface with the acids, and as a result, for the increase in the effective cross-sectional solute size. In turn, this reasons the more intensive lyophobic solute assembling within the nematic transition observed by SANS in concentrated solutions.

To summarize this part of the work we can state the following:

- For high surfactants excess a sharp break in the stability of non-polar ferrofluids is found. A significant increase in the attraction is observed for acid molecules in the ferrofluids, which is related to the loss of magnetic fluids stability at high excess of acid.
- It was shown that attractive component affects transition into the liquid crystalline state. The fact that the nematic transition in the SA case is significantly shifted to small concentrations because of the strong van der Waals attraction.
- The formation of the nematic phase in bulk solutions of mono-carboxylic acids is an important factor in the stabilization procedure of magnetic fluids. Formation of acid aggregates would hinder process of chemisorption of the acid heads on the magnetite surface.

10.3 Structure Diagnostics of Polar Magnetic Fluids by SANS

Different aggregate classes depending on the stabilization mechanism (steric, electrostatic and steric/electrostatic stabilization) of magnetic particles (magnetite) in physiological conditions are studied by SANS [23, 50–54]. Water-based magnetic fluids used as a source of magnetic nanoparticles in the therapy of the brain cancer glioblastoma were studied by SANS contrast variation [5, 55]. These fluids are characterized by record achievable concentrations of magnetic material (up to 10 vol%) while keeping high stability [56]. The nanomagnetite was stabilized by a double layer of fatty mono-carboxylic acids with short alkene chains, namely lauric (C12) and myristic (C14) acids. Despite the high concentration and long-time stability, SANS shows the presence of aggregates in the systems. The found effective match points are shifted and show a difference in the composition of the aggregates. The main important conclusion of the structure analysis: there is a different extent in the surfactant coating of the particles in the aggregates, which is consistent with the longer chain of myristic acid. In the case of stabilization of different magnetic materials in ferrofluids by the dodecylbenzene sulfonic acid, the distribution function of magnetic nanoparticles over sizes (the average radius is 6 nm) is not typical and differs from the log-normal distribution. In this case, the polydispersion of particles is large (up to 50% and more). The volume fraction of particles in clusters is approximately equal to 10%. The use of monocarboxylic acids for the stabilization results in the dispersion of individual magnetite particles in water with a typical size distribution (average radius, 3.7 nm; polydispersity, 40%), which coincides with the distribution for magnetite produced in the condensation reaction. A number of magnetic particles form clusters with characteristic radii in the range of 10–20 nm depending on the acid used. Among the studied acids, the best stabilization properties are observed for the lauric acid, C12; the volume fraction of clusters in this case is only 5%. The results obtained suggest that the use of monocarboxylic acids in the preparation of highly stable aqueous magnetic fluids is very promising. An important aspect of study is the fact that these acids are biocompatible, which opens up the possibilities of biomedical applications of the magnetic fluids under investigation.

Among the studied systems by SANS method are water-based magnetic fluids with substitution of sodium oleate as surfactant by biocompatible polymer polyethylene glycol at the magnetite surface, which aims at the increase in the life time of magnetic nanoparticles in living organisms by reducing the response of immune systems. This fluid was used as an initial component in the synthesis of the magnetic carrier containing anticancer drug Taxol. It is revealed that quite large amounts of polymer in the fluid structure results in a decrease in the aggregation stability, thus requiring that an optimal polymer content to be chosen.

The impact of surfactant type on the structure organization of aqueous ferrofluids was considered relying on the data of small-angle neutron scattering. Thus, the aggregates of different size and type were observed (Fig. 10.6) when stabilizing

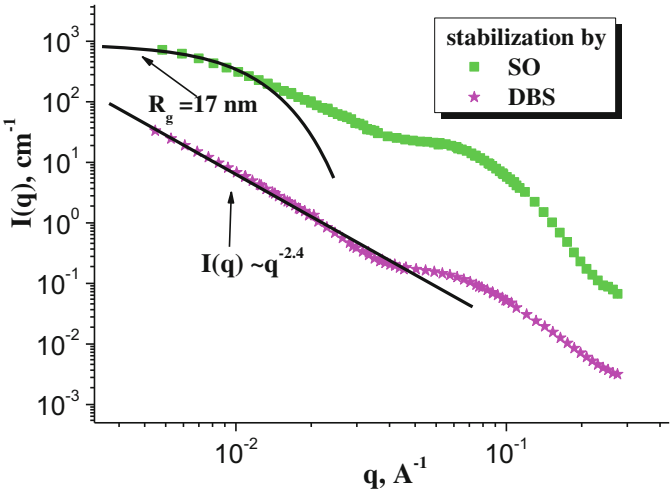

Fig. 10.6 Experimental SANS curves for aqueous MFs with double layer stabilization by sodium oleate, SO, (green square) and dodecylbenzene sulphonic acid, DBS (pink star). Solid lines represent the Guinier function and power-law behavior of scattered intensity

magnetic nanoparticles (MNPs) of magnetite in heavy water by sodium oleate (SO) or dodecylbenzene sulphonic acid (DBS) which, according to the surface tension measurements, show significantly different critical micelle concentrations. The found aggregate difference was related to the behavior of surfactant molecules in aqueous solutions including the structure and interaction parameters of micelles (micelle aggregation number, fractional charge, charge per micelle and surface potential, etc.) derived from the SANS analysis [57, 58].

From the comparison of the behaviour of the aqueous micellar solutions of DBS and SO with the structure characteristics of aqueous MF one can see a distinct correlation between a number of monomers of surfactants molecules (*cmc*-value) and MNPs structure in ferrofluids, namely the higher *cmc* the less aggregated is the MF. From the structural viewpoint, the MF stabilized by DBS is very similar to the MF with PEG modification when large branched fractal-like aggregates were observed at addition of some amount of PEG into the solutions [50]. For both ferrofluids the power-law behaviour at small q-values is observed together with a distinct contribution from surfactants (stabilizing shell around magnetite particles and micelles in the solution). This is a strong indication that not only the number of free surfactant molecules in the solutions but also the surfactant-MNP and surfactant-solvent interactions affect the stabilization mechanism in MFs.

To summarize, various structure organizations of aqueous MFs stabilized by SO and DBS is detected in SANS experiments. While comparatively small and compact MNPs aggregates are observed in the case of the SO stabilization, large and developed fractal type aggregates are revealed in water-based MF with the DBS stabilization. DBS and SO micelle structure and interaction parameters are obtained

as a function of the surfactant concentration in aqueous solutions. The determined dependences can be used in the study of complex systems with DBS and SO where potential presence of micelles takes a strong effect on the properties and synthesis of such systems. In particular, the micelle size is comparable with the size of surfactant aggregates in water-based ferrofluids with the double layer stabilization. Finally, the behaviour of the surfactants in aqueous solutions correlates with their stabilizing properties in ferrofluids.

DBS is actively used in the double sterical stabilization of technical water-based ferrofluids [56, 59–62], aqueous dispersions of magnetic (mostly magnetite) nanoparticles. The second surfactant layer at the surface of magnetite in such ferrofluids is formed due to physical adsorption in excess of the acid. The equilibrium of this process is strongly affected by free surfactant whose concentration is restricted by the critical micelle concentration. So, the micelle formation in this stabilization scheme should be considered among the factors, which determine stability of ferrofluids.

Small-angle neutron scattering is used to find out parameters of the structure and interaction of the DBSA micelles in deuterated water (d-water) as a function of the surfactant concentration in solution. Deuterated water is used to achieve a sufficient scattering contrast between the surfactant and liquid carrier and also for reduction of incoherent scattering background from hydrogen. The surfactant content in the bulk of ferrofluids is found [57].

The $Ic(q)$ function (the shape scattering function, which is one of the modified basic functions, introduced and applied recently to the analysis of the contrast variation from ferrofluids [23]) obtained from the experimental scattering curves at various contrasts [61] for the discussed ferrofluid is given in Fig. 10.7, where three scattering levels can be distinguished. The first level shows presence of fractal aggregates (size >250 nm), while the second level corresponds to primary particles (size ~20 nm) composing the aggregates. The third level can be associated with the micelles of surfactant in water (DBS or SO). It is comparable with scattering from the micelles in pure heavy water. The $Ic(q)$ basic function can also be compared directly with the scattering from micelles in pure d-water. In Fig. 10.7 this is done for the rescaled scattering curve from solution of free DBS. Good consistency can

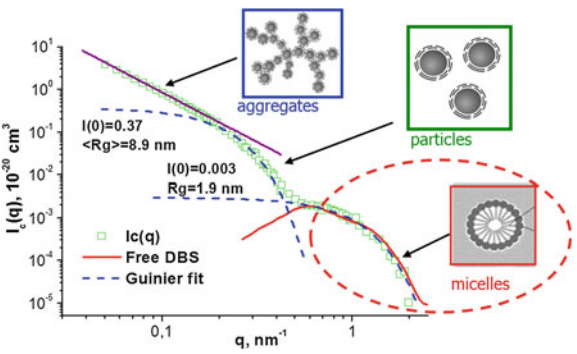

Fig. 10.7 Surfactant excess in water-based ferrofluids

be seen. From the data analysis one obtains the total volume fraction of the non-adsorbed surfactant in the ferrofluid to be 0.00091. This value takes about 5% of the whole surfactant content in the system, with the approximate ratio of 1:4 for the free monomer surfactant and micelles. So, one can conclude that almost 95% of DBS acid are effectively adsorbed on the magnetite surface and form the stabilizing shell.

The decrease in the micelle aggregation number value as well as the change in the power-law dependence of the aggregation number versus surfactant concentration are clearly seen [58] for the same values of the added PEG (about 2.5 wt%) in various SO solutions. Other micellar parameters (degree of micelle ionization, charge per micelle and surface potential) keep constant or just slightly decrease with increasing SO concentration. It should be mentioned that the well-known tendency of SO to form soaps at near-neutral pH is of little significance in the studied natural solutions of SO (pH $\sim$ 10).

The most pronounced effect of the presence of PEG on the SO micelles is observed for the micelle aggregation number, which significantly decreases with the addition of PEG as compared to the neat SO solutions and does not change much with the growth of the PEG concentration. Behavior of neat PEG solutions of different molecular weight was also studied by SANS [40, 63]. Other parameters vary sharply with the PEG concentration. Thus, the degree of micelle ionization, charge per micelle and surface potential show an increase on the small addition of the polymer of about 2 wt% and a decrease at the PEG concentration of about 10 wt%. A reasonable explanation for this effect is some adsorption of free surfactant on the PEG coils, which unbalances the ratio between the SO molecules in a free state and in micelles.

The decrease in the micelle-micelle distance (as it follows from the shift of the interaction maximum towards larger q-values) on addition of PEG can be connected with a possible decrease in *cmc*, which could result in an increase in the micelle concentration. However, this is highly unlikely if one takes into account the studied SO concentration range, which exceeds *cmc* in the neat SO solutions by at least two orders of magnitude. So, the discussed change in the scattering is related probably to an effective attraction between micelles, which partly compensates the electrostatic repulsion, and depends on the PEG content in a complex way as it follows from the significant variations in the maximum position and the width of the interaction peak. At small PEG concentrations, the most probable candidate for the attraction mechanism is depletion forces between small polymer coils and comparatively large colloidal micelles. At high PEG concentrations it is reasonable to assume that the polymer adsorbs on the micelle surface or in other words, the micelles are wrapped by some part of the polymer.

The obtained results are consistent with the analysis of the interaction of PEG with SO-coated magnetite nanoparticles in water-based magnetic fluids [50], where the structure reorganization of the particle aggregates at sufficiently high PEG content was explained by the formation of the "polymer layer" around colloidal particles as a result of partial replacement of SO with PEG on the surface of magnetite.

Self-assembly of the nanoparticles occurs during the solvent evaporation, therefore interaction between the film and a substrate plays an important role in the ordering. An additional point is that a possible difference in the stability of MFs in bulk and at interfaces should be taken into account in the requirements for the stabilization of these systems with respect to their storage, namely to the interaction of the MF particles with container walls under different conditions. Adsorption of nanoparticles from MFs on solid surface was studied by neutron reflectometry (NR) and related to the bulk structural organization of MFs concluded from SANS. The neutron reflectometry experiments with highly stable magnetic fluids of two types, non-polar organic solvent (benzene) and highly polar solvent (water) at the silicon interface show that, along with the structural stability in a bulk, the considered MFs are characterized by high interface stability as well [64–67]. This fact differs from the previously studied over-saturated aqueous MFs [67] which form the ordered structures of the particles on the surface. In the stable MFs only one adsorption layer of colloidal polydisperse particles from MFs is adsorbed on the silicon surface. The concentration of free particles at the interface is higher than that in a bulk for concentrated non-polar MFs, thus indicating to a wide spatial transition from the adsorption layer to bulk. In the aqueous MF this transition is significantly sharper, so that the mean scattering length density of the interface and bulk are very close. In the partially aggregated aqueous MF the preferable adsorption of free (non-aggregated) particles on the silicon surface takes place. No effect of the external magnetic field on the interface structure of the both types of MFs was observed.

Different structural organizations of MFs at interface with silicon were also concluded from neutron reflectometry experiments for two aqueous MFs with various bulk structures revealed by SANS. It was obtained that individual non-aggregated nanoparticles are preferably adsorbed on the oxidized silicon surface from the initial aqueous MF to form a single adsorption layer. The reorganization of the cluster structure in a bulk after the modification of MF with PEG results in disappearing of the adsorption layer, which is correlated with the fact that as compared to the initial MF all nanoparticles in the PEG modified MF compose large developed aggregates that are not adsorbed by the surface. The gravity effect showed less than 10% difference in the mean SLD for the two configurations of the MF/Si interface with Si substrate above and below MF caused by a corresponding increase in the particle and aggregate concentration at the interface in the second case.

Thus from the SANS structural characterization of aqueous ferrofluids we could summarize the following:

- The best combination of surfactant for water-based ferrofluids from structural point of view is found, namely double layer of LA results closely to the original size distribution of the magnetic nanoparticles obtained in the co-precipitation reaction.

- Estimation of surfactants fractions in the bulk and adsorbed on nanoparticles in aqueous ferrofluids were done. It was observed that the adsorption rate depends on surfactant type used for aqueous magnetic fluids stabilization.
- Structure and interaction parameters of the micelles in polymer—surfactant aqueous solutions are obtained. Influence of polymer on surfactant micelle is observed: Change in the behavior of aggregation number is observed at 2% addition of PEG. Effect of screening of interaction takes place at PEG addition above 5 vol%.

10.4 Conclusions

According to presented information, we can conclude that small-angle neutron scattering is a very informative method of analyzing the microstructure of magnetic fluids, which allows to determine particle structure and their interactions in a number of magnetic fluids and complex multicomponent liquids systems. Effect of different stabilization properties of mono-carboxylic acids in non-polar carriers were successfully described by small-angle scattering methods. Structural stability and reorganization of magnetic nanoparticles in water based ferrofluids were studied in details.

References

1. B. Berkovski, in *Magnetic Fluids and Applications Handbook*, ed. by V. Bashtovoy (Begell House, Inc. New York, 1996), p. 350
2. L. Vekas, M.V. Avdeev, D. Bica, Magnetic nanofluids: synthesis and structure, in *Nanoscience in Biomedicine*, Ch. 25, ed. by D. Shi. (Springer, Berlin, 2009), pp. 650–728, https://doi.org/10.1007/978-3-540-49661-8_25
3. *Proceedings of the Seventh International Conference on the Scientific and Clinical Applications of Magnetic Carriers*, ed. by Urs. Häfeli, M. Zborowski. J. Mag. Mag. Mater. **321**, 1335–1688 (2009), https://doi.org/10.1016/j.jmmm.2009.03.008
4. A.B. Jódar-Reyes, A. Martín-Rodríguez, J.L. Ortega-Vinuesa, J. Coll. Int. Sci. **298**(1), 248–257 (2006), https://doi.org/10.1016/j.jcis.2005.12.035
5. M.V. Avdeev, B. Mucha, K. Lamszus, L. Vékás, V.M. Garamus, A.V. Feoktystov, O. Marinica, R. Turcu, R. Willumeit, Structure and in vitro biological testing of water-based ferrofluids stabilized by monocarboxylic acids. Langmuir **26**(11), 8503–8509 (2010), https://doi.org/10.1021/la904471f
6. E. Tombácz, D. Bica, A. Hajdú, E. Illés, A. Majzik, L. Vékás, Surfactant double layer stabilized magnetic nanofluids for biomedical application. J. Phys.: Condens. Matter **20**(20), 204103(6) (2008), https://doi.org/10.1088/0953-8984/20/20/204103
7. R.W. Chantrell, J. Sidhu, P.R. Bissell, P.A. Bates, Dilution induced instability in ferrofluids. J. Appl. Phys. **53**, 8341 (1982), https://doi.org/10.1063/1.330358

8. V. Socoliuc, C. Daia, A. Taculescu, L. Vekas, Colloidal stability loss with increasing dilution of polar carrier based magnetic colloids stabilized by steric repulsion. Rev. de Chimiel. **64**(10), 1194–1196 (2013), https://www.researchgate.net/profile/V_Socoliuc/publication/260405832_Colloidal_Stability_Loss_with_Increasing_Dilution_of_Polar_Carrier_based_Magnetic_Colloids_Stabilized_by_Steric_Repulsion/links/561df40908aecade1acb4399.pdf?origin=publication_list
9. R.E. Rosensweig, *Ferrohydrodynamics* (Cambridge University Press, Cambridge, 1985), p. 344, https://doi.org/10.1017/S0022112089220773
10. V.I. Petrenko, M.V. Avdeev, V.L. Aksenov, L.A. Bulavin, L. Rosta, Magnetic fluids with excesses of a surfactant according to the data of small-angle neutron scattering. J. Surf. Invest. **3**(1), 161–164 (2009), https://doi.org/10.1134/S1027451009010261
11. D. Bica, Preparation of magnetic fluids for various applications. Rom. Rep. Phys. **47**, 265 (1995)
12. M.S. Dababneh, N.Y. Ayoub, The effect of oleic acid on the stability of magnetite ferrofluid. IEEE Trans. Magn. **31**(6), 4178–4180 (1995), https://doi.org/10.1109/20.489918
13. P. Izquierdo, J. Esquena, Th.F Tadros, C. Dederen, M.J. Garcia, N. Azemar, C. Solans, Formation and stability of nano-emulsions prepared using the phase inversion temperature method. Langmuir **18**(1), 26–30 (2002), https://doi.org/10.1021/la010808c
14. V.L. Alexeev, The instability of silica sol in concentrated solutions of triton X100. J. Coll. Interface Sci. **206**(2), 416–423 (1998), https://doi.org/10.1006/jcis.1998.5709
15. J. Bibette, D. Roux, B. Pouligny, Creaming of emulsions: the role of depletion forces induced by surfactant. J. Phys. II France. **2**, 401–424 (1992), https://doi.org/10.1051/jp2:1992141
16. Y.-J. Yang, A.V. Kelkar, X. Zhu, G. Bai, H.T. Ng, D.S. Corti, E.I. Franses, Effect of sodium dodecylsulfate monomers and micelles on the stability of aqueous dispersions of titanium dioxide pigment nanoparticles against agglomeration and sedimentation. J. Colloid Interface Sci. **450**, 434–445 (2015), https://doi.org/10.1016/j.jcis.2015.02.051
17. O.Z. Durham, D.A. Shipp, Suspension thiol-ene photopolymerization: effect of stabilizing agents on particle size and stability. Polymer **55**(7), 1674–1680 (2014), https://doi.org/10.1016/j.polymer.2014.02.044
18. T. Dederichs, M. Möller, O. Weichold, Colloidal stability of hydrophobic nanoparticles in ionic surfactant solutions: definition of the critical dispersion concentration. Langmuir **25**(4), 2007–2012 (2009), https://doi.org/10.1021/la8033676
19. T. Dederichs, M. Möller, O. Weichold, Temperature-dependent colloidal stability of hydrophobic nanoparticles caused by surfactant adsorption/desorption and depletion flocculation. Langmuir **25**(18), 10501–10506 (2009), https://doi.org/10.1021/la901216g
20. F. Tardani, C. La Mesa, Attempts to control depletion in the surfactant-assisted stabilization of single-walled carbon nanotubes. Colloids Surf. A **443**, 123–128 (2014), https://doi.org/10.1016/j.colsurfa.2013.11.001
21. E. Tombácz, M. Szekeres, A. Hajdú, I.Y. Tóth, R.A. Bauer, D. Nesztor, E. Illés, I. Zupkó, L. Vékás, Colloidal stability of carboxylated iron oxide nanomagnets for biomedical use. Period. Polytech. Chem. Eng. **58**, 3–10 (2014), https://doi.org/10.3311/PPch.7285
22. W. Huang, X. Wang, Study on the properties and stability of ionic liquid-based ferrofluids. Colloid Polym. Sci. **290**(16), 1695–1702 (2012), https://doi.org/10.1007/s00396-012-2773-0
23. M.V. Avdeev, V.L. Aksenov, Small-angle neutron scattering in structure research of magnetic fluids. Phys. Usp. **53**(10), 971–993 (2010), https://doi.org/10.3367/UFNe.0180.201010a.1009
24. J.S. Pedersen, Analysis of small angle scattering data from colloids. J. Coll. Interf. Sc. **70**, 171–210 (1997), https://doi.org/10.1016/S0001-8686(97)00312-6
25. L.A. Feigin, D.I. Svergun, in *Structure Analysis by Small-Angle X-ray and Neutron Scattering*, ed. by G.W. Taylor (Plenum Press, New York, 1987), p. 335, https://doi.org/10.1007/978-1-4757-6624-0
26. V.I. Petrenko, M.V. Avdeev, V.L. Aksenov, L.A. Bulavin, L. Rosta, Effect of surfactant excess in non-polar ferrofluids probed by small-angle neutron scattering. Solid State Phenom. **198**(152–153), 198–201 (2009), https://doi.org/10.4028/www.scientific.net/SSP.152-153.198

27. A.V. Nagornyi, V.I. Petrenko, L.A. Bulavin, M.V. Avdeev, L. Almásy, L. Rosta, V.L. Aksenov, Structure of the magnetite-oleic acid-decalin magnetic fluid from small-angle neutron scattering data. Phys. Solid State **56**(1), 91–96 (2014), https://doi.org/10.1134/S1063783414010259
28. L.A. Bulavin, A.V. Nagornyi, V.I. Petrenko, M.V. Avdeev, L. Almásy, L. Rosta, V.L. Aksenov, Neutron studies of the structure of non-polar magnetic fluids with surfactant excess. Ukr. J. Phys. **58**(12), 1143–1148 (2013), https://doi.org/10.15407/ujpe58.12.1143
29. V.I. Petrenko, M.V. Avdeev, L. Almásy L.A. Bulavin, V.L. Aksenov, L. Rosta, V.M. Garamus, Interaction of mono-carboxylic acids in benzene studied by small-angle neutron scattering. Coll. Surf. A. **337**(1–3), 91–95 (2009), https://doi.org/10.1016/j.colsurfa.2008.12.001
30. V.I. Petrenko, M.V. Avdeev, L.A. Bulavin, L. Almasy, N.A. Grigoryeva, V.L. Aksenov, Effect of surfactant excess on the stability of low-polarity ferrofluids probed by small-angle neutron scattering. Crystallogr. Rep. **61**(1), 121–125 (2016), https://doi.org/10.1134/S1063774516010168
31. M.V. Avdeev, D. Bica, L. Vékás, V.L. Aksenov, A.V. Feoktystov, O. Marinica, L. Rosta, V. M. Garamus, R. Willumeit, Comparative structure analysis of non-polar organic ferrofluids stabilized by saturated mono-carboxylic acids. J. Coll. Inter. Sci. **334**(1), 37–41 (2009), https://doi.org/10.1016/j.jcis.2009.03.005
32. A.V. Nagornyi, V.I. Petrenko, M.V. Avdeev, L.A. Bulavin, V.L. Aksenov, Analysis of small-angle neutron scattering from very dilute magnetic fluids. J. Surf. Invest. **4**(6), 976–981 (2010), https://doi.org/10.1134/S1027451010060169
33. A.V. Nagornyi, L.A. Bulavin, V.I. Petrenko, M.V. Avdeev, V.L. Aksenov, Sensitivity of small-angle neutron scattering method at determining the structural parameters in magnetic fluids with low magnetite concentrations. Ukr. J. Phys. **58**(8), 735–741 (2013), https://doi.org/10.15407/ujpe58.08.0735
34. A.V. Nagornyi, V.I. Petrenko, M.V. Avdeev, L.A. Bulavin, L. Rosta, V.L. Aksenov, On determination of the structural parameters of polydisperse magnetic fluids by small-angle neutron scattering. J. Surf. Invest. **7**(1), 99–104 (2013), https://doi.org/10.1134/S1027451013010291
35. VYu. Bezzabotnov, L. Cser, T. Grosz, G. Jancso, YuM Ostanevich, Small-angle neutron scattering in aqueous solutions of tetramethylurea. J. Phys. Chem. **96**, 976 (1992), https://doi.org/10.1021/j100181a079
36. J. Bloustine, T. Virmani, G.M. Thurston, S. Fraden, Light scattering and phase behavior of lysozyme-poly (ethylene glycol) mixtures. Phys. Rev. Lett. **96**, 087803 (2006), https://doi.org/10.1103/PhysRevLett.96.087803
37. V.L. Aksenov, M.V. Avdeev, A.V. Shulenina, Y.V. Zubavichus, A.A. Veligzhanin, L. Rosta, V.M. Garamus, L. Vekas, Neutron and synchrotron radiation scattering by nonpolar magnetic fluids. Crystallogr. Rep. **56**(5), 792–801 (2011), https://doi.org/10.1134/S1063774511050026
38. V.I. Petrenko, L.A. Bulavin, M.V. Avdeev, V.L. Aksenov, L. Rosta, Neutron investigations of the interaction of surfactant molecules in non-polar solvent. Ukr. J. Phys. **53**(3), 229–233 (2008), https://www.ujp.bitp.kiev.ua/files/journals/53/3/530304p.pdf
39. G. Lancz, M.V. Avdeev, V.I. Petrenko, V.M. Garamus, M. Koneracká, P. Kopčanský, SANS study of poly (ethylene glycol) solutions in D_2O. Acta Phys. Pol. A. **118**(5), 980–982 (2010), https://doi.org/10.12693/APhysPolA.118.980
40. V.I. Petrenko, M.V. Avdeev, V.M. Garamus, L.A. Bulavin, V.L. Aksenov, L. Rosta, Micelle formation in aqueous solutions of dodecylbenzene sulfonic acid studied by small-angle neutron scattering. Colloids Surf. A: Physicochem. Eng. Aspects. **369**(1–3), 160–164 (2010), https://doi.org/10.1016/j.colsurfa.2010.08.023
41. R.A. Eremin, K.T. Kholmurodov, V.I. Petrenko, L. Rosta, N.A. Grigoryeva, M.V. Avdeev, On the microstructure of organic solutions of mono-carboxylic acids: combined study by infrared spectroscopy, small-angle neutron scattering and molecular dynamics simulations. Chem. Phys. **461**(5), 1–10 (2015), https://doi.org/10.1016/j.chemphys.2015.08.017

42. V.I. Petrenko, L.A. Bulavin, M.V. Avdeev, P. Kopcansky, Structure diagnostics of biorelevant associates and complexes in liquid nanosystems by small-angle scattering, in *Nanobiophysics: Fundamentals and Applications* (Pan Stanford, 2015), pp. 129–161, https://doi.org/10.1201/b20480-6
43. R.A. Eremin, K.T. Kholmurodov, V.I. Petrenko, L. Rosta, M.V. Avdeev, Effect of the solute-solvent interface on small-angle neutron scattering from organic solutions of short alkyl chain molecules as revealed by molecular dynamics simulation. J. Appl. Crystallogr. **46**(2), 372–378 (2013), https://doi.org/10.1107/S002188981205131X
44. R.A. Eremin, K.T. Kholmurodov, V.I. Petrenko, M.V. Avdeev, Calculating the bulk properties of decalins and fatty acids in decalin according to data from molecular dynamics simulation. Russ. J. Phys. Chem. A **87**(5), 745–751 (2013), https://doi.org/10.1134/S0036024413040092
45. R.A. Eremin, K.T. Kholmurodov, V.I. Petrenko, M.V. Avdeev, Solute-solvent interaction in nonpolar solutions of oleic acid as revealed by molecular dynamics simulation. J. Surf. Invest. **7**(6), 1128–1132 (2013), https://doi.org/10.1134/S1027451013060281
46. R.A. Eremin, K.T. Kholmurodov, V.I. Petrenko, L. Rosta, M.V. Avdeev, Molecular dynamics simulations for small-angle neutron scattering: scattering length density spatial distributions for mono-carboxylic acids in d-decalin, in *Models in Bioscience and Materials Research: Molecular Dynamics and Related Techniques* (Nova Science Publishers, Inc., 2013), pp. 139–154 https://www.scopus.com/inward/record.url?scp=84895354238&partnerID=8YFLogxK
47. R.A. Eremin, K.T. Kholmurodov, V.I. Petrenko, L. Rosta, M.V. Avdeev, Molecular dynamics simulation analysis of small-angle neutron scattering by a solution of stearic acid in benzene. Phys. Solid State **56**(1), 81–85 (2014), https://doi.org/10.1134/S1063783414010132
48. R.A. Eremin, K.T. Kholmurodov, V.I. Petrenko, M.V. Avdeev, Oleic acid in benzene and decalin solutions: solvation shell effect on small-angle neutron scattering, in *Computational Materials and Biological Sciences* (Nova Science Publishers, Inc., 2015), pp. 25–34
49. M.V. Avdeev, E. Dubois, G. Mériguet, E. Wandersman, V.M. Garamus, A.V. Feoktystov, R. Perzynski, Small-angle neutron scattering analysis of a water-based magnetic fluid with charge stabilization: contrast variation and scattering of polarized neutrons. J. Appl. Crystallogr. **42**(6), 1009–1019 (2009), https://doi.org/10.1107/S0021889809036826
50. M.V. Avdeev, A.V. Feoktystov, P. Kopcansky, G. Lancz, V.M. Garamus, R. Willumeit, M. Timko, M. Koneracka, V. Zavisova, N. Tomasovicova, A. Jurikova, K. Csach, L.A. Bulavin, Structure of water-based ferrofluids with sodium oleate and polyethylene glycol stabilization by small-angle neutron scattering: contrast-variation experiments. J. Appl. Crystallogr. **43**(5), 959–969 (2010), https://doi.org/10.1107/S0021889810025379
51. A.V. Nagornyi, L.A. Bulavin, V.I. Petrenko, O.I. Ivankov, O.V. Tomchuk, M.V. Avdeev, L. Vékás, Determination of the structure factor of interparticle interactions in the ferrofluid by small-angle neutron scattering. Nucl. Phys. At. Energy. **15**(1), 59–65 (2014), https://jnpae.kinr.kiev.ua/15.1/Articles_PDF/jnpae-2014-15-0059-Nagornyi.pdf
52. A.V. Nagornyi, V.I. Petrenko, M.V. Avdeev, S.O. Solopan, O.V. Yelenich, A.G. Belous, A. A. Veligzhanin, A.Yu. Gruzinov, Ya.V. Zubavichus, L.A. Bulavin, Structure of water-based magnetic liquids by small-angle x-ray scattering. Rom. J. Phys. **61**(3–4), 483–490 (2016), https://www.nipne.ro/rjp/2016_61_3-4/0483_0490.pdf
53. A.V. Nagornyi, V.I. Petrenko, M.V. Avdeev, O.V. Yelenich, S.O. Solopan, A.G. Belous, AYu. Gruzinov, O.I. Ivankov, L.A. Bulavin, Structural aspects of magnetic fluid stabilization in aqueous agarose solutions. J. Mag. Mag. Mater. **431**, 16–19 (2017), https://doi.org/10.1016/j.jmmm.2016.10.018
54. A.V. Feoktystov, M.V. Avdeev, V.L. Aksenov, V.I. Petrenko, L.A. Bulavin, D. Bica, L. Vekas, V.M. Garamus, R. Willumeit, Contrast variation in small-angle neutron scattering from magnetic fluids stabilized by different mono-carboxylic acids. Solid State Phenom. **152–153**, 186–189 (2009), https://doi.org/10.4028/www.scientific.net/SSP.152-153.186

55. V.I. Petrenko, V.L. Aksenov, M.V. Avdeev, L.A. Bulavin, L. Rosta, L. Vekas, V.M. Garamus, R. Willumeit, Analysis of the structure of aqueous ferrofluids by the small-angle neutron scattering method. Phys. Solid State **52**(5), 974–978 (2010), https://doi.org/10.1134/S1063783410050185
56. V.I. Petrenko, M.V. Avdeev, V.M. Garamus, L.A. Bulavin, V.L. Aksenov, L. Rosta, Micelle formation in aqueous solutions of dodecylbenzene sulfonic acid studied by small-angle neutron scattering. Colloids Surf. A **369**, 160–164 (2010), https://doi.org/10.1016/j.colsurfa.2010.08.023
57. V.I. Petrenko, M.V. Avdeev, V.M. Garamus, L.A. Bulavin, P. Kopcansky, Impact of polyethylene glycol on aqueous micellar solutions of sodium oleate studied by small-angle neutron scattering. Colloids Surf. A **480**, 191–196 (2015), https://doi.org/10.1016/j.colsurfa.2014.11.064
58. D. Bica, L. Vékás, M.V. Avdeev, O. Marinică, V. Socoliuc, M. Bălăsoiu, V.M. Garamus, Sterically stabilized water based magnetic fluids: synthesis, structure and properties. J. Mag. Mag. Mater. **311**(1) 17–21 (2007), https://doi.org/10.1016/j.jmmm.2006.11.158
59. L. Vekas, D. Bica, M.V. Avdeev, Magnetic nanoparticles and concentrated magnetic nanofluids: synthesis, properties and some applications. China Particuol. **5**, 43–49 (2007), https://doi.org/10.1016/j.cpart.2007.01.015
60. M.V. Avdeev, V.L. Aksenov, M. Balasoiu et al., Comparative analysis of the structure of sterically stabilized ferrofluids on polar carriers by small-angle neutron scattering. J. Coll. Inter. Sci. **295**, 100–107 (2006), https://doi.org/10.1016/j.jcis.2005.07.048
61. M. Balasoiu, M.V. Avdeev, V.L. Aksenov et al., Structural organization of water-based ferrofluids with sterical stabilization as revealed by SANS. J. Mag. Mag. Mater. **300**, e225–e228 (2006), https://doi.org/10.1016/j.jmmm.2005.10.085
62. V. Petrenko, L. Bulavin, M. Avdeev, V. Garamus, M. Koneracka, P. Kopcansky, Structure and interaction of poly (ethylene glycol) in aqueous solutions Small-angle neutron scattering data. Macromolecular Symposia **335**, 20–23 (2014), https://doi.org/10.1002/masy.201200117
63. I.V. Gapon, V.I. Petrenko, M.V. Avdeev, L.A. Bulavin, YuN Khaydukov, O. Soltwedel, V. Zavisova, I. Antal, P. Kopcansky, Consideration of diffuse scattering in the analysis of specular neutron reflection at the magnetic fluid-silicon interface. J. Surf. Invest. **9**(2), 320–325 (2015), https://doi.org/10.1134/S1027451015010073
64. M.V. Avdeev, V.I. Petrenko, I.V. Gapon, L.A. Bulavin, A.A. Vorobiev, O. Soltwedel, M. Balasoiu, L. Vekas, V. Zavisova, P. Kopcansky, Comparative structure analysis of magnetic fluids at interface with silicon by neutron reflectometry. Appl. Surf. Sci. **352**, 49–53 (2015), https://doi.org/10.1016/j.apsusc.2015.02.170
65. M. Kubovcikova, I.V. Gapon, V. Zavisova, M. Koneracka, V.I. Petrenko, O. Soltwedel, L. Almasy, M.V. Avdeev, P. Kopcansky, On the adsorption properties of magnetic fluids: impact of bulk structure. J. Mag. Mag. Mater. **427**, 67–70 (2016), https://doi.org/10.1016/j.jmmm.2016.10.104
66. I.V. Gapon, V.I. Petrenko, L.A. Bulavin, M. Balasoiu, M. Kubovcikova, V. Zavisova, M. Koneracka, P. Kopcansky, M.V. Avdeev, Structure analysis of aqueous ferrofluids at interface with silicon: neutron reflectometry data. J. Phys.: Confer. Series. 848 (2017) 012015, https://doi.org/10.1088/1742-6596/848/1/012015
67. A. Vorobiev, J. Major, H. Dosch, G. Gordeev, D. Orlova, Magnetic field dependent ordering in ferrofluids at SiO_2 interfaces. Phys. Rev. Lett. **93,** 267203 (2004), https://doi.org/10.1103/PhysRevLett.93.267203

Part IV
Phase Transitions and Critical Phenomena

Chapter 11
Phase Transitions in a Continuum Curie-Weiss System: A Quantitative Analysis

Yuri Kozitsky, Mykhailo Kozlovskii and Oksana Dobush

Abstract Phase transitions in a continuum Curie-Weiss system of interacting particles are studied quantitatively. The interaction is determined by a division of the underlying space $\mathbb{R}^d$ into congruent cubic cells. For a region $V \subset \mathbb{R}^d$ consisting of $N \in \mathbb{N}$ cells, each two particles contained in V attract each other with intensity J_1/N. The particles contained in the same cell repel each other with intensity $J_2 > J_1$. For fixed values of the intensities J_1, J_2, the temperature and the chemical potential, the thermodynamic phase is defined as a probability measure on the space of occupation numbers of cells. There is shown that the half-plane $J_1 \times$ *chemical potential* contains phase coexistence points, and thus multiple thermodynamic phases of the system may exist at the same values of the temperature and chemical potential. The numerical calculations describing such phenomena are presented.

11.1 Introduction

The rigorous theory of phase transitions in continuum particle systems has much more modest account of the results than its counterpart dealing with lattices, graphs, etc. It is then quite natural to employ here mean field models. In [1] one can find mathematical realization of the mean field approach by using a Kac-like infinite range attraction combined with a binary repulsion. By means of rigorous upper and lower bounds obtained in that paper for the canonical partition function, the authors derived the equation of state indicating the possibility of a first-order phase

Y. Kozitsky
Maria Curie-Skłodowska University, Pl. Marii Curie-Skłodowskiej 5,
20-031 Lublin, Poland
e-mail: jkozi@hektor.umcs.lublin.pl

M. Kozlovskii (✉) · O. Dobush
Institute for Condensed Matter Physics of the National Academy
of Sciences of Ukraine, 1, Svientsitskii Str., Lviv 79011, Ukraine
e-mail: mpk@icmp.lviv.ua

O. Dobush
e-mail: dobush@icmp.lviv.ua

L. A. Bulavin and A. V. Chalyi (eds.), *Modern Problems of Molecular Physics*,
Springer Proceedings in Physics 197, https://doi.org/10.1007/978-3-319-61109-9_11

transition. Later on, this result was employed in [2], see also [3], to go beyond the mean field frames. Another mean-field approach is based on the use of Curie-Weiss interactions and appropriate methods of calculating asymptotics of integrals. Recently it was turned into a mathematical theory in the framework of which the thermodynamic phases are constructed as probability measures on an appropriate phase space, see [4, Sect. 11.2]. In this context, in [4] there was introduced a simple Curie-Weiss type model of a continuum particle system, for which it was proved in [5] that multiple thermodynamic phases may exist at the same values of the temperature and chemical potential. In the present work, we numerically investigate this model in more detail.

In the model which we study, the interaction is determined by a division of the underlying space $\mathbb{R}^d$ into congruent cubic cells. For a region $V \subset \mathbb{R}^d$ which consists of N such cells, J_1/N is set to be the attraction between each two particles in V, regardless their positions. If such two particles are hosted in the same cell, they are subject to repulsion of each other with intensity $J_2 > J_1$. Unlike to [1], we work in the grand canonical ensemble, and thus the initial thermodynamic variables are the inverse temperature $\beta = 1/k_B T$ and the physical chemical potential. However, we use the variables $p = \beta J_1$ and $\mu = \beta \times$*physical chemical potential* and define single-phase domains of the half-plane $\{(p, \mu) : p > 0, \mu \in \mathbb{R}\}$, (see Definition 1), by a condition determining a unique probability measure $\mathbf{Q}_{p,\mu}$, given in (11.16) and (11.15). This measure is set to be the thermodynamic phase of the system, in the grand canonical formalism and the approach of [4]. The points (p, μ) correspond to the coexistence of multiple thermodynamic phases. There the mentioned single-phase condition fails to hold due to the existence of multiple $\bar{y}$.

Section 11.3 is dedicated to numerical results related to description of the phase transition in the system with Curie-Weiss interaction. An analysis of the chemical potential behavior $\bar{\mu}(y)$ which meet the condition of maximum of $E(y, p, \mu)$ is provided. To make quantitative analysis we considered fixed values of the parameters $\upsilon = 12$, $p = 6$. The former parameter determine the volume of a cell, the latter is connected to attractive part of the interaction potential. We found the critical value of $p = p_c(a)$ dividing the monotonic and non-monotonic dependence of $\bar{\mu}(y)$. The explicit form of the state equation of the model is obtained in the region of $p < p_c(a)$ (matching to $T > T_c$, T_c is defined in (11.23)) describing a single-phase domain. The pressure as a function of density and temperature is represented. In the region of $p > p_c(a)$ we found values of the chemical potential μ_c at which the first order phase transition occurs for different temperatures. In Sect. 11.3.3 the equation of state of the model in the region of low densities and temperatures below the critical one is represented. The second and third cascades of phase transitions are considered in Sect. 11.3.4. In this case the pressure as a function of density at $T < T_c$ is obtained. Section 11.3.5 represents numerical results stated above for the case of another ratio of repulsive and attractive parameters.

11.2 The Model: A Theoretical Study

The following theoretical study is given in our recent paper [5] in more detail. In this work we briefly summarize the theory and pay much attention to a quantitative analysis of the phenomenon.

By $\mathbb{N}$, $\mathbb{R}$ we denote the sets of natural and real numbers, respectively. We also put $\mathbb{N}_0 = \mathbb{N} \cup \{0\}$. For $d \in \mathbb{N}$, by $\mathbb{R}^d$ we denote the Euclidean space of vectors $x = (x^1, \dots, x^d)$, $x^i \in \mathbb{R}$. In the sequel, its dimension d will be fixed. By dx we mean the Lebesgue measure on $\mathbb{R}^d$.

11.2.1 The Grand Canonical Partition Function

For some $c > 0$, we let $\Delta = (-c/2, c/2]^d \subset \mathbb{R}^d$ be a cubic cell of volume $v = c^d$ centered at the origin. Let also $V \subset \mathbb{R}^d$ be the union of $N \in \mathbb{N}$ disjoint translates Δ_ℓ of Δ, i.e.

$$V = \bigcup_{\ell=1}^{N} \Delta_\ell .$$

As is usual for Curie-Weiss theories, cf. [4], the form of the interaction energy of the system of particles placed in V depends on V. In our model, the energy of a configuration $\gamma = \{x_1, \dots, x_n\} \subset V$, $n \in \mathbb{N}$, is

$$W_N(\gamma) = \frac{1}{2} \sum_{x,y \in \gamma} \Phi_N(x, y),$$

where

$$\Phi_N(x, y) = -J_1/N + J_2 \sum_{\ell=1}^{N} \mathbb{I}_{\Delta_\ell}(x) \mathbb{I}_{\Delta_\ell}(y). \tag{11.1}$$

Here $\mathbb{I}_{\Delta_\ell}$ is the indicator of Δ_ℓ, that is, $\mathbb{I}_{\Delta_\ell}(x) = 1$ if $x \in \Delta_\ell$ and $\mathbb{I}_{\Delta_\ell}(x) = 0$ otherwise. For convenience, in W_N above we have included the self-interaction term $\Phi_N(x, x)$, which does not affect the physics of the model. We also write W_N and Φ_N instead of writing W_V and Φ_V since these quantities depend only on the number of cells in V but not on its particular location. The first term in Φ_N with $J_1 > 0$ describes attraction. By virtue of the Curie-Weiss approach, it is taken equal for all particles. The second term with $J_2 > 0$ describes repulsion between two particles contained in one and the same cell. That is, in our model every two particles in V attract each other independently of their location, and repel if they are in the same cell. The intensities J_1 and J_2 in (11.1) are assumed to satisfy the following condition

$$J_2 > J_1. \tag{11.2}$$

The latter is to secure the stability of the interaction, see [6], that is to satisfy

$$\int_V \Phi_N(x,y)dy > 0, \qquad \text{for all } x \in V.$$

Let $\beta = 1/k_{\mathrm{B}}T$ be the inverse temperature. To optimize the thermodynamic variables we introduce the following

$$p = \beta J_1, \qquad a = J_2/J_1, \tag{11.3}$$

and the dimensionless chemical potential $\mu = \beta \times$(physical chemical potential). Then $(p, \mu) \in \mathbb{R}_+ \times \mathbb{R}$ is considered as the basic set of thermodynamic variables, whereas a and υ are model parameters.

The grand canonical partition function in region V is

$$\Xi_N(p,\mu) = 1 + \sum_{n=1}^{\infty} \frac{1}{n!} \int_{V^n} \exp\left(\mu n - \frac{\beta}{2} \sum_{i,n=1}^{n} \Phi_N(x_i, x_j) \right) dx_1 \cdots dx_n. \tag{11.4}$$

In [5], the representation in (11.4) was transformed into the following one

$$\Xi_N(p,\mu) = \sum_{\rho \in \mathbb{N}_0^N} \exp\left(\frac{p}{2N} \left(\sum_{\ell=1}^{N} \rho_\ell \right)^2 \right) \prod_{\ell=1}^{N} \pi(\rho_\ell, \mu), \tag{11.5}$$

where p is as in (11.3) and

$$\pi(n,\mu) = \frac{\upsilon^n}{n!} \exp\left(\mu n - \frac{1}{2} a p n^2 \right), \qquad n \in \mathbb{N}_0. \tag{11.6}$$

Note that, for $p = 0$, π turns into the (non-normalized) Poisson distribution with parameter υe^{μ}. Hence, alternating the cell size amounts to shifting μ.

We write Ξ_N instead of Ξ_V for the reasons mentioned above. Such type of distribution was used in [7].

11.2.2 Single-Phase Domains and Phase Transitions

For the reader's convenience, we repeat here some definitions and facts from [5]. By a standard identity involving Gaussian integrals one gets

$$\exp\left(\frac{p}{2N} \left(\sum_{\ell=1}^{N} \rho_\ell \right)^2 \right) = \sqrt{\frac{N}{2\pi p}} \int_{\mathbb{R}} \exp\left(-N \frac{y^2}{2p} + y \sum_{\ell=1}^{N} \rho_\ell \right) dy.$$

Applying this in (11.5) one arrives at

$$\Xi_N(p,\mu) = c_N \int_{\mathbb{R}} \exp\left(NE(y,p,\mu)\right) dy, \quad c_N = \sqrt{\frac{N}{2\pi p}}, \tag{11.7}$$

where

$$E(y,p,\mu) = -\frac{y^2}{2p} + \ln K(y,p,\mu), \tag{11.8}$$

and, cf. (11.3) and (11.6),

$$K(y,p,\mu) = \sum_{n=0}^{\infty} \frac{v^n}{n!} \exp\left((y+\mu)n - \frac{ap}{2}n^2\right). \tag{11.9}$$

Note that E is an infinitely differentiable function of all its arguments. Set

$$P_N(p,\mu) = \frac{1}{vN} \ln \Xi_N(p,\mu). \tag{11.10}$$

By the following evident inequality

$$(y+\mu)n - \frac{ap}{2}n^2 \le \frac{(y+\mu)^2}{2ap}, \qquad n \in \mathbb{N}_0,$$

we obtain from (11.9) and (11.8) that

$$E(y,p,\mu) \le -\frac{a-1}{2ap}y^2 + \frac{\mu}{2ap}(2y+\mu) + v. \tag{11.11}$$

As is usual for Laplace's method, see [8], the calculation of the large N limit in (11.10) is based on finding global maxima of $E(y,p,\mu)$ as a function of $y \in \mathbb{R}$ (i.e. for fixed values of $p > 0$ and $\mu \in \mathbb{R}$). By (11.11) we have that $\lim_{|y|\to+\infty} E(y,p,\mu) = -\infty$; hence, each point $\bar{y}$ of global maximum belongs to a certain interval $(\bar{y}-\varepsilon, \bar{y}+\varepsilon)$, where it is also a maximum point. Since E is everywhere differentiable in y, then $\bar{y}$ is the point of global maximum only if it solves the following equation

$$E_1(y,p,\mu) := \frac{\partial}{\partial y} E(y,p,\mu) = 0. \tag{11.12}$$

By (11.8) and (11.9) this equation can be rewritten in the form

$$-\frac{y}{p} + \frac{K_1(y,p,\mu)}{K(y,p,\mu)} = 0, \tag{11.13}$$

$$K_1(y,p,\mu) := \sum_{n=1}^{\infty} \frac{nv^n}{n!} \exp\left((y+\mu)n - \frac{ap}{2}n^2\right).$$

The equation in (11.13) has at least one solution for all $p > 0$ and $\mu \in \mathbb{R}$. Since both K_1 and K take only strictly positive values, these solutions are also strictly positive.

Definition 1 We say that (p, μ) belongs to a single-phase domain if $E(y, p, \mu)$ has a unique global maximum $\bar{y} \in \mathbb{R}$ such that

$$E_2(\bar{y}, p, \mu) := \frac{\partial^2}{\partial y^2} E(y, p, \mu)|_{y=\bar{y}} < 0. \tag{11.14}$$

Note that $\bar{y}$ can be a point of maximum if $E_1(\bar{y}, p, \mu) = E_2(\bar{y}, p, \mu) = 0$. That is, not every point of global maximum corresponds to a point in a single-phase domain.

The condition in (11.13) determines the unique probability measure $Q_{p,\mu}$ on $\mathbb{N}_0$ such that

$$Q_{p,\mu}(n) = \frac{1}{K(\bar{y}, p, \mu) n!} \upsilon^n \exp\left((\bar{y} + \mu) n - \frac{ap}{2} n^2 \right), \quad n \in \mathbb{N}_0, \tag{11.15}$$

which yields the probability law of the occupation number of a single cell. Then the unique thermodynamic phase of the model corresponding to $(p, \mu) \in \mathscr{R}$ is the product

$$\mathbf{Q}_{p,\mu} = \bigotimes_{\ell=1}^{\infty} Q_{p,\mu}^{(\ell)} \tag{11.16}$$

of the copies of the measure defined in (11.15). It is a probability measure on the space of all vectors $\mathbf{n} = (n_\ell)_{\ell=1}^{\infty}$, in which $n_\ell \in \mathbb{N}_0$ is the occupation number of ℓ-th cell.

The role of the condition in (11.14) is to yield the possibility to apply Laplace's method for asymptotic calculating the integral in (11.7). By direct calculations it follows that

$$\begin{aligned} E_2(y, p, \mu) = &- \frac{1}{p} + \frac{1}{2\left[K(y, p, \mu)\right]^2} \\ &\times \sum_{n_1, n_2 = 0}^{\infty} \frac{\upsilon^{n_1 + n_2}}{n_1! n_2!} (n_1 - n_2)^2 \exp\left((y + \mu)(n_1 + n_2) - \frac{ap}{2}(n_1^2 + n_2^2) \right). \end{aligned} \tag{11.17}$$

In dealing with the equation in (11.13) we will fix $p > 0$ and consider E_1 as a function of $y \in \mathbb{R}$ and $\mu \in \mathbb{R}$. Then, for a given μ, we solve (11.12) to find $\bar{y}$ and then check whether it is the unique point of global maximum and (11.14) is satisfied, i.e. whether (p, μ) belongs to a single-phase domain. As it was shown in [5] each single-phase domain, $\mathscr{R}$, has the following properties: (a) it is an open subset of $\mathbb{R}_+ \times \mathbb{R}$; (b) for each $(p_0, \mu_0) \in \mathscr{R}$, the function $\mathscr{I}_{p_0} := \{\mu \in \mathbb{R} : (p_0, \mu) \in \mathscr{R}\} \ni \mu \mapsto \bar{y}(\mu)$ is continuously differentiable on $\mathscr{I}_{p_0}$. Moreover,

$$\frac{d\bar{y}(\mu)}{d\mu} > 0, \qquad \text{for all } \mu \in \mathscr{I}_{p_0}. \tag{11.18}$$

By (11.15) and (11.13) we get the $Q_{p,\mu}$-mean value $\bar{n} = \bar{n}(p, \mu)$ of the occupation number of a given cell in the form

$$\bar{n}(p, \mu) = \sum_{n=0}^{\infty} nQ_{p,\mu}(n) = \frac{K_1(\bar{y}(p, \mu), p, \mu)}{K(\bar{y}(p, \mu), p, \mu)} = \frac{\bar{y}(p, \mu)}{p}. \tag{11.19}$$

Note that, up to the factor υ^{-1}, $\bar{n}(p, \mu)$ is the particle density in phase $\mathbf{Q}_{p,\mu}$. For a fixed p, $\bar{n}(p, \cdot)$ in an increasing function on $\mathscr{I}_p$, which thus can be inverted to give $\bar{\mu}(p, \bar{n})$. By Laplace's method we get that for each $(p, \mu) \in \mathscr{R}$, the limiting pressure $P(p, \mu) = \lim_{N\to+\infty} P_N(p, \mu)$, see (11.10), exists and is continuously differentiable on $\mathscr{R}$. Moreover, it is given by the following formula

$$P(p, \mu) = \upsilon^{-1} E(\bar{y}(p, \mu), p, \mu). \tag{11.20}$$

Let $\mathscr{N}_p$ be the image of $\mathscr{I}_p$ under the map $\mu \mapsto \bar{n}(p, \mu)$. Then the inverse map $\bar{n} \mapsto \bar{\mu}(p, \bar{n})$ is continuously differential and increasing on $\mathscr{N}_p$. By means of this map, for a fixed p, the pressure given in (11.20) can be written as a function of $\bar{n}$

$$P = \bar{P}(\bar{n}) = \upsilon^{-1} E(p\bar{n}, p, \bar{\mu}(p, \bar{n})), \qquad \bar{n} \in \mathscr{N}_p, \tag{11.21}$$

which is the equation of state.

By virtue of Definition 1 each single-phase domain is an open subset of the open right half-plane $\{(p, \mu) : p > 0, \ \mu \in \mathbb{R}\}$, see (11.18). In the context of this work, a phase transition is understood as the possibility to have different phases at the same value of the pair (p, μ). If this is the case, (p, μ) is called a *phase coexistence point*. Clearly, such a point should belong to the common topological boundary of at least two distinct single-phase domains. In [5], we demonstrated the existence of phase transitions in this sense. Namely, we proved the following statements.

Theorem 1 *There exists $p_0 = p_0(a) > 0$ such that the set $\mathscr{R}(p_0) := \{(p, \mu) : p \in (0, p_0]\}$ is a single-phase domain.*

Theorem 2 *For each $a > 1$, there exists $p_1 = p_1(a) > 0$ such that, for each $p \geq p_1$, the line $l_p = \{(p, \mu) : \mu \in \mathbb{R}\}$ contains at least one phase-coexistence point.*

11.3 The Quantitative Analysis

In the remaining part of the work, we provide our numerical results related to the facts just stated. Let us fix the following values of the parameters

$$a = J_2/J_1 = 1.2, \quad \upsilon = 12. \tag{11.22}$$

Below we return to the question how the results depend on the values of a and υ.

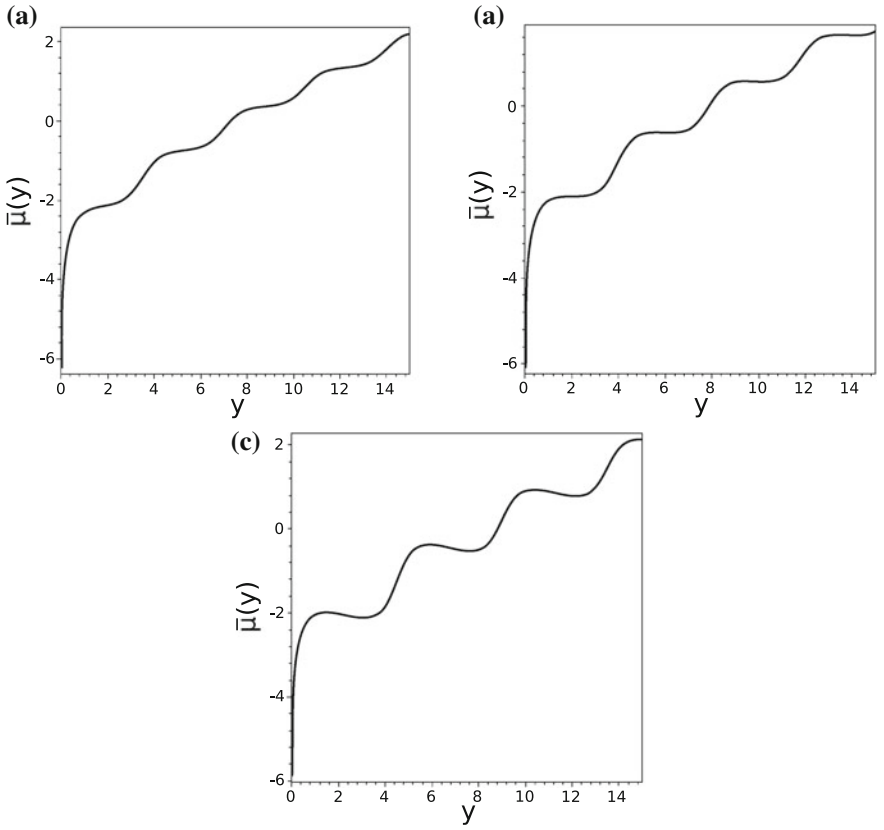

Fig. 11.1 Plot of the chemical potential $\bar{\mu}(y)$ as a function of y for values of the attraction parameter $p = 3.5$ (curve a), $p = p_c(1.2)$ (curve b), $p = 4.5$ (curve c)

As follows from Theorems 1 and 2, for small $p_0 > 0$ the stripe $\{(p, \mu) : \mu \in \mathbb{R},\ p \in (0, p_0]\}$ is a single-phase domain, whereas the lines $l_p = \{(p, \mu) : \mu \in \mathbb{R}\}$ contain phase coexistence points if $p \geq p_1$ for sufficiently big $p_1 > p_0$. Thus, there should be some critical $p_c \in (p_0, p_1)$ which separates these two regimes. Our aim now is to find its numerical value for the parameters fixed in (11.22).

Figure 11.1 below shows the plot of $\bar{\mu}(y)$ which is the function inverse to that in (11.18). That is, given $y > 0$, $\bar{\mu}(y)$ is the value of μ for which y solves (11.13), see [5] for more detail. In view of (11.18), a monotone dependence of $\bar{\mu}(y)$ on y corresponds to a single-phase domain. Case (a) of Fig. 11.1 corresponds to $p = 3.5$, case (b) to $p = p_c = 3.928236$, and case (c) to $p = 4.5$. Easily seen that $p_c = 3.928236$ is indeed the critical value. Recall that it corresponds to $a = 1.2$. By means of $p_c(a)$ one may define the corresponding value of the critical temperature, cf. (11.3),

$$T_c(a) = J_1/p_c(a). \tag{11.23}$$

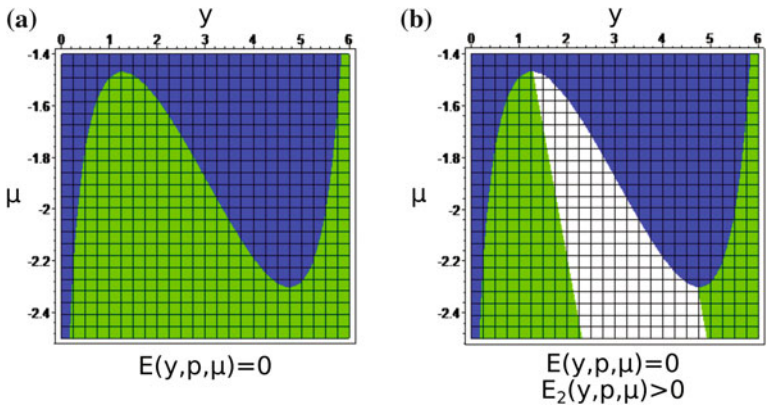

Fig. 11.2 **a**—division boundary of two surfaces which give the line of extremes (11.12) of the function $E(\bar{y}, p, \mu)$. Figure 11.2b—the imposed (white) part meet the condition of minimum of $E(\bar{y}, p, \mu)$ ($p = 6$ $a = 1.2$, $\upsilon = 12$)

At $p < p_c(a)$ the equation (11.13) gives the line of extremes of the function $E(\bar{y}, p, \mu)$. Using this equation the chemical potential $\bar{\mu}(y)$ is a monotonic increasing function of y (see Fig. 11.1a).

According to Theorem 2 for all $p > p_c(a)$ multiple solutions $\bar{y}$ correspond to the same value of $\bar{\mu}(y)$, as it is shown on Fig. 11.1c. In this case some part of the curve represented on Fig. 11.1c expresses the max $E(\bar{y}, p, \mu)$, and the other part of it meets the condition of min $E(\bar{y}, p, \mu)$ at equal values of μ. As a consequence of inequality (11.14) the parts of the curve for (11.13) meets the condition of max $E_0(\bar{y}, \mu)$ if $\bar{\mu}(y)$ behaves as an increasing function of y. The condition min $E(\bar{y}, p, \mu)$ is implemented on the areas where $\bar{\mu}(y)$ is a decreasing function of y, which means that this condition is not applicable since we use the Laplace method for calculating (11.7).

It is easy to make sure about the latter fact directly from calculations. Figure 11.2a shows the intersection of the surface $E_1(y, p, \mu)$ (11.12) with the plane of zeroth level corresponding to the line of extremes $\bar{\mu}(y)$. On Fig. 11.2b the image of the surface $E_2(y, p, \mu) > 0$ projection (white part) is imposed on the projection from Fig. 11.2a. Positive part of the second derivative of the function $E_0(\bar{y}, y)$ coincide with the area where $\bar{\mu}(y)$ as a function of $\bar{y}$ decrease. The condition $E_2(y, p, \mu) < 0$ is held only on the areas where $\bar{\mu}(y)$, is an increasing function of its argument.

11.3.1 The Equation of State in a Single-Phase Domain

In a single-phase domain, the function in (11.8) has a unique global maximum $\bar{y}(p, \mu)$, and hence the Laplace method yields in (11.7) that

$$\Xi_N \simeq c_N \exp\left[NE(\bar{y}(p, \mu)p, \mu)\right],$$

where the asymptotic equality is understood in the large N limit.

Let us write the equation of state of the model in case of $p < p_c(a)$ in the region of temperature $T > T_c$. At this range of parameter p the chemical potential $\bar{\mu}(y)$ behaves as a monotonic increasing function of $\bar{y}$ (Fig. 11.1a). The explicit form of the pressure is given in (11.20) This equation expresses the pressure P as a function of temperature and chemical potential since $\bar{y}$ is a monotonic increasing function of μ as it is seen from (11.13). This equation can be rewritten in terms of the mean density $\bar{n}$ as the mean value of the occupation number n over probability measure $Q_{p,\mu}(n)$ from (11.15). Taking into account (11.19) we have

$$\bar{n} = \sum_{m=0}^{\infty} \frac{\upsilon^m}{m!} m \exp\left(-\frac{ap}{2}m^2\right) \exp\left(p\bar{n}m + \beta\mu(p,\bar{n})m\right) / \sum_{m=0}^{\infty} \frac{\upsilon^m}{m!} \exp\left(-\frac{ap}{2}m^2\right) \exp\left(p\bar{n}m + \beta\mu(p,\bar{n})m\right). \tag{11.24}$$

The equation (11.24) holds a central place in the grand canonical ensemble formalism. It gives a possibility to find the chemical potential as a function of density and express the pressure in terms of density and temperature. In range of values of the parameter $p < p_c(a)$ for (11.21) we obtain the explicit form of the equation of state

$$P\upsilon = -\frac{1}{2}p\bar{n}^2 + \ln \sum_{m=0}^{\infty} \frac{\upsilon^m}{m!} \exp\left(-\frac{ap}{2}m^2\right) \exp\left(p\bar{n}m + \beta\mu(p,\bar{n})m\right), \tag{11.25}$$

here $\mu(p,\bar{n})$ is a function of temperature and average density as it can be seen in (11.24).

Figure 11.3 shows pressure as a function of average density $\bar{n}$ and the parameter p, which is inversely proportional to temperature. Easy to see that pressure is a monotonic increasing function of temperature and density.

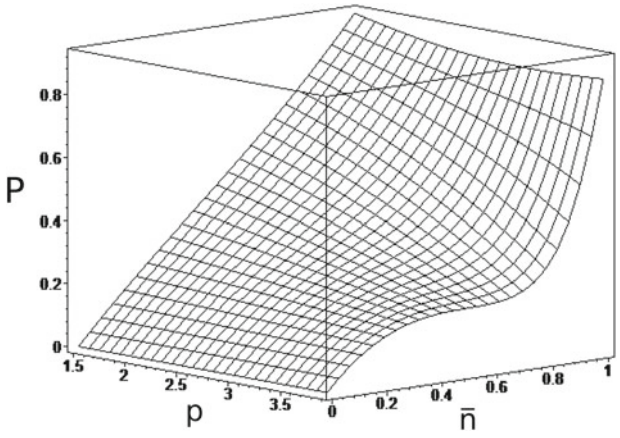

Fig. 11.3 Plot of pressure as a function of density and parameter of attraction p (see Eq. (11.25)) at temperature higher then critical one ($a = 1.2$, $\upsilon = 12$)

11.3.2 The Case of $T < T_c$

Consider calculation of the grand partition function in the region of $p > p_c(a)$, that correspond to temperatures $T < T_c$. Here the chemical potential $\bar{\mu}(y)$ is a monotonic function of $\bar{y}$. Let as explore the behavior of $\bar{\mu}(y)$ in this range of values of the parameter p. It is represented on Fig. 11.4 at $p = 6$. For example, here we have chosen a large (in comparison to the critical one) value of this parameter so the maximum coordinates $\bar{\mu}(y)$ are not too close to each other.

The points of extremes of $\bar{\mu}(y)$ can be found from the equation (11.13). This equation allows us to determine the local maximums y_1, y_{11}, y_{12} and local minimums y_2, y_{21}, y_{22} of the function $\bar{\mu}(y)$. Taking into account the equality (11.17) we obtain the following equation

$$K_2(\bar{y}, p, \mu)/K_0(\bar{y}, p, \mu) - (K_1(\bar{y}, p, \mu)/K_0(\bar{y}, p, \mu)) = 1/p \tag{11.26}$$

for the extremum points of the function $\bar{\mu}(y)$. Comparing the latter expression to the condition (11.14) easy to see that the solutions $\bar{y}$ of this equation do not meet the condition $\max E(\bar{y}, p, \mu)$. However this solutions determine specific points, which divide the region of values $\bar{y}$ into intervals. In particular, in the interval (Fig. 11.4)

$$\bar{y} \in (0, y_1) \tag{11.27}$$

where $y_1 = 1.267510$, the function $E_0(\bar{y}, \mu)$ has its maximum ($E_2(\bar{y}, p, \mu) < 0$), while at

$$\bar{y} \in (y_1, y_2) \tag{11.28}$$

where $y_2 = 4.755127$, this function meet the condition of minimum ($E_2(\bar{y}, p, \mu) > 0$). The following range of values (see also Fig. 11.7)

$$\bar{y} \in (y_2, y_{11}); \quad \bar{y} \in (y_{21}, y_{12}) \tag{11.29}$$

correspond to the maximum of $E(\bar{y}, p, \mu)$ etc. This function has its minimum at

$$\bar{y} \in (y_1, y_2); \quad \bar{y} \in (y_{11}, y_{21})$$

therefore there is no need to consider them anymore. Here $y_{11} = 7.244287$, $y_{21} = 10.763368$. For the purpose of calculating the integral (11.7) we are interested in $\max E(\bar{y}, p, \mu)$ and intervals of values of $\bar{y}$ in (11.27), (11.29).

In the region of values $\bar{y} \in (0, y_2')$ the function $\mu(\bar{y})$ is monotonic increasing. Here each value of $\bar{y}$ has specific corresponding value of $\bar{\mu}(y) < \mu_2$. So the form of the equation of state for $\bar{y}$ in this interval coincides with (11.20).

Consider in more details the region of the first maximum of the function $\bar{\mu}(y)$ (Fig. 11.4). There are multiple solutions $\bar{y}$ in the interval

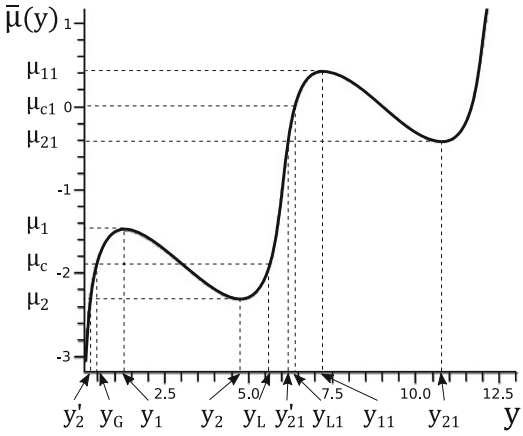

Fig. 11.4 Plot of the chemical potential as a function of $\bar{y}$ at $p = 6$ in he region of monotonic dependence

$$\bar{\mu}(y) \in (\mu_2, \mu_1) \tag{11.30}$$

where $\mu_2 = -2.308041$, $\mu_1 = -1.470040$. It is necessary to find out which one leads to max $E(\bar{y}, p, \mu)$.

Let us introduce the function

$$E_G(\bar{y}, p, \bar{\mu}(y)) = E(\bar{y}, p, \bar{\mu}(y))\Theta(y_1 - \bar{y}), \tag{11.31}$$

corresponding to the values $\bar{y} \in (0, y_1)$, and the function

$$E_L(\bar{y}_1, p, \bar{\mu}(y)) = E(\bar{y}, p, \bar{\mu}(y))\Theta(\bar{y} - y_2)\Theta(y_{11} - \bar{y}), \tag{11.32}$$

defined in the interval $\bar{y} \in (y_2, y_{11})$, y_{11} is the coordinate of the second local maximum of $\bar{\mu}(y)$ (Fig. 11.4). Each of this functions is a function of chemical potential. The interval of values (11.28) is not taken into account since $E(\bar{y}, p, \mu)$ fails to meet the condition of maximum there.

The function $E(\bar{y}, p, \mu)$ at $p = 6$ is monotonic for all

$$\bar{\mu}(y) \in (-\infty, \mu_2), \tag{11.33}$$

and also for

$$\bar{\mu}(y) \in (\mu_1, \mu_{21}). \tag{11.34}$$

where $\mu_{21} = -0.4173780$. The value μ_{21} of the chemical potential correspond to the solution of the equation (11.29) at $\bar{y} = y_{21}$. Appliance of the Laplace method for calculation of the integral (11.7) in regions of the chemical potential (11.33) and (11.34) is obvious, since for each $\bar{y}$ one has a single extremum (maximum) value of $E(\bar{y}, p, \mu)$. One should pay additional attention to values of the chemical potential (11.30). It is necessary to find which function either (11.31) or (11.32) has larger

value. Easy to make sure that at $\bar{\mu}(y) = \mu_2$ we have

$$E_G(\bar{y}, p, \mu_2) > E_{0L}(\bar{y}, \mu_2),$$

and at $\bar{\mu}(y) = \mu_1$

$$E_G(\bar{y}, p, \mu_1) < E_L(\bar{y}, p, \mu_1).$$

Therefore in range of values (11.30) for all $p > p_c(a)$ there exist such μ_c that

$$E_G(y_G, p, \mu_c) = E_L(y_L, p, \mu_c), \tag{11.35}$$

moreover $y_G \leq y_L$. Here the sign of equality refer to case of $T = T_c$. Easy to see that for all $\mu < \mu_c$ we have $E_G > E_L$, and for $\mu > \mu_c$ the maximal one will be $E_L > E_G$.

Figure 11.5 represent the plot of $E(\bar{y}, p, \mu)$ at two fixed values of $\bar{\mu}(y)$ (at $p = 6, \upsilon = 12, a = 1.2$). The critical value of the chemical potential in case of mentioned above values of the parameters is $\mu_c = -1.890291$. Case (a) correspond to $\mu_a < \mu_c$, case (b) to $\mu_b > \mu_c$. Note that μ_a is close to μ_2 ($\mu_a \geq \mu_2$), and μ_b is close to μ_1 ($\mu_b \leq \mu_1$). At smaller value of the chemical potential μ_a the maximum on the left-hand side is larger then the one on the right-hand side. At larger one μ_b we have the opposite situation. In other words, at small values of the chemical potential $\mu \in (-\infty, \mu_c)$ the function $E_G > E_L$, and at larger ones $\mu \in (\mu_c, \mu_{21})$ we have $E_L > E_G$. Same situation occurs in the region of values $\mu \in (\mu_{21}, \mu_{11})$. In the next section we consider this in more details.

Numerical calculation of μ_c is the following. Firstly we consider the coordinates of extremes point of the curve $\mu(\bar{y})$ in the interval

$$\bar{y} \in (0, y_{11}), \tag{11.36}$$

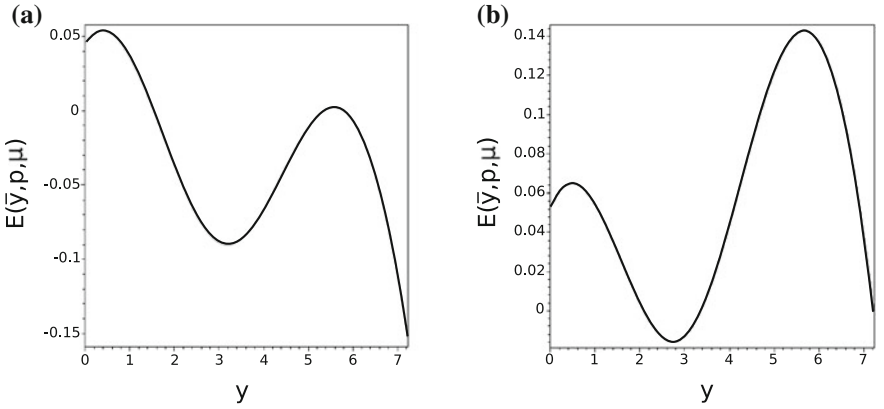

Fig. 11.5 Plot of the function $E(\bar{y}, p, \mu)$ at two fixed values of the chemical potential **a** $\mu_a = -1.950$, **b** $\mu_b = -1.800$ ($\mu_c = -1.890291, p = 6, a = 1.2, \upsilon = 12$)

where y_{11} is the coordinate of the second larger maximum of this function (Fig. 11.4). Applying the equation (11.26) for this purpose allows us to find the extremum points $y_1, y_2; y_{11}, y_{21}$ and so on. Using this values in (11.13) we obtain corresponding values of the chemical potential μ_1, μ_2, μ_{11}, μ_{21} (Fig. 11.4).

The following scheme serves to calculate the chemical potential μ_c, see (11.35). The value of $\mu^{(1)}$ matching the coordinate $y_s = (y_1 + y_2)/2$ is obtained from the equation (11.13)

$$\mu^{(1)} = \bar{\mu}(y_s).$$

In the interval (11.36) there are two more values of $\bar{y}$, namely $y_G^{(1)} < y_s$ and $y_L^{(1)} > y_s$, corresponding to $\mu^{(1)}$

$$\begin{aligned} y_G^{(1)} &= \bar{y}(\mu^{(1)}), \quad y_G^{(1)} \in (0, y_1), \\ y_L^{(1)} &= \bar{y}(\mu^{(1)}), \quad y_L^{(1)} \in (y_2, y_{11}) \end{aligned}$$

Then $E_G(y_G^{(1)}, p, \mu^{(1)})$ should be compared with $E_L(y_L^{(1)}, p, \mu^{(1)})$. In case they are not equal one has to find $\mu^{(2)}$ from the condition

$$E_G(y_G^{(2)}, p, \mu^{(2)}) = E_L(y_L^{(2)}, p, \mu^{(2)}).$$

and to repeat the applied for $\mu^{(1)}$ procedure of calculation for the value $\mu^{(2)}$. This is the way to find μ_c which meet the condition (11.35) with pre-set accuracy. The value $\mu_c = \lim_{n\to\infty} \mu^{(n)} = -1.890291$ allows to set the mechanism of the first order phase transition. The chemical potential is the control parameter since we consider the grand canonical partition. In the limit $\mu \to -\infty$ we have $\bar{y} = 0$, as follows from (11.13). The increase of μ cause the increase of $\bar{y}$. In the range of values

$$\mu \in (-\infty, \mu_c)$$

the value $\bar{y}$ increase starting from $\bar{y} = 0$ to $\bar{y} = y_G$ ($y_G = \lim_{n\to\infty} y_G^{(n)} = 0.420875$). The further increase of μ cause changing the function $E(\bar{y}, p, \mu)$ from $E_G(\bar{y}, p, \mu)$ at $\mu = \mu_c - 0$, to the function $E_G(\bar{y}, p, \mu)$ at $\mu = \mu_c + 0$. This situation is accompanied by jump of $\bar{y}$ starting from y_G to y_L ($y_L = \lim_{n\to\infty} y_L^{(n)} = 5.621854$). Moreover at $T = T_c$ we have $y_L(T_c) = y_G(T_c)$. With decrease of temperature ($T < T_c$) the value

$$\Delta y(T) = y_L(T) - y_G(T)$$

increases.

11.3.3 Equation of State in the Region of Low Densities and Temperatures $T < T_c$

Taking into account previous results we can write the equation of state in the region of low densities $\bar{n}$ at $p > p_c(a)$. Let us denote

$$P_{\bar{n}}\upsilon = -\frac{p}{2}\bar{n} + \ln \sum_{m=0}^{\infty} \frac{\upsilon^m}{m!} e^{-\frac{ap}{2}m^2} e^{p\bar{n}m} e^{\beta\mu(p,\bar{n})m}, \tag{11.37}$$

where $\mu(p, \bar{n})$ is the solution of the equation (11.24). There are some fixed values of the density $\bar{n} = \bar{y}/p$ at $T < T_c$. The first one appear in the region of the first maximum of $\bar{\mu}(y)$ (Fig. 11.4)

$$n_G = y_G/p \tag{11.38}$$

It correspond to the value $\bar{y}$ in the interval $\bar{y} \in (0, y_1)$ for the chemical potential μ_c (11.35). At $p = 6$ we have $n_G = 0.070146$.

The second fixed value is

$$n_L = y_L/p \tag{11.39}$$

($n_L = 0.936975$ at $p = 6$). This one correspond to the value $\bar{y}$ on the interval $\bar{y} \in (y_2, y_{11})$ at $\mu = \mu_c$. Moreover $n_L \geq n_G$ for all $T \leq T_c$.

There is a fixed value of the chemical potential in the region of the second maximum

$$n'_{21} = \bar{y}'_{21}/p, \tag{11.40}$$

(for $p = 6$ we have $\bar{y}'_{21} = 6.163534, n'_{21} = 1.027256$), corresponding to the coordinate y'_{21} which is calculated at μ_{21} (Fig. 11.4). The values (11.38), (11.39) and (11.40) can be obtained from the equation (11.24) in different intervals of the variable $\bar{y}$.

The equation of state of the system in the region of densities

$$n \in (0, n'_{21}) \tag{11.41}$$

including the values of $\bar{y}$ starting from zero to y'_{21} has the following form

$$P\upsilon = P_{\bar{n}}\upsilon\Theta(n_G - \bar{n}) + P_{n_G}\upsilon\Theta(\bar{n} - n_G)\Theta(n_L - \bar{n}) + P_{\bar{n}}\upsilon\Theta(\bar{n} - n_L)\Theta(n'_{21} - \bar{n}). \tag{11.42}$$

Moreover the first term in (11.42) describes the behavior of the phase I with the lowest density, the third term–the phase II, which has larger density than the phase I at all $T < T_c$. At $T = T_c$ both phases has equal densities and at $T > T_c$ there exist only one density which is a monotonic increasing function of pressure (Fig. 11.3).

The second term in (11.42) indicate that pressure remains constant and equal to

$$P_{n_G}\upsilon = -\frac{p}{2}\bar{n}_G + \ln\sum_{m=0}^{\infty}\frac{\upsilon^m}{m!}e^{-\frac{ap}{2}m^2}e^{p\bar{n}_G m}e^{\beta\mu_c m}.$$

in the interval

$$\bar{n} \in (n_G, n_L) \tag{11.43}$$

Note that the condition (11.35) gives $P_{n_G} = P_{n_L}$, where P_{n_L} is as follows

$$P_{n_L}\upsilon = -\frac{p}{2}\bar{n}_L + \ln\sum_{m=0}^{\infty}\frac{\upsilon^m}{m!}e^{-\frac{ap}{2}m^2}e^{p\bar{n}_L m}e^{\beta\mu_c m}.$$

In case of $p > p_c(a)$ there are unattainable densities in the interval (11.43) from the point of varying the chemical potential $\bar{\mu}(y)$. When $\bar{\mu}(y)$ tends to μ_c from the left-hand side we have the density region

$$\bar{n} \in (0, n_G). \tag{11.44}$$

When $\bar{\mu}(y)$ tends to μ_c from the right-hand side

$$\bar{n} \in (n_L, n'_{21}). \tag{11.45}$$

The density region (11.43) in between does not exist. The solutions of the phase I, where the density varies in the interval (11.44), transit by jump into the solutions of the phase II, with (11.45). This is connected with change of derivative value of the chemical potential in the point μ_c.

Figure 11.6 shows the isotherms of pressure in the interval (11.41) at different values of the parameter p.

11.3.4 Transition Between the Phase II and the Phase III

The previous section was dedicated to description of behavior of the model in the region of low densities (11.41). It can be conditionally linked to the gas-liquid phase transition, since density in this case vary starting from zero up to some fixed value. Let us describe the behavior of the system for larger values of density $\bar{n} > n'_{21}$ (Fig. 11.7) and show that transition from the phase II to the phase III (with larger density than in the phase II) is possible here. Behavior of $\bar{\mu}(y)$ is of most importance here.

Figure 11.7 shows the characteristic points of the function $\bar{\mu}(y)$ in the region of the second and the third maximums of the value $\bar{\mu}(y)$ from (11.13).

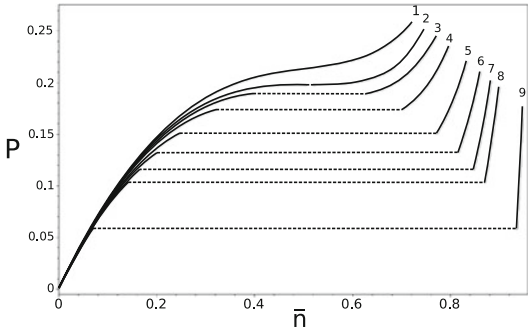

Fig. 11.6 Isotherms of pressure as a function of density at $p > p_c(1.2)$ in the region of low densities (11.41). Curve 1 corresponds to $p = 3.8 < p_c(1.2)$. The curves 2–9 correspond to $p \geq p_c$: $p = p_c(1.2)$ (curve 2), $p = 4$ (curve 3), $p = 4.135$ (curve 4), $p = 4.3647$ (curve 5), $p = 4.5824$ (curve 6), $p = 4.8$ (curve 7), $p = 5$ (curve 8), $p = 6$ (curve 9)

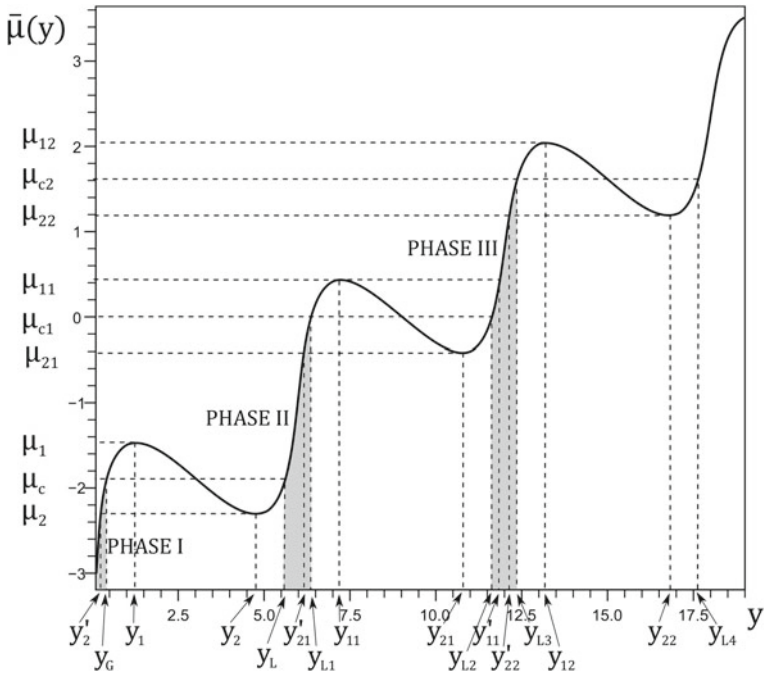

Fig. 11.7 Plot of $\bar{\mu}(y)$ in the region of the second maximum at $p = 6$, $a = 1.2$, $v = 12$

In the interval of the chemical potential values

$$\bar{\mu}(y) \in (\mu_{21}, \mu_{11}) \tag{11.46}$$

($\mu_{21} = -0.417380, \mu_{11} = 0.431080$) we have a non-monotonic behavior of $\bar{\mu}(y)$. Let us define the function

$$E_S(\bar{y}, p, \mu) = E(\bar{y}, p, \mu)\Theta(y_{12} - \bar{y})\Theta(y_{21} - \bar{y}), \tag{11.47}$$

which is nonzero in the interval

$$\bar{y} \in (y_{21}, y_{12}).$$

where $y_{12} = 13.236413$. The function $\bar{\mu}(y)$ is monotonic in the interval

$$\bar{y} \in (y_L, y'_{21})$$

so the function $E(\bar{y}, p, \mu)$ is characterized by one value $\bar{y}$ determining the integral (11.7), therefore it determines the expression of pressure (11.37). The phase II exists here in "pure" form.

The interval of values

$$\bar{y} \in (y'_{21}, y'_{11})$$

($y'_{21} = 6.163534, y'_{11} = 11.862089$) correspond to non-monotonic dependence of $E(\bar{y}, p, \mu)$ on $\bar{y}$. Therefore it is worthily to compare the functions $E_L(\bar{y}, p, \mu)$ from (11.32) and $E_S(\bar{y}, p, \mu)$ from (11.47) at all values of the chemical potential from the interval (11.46). As well as in case of transition from the phase I to the phase II, there exist the chemical potential μ_{c_1}, such that

$$E_L(y_{L1}, p, \mu_{c_1}) = E_S(y_{L2}, p, \mu_{c_1}),$$

where

$$y_{L1} \in (y'_{21}, y_{11}) \quad \text{and} \quad y_{L2} \in (y_{21}, y_{12}).$$

The way of calculating μ_{c_1} is the same as represented in Sect. 11.4 for the case of μ_c. Figure 11.8 shows the pressure as a function of $\bar{y}$ at $p = 4, p = 5, p = 6$ and $p = 8$ including the region of the first and the second local maximums of the curve $\bar{\mu}(y)$. Evidently, except the transition from the phase I to the phase II (at $y \in (y_G, y_L)$) there exist the transition from phase II to phase III, where the jump of the order parameter occurs in the interval of values

$$\bar{y} \in (y_{L1}, y_{L2}),$$

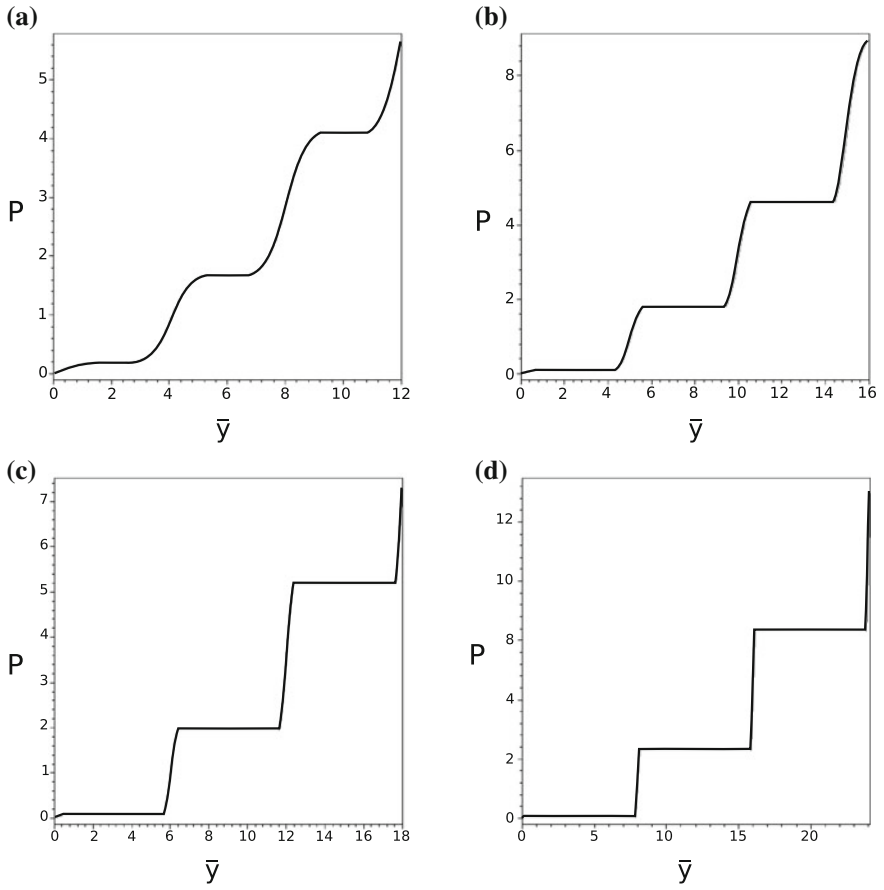

Fig. 11.8 Plot of the pressure as a function of density in the region of first three maximums of dependence $\bar{\mu}(y)$ at $a = 1.2$, $\upsilon = 12$: **a** $p = 4$, **b** $p = 5$, **c** $p = 6$, **d** $p = 8$

where $y_{L1} = 6.373312$, $y_{L2} = 11.641773$, moreover y_{L1} characterizes the maximal density of the phase II, and y_{L2}—the minimal density of the phase III at correspondent values of p.

The further growth of the chemical potential yield the cascade of phase transitions from the phase f to the phase $(f + 1)$. Each subsequent cascade correspond to larger densities. Note that this model has more than a single critical point. Each of them is characterized by its critical temperature, critical density, and exist in appropriate cascade.

Sufficient growth of the attraction parameter p causes the possibility of transition of the system from the phase I to the phase III omitting the phase II. As we can see from the quantitative results there exist some value of the parameter p_T, that at $p > p_T$ there occurs a competition between $E_G(\bar{y}, p, \mu)$, $E_L(\bar{y}, p, \mu)$ and $E_s(\bar{y}, p, \mu)$

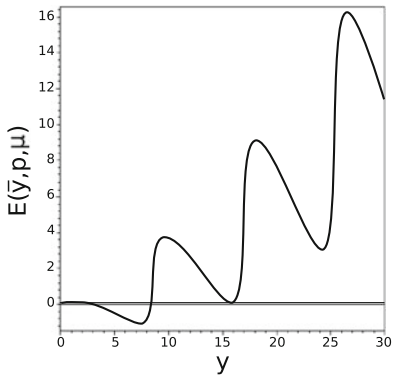

Fig. 11.9 Comparison of values of the function $E(\bar{y}, p, \mu)$ at large attraction parameter $p = p_T$

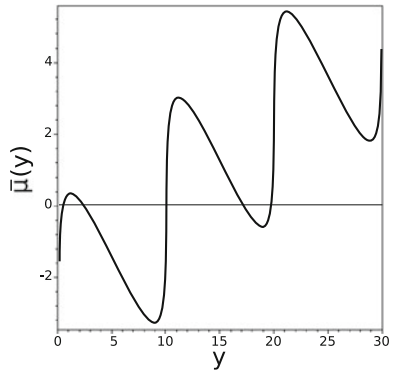

Fig. 11.10 Plot of the function $\bar{\mu}(y)$ at $p = 10$

aimed to find out which one of this functions is maximal at the same value of the chemical potential (see Fig. 11.9). According to the definition (11.31) the variable $\bar{y}$ of the function $E_G(\bar{y}, p, \mu)$ takes small values $\bar{y} \in (0, y_1)$, in $E_L(\bar{y}, p, \mu)$ this variable changes in the interval $\bar{y} \in (y_2, y_{11})$, where $y_2 > y_1$, and in $E_s(\bar{y}, p, \mu)$ $-\bar{y} \in (y_{21}, y_{12})$, moreover $y_{21} > y_{11}$. Note that in the region of values $p_c(1.2) < p < p_T$ correspondent to the temperature interval

$$T_T < T < T_c \tag{11.48}$$

there occur only the sequence of phase transitions phase I—phase II, phase II—phase III etc. This is because each $\bar{\mu}(y)$ has not more than three extremum points (two of them correspond to max $E(\bar{y}, p, \mu)$).

At $p > p_T$ there is a situation where five extremum points of the function $E(\bar{y}, p, \mu)$ (three of them are maximums of $E(\bar{y}, p, \mu)$) correspond to single value of $\bar{\mu}(y)$ (see Fig. 11.10). In this case it is worthily to find out which one of them is the largest. To do this we have to compare the functions $E_G(\bar{y}, p, \mu)$, $E_L(\bar{y}, p, \mu)$ and $E_s(\bar{y}, p, \mu)$ at some values of μ. There are two possible cases. In the former $E_G(\bar{y}, p, \mu)$ transits to $E_L(\bar{y}, p, \mu)$ at $\mu = \mu_c$, and $E_L(\bar{y}, p, \mu)$ transits to $E_s(\bar{y}, p, \mu)$ at $\mu = \mu_{1c}$. Moreover $\mu_{1c} > \mu_c$. This situation occurs in the region of temperatures (11.48). In the latter case

$E_G(\bar{y}, p, \mu)$ transits to $E_s(\bar{y}, p, \mu)$ at once at $\mu = \mu_s$, namely there occur the transition of the phase I to the phase III, omitting the phase II. This situation can happen only in the region of $p > p_T$ which match the temperature region $T < T_T < T_c$. There are important numerical results which show that first of all for (11.22) we have at $a = 1.2$

$$p_T = 8.440525.$$

and secondly the direct transition between the phases I and III is impossible. Therefore we have the sequence of phase transitions between neighboring phases.

11.3.5 Investigation of Dependence on the Parameter a

This parameter characterizes the relation between repulsive J_1 and attractive J_2 components of the interaction potential. The represented above calculations were executed at $a = 1.2$ and $\upsilon = 12$ from (11.22). Let us see how the results change when the parameter a vary in the interval $1 < a < 10$. In accordance to the condition of stability (11.2) $a > 1$. The parameter υ will be the same as previously $\upsilon = 12$.

The numerical results show that changing the value of a has no influence on existence of the phase transition in the model. It only lead to slightly different absolute value of the critical temperature which is defined in (11.23). The latter fact is natural, since T_c depends on the parameter p which is the repulsive component of the interaction potential and on the value $p_c(a)$ separating monotonic behavior of the extremum value of the chemical potential from non-monotonic one.

However note that the critical value of the chemical potential increases sufficiently when a grows ($\upsilon = 12$):

$$\begin{aligned}
&a = 0.0001 \quad \mu_{c_1}^{1} = -2.516, \quad p_c(1) = 3.8255,\\
&a = 1.2 \quad\;\; \mu_{c_1}^{1.2} = -2.105, \quad p_c(1.2) = 3.9282,\\
&a = 2 \quad\;\; \mu_{c_1}^{2} = -0.4866, \quad p_c(2) = 3.9973,\\
&a = 10 \quad\;\; \mu_{c_1}^{10} = 15.5196, \quad p_c(10) = 4.0000.
\end{aligned}$$

It means that with growth of repulsive part of the interaction potential (with respect to the attractive one) the phase transition occur at more larger value of the chemical potential.

Numerical way of calculating $p_c(a)$ is the following. The function $\bar{\mu}(y)$ has an inflection point in the critical point. Namely the following equalities are held

$$\frac{\partial \bar{\mu}(y)(y)}{\partial \bar{y}} = 0.$$

$$\frac{\partial^2 \bar{\mu}(y)(y)}{\partial \bar{y}^2} = 0,$$

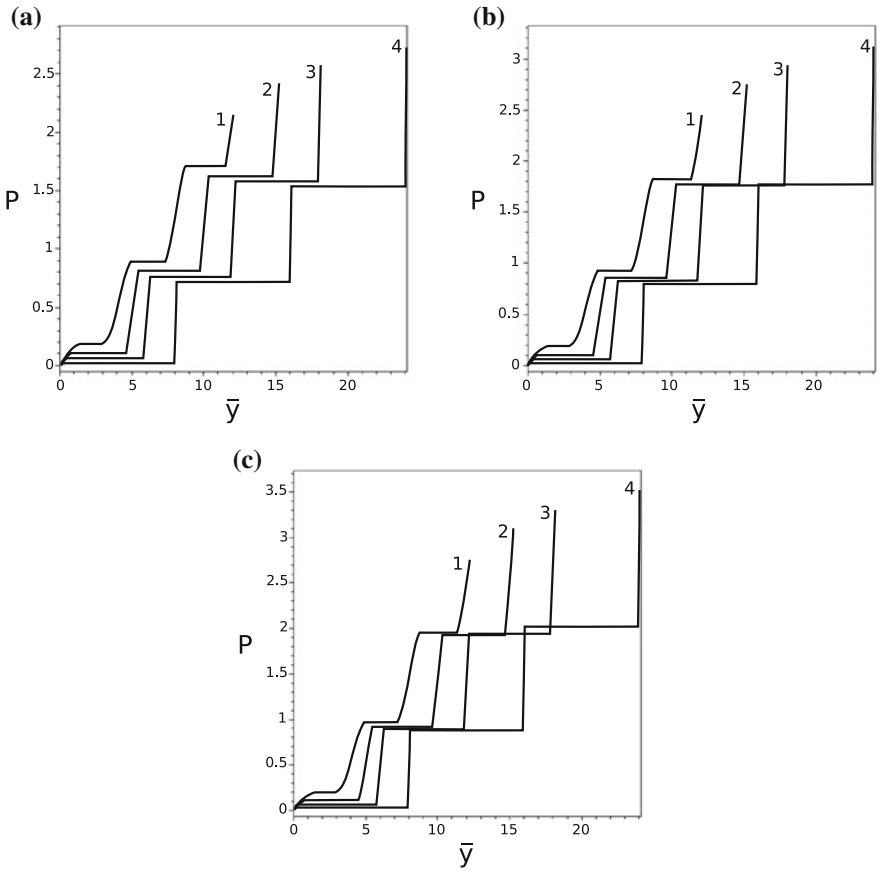

Fig. 11.11 Isotherms of pressure as a function of density at $\upsilon = 12$, **a** correspond to $a = 1.0001$, **b** $a = 1.01$ and **c** $a = 1.02$. Curve 1 is for $p = 4$, curve 2 $p = 5$, curve 3 $p = 6$ and curve 4 $p = 8$

If these equalities are held simultaneously we obtain $\bar{y} = \bar{y}_c$ and $p = p_c(a)$.

Figure 11.11a represent the isotherms of the equation of state at $\upsilon = 12, a = 1.0001$, and different p. Easy to see that curves of isotherms have no intersection at any p.

The case of $a = 1.0001$ is shown on Fig. 11.11b. At low p this curves also don't intersect but the isotherms where $p = 6$ and $p = 8$ cross in the phase transition in the third cascade. The same situation occur at $a = 1.02$ (Fig. 11.11c). Here we have a crossing in the third cascade of the phase transition (particularly in case of $p = 5$, $p = 6$ and $p = 8$). Besides the values of pressure coincide in cases of $p = 6$ and $p = 8$ in the phase transition point of the second phase transition cascade.

In case of $a = 1.2$ and different p isotherms in the first cascade has no crossing, but there are numerous intersections in the second and the third cascades.

11.4 Conclusions

We made the accurate calculation of the grand partition function of single-sort cell model with Curie-Weiss potential. Consequently it is found that this model has a sequence of first order phase transitions at temperatures below the critical one T_c. The critical temperature value depends on two parameters: attractive component of the interaction potential J_1 and the parameter a. We proved the existence of multiple thermodynamic phases at the same values of temperature and chemical potential, which are the extensive model parameters. We deal directly with thermodynamic phases in the grand canonical ensemble, in contrast to the approach of [1]. We provided detailed quantitative study at fixed values of parameters of the model in wide region of densities and temperature. Behavior of the pressure as a function of density is explored for first three cascades of first-order phase transitions at temperatures below the critical one T_c. To the best of our knowledge, this is the first result of this kind.

Acknowledgements This work was supported in part by the European Commission under the project STREVCOMS PIRSES-2013-612669, which is cordially acknowledged by the authors.

References

1. J.L. Lebowitz, O. Penrose, Rigorous treatment of the van der Waals-Maxwell theory of the liquid-vapor transition. J. Math. Phys. **7**, 98–113 (1966)
2. J.L. Lebowitz, A.Z. Mazel, E. Presutti, Liquid-vapor phase transition for systems with finite range interactions. J. Stat. Phys. **94**, 955–1025 (1999)
3. E. Presutti, Phase transitions for point particle systems. Physica A **263**, 141–147 (1999)
4. C. Külske, A. Opoku, Continuous spin mean-field models: limiting kernels and Gibbs properties of local transforms. J. Math. Phys. **49**(31), 125215 (2008)
5. Y. Kozitsky, M. Kozlovskii, A Phase Transition in a Continuum Curie-Weiss System with Binary Interactions (2016), http://arxiv.org/abs/1610.01845 [math-ph]
6. D. Ruelle, Superstable interactions in classical statistical mechanics. Comm. Math. Phys. **18**, 127–159 (1970)
7. M. Kozlovskii, O. Dobush, Representation of the grand partition function of the cell model: the state equation in the mean-field approximation. J. Mol. Liq. **215** 58–68 (2016)
8. M.V. Fedoryuk, Asymtotic methods in analysis, in Analysis I: Integral Representations and Asymptotic Methods, ed. by M.A. Evgrafov, R.V. Gamkrelidze. Encyclopaedia of Mathematical Sciences, vol. 13 (Springer-Verlag, Berlin, Heidelberg, 1989), pp. 83–191

Chapter 12
Dynamic Anomalies in Confined Supercooled Water and Bulk Fluids

Alexander V. Chalyi

Abstract This review paper is aimed at studying the problems as follows: (1) the Widom line and its analogues in supercooled and supercritical regions; (2) effects of dimensional crossover (DC) on the critical exponents, effective spatial d_{eff} and fractal d_{fr} dimensionalities; (3) anomalous behavior of the diffusion coefficient D and the shear viscosity coefficient η in bulk fluids and confined supercooled water (CSW) near the critical points; (4) spectra of the light molecular scattering (LMS) and quasi-elastic neutron scattering (QENS) and its possible medical applications. The effective critical exponents as well as the effective spatial d_{eff} and fractal d_{fr} dimensionalities were calculated for confined fluids like CSW. A $3d \leftrightarrow 2d$ DC between the critical exponents $\alpha = 0, \beta = 1/8, \delta = 15, \gamma = 7/4, \nu = 1$ and $\alpha = 0.110, \beta = 0.3265, \delta = 4.789, \gamma = 1.237, \nu = 0.630$ for 2d and 3d systems belonging to the Ising-model universality class were taken into account. Anomalies of the diffusion coefficient were examined in bulk water and CSW in wide intervals of the size and thermodynamic variables corresponding to crossover phenomena between the dynamic fluctuation, crossover and regular regions. The transition between dynamic crossover and regular regions in bulk fluids, including bulk water, is illustrated by changes in the diffusion-coefficient dependences on: (a) the size variable—from $D \sim L^{-1.963}$ to $D \sim L^{-2}$, (b) the temperature variable—from $D \sim (T - T_{\text{c}})^{1.237}$ to $D \sim (T - T_{\text{c}})$, (c) the concentration variable—from $D \sim (x - x_{\text{c}})^{3.789}$ to $D \sim (x - x_{\text{c}})^2$, (d) the pressure variable $D \sim (p - p_{\text{c}})^{0.791}$ to $D \sim (p - p_{\text{c}})^{0.667}$. In confined 2d fluids like CSW such a transition between crossover and regular behaviors should be treated as 2d $\leftrightarrow$ 4d crossover phenomena because results of the Landau mean-field theory are valid for $d = 4$ (with a logarithmic accuracy). A $2d \leftrightarrow 4d$ crossover leads to the following changes in dependence of the diffusion coefficient D on: (a) the size variable from $D \sim L^{-1.75}$

A. V. Chalyi (✉)
Department of Medical and Biological Physics, Bogomolets National Medical University, 13, Shevchenko Blvd, Kiev 01601, Ukraine
e-mail: avchal@nmu.ua

L. A. Bulavin and A. V. Chalyi (eds.), *Modern Problems of Molecular Physics*,
Springer Proceedings in Physics 197, https://doi.org/10.1007/978-3-319-61109-9_12

to $D \sim L^{-2}$, (b) the temperature variable from $D \sim (T - T_c)^{1.75}$ to $D \sim (T - T_c)$, (c) the concentration variable from $D \sim (x - x_c)^{14}$ to $D \sim (x - x_c)^2$, (d) the pressure variable from $D \sim (p - p_c)^{0.933}$ to $D \sim (p - p_c)^{0.667}$. Near the glass-transition critical point of CSW the shear viscosity has much stronger power-law singularity: $\eta \sim (T - T_c)^{-1.81} \sim (x - x_c)^{-14.48} \sim (p - p_c)^{-0.965}$ than in the vicinity of the 3d high-temperature critical point: $\eta \sim (T - T_c)^{-0.065} \sim (x - x_c)^{-0.199} \sim (p - p_c)^{-0.042}$. An important problem of the violation of the Stokes-Einstein relation (SER) in CSW is discussed. Specific properties of LMS and QENS spectra in confined liquids were studied. It was shown that with increasing the characteristic system's size L: (1) the widths Γ_c of the central Rayleigh line and $\Delta E(q^2)$ of the QENS peak, being proportional L^{-2}, are rapidly decreasing; (2) the width Γ_{MB} of Mandelstam-Brillouin components is strongly shortening (broadening) according to $\Gamma_{MB} \sim L^3$; (3) the frequency shift $\Delta\Omega_{MB}$ of the Mandelstam-Brillouin components is weakly increasing (decreasing) in accordance with $\Delta\Omega_{MB} \sim L^{-0.087}$; (4) the Landau-Placzek relation is essentially decreasing (increasing) as is seen from $I_c/2I_{MB} \sim L^{-1.79}$. These results create a reliable background to introduce a new additional diagnostic method of early detecting the tumor formation in practical medicine.

Abbreviations

CSW	Confined supercooled water
LLCP	Liquid-liquid critical point
LDW	Low density water
HDW	High density water
CF	Correlation function
OZ	Ornstein-Zernike
DCF	Direct correlation functions
DC	Dimensional crossover
D	Diffusion coefficient
d	Spatial dimensionality
3d ⇔ 2d	Crossover between 3-dimensional and 2-dimensional systems
d_{eff}	Effective spatial dimensionality
d_{fr}	Fractal dimensionality
SER	Stokes-Einstein relation
LMS	Light molecular scattering
MBC	Mandelstam-Brillouin components
LPR	Landau-Placzek relation
HB	Hydrogen bond
NMR	Nuclear magnetic resonance
QENS	Quasi-elastic neutron scattering

12.1 Introduction

Effects of confinement on phase transitions and critical phenomena and its differences from bulk critical behavior were actively studied in many systems of experimental, theoretical, and practical interest such as bounded fluids and liquid crystals, non-homogeneous liquids in external fields, low-dimensional magnetic systems, few-layer graphene, carbon nanotubes, porous media, biological membranes, vesicles, synaptic clefts, etc. [1–20].

This list of confined systems should be extended, without any doubts, by the most mysterious and unique substance—liquid water. Theoretical and experimental studies as well as computer simulations predict an anomalous behavior of the supercooled water that obviously has, besides a high-temperature critical point at the critical temperature $T_{1c} \approx 647$ K ($t_{1c} \approx 374$ °C), another low-temperature critical point at the critical temperature $T_{2c} \approx 228$ K ($t_{2c} \approx -45$ °C) [21–53]. It should be noted that bulk water, supercooled to such low temperatures, cannot exist in an ordinary liquid state because of its freezing. At the same time in confined fluid systems with hydrophobic boundary surfaces the critical parameters as the critical temperature T_c, critical pressure P_c, critical density ρ_c (or critical concentration x_c in mixtures) are shifted to lower values, preventing such systems from crystallization. It allows studying low-temperature critical anomalies of confined supercooled water (CSW) by experimental methods and computer simulations even near and below $T_{2c} \approx 228$ K.

The recent review "A Tale of Two Liquids" was written by 16 authors actively studying the anomalous properties of water [21]. Four different scenarios were proposed to explain the water anomalies from ambient conditions to the deep-quenched supercooled metastable region, being as follows: (a) the first scenario known as the "stability limit conjecture" [22] was proposed be Speedy in 1982, using empirical equations of state for water and water phase diagram in the metastable region; (b) the second scenario known as the "2nd critical-point hypothesis" [23] was proposed by Poole, Sciortino, Essmann, and Stanley 10 years later in 1992, using ideas of the fluctuation theory of phase transitions; (c) the third "critical-point free" scenario [24, 25] was proposed by Poole, Sciortino, Grande, Stanley, and Angell in 1994, taking into account effects of hydrogen bonds on the thermodynamic behavior of liquid water and its glass-forming properties; (d) the fourth scenario known as the "singularity-free" [26] was proposed by Sastry, Debenedetti, Sciotino, and Stanley in 1996, using the thermodynamics of supercooled water and lattice-model calculations.

Summarizing all the results on anomalous physical properties of water obtained in molecular dynamic simulations and real experiments, one may formulate the following important conclusions [21–53]:

(a) Such thermodynamic properties of CSW as the isobaric heat capacity $C_P = T(\partial S/\partial T)_P$, the isothermal susceptibility χ_T or, better saying, for fluids—the isothermal compressibility $\chi_T = -(\partial V/\partial P)_T/V$, and the isobaric thermal

expansion coefficient $\alpha_T = -(\partial V/\partial T)_P/V$ diverge with power laws as the temperature is approaching the 2nd low-temperature critical point.

(b) Not only thermodynamic but also dynamic physical properties like the diffusion coefficient D and the shear viscosity η demonstrate a singular power-law behavior near the critical point of CSW.

(c) Theoretical explanation of critical anomalies of CSW is based on the most probable "2nd critical-point hypothesis" together with the notion of "the liquid-liquid critical point (LLCP)", located in a deeply quenched metastable state. The hypothesis predicts an existence of two CSW phases: (1) a low density water (LDW) with a disordered structure and Arrehenious behavior, (2) a high density water (HDW) with an ordered tetrahedral structure and non-Arrehenious behavior of dynamic properties. These two CSW phases are separating from each other by the Widom line [54].

The proposed review paper is based on the "2nd critical-point hypothesis" and aimed at studying the problems as follows:

(1) the Widom line and its analogues in supercooled and supercritical fluids;
(2) effects of dimensional crossover (DC) on the critical exponents, effective spatial d_{eff} and fractal d_{fr} dimensionalities;
(3) anomalous behavior of the diffusion coefficient D and the shear viscosity coefficient η in bulk fluids and CSW near the critical points;
(4) spectra of the light molecular scattering (LMS) and quasi-elastic neutron scattering (QENS) and its possible medical applications.

12.2 The Widom Line and its Analogues in Bulk and Confined Fluids

As is known, it is possible to introduce different lines or boundaries to divide "liquid-like" and "gas-like" states of supercritical and supercooled fluids, most popular among them being as follows:

the ***Frenkel line*** characterizing a boundary between "rigid" or "solid-like" and "soft" or "gas-like" states of a fluid [55],
the ***Fisher-Widom line*** giving the boundary between oscillatory and monotonic behavior of the $G_2(r) = g(r) - 1$, where $G_2(r)$ is a pair correlation function, $g(r)$ is a radial distribution function [56],
the ***Widom line*** defining a line of the correlation length ξ maximum points (this name was proposed by Stanley and his collaborators [54, 57]).

Without claiming to give a complete chronology of the Widom-line studies, first it should be noted papers [54, 58–64] in which one can find different definitions of this line. As was mentioned above, a key notion of the Widom line in [54] is connected with a line of the correlation length extrema points. Another definition

was used in [60–63] where the Widom line corresponds to a line of zero ordering field. In [64] one can find references on studies the Widom line near the low-temperature LLCP of CSW.

To author's best knowledge, a similar line was independently established in [58] as a line of susceptibility (compressibility) χ_T maxima points for bulk fluids. This line was found on the basis of experimental data on light scattering with a corresponding theoretical interpretation in the supercritical region of one-component fluid n-pentane and two-component fluid mixture n-pentane—cyclopentane. It seems to be obvious an analogy between both definitions of the Widom line as loci of the correlation length ξ maxima [54] and the susceptibility (compressibility) χ_T maxima [58] due to fluctuation and/or fluctuation-dissipative theorems like a so-called "integral of compressibility" introduced in the statistical theory of condensed matter (see e.g. [65–67])

$$\rho kT\chi_T = 1 + \rho \int G_2(r)dV \propto \xi^{2-\eta^*}, \tag{12.1}$$

where η^* is a critical exponent of the pair correlation function $G_2(r)$ of the order-parameter fluctuations [68].

Supercritical bulk fluids. Here, we shall pay special attention to results obtained in [58] where an analogue of the Widom line was introduced with taking into account the experimental and theoretical studies a line of maxima susceptibility (isothermal compressibility) points of fluids in the supercritical region. Let us consider the data [58] on the light scattering near the liquid-gas critical point in supercritical bulk fluids. We studied the properties of a substance for values of the temperature variable τ_M and order parameter φ_M corresponding to maxima points of the isothermal compressibility $\beta_T(\tau_M, \varphi_M)$ at $T > T_c$. An analysis of the experimental data in the single-scattering approximation shows that the light scattering intensity at small scattering angles

$$I = I_0 \frac{\pi^2 V k_B T}{2\lambda^4 R^2} \left(\frac{\partial \varepsilon}{\partial \varphi}\right)^2 \frac{\partial \varphi}{\partial h}, \tag{12.2}$$

passed through its maxima points at non-zero temperature values $\tau_M = (T - T_c)/T_c \neq 0$ and at fixed heights $H \neq 0$ (Fig. 12.1a and b). Here, in (12.2) φ is the order parameter; $h = \rho_c g H / P_c$ is the conjugated external field variable associated with the gravitational field; H is the height which is measured at $T > T_c$ from the level $H = 0$ where the order parameter φ (the deviation of the density in a one-component fluid or the composition in a two-component solution) is equal to zero. A fundamental question should be mentioned of how close to the critical point one can regard the single-scattering contribution as primary, adequately describing the experimental data, and double and multiple scattering as corrections. An answer to this question and the convergence of the iterative series in the scattering orders was discussed in [69–75].

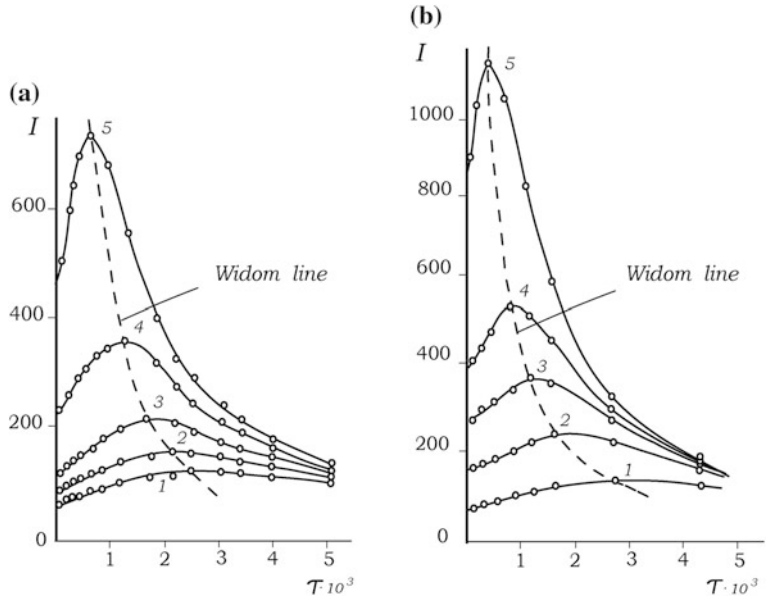

Fig. 12.1 The temperature dependence of the light single-scattering intensity: **a** in n-pentane at different heights H = 1.30 cm (curve 1), H = 1.00 cm (curve 2), H = 0.75 cm (curve 3), H = 0.40 cm (curve 4), and H = 0.15 cm (curve 5); **b** in n-pentane-cyclopentane solution at different heights H = 1.40 cm (curve 1), H = 0.70 cm (curve 2), H = 0.40 cm (curve 3), H = 0.25 cm (curve 4), and H = 0.10 cm (curve 5)

The scaling theory of critical phenomena and phase transitions in bulk systems allows to investigate the experimentally observed behavior of the light scattering intensity using the following equation of state for fluid systems or an equivalent form for magnetic systems (see e.g. [3, 7, 9]:

$$\Delta\mu = \tau^{\beta\delta} G(y) signh,\ H = M|M|^{\delta-1} f(x). \tag{12.3}$$

Here $\Delta\mu$ is the deviation of the chemical potential, $G(y)$ is a scaling function, and $y = \varphi/\tau^{\beta}$ for fluids; H is the magnetic field, M is the magnetization, $f(x)$ is a scaling function of an argument $x = \tau/M^{1/\beta}$ for magnetic systems. At susceptibility extrema points in bulk fluids for fixed external fields h in the vicinity of the critical point one has

$$\left(\frac{\partial I}{\partial \tau}\right)_h = -I\frac{\beta\delta G(y)}{\tau G'(y)}\left[\frac{d}{dy}\left(\ln\frac{G^{\gamma/\beta\delta}}{G'}\right)\right] = 0. \tag{12.4}$$

Equation (12.4) and the 2nd extremum condition $(\partial I/\partial\phi)_h = 0$ are satisfied for a constant value $y = y_M$ which gives a zero value of the derivative

$$\frac{d}{dy}\left(\ln\frac{G^{\gamma/\beta\delta}}{G'}\right)=0. \tag{12.5}$$

Numerical experimental values of $y_M, G(y_M), G'(y_M)$ at susceptibility extrema points in n-pentane and solution of 0.386 mol fraction cyclopentane in n-pentane obtained by Alekhin and Krupskii, together with theoretical interpretation proposed by Chalyi [58], show the constancy of these scaling quantities in the supercritical region.

Thus, it gives a possibility to conclude that an experimentally observed in the supercritical region and theoretically confirmed line of susceptibility extrema points in bulk fluid systems, being similar to the Widom line, possesses the following important properties:

- the order parameter behaves along this line $\varphi_M \sim \tau_M^{\beta}$ as on the coexistence curve,
- the condition $y_M = const$, together with conditions $G(y_M) = const$, $G'(y_M) = const$, is equivalent to the temperature dependence of susceptibility $\chi_M \sim \tau_{\mathrm{M}}^{-\gamma}$ as on the critical isochore,
- the heat capacity $C_{VM} \sim \tau_M^{-\alpha}$ as on the critical isochore,
- the "field" dependences of the order parameter $\varphi_M \sim h_M^{1/\delta}$ as on the critical isotherm,
- the susceptibility $\chi_M \sim h_M^{-(\delta-1)/\delta}$ as on the critical isotherm,
- the heat capacity $C_{VM} \sim h_M^{-\alpha/\beta\delta}$ as on the critical isotherm.

It should be mentioned that a line of the susceptibility maxima observed in [58] is not the only analogue of the Widom line in the supercritical region. Another example of an analogue of the Widom line was discovered in [59]. Here, authors determined the velocity of acoustic waves with nanometer wavelength in supercritical fluid argon at high pressure using inelastic X-ray scattering and molecular dynamic simulations. The obtained results allow finding the Widom line which divides the supercritical region into gas-like and liquid-like parts.

Supercritical confined fluids. Now, let us discuss a line of susceptibility maxima points as an analogue of the Widom line for supercritical confined fluids. However, there is a problem that put this statement under a certain doubt for confined systems. To explain this problem, let us consider specific conditions of the universality classes for which one has a similar critical behavior of different physical properties. As is known [3, 7, 9, 18], these conditions of universality classes for bulk systems with $L \gg \xi$ are as follows: (a) the same space dimensionality D; (b) the same dimensionality (number of components) n of a system's order parameter; (c) the same type (short- or long-range) of the intermolecular interaction; (d) the same symmetry of Hamiltonian (fluctuation part of the thermodynamic potential).

While changing one (or more) of these four conditions, the crossover phenomena may appear in the bulk as well as in systems under confinement. In latter case, i.e. in confined systems with $\xi \geq L$, the following additional conditions of

universality classes have to be taken into account [18, 76]: (e) the same type (hydrophilic, hydrophobic or partial wetting) boundary conditions, (f) the same geometric form of system's limiting surfaces or the same lower crossover dimensionality D_{cros}, (g) the same physical property under consideration.

The lower crossover dimensionality D_{cros} mentioned in the condition (f) means such a dimensionality which characterizes a limiting volume in the case when one (two or all three) its linear size is approaching a monomolecular thickness. Thus, thin films have a form of monomolecular planes with $D_{cros} = 2$, cylindrical pores receive a form of monomolecular wires with $D_{cros} = 1$, while quantum dots or vesicles have a limiting form of a single molecule with $D_{cros} = 0$.

The final condition (g) considers to be important just for a problem mentioned above, because the equations for coordinates of maxima or minima for the physical properties in systems with confinement contain non-universal amplitudes in the scaling laws. Therefore, in contrast to the critical behavior in bulk fluid systems with $L \gg \xi$ having the single critical point, these equations give (a) analogues of critical parameters which are different due to non-universal amplitudes, say, for the heat capacity or the isothermal susceptibility, etc. as well as (b) a non-singular "rounding" extrema points for physical properties in reduced geometry with $\xi \geq L$ and (c) different and non-universal characteristics of the Widom line and its analogues for confined fluids.

12.3 Effects of DC on the Low-Temperature LLCP of CSW

This section will be devoted to a particular case of crossover (transitional) phenomena—a DC describing a smooth transition between systems of different spatial dimensionalities [18, 76–87]. A DC is usually governed by a relationship between the correlation length ξ of order parameter fluctuations and a linear size L of a system's restricted volume under consideration.

It was shown that: (a) in the case of the 1st type DC, the dependence of various physical properties on temperature, density, pressure, and other thermodynamic variables in $3d$ bulk fluids with $L \gg \xi$ transfer to dependence of these properties on linear sizes in $3d$ confined fluids with $L \leq \xi$; (b) in the case of the 2nd type DC, a further decrease of linear sizes in 3d confined fluids converted into a change of the spatial dimensionality, i.e. into a smooth crossover phenomena between 3-dimensional and 2-dimensional fluid systems. Such a smooth $3d \Leftrightarrow 2d$ DC of the effective critical exponents $\alpha_{eff}, \gamma_{eff}, \nu_{eff}$ for the temperature dependence of the isochoric heat capacity C_V, the isothermal compressibility β_T, and the correlation length ξ was examined for fluids in reduced geometry in [85].

Here, we shall study the influence of a $3d \leftrightarrow 2d$ DC on the effective critical exponent β_{eff} of the coexistence curve and on the effective critical exponent δ_{eff} of

the critical isotherm as well as on the effective spatial d_{eff} and fractal d_{fr} dimensionalities for bulk and confined fluids.

To study the properties of confined fluids (generally saying, any soft-matter confined substances), we used a method of finding the pair correlation function (CF) $G_2(r)$ as a Green function of the Helmholtz operator, corresponding to the differential Ornstein-Zernike (OZ) equation with appropriate boundary conditions at limiting surfaces [4, 13, 15]. These differential equations derived from the exact integral OZ equation for short-range direct correlation functions (DCF) C(r) considering any number of its spatial moments C_i and real intermolecular potentials. In the approach that takes into account only the main contributions to CF $G_2(r)$ and zero (hydrophobic) boundary conditions the following formulas were obtained for spatially confined systems in geometry of plane-parallel layers (slitlike pores) and cylindrical samples:

$$G_2(\rho, z) = (2\pi L_0)^{-1} K_0[\rho(\kappa^2 + n^2\pi^2/4L_0^2)^{1/2}] \cos(\pi z/2L_0), \tag{12.6}$$

$$G_2(r, z) = D_1 J_0(\mu_1 r/a) \exp[-(\kappa^2 + \mu_1^2/a^2)^{1/2}|z|], \tag{12.7}$$

where $K_0(u)$, $J_0(u)$ are the Biessel and Macdonald functions. These formulas demonstrate the dependence of the correlation properties on linear sizes of confined fluids such as layer thickness $H = 2L_0$ or cylinder radius a as well as on boundary conditions in accordance with requirements (e) and (f) for universality classes.

Since the pair CF $G_2(r)$ for confined systems does not have in general an exponential form, it is natural to define the correlation length ξ of fluctuations as a normalized second spatial moment M_2 as follows:

$$\xi = \sqrt{M_2} = \sqrt{\int G_2(r) r^2 dr / \int G_2(r) dr}. \tag{12.8}$$

The corresponding formulae for the correlation length of slitlike and cylindrical pores contain not only the thermodynamic variables, but also the geometrical parameter $S = L/d_0$ characterizing the number of molecular layers along the direction of pore's spatial limitation (for slitlike pores $L = H$, where H is its thickness, while for cylindrical pores $L = a$, where a is its radius), d_0 is a diameter of molecules (for water molecules $d_0 \approx 0.3$ nm).

To calculate the dependence of physical properties on linear sizes of a fluid's volume, it is necessary to introduce, instead of the temperature variable $\tau = [T - T_c(\infty)]/T_c(\infty)$ in bulk fluids, the following new temperature variable for fluids in confined geometry [86]:

$$\tau(S, \xi) = (G/S)^{1/\nu} + [1 + (G/S)^{1/\nu}](\xi_0/\xi)^{1/\nu} sign\tau, \tag{12.9}$$

where the geometrical factor $G = \pi$ for plane-parallel layers or slitlike pores, and $G = \mu_1 = 2.4048$ for cylindrical pores where μ_1 is the first zero of the Biessel function.

It follows from (12.9) that:

(a) for relatively large sizes $L \gg \xi$ it is easy to find that due to an inequality $S = L/d_0 \gg 1$ the correlation length ξ is approaching its bulk value $\xi = \xi_0 \tau^{-\nu}$. In this case one has

$$\xi_0/\xi \gg (G/S)[1 + (S/G)^{1/\nu}]^{\nu}, \tag{12.10}$$

and a term with (G/S) in (12.9) may be omitted. Therefore, all the physical properties depend on the thermodynamic variables (temperature, pressure, density or concentration, etc.);

(b) in the opposite case of small fluid's volumes with $L \ll \xi$, when such an inequality takes place

$$S = L/d_0 \gg G(\xi/\xi_0)[1 + (G/S)^{1/\nu}]^{-\nu}, \tag{12.11}$$

all the physical properties depend only on linear sizes in confined fluids, as it is really predicted for the 1st type of a DC.

As an example, let us consider the case of relatively small linear sizes S and relatively large correlation lengths ξ. Say, let the number S of molecular layers along the direction of spatial limitation be changing from 10 to 30, while the temperature variable $\tau \approx 10^{-3}$–10^{-4}, i.e. the correlation length $\xi/\xi_0 \approx 10^{-2}$–$10^{-2.5}$. Then the first term in the braces in (12.9) is 10 times larger than the second one. Therefore, by omitting the second term depending on the correlation length, one receives the expressions for physical properties depending only on the size variable.

Similar to the temperature variable $\tau(S, \xi)$ for confined fluids given by (12.9), the density $\Delta\rho(S, \xi)$ and pressure $\Delta p(S, \xi)$ variables should be introduced according to the following formulae [87]

$$\Delta\rho(S, \xi) = (G/S)^{\frac{\beta}{\nu}} + \left(1 + (G/S)^{\frac{\beta}{\nu}}\right)(\xi_0/\xi)^{\frac{\beta}{\nu}} sign\Delta\rho, \tag{12.12}$$

$$\Delta p(S, \xi) = (G/S)^{\frac{\beta\delta}{\nu}} + \left(1 + (G/S)^{\frac{\beta\delta}{\nu}}\right)(\xi_0/\xi)^{\frac{\beta\delta}{\nu}} sign\Delta p. \tag{12.13}$$

To study a DC of the 2nd type, the following expression for any effective critical exponents n_{eff} may be used to describe a smooth transition between its $3d$ value n_3 and $2d$ value n_2 [18]:

$$n_{eff} = n_3 + [(2/\pi)arctg(ax - b) - 1](n_3 - n_2)/2, \tag{12.14}$$

where the dimensionless size $x = H/H_{cr}$ depends on the thickness H_{cr} at which a $3d \leftrightarrow 2d$ DC occurs. Our theoretical calculations demonstrate a good agreement with computer experiment studies [16], in which the authors consider $H_{cr} \approx 2.4$ nm for a slitlike pore filled by water. Equation (12.14) looks similar to the (12.58) giving a crossover between hydrodynamic and fluctuation regions for the width Γ_c of the central Rayleigh component of the light-scattering spectrum in the mode-mode coupling dynamic theory of critical phenomena [12, 88–90].

Table 12.1 contains the results of effective critical exponents for confined fluids like CSW with a scalar order parameter. A $3d \leftrightarrow 2d$ DC is taken into account between values of critical exponents $\alpha = 0, \beta = 1/8, \delta = 15, \gamma = 7/4, \nu = 1$ for $2d$-systems and $\alpha = 0.110, \beta = 0.3265, \delta = 4.789, \gamma = 1.237, \nu = 0.630$ proposed by Anisimov and his collaborators [60–63] for 3d-systems belonging to the Ising-model universality class.

In addition, the effective spatial d_{eff} and fractal d_{fr} dimensionalities, accompanying a $3d \leftrightarrow 2d$ DC, are given in the last two columns. Here we use a known hyperscaling formula for the effective spatial dimensionality $d_{eff} = (2 - \alpha_{eff})/\nu_{eff}$ and the Mandelbrot's formula for the fractal dimensionality $d_{fr} = d_{eff} - \beta_{eff}/\nu_{eff}$.

An important conclusion may be formulated on the basis of these results: the spatial and fractal dimensionalities are gradually varying with change of linear size of a system. Figure 12.2 illustrates the dependence of d_{eff} and d_{fr} on number S of molecular layers in confined fluid systems.

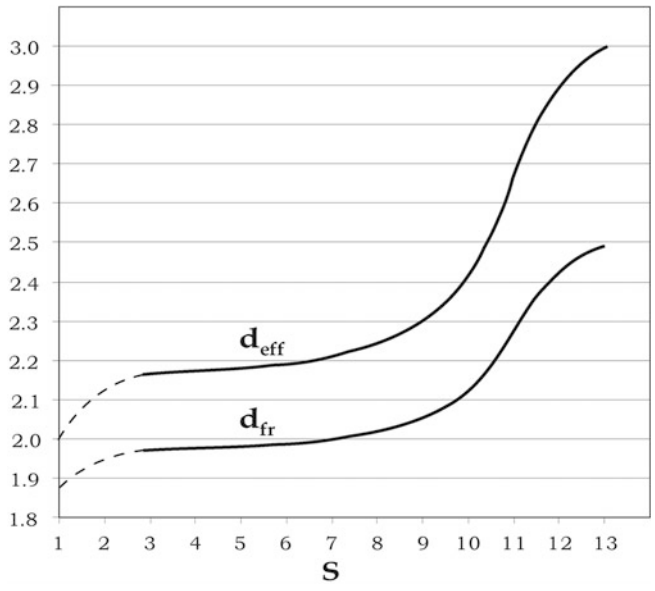

Fig. 12.2 The dependence of the effective spatial d_{eff} and fractal d_{fr} dimensionalities on number S of molecular layers in a confined system

Table 12.1 Effective critical exponents, spatial and fractal dimensionalities

S	α	β	δ	γ	ν	$d_{eff} = (2 - \alpha_{eff})/\nu_{eff}$	$d_{fr} = d_{eff} - \beta_{eff}/\nu_{eff}$
1	$\to 0$	$\to 0.125$	$\to 15.00$	$\to 1.750$	$\to 1.000$	2.000	1.875
2	0.025	0.171	12.649	1.632	0.915	2.158	1.971
3	0.026	0.173	12.585	1.629	0.912	2.163	1.973
4	0.027	0.174	12.503	1.625	0.910	2.168	1.977
5	0.028	0.176	12.394	1.619	0.906	2.177	1.982
6	0.030	0.179	12.240	1.611	0.900	2.189	1.990
7	0.032	0.184	12.011	1.600	0.892	2.206	2.000
8	0.036	0.191	11.638	1.581	0.878	2.237	2.019
9	0.044	0.205	10.952	1.547	0.853	2.293	2.053
10	0.059	0.233	9.546	1.476	0.802	2.420	2.129
11	0.084	0.278	7.243	1.360	0.719	2.665	2.278
12	0.102	0.313	5.487	1.272	0.655	2.898	2.742
13	$\to 0.110$	$\to 0.3265$	$\to 4.789$	$\to 1.237$	$\to 0.630$	3.000	2,482

Studies of the fractal dimensionality d_{fr} and its dependence on a geometrical number S are important for understanding the basic principles of nucleation processes. Most considerations and results of the theory of the formation of a new phase are based on the convenient concept of a spherical nucleus. However, this assumption is not valid for deep quenches to the metastable region because of the fractal nature of new-phase nucleus. New phase nuclei are fractal objects in early stages of its formation [91]. Conclusions on the fractal nature of clusters of a new phase are also supported by computer-simulation studies [92]. Another proof of this fact is as follows: the mean-square fluctuation of the number of particles $\langle \Delta N^2 \rangle^{1/2}$ in clusters of a new phase is directly determined by its fractal dimensionality d_{fr} according to the scaling formula [93, 94]

$$\sqrt{\langle \Delta N^2 \rangle} = L^{d_{fr}} f_N(x, y). \tag{12.15}$$

Here, the fractal dimensionality d_{fr} is connected with the spatial dimensionality d and critical exponents β and ν by the above-mentioned Mandelbrot's formula, L is a cluster's linear size, $f_N(x, y)$ is a corresponding scaling function of arguments $x = \tau L^{1/\nu}$ and $y = hL^{\beta/\nu}$, τ and h are the temperature and field variables.

A considerable difference between the effective spatial and fractal dimensionalities given in Table 12.1 means that the nuclei of a new phase are not compact and spherical but rather branching objects. The specific features of physical properties and fractal structures in the metastable region were discussed in detail (see e.g. [12, 91, 95]).

In particular, the studies of the effective values of dimensionalities and co-dimensionalities [96, 97] show that the growth of fluctuating clusters due to its coalescence is a less probable process with transfer from $2d$ to $3d$ geometry, i.e. with increasing a geometrical parameter S and numerical values of difference $d_{\text{eff}} - d_{\text{fr}}$.

12.4 Anomalies of Diffusion Coefficient in Bulk Water and CSW

As it was mentioned in Introduction, the diffusion coefficient D has an unusual behavior along isobars crossing the Widom line generated from a LLCP. In particular, the diffusion coefficient D demonstrates a crossover right at the Widom line from a non-Arrhenius ("fragile") HDW with the power-law temperature dependence

$$D \propto (T - T_{MCT})^{\gamma}, \tag{12.16}$$

where T_{MCT} is the corresponding crossover temperature from the mode coupling theory with $T_{MCT} = 231$ K and $\gamma = 1.7$–1.9, to an Arrhenius ("strong") LDW with

the exponential-law temperature dependence $D \propto \exp(-E_{act}/kT)$, where E_{act} is the activation energy [42–46].

Here, we shall study a critical behavior of the diffusion coefficient D for a non-Arrhenius phase of CSW near the low-temperature critical point. Taking into account ideas of the finite-size scaling theory in binary liquid mixtures and results of a 2d ⇔ 3d dimensional crossover, one may testify that properties of fluids near phase transitions and critical points for a certain class of universality demonstrate identical dependence on the characteristic size L of a system and thermodynamical parameters. It is seen from the hypothesis of finite-size scaling which can be formulated for a singular part of the Gibbs free energy as follows:

$$G_s = L^{-d} f_G(\Delta x L^{1/\nu}, hL^{\beta\delta/\nu}). \tag{12.17}$$

For definiteness, a binary liquid mixture like CSW near the LLCP is examined, which belongs to the class of universality of 3-dimensional Ising model and for which the critical exponents have such values: $\beta = 0.3265$, $\delta = 4.789$, $\nu = 0.630$ [60–63].

Formulae (12.9), (12.12) and (12.13) for $\tau, \Delta p, \Delta x$ allow to examine the limiting cases, namely: (1) for nanoscale confined systems, when $S \leq \xi^*$, the first addends in these expressions depending on linear sizes play a basic role; (2) for bulk systems, when $S \gg \xi^*$, a dominant role belongs to the second addends, which contain the correlation length depending on thermodynamics variables.

Let us consider any dynamic physical properties (namely, the diffusion coefficient D) of confined systems with taking into account its vicinity to the points of phase transitions or critical points.

Dynamic fluctuation region. The term "fluctuation region" will be used in two senses. Firstly, as a dynamic fluctuation region, where singular parts a_S of the Onsager kinetic coefficients substantially prevail their regular parts a_0 and where the following inequalities are fulfilled for thermodynamics variables: $0 \leq \tau < \tau_D$, $0 \leq \Delta p < \Delta p_D$, $0 \leq \Delta x < \Delta x_D$. Here $\tau_D = (T_D - T_c)/T_c, \Delta p_D = (p_D - p_c)/p_c$, $\Delta x_D = (x_D - x_c)/x_c$ are so-called the crossover temperature [98], pressure and concentration [87], for which $a_S \approx a_0$. Secondly, as a region in the immediate vicinity of the phase transition (critical) points, where the role of fluctuation effects becomes decisive due to the Ginzburg-Levanyuk criterion [99, 100] expressed by the following inequalities for thermodynamic variables $\tau, \Delta p, \Delta x$ and the Ginzburg number Gi:

$$0 \leq \tau \ll Gi,\ 0 \leq \Delta p \ll Gi^{1/\beta\delta},\ 0 \leq \Delta x \ll Gi^{1/\beta}, \tag{12.18}$$

The dynamic scaling theory provides for a singular part a_S of the Onsager kinetic coefficients such divergences:

$$a_S/a_0 \sim \xi/\xi_0 \sim \tau(S,\xi^*)^{-\nu} \sim \Delta p(S,\xi^*)^{-\nu/\beta\delta} \sim \Delta x(S,\xi^*)^{-\nu/\beta}, \tag{12.19}$$

where indexes equal $\nu/\beta\delta = 0403, \nu/\beta = 1,930$. The compressibility $\chi_{p,T} \sim (\partial x/\partial\mu)_{p,T}$ of a binary liquid mixture at constant pressure and temperature (in general case—susceptibility) is determined by fluctuation theorems (or fluctuation-dissipative theorems for non-equilibrium properties) and described by the following formulae:

$$\chi \sim \left(\partial^2 G_{cum}/\partial z^2\right)_y (\partial z/\partial h)^2 \sim L^{-d+2\beta\delta/\nu} \sim L^{-\gamma/\nu} \sim \tau^{-\gamma} \sim \Delta x^{\gamma/\beta} \sim \Delta p^{-\gamma/\beta\delta} \tag{12.20}$$

where such equalities between critical exponents $d\nu = 2-\alpha$, $\beta\delta = \beta+\gamma$, $\alpha+2\beta+\gamma = 2$ are taken into account and the critical exponent $\alpha = 0.110$.

The diffusion coefficient of a binary liquid mixture in a fluctuation region is determined by a product of singular part of the Onsager kinetic coefficient and reverse value of the isobaric-isothermal compressibility

$$D = a_S(\partial\mu/\partial x)_{p,T} \sim L^{1-\gamma/\nu} f_D^{(1)}(y,z) \sim \tau^{\gamma-\nu} f_D^{(2)}(y,z) \sim \Delta x^{(\gamma-\nu),\beta} f_D^{(3)}(y,z) \sim \\ \sim \Delta p(S,\xi^*)^{(\gamma-\nu)/\beta\delta} f_D^{(4)}(y,z). \tag{12.21}$$

This formula foresees an approaching the diffusion coefficient D of bulk $3d$ fluids to zero value in a binary mixture according to such power laws:

$$D \sim L^{-0.963} \sim \tau^{0.607} \sim \Delta x^{1.859} \sim \Delta p^{0.388}. \tag{12.22}$$

The diffusion coefficient of $2d$ fluids like CSW belonging to the Ising-model universality class may have the following power-law critical behavior near the LLCP with taking into account such values of the critical exponents $\alpha = 0, \beta = 0.125, \delta = 15, \gamma = 1.75, \nu = 1$:

$$D \sim L^{-0.75} \sim \tau^{0.75} \sim \Delta x^{6.0} \sim \Delta p^{0.4}. \tag{12.23}$$

An effect of the spatial dispersion (non-locality) for the diffusion coefficient D allows avoiding a non-physical results in D, namely its zero value $D \to 0$ and, correspondingly, in the width of central (Rayleigh) line of the light-scattering spectrum $\Gamma_c \to 0$ and an infinite value in the relaxation time $t_c \sim 1/\Gamma_c \to \infty$ in the critical and phase-transition points.

In particular, experimental confirmation of these results is as follows:(a) a finite decreasing the width Γ_c of central (Rayleigh) line in light-scattering spectrum, allowing for the spatial and/or temporal dispersion of the critical fluctuations, (b) a finite narrowing the width Γ_c and, correspondingly, a large but finite increasing the relaxation time $t_c \sim 1/\Gamma_c$ at the critical (phase transition) points.

At the same time, studies of the non-equilibrium critical phenomena such as the diffusion processes and viscous flow are difficult to conduct in the dynamic

fluctuation region. One of possible reasons is a small value of the dynamic crossover temperature $\tau_D \approx 10^{-5}$.

Dynamic crossover region. Inequalities

$$\tau_D < \tau < Gi,\ \Delta p_D < \Delta p < Gi^{1/\beta\delta},\ \Delta x_D < \Delta x < Gi^{1/\beta} \tag{12.24}$$

are valid in this region, where singular and regular parts of the Onsager kinetic coefficients become the same order ($a_S \approx a_0$). Then, peculiarities of the diffusion coefficient D are determined only by a derivative $(\partial\mu/\partial x)_{p,T}$, according to formula as follows:

$$D \approx 2a_0(\partial\mu/\partial x)_{p,T} \sim L^{-\gamma/\nu} f_D^{(1)}(y,z) \sim \tau^{\gamma} f_D^{(2)}(y,z) \sim \Delta x^{\gamma/\beta} f_D^{(3)} \sim \Delta p^{\gamma/\beta\delta} f_D^{(4)}(y,z). \tag{12.25}$$

For certain liquids including water the Ginzburg number $Gi \approx 0.3$ [91], that is why experimental studies of the diffusion coefficient D may be conducted in the dynamic crossover region $10^{-4} < \tau < 0.3$.

In this region one has such theoretic predictions on the dependence of the bulk $3d$ diffusion coefficient on linear sizes and thermodynamic variables

$$D \approx 2a_0(\partial\mu/\partial x) \sim L^{-1.963} \sim \tau^{1.237} \sim \Delta x^{3.789} \sim \Delta p^{0.791} \tag{12.26}$$

On the other hand, the corresponding expressions for the $2d$ diffusion coefficient in CSW may be written in the following form:

$$D \sim L^{-1.75} \sim \tau^{1.75} \sim \Delta x^{14} \sim \Delta p^{0.933}. \tag{12.27}$$

Dynamic regular region. In a dynamic regular region, where such conditions take place for thermodynamic variables and the Ginzburg number:

$$Gi < \tau \leq 1,\ Gi^{1/\beta\delta} < \Delta p \leq 1,\ Gi^{1/\beta} \ll \Delta x \leq 1 \tag{12.28}$$

fluctuation effects do not play a substantial role. The proper critical exponents in formulae for the diffusion coefficient receive their values from the Landau theory, namely: $\beta = \nu = 1/2, \gamma = 1, \delta = 3$. As a result, one has such an expression for the diffusion coefficient:

$$D \sim L^{-2} \sim \tau \sim \Delta x^2 \sim \Delta p^{2/3}, \tag{12.29}$$

being valid for fluids like water in the intervals of temperature $0.30 < \tau \leq 1$, pressure $0.45 < \Delta p \leq 1$, and concentration $0.09 \ll \Delta x \leq 1$.

As is well-known, the Landau theory of the 2-order phase transition and critical phenomena is valid for the spatial dimensionality $d = 4$ (with a logarithmic accuracy). It means that a transition between the dynamic crossover behavior and the dynamic regular behavior may be treated as a $3d \Leftrightarrow 4d$ crossover phenomena.

An important illustrations of such a crossover in bulk fluids (including bulk water) are changes in the diffusion-coefficient dependences on: (a) size—from $D \sim L^{-1.963}$ to $D \sim L^{-2}$, (b) temperature—from $D \sim (T - T_c)^{1.237}$ to $D \sim (T - T_c)$, (c) concentration—from $D \sim (x - x_c)^{3.789}$ to $D \sim (x - x_c)^2$, (d) pressure $D \sim (p - p_c)^{0.791}$ to $D \sim (p - p_c)^{0.667.}$

In confined $2d$ fluids like CSW such a transition between crossover and regular behaviors should be treated, obviously, as a $2d \Leftrightarrow 4d$ crossover phenomena omitting $3d$ case because results of the Landau theory are independent on a spatial dimensionality. This $2d \Leftrightarrow 4d$ crossover phenomena leads to the following changes in dependence of the diffusion coefficient D on: (a) the size variable from $D \sim L^{-1.75}$ to $D \sim L^{-2}$, (b) the temperature variable from $D \sim (T - T_c)^{1.75}$ to $D \sim (T - T_c)$, (c) the concentration variable from $D \sim (x - x_c)^{14}$ to $D \sim (x - x_c)^2$, (d) the pressure variable from $D \sim (p - p_c)^{0.933}$ to $D \sim (p - p_c)^{0.667.}$

12.5 The Shear-Viscosity Anomalies in Bulk Water and CSW

The theoretical and experimental studies of the dynamic critical phenomena, including the dynamic anomalies in bulk and confined aqueous systems, require taking into account the most important problems in this field as follows.

12.5.1 The Dynamic Critical Exponent

In the dynamic scaling theory the relaxation (life) time t_r of the order-parameter fluctuations and therefore the width $\Gamma_c = 1/t_r$ of the central Rayleigh component of the critical-opalescence spectrum is given by the following formula in individual ***bulk*** fluids:

$$\Gamma_c^s = q^{z^*} f_\Gamma(q\xi). \tag{12.30}$$

Here $q = \frac{2\pi\sqrt{2}}{\lambda}(1 - \cos\theta)^{1/2}$ is the change in the wave vector on scattering by an angle θ for a light beam with the wavelength λ, $f_\Gamma(q\xi)$ is the corresponding scaling function.

The main problem is to establish the value of the dynamic critical exponent z^* because the known scaling equalities for the critical exponents do not contain this critical index. Far from the critical point, where $\Gamma_c^b \gg \Gamma_c^s$, one has $z^* = 2$ or

$z^* = 2 - \eta^*$ depending on whether the OZ approximation or a scaling-invariant form of the pair CF G_2 is used. In the immediate vicinity of the critical point, if one neglects Γ_c^b, it follows that $z^* = 3$ (see (12.59)). Such a value of z^* corresponds to an additional assumption that the shear viscosity η^s is regular or has a weak logarithmic divergence at the critical point. In reality, the shear viscosity has a weak power-law singularity at a high-temperature critical point [101]:

$$\eta^s \sim \xi^{X_\eta}, \tag{12.31}$$

where the critical exponent $X_{\eta\,\mathrm{theor}} = 0.065$. Experimental studies (see e.g. [9, 12, 73] confirm this theoretical result: $X_{\eta\,\mathrm{exp}} = 0.063 \pm 0.024$. Therefore, the dynamic critical exponent in bulk fluids is: $z^*_{\mathrm{theor}} = 3 + X_{\eta\,\mathrm{theor}} = 3.065$ and $z^*_{\mathrm{exp}} = 3.063 + 0.024$ (say for the mixture 3-methylpentane-nitroethane [102]. The temperature dependence of the dynamic critical exponent z^* showing a smooth transition from $z^* = 2$ to $z^* = 3.06$ is given in Fig. 12.3.

The dependence of the shear viscosity on the temperature τ, concentration Δx, and pressure Δp variables is given by the following power-law relations for 3d bulk fluids:

$$\eta_c^s \sim \xi^{0.065} \sim \tau^{-0.041} \sim \Delta x^{-0.124} \sim \Delta p^{-0.026}. \tag{12.32}$$

12.5.2 The Dynamic Scaling Function $F_I(x)$ and Diffusion Coefficient D

Existing versions of the dynamic scaling hypothesis predict different scaling functions $f_I(x)$ in (12.30). The exact structures of these scaling functions are necessary to verify the attractive universality hypothesis of the equilibrium phenomena as well as the non-equilibrium phenomena near the critical and phase-transition points.

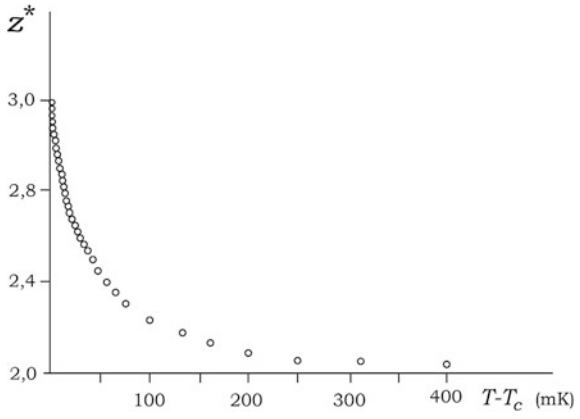

Fig. 12.3 The temperature dependence of the dynamic critical exponent z^*

The diffusion coefficient D determined experimentally from the Rayleigh linewidth Γ_c in bulk binary fluid mixtures satisfies the SER relation

$$D = \lim_{x \to 0} \Gamma_c(x) \mathrm{q}^{-2} = R k_B T / \eta \xi. \tag{12.33}$$

Numerical calculations of the coefficient R in various variants of the dynamic scaling theories (mode-mode coupling theory, decoupled-mode theory, etc.) give $R = 1/6\pi$ as in the initial SER, while the renormalization-group calculations predict that $R = 1/5\pi$. A number of experiments have shown values of $R \approx 1.2/6\pi$, while another studies of Γ_c have confirmed results which agree with the mode-mode coupling theory (see e.g. [9, 12]).

12.5.3 Peculiarities of Shear Viscosity and Central Linewidth in CSW

Near the glass-transition critical point of CSW the shear viscosity has much stronger power-law singularity than in the vicinity of the $3d$ high-temperature critical point (see formula (12.31) with $X_\eta \approx 0.065$):

$$\eta^s = \eta_0 \left(\frac{T}{T_g} - 1 \right)^{-\mu}, \tag{12.34}$$

where $T_g \approx 228$ K is the glass-transition critical temperature, $\mu \approx 1.81$ is the critical exponent of the shear-viscosity temperature dependence [103].

Allowance for formula (12.34) and the critical exponents $\beta = 1/8, \delta = 15, \nu = 1$ leads to the shear-viscosity dependence on linear sizes L, concentration $\Delta x = (x - x_g)/x_g$, and pressure $\Delta p = (p - p_g)/p_g$ in $2d$ CSW:

$$\eta^s \sim L^{\mu/\nu} \sim L^{1.81}, \ \eta^s = \eta_0 \left(\frac{x}{x_g} - 1 \right)^{-\mu/\beta} \sim \Delta x^{-14.48}, \ \eta^s = \eta_0 \left(\frac{p}{p_g} - 1 \right)^{-\mu/\beta\delta} \sim \Delta p^{-0.965}. \tag{12.35}$$

The singular part of the width Γ_{c}^s of the central Rayleigh component in $2d$ CSW depends on $L, \tau, \Delta x, \Delta p$ as follows:

(a) in the dynamic fluctuation region

$$\Gamma_{\mathrm{c}}^s \sim L^{-(1+\mu/\nu)} \sim L^{-2.81}, \ \Gamma_{\mathrm{c}}^s \sim \tau^{\nu+\mu} \sim \tau^{2.81}, \ \Gamma_{\mathrm{c}}^s \sim \Delta x^{(\nu+\mu)/\beta} \sim \tau^{22.48}, \\ \Gamma_{\mathrm{c}}^s \sim \Delta p^{(\nu+\mu)/\beta\delta} \sim \Delta p^{1.499}, \tag{12.36}$$

(b) in the dynamic crossover region

$$\Gamma_{\mathrm{c}}^{s} \sim L^{-\mu/\nu} \sim L^{-1.81}, \Gamma_{\mathrm{c}}^{s} \sim \tau^{\mu} \sim \tau^{1.81}, \Gamma_{\mathrm{c}}^{s} \sim \Delta x^{\mu/\beta} \sim \Delta x^{14.48}, \Gamma_{\mathrm{c}}^{s} \sim \Delta p^{\mu/\beta\delta} \sim \tau^{0.965}, \tag{12.37}$$

Taking into account effects of the spatial dispersion (non-locality) of order-parameter fluctuations allows avoiding non-physical results $\eta^{s} \to \infty$ and $\Gamma_{\mathrm{c}}^{s} \to 0$ in the glass-transition critical point.

In the case of a weak power-law singularity one has for the temperature dependence of the shear viscosity and the width of the central Rayleigh line the following results near the $3d$ high-temperature critical point:

$$\eta^{-1}(\tau, q) = \eta_0^{-1}(\tau^{0.041} + bq^2),\ \Gamma_c^s = (k_B T/16\eta_0 q^3)(\tau^{0.041} + bq^2), \tag{12.38}$$

which lead to its finite values $\eta = \eta_0/bq^2 \neq 0$ and $\Gamma_{\mathrm{c}}^{s} = bk_B T/16\eta_0 q \neq 0$ for $\tau = (T - T_c)/T_c \to 0$.

In the case of a strong power-law singularity of the shear viscosity near the glass-transition critical point of $2d$ CSW one has such expressions for the temperature dependence of the shear viscosity and the width of the central line

$$\eta^{-1}(\tau, q) = \eta_0^{-1}(\tau^{1.81} + b_0 q^2),\ \Gamma_c^s = (k_B T/16\eta_0 q^3)(\tau^{1.81} + b_0 q^2) \tag{12.39}$$

and its finite values $\eta = \eta_0/b_0 q^2 \neq 0,\ \Gamma_c^s = b_0 k_B T/16\eta_0 q \neq 0$ with approaching to the critical glass-transition temperature ($T \to T_g$).

12.5.4 The Crossover Function for the Shear Viscosity and the Breakdown of the Stokes-Einstein Relation

To find the dynamic critical exponent z*, the dynamic scaling functions $f_{\Gamma}(x)$ in (12.30), and the coefficient R in (12.33), one must solve the problem of determining the crossover functions $f_{\eta}(q\xi)$ and $f_{\eta}^{(1)}(qL, \tau L^{1/\nu}, \Delta x^{\beta/\nu})$ for the shear viscosity in bulk and confined fluids according to the following formulae, respectively:

$$\eta^{s} = \xi^{X_{\eta}} f_{\eta}(q\xi), \tag{12.40}$$

$$\eta^{s} = \xi^{\mu/\nu} f_{\eta}^{(1)}(qL, \tau L^{1/\nu}, \Delta x^{\beta/\nu}). \tag{12.41}$$

The important problem of the dynamic critical phenomena is the validity of the SER (12.33) with $R = 1/6\pi$ in bulk and confined fluids. As it is well known, the

SER gives the relationship between the diffusion coefficient D and relaxation time t_r, which is proportional to the viscosity η,

$$t_r \propto \eta/D. \tag{12.42}$$

Really, one has such a relationship

$$\Gamma_c \propto 1/t_c \propto D \propto \mathrm{T}/\eta, \tag{12.43}$$

which leads directly to the SER (12.42).

An experimental evidence of the SER violation was obtained from the nuclear magnetic resonance (NMR) and the quasi-elastic neutron scattering (QENS) data in CSW in the temperature interval from 280 to 190 K (see, e.g. [103–105]). Specifically, the authors [103] presented a well-defined non-monotonic decoupling of D and $t_r \sim \eta$ which implied the SER breakdown as a change in the hydrogen-bond (HB) structure of CSW. The authors [104] considered 3 types of different water geometry: (a) confined water in a quasi-1d nanotube filled by water, (b) confined water in a quasi-2d layer of the lysozyme protein, and c) bulk quasi-3d water in methanol-diluted mixture. The NMR and QENS experimental results showed that observed processes were independent on the system dimensionality d and caused by the HB network governing the dynamic properties of water. On the other hand, results from simulations of model glass formers in [105] showed that the degree of the SER breakdown decreased with increasing spatial dimensionality d, while the fragility of the studied liquids was found to increase with d.

12.6 Dynamic Light Scattering in Bulk and Confined Fluids

Theoretical and experimental studies of the dynamic light scattering near the critical and phase-transition points are the subject of a number of papers (see e.g. [9, 12, 73] and references there). First we shall consider this problem for the case of bulk fluids in a single-scattering approximation. The problem of multiple light scattering in fluids near the critical points was discussed in [12] with taking into account its contributions to the integrated intensity and spectra of the light critical opalescence.

12.6.1 Characteristics of Dynamic Light-Scattering Spectrum in Bulk Fluids

The hydrodynamic theory predicts that such characteristics of the dynamic light scattering as the widths of the central Rayleigh component Γ_c and side Mandelstam-Brillouin components (MBC) Γ_{MB} of the single-scattering triplet as

well as the frequency shift of the side components $\Delta\Omega_{MB}$ depend on the thermal conductivity λ, the shear viscosity η, the bulk viscosity ς, the specific heat capacities C_{p} and C_{v}, and the velocity of sound υ in a one-component bulk fluid:

$$\Gamma_c = \lambda(q)q^2/\rho C_p(q), \tag{12.44}$$

$$\Gamma_{MB} = \left[(\frac{4}{3}\eta(q) + \varsigma(q))\rho^{-1} + \frac{\lambda(q)}{\rho C_p(q)} - \frac{\lambda(q)}{\rho C_v(q)}\right]q^2, \tag{12.45}$$

$$\Delta\Omega_{MB} = \upsilon(q)q^2. \tag{12.46}$$

Here $q = (2\pi/\lambda)\sqrt{2\varepsilon_0}(1 - \cos\theta)^{1/2}$ is the change of the wave vector on scattering by an angle θ, λ is the light wave length, ε_0 is an average part of the dielectric permittivity.

In a binary fluid mixtures

$$\Gamma_c = L(q)\chi^{-1}(q)q^2 = D(q)q^2, \tag{12.47}$$

where L is the Onsager coefficient, χ is the susceptibility, which is equal to $(\partial\rho/\partial\mu)_{T,\mu=\mu_1-\mu_2}$ or to $(\partial x/\partial\mu)_{P,T}$ near the critical vaporization or mixing points, respectively, and D is the diffusion coefficient.

Correct interpretation of the experimental data on the critical opalescence spectrum in bulk fluids necessitates taking into account the background parts of the kinetic coefficients into account. In the region enough far from the critical point in which the background parts of the thermal conductivity λ^b and the Onsager coefficient L^b exceed their singular parts $\lambda^s(q)$ and $L^s(q)$, the narrowing of Γ_c and therefore the increase in the relaxation time $t_c = 1/\Gamma_c$ is completely determined by the strongly diverging properties C_p and χ:

(a) in a bulk one-component fluid

$$\Gamma_c = \lambda^b q^2(1 + q^2\xi^2)/\rho C_p(q = 0), \tag{12.48}$$

(b) in a bulk binary mixture

$$\Gamma_c = L^b\chi(q = 0)q^2(1 + q^2\xi^2). \tag{12.49}$$

Extrapolation of the hydrodynamic formulae (12.44) and (12.47) for the width Γ_c to the dynamic fluctuation region, where $\lambda^s \sim \tau^{-\nu} \gg \lambda^b$ and $L^s \sim \tau^{-\nu} \gg L^b$ according to the dynamic theory of critical phenomena, leads to not so strong narrowing of the central linewidth:

$$\Gamma_c \sim \tau^{\nu}(\rho = \rho_c), \Gamma \sim \Delta\rho^{\nu/\beta}(T = T_c). \tag{12.50}$$

This result follows from simple consideration based on the SER in which one has to replace the radius of a droplet by the correlation length ξ:

$$D = k_B T/6\pi\eta\xi. \tag{12.51}$$

The behavior of the side MBC near the critical point of bulk fluids is governed by specific features of the velocity and damping of sound waves. For the singular part of the sound velocity at low frequencies one has

$$v^s(\omega \to 0) \sim \tau^{\alpha/2} f_v(\Delta\rho/\tau^{\beta}), \tag{12.52}$$

where the scaling function $f_v(x)$ has the following asymptotic representations:

$$f_v(x \to 0) = const, f_v(x \to \infty) \sim x^{\alpha/2\beta}. \tag{12.53}$$

A decrease in v^s according to (12.52) and therefore a decrease in the frequency shift $\Delta\Omega_{MB}$ should be observable only at frequencies $\omega \ll \omega_r$. The relaxation frequency $\omega_r = \lambda/\rho C_V \xi^2$ decreases rapidly and the dispersion of the sound velocity $v(\omega)$ should be observed with approaching to the critical point. In the immediate vicinity of the critical point, where the background width of the MBC $\Gamma^{\mathrm{b}}_{\mathrm{MB}}$ is small, the growth of the acoustic damping and, accordingly, the broadening of Γ_{MB} are determined by the singular part of the bulk viscosity ς^s:

$$\Gamma_{\mathrm{MB}} \approx \Gamma^{\mathrm{s}}_{\mathrm{MB}} \sim \varsigma^s = \tau^{-(3\nu+\alpha)} f_{\varsigma}(\Delta\rho/\tau^{\beta}),$$

$$3\nu + \alpha = 2, f_{\varsigma}(x \to 0) = const, f_{\varsigma}(x \to \infty) \sim x^{-2/\beta}. \tag{12.54}$$

The dispersion of the sound velocity and damping at the acoustic wavelength

$$\frac{v(\omega)}{v(\omega \to 0)} - 1 = [\omega/2\rho v(\omega \to 0)]\mathrm{Im}\varsigma^{-1}(\omega),$$

$$\alpha(\omega) = [\pi\omega/\rho v(\omega \to 0)]\mathrm{Re}\varsigma^{-1}(\omega). \tag{12.55}$$

should be universal functions of the reduced frequency $\omega^* = \omega/2\omega_r$. All features of the behavior of the MBC were confirmed experimentally by techniques based on light-beating spectroscopy and ultrasound studies (see e.g. [9, 106]).

The rapidly growing central Rayleigh component of the single-scattering triplet is of primary interest to study of the critical-opalescence spectrum. It follows from the Landau-Placzek relation (LPR)

$$I_c/2I_{MB} \sim \tau^{-\gamma+\alpha}(q \to 0,\ \Delta\rho \ll \tau^{\beta}) \tag{12.56}$$

that the ratio $I_c/2I_{MB}$ increases by an order of magnitude $(\gamma - \alpha \approx 1.1)$ as the temperature deviation τ becomes one decade close to the critical point. Naturally, allowing for the spatial dispersion of fluctuations, the value of $I_c/2I_{MB}$ at $q \neq 0$ should be large, but finite, at the critical point.

To study the width of the central Rayleigh component, which characterizes the relaxation frequency ω_r (the relaxation time t_c) of the order-parameter fluctuations near the critical point, several versions of dynamic theory of critical phenomena have been developed [9, 12]. Allowance for coupling between the modes (the most important being the coupling between the order-parameter fluctuations and the viscous mode) leads to the following result for the singular part Γ_c^s of the width of the central component

$$\Gamma_c^s = \frac{k_B T}{6\pi\eta^* \xi^3} K_0(q\xi), \tag{12.57}$$

where $\eta^* = f(\eta, q\xi)$ is the 'high-frequency' shear viscosity and the crossover function

$$K_0(x) = 3[1 + x^2 + (x^2 + 1/x)arctgx]/4 \tag{12.58}$$

was introduced in [88] to give a correct interpolation between the hydrodynamic $(q\xi \ll 1)$ and non-hydrodynamic $(q\xi \gg 1)$ regions.

For $q\xi \ll 1$ one has $\lim_{x\to 0} K_0(x) = x^2$ and $\Gamma_c^c = Dq^2$ in agreement with the hydrodynamic theory. In the non-hydrodynamic (fluctuation) region, where $q\xi \gg 1$, one has

$$\lim_{x\to\infty} K_0(x) = 3\pi x^3/8 \text{ and } \Gamma_c^s = (k_B T/16\eta^*)q^3. \tag{12.59}$$

As a result, the width of the central Rayleigh component does not depend on ξ and, hence, on the thermodynamic variables.

Figure 12.4 shows the dependence of the dimensionless width of the central component $\Gamma_{c*}^s = \Gamma_c^s 6\pi\eta^*/k_B T q^3$ on $q\xi$ for the mode-mode coupling theory (curve 1), the decoupled-mode theory (curve 2) and the dynamic droplet model (curve 3). In the hydrodynamic region $(q\xi \ll 1)$ all these theoretical approaches give practically the same result: $\Gamma_c^{s*} = 1/q\xi$.

A difference appears in the non-hydrodynamic (fluctuation) region $1 \leq q\xi \leq 10$. Experimental studies of Γ_c^{s*} in individual fluids and fluid mixtures agree better in same cases (Xe, aniline-cyclohexane and 3-methylpentane-nitroethane) with the mode-mode coupling theory while in other cases (water-isobutyric acid) with the decoupled-mode theory. The disparity between these theories, however, does not exceed 10% for $q\xi \gg 1$.

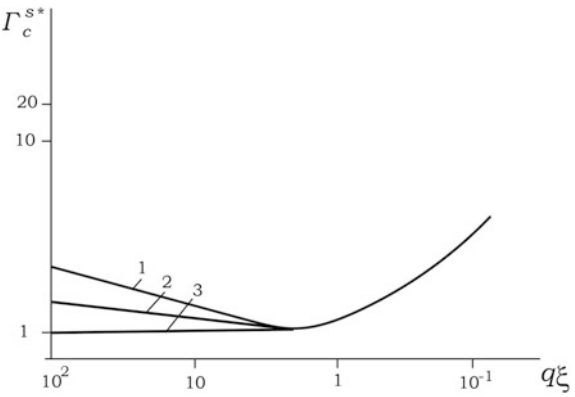

Fig. 12.4 The dependence of the width Γ_c^{s*} of the central Rayleigh component on $q\xi$ in dynamic theories of critical phenomena

Here in this section, we considered the width of the central Rayleigh component in binary liquid mixtures using an approximation when one may neglect the contribution from the thermal conductivity. More consistent studies of the dynamic light scattering in bulk and confined binary mixtures were conducted near its criticality in [89, 107–110].

Strictly saying, the time-dependent single-scattering light intensity in binary mixtures is proportional to the dynamic structure factor

$$S(q,t) = A_1 \exp(-D_1 q^2 t) + A_2 \exp(-D_2 q^2 t), \tag{12.60}$$

where A_1 and A_2 are the amplitudes, D_1 and D_2 are the effective diffusion coefficients of relaxation modes describing by such expressions in the hydrodynamic relaxation theory:

$$D_{1,2} = \frac{1}{2}(\chi + \Delta) \mp \frac{1}{2}\sqrt{(\chi + \Delta)^2 + 4\chi D}. \tag{12.61}$$

Here $\chi = \lambda/\rho C_{P,x}$ corresponds to the contribution from the thermal conductivity given by the Fourier law, where λ is the coefficient of thermal conductivity, ρ is the total mixture density, and $C_{\mathrm{P,x}}$ is the specific heat capacity at constant pressure and concentration. Another quantity in (12.61)

$$\Delta = D\left[1 + \frac{k_T^2}{TC_{P,x}}\left(\frac{\partial \mu}{\partial x}\right)_{P,T}\right] \tag{12.62}$$

describes the contribution from the diffusion given by the Fick law and the thermal diffusivity given by the Soret effect, where D is the mass diffusion coefficient, $k_T = D_T/D$ and D_{T} are the thermal diffusivity ratio and the thermal diffusivity coefficient, respectively, μ is the difference of chemical potentials of solvent and solute per unit of mass.

Taking (12.60)–(12.62) into account and omitting details of calculations [89], the following conclusions for the critical behavior of relaxation processes in binary mixtures can be formulated: (a) the dynamic process with the effective diffusion coefficient D_1 is slow (critical), (b) the dynamic process with the effective diffusion coefficient $D_2 \gg D_1$ is relatively quick (noncritical).

It should be mentioned that both effective diffusion coefficients D_1 and D_2 of relaxation processes in binary mixtures are not determined either by a pure diffusion or by a pure thermal diffusion. A main reason of this fact can be explained by a strong dependence of quantities χ and D on the concentration of binary mixtures. For instance, coefficients of the thermal conductivity χ and diffusion D are changing with the concentration x of ethane at studies of the Rayleigh scattering from a methane-ethane mixture [109] as follows:

(a) $\chi = 8 \times 10^{-8}\,\mathrm{m}^2/\mathrm{s},\ D = 4 \times 10^{-10}\,\mathrm{m}^2/\mathrm{s}\ at\ x = 28.53\,\mathrm{mole\%}$;
(b) $\chi = 10^{-8}\,\mathrm{m}^2/\mathrm{s},\ D = 2 \times 10^{-9}\,\mathrm{m}^2/\mathrm{s}\ at\ x = 1\,\mathrm{mole\%}$;
(c) $\chi = 1.8 \times 10^{-9}\,\mathrm{m}^2/\mathrm{s},\ D = 10^{-8}\,\mathrm{m}^2/\mathrm{s}\ at\ x = 0.1\,\mathrm{mole\%}$.

In concluding this section let us note a recent paper [111] in which the authors examined collective excitations in supercritical soft-sphere fluids. Such systems without attractive forces did not have a liquid-gas coexistence curve, or binodal line, and therefore the Widom line. Nevertheless, authors received a principal and somewhat unexpected result: the extrema points of thermal diffusivity and kinematic viscosity allowed finding the boundary between liquid-like and gas-like regions which resembled the Widom line in the supercritical soft-sphere fluids.

12.6.2 Dynamic Light-Scattering Spectrum in Confined Fluids and CSW

Now let us consider the case of dynamic light scattering in ***confined fluids*** near the critical (phase-transition) point. The scaling hypothesis for confined one-component fluids has to include not only the temperature variable τ, the order parameter $\Delta\rho$ (or another density variable like the entropy), and the external field h associated with the order parameter, but also a characteristic linear size L in the direction(s) of spatial limitation of a system under consideration. Such a scaling hypothesis formulated first in [2] and later in other papers [11, 13] can be written in the following form for the singular (fluctuation) part of the Helmholtz free energy in confined fluids:

$$F^s = L^{-d} f_F(x, y), \tag{12.63}$$

where d is a space dimensionality, $x = \tau L^{1/\nu}$, $y = \Delta\rho L^{\nu/\beta}$ are the scaling arguments, and the scaling function $f_F(x, y)$ has such asymptotic representations:

$$f_F(x \to 0, 0) = const,\ f_F(x \to \infty, 0) \sim x^{2-\alpha},$$
$$f_F(0, y \to 0) = const,\ f_F(0, y \to \infty) \sim y^{(2-\alpha)/\beta}. \tag{12.64}$$

The width the central Rayleigh component in confined fluids. The dynamic hypothesis (12.30) for the width of the central Rayleigh component in bulk fluids can be generalized in the case of ***confined fluids*** as follows:

$$\Gamma_c^s = 1/t_r = L^{-z^*} f_\Gamma(qL, \tau L^{1/\nu}, \Delta\rho/L^{\nu/\beta}), \tag{12.65}$$

where $f_\Gamma(x, y, z)$ is the scaling function. In fluids with linear sizes L exceeding the correlation length ξ, one may obtain

$$\Gamma_c^s = \xi^{-z^*} f_\Gamma(q\xi, \tau\xi^{1/\nu}, \Delta\rho/\xi^{\nu/\beta}). \tag{12.66}$$

Such a consideration can explain the transition between the size dependence of the Rayleigh linewidth and its dependence on the correlation length. If any physical quantity A characterizes by the following scaling formula near the critical point:

$$A = \tau^{-n} f_A(L/\xi), \tag{12.67}$$

where n is the critical exponent of the temperature dependence $A(\tau)$, then this quantity has to have such asymptotic representations:

(a) for $L \gg \xi$, i.e. in bulk fluids or other bulk systems near its phase-transition points

$$A \sim \xi^{n/\nu}, \tag{12.68}$$

(b) for $L \ll \xi$, i.e. in confined systems

$$A \sim L^{n/\nu}. \tag{12.69}$$

The dynamic scaling hypothesis (12.65) and (12.66) for confined fluids can be rewritten as follows:

$$\Gamma_c^s = \tau^{\nu z^*} f_\Gamma^{(1)}(qL, \tau L^{1/\nu}, \Delta\rho/L^{\beta/\nu}), \tag{12.70}$$

$$\Gamma_c^s = \rho^{\nu z^*/\beta} f_\Gamma^{(2)}\left(qL, \tau L^{1/\nu}, \Delta\rho/L^{\beta/\nu}\right). \tag{12.71}$$

The scaling functions in (12.65), (12.70) and (12.71) are connected by the following relationships:

$$f_{\Gamma}^{(1)}(\mathrm{x},\mathrm{y},\mathrm{z}) = \mathrm{y}^{-\nu z^{*}} f_{\Gamma}(\mathrm{x},\mathrm{y},\mathrm{z}), f_{\Gamma}^{(2)}(\mathrm{x},\mathrm{y},\mathrm{z}) = \mathrm{z}^{-\nu z^{*}/\beta} f_{\Gamma}(\mathrm{x},\mathrm{y},\mathrm{z}), \tag{12.72}$$

because one has $L = (y/\tau)^{\nu} = (z/\Delta\rho)^{1/\beta}$.

The dynamic scaling hypothesis predicts an anomalous behavior of physical properties in experiments on the critical-opalescence spectra in confined fluids. For individual fluids in small volumes with linear sizes L having the same order of magnitude as the correlation length ξ, one has the following formulae for the width of the central Rayleigh component Γ_c:

(a) in such a vicinity of the critical point where regular part of the thermal conductivity λ^b exceeds its singular part λ^s, i.e. in the dynamic regular region,

$$\Gamma_c = \Gamma_{c0} \frac{\tau^{\gamma}(1+\mathrm{q}^2\xi^2)}{f_c(\Delta\rho/\tau^{\beta})}, \tag{12.73}$$

where $\Gamma_{c0} = \lambda_0/\rho C_{P0}$ is the amplitude of the width of the central Rayleigh component, $f_{C_P}(y)$ is the scaling function of the heat capacity at a constant pressure with such asymptotics: $f_{C_P}(y \to 0) = const, f_{C_P}(y \to \infty) \sim y^{-\gamma/\beta}$, and effects of the weak spatial dispersion in the Ornstein-Zernike approximation $(q\xi \ll 1)$ were taken into account.

(b) in the opposite case, when $\lambda^s \gg \lambda^b$, the width of the central Rayleigh component

$$\Gamma_c = \Gamma_{c0} L^{1-\gamma/\nu} f_{\Gamma}(qL, \Delta\rho^{\beta/\nu}). \tag{12.74}$$

Let us pay a special attention to such characteristics of the light critical opalescence spectrum in confined liquids as: (1) the width Γ_{MB} of MBC, (2) the frequency shift $\Delta\Omega_{\mathrm{MB}}$ of the side MBC from the central Rayleigh line, (3) the LPR $I_{\mathrm{c}}/2I_{\mathrm{MB}}$.

The width of MBC. In accordance with the finite-size scaling hypothesis, the critical behavior of any quantity is determined by the singularity of the correlation length ξ of a system under consideration.

For a plane-parallel liquid layer with its thickness $H \leq \xi$ (this geometry fits good to such biological object as a synaptic cleft) the correlation length ξ of density fluctuations in confined liquids was found in [13] as follows:

$$\xi = \xi_0 \left[\tau + \left(\frac{\pi\xi_0}{H} \right)^{1/\nu} (1+\tau) \right]^{-\nu}. \tag{12.75}$$

Here ξ_0 is the amplitude of the correlation length, $\tau = (T - T_c)/T_c$ is the temperature variable, $\nu \approx 0.63$ is the critical exponent.

Another geometry of a liquid volume of the cylindrical form with a linear size along its axis $L_z \gg \xi$ and radius $R \leq \xi$ corresponds to porous structures or ion channels in biological membranes. In this case the correlation length of density fluctuation is given by the formula [13]:

$$\xi = \xi_0 \left[\tau + \left(\frac{\mu_1 \xi_0}{R} \right)^{1/\nu} (1 + \tau) \right]^{-\nu} \tag{12.76}$$

with $\mu_1 = 2.4048$ being the first naught of the Bessel function $J_0(z)$.

A quantity with the strongest singularity in (12.45) is the bulk viscosity $\varsigma = \varsigma_r + \varsigma_s$ where ς_r is a regular part without any singularity while a singular part $\varsigma_s \propto \xi(L)^3$ is approximately proportional to $\varsigma_s \propto \tau(L)^{-2}$ due to the hyperscaling equality $3\nu = 2 - \alpha \approx 1.9$ with the critical exponents $\nu \approx 0.63$ and $\alpha \approx 0.1$. As for other quantities in (12.45), their singularities are essentially weaker: (a) the shear viscosity $\eta = \eta_r + \eta_s$ with a singular part $\eta_s \sim \xi^{X_\eta} \sim \tau(L)^{-X\eta^\nu}$ where the critical exponent $x_\eta \approx 0.065$; (b) the coefficient of thermal conductivity $\kappa = \kappa_r + \kappa_S$ where a singular part $\kappa_S \propto \xi \propto \tau(L)^{-\nu}$ while a regular part κ_r is practically constant in the vicinity of the critical point; (c) the specific heat at constant pressure $C_P \propto \tau(L)^{-\gamma}$ where the critical exponent $\gamma \approx 1.24$ while the specific heat at constant volume $C_V \propto \tau(L)^{-\alpha}$.

Thus, the width Γ_{MB} of the MBC in the light critical opalescence spectrum satisfies the following formula for confined liquids:

(a) for a cylindrical geometry (e.g. channels, pores, etc.)

$$\Gamma_{MB} \propto \Gamma^0_{MB} \left[\tau + \left(\frac{\mu_1 \xi_0}{R} \right)^{1/\nu} (1 + \tau) \right]^{-3\nu}; \tag{12.77}$$

(b) for a plane-parallel geometry (interfaces, biological membranes, etc.)

$$\Gamma_{MB} \propto \Gamma^0_{MB} \left[\tau + \left(\frac{\pi \xi_0}{H} \right)^{1/\nu} (1 + \tau) \right]^{-3\nu}, \tag{12.78}$$

where $\Gamma^0_{MB} \cong \varsigma_0 q^2/\rho$, ς_0 is the amplitude of the singular part of the bulk viscosity.

These results enable us to formulate the following conclusions:

1. A maximal value of the width Γ_{MB} takes place as the new "critical temperature" $T_c^*(L)$ of a confined liquid is approached. One has such formulae for this new

"critical temperature" $T_c^*(L)$ which is in fact the temperature corresponding to the maximum (minimum) values of a physical quantity under consideration (in our case—the width Γ_{MB}):

$$T_c^*(R) = T_c(\infty)\left\{1 + \left(\frac{\mu_1 \xi_0}{R}\right)^{1/\nu}\right\}^{-1} \text{ for a cylindrical geometry;} \tag{12.79}$$

$$T_c^*(H) = \frac{T_c(\infty)}{1 + \left(\frac{\pi\xi_0}{H}\right)^{1/\nu}} = T_c(\infty)\left\{1 + \left(\frac{\pi\xi_0}{H}\right)^{1/\nu}\right\}^{-1} \text{ for a plane} - \text{parallel geometry.}$$

As is seen from (12.79), the new "critical temperature" $T_c^*(L)$ of a confined liquid is shifted from the critical temperature $T_c(\infty)$ of a bulk liquid system. The shift given by formulae (12.79) demonstrates that (a) $T_c^*(L) < T_c(\infty)$, i.e. $T_c^*(L)$ is shifted towards lesser temperature; (b) $T_c^*(L)$ is approaching $T_c(\infty)$ with increasing a geometric factor L.

2. The width Γ_{MB} in confined liquids has no singularity at the critical temperature of a bulk liquid system ($\tau = 0$) and depends only on a geometric factor L according to the relations

$$\begin{aligned} \Gamma_{MB} &\propto R^3 \text{ for a cylindrical geometry;} \\ \Gamma_{MB} &\propto H^3 \text{ for a plane} - \text{parallel geometry.} \end{aligned} \tag{12.80}$$

Thus, with decreasing a geometric factor L of confined liquids, say, by an order of magnitude, i.e. ten times, the width Γ_{MB} of the MBC of the light critical opalescence spectrum at the bulk critical temperature $T_c(\infty)$ is shortening very strong—one thousand times. Figure 12.5 shows a schematic dependence of the dimensionless width of the MDC in liquids with different linear sizes of its volumes.

The frequency shift of MBC. The shift $\Delta\Omega_{\mathrm{MB}}$ of the side MBC from the central Rayleigh line is governed by the sound velocity $v(q)$ and in the hydrodynamic theory can be represented by the formula

$$\Delta\Omega_{\mathrm{MB}} = v[\tau(L, q)]q^2. \tag{12.81}$$

The regular part of $\Delta\Omega_{\mathrm{MB}}$ connected with the background part of the specific heat C_v at the constant volume due to the relation $v_{reg} \sim C_{Vreg}^{-1/2}$, while the singular part of the frequency shift $\Delta\Omega_{\mathrm{MB}}$ at low frequencies can be written as follows:

$$\Delta\Omega_{\mathrm{MBs}} = \upsilon_s[\tau(L,q)]q^2 \sim C_{Vs}^{-1/2} \sim \tau(L,q)^{\alpha/2}. \tag{12.82}$$

The main consequences obtained from (12.82) can be formulated as follows:

1. A decrease in the frequency shift $\Delta\Omega_{\mathrm{MB}}$ is small because a numerical value $\alpha/2 \approx 0.055$ for classical liquids.
2. The minimal value of $\Delta\Omega_{\mathrm{MB}}$ does not take place at the bulk critical temperature $T_c(\infty)$ but at the new "critical temperature $T_c^*(L)$ given by (12.79), as in the case of the width Γ_{MB}.
3. The frequency shift $\Delta\Omega_{\mathrm{MB}}$ in confined liquids has also no singularity at the critical temperature $T_c(\infty)$ of a bulk liquid system and depends on a geometric factor L:

$$\begin{aligned} \Delta\Omega_{\mathrm{MB}} &\propto R^{-\alpha/2\nu} \text{ for a cylindrical geometry;} \\ \Delta\Omega_{\mathrm{MB}} &\propto H^{-\alpha/2\nu} \text{ for a plane}-\text{parallel geometry.} \end{aligned} \tag{12.83}$$

Equations (12.83) give such a result: with decreasing a geometric factor L of confined liquids (correspondingly, the thickness H of a liquid film (e.g. biologic membranes, synaptic clefts, etc.) or the radius R of cylindrical samples (e.g. ion channels, pores, etc.), the frequency shift of the side MBC of the light critical opalescence spectrum is weakly increasing: $\Delta\Omega_{\mathrm{MB}} \sim L^{-\alpha/2\nu} \sim L^{-0.087}$. It is worthy to mention that results obtained for the width Γ_{MB} and frequency shift $\Delta\Omega_{\mathrm{MB}}$ are valid only at frequencies $\omega \gg \omega_r$ where $\omega_r = \lambda/\rho C_V \xi^2 \propto \xi(L)^{-(1+\alpha/\nu)}$ is the relaxation frequency which decreases with approaching the new "critical temperature" $T_c^*(L)$ of confined fluids.

The Landau-Placzek relation. As is known, the ratio $I_c/2I_{MB}$ of the integral intensities of the central Rayleigh line and side MBC is given by the LPR

$$I_c/2I_{MB} = (C_P - C_V)/C_V. \tag{12.84}$$

While studying the light critical opalescence spectrum for confined liquids, one has such a formula for the LPR in the hydrodynamic approximation:

$$I_c/2I_{MB} \sim \tau(L)^{-\gamma+\alpha}, \tag{12.85}$$

with $-\gamma + \alpha \approx -1.1$. Thus, the LPR demonstrates a rapid growth of the integral intensity I_c of the central component which becomes finite at the new "critical temperature" due to the spatial dispersion of the order-parameter fluctuation. Again, the largest value for the ratio $I_c/2I_{MB}$ should be observed at the temperature $T_c^*(L)$ given by (12.79). At the bulk critical temperature $T_c(\infty)$, (12.85) gives the following dependence of $I_c/2I_{MB}$ on the geometric factor L:

$$I_c/2I_{MB} \sim R^{(\gamma-\alpha)/\nu} \text{ for a cylindrical geometry;}$$
$$I_c/2I_{MB} \sim H^{(\gamma-\alpha)/\nu} \text{ for a plane}-\text{parallel geometry.} \tag{12.86}$$

This formula shows that the ratio $I_c/2I_{MB}$ decreases for lesser linear sizes of liquid systems at the direction of its spatial limitation, namely $I_c/2I_{MB} \sim L^{1.79}$.

Similarity between light and neutron scattering spectra. The method of QENS is a powerful physical method of studying the dynamic properties of confined fluids. In accordance with the hypothesis of dynamic scaling and formulae for kinetic coefficients in confined fluids, we may write the following expression for the width of quasi-elastic peak of slow neutron scattering in spatially limited liquid volumes with a linear size S [18, 112–114]:

$$\Delta E(q^2,\tau) = \Delta E(q^2)\{(G/S)^{1/\nu} + [1+(G/S)^{1/\nu}](\xi/\xi_0)^{-1/\nu} sign\tau\}^{\gamma} \tag{12.87}$$

Here, $\Delta E_0(q^2) = (h/\pi)D_0q^2$ is the amplitudes of the width of QENS peak, D_0 is the amplitude of diffusion coefficient [86]

$$D = D_0\{(G/S)^{1/\nu} + [1+(G/S)^{1/\nu}](\xi/\xi_0)^{-1/\nu} sign\tau\}^{\gamma} \tag{12.88}$$

in the dynamic crossover region.

Biomedical applications of the light scattering spectra and QENS. The principle goal of this section is to emphasize the peculiarities of the light scattering spectra and QENS in confined liquids, in particular of the medical and biological nature. Main reasons for such a study are as follows (see e.g. [18, 112–119]):

(a) large responses of a system to external fields are mostly connected with its critical (bifurcation) states;
(b) biological liquids are usually located in small volumes such as cells, synaptic clefts, ion channels, vesicles, porous structures, etc.;
(c) phase transitions and critical phenomena undergoing in fluids at restricted geometry have a very specific behavior;
(d) spectra of the light scattering spectra as well as the method of QENS give the broad information on the equilibrium and non-equilibrium properties of biological mesostructures.

Therefore, the above-mentioned problem seems to be of a great importance for a deeper understanding the peculiar features of confined water and aquatic biological solutions. In particular, a precise analysis of the dynamic light and neutron scattering in aquatic solutions of plasmatic membranes of tumor cells is a promising biomedical direction of studies near structural phase transitions such as the cell proliferation, i.e. an anomalous growth of cell and membrane sizes.

Results obtained in this direction may give a reliable background to introduce a new diagnostic method of the crucial process of tumor formation. This method is based upon the following conclusions: with *increasing* the characteristic system's size L in water suspension of plasmatic membranes of tumor cells:

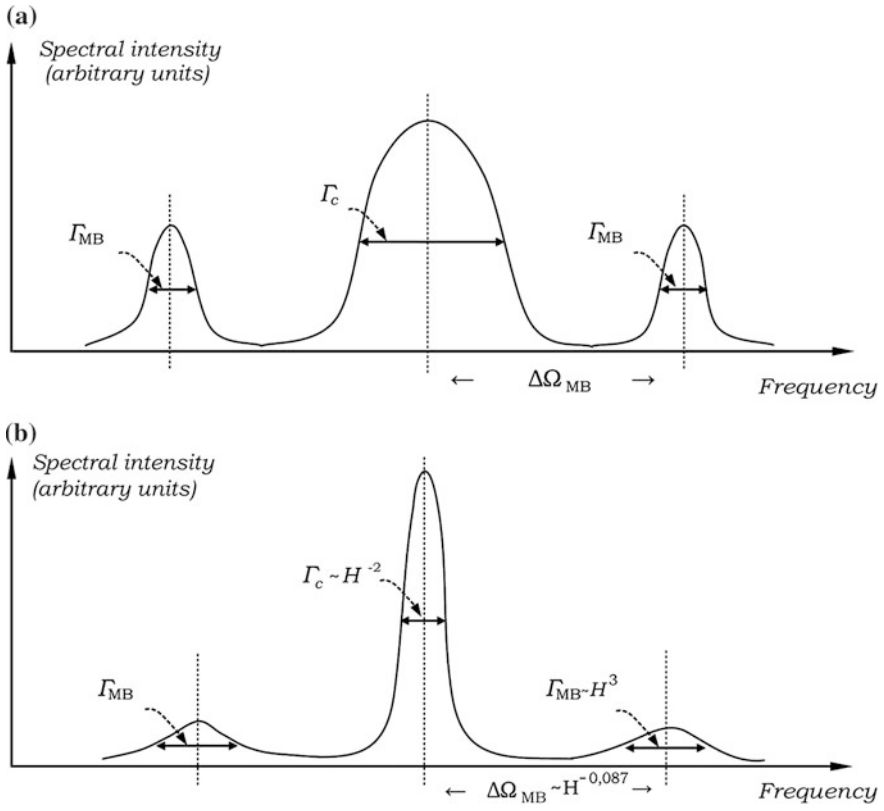

Fig. 12.5 The LMS spectra in suspensions of plasmatic membranes: **a** normal cells, **b** proliferated cells

1. The width Γ_c of the central Rayleigh line, being proportional L^{-2}, *is rapidly decreasing* because the dynamic critical exponent z* ≈2 in the hydrodynamic region (see formula (12.62) and Fig. 12.5).
2. The width Γ_{MB} of MDC is *strongly broadening* according to the relation $\Gamma_{MB} \propto L^3$ (see (12.80)) and due to the diffusion mechanism being in fact a governing factor also for the size dependence (12.87) of the quasi-elastic peak of the neutron scattering studies in the water suspensions of plasmatic membranes of tumor cells [18].
3. The frequency shift $\Delta\Omega_{MB}$ of the side MBC from the central Rayleigh line is *weakly decreasing* in accordance with such a relation $\Delta\Omega_{MB} \propto L^{-0.087}$ (see (12.83)).
4. The LPR is *essentially increasing* as is seen from $I_c/2I_{MB} \propto L^{1.79}$ (see (12.86)).

Figure 12.5 illustrates these results which should be observed in mesoscale biomedical systems such as suspensions of membranes of oncologic cells during the process of its proliferation connected with an increase of the membrane's thickness H. The same conclusion on the size dependence of the width line $\Delta E(q, H) \sim H^{-2}$ of the QENS, as compared with the size dependence of the width $\Gamma_c \sim L^{-2}$ of the central Rayleigh line, was received in [18, 112].

Thus, while the membrane thickness H is increasing 1.5 times during the process of proliferation, one should expect that (1) the widths of the central Rayleigh line Γ_c and the QENS peak $\Delta E(q^2)$ are shortening twice, (2) the frequency shift $\Delta\Omega_{\mathrm{MB}}$ of the side components is increasing by 3.6%, (3) the width of the side MBC is broadening 3 times, and (4) the LPR is increasing more than 2 times.

12.7 Conclusion

In this paper, we have investigated the features of bulk and confined fluids, including peculiar physical properties of CSW near its 2nd critical point in a deep-quenched metastable state.

Our theoretical approach allows finding the pair correlation function and the correlation length of order-parameter fluctuations in confined systems undergoing phase transitions and critical phenomena. It is shown that, by considering the actual factor of a dimensional crossover, the effective spatial d_{eff} and fractal d_{fr} dimensionalities are gradually varying with increasing a number S of molecular layers in confined fluid systems. These findings are important for a deeper understanding the basic principles of nucleation processes. In particular, the growth of fluctuating clusters due to its coalescence appears to be a less probable event with transfer from $2d$ to $3d$ geometry, i.e. with increasing S and numerical values of $d_{\mathrm{eff}} - d_{\mathrm{fr}}$.

We also show how the dynamic anomalies in confined fluids and CSW (namely, the coefficients of diffusion and shear viscosity, the linewidth of the quasi-elastic neutron scattering (QENS) as well as the main characteristics of the light molecular scattering spectrum such as the width Γ_{c} of the central Rayleigh line, the width Γ_{MB} and frequency shift $\Delta\Omega_{\mathrm{MB}}$ the of MBC, and the LPR are essentially changed as compared with the dynamic anomalies in bulk fluids. These results create a reliable background to introduce a new additional diagnostic method of early detecting the tumor formation in practical medicine.

We hope for that the existing theory of CSW behavior near the low-temperature phase transitions, including theoretical results presented in our paper, will help one to stimulate new experimental studies and simulations in this difficult and important direction.

Acknowledgements The author would like to thank Prof. M. A. Anisimov, Prof. T. M. Bryk, Prof. L. A. Bulavin, Prof. K. A. Chalyy, Prof. M. F. Holovko, Prof. M. P. Kozlovskii, Prof. H.-J. Moegel, Prof. W. Schroer, Prof. V. M. Sysoev, Prof. A. N. Vasilev, Dr. L. M. Chernenko, Dr. G. V. Hrapijchuk, Dr. A. V. Oleinikova, and Dr. E. V. Zaitseva for helpful remarks and collaboration.

References

1. L.P. Kadanoff, Physica **2**, 263 (1966)
2. M.E. Fisher, in *Critical Phenomena*, ed. by M.S. Green (Academic Press, New York, 1971)
3. H.E. Stanley, *Introduction to Phase Transitions and Critical Phenomena* (Glarendon Press, Oxford, 1971)
4. E.L. Lakoza, V.M. Sysoev, A.V. Chalyi, JETP **65**, 605 (1973)
5. M.E. Fisher, Rev. Mod. Phys. **46**, 597 (1974)
6. K.G. Wilson, J. Kogut, Phys. Rep. **12**, 75 (1974)
7. A.Z. Patashinskii, V.L. Pokrovskii, *The Fluctuation Theory of Phase Transitions* (Pergamon Press, Oxford, 1979)
8. M.N. Barber, in *Phase Transitions and Critical Phenomena*, ed. by C. Domb, J.L. Lebowitz (Academic Press, New York, 1983)
9. M.A. Anisimov, *Critical Phenomena in Liquids and Liquid Crystals* (Gordon & Breach, Philadelphia, 1991)
10. V. Privman, P.C. Hohenberg, A. Aharony, in *Phase Transitions and Critical Phenomena*, ed. by C. Domb, J.L. Lebowitz (Academic Press, New York, 1991)
11. K. Binder, Annu. Rev. Phys. Chem. **43**, 33 (1992)
12. A.V. Chalyi, A.V. Lebed, *Non-homogeneous Liquids Near the Critical Point and the Boundary of Stability and Theory of Percolation in Ceramics* (Harwood Academic Publishers, London, 1993)
13. A.V. Chalyi, J. Mol. Liquids **58**, 179 (1993)
14. A.V. Chalyi, L.M. Chernenko, in *Dynamic Phenomena at Interfaces, Surfaces and Membranes*, ed. by D. Beysens, N. Baccara, G. Forgacs (Nova Science Publishers, New York, 1993)
15. A.V. Chalyi, A.N. Vasilev, J. Mol. Liquids **84**, 203 (2000)
16. I. Brovchenko, A. Oleinikova, Handb. Theor. Comput. Nanotechnol. **62**, 1 (2005)
17. M.P. Kozlovskii, *The Influence of External Field on Critical Behavior of 3- Dimensional Systems* (Galitskij Publisher, Lviv, 2012)
18. A.V. Chalyi, L.A. Bulavin, V.F. Chekhun, K.A. Chalyy, L.M. Chernenko, A.M. Vasilev, E.V. Zaitseva, G.V. Khrapijchuk, A.V. Severin, M.V. Kovalenko, Condens. Matter Phys. **16**, 23008 (2013)
19. M. Holovko, V. Shmotolokha, T. Patsahan, in *Physics of Liquid Matter: Modern Problems*, ed. by L. Bulavin, N. Lebovka (Springer, Switzerland, 2015)
20. A.V. Chalyi, in *Physics of Liquid Matter: Modern Problems*, ed. by L. Bulavin, N. Lebovka (Springer, Switzerland, 2015)
21. P. Gallo, K. Amman-Winkler, C.A. Angell, M.A. Anisimov, P. Caupin, C. Chakravarty, E. Lascaris, T. Loerting, A.Z. Panagiotopoulos, J. Russo, J.A. Sellberg, H.E. Stanley, H. Tanaka, C. Vega, L. Xu, L.G.M. Pettersson, Chem. Rev. **116**, 7463 (2016)
22. R.J. Speedy, J. Chem. Phys. **86**, 982 (1982)
23. P.H. Poole, F. Sciortino, U. Essmann, H.E. Stanley, Nature **360**, 324 (1992)
24. P.H. Poole, F. Sciortino, T. Grande, H.E. Stanley, C.A. Angell, Phys. Rev. Lett. **73**, 1632 (1994)
25. C.A. Angell, Science **319**, 582 (2008)
26. S. Sastry, P.H. Debenedetti, F. Sciortino, H.E. Stanley, Phys. Rev. E **53**, 6144 (1996)
27. C.A. Angell, Ann. Rev. Phys. Chem. **34**, 593 (1983)
28. F. Sciortino, P. Gallo, P. Tartaglia, S.-H. Chen, Phys. Rev. **54**, 6331 (1996)
29. P.G. Debenedetti, H.E. Stanley, Phys. Today **56**, 40 (2003)
30. P.G. Debenedetti, J. Phys, Condens. Matter **15**, R1669 (2003)
31. I. Brovchenko, A. Geiger, A. Oleinikova, D. Paschek, Eur. Phys. J. **12**, 69 (2003)
32. K.A. Chalyy, K. Hamano, A.V. Chalyi, J. Mol. Liq. **92**, 153 (2001)
33. D.A. Fuentevilla, M.A. Anisimov, Phys. Rev. Lett. **97**, 195702 (2006)
34. I. Brovchenko, A. Oleinikova, J. Chem. Phys. **126**, 214701 (2007)

35. H.E. Stanley, Z. Phys, Chem. **223**, 939 (2009)
36. O. Mishima, J. Chem. Phys. **133**, 144503 (2010)
37. V. Holten, M.A. Anisimov, Sci. Rep. **2**, 713 (2012)
38. F.X. Prielmeier, E.W. Lang, R.J. Speedy, H.-D. Lüdemann, Phys. Rev. Lett. **59**, 1128 (1987)
39. Yu.A. Osipov, B.V. Zheleznyi, N.F. Bondarenko, Zh. Fiz. Khim. **51**, 1264 (1977)
40. W. Koch, V. Dohm, Phys. Rev. E **58**, R1179 (1998)
41. T.V. Lokotosh, S. Magazu, G. Maisano, N.P. Malomuzh, Phys. Rev. E **62**, 3572 (2000)
42. P. Kumar, Proc. Natl. Acad. Sci. USA **103**, 12955 (2006)
43. L. Xu, P. Kumar, S.V. Buldyrev, S.-H. Chen, P.H. Poole, F. Sciortino, H.E. Stanley, Proc. Natl. Acad. Sci. USA **102**, 16558 (2005)
44. P. Kumar, S.V. Buldyrev, S.R. Becker, P.H. Poole, F.W. Starr, H.E. Stanley, Proc. Natl. Acad. Sci. USA **104**, 9575 (2007)
45. J.D. Eaves, D.R. Reichman, Proc. Natl. Acad. Sci. USA **106**, 15171 (2009)
46. A. Dehaoui, B. Issenmann, F. Caupin, Proc. Natl. Acad. Sci. USA **112**, 12020 (2015)
47. C.A. Angell, J. Shuppert, J.C. Tucker, J. Phys. Chem. **77**, 3092 (1973)
48. R.J. Speedy, C.A. Angell, J. Chem. Phys. **65**, 851 (1976)
49. R. Kurita, H. Tanaka, Science **306**, 845 (2004)
50. S. Sen, S. Gaudio, B.G. Aitken, C.E. Lesher, Phys. Rev. Lett. **97**, 025504 (2006)
51. M.H. Bhat, V. Molionero, E. Soignard, V.C. Solomon, S. Sastry, J.L. Yarger, C.A. Angell, Nature **448**, 787 (2007)
52. K. Stokely, M.G. Mazza, H.E. Stanley, G. Franzese, Proc. Natl. Acad. Sci. USA **107**, 1301 (2010)
53. P. Kumar, S. Han, H.E. Stanley, J. Phys.: Condens. Matter **21**, 504108 (2009)
54. B.J. Widom, in *Phase Transitions and Critical Phenomena*, ed. by C. Domb, M.S. Green (Academic Press, Waltham, 1972)
55. J. Frenkel, *Kinetic Theory of Liquids* (Oxford University Press, Oxford, 1947)
56. M.E. Fisher, B.J. Widom, J. Chem. Phys. **50**, 3759 (1969)
57. *Water Wisdom and Widom* (Boston University Research Briefs, 2005)
58. A.D. Alekhin, N.P. Krupskii, A.V. Chalyi, JETP **63**, 1417 (1972)
59. G.G. Simeoni, T. Bryk, F.A. Gorelli, M. Krisch, G. Ruocco, M. Santoro, T. Scopigno, Nat. Phys. **6**, 503 (2010)
60. M.A. Anisimov, V.F. Agayan, P.I. Collings, Phys. Rev. E **57**, 582 (1998)
61. D.A. Fuentevilla, M.A. Anisimov, Phys. Rev. Lett. **98**, 149904 (2007)
62. C.E. Bertrand, M.A. Anisimov, J. Phys. Chem. B **115**, 14099 (2011)
63. V. Holten, C.E. Bertrand, M.A. Anisimov, J.V. Sengers, J. Chem. Phys. **136**, 094507 (2012)
64. J. Luo, L. Xu, E. Lascaris, H.E. Stanley, S.V. Buldyrev, Phys. Rev. Lett. **112**, 135701 (2014)
65. R. Balescu, *Equilibrium and Nonequilibrium Statistical Mechanics* (Publication, Wiley, 1975)
66. I.R. Yukhnovskyi, M.F. Holovko, *Statistical Theory of Classical Equilibrium Systems* (Naukova Dumka, Kyiv, 1980)
67. I.R. Yukhnovskii, M.P. Kozlovskii, I.V. Pelyuk, *Microscopic Theory of Phase Transitions in 3-Dimensional Systems* (Evrosvit, Lviv, 2001)
68. M.E. Fisher, J. Math. Phys. **5**, 944 (1964)
69. E.L. Lakoza, A.V. Chalyi, JETP **40**, 521 (1974)
70. D.W. Oxtoby, W.M. Gelbart, J. Chem. Phys. **60**, 3359 (1974)
71. V.L. Kuzmin, Opt. Spectrosk. **38**, 423 (1975)
72. L.V. Adzhemyan, L. Ts, L.A. Adzhemyan, V.P.R. Zubkov, JETP **51**, 530 (1981)
73. E.L. Lakoza, A.V. Chalyi, Usp. Fiz. Nauk **140**, 393 (1983); Sov. Phys. Usp. **26**, 573 (1983)
74. V.L. Kuzmin, Phys. Rep. **123**, 365 (1985)
75. L.A. Zubkov, V.P. Romanov, Usp. Phys. Nauk **14**, 615 (1988); Sov. Phys. Usp. **31**, 328 (1988)
76. M.O. Kimball, K.P. Mooney, F.M. Gasparini, Phys. Rev. Lett. **92**, 15301 (2004)
77. E.K. Riedel, F.J. Wegner, Phys. Rev. Lett. **29**, 349 (1972)
78. D.J.O. Conner Phys. A **25**, 101 (1992)

79. S. Berber, Y.-K. Kwon, D. Tomanek, Phys. Rev. Lett. **84**, 4613 (2000)
80. L. Yang, P. Grassburger, B. Hu, Phys. Rev. E **74**, 062101 (2006)
81. S. Ghosh et al., Nat. Mater. **9**, 555 (2010)
82. M.H. Fischer, M. Sigrist, J. Phys: Conf. Ser. **200**, 012034 (2010)
83. S. Krali et al., Soft Matter **8**, 2460 (2012)
84. S. Karimi, C.A. Ullrich, Phys. Rev. B **90**, 245304 (2014)
85. A.V. Chalyi, E.V. Zaitsea, K.A. Chalyy, G.V. Khrapijchuk, Ukr. Phys. J. **60**, 888 (2015)
86. A.V. Chalyi, E.V. Zaitseva, Bull. Kiev Univ. (Phys. Math.), no. 1, 287 (2009)
87. A.V. Chalyi, G.V. Hrapijchuk, L.M. Chernenko, K.A. Chalyy, E.V. Zaitseva, Ukr. Phys. J. **55**, 1113 (2010)
88. K. Kawasaki, in *Phase Transitions and Critical Phenomena*, ed. by C. Domb, M.S. Green (Academic Press, New York, 1976)
89. A.V. Chalyi, V.P. Lukomskii, I.S. Gandzha, Ya.V. Tsekhmister, K.A. Chalyi, *Non-Linear Processes in Physics: Oscillations, Waves and Self-Organization* (Chetvertaya Khvylja, Kyiv, 2004)
90. K.A. Chalyi, L.A. Bulavin, A.V. Chalyi, J. Phys. Studies **9**, 66 (2005)
91. V.G. Boiko, H.-J. Moegel, V.M. Sysoev, A.V. Chalyi, Usp. Fiz. Nauk **161**, 77 (1991)
92. K. Binder, D.W. Heermann, *Monte Carlo Simulation in Statistical Physics* (Springer, Berlin, 2002)
93. V.G. Boiko, V.M. Sysoev, A.V. Chalyi, JETP **96**, 842 (1990)
94. Y.B. Zel'dovich, D.D. Sokolov, Usp. Fiz. Nauk **146**, 493 (1985)
95. P.G. Debenedetti, *Metastable Liquids: Concepts and Principles* (Princeton University Press, Princeton, 1996)
96. V.I. Arnold, *Catastrophe Theory* (Moscow University Press, Moscow, 1983)
97. T. Poston, I. Stewart, *Catastrophe Theory and its Applications* (Pitman, London, 1978)
98. A. Onuki, J. Chem. Phys. **85**, 1122 (1986)
99. A.P. Levanyuk, JETP **9**, 571 (1959)
100. V.L. Ginzburg, Phys. Solid State **2**, 1824 (1961)
101. P.C. Hohenberg, B.I. Halperin, Rev. Mod. Phys. **49**, 435 (1977)
102. H.C. Burstyn, J.V. Sengers, P. Esfandiari, A **19**, 2402 (1980)
103. F. Mallamace, C. Branca, C. Corsaro, N. Leone, J. Spooren, H.E. Stanley, S.-H. Chen, J. Phys. Chem. B **114**, 1870 (2010)
104. S.-H. Chen, F. Mallamace, C.-Y. Mou, M. Brocco, C. Corsaro, A. Faraone, L. Liu, Proc. Natl. Acad. Sci. USA **103**, 2974 (2006)
105. S Sengupta, S Karmakar, C Dasgupta, and S Sasry, J. Chem. Phys. **138**, 10.1063 (2013)
106. H.S. Cummins, E.R. Pike, *Photon Correlation and Light Beating Spectroscopy* (Plenum Press, New York, 1974)
107. M.A. Anisimov, V.A. Agayan, A.A. Povodyrev, J.A. Sengers, E.E. Gorodetskii, Phys. Rev. E **57**, 1946 (1998)
108. B.W. Law, J.C. Nieuwoudt, Phys. Rev, A. **40**, 3880, 1989
109. B.J. Askerson, H.J.M. Hanley, J. Chem. Phys. **73**, 3568 (1980)
110. R.D. Mountain, J.M. Deutch, J. Chem. Phys. **50**, 1103 (1969)
111. T. Bryk, F. Gorelli, G. Ruocco, M. Santoro, T. Scopigno, Phys. Rev. E **90**, 042301 (2014)
112. L.A. Bulavin, K.A. Chalyy, *Neutron Optics of Mesoscale Liquids* (Naukova Dumka, 2006)
113. L.A. Bulavin, V.F. Chekhun, K.A. Chalyy et al., Phys. Alive **12**, 94 (2004)
114. L.A. Bulavin, I.M. Vyshnevskii, V.F. Chekhun, R.V. Bila, V.P. Tryndyak, K.A. Chalyy, Rep. Natl. Acad. Sci. Ukraine **7**, 176 (2004)
115. A.V. Chalyi, *Non-Equilibrium Processes in Physics and Biology* (Naukova Dumka, Kyiv, 1997)

116. A.V. Chalyi, Ya.V. Tsekhmister, K.A. Chalyi, *Processes of Ordering and Self-organization in Fluctuation Models of Open Systems* (Bogomolets National Medical University, Kyiv, 2001)
117. *Medical and Biological Physics*, ed. by A.V. Chalyi (Nova Knyha, Vinnytsia, 2013)
118. *Oncology. Selected Lectures for Students and Physicians*, ed. by V.F. Chekhun (Zdorovje Ukrainy, Kyiv, 2010)
119. A.V. Chalyi, Rep. Natl. Acad. Sci. Ukraine **9**, 170 (2012)
120. F. Mallamace et al., Adv. Chem. Phys. **152**, 203 (2013)
121. F. Mallamace, C. Corsaro, D. Mallamace, C. Vasi, S. Vasi, H.E. Stanley, *Material Research Society (MRS) Advances*, pp. 1–12 (2016)

Chapter 13
The Polycluster Theory for the Structure of Glasses: Evidence from Low Temperature Physics

Giancarlo Jug

Abstract The problems of the intermediate-range atomic structure of glasses and of the mechanism for the glass transition are approached from the low-temperature end in terms of a scenario for the atomic organization that justifies the use of an extended tunneling model. The latter is crucial for the explanation of the magnetic and compositional effects discovered in non-metallic glasses in the Kelvin and milli-Kelvin temperature range. The model relies on the existence of multi-welled local potentials for the effective tunneling particles that are a manifestation of a non-homogeneous atomic structure deriving from the established dynamical heterogeneities that characterize the supercooled liquid state. It is shown that the extended tunneling model can successfully explain a range of experiments at low temperatures, but the proposed non-homogeneous atomic structure scenario is then tested in the light of available high resolution electron microscopy imaging of the structure of some glasses and of the behaviour near the glass transition.

13.1 Introduction

The physics of glass-forming liquids, especially at higher temperature, continues to generate considerable research effort. These substances of extraordinary practical and technological importance still present considerable scientific challenges in the description of the glass-formation mechanism (nature of the glass transformation) and of the nature of the atomic structure at intermediate- and long-range length scales that characterize the solid. Standard X-ray and other scattering techniques fail in this respect to give a conclusive answer about the atomic structure of topologically disordered solids and the development of new investigation tools is desirable since there is no way to distinguish via scattering the structure of the liquid from that of

G. Jug (✉)
Dipartimento di Scienza ed Alta Tecnologia and To.Sca.Lab,
Università dell'Insubria, Via Valleggio 11, 22100 Como, Italy
e-mail: giancarlo.jug@uninsubria.it

G. Jug
INFN – Sezione di Pavia, Pavia, Italy

L. A. Bulavin and A. V. Chalyi (eds.), *Modern Problems of Molecular Physics*,
Springer Proceedings in Physics 197, https://doi.org/10.1007/978-3-319-61109-9_13

the topologically disordered solid except through the vastly different relaxation time scales. Opinions as to why divergent time scales characterize the formation of the topologically disordered solid differ, however, and no agreement on a justification from structure for the mechanical properties below the glass transformation temperature T_g has to date been reached. Why should indeed a microscopically liquid-looking assembly of interacting particles behave (mechanically) like a crystalline solid remains to date a true mystery. Owing to such difficulties much theoretical and computational research on the description of the topologically disordered solid and its properties takes its moves from the study of the corresponding liquid for which much has been understood thanks to equilibrium statistical mechanics. Though understandable, this approach would correspond to be wanting to understand the physical properties of a crystalline solid from the study of its melt, which of course would present some formidable challenges given the ergodicity-breaking phenomenon that characterizes crystallization. In this essay it is proposed that the glass transition is of a purely kinetic nature and the use of equilibrium statistical mechanics is at its very limit of applicability since ergodicy also gets broken, though perhaps not so sharply and completely as for crystals, through the onset of the glassy state. The idea is then to try to learn something about the structure below T_g and the kinetic character of the glass transition starting from the phenomenology of the better understood supercooled liquid state (defined for temperatures T in the range $T_g \leq T \leq T_c$, with T_c the (equilibrium) crystallization temperature) and folding that knowledge in the study of the low-temperatures properties of laboratory amorphous solids. The return to low-temperatures is for glasses in a sense akin to starting to study the crystalline solid through X-ray and other (e.g. neutron-) scattering techniques at "zero" temperatures assuming the atoms in fixed positions. However since at those temperatures the glass would look like a liquid in a static scattering experiment, one has to exploit other specific degrees of freedom of the cold, topologically disordered solid that are not present for the perfectly ordered crystals. These are the so-called tunneling systems (TSs), local defects described in terms of new local degrees of freedom and that can be exploited—much as the atomic nuclei in NMR research—to probe the atomic structure and properties of the glassy state. The only difficulty is that these TS probes are not entirely localized, each comprising several atoms as a rule, and have not been fully understood to date. However, progress in their characterization and in the understanding of their microscopic nature is advancing also in view of some recent challenges posed by the discovery of puzzling magnetic effects in non-magnetic glasses that cannot be attributed (despite some interesting attempts) to trace paramagnetic impurities. Moreover, in the strategic research for reliable solid-state qubits to be deployed for the fabrication of working quantum computers (e.g. through use of Josephson-junction superconducting devices) the problems posed by the TSs (ubiquitous in the junctions) are paramount. These new challenges foster enhanced research efforts that have culminated in the development of an extended tunneling model [1] that relies on a new scenario for the intermediate-range atomic structure of glasses. The new model and structural scenario afford a reasonable—though not complete—explanation for the low-T anomalies in glasses and in turns the structural scenario can be evolved at higher temperatures to formulate a possible mechanism

for the onset of the glass transition from the supercooled state. Preliminary aspects of the structure that is expected are tested in this essay and seem to corroborate some known facts about the glassy state. In this new framework of ideas, research in the previously-exotic low-T regime begins to give very useful hints about the onset of the glassy state from the supercooled liquid at much higher temperatures. The interplay of knowledge coming from the high-T supercooled liquid state and from the low-T cryogenic properties thus begins to provide a productive symbiosis for the understanding of this still mysterious, though ubiquitous, state of matter.

At low temperatures (cryogenic) glasses are believed to be characterized by special low-energy excitations (TSs) which are usually described through the use of double-welled potentials (DWPs) and of so-called two-level systems (2LSs) with energy asymmetry and tunneling barrier broadly distributed throughout the mass of the amorphous solid [2, 3]. While little is still known about the character (atomic, polyatomic or cluster-like) of the TSs, the general agreement is still that the intermediate-range atomic structure of glasses should be conveniently well described by Zachariasen's 1932 continuous random network (CRN) model [4, 5] (thus homogeneously disordered, just like for a liquid) and the 2LSs therefore result out of two slightly similar, probably localized atomic configurations. With this by now classic characterization, the 2LSs have been employed mainly in the 1970s and 1980s to explain with some success the anomalies in the physical properties of glasses at low and ultra-low temperatures, a research field thus far completely detached from the quest for the nature of the glass transition.

Yet, systematic deviations from the behaviour predicted by the standard tunneling model (STM) occasionally challenge (or have challenged) the validity of the model in the case of multi-component glasses with tunable content of the good crystal-forming (GCF) component (e.g. $(SiO_2)_{1-x}(K_2O)_{1-x}$ with changing x, the concentration of the alkali component, [6, 7]) and especially in glasses of the compositions type $BaO–Al_2O_3–SiO_2$ and then in the presence of a weak magnetic field [8]. In such glasses (unfortunately the mixed alkali-silicate glasses have not yet been investigated in a field, but the prediction is for important magnetic effects there, and x-dependent too) a puzzling non-monotonous magnetic-field dependence in many properties has been unveiled in some physical properties [9–11]. The magnetic effect is typically (but not always) weak, but orders of magnitude larger than expected from basic thermodynamic-science considerations. The STM by itself is unable to account for the compositional and magnetic effects, therefore a suitable extension of the celebrated tunneling model for both situations has been proposed by the present Author [1]. This so-called extended tunneling model (ETM) rests upon the existence (particularly in the multi-component glasses) of small regions of enhanced regularity (RERs) in the intermediate-range atomic structure of the somewhat incompletely-frozen (in fact) amorphous solid. A complete mathematical description and ultimate physical justification of the ETM thus requires at the very least a partial (or complete) demise of the Zachariasen-Warren's vision of the intermediate-scale structure of glasses and amorphous solids in general.

As it happens, an alternative to the homogeneously-disordered approach of Zachariasen-Warren has been proposed and developed in the former Soviet Union

and in some places in the West. Well before Zachariasen-Warren, Lebedev [12] and his followers in Skt. Petersburg (but Randall in London, UK, too [13]) proposed that glasses should be made up of (initially, true) polycrystallites of sufficiently small size as to justify the X-ray peak rounding which was observed experimentally in diffractometers. Since the thermal and mechanical properties of glasses are reported not the same as those of polycrystalline solids, the concept of "crystallite" has evolved, meaning finally a failed micro-crystal of some sort. Also because finite clusters cannot be crystalline, strictly speaking. The evolution of the crystallite concept can be found in reviews by Porai-Koshits (see, e.g., [14]) and the latest views rely on concepts such as "cybotactic groupings", meaning atomic regions that can be rather extended and interpenetrating, but where the atomic ordering—though not complete due to finite size, thus highly defective—is better achieved than in the rest of the solid. A recent overview can be found in the works by Wright [15], and in the Russian literature recent ideas have been put forward also by Bakai [16, 17]. The latter Author envisages in fact better-ordered clusters being preferentially nucleated below T_c through some kinetic mechanisms that have the clusters survive and grow at the expense of true micro-crystalline nuclei that have no time to grow. At the glass transition these ill-formed, but better-ordered clusters merge together and get to form a polycluster that is the macroscopic skeleton of the solid glass. Evidently, looser material is also present in a patchwork atomic structure, characterized by spatial and (above T_g) temporal heterogeneities.

In this review we provide a scenario for the intermediate-range atomic structure of glasses, the cellular model, which is very much reminiscent of the polycluster theory of Bakai and a formulation within which the phenomenological assumptions for the ETM's mathematical framework (given in several papers by the present Author) become completely—or at least to a large extent—justified. The cellular or polycluster model provides for a definitely more realistic mathematical formulation of this framework in terms of a tetrahedric four-welled tunneling quasi-particle potential, as said, the simplified triangular three-welled version of which is nothing but a poor-man's, probably rather realistic, version affording a much speedier mathematical description. Within this cellular approach to the structure of glasses the most significant local tunneling potentials (probably in terms of number density) turn out to be the DWPs, this for a single (or very few) atomic particle(s), and the said tetrahedric four-welled potential (TFWP) for a correlated cluster of $N \gg 1$ charged real atomic particles. A reasonable and very useful simplification for the TFWP is thus the replacement of the N interacting and tunneling atomic particles with a single fictive quasi-particle subject to a triangular tunneling potential (TWP) and carrying renormalized parameters (charge, magnetic threaded area, energy asymmetry as well as tunneling probability), quantum-mechanically moving about one face of the full tetrahedric potential. The renormalization gets fully justified by the proximity of (on average) four similarly quasi-ordered, close-packed atomic cells (RERs or better-ordered regions) and the reasonable assumption that most of the charged particles will avoid the interstice's tetrahedral potential's centre. We present again, therefore, a brief mathematical description of the TWP and its quantum mechanics in those limits appropriate for practical applications. We then show the main results obtained

for the description of the density of states (DOS) and the temperature and magnetic-field dependence for the specific heat of some specific glasses, then for the dielectric constant (real and imaginary parts) in the linear-response regime, and for the polarization echo—always in the presence of a magnetic field (limiting to results obtained for the multi-silicates).

With this scenario of the cellular, or polycluster structure of real glasses assimilated, the question of the description of the glass transition is one of the next challenges. Having nucleation theory, and for better-ordered or Bakai clusters in mind the growth of such clusters with a cooling rate κ can be considered and the temperature at which the polycluster appears is taken to be T_g. With some phenomenological assumptions in the light of standard Adam-Gibbs theory (where the RERs, or Wright's better-ordered clusters, appear as CRCs or coherently-rearranging clusters) [18], the dependence of T_g from κ is worked out and the known logarithmic dependence can be recovered.

The paper is organized as follows. In Sect. 13.2 we introduce the cellular model for the structure of glasses, now a complete departure from Zachariasen's continuous random-network model, and then examine the likely tunneling states that would emerge from such cellular picture, to conclude that only DWPs and TFWPs should be relevant for the physics of glasses below the glass transition temperature T_g. In Sect. 13.2 we also review the basic relevant quantum mechanics of the three-welled, poor man's version of the TFWP, a version that has been used to date to obtain a reasonable single explanation for all of the anomalies (and deviations from the STM predictions) due to composition changes and to the presence of a magnetic field. We also show how to evaluate the magnetic density of states (DOS) $g(E, B)$ and, in Sect. 13.3, we briefly review some of the magnetic-field dependent low-temperature physical properties that have been studied to date, such as the heat capacity $C_p(T, B)$ comparing with some of the published data for the multi-silicate glasses. We then do the same for the dielectric constant, real part ϵ' and (just comment on the) imaginary part ϵ'' as well, also showing some comparison with available data at low (kHz) frequency, and then we examine the application of the ETM to the explanation of some of the data for the polarization (or, electric) echoes in the silicates (only commenting about glycerol, for which case the ETM has been able to explain the so-called isotope effect, which is in fact a mere mass substitution effect). Section 13.4 contains a discussion on how the cellular model can be implemented to gain information on the size of the better-ordered cells making up the polycluster structure of amorphous solids. The typical values for the cell size extracted from low-temperature experiment parameters are then compared with available high resolution electron microscopy (HREM) imaging of insulating glasses that show such structure. It is shown that estimates from low temperatures and from HREM imaging compare reasonably well. A brief derivation of the model's prediction for the cooling rate dependence of T_g is also provided and this Sect. 13.4 contains also our Conclusions.

13.2 The Cellular Model for the Atomic Structure of Glasses and the Three-Welled Tunneling Potential

Glass-forming liquids are an important class of materials for technology and ubiquitous applications, nevertheless the atomistic structure of glass in relation to its physical properties remains a mystery. As stated in the Introduction, the widespread conception is that the atomic arrangement of a glass should be the same as that for a liquid, as is indeed implicit in Zachariasen's 1932 proposed continuous network picture [4, 5], which has been widely adopted by scholars (at least in the West, see below). This picture differs from that of a liquid only in that a dynamical arrest has occurred, without specifying its ultimate origin. Relaxation times diverge "near" T_g, but why? In a spin-glass the ultimate origin of dynamical arrest is magnetic frustration (with or without disorder), but for ordinary structural glasses it remains mysterious and an important open issue [19–22]. In the opinion of the present Author, lack of justification for this arrest is the primary roadblock for the achievement of a theory of the glassy state encompassing all aspects of glass physics in every possible temperature range. As mentioned in the Introduction, prior to Zachariasen's scheme, however, the Soviet scientist A.A. Lebedev had proposed, in 1921, the concept of "crystallites" [12], small crystal-like (yet not truly ordered) regions jammed against each other in random orientation to contain altogether all (actually, almost all) atoms in the glassy substance. Later, Randall proposed that these be real microcrystals and explained the rounded-up X-ray spectra from glasses in this manner [13]. However, the density of glasses is typically some 10% less than that of polycrystalline aggregates and the thermal properties of glasses too cannot be explained by means of the Lebedev-Randall picture. Despite these observations, the East-West dychotomy continued to these days. The Zachariasen-Warren model of glass structure was for instance criticized by Hägg [23] in the West right in the early days of X-ray crystallography and a good review of the status quo of this controversy has been recently provided by Wright [15] who concludes, from a re-analysis of X-ray and neutron-scattering data from many different covalent-bonded and network glasses that indeed so-called *cybotactic groupings* (better-ordered regions) may well be present and frozen-in in most glasses, particularly if multi-component (or—one could add—polymeric [24]). The formation of *polyclusters*, instead of jammed crystallites, in most glasses is the latest scenario by the Eastern school [16, 17], which is based on observations and kinetic reasoning. As nicely set out by Bakai [16], the incipient crystals forming at and below T_c (melting point) are in constant competition with kinetically swifter (for glass-forming liquids) embryo clusters (or crystallites) that can win thermodynamically and kinetically over crystals during a rapid enough quench forming a polycluster spanning the whole of the sample.

On the experimental side, the concept of de-vitrification has been gradually taking sway with reports of metallic glasses [25] and also of monocomponent high-coordination covalent solids, like amorphous Si, forming *paracrystals* in their amorphous solids [26]. Therefore, the stance will be taken in this new review that only

the purest mono-component glasses may (perhaps) abide to the Zachariasen-Warren dogma of the continuous random-network model for a glass, whilst the vast majority of real glasses [27] will be organized differently at the intermediate-range atomic structure level. Solid-like fluctuations of finite size are, in fact, likely to form already around and below the crystallization temperature T_c, the formed solid-like clusters continuously breaking up and reforming in the supercooled state between T_c and T_g, which is indeed widely known to be characterised by the so-called dynamical heterogeneities (DH). The slower-particle regions of the DH are, in the present Author's view, to be identified with the solid-like (better-ordered) clusters and the faster-particle DH regions with the liquid-like (completely disordered) clusters that become thinner and thinner as T_g is approached. In this vision, the lower temperature glassy structure (now almost entirely solid-like) inherits the inhomogeneous DH structure of the supercooled state, the slower, solid-like better-ordered regions having grown to a limit size (e.g. a maximum average radius ξ_0) that is determined by the onset of the polycluster.

The structure now proposed is a cellular-type arrangement of better-ordered atomic regions (regions of enhanced ordering, RERs) that can have complicated, maybe fractal, but definitely compact shapes with a narrow size distribution and the interveening regions (let us call them interstitials) between them populated by still fast-moving particles (normally charged and possibly dangling-bonded ions). The insterstitial regions between the RERs are here the equivalent of the concept of *cages*, that is often discussed in the glass structure's literature (see e.g. [19]). We remark that a cellular-type structure was already embodied within the "crystallite" idea of Lebedev, but now no micro-crystals are claimed here to exists (except definitely in the ceramic-glasses case, to a good extent). The RERs are more like Wright's "cybotactic regions" [15] or Treacy's "paracrystals" [26] (there for a-Si, not a quenched-melt solid) and issue from the DH picture for the glass-forming supercooled liquid state above T_g (see e.g. Fig. 13.1) [19, 28–30]. The DH picture does indeed recognise the presence of regions of "slower" and "faster" particles, and an inspection of the slower-particle regions of the supercooled liquid reveals that these are also better ordered (solid-like) whilst the faster-particle regions are rather much more liquid-like. DH are ubiquitous in perhaps all supercooled liquids [30] and the claim (though still somewhat speculative) here is that the slower-particle regions will grow on approaching T_g, albeit only up to a finite size and will now be giving rise to the RERs in the frozen, glassy state below T_g. In fact, simulations in the frozen glassy state of the slower- and faster-particle regions do confirm that a DH-like picture applies also below T_g [31] and with the slower-regions's size ξ increasing as $T \to 0$. Earlier simulations (always for model systems) [32] did point out the difficulty of simulating the DH picture below T_g and came up with a picture of these slower-regions growing, and possibly diverging in size, on approaching T_g. In the present review, however, the stance will be taken that the slower-regions' average (even maximum) size growths in real systems, but does not diverge at T_g or at any other characteristic temperature. Full experimental or numerical proofs of this fact are, unfortunately, still lacking and should be considered as a reasonable working hypothesis in this paper. Indeed, the absence of a diverging characteristic length is,

in a nutshell, the central enigma of the problem of the glass transition. We remark in passing that a cellular structure (mosaic-like) for the glasses had been proposed by de Gennes [33] in the past and, in the context of the low-temperature anomalies, by Baltes [34] who was able to explain the linear in T anomaly in the heat capacity C_p (but not those in the acoustic properties, though, which require the introduction of tunneling). A very similar picture is that of the polyclusters of Bakai [16], as was already mentioned, but in the present approach the thermal genesis of the cells, or RERs, is ascribed directly to the DH scenario already present above T_g. In this approach the RERs, like grains or domains in the frozen structure below T_g, are the thermal-history continuation of the slower-particle regions of the DH above T_g. In Fig. 13.2 we show how the RERs themselves (not single particles) can get to grow to a limit intermediate average size ξ_0 and randomly close-pack together in the proximity of the glass transition temperature T_g, thus forming a highly correlated polycluster. The random close-packing process gets to be completed at a lower temperature $T_K < T_g$ (T_K possibly to be identified with the Kauzmann temperature) thus giving the glass transition more the character of a crossover. As temperature drops further below T_K, the cells or RERs can slightly increase in size, consolidating their growth at the expense of the species present in the interestitials between the RERs. This idea of consolidation at lower temperatures is shown pictorially in Fig. 13.3. The cells and interfaces between the cells will contain the bulk of the tunneling systems. These 2LSs are atomic tunneling states arising from the cells' own disorder, but most of the 2LSs should be located at the meeting point between two cells (two RERs). In the interstitial spaces between cells the remnant faster particles of the DH at $T > T_g$ give rise for $T < T_g$ to regions where a large number N (on average, per interstitial) of charged atomic tunneling particles are constrained to move in a coherent fashion due to the high Coulomb repulsion forces between them. Figure 13.4 shows in a schematic way how the atomic/ionic matter can get organised below T_g in a real glass. Since the interstitial's charged ions (dangling bonds, most likely) should act as a coherently tunneling ensemble, it seems natural to simplify the description of the physics at the lower temperatures using only phonons, propagating in the collection of cells now jammed against each other, and remnant ergodic localized degrees of freedom acting as TSs. These TSs will be of two types: the 2LSs within the cells and at their points of contact (owing to inherent disorder in the cells' atomic arrangement) and effective quasi-particles sitting in the close-packed cells' interstices and now representing the collective motion of the coherently-tunneling ions which are trapped in each interstice (Fig. 13.4). The quasi-particle will be subjected to an effective potential of distorted tetrahedral topology characterized by four wells for each RER interstice, with minima inside each RER or—depending on the material—at the RER meeting points and a high barrier in the interstice's centre. De facto this 3D interstitial TFWP potential can be replaced by four local 2D potentials for the four quasi-particles describing the coherent tunneling of the faster-moving particles sitting near each face of the distorted tetrahedron, close to a group of three (on average) quasi-ordered cells (Fig. 13.5). Because of the better-ordering implicit in this model of the glassy intermediate-range atomic structure, and in each cell, the three wells of each effective local 2D potential for the tunneling quasi-particles (four per interstice,

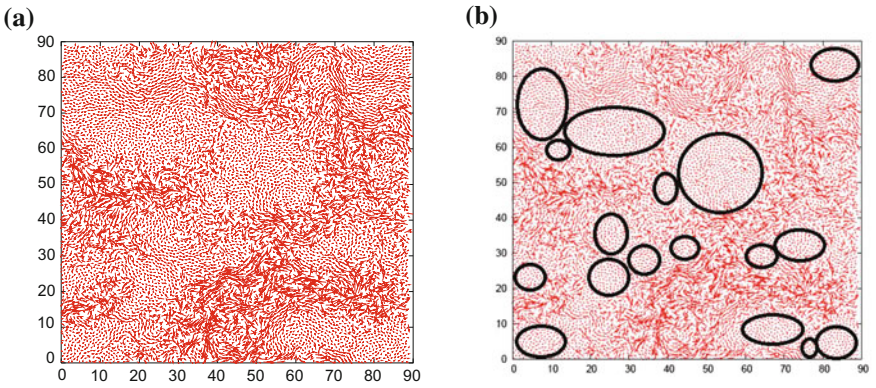

Fig. 13.1 **a** Spatial map of a single-particle displacements in the simulation of a binary Lennard-Jones mixture in two dimensions. Arrows show the displacement of each particle in a trajectory of length comparable to the structural relaxation time. The map (courtesy of G. Biroli, from [19]) reveals the existence of particles with different mobilities during relaxation, also the existence of spatial correlations between these dynamical fluctuations. Faster and slower particle regions are clearly visible and a closer inspection reveals that the slower particles form better-ordered regions, while the faster particles form liquid-like regions. Note the distinct clustering of slow particles (dynamical heterogeneities, DH). **b** The slower regions have been schematically highlighted to show their incipient cellular structure. At the temperature of the simulation ($T > T_g$) the slower regions are continuously breaking up and reforming, the idea is that as T_g is approached their size grows to a finite limit value and their mutual hindering significally slows down their dynamics. The ringed regions of slower moving particles become, below T_g, the RERs or cells characterizing glassy intermediate-range atomic structure

on average) should be near-degenerate in terms of their ground-state energy asymmetries: $E_1 \simeq E_2 \simeq E_3 \simeq 0$. With this, still qualitative, picture in mind we now turn to the mathematical description of the physics of the remnant and still ergodic degrees of freedom (phonons in the cells' network—likely the origin of the Boson peak—2LSs and ATSs (anomalous tunneling systems, four in each interstice)). For our model of a real glass, by construction the 2LSs will be much more numerous than the ATSs.

In this approach [1] the relevant degrees of freedom, beside the phonons, are generalised dilute gases of independent 2LSs described by the STM and of fictitious quasi-particles tunneling in TWPs. The formulation of the STM (the 2LS model) for the low temperature properties of glasses is very well known [2, 3]. One assumes a collection of DWPs distributed in the substance and represented each by a 2×2 effective Hamiltonian of the form, in the potential-well (or real-space) representation:

$$\mathcal{H}_{2LS} = -\frac{1}{2}\begin{pmatrix} \Delta & \Delta_0 \\ \Delta_0 & -\Delta \end{pmatrix}. \tag{13.1}$$

Here the two parameters Δ (the energy asymmetry) and Δ_0 (twice the tunneling parameter) are typically characterized by a probability distribution that views

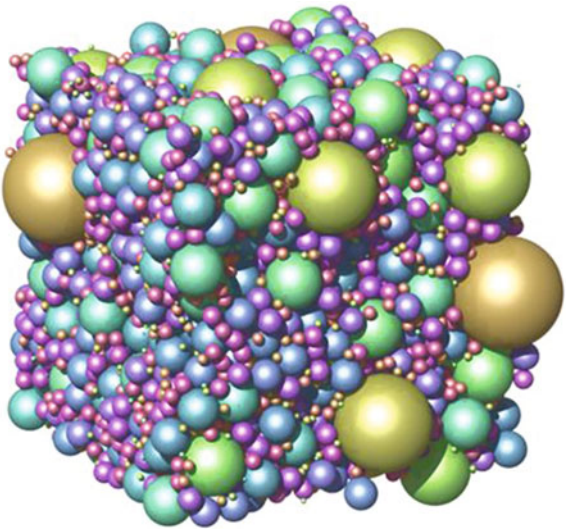

Fig. 13.2 Random close packing of compact RERs in the proximity of the glass transition temperature T_g. The spheres represent regions of better-ordered atomic particles that have grown to a limit maximum size and hinder each other's further growth. In the interstitial regions (voids between the spheres), not shown, are the remainder of the incipient glass particles: these are more liquid-like and mobile, while the RERs that are shown need not be spherical nor completely mutually exclusive, partial coalescence being allowed

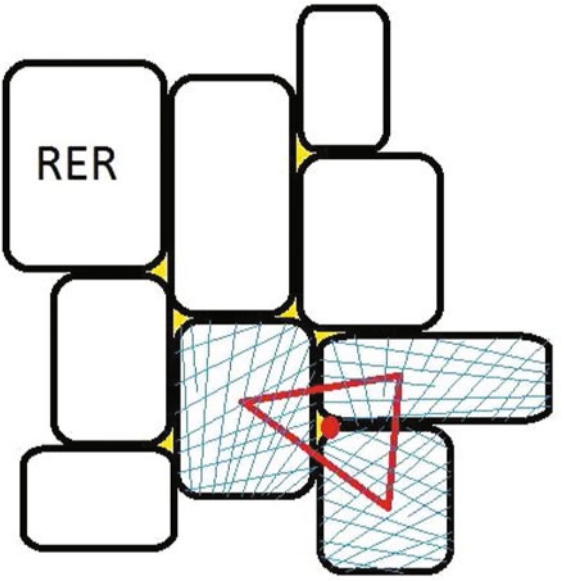

Fig. 13.3 2D cartoon of the consolidation of the RERs at the lower temperatures, where the better-ordered regions have grown at the expense of the particles in the interstitials. Ultimately this leads to a temperature-dependent number of liquid-like tunneling particles in each interstitial

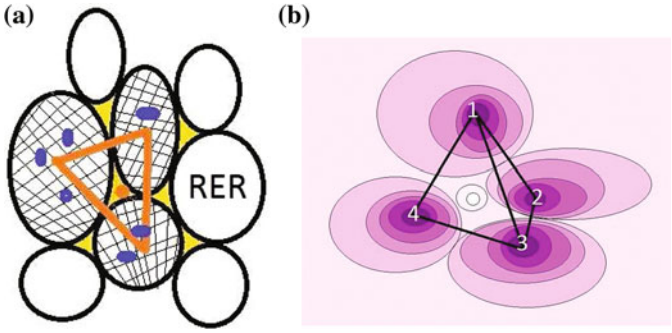

Fig. 13.4 **a** A 2D cartoon of the cellular structure of an amorphous (melt-quenched) solid just below T_g. The RERs (black-circled blobs, an oversimplified schematics for fractal-like, but compact objects) have grown to completely fill the space and enclose atomistic tunneling states of the 2LS type (blue blobs). At the same time, in the RER interstitials (yellow regions, connecting to each other) the trapped, charged and faster particles of the DH existing above T_g (now probably charged dangling bonds), give rise to coherently-tunneling large groups of ions here represented by a single, fictitious, quasi-particle (orange dot) subjected to an effective tunneling potential having typically four natural wells in distorted-tetrahedral configuration (**b**) for close-packed RERs. **b** The tetrahedral four-welled potential (TFWP) in a 3D representation with a colour-coded potential intensity (dark = deepest, light = highest)

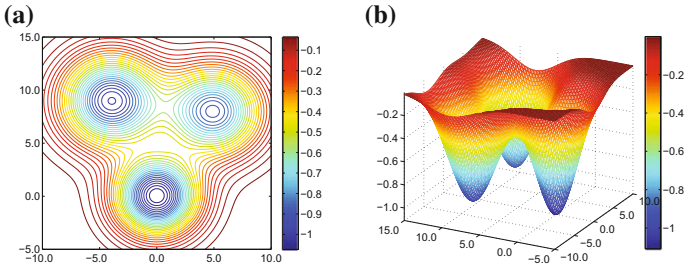

Fig. 13.5 **a** Contour-plot of a possible realization of the 2D effective three-welled potential (TWP) very likely felt by the quasi-particle of those charged real particles dangling from, or being trapped by, a group of three RERs on each one face of the tetrahedral configuration for an interstice formed by close-packed RERs well below T_g (and T_K). **b** 3D attempted visualization of the same example of a TWP potential

Δ and $\ln(\Delta_0)$ (the latter linked to the particular DWP energy barrier) broadly (in fact, uniformly) distributed throughout the topologically disordered solid [35]:

$$\mathcal{P}_{2LS}(\Delta, \Delta_0) = \frac{\bar{P}}{\Delta_0} \tag{13.2}$$

where some cutoffs must be introduced when needed and where $\bar{P}$ is an elusive material-dependent parameter, like the cutoffs. In fact, Eq. (13.2) embodies entirely the Zachariasen-Warren hypothesis for the intermediate atomic structure of a glass,

assuming broadly-distributed the energy asymmetry $\Delta = E_2^{(0)} - E_1^{(0)}$, hence the single-well ground state energies $E_1^{(0)}$ and $E_2^{(0)}$ themselves, as well as the potential barrier height V_0 appearing typically in relations such as:

$$\Delta_0 \simeq \hbar\Omega e^{-\frac{d}{\hbar}\sqrt{2mV_0}} \tag{13.3}$$

$$\Delta_0 = \frac{\hbar\Omega}{2}\left[3 - \sqrt{\frac{8V_0}{\pi\hbar\Omega}}\right] e^{-2\frac{V_0}{\hbar\Omega}} \tag{13.4}$$

Here, the first relation is the generic WKB result for an arbitrarily shaped DWP (where m is the particle's mass, Ω its single-well harmonic frequency (or tunneling attempt frequency) and d the tunneling distance) and the second formula refers instead to a symmetric ($\Delta = 0$) DWP made up by two superimposed parabolic wells. In fact, in the end the distribution (13.2) refers to the combination of parameters $\Delta_0/\hbar\Omega$. The energies of the two levels $|0>$ and $|1>$ are then given by $\mathcal{E}_{0,1} = \pm\frac{1}{2}\sqrt{\Delta^2 + \Delta_0^2}$, and so on [2, 35].

The tunneling Hamiltonian of a particle in a TWP is also easily written down, in the same low-T spirit as for a 2LS, as a generalization of the above matrix formulation to the case of three wells [1]:

$$\mathcal{H}_{3LS} = \begin{pmatrix} E_1 & D_0 & D_0 \\ D_0 & E_2 & D_0 \\ D_0 & D_0 & E_3 \end{pmatrix} \tag{13.5}$$

where E_1, E_2, E_3 are now the energy asymmetries between the wells and where D_0 is the most relevant tunneling amplitude (through saddles of the glassy potential energy landscape, or PEL, in fact). No disorder in D_0 is considered, for simplicity, within each single DWP. This 3LS Hamiltonian has the important advantage of readily allowing for the inclusion of a magnetic field $B > 0$, when this is coupling orbitally with a tunneling "particle" (in fact, a quasi-particle) having charge q (q being some multiple of the electron's charge e) [1]:

$$\mathcal{H}_{3LS}(B) = \begin{pmatrix} E_1 & D_0 e^{i\varphi/3} & D_0 e^{-i\varphi/3} \\ D_0 e^{-i\varphi/3} & E_2 & D_0 e^{i\varphi/3} \\ D_0 e^{i\varphi/3} & D_0 e^{-i\varphi/3} & E_3 \end{pmatrix} \tag{13.6}$$

where $\varphi/3$ is the so-called Peierls phase for the tunneling particle through a saddle and in the field, and φ is the Aharonov-Bohm (A-B) phase for a tunneling loop (triangular shaped) and is given by the usual formula:

$$\varphi = 2\pi\frac{\Phi}{\Phi_0}, \qquad \Phi_0 = \frac{h}{|q|} \tag{13.7}$$

Φ_0 being the appropriate magnetic flux quantum (h is Planck's constant) and $\Phi = \mathbf{B} \cdot \mathbf{S}_{\triangle}$ the magnetic flux threading the area $S_{\triangle}$ and formed by the tunneling paths of the particle in this now simplified (poor man's, yet as we have seen realistic) model. The three energy asymmetries E_1, E_2, E_3 typically enter through their natural combination $D \equiv \sqrt{E_1^2 + E_2^2 + E_3^2}$.

For $n_w = 3$ wells an exact solution for the $k = 0, 1, 2$ eigenvalues of the multi-welled tunneling Hamiltonian Eq. (13.6) is still possible (but not in the $n_w = 4$ TFPW case):

$$\mathcal{E}_k = 2D_0 \sqrt{1 - \frac{\sum_{i \neq j} E_i E_j}{6D_0^2}} \cos\left(\frac{1}{3}\theta + \theta_k\right) \tag{13.8}$$

$$\cos\theta = \left(\cos\varphi + \frac{E_1 E_2 E_3}{2D_0^3}\right)\left(1 - \frac{\sum_{i \neq j} E_i E_j}{6D_0^2}\right)^{-3/2}$$

$\theta_k = 0, +\frac{2}{3}\pi, -\frac{2}{3}\pi$ an index distinguishing the three eigenstates. In the physically relevant limit, which we now consider, and in which $\varphi \to 0$ (weak fields) and $D = \sqrt{E_1^2 + E_2^2 + E_3^2} \to 0$ (near-degenerate distribution), and always at low temperatures, we can approximate (in a now simplified calculation) the $n_w = 3$—eigenstate system with an *effective 2LS* having its energy gap $\Delta\mathcal{E} = \mathcal{E}_1 - \mathcal{E}_0$ widening with increasing φ provided $D_0 > 0$ (see below):

$$\lim \Delta\mathcal{E} \simeq \frac{2}{\sqrt{3}} \sqrt{D_0^2\varphi^2 + \frac{1}{2}(E_1^2 + E_2^2 + E_3^2)} \to \sqrt{D_0^2\varphi^2 + D^2} \tag{13.9}$$

(a trivial rescaling of D_0 and of the E_i has been applied). One can easily convince oneself that if such TWP is used and with the standard parameter distribution, Eq. (13.2) (with D, D_0 replacing Δ, Δ_0) for the description of the TS, one would then obtain essentially the very same physics as for the STM's 2LS-description. In other words, there would be no need to complicate the popular, minimal 2LS-description in order to study glasses at low temperatures, unless structural inhomogeneities of the RER-type and a magnetic field are present. Without the RERs, hence no distribution of the type (13.10) below, the phase interference from separate tunneling paths is only likely to give rise to an exceedingly weak quantum effect. Hence, it will be those TSs nesting between the RERs that will give rise to an enhanced quantum phase interference and these TSs can be minimally described—most appropriately and conveniently—through Hamiltonian (13.6) and with a distribution of asymmetries thus modified in order to favour near-degeneracy [1]:

$$\mathcal{P}^*_{3LS}(E_1, E_2, E_3; D_0) = \frac{P^*}{D_0(E_1^2 + E_2^2 + E_3^2)} \tag{13.10}$$

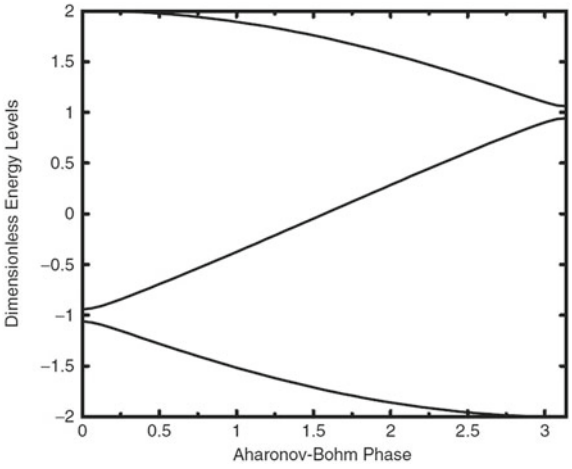

Fig. 13.6 The energy spectrum (for $D_0 = 1$ units) of the ATS (3LS, TWP) model, in the physically appropriate limits of a weak magnetic field and near-degeneracy due to the embedding within RER's interstitials. On the horizontal axis is the A-B phase $\varphi \propto B$

P^* being a dimensionless (which is pleasing) material parameter. We remark that the incipient "crystallinity" (better-ordering, in fact) of the RERs calls for near-degeneracy in E_1, E_2, E_3 simultaneously and not in a single one of them, whence the correlated form of (13.10). We now have basically three-level systems (3LSs) with energy levels $\mathcal{E}_0 < \mathcal{E}_1 \ll \mathcal{E}_2$, periodic in φ. The typical ATS spectrum, with $D_0 > 0$ (see below), is shown in Fig. 13.6 as a function of φ and one can now see that the third and highest level $\mathcal{E}_2$ can be safely neglected for most low-field applications. Other descriptions, with TFWPs or modified three-dimensional DWPs are possible for the TSs nested in the RERs and yet they lead to the same physics as that from Eqs. (13.6) and (13.10) above (which describe what we like to call the anomalous tunneling systems, or ATSs, nesting in the interstitials between the RERs). The final and a most important consideration for the construction of a suitable mathematical model of such complex systems is that the TSs appear to be rather diluted defects in the glass (indeed their concentration is of the order of magnitude of that for trace, paramagnetic (e.g. Fe), impurities, as we shall see). Hence the tunneling "particles" are, de facto, embedded in a medium otherwise characterized only by fairly simple acoustic-phonon degrees of freedom. This embedding, however, does mean that the rest of the material takes its part in the making of the tunneling potential for the TS's "particle", which itself is not moving quantum-mechanically in a true vacuum. Sussmann [36] has shown that this should lead to local trapping potentials that (for the case of triangular and tetrahedral perfect symmetry, like in our limit no-disorder case) must be characterized by a degenerate ground state. This should mean that, as a consequence of the TS embedding, our poor man's model, Eq. (13.6), for the ATSs should be chosen with a strictly positive tunneling parameter [1]:

$$D_0 > 0 \tag{13.11}$$

where of course perfect degeneracy gets always removed through weak disorder in the asymmetries. Intrinsic near-degeneracy of (13.10) of course implies that the

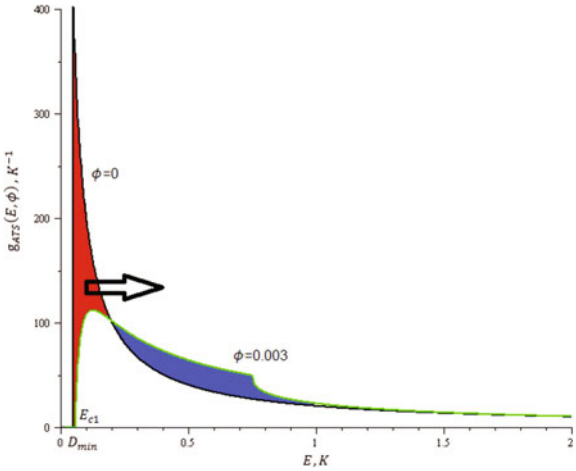

Fig. 13.7 The magnetic-sensitive contribution of the density of states (DOS) as the function of the energy gap E and selected Aharon-Bohm (A-B) phases φ (proportional to the magnetic field B) (here $n_{ATS}P^*$ has been set to 1). The rapid transfer of quantum states to higher energy when a very weak magnetic field B is switched on is the basic explanation for the origin of the magnetic effects

model should be used in its $D/D_0 \ll 1$ limit, and that in turn reduces the ATSs to effective magnetic-field dependent 2LSs, greatly simplifying the mathematical analysis when the limit $\varphi \to 0$, which we always take for relatively weak magnetic fields, is used. The ETM was first proposed in [1], and consists basically in a collection of independent, non-interacting 2LSs which are described by the STM and also 3LS-TWPs, which are described by Eqs. (13.6) and (13.10) above, in the mentioned $D/D_0 \ll 1$ and $\varphi \to 0$ limits. The 3LSs are meant to be nested in the interstitials between the close-packed RERs while the magnetic-field insensitive 2LSs are distributed in the remaining homogeneously-disordered granular matrix of RERs and at their touch points or interfaces [37]. In Fig. 13.7 we illustrate the behaviour of the magnetic part of the density of states (DOS) for this model as a function of the ATS gap energy, E, for different values of the A-B phase φ. This figure demonstrates the physical origin of the magnetic effects: the number of quantum states being conserved, they get to be very rapidly shifted towards high values of the energy when a magnetic field, even very weak, is turned on. The ETM, proposed in this form by the present Author in 2004, has been able to explain so far the magnetic effects in the heat capacity [1], in the real [38] and imaginary [39] parts of the dielectric constant and in the polarization echo amplitude [39] data reported to date for a variety of glasses at low temperatures. The ETM has also shed much new light into the composition-dependent anomalies [7, 37]. The new physics provided by the magnetic-field dependent TS DOS, as mentioned, comes from a term due to the near-degenerate TWPs [1] and that gets to be added up to the constant DOS from the STM 2LSs (having constant density n_{2LS}):

$$\begin{aligned} g_{tot}(E,B) &= n_{2LS}\bar{P} + n_{ATS}\frac{P^*}{E}f_{ATS}(E,B)\theta(E-E_{c1}) \\ &= g_{2LS}(E) + g_{ATS}(E,B) \end{aligned} \tag{13.12}$$

where n_{ATS} is the ATSs' concentration, while f_{ATS} is a magnetic-field dependent dimensionless function already described in previous papers [1] and E_{c1} is a material and weakly B-dependent energy cutoff:

$$g_{ATS}(E,\varphi) = \int \Pi_i dE_i \delta(\Sigma_j E_j) \int dD_0 \mathcal{P}^*_{3LS}(\{E_k\}, D_0)\delta(E-\Delta\mathcal{E}) = \begin{cases} \frac{2\pi P^*}{E} \ln\left(\frac{D_{0max}}{D_{0min}}\sqrt{\frac{E^2-D^2_{0min}\varphi^2}{E^2-D^2_{0max}\varphi^2}}\right) & \text{if} \quad E > E_{c2} \\ \frac{2\pi P^*}{E} \ln\frac{\sqrt{(E^2-D^2_{0min}\varphi^2)(E^2-D^2_{min})}}{D_{0min}D_{min}\varphi} & \text{if} \quad E_{c1} \le E \le E_{c2} \\ 0 & \text{if} \quad E < E_{c1}. \end{cases} \tag{13.13}$$

Moreover, after an irrelevant renormalization of parameters: $E_{c1} = \sqrt{D^2_{min} + D^2_{0min}\varphi^2}$, $E_{c2} = \sqrt{D^2_{min} + D^2_{0max}\varphi^2}$, D_{min}, D_{0min} and D_{0max} being suitable (material parameters) cutoffs. A more microscopic model does not exist, at present. The gross $1/E$ dependence of the ATS DOS is one consequence of the chosen tunneling parameters' distribution, Eq. (13.10), and it gives rise to a peak in g_{tot} near E_{c2} that is rapidly eroded away as soon as a (weak, depending on material parameters) magnetic field is switched on. The form and evolution of the magnetic part of the DOS is shown in Fig. 13.8 for some chosen parameters and as a function of $\varphi \propto B$ for different values of the ATS energy gap E. This behaviour of the

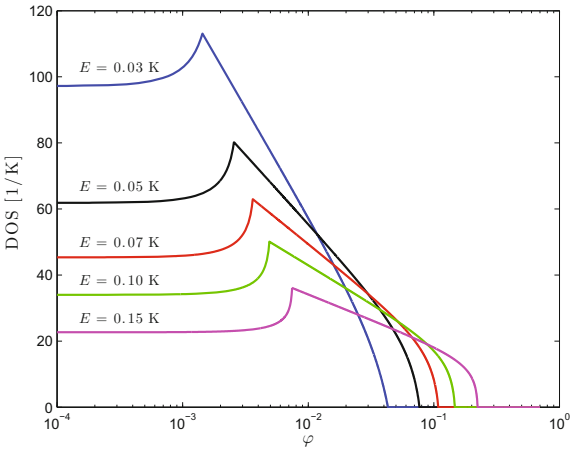

Fig. 13.8 The magnetic-sensitive part of the density of states (DOS) as a function of the A-B phase φ (proportional to the magnetic field B, upon averaging) and different energies (again $n_{ATS}P^*$ has been set equal to 1). The shape of this DOS contribution (coming from the TWPs with a parameter distribution (13.10) which is favouring near-degeneracy) is the ultimate source of all the magnetic effects (see also Fig. 13.17). The cusp is an artifact of the effective 2LS approximation [1], albeit also of the existence of upper and lower bounds for D_0 due to the disordered nature of the RER glassy atomic structure

DOS with B is essentially the underlying mechanism for all of the experimentally observed magnetic-field effects in the studied cold glasses within this model: the measured physical properties turn out to be convolutions of this DOS (with some appropriate B-independent functions) and in turn they reproduce the shape of this DOS as functions of B (see also Fig. 13.17). We remark that already at $B = 0$ the TS total DOS $g_{tot}(E)$ that is here advocated, Eq. (13.12) above (see also Fig. 13.7, has the correct qualitative form that was solicited by Yu and Leggett [40] in order to achieve a better qualitative explanation for many experiments at low temperatures in the real glasses. Namely, a broad constant (due to the majority 2LSs), surmounted by a triangular-shaped contribution in a range of energy E (this part, coming from the minority ATSs). This shape is now being to a large extent justified by our model and indeed explains experimental data rather well.

13.3 The Magnetic Field Effects (Multi-silicate Glasses Only)

We now come to the main theme for this article, the crucial piece of new experimental evidence for the cellular, RER-based scenario for glass structure. As mentioned in the Introduction, a large number of magnetic-field dependent effects have been reported in the late 1990s and early 2000s for several insulating glasses and that could not be ascribed to the (ubiquitous) trace paramagnetic impurities. We refer the reader to a review article of this Author's work so far [41], here we just review the main results that have been obtained through the proposed cellular approach and ETM low-temperature model in order to explain all such magnetic effects.

13.3.1 The Magnetic Field Dependent Specific Heat

Though unrecognized by the experimentalists, the heat capacity measured in some multi-component silicate glasses (pure, mono-component silica does not display such effect) has shown a strong dependence on the applied magnetic field. Such dependence was the first to be explained by the present approach [1, 42]. The total TS heat capacity is easily evaluated for this model (ETM) and obtained from the above calculated DOS

$$C_{pTS}(T,B) = \int_0^\infty dE\; g_{tot}(E,B) C_{p0}(E,T) \tag{13.14}$$

Table 13.1 Extracted parameters (from the specific heat data [43]) for the concentrations of ATSs and Fe-impurities for the BAS glass

BAS glass	Concentration [g^{-1}]	Concentration [ppm]
$n_{Fe^{2+}}$	1.06×10^{17}	14.23
$n_{Fe^{3+}}$	5.00×10^{16}	6.69
$P^* n_{ATS}$	5.19×10^{16}	–

Table 13.2 Extracted tunneling parameters (from the C_p data [43]) for the BAS glass

Temperature [K]	D_{min} [K]	$D_{0min}\|\frac{q}{e}\|S$ [KÅ^2]	$D_{0max}\|\frac{q}{e}\|S$ [KÅ^2]
0.60	0.49	4.77×10^4	3.09×10^5
0.90	0.53	5.07×10^4	2.90×10^5
1.36	0.55	5.95×10^4	2.61×10^5

where

$$C_{p0}(E,T) = k_B \left(\frac{E}{2k_B T}\right)^2 \cosh^{-2}\left(\frac{E}{2k_B T}\right) \tag{13.15}$$

is the heat capacity contribution from each single TS having energy gap E and where $g_{tot}(E,B)$ is given by Eq. (13.12). We have made use of the resulting expression to fit the available data [43] that display a magnetic effect in the heat capacity in the case of two multi-component silicate glasses: commercial borosilicate Duran (from Schott GmbH) and barium-allumo-silicate (AlBaSiO, or BAS in short) glass (from Heraeus GmbH), in order to show that the ATS-ETM model works well for the magnetic-field dependent C_p. In order to fit the data, the standard phonon (T^3) contribution as well as the Langevin-paramagnetism contribution from the trace iron impurities [mostly Fe^{2+} as it turns out] need to be added to the said tunneling contributions (Tables 13.1 and 13.2).

The best fit for the available data is reported in Fig. 13.9a in the case of BAS glass. The concentrations of the ATSs and Fe-impurities extracted from the best fit of the heat capacity data [43] as a function of B, for Duran, are reported in Table 13.3; having fixed the concentrations, it is then possible to extract the remaining parameters for Duran (Table 13.4). The fit of the available data [43] is reported in Fig. 13.9b for Duran.

The results of our repeated [1] C_p analysis definitely indicate that the magnetic-field sensitive ATSs give a significant contribution to the low temperature heat capacity data. The explanation of these data [1] was the first test of the ETM and gave the first indication that the cellular structure of glass has a manifestation in experiments outside the traditional X-ray scattering domain of investigation.

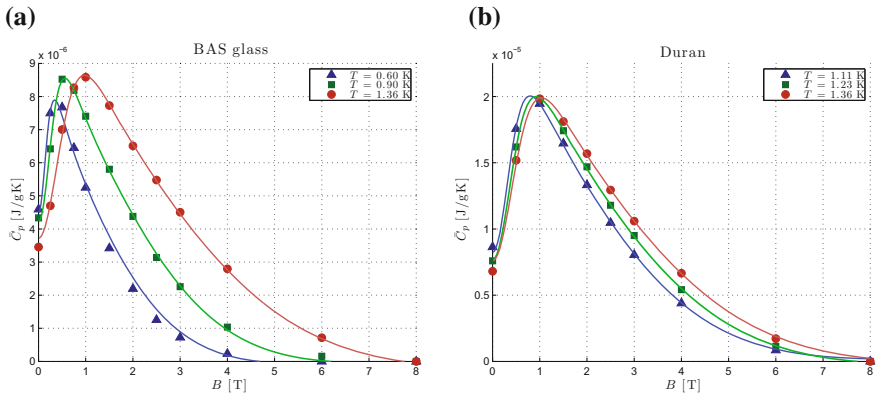

Fig. 13.9 The heat capacity best fit for the **a** BAS (or AlBaSiO) and **b** Duran glasses. The continuous lines are the predictions from the ETM. Data from Ref. [43]

Table 13.3 Extracted parameters (from the heat capacity data [43]) for the concentration of ATSs and Fe-impurities for Duran

Duran	Concentration [g^{-1}]	Concentration [ppm]
$n_{Fe^{2+}}$	3.21×10^{17}	33.01
$n_{Fe^{3+}}$	2.11×10^{17}	21.63
$P^* n_{ATS}$	8.88×10^{16}	–

Table 13.4 Extracted tunneling parameters (from the C_p data [43]) for Duran

Temperature [K]	D_{min} [K]	$D_{0min}\|\frac{q}{e}\|S$ [KÅ^2]	$D_{0max}\|\frac{q}{e}\|S$ [KÅ^2]
1.11	0.34	4.99×10^4	2.68×10^5
1.23	0.32	5.30×10^4	2.50×10^5
1.36	0.32	5.54×10^4	2.46×10^5

13.3.2 The Magnetic Field Dependent Dielectric Constant

As it turns out, historically the magnetic effect on the dielectric properties of the multi-silicate glasses was the first to be discovered [9]. Only the present approach—at the time of writing—is able to explain the data, qualitatively [38] and then quantitatively [39]. We consider the contribution to the dielectric constant $\epsilon(\omega)$ from the TWPs (or ATSs) that are sitting in the interstices between the RERs. One can then treat each ATS again as an *effective* 2LS having first energy gap $\Delta\mathcal{E} = \mathcal{E}_1 - \mathcal{E}_0 = E = \sqrt{D^2 + D_0^2\varphi^2}$ for relatively weak fields. Within this simplified picture, the linear-response, quasi-static resonant and relaxational contributions to the polarizability tensor $\alpha_{\mu\nu}$ can be extracted according to the general 2LS approach described in various papers [44], as well as in the review in Ref. [41], to obtain

$$\alpha_{\mu\nu}^{RES} = \int_0^\infty \frac{dE}{2E} \mathcal{G}_{\mu\nu}\left(\left\{\frac{E_i}{E}\right\}; \mathbf{p}_i\right) \tanh\left(\frac{E}{2k_BT}\right)\delta(E-\Delta\mathcal{E}) \tag{13.16}$$

as well as

$$\alpha_{\mu\nu}^{REL} = \frac{1}{4k_BT}\int_0^\infty dE\left(\sum_{i,j=1}^{3}\frac{E_iE_j}{E^2}p_{i\mu}p_{j\nu}\right)\cosh^{-2}\left(\frac{E}{2k_BT}\right)\delta(E-\Delta\mathcal{E}) \tag{13.17}$$

where

$$\mathcal{G}_{\mu\nu}\left(\left\{\frac{E_i}{E}\right\}; \mathbf{p}_i\right) = \sum_{i=1}^{3} p_{i\mu}p_{i\nu} - \sum_{i,j}\frac{E_iE_j}{E^2}p_{i\mu}p_{j\nu} \tag{13.18}$$

is a disorder correlator that makes use of the single-wells' electric dipoles $\mathbf{p}_i = q\mathbf{a}_i$ ($i = 1, 2, 3$). This expression assumes vanishing electric fields and no TS-TS interactions yet, an approximation which indeed does not realistically apply to experiments at the lowest temperatures. To keep the theory treatment simple, however, one can still make use of Eq. (13.16) and of the analogous one for the relaxational contribution to the polarizability. Interactions will play a role, though from estimates this should only happen around the 1 to 10 mK range. Equation (13.16) must be averaged over the random energies' distribution (13.10) (denoted by $[\dots]_{av}$, responsible for the high sensitivity to weak fields) and also over the dipoles' orientations and strengths (denoted by $\overline{(\dots)}$). For a collection of ATS with $n_w > 2$ wells this averaging, as it turns out, presents serious difficulties and one must resort to the reasonable decoupling:

$$\overline{\mathcal{G}_{\mu\nu}\delta(E-\Delta\mathcal{E})} \simeq \overline{\mathcal{G}_{\mu\nu}}\cdot\overline{\delta(E-\Delta\mathcal{E})}, \tag{13.19}$$

where now $\overline{[\delta(E-\Delta\mathcal{E})]_{av}} = g_{ATS}(E,B)$ is the fully-averaged DOS. To calculate $\overline{\mathcal{G}_{\mu\nu}}$, one can begin by envisaging a fully-isotropic distribution of planar n_w-polygons to then obtain:

$$\overline{\mathcal{G}_{\mu\nu}} = \frac{1}{3}\left(\frac{n_w}{n_w-1}\right)\overline{p_i^2}\frac{(n_w-2)E^2 + D_0^2\varphi^2}{E^2}\delta_{\mu\nu}. \tag{13.20}$$

The second term in the numerator of Eq. (13.20) gives rise, one discovers, to a peak in $\delta\epsilon/\epsilon$ as a function of B at very low fields, while the first term (which is present only if $n_w > 2$) produces a *negative* contribution to $\delta\epsilon/\epsilon$ at larger B which can dominate over the enhancement term for all values of B when $D_{0max} \gg D_{0min}$, where D_{0min}, D_{0max} correspond to material-dependent cutoffs in the distribution of ATS energy barriers (V_{0max}, V_{0min} respectively). Observations in Duran and BK7 indeed show a significant depression of $\epsilon'(B)$ for weak fields [10], thus presenting direct evidence for the existence of ATSs carrying $n_w > 2$ in the multi-silicate glasses. Performing the averaging $[\dots]_{av}$ one then gets some analytical expressions for the polarizability. The uniform average over orientation angles θ must be performed numerically (although it was checked that a very good approximation con-

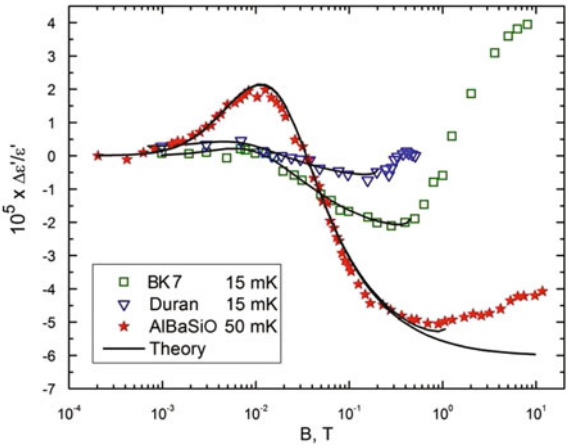

Fig. 13.10 Relative dielectric constant variation versus the magnetic field for AlBaSiO (or BAS) [10]b, BK7 [10] and Duran [10]b glasses. With best-fit parameters given in Table 13.5, the continuous curves are the results of our theory in the "weak field" approximation with (and—for AlBaSiO—also without) higher order correction. From [45]

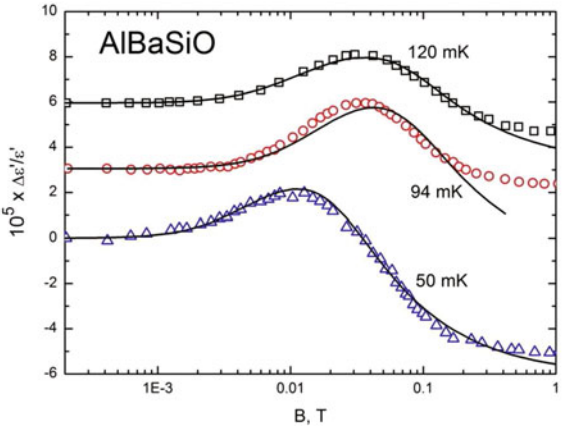

Fig. 13.11 Relative dielectric constant variation versus the magnetic field and temperature for AlBaSiO (or BAS) glass [10]b. With fitting parameters as in Table 13.5, the continuous curves are the result of our theory in the "weak field" approximation. From [45]

sists in the replacement $\varphi^2 \to \frac{1}{3}\varphi^2$ for averaged expressions, which corresponds to the replacement $\overline{\cos^2\theta} \to \frac{1}{3}$).

Details of the evaluation of the dielectric constant can be found in [41] and the resulting expressions appear to describe well most experimental data and for different glasses, as is shown in Figs. 13.10, 13.11 and 13.12 using the fitting parameters presented in the Tables 13.5 and 13.6.

For the sake of clarity, the data and theoretical curves in Figs. 13.11 and 13.12 have been shifted apart vertically. The quantity x_{ATS} now refers to volume concentrations of ATSs, linked to mass concentrations n_{ATS} through use of the solid's density ρ : $x_{ATS} = n_{ATS}\rho$.

Analogous results have been obtained for the explanation of the dielectric loss data in a magnetic field, the theory and fits of the available experimental data can be found in [41]. The tunneling parameters extracted from the data fitting compare well with those given above, so that in fact a single model with a single set of material parameters per specimen could be used in all these studies (except that the fit of all

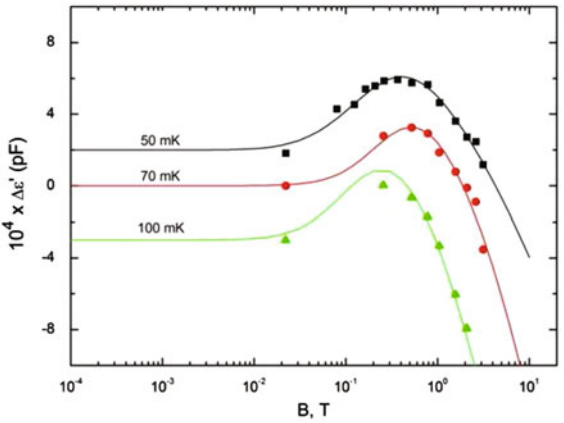

Fig. 13.12 Dielectric constant variation as a function of the magnetic field and temperature for the (non nuclear-quadrupole moments containing) $SiO_{2+x}C_yH_z$ glass [46]. Fitting parameters as in Table 13.6. From [45]

Table 13.5 Fitting parameters extracted for the dielectric constant in a magnetic field and for three different types of glasses

Material and temperature	$\pi x_{ATS} P^* \overline{p_1^2}/\epsilon_r\epsilon_0$	D_{min}, K	$D_{0min}\left\|\frac{q}{e}\right\| S_\Delta$, K^2	$D_{0max}\left\|\frac{q}{e}\right\| S_\Delta$, K^2
BK7 15 mK	0.089×10^{-5}	0.030	1.668×10^5	4.576×10^5
Duran 15 mK	0.052×10^{-5}	0.021	2.457×10^5	4.151×10^5
AlBaSiO 50 mK	0.89×10^{-5}	0.015	2.440×10^5	3.080×10^5
AlBaSiO 94 mK	3.75×10^{-5}	0.025	1.225×10^5	1.589×10^5
AlBaSiO 120 mK	3.09×10^{-5}	0.023	1.767×10^5	2.248×10^5

Table 13.6 Fitting parameters for the (non nuclear-quadrupole moments containing) $SiO_{2+x}C_yH_z$ glass for different temperatures

Temperature	$\pi x_{ATS} P^* \overline{p_1^2}/\epsilon_r\epsilon_0$	D_{min}, K	$D_{0min}\left\|\frac{q}{e}\right\| S_\Delta$, K^2	$D_{0max}\left\|\frac{q}{e}\right\| S_\Delta$, K^2
50 mK	4.38×10^{-5}	0.0150	0.076×10^3	3.047×10^4
70 mK	12.22×10^{-5}	0.0486	0.600×10^3	2.662×10^4
100 mK	13.63×10^{-5}	0.0486	3.035×10^3	7.616×10^4

the data sets would not be so good). Here we only like to remark that for the loss the theory must also describe the magnetic-field dependence of a phenomenological relaxation time, a new parameter entering in the description of dielectric dissipation. This relaxation time for ATSs at low temperature and in a magnetic field is now found to be given by the following expression (derived, yet no detailed published, by the present Author) [41]:

$$\tau_{ATS}^{-1} = \tau^{-1}(E,\varphi) = \frac{E^3\left(D_0^2\varphi^2 + \frac{5}{6}D^2\right)}{\Gamma \tanh\left(\frac{E}{2k_BT}\right)} = \frac{E^3\left(E^2 - \frac{1}{6}D^2\right)}{\Gamma \tanh\left(\frac{E}{2k_BT}\right)} = \tau^{-1}(E,D) \quad (13.21)$$

where, as usual, the A-B phase φ is directly proportional to the magnetic field B. It appears, therefore, that the total dielectric relaxation time, obtained through its inverse:

$$\frac{1}{\tau_{tot}} = \frac{1}{\tau_{2LS}} + \frac{1}{\tau_{ATS}(\varphi)} \tag{13.22}$$

must diminish in a non-trivial manner as the magnetic field is switched on. This very interesting prediction of the present theory appears to be confirmed explicitly, albeit only qualitatively, in laboratory experiments and for some special multi-silicate glasses so far only via the work of a Russian group at liquid-He temperatures [47]. A systematic study of the magnetic-field dependence of τ_{tot} in the multi-component glasses is lamentably still lacking.

13.3.3 The Magnetic Field Dependent Polarization Echo Amplitude

The experimental detection of electric and phonon echoes in glasses is one strongly convincing argument for the 2LSs' existence. Echoes in glasses are similar (yet with important differences) to other echo phenomena such as nuclear spin echo, photon echo and so on. But only at very low temperatures the relaxation of the TSs becomes so slow that coherent phenomena like polarization echoes become observable in the insulating glasses [35].

The essence of the effect is as follows (see Fig. 13.13). A glass sample placed in a reentrant resonating cavity ("Topfkreisresonator") is subjected to two very short ac electromagnetic pulses at the nominal frequency of about 1 GHz and separated by a time interval τ_{12}. The durations τ_1 and τ_2 of the pulses must be much shorter that all relaxation process times in the observed system. The macroscopic polarization produced by the first pulse then vanishes rapidly, due to the broad distribution

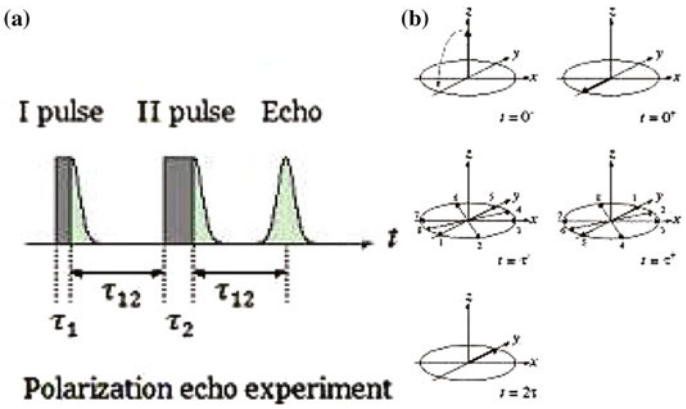

Fig. 13.13 Schematics of the two-pulse polarization echo experiment. Hahn's vectorial interpretation on the right hand side is for NMR's spin-echo experiment

of parameters of the TSs in glasses. This phenomenon is similar to the well-known free-induction decay that is observed in nuclear magnetic resonance (NMR) experiments. The "phase" (energy-level populations) of each 2LS develops freely between the two exciting pulses. The second pulse causes an effective "time reversal" for the development of the phase of the 2LSs. The initial macroscopic polarization of the glass is then recovered at a time τ_{12}, roughly, after the second pulse. Because the thermal relaxation processes and (see below) spectral diffusion are strongly temperature dependent, polarization echoes in glasses can be observed, in practice, only at very low temperatures: typically below 100 mK. The echo amplitude is clearly proportional to the number of 2LSs that are in or near resonance with the exciting microwave pulse and that do not loose their phase coherence during the time $2\tau_{12}$ [35]. It should be stressed that, because of the wide distribution for the parameters of the two-level systems in glasses, the theoretical description of polarization echoes in glasses is considerably more complicated than in the case of nuclear spin systems. In analogy to the two-pulse echo in NMR experiments this phenomenon is referred to as the spontaneous electric echo.

Polarization echo phenomena can help us understand more about the microscopic structure of TSs in general in glasses and give different kinds of information. The analysis of these experiments is similar to that for the analogous NMR case, except that the TS problem is complicated by three new factors. First, the elastic (or electric) dipoles are not aligned with respect to the driving field(s) and a calculation of the echo signal involves averaging over their orientations. Second, for a given pumping frequency ω there exists a distribution of induced moments (elastic or electric) and relaxation times, which must be included in the theoretical analysis. Finally, in electric echo experiments the local field as seen by the TSs is not equal to the externally applied field, and a local-field correction factor must be used when evaluating absolute values of the polarization [35].

In the polarization echo experiments, done typically at radio frequencies and at very low temperature (about 10 to 100 mK), it has been established that the TSs in glasses couple directly to the magnetic field B [48, 49]. This time, the amplitude of two-pulse echoes in the BAS, Duran and BK7 glasses was found to dependent strongly on the applied magnetic field showing a non-monotonic (perhaps oscillatory) field variation and for all glass types. Since the very beginning [11, 50], such behavior was attributed to the existence of nuclear electric quadrupole moments (NEQM) carried by some of the tunneling species (having nuclear spin $I > \frac{1}{2}$) interacting via their nuclear magnetic dipole with the magnetic field and also with gradients of the internal microscopic electric field. The NEQM model is based on the consideration that the levels of tunneling particles with non-zero nuclear quadrupole moment experience a nuclear quadrupole splitting, which is different in the ground state and in the excited state of a tunneling 2LS. The magnetic field then causes an additional Zeeman splitting of these levels, giving rise to interference effects. In turn, these two different nuclear interactions, though very weak, are thought to be causing the non-monotonic magnetic field variation of the echo amplitude.

The amplitude (in fact, integrated amplitude) of two-pulse polarization echoes of four types of silicate glasses is now shown in Fig. 13.14a and as a function of

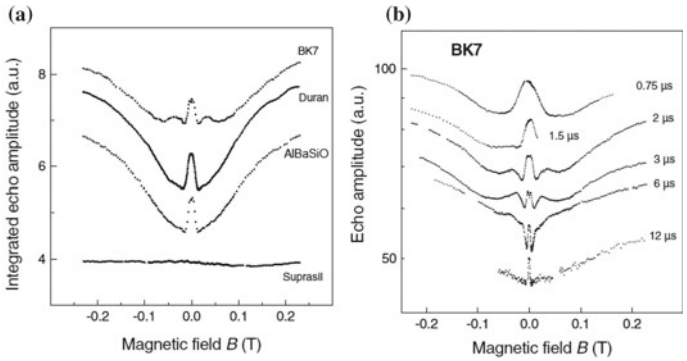

Fig. 13.14 Data from [48] **a** The integrated echo amplitude plotted as a function of the magnetic field for different silicate glasses: BK7, Duran, AlBaSiO (BAS) and Suprasil I. All data were taken at $T = 12$ mK, $\tau_{12} = 2\,\mu$s, and nominally 1 GHz, except for Duran, where the delay time was $\tau_{12} = 1.7\,\mu$s. **b** The amplitude of two-pulse echoes in BK7 glass versus the magnetic field for different values of the waiting time τ_{12} between pulses. All data sets were taken at 4.6 GHz and 12 mK except that for $\tau_{12} = 2\,\mu$s which was taken at 0.9 GHz (this behaviour, right panel, remains unexplained by all existing theories and a real challenge)

the magnetic field [49]. In contrast to various other low-temperature properties of glasses, the influence of the magnetic field on the amplitude of spontaneous echoes is manifestly not universal on the qualitative level already. BK7 and Duran show similar effects, and yet the concentration of magnetic impurities differs by at least a factor of 20 (a clear indication, that such impurities are irrelevant for such effects). The most remarkable result of these measurements is the fact that Suprasil I (very pure a-SiO_2) shows no detectable magnetic-field effect. While Duran, BAS and BK7 contain nuclei with non-zero nuclear quadrupole moment, Suprasi I is virtually free of such nuclei, except for a tiny % of ^{17}O. This fact has been used to provide the justification for the nuclear quadrupole theory. The variation of the echo amplitude with the applied magnetic field is similar for Duran, BK7 and BAS, but not at all qualitatively identical. All three samples exhibit a marked principal maximum at very weak fields, $B \sim 10$ mT, but only BK7 has a relevant second maximum and some hint to an oscillation as a function of B. Unexplained by the NEQM theory, at high fields the amplitude of the echo rises well above its value at zero magnetic field and seemingly saturates (yet, see Figs. 13.9 and 13.17 below, this is very similar to what happens to the inverted heat capacity, $-C_p$, as a function of B). Again unexplained by NEQM theory, there is a piece of linear dependence on B at intermediate fields.

In Fig. 13.14b the amplitude of spontaneous echoes for the BK7 glass is reproduced as a function of the applied magnetic field and for different delay times τ_{12} between the exciting pulses. We can see some obvious qualitative differences for different values of τ_{12} and that a second maximum (the "oscillation") is not always present. These findings necessitate a good theory for spectral diffusion [51] in real glasses (containing both 2LSs and ATSs) and this theory remains to date unaccomplished.

One of the most remarkable facts about the experiments on echoes from glasses in a weak magnetic field is that strong magnetic response is not confined to the inorganic, multi-silicate glasses. The amplitude of spontaneous echoes in part-deuterated and in undeuterated amorphous glycerol as a function of the weak magnetic field B has been demontrated to show completely different behaviour [11]. In the case of ordinary glycerol there is some, very small change of the echo amplitude with B. However, for partially deuterated glycerol the change is considerably more noticeable, of different shapes and duration. These experiments *seemingly* provide proof that the magnetic effects are of nuclear origin, since the two amorphous glycerol samples differ only in the content of nuclei carrying a NEQM. As it turns out, a comparative analysis of experiments in different isotope-concentration samples hints to the fact that the effect does not scale at all with NEQM concentration. The explanation of the magnetic effects in amorphous glycerol echo experiments goes beyond the aims of this review and an explanation based on the ETM can be found in the review [41] and first published in [39]. The vitreous-glycerol experiments show, however, that the tunneling species are H^+ and/or D^+ in these samples: correctly, the lighter atomic species. Then, in the multi-silicates the tunneling particles ought to be overwhelmingly O^{2-}, hardly the NEQM-carrying B^{3+}, Na^+, K^+, or Al^{3+} as claimed by NEQM-theory supporters. The status of the NEQM-theory remains unclear.

We will discuss in this essay principally the echo experiments on the silicates. A theory for the echo signal from a collection of 2LSs can be obtained—and from first principles—from a lengthy but straightforward Schrödinger equation (or density matrix) treatment in which high-frequency modes are neglected and the phonon-damping is treated in a phenomenological way [45]. In the more rigorous way, we have obtained for the echo signal an expression which confirms and in fact improves on the theory of 2LSs' electric echos by Gurevich et al. [52] [some details can also be found in [41]]. It is then possible to extend this polarization echo's calculation to the case of the ATS-ETM describing glasses in a magnetic field [39, 45]. The point of view is taken that a background of ordinary 2LSs—insensitive to the magnetic field—also exists in the glass, but is not needed in order to explain the data as a function of the magnetic field.

One begins with a collection of 3LSs (now $n_w = 3$ is not just computationally convenient, but physically correct as explained in Sect. 13.2), but with each single ATS Hamiltonian written in the (diagonal) energy representation:

$$H' = SHS^{-1} = \begin{pmatrix} \mathcal{E}_0 & 0 & 0 \\ 0 & \mathcal{E}_1 & 0 \\ 0 & 0 & \mathcal{E}_2 \end{pmatrix} + S \begin{pmatrix} -\mathbf{p}_1 \cdot \mathbf{F} & 0 & 0 \\ 0 & -\mathbf{p}_2 \cdot \mathbf{F} & 0 \\ 0 & 0 & -\mathbf{p}_3 \cdot \mathbf{F} \end{pmatrix} S^{-1} \tag{13.23}$$

Here the transformation matrix $S = S(\varphi)$ is magnetic-field dependent, the $\mathcal{E}_i$ are the (B-dependent) ATS energy levels and the $\mathbf{p}_i$ are the single wells' electric dipoles. As in the treatment of Gurevich et al. [52] there is also a phonon bath and this will be treated—as usual—phenomenologically and resulting in a standard phonon-damping exponential. The second term in Eq. (13.23) causes irrelevant energy-level

shifts and also produces an extra matrix term $\Delta H'(t) = (A_{ij})$ of which the only relevant element is of the form

$$A_{01} = A_{10}^{*} = \sum_{k=1}^{3} -\mathbf{p}_k \cdot \mathbf{F}_0 \, \mathrm{S}_{0k}(\varphi)\mathrm{S}_{1k}^{*}(\varphi) \cos \omega t \tag{13.24}$$

These A_{ij} cause quantum transitions between the ATS levels ($|0>, |1>, |2>$) when the electric-field pulses are applied. In the weak magnetic field limit (now most appropriate for these experiments) and in the usual approximation $D \ll D_0$ (which is always consistent with our best fits to the data), one discovers that the second excited level $|2>$ remains unperturbed and one can make use of the effective 2LS approximation (where, however, the ground-state single-well wavefunctions mix). One can then repeat the Schrödinger equation (or density-matrix) calculation carried out for the 2LS case, introducing though the complex Rabi frequency:

$$\Omega_0 = \frac{A_{01}}{\hbar} \tag{13.25}$$

The evolution of the generic ATS during, or in the absence, of pulses then gets to be followed exactly in much the same way as before, except that in order to simplify the formalism it is convenient to introduce right from the beginning the orientationally-averaged Rabi frequency (which is now a real quantity):

$$\Omega_R = \sqrt{\overline{|\Omega_0|^2}} \tag{13.26}$$

the bar denoting averaging over the 3LS base-triangle's orientation. Replacing Ω_0 with Ω_R before carrying out this averaging of the sample's polarization is here our main approximation, allowing for a considerably simplified treatment and leading to the following magnetic-field dependent Rabi frequency:

$$\Omega_R = \frac{\mathrm{p}_1 \mathrm{F}_0}{\hbar} \sqrt{\frac{D_0^2\varphi^2 + \frac{5}{6}D^2}{6E^2}} \tag{13.27}$$

Here, $\mathbf{p}_1$ is the single-well (orientation-averaged) electric dipole and $E = \hbar\omega_0 = \sqrt{D^2 + D_0^2\varphi^2}$ is the usual magnetic-field dependent lower energy gap, in the weak field and near-degenerate approximations. The above form for Ω_0 of course treats incorrectly the ATSs that have $\mathbf{F}_0$ roughly orthogonal to the ATS base triangle; fortunately these have $\Omega_0 \approx 0$ and in fact do not contribute to the echo signal.

Proceeding as in our own derivation of the ordinary 2LSs echo [45], one finds that there is indeed a magnetic contribution to the polarization of the sample from the generic ATS and (partly averaged) given by:

$$\Delta\wp_{\parallel}(t) \cong -\frac{\hbar}{\mathrm{F}_0}\tanh\left(\frac{E}{2k_BT}\right)e^{-\frac{\overline{\gamma}}{2}t}\frac{\Omega_R^4}{\Omega_G^3}$$
$$\mathrm{Im}\left\{\sin^2\left(\frac{\Omega_G\tau_2}{2}\right)\left[\sin\left(\Omega_G\tau_1\right)-2i\frac{\omega_0-\omega}{\Omega_R}\sin^2\left(\frac{\Omega_G\tau_1}{2}\right)\right]\right\}e^{i\Phi(t)-i\int_0^t\Delta\omega(t')s(t')dt'} \tag{13.28}$$

Here, $\frac{\overline{\gamma}}{2}=\tau^{-1}$ is the magnetic ATS relaxation rate due to phonons and given by Eq. (13.21), so the generalized Rabi frequency is still given by $\Omega_G=\sqrt{\Omega_R^2+(\omega_0-\omega)^2}$ and, moreover:

$$\Phi(t)=\omega_0\left(t-2\overline{\tau}_{12}\right)+\omega\Delta\tau \tag{13.29}$$

is what we find to be the appropriate time argument. From this, it is obvious that the time at which all the ATSs (regardless of energy gap $E=\hbar\omega_0$ value) get to be refocused is $t=2\overline{\tau}_{12}$ and this determines the correct echo's peak position (when the echo signal has a reasonable shape, this not being always the case [48]). The measured echo amplitude's contribution from the magnetic ATS is then (also allowing for an arbitrary amplification factor A_0):

$$\begin{aligned}\Delta A(\varphi) =& A_0\frac{d}{\varepsilon_0\varepsilon_r}x_{ATS}2\pi P^*\int_0^\infty dE\int\frac{dD}{D}\int\frac{dD_0}{D_0}\Theta(D,D_0)\\ &\times\delta\left(E-\sqrt{D^2+D_0^2\varphi^2}\right)\Delta\wp_{\parallel}\left(2\overline{\tau}_{12}\right)\end{aligned} \tag{13.30}$$

where now d is the sample's thickness, $\Theta(D,D_0)$ is a Dirichlet's theta-function restriction for the integration domain (see [45]) and where a final orientational-averaging with respect to the angle (defining the A-B phase φ, see Eq. (13.7)) $\beta=\widehat{\mathbf{BS}_{\triangle}}$ is in order. One deals with the delta-function's constraint and the energy parameters' integrations in the usual way to arrive at, after a lengthy calculation:

$$\begin{aligned}\Delta A(\varphi) \cong& -A_0\frac{d}{\varepsilon_0\varepsilon_r}x_{ATS}\frac{4\pi\hbar^2P^*}{\mathrm{F}_0}\cos(\omega\Delta\tau)\\ &\times\int_{E_{c_1}}^{E_{c_2}}\frac{dE}{E}\int_{D_{min}}^{D_2(\varphi)}\frac{dD}{D}\tanh\left(\frac{E}{2k_BT}\right)\frac{E^2}{E^2-D^2}\\ &\cdot e^{-w2\overline{\tau}_{12}}\Omega_R^2\sigma(E)\left[\mathrm{S}(\theta_1,\theta_2)\tan(\omega\Delta\tau)+\mathrm{C}(\theta_1,\theta_2)\right]\\ &+\int_{E_{c_2}}^{\infty}\frac{dE}{E}\int_{D_1(\varphi)}^{D_2(\varphi)}\frac{dD}{D}(\text{same integrand as above}\ldots)\end{aligned} \tag{13.31}$$

where we have defined the special functions:

$$\begin{aligned}
\sigma\,(\mathrm{E}) &= \frac{\Omega_{\mathrm{R}}^2}{2\hbar\Omega_{\mathrm{G}}^3} = \frac{\Omega_R^2}{2\hbar\left(\Omega_R^2+(\omega_0-\omega)^2\right)^{3/2}} \\
\mathrm{S}\left(\theta_1,\theta_2\right) &= \sin\left(\Omega_G\tau_1\right)\sin^2\left(\Omega_G\tau_2/2\right) \\
\mathrm{C}\left(\theta_1,\theta_2\right) &= -2\frac{\omega_0-\omega}{\Omega_R}\sin^2\left(\Omega_G\tau_1/2\right)\sin^2\left(\Omega_G\tau_2/2\right)
\end{aligned} \tag{13.32}$$

and where $\theta_{1,2} = \Omega_G\tau_{1,2}$ are the so-called pulse areas. $E_{c_{1,2}}$ are as in the previous Sections whilst now: $D_{1,2}\,(\varphi) = \sqrt{E^2 - D_{0max,min}^2\varphi^2}$ and $E = \hbar\omega_0$.

In going from Eqs. (13.28)–(13.31) we have tacitly made some assumptions on the (to be fully averaged) spectral diffusion term, $e^{-i\int_0^{2\tau_{12}}\Delta\omega(t')s(t')dt'}$ (where $\hbar\Delta\omega(t) = E(t) - E$ represents the time fluctuation of the ATS's energy gap which is due to local strain and/or electric field fluctuations [51]). The theory of spectral diffusion (SD) [51] for the ATSs is still to be accomplished, but we can safely assume that what was found by many Authors for NMR's spin-echoes as well as for the 2LS polarization echoes in glasses holds good for the ATSs too. Namely: there is a wide range of waiting times τ_{12} values where the decay of the echo amplitude well approximates a simple exponential form, so that one can replace the SD term with $e^{-2\tau_{12}/\tau_\phi}$, $\tau_\phi(T)$ being a SD characteristic time depending only on temperature. There should be a SD time $\tau_{\phi(3)}$ for the ATSs just like there is a SD time $\tau_{\phi(2)}$ for the standard 2LSs' ensemble. For the latter, STM theory has shown [51, 53] that the latter parameter is independent of E and thus for the ATS we shall assume the very same and, moreover, that (just as for the phonon damping rate and for Rabi frequency) its own dependence on B is weak or absent. This allows us to lump the SD problem together with phonon damping, yielding—in essence—an overall exponential relaxation rate:

$$w(E,D) = \tau_\phi{}^{-1} + \tau^{-1}(E,D) \tag{13.33}$$

where the SD-time $\tau_{\phi(3)}$ is typically much shorter than the phonon-damping time τ and depends on temperature only, through:

$$\tau_{\phi(3)}{}^{-1} = c_{ATS}T \tag{13.34}$$

where c_{ATS} is an appropriate constant. The assumption of an overall simple-exponential decay of the echo amplitude with waiting time τ_{12} and characteristic time $\tau_{\phi(2)} = 1/c_{2LS}T$ seems to be well verified experimentally [54] for single-component glasses (uncontaminated a-B_2O_3, a-SiO_2 etc.). Clearly, a better theory for SD in multi-component glasses is however in order.

We now make use of Eq. (13.31) to fit some of the available experimental data for the multi-silicates, the idea being that the total amplitude is given by a sovrapposition of 2LS and ATS contributions: $A\,(\varphi) = A_{2LS} + \Delta A\,(\varphi)$ (which must still be

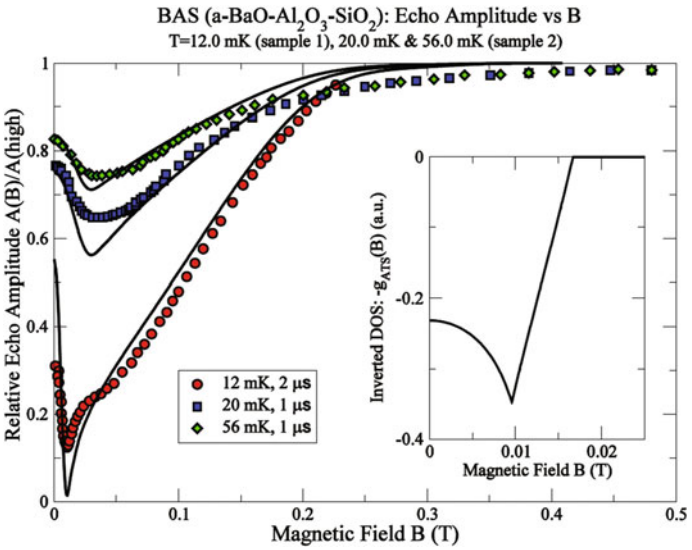

Fig. 13.15 Magnetic field dependence of the polarization echo *relative* amplitude (relative to its value at "high" fields, where saturation occurs) for the AlBaSiO glass [49] (also referred to as BAS glass) at given experimental conditions. We believe that two separate samples have been used. The continuous curves are from our theory. Nominal frequency 1 GHz, $\tau_2 = 2\tau_1 = 0.2\,\mu$s. Inset: behaviour of the ATS DOS for the same parameters (this is the physical origin of the effect)

averaged with respect to the ATS magnetic-orientation angle β). Figure 13.15 shows the experimental results for the *relative* echo amplitude in AlBaSiO (or BAS glass) as a function of B. Values of B up to 0.6 T have been explored, and for three distinct temperatures. The data are then fitted with our theory (full curves) with the parameters reported in Table 13.7. The agreement between theory and experiment is indeed highly satisfactory, given the discussed simplifications and assumptions that have been used in the theory. Only one minimum in $A(B)$ is found and the inset in Fig. 13.15 shows that, again, it is the ATS magnetic DOS that is causing the magnetic effect (Sect. 13.3). In fact, by enforcing the strict-resonance condition $\sigma(E) \to \delta(E - \hbar\omega)$ Eq. (13.31) would collapse to a quantity very much like the DOS (convoluted with slow-varying, in E, corrections) and with the very same DOS behaviour, reproducing in this way the qualitative shape of $\Delta A(B)$. It is however the non-resonant convolution of this quasi-DOS with other (smooth) E-dependent functions that produces the rounding of the minimum in $\Delta A(B)$ and the B^{-2} saturation that is always observed. Interestingly enough, now τ (though $\tau_\phi \ll \tau$) the phonon-damping term plays a main role in the rounding of the high-B tail of $\Delta A(B)$ to the B^{-2} (as observed) saturation. The ATS approach is the only theory that predicts also a linear-in-B intermediate decay regime of the echo amplitude, and this is often experimentally observed. Details of the ETM theory for the electric echo are interesting and will be published elsewhere. Next, in Fig. 13.16 we produce the comparison of theory and experiment for data for the echo amplitude in BK7 (this is

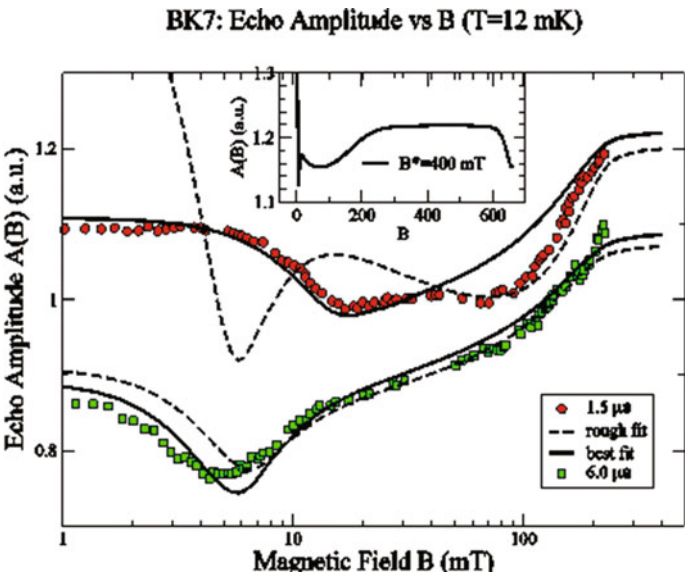

Fig. 13.16 Magnetic-field dependence of the polarization echo amplitude for borosilicate BK7 glass [49] at given experimental conditions. Dashed curves (preliminary rough fit) and continuous curves from our theory: there are no more than two observable maxima or minima (so, no true oscillations). Nominal frequency 0.9 GHz, $\tau_2 = 2\tau_1 = 0.2\,\mu$s. Inset: our prediction for the higher magnetic field regime (B^* as defined in Sect. 5, Ref. [41])

good optical glass, hence devoid of true microcrystals, but nevertheless containing the (large) RERs) at two different values of the waiting time τ_{12}. It is truly remarkable how our ETM theory, despite the many simplifications and assumptions and the total absence of multi-level quantum physics (as advocated by the NEQM approach), can reproduce all the features qualitatively characterizing the experimental data, including every change in curvature of $A(B)$ vs. B. A preliminary rough fit, reported, not aiming at high χ^2 agreement, reproduces also two maxima (and minima) that the NEQM approach takes as indication of the multiple (rapid) oscillations ensuing from the quantum beatings ascribed to the Zeeman- and NEQM-splitting of the generic 2LS [50] and NEQM-carrying tunneling particle. There are in fact never more than two observed minima, in the experimental data, and these can be reproduced by the present, simpler ATS-ETM approach. Finally, in the inset of Fig. 13.16 we show what the experimentalists overlooked, by not exploring higher magnetic-field values. Using a simple-minded low-φ correction for the lower energy gap at higher fields, we plot the expected behaviour of $A(B)$ for intermediate fields. After the two observed minima, there is only an apparent saturation, yet new interesting features ought to characterise $A(B)$ at higher fields ($B >$600 mT). This, just as it happens for the dielectric constant (Sect. 5). A full description of the high field effects, however, requires a calculation involving all three ATS energy levels (this was never done).

This concludes this very short survey of the main results obtained within the ETM model for the low-temperature magnetic-field effects. The treatment shows that all the magnetic effects (basically: an enhancement at low fields, followed by a decrease in each probed quantity at the higher fields) appear to be the consequences of the very same magnetic behaviour of the ATS DOS (described in Sect. 13.2). In Fig. 13.17 we have re-drawn the magnetic-field dependence of the relative dielectric constant's change and (different scale) of the *inverted* relative echo amplitude variation. The variation of the heat capacity C_p has not been inserted for clarity, nevertheless it follows exactly the very same trend as for $-A(B)/A(\text{high})$ (see Fig. 13.9a, b). The schematic change of the ATS DOS, $g_{ATS}(B)$ is also shown (not to scale) and it appears to determine the trend observed in all three experiments.

Table 13.7 Fitting parameters for the echo amplitude's magnetic-field dependence. (*) For BK7 (best-fit parameters only), only c_{ATS} is involved

Glass type	D_{min} (mK)	$D_{0min}\left\|\frac{q}{e}\right\|S_\Delta$ (KÅ^2)	$D_{0max}\left\|\frac{q}{e}\right\|S_\Delta$ (KÅ^2)	Γ^{-1} $(\mu\text{sK}^5)^{-1}$	$c_{ATS}-c_{2LS}$ $(\mu\text{sK})^{-1}$	p_1F_0 D kV m^{-1}	$\tan\omega\Delta\tau$
AlBaSiO (sample 1)	17.74	0.95×10^3	2.13×10^4	9.22×10^6	5.008	0.461	0.247
AlBaSiO (sample 2)	27.20	1.14×10^3	8.96×10^3	2.57×10^5	3.825	0.450	0.245
BK7 (1.5 μs)	16.76	0.92×10^3	1.34×10^4	8.91×10^6	1.03 (*)	0.60	0.207
BK7 (6 μs)	15.94	0.89×10^3	3.31×10^4	3.25×10^6	5.72 (*)	0.98	0.204

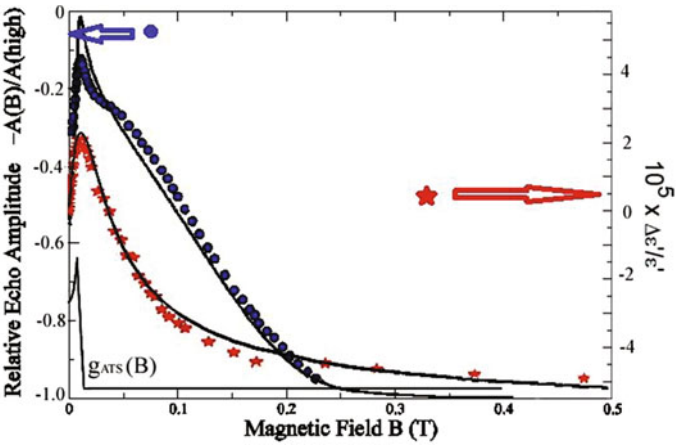

Fig. 13.17 Some data (for the same glass type, BAS) showing the magnetic-field variation of (minus) the echo amplitude $-A(B)/A(\text{high})$ (blue dots) and of the dielectric constant variation (different scale, red stars). The qualitative variation (which mimicks that of the heat capacity C_p, see Fig. 13.9a, b) derives from that of the magnetic DOS, $g_{ATS}(B)$, drawn not to scale. The black lines are all theory predictions

13.4 Consequences, Conclusions and Outlook

13.4.1 A New Scenario for the Glass Transition?

Having conceived a heterogeneously disordered, cellular make-up of the glassy state, it seems natural to ask what the implications for the onset of the glassy state would be. The crucial question is the definition of the glass transition, which can only be kinetic in nature given the continuity that is being advocated between the dynamical heterogeneities of the supercooled state and those of the glassy state. Namely, it is envisaged that the better-ordered regions, or RERs or solid-like clusters in the supercooled state grow in size with decreasing temperature till a limit size ξ_0 is reached. Thereafter a mutually hindering state sets in for the maximally grown RERs and they must grow through a completely different (and much slower) mechanism for consolidation to take place at the expense of the material (if any) in the interstitial spaces. Naively we can take the temperature where ξ_0 is attained as the glass transition temperature T_g. At this temperature the substance is made up of close-packed RERs of maximum size ξ_0 which are better ordered, though not crystalline, and—depending on composition—of fluid-like atomic species in the interstitial spaces (or cages) between the RERs. The true crystals have not had the chance to grow, either because kinetically disfavoured or because their size does not allow for true order (thus RERs have formed instead). The time necessary for the coalescence and grow of true crystals has not been made available in the quench.

We can describe the dependence of T_g, the temperature where the polycluster forms, on the cooling rate κ by envisaging a characteristic microscopic time τ_0 for the cells' rearrangement and an entropy (per atomic species) for the many ways the polycluster can be formed from the cooperative nucleation of such cells:

$$s(T) = k_B \ln\left[\frac{T_c - T}{\kappa\tau_0}\right] \tag{13.35}$$

much in the same spirit as in Adam-Gibbs' treatment for the onset of the glassy state [18]. On dimensional grounds, and treating this entropy as a response susceptibility for the glass transition, one then writes (if w_0 is a characteristic energy, per atomic species, for the polycluster formation):

$$s(T_g) = k_B \ln\left[\frac{T_c - T_g}{\kappa\tau_0}\right] = \frac{w_0}{T_g} \tag{13.36}$$

If the written form of the above susceptibility is regarded as a Curie-like approximation in which the nucleating cells are not yet interacting, then the molecular-field improved form of the Curie-Weiss type would lead us to write

$$k_B \ln\left[\frac{T_c - T_g}{\kappa\tau_0}\right] = \frac{w_0}{T_g - \Theta} \tag{13.37}$$

where Θ is a characteristic temperature below T_g that takes nucleating cell-cell interactions into account. A graphical study of the above Eq. (13.37) for $T_g(\kappa)$ shows that T_g increases logarithmically with κ, as is known experimentally (see e.g. [55]) and from computer simulations (see e.g. [56]). A full derivation from nucleation theory of the above reasoning will be reported elsewhere.

13.4.2 Some Conclusions from the Magnetic Effects: Estimate of Cell Size

Qualitatively at least, our cellular-structure based ETM explains all low-temperature experimental observations so far [for a more complete discussion see [41]]. Looking at the parameters which have been used for the best fits, one cannot fail to recognize (see e.g. Table 13.7) that for the echo experiments the extracted values of the cutoffs for the parameter combinations $D_0 \frac{q}{e} S_{\triangle}$ are approximately one order of magnitude smaller than those used for the other experiments, namely for C_p and ϵ. The latter have been carried out inside higher temperature ranges, as it turns out. This could be explained through a mechanism where the number of elementary atomic tunneling systems N within each single ATS (hence inside each interstice, or cage, between the RERs or mosaic cells or grains) gets to be characterised by a temperature dependence $N(T) = N_0 \exp\{-E_0/(k_B T)\}$. Namely: there is a consolidation mechanism especially important at the lowest temperatures where ions from the interstices get to be absorbed in the cells (see Fig. 13.3) and the resulting number of coherently tunneling particles making up each ATS diminishes with diminishing temperature. We have conducted an analysis of the paramagnetic magnetization of samples of Duran, BAS and BK7 glass reported in the literature as a function of temperature using the idea of the cell model and ATS tunneling in the interstices with a temperature-dependent $N(T)$ [42]. We have obtained in this way good fits to the data and an estimate of the Fe impurity concentrations that are in agreement with the concentrations extracted from the low-temperature C_p data (Tables 13.1 and 13.3). The number N of coherently tunneling ions making up each ATS then enters the parameter combination $D_0 \frac{q}{e} S_{\triangle}$ as $[N(T)]^3$ times a combination of factors specific for a single atomic tunneling particle and the T—dependence of the extracted combination of cutoff and other tunneling parameters receives its rationale. Though it might seem surprising that the tunneling parameter D_0 of a collection of N coherently tunneling atomic particles gets to scale like N times a microscopic tunneling parameter, we remark that this is similar to what happens in the theory and experiments of a drop of coherent atoms in a Bose-Einstein condensate trapped and subject to a double-welled tunneling potential [57, 58]

At this point one could ask if the low temperature experiments hold some information on the cell size for the proposed polycluster structure of glass, given that we have extracted values of the ATS concentration in the form of the quantity $n_{ATS}P^*$ (where n_{ATS} is the ATS number (mass) density) (see Tables). It is reasonable to assume, in

fact, that on average four ATSs sit in each interstice between four tetrahedrally close-packed cells and this allows for a determination of the cell size ξ. If ξ is the cell's radius, the volume of the interstitial space is $2\sqrt{2}\xi^3/3$ and therefore we have, on average:

$$\frac{4}{\frac{2\sqrt{2}}{3}\xi^3} = x_{ATS} = n_{ATS}\rho = \frac{n_{ATS}P^*\rho}{P^*} \tag{13.38}$$

where ρ is the solid's mass density. The parameter P^* could be determined, in principle, from the normalization condition for the ATS parameter distribution:

$$2\pi P^* \ln\left(\frac{D_{max}}{D_{min}}\right) \ln\left(\frac{D_{0max}}{D_{0min}}\right) = 1. \tag{13.39}$$

However D_{max} remains unknown from the fits to the data, so we can only make the reasonable guess that the quantity $\ln\left(\frac{D_{max}}{D_{min}}\right) \ln\left(\frac{D_{0max}}{D_{0min}}\right)$ is of order 1, to estimate $P^* \approx 1/(2\pi)$. We then get the estimating formula for the average cell radius

$$\xi \approx \left[\frac{3}{\pi\sqrt{2}(n_{ATS}P^*)\rho}\right]^{1/3} \tag{13.40}$$

so that at this point we can use the values of $n_{ATS}P^*$ obtained in Sect. 13.3 to give cell size estimates. We use, for the silicates: $n_{ATS}P^* \approx 5 \times 10^{16}\,\mathrm{g}^{-1}$ (BAS glass), $9 \times 10^{16}\,\mathrm{g}^{-1}$ (Duran) and [as obtained in [42]] $1 \times 10^{16}\,\mathrm{g}^{-1}$ (BK7 glass). Then, from the literature [43] we get: $\rho \simeq 3.1\,\mathrm{g\,cm}^{-3}$ (BAS glass), $2.3\,\mathrm{g\,cm}^{-3}$ (Duran) and $2.5\,\mathrm{g\,cm}^{-3}$ (BK7 glass). Using the above estimating formula Eq. (13.40) we arrive at the size of the cells in terms of their radius: $\xi \approx 1.63 \times 10^{-6}$ cm or 163 Å (BAS glass), 1.54×10^{-6} cm or 154 Å (Duran) and finally 3.00×10^{-6} cm or 300 Å (BK7 glass). Thus, from the low temperature experiments we get to estimate that for these silicates the cell size should be some 300–600 Å in diameter (2ξ). Is this a reasonable estimate?

While high-resolution electron microscopy (HREM) images for the mentioned silicate glasses are not available in the literature, some HREM images of (inevitably) very thin samples of related glasses can be found. These are presented below, for the case of amorphous SiO_2 (Fig. 13.18a), amorphous $(B_2O_3)_{0.75}-(PbO)_{0.25}$ (Fig. 13.18b) and amorphous $LiO_2 \cdot SiO_2$ (equimolar mixture, Fig. 13.18c). The cellular structure of these thin glass samples is clearly visible in these images, with the estimates for the diameter size $2\xi \approx 500$ Å, 600 Å and, respectively, 500 Å. While the second glass is not a silicate, the size of the cells as seen in HREM imaging for the two other silicates compares very favourably with the estimates for other silicates obtained from the low temperature work. It is therefore tempting to conclude that the estimate from the tunneling data at low temperatures lead to cellular sizes that are compatible with HREM imaging. This is also consistent with estimates for the number N of coherently tunneling atomic particles that make up each ATS. While

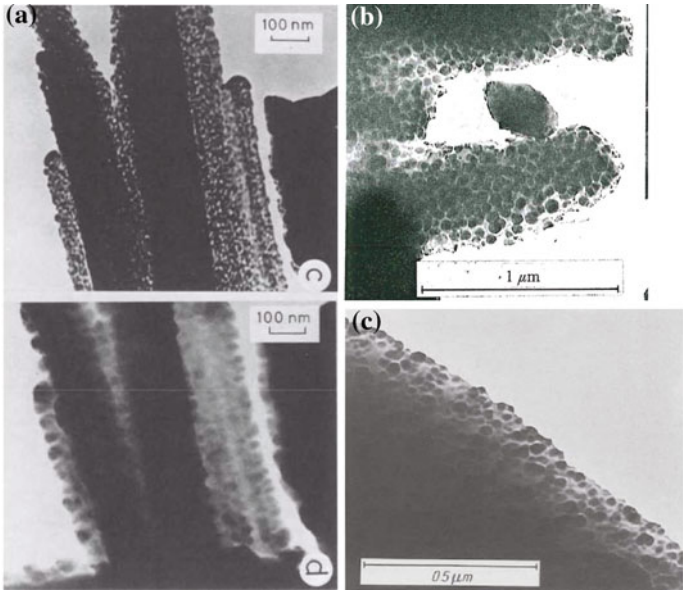

Fig. 13.18 HREM images of the cellular structure of thin glass samples. **a** Amorphous SiO_2 (especially panel d, from [59], see also [60]), **b** amorphous B_2O_3-PbO (from [60]), **c** amorphous Li_2O–SiO_2 (from [61])

N depends on temperature as stated, estimates [45] range from 10 to 10^2 and while the nature of the microscopic tunneling entities is still unknown and should depend on composition (in the case of pure SiO_2 this N should be close to 1) these values are not incompatible with a cell size of some 500 Å in diameter. The question of the nature of the atomic coherently tunneling particles making up each ATS in each cellular interstice remains completely unanswered.

13.4.3 Conclusions

In conclusion, the cellular glass-structure backed ATS ETM for the magnetic effects in multi-component glasses (the multi-silicates BAS (or AlBaSiO), Duran and BK7) and contaminated mono-component vitreous glycerol has been fully justified in terms of a (not entirely) new vision for the intermediate-range structure of real glasses. In this scheme the particles are organized in regions of enhanced regularity (RERs) and more mobile *charged* particles trapped in the interstices (or cages) between the close-packed RERs. These are coherent (owing to proximity and strong Coulomb forces) atomic tunnelers that can be modeled in terms of single quasi-particles with highly renormalized tunneling parameters. This model explains a large number of experimental data and facts with remarkable consistency also in terms of

cross-checks like the determination of the concentration of trace paramagnetic impurities [42].

The fact that pure amorphous silica (Spectrosil-I, for example [48]) shows no detectable magnetic effects is a consequence of the relatively small size of the RERs for pure a-SiO_2, deprived of almost any nucleation centres for both mosaic cells (RERs) and polycluster formation. These RERs will therefore trap a very small number N of dangling-bond ionic particles, or none at all given the covalent nature of the Si-O bonds. Hence, no magnetic effects are observable in this purest, single-component SiO_2 glass.

We remark at this point that the ETM with two types of TSs is not the only theoretical explanation that has been put forth for the explanation of the magnetic effects at low temperatures in the multi-silicate glasses. It is however the only theory that successfully explains all of the experimental data so far, including those for the compositional effects, and that links the deviations from the STM to the real structure of glasses at the intermediate atomic range. Two other approaches have been in fact proposed to date, the one already mentioned based on the coupling of the 2LSs to nuclei in the sample carrying NEQMs [50] and the one based on the coupling of the 2LSs to paramagnetic Fe^{3+} impurities [62, 63]. These two other approaches have shortcomings that will not be discussed here, since their model justification has no bearing on the real atomic structure of glasses and on the glass-forming process from glass-forming liquids (the Zachariasen-Warren picture being—in fact—always tacitly assumed). Polymeric glasses should also be well described by the present cellular model (possibly also their surfaces [64]).

The present theory on the one hand bears heavily on the true structure of real glasses and it implies that the amorphous state should no longer be regarded as a dynamically arrested liquid, but rather as a new type of solid. It also shows on the other hand that the magnetic (and compositional) effects are a mere manifestation of the heterogeneous, cellular-type intermediate atomic structure of real glasses which abandons the Zachariasen-Warren picture for good. A cellular-type structure that has been advocated for by scientists, especially (but not only) in the ex-USSR, now for almost a century. It is not impossible that with this vision in mind the TSs could become in the near future the right probes with which to study the structure of real glasses in the laboratory.

Acknowledgements The Author is very grateful to Maksym Paliienko and Silvia Bonfanti for their help with data fitting. He gratefully acknowledges stimulating discussions with A.S. Bakai. Part of this work was carried out whilst visiting the Physics Department of McGill University in Montreal (CA). The Author is grateful to Hong Guo for support and to him, to Martin Grant and Mark Sutton for useful discussions. On-going support from INFN-Pavia through Iniziativa Specifica GEOSYM-QFT is gratefully acknowledged.

References

1. G. Jug, Theory of the thermal magnetocapacitance of multi-component silicate glasses at low temperature. Phil. Mag. **84**(33), 3599–3615 (2004)
2. W.A. Phillips (ed.), *Amorphous Solids: Low Temperature Properties* (Springer Verlag, Berlin, 1981)
3. P. Esquinazi (ed.), *Tunneling Systems in Amorphous and Crystalline Solids* (Springer, Berlin, 1998)
4. W.H. Zachariasen, The atomic arrangement in glass. J. Am. Chem. Soc. **54**, 3841–3851 (1932); *ibid.*: The vitreous state. J. Chem. Phys. **3**, 162–163 (1935)
5. B.E. Warren, The diffraction of X-rays in glass. Phys. Rev. **45**, 657–661 (1934)
6. W.M. MacDonald, A.C. Anderson, J. Schröder, Low-temperature behavior of potassium and sodium silicate glasses. Phys. Rev. B **31**, 1090–1101 (1985)
7. G. Jug, M. Paliienko, Evidence for a two-component tunnelling mechanism in the multicomponent glasses at low temperatures. Europhys. Lett. **90**, 36002 (2010)
8. C. Enss, Anomalous behavior of insulating glasses at ultra-low temperatures. Adv. Solid State Phys. **42**, 335–346 (2002)
9. P. Strehlow, M. Wohlfahrt, A.G.M. Jansen, R. Haueisen, G. Weiss, C. Enss, S. Hunklinger, Magnetic field dependent tunneling in glasses. Phys. Rev. Lett. **84**, 1938–1941 (2000)
10. M. Wohlfahrt, P. Strehlow, C. Enss, S. Hunklinger, Magnetic-field effects in non-magnetic glasses. Europhys. Lett. **56**, 690–694 (2001); M. Wohlfahrt, Ph.D. Thesis (Heidelberg 2001), www.ub.uni-heidelberg.de/archiv/1587
11. P. Nagel, A. Fleischmann, S. Hunklinger, C. Enss, Novel isotope effects observed in polarization echo experiments. Phys. Rev. Lett. **92**, 245511 (2004)
12. A.A. Lebedev, O Polimorfizme i Otzhige Stekla. Trud'i Gos. Opt. Inst. **2**, 1–20 (1921) (in Russian); ibid., Izv. Akad. Nauk SSSR, Otd. Mat. Estestv. Nauk, Ser. Fiz. **3**, 381 (1937)
13. J.T. Randall, H.P. Rooksby, B.S. Cooper, The diffraction of X-rays by vitreous solids and its bearing on their constitution. Nature **125**, 438 (1930); ibid: X-ray diffraction and the structure of vitreous solids. I. Z. Kristallogr. **75**, 196–214 (1930)
14. E.A. Porai-Koshits, Genesis of concepts on structure of inorganic glasses. J. Non-cryst. Sol. **123**, 1–13 (1990)
15. A.C. Wright, Crystalline-like ordering in melt-quenched network glasses? J. Non-cryst. Solids **401**, 4–26 (2014); ibid.: The great crystallite versus random network controversy: a personal perspective. Int. J. Appl. Glass Sci. **5**, 31–56 (2014)
16. A.S. Bakai, The polycluster concept of amorphous solids, in *Glassy Metals III*, H. Beck and H. -I. Günterodt (eds.), *Topics in Applied Physics*, vol. 72, 209–255 (Springer, Berlin, 1994)
17. A.S. Bakai, *Poliklastern'ie Amorfn'ie Tela*, Khar'kov "Synteks" (Khar'kov, Ukraine, 2013). (in Russian)
18. G. Adam, J.H. Gibbs, On the temperature dependence of cooperative relaxation properties in glass-forming liquids. J. Chem. Phys. **43**, 139–146 (1965)
19. L. Berthier, G. Biroli, Theoretical perspective on the glass transition and amorphous materials. Rev. Mod. Phys. **83**, 587–645 (2011)
20. C.A. Angell, Perspective on the glass transition. J. Phys. Cem. Solids **49**, 863–871 (1988)
21. V. Lubchenko, P.G. Wolynes, Theory of structural glasses and supercooled liquids. Annu. Rev. Phys. Chem. **58**, 235–266 (2007)
22. S.L. Simon, G.B. McKenna, Experimental evidence against the existence of an ideal glass transition. J. Non-Cryst. Solids **355**, 672–675 (2009)
23. G. Hägg, The vitreous state. J. Chem. Phys. **3**, 284–349 (2016)
24. U. Satoshi, H. Koibuchi, Finsler geometry modeling of phase separation in multi-component membranes. Polymers **8**, 284 (2016)
25. J. Hwang, Z.H. Melgarejo, Y.E. Kalay, I. Kalay, M.J. Kramer, D.S. Stone, P.M. Voyles, Nanoscale structure and structural relaxation in $Zr_50Cu_45Al_5$ bulk metallic glass. Phys. Rev. Lett. **108**, 195505 (2012)

26. M.M.J. Treacy, K.B. Borisenko, The local structure of amorphous silicon. Science **335**, 950–953 (2012)
27. J.C. Phillips, Realization of a Zachariasen glass. Solid State Comm. **47**, 203–206 (1983)
28. M.M. Hurley, P. Harrowell, Kinetic structure of a two-dimensional liquid. Phys. Rev. E **52**, 1694–1698 (1995)
29. H. Sillescu, Heterogeneity at the glass transition: a review. J. Non-Cryst. Solids **243**, 81–108 (1999)
30. M.D. Ediger, Spatially heterogeneous dynamics in supercooled liquids. Annu. Rev. Phys. Chem. **51**, 99–128 (2000)
31. K. Vollmayr-Lee, A. Zippelius, Heterogeneities in the glassy state. Phys. Rev. B **72**, 041507 (2005); K. Vollmayr-Lee, W. Kob, K. Binder, A. Zippelius, Dynamical heterogeneities below the glass transition. J. Chem. Phys. **116**, 5158–5166 (2002)
32. C. Donati, S.C. Glotzer, P.H. Poole, W. Kob, S. Plimpton, Spatial correlations of mobility and immobility in a glass-forming Lennard-Jones liquid. Phys. Rev. E **60**, 3107–3119 (1999)
33. P.-G. de Gennes, A simple picture for structural glasses. C. R. Phys. **3**, 1263–1268 (2002)
34. H.P. Baltes, A cellular model for the specific heat of amorphous solids at low temperatures. Solid State Commun. **13**, 225–228 (1973)
35. W.A. Phillips, Two-level states in glasses. Rep. Prog. Phys. **50**, 1657–1708 (1987)
36. J.A. Sussmann, Electric dipoles due to trapped electrons. Proc. Phys. Soc. **79**, 758–774 (1962). (London)
37. G. Jug, M. Paliienko, Multilevel tunneling systems and fractal clusters in the low-temperature mixed alkali-silicate glasses. Sci. World J. **2013**, 1–20 (2013)
38. G. Jug, Multiple-well tunneling model for the magnetic-field effect in ultracold glasses. Phys. Rev. B **79**, 180201 (2009)
39. G. Jug, M. Paliienko, S. Bonfanti, The glassy state magnetically viewed from the frozen end. J. Non-Crys. Solids **401**, 66–72 (2014)
40. C.C. Yu, A.J. Leggett, Low temperature properties of amorphous materials: through a glass darkly. Comm. Cond. Mat. Phys. **14**, 231–251 (1988)
41. G. Jug, S. Bonfanti, W. Kob, Realistic tunneling systems for the magnetic effects in non-metallic real glasses. Phil. Mag. **96**, 648–703 (2016)
42. S. Bonfanti, G. Jug, On the paramagnetic impurity concentration of silicate glasses from low-temperature physics. J. Low Temp. Phys. **180**, 214–237 (2015)
43. L. Siebert, Ph.D. Thesis (Heidelberg University, 2001), www.ub.uni-heidelberg.de/archiv/1601
44. H.M. Carruzzo, E.R. Grannan, C.C. Yu, Non-equilibrium dielectric behavior in glasses at low temperatures: evidence for interacting defects. Phys. Rev. B **50**, 6685–6695 (1994)
45. M. Paliienko, Multiple-welled tunnelling systems in glasses at low temperatures. Ph.D. Thesis (Università degli Studi dell'Insubria, 2011), http://insubriaspace.cineca.it/handle/10277/420
46. F. LeCochec, F. Ladieu, P. Pari, Magnetic field effect on the dielectric constant of glasses: evidence of disorder within tunneling barriers. Phys. Rev. B **66**, 064203 (2002)
47. B.P. Smolyakov, E.P. Khaimovich, Pis'ma Zh. Eksp. Teor. Fiz. **29**, 464 (1979) (in Russian); ibid.: Dynamic processes in dielectric glasses at low temperatures. Sov. Phys. Uspekhi, **25**, 102–115 (courtesy A. Borisenko) (1982)
48. S. Ludwig, P. Nagel, S. Hunklinger, C. Enss, Magnetic field dependent coherent polarization echoes in glasses. J. Low Temp. Phys. **131**, 89–111 (2003)
49. S. Ludwig, P. Nagel, S. Hunklinger, C. Enss, Direct coupling of magnetic fields to tunneling systems in glasses. Phys. Rev. Lett. **88**, 075501 (2002)
50. A. Würger, A. Fleischmann, C. Enss, Dephasing of atomic tunneling by nuclear quadrupoles. Phys. Rev. Lett. **89**, 237601 (2002)
51. J.L. Black, B.I. Halperin, Spectral diffusion, phonon echoes and saturation recovery in glasses at low temperatures. Phys. Rev. B **16**, 2879–2895 (1977)
52. V.L. Gurevich, M.I. Muradov, D.A. Parshin, Electric dipole echo in glasses. Sov. Phys. JETP **70**, 928 (1990)

53. Y.M. Galperin, V.L. Gurevich, D.A. Parshin, Nonlinear resonant attenuation in glasses and spectral diffusion. Phys. Rev. B **37**, 10339–10349 (1988)
54. C. Enss, S. Ludwig, R. Weis, S. Hunklinger, Decay of spontaneous echoes in glasses. Czechoslovak J. Phys. **46**, 2247–2248 (1996)
55. D. Simatos, G. Blond, R. Roudaut, D. Champion, J. Perez, A.L. Faivre, Influence of heating and cooling rates on the glass transition temperature and the fragility parameter of sorbitol and fructose as measured by DSC. J. Thermal Anal. **47**, 1419–1436 (1996)
56. J. Buchholz, W. Paul, F. Varnik, K. Binder, Cooling rate dependence of the glass transition temperature of polymer melts: molecular dynamics study. J. Chem. Phys. **117**, 7364–7372 (2002)
57. A. Smerzi, S. Fantoni, S. Giovanazzi, S.R. Shenoy, Quantum coherent atomic tunneling between two trapped Bose-Einstein condensates. Phys. Rev. Lett. **79**, 4950 (1997)
58. M. Albiez, R. Gati, J. Fölling, S. Hunsmann, M. Cristiani, M.K. Oberthaler, Direct observation of tunneling and nonlinear self-trapping in a single Bosonic Josephson junction. Phys. Rev. Lett. **95**, 010402 (2005)
59. J. Zarzycki, *Proceedings of X International Congress on Glass*, No. 12 (Kyoto, Japan, 1974), p. 28
60. J. Zarzycki, *Glasses and the Vitreous State* (Cambridge University Press, Cambridge, 1991), p. 172
61. W. Vogel, *Glass Chemistry*, 2nd edn. (Springer, Berlin, 1992), p. 74
62. A. Borisenko, Hole-compensated Fe^{3+} impurities in quartz glasses: a contribution to Subkelvin thermodynamics. J. Phys.: Condens. Matter **19**, 416102 (2007)
63. A. Borisenko, G. Jug, Paramagnetic tunneling systems and their contribution to the polarization echo in glasses. Phys. Rev. Lett. **107**, 075501 (2011)
64. E. Proutorov, H. Koibuchi, Orientation asymmetric surface model for membranes: Finsler geometry modeling. Axioms **6**, 10 (2017)

Chapter 14
Relaxation and Vitrification Processes of Disordered Iron Based Systems

Leonid A. Bulavin, Volodymyr Karbivskyy, Viktor Artemyuk and Love Karbivska

Abstract The influence of processes occurring at various stages of crystallization on morphological features and the electronic structure of the surface of iron-based amorphous metallic alloys (AMA) was investigated with use of scanning tunneling microscopy, atomic resolution, tunneling spectroscopy, XPS and EXAFS spectroscopy methods.The results of morphological changes on surface of iron-based AMA during the structural relaxation under heat treatment of amorphous tapes in the range from 250 to 700 °C are shown. The nonmonotonic dependence of subroughness parameters of AMA surface in the annealing range from room temperature to 700 °C is established. The formation of regular shape nanostructures in the form of rods was observed at annealing temperature about 500 °C.For initial amorphous iron-based samples the presence of significantly oxidized surface layer down to a depth of 150 nm was shown. In the case of alloying of amorphous Fe-B system by metalloid its segregation at the surface is observed. During structural relaxation induced by heat treatment a higher redistribution of boron atoms in comparison with Fe and Si atoms occurs. On the surface of investigated AMA carbon is appeared mainly in the oxidized state while in the bulk it forms compounds with silicon.The low conductivity regions typical for the Fe-Si and Fe-B nanophase formation were detected by tunneling spectroscopy method. The substantial inhomogeneity of electron density of states at the intercluster boundaries is observed indicating on their complex organization. The Fermi level of investigated

L. A. Bulavin
Faculty of Physics, Taras Shevchenko National University of Kyiv,
Volodymyrska Str., 64, Kiev 01601, Ukraine
e-mail: bulavin221@gmail.com

V. Karbivskyy (✉) · V. Artemyuk · L. Karbivska
G.V. Kurdymov Institute for Metal Physics of the NAS of Ukraine,
blvd. Vernadsky, 36, Kiev 03680, Ukraine
e-mail: karb@imp.kiev.ua

V. Artemyuk
e-mail: artemyukviktor@ukr.net

L. Karbivska
e-mail: karb000@i.ua

L. A. Bulavin and A. V. Chalyi (eds.), *Modern Problems of Molecular Physics*,
Springer Proceedings in Physics 197, https://doi.org/10.1007/978-3-319-61109-9_14

alloys is situated at local minimum of electron density of states and thus meets the criterion of Nagel-Tauk for amorphous state formation.Under complete crystallization conditions at 700 °C terraced structures were observed which formed a practically smooth planes of size more than 200 nm. According to EXAFS-studies the increase of Co atoms concentration in the AMA Fe-Co-B system leads to reduction of the radius of the first coordination sphere of a boron atom and reduction of the unit cell volume in the crystalline alloy $(Co\ Fe)_3B$ indicating bounds strengthening of the transition metal—boron bond. The results of the EXAFS-spectroscopy studies of amorphous systems Fe-Co-B and Fe-Cr-B are well interpreted in terms of the cluster model of microinhomogeneous AMA structure.

14.1 Introduction

Investigation of amorphous metallic alloys (AMA) remains to be the crucial direction in experimental physics. Crystal transition into amorphous state is accompanied by changes in the variety physical-chemical properties of materials, particularly, by huge change in density, viscosity, coefficient of thermal expansion, thermal capacity, elastic constants. Such changes are very close to second order phase transition. In the vitrification temperature interval reformation of liquid's short-range order (SRO) is retarded, and at the temperature below vitrification such a reformation stops completely. Particles remain only ability to rotational and oscillatory movements. The translational mobility, which is characteristic of liquid state, is lost. The difference in properties of amorphous and liquid states is determined by the character of thermal motion of particles. Thermodynamic parameters of vitreous amorphous state are specified by not only temperature and pressure, but also are dependent on the history of the sample, particularly, on the speed of cooling. AMA are better than traditional materials by their electric, magnetic and mechanical characteristics, corrosive and radiational stabilities. As soft ferrites, AMA are often used as transformer cores in communications systems in building different kinds of electromagnetic components in electronics. Thus, AMA have the variety of unique physicochemical properties.

Recently, in the fabrication of modern commercial high density hard drives with the "system of perpendicular magnetic records" was used. To achieve a high signal to a noise ratio in those drives application of the soft ferrites substrates with a low value of coercive force has become quite popular [1–5]. Using thin magnetic amorphous alloys as a substrate guarantees not only good soft magnetic properties, but also provides less impulse noise due to the absence of domain walls. Therefore, study of films surfaces of amorphous alloys attracts significant interest due to the fact that surface has the highest influence the quality of magnetic disk.

Today, amorphous soft ferrites are commonly based on Fe-B-Si system with the addition of various dopants to achieve the desired properties. For example, in metallic glasses $(Co,Fe)_{71}(Si,B)_{29}$ losses of the frequency of 1 MHz at 0.1 T is 1.8 W/cm^3, that is substantially less than for the Mn-Zn ferrites. Explanation of a variety of physical properties can be based on knowledge of electronic structure, which can be more directly investigated by X-ray photoelectron, emission and tunneling spectroscopies. For understanding of the electronic structure features of amorphous alloys and in particular, the interpretation of X-ray photoelectron and X-ray emission spectra the knowledge of the atomic structure of these substances is very important. Any modification in the amorphous structure leads to fluctuations of quantities of the exchange interaction, consequently, to changes of magnetic properties. Decisive influence on the magnetic properties of such materials has the size of nanocrystals which forms the structure. Such a behavior of the materials can be explained in terms of the Herzer model [6], according to which a decrease of nanocrystals sizes to values smaller than the length of the magnetic exchange correlation leads to a spatial averaging of magnetic anisotropy, and, as a consequence, to a substantial reduction of coercive force.

Required structure of amorphous material usually is achieved by the annealing process. Thus, an amorphous alloy annealed at the 550 °C during one hour leads to formation of nanocrystals with size about 15 nm [7, 8]. Since amorphous ferromagnetic films produced by rapid cooling were thermodynamically unstable and the heating of these films is accompanied by a structural relaxation and the formation of a more stable structure. Thus, annealing of amorphous films at temperatures below the crystallization temperature is accompanied by a significant improvement of their properties. Structural relaxation in this case is effected by compositional and topological short-range ordering [9–14].

Due to the fact that structural relaxation has an impact on various physical, chemical and mechanical properties, the study of relaxation phenomena causes some interest not only because of amorphous films applications, but also provides better understanding of the nature of the amorphous structure.

In view of the above mentioned difficulties, today there is no unambiguous approach in predicting of physical properties of amorphous metal alloys design by synthesis or further heat treatment. Therefore, the study of physical and chemical properties of the available AMA is a necessary task for the accumulation of the experimental basis for the purpose of development of the theory of disordered state of complex metallic systems and important for targeted prediction of amorphous materials properties.

In this paper, the morphological features and electronic structure of the amorphous metal alloy $Fe_{82}Si_4B_{14}$ after heat treatment over a wide temperature range (from room temperature to 700 °C), as well as subroughness (hereinafter roughness) were studied by the methods of high vacuum tunneling microscopy with atomic resolution, tunneling and XPS spectroscopies. SRO of the amorphous metal iron-based alloys was investigated by the method of EXAFS—spectroscopy.

14.2 The Methods Used to Study of Local Atomic and Electronic Structure of Disordered Metallic Systems

One of the major problems which are resolved by physical methods is determination of material atomic and electronic structure. The accumulation of the variety of data allows identifying patterns and establishing correlations between different properties. Data acquired from each method is unique, but despite the perfection achieved by a variety of methods, processes of development, broadening and expanding of applications for almost all methods still continue. One of the most important problems remains the optimal choice of method or group of methods taking into account their potentials. Regardless of practical accessibility of certain method, the crucial capabilities of methods have a great value and their development should promote better understanding and effective problems solving.

Adaptation of comprehensive approach to the study of AMA generates multiview presentation of the studied system. Comprehensive approach to investigations may result in compound compositions with attractive properties; however, the aim of preparative research and the basis for synthesis of compounds with targeted composition, three-dimensional structure, and ultimate properties can become exclusively the comprehension and mastering of initiated transformations mechanism. Direct new materials synthesis is possible under condition that deep and detailed study of compounds is available for researchers as well as empirically predicted and synthesized at the time of the research.

The various properties of AMA, as it is known, are largely determined by their electronic structure. As a result, determination of the formation regularities of electronic structure for existing compounds is an important step in methods development for obtaining of new analogous materials with desired characteristics.

In the view of the importance of the indicated problem at present it is difficult to point out the methods unused in study of disordered compounds and among them spectral methods are the ones of the most efficient in the study of the compounds electronic properties.

By now, the theory of electronic structure of disordered compounds is still far from complete, despite the fairly great number of works devoted to the study of a number of specific substances of the aforesaid type. This circumstance is caused, primarily, by absence of conclusive systematic data of the nature of interatomic interactions, charge and spin states of atoms, valence electrons energy distribution for the different symmetries and especially inapplicability of such universal approach as the Bloch theorem.

As literature data analysis shows, regardless of high scientific and practical attention to AMA, there are plenty of remaining challenges. The solution of the mentioned problems is temporary and possible exclusively by taking advantages of complex techniques.

Production of iron-based AMA. The amorphous $Fe_{82}Si_4B_{14}$ metal alloy in the form of a tape with width of 12.8 mm and a thickness of 28–30 μ in a rarefied

atmosphere of carbon dioxide at the rate of rotation of the copper disk with diameter of 180 mm and 1750 rpm were obtained by fast cooling. Overpressure of the melt ejection was 0.2 atm CO_2. The nozzle was located above the disk surface at the distance of 0.2 mm. Liquidus temperature of the alloy was 1160 °C. Sample melting mode starts with heating to 1470 °C, then 1 min holding at this temperature, then cooling ejection at 1350 °C. The tape was mechanically removed from the disk by the sliding knife-stripper through 3/4 turn. Estimated cooling rate of melt was about 10^{-6} K/s.

Study of surface morphological features and subroughness. Investigation of subroughness can provide a new understanding for the theory of friction, lubrication and wear. Determination of subroughness describes a very smooth surface, the roughness of which is at nanometer scale. Amorphous metal alloy $Fe_{82}Si_4B_{14}$ morphological properties were investigated with use of high resolution ultra high vacuum scanning tunneling microscope *(JEOL JSPM-4610)*.

Thermal impact on the specimen was performed by indirect heating of ceramic base heater. The heating current of ceramic holder was varied from 0.2 to 0.7 A. The temperature of the sample was determined from the curve load of the holder and also by pyrometric measurements. The accuracy of sample surface temperature measurements was at least 3 K. The sample heating rate was 2 K/min. Images were acquired after annealing for 15 min at the specified temperature. Tunneling images of AMA surfaces were taken at a bias voltage of up to ± 3.0 V and tunneling current of about ~2 *nA*. Residual pressure was less than 10^{-7} Pa.

Subroughness were determinated from STM images. For quantitative evaluation of surface subroughness the next parameters were used:

R_a—the arithmetic mean deviation of the absolute values of profile within a base length l:

$$R_\alpha = \frac{1}{l}\int_0^l |y(x)|dx,$$

where y—profile deviation.

R_q—the mean-square deviation values of profile within a base length l:

$$R_\alpha = \sqrt{\frac{1}{l}\int_0^l y^2(x)dx},$$

R_{zjis}—the sum of average absolute values of five biggest profile protrusions and five biggest profile depressions within a base length:

$$R_{zjis} = \frac{\sum_{l=1}^{5} |y_{pi}| + \sum_{l=1}^{5} |y_{\nu i}|}{5},$$

where y_{pi}—height of i-th protrusion profile, $y_{\nu i}$—depth of i-th depressions profile.

R_z—maximum difference between protrusions and depressions for tens points [15]:

$$R_z = Z_{max} - Z_{min},$$

where Z_{max} and Z_{min} represent the values of protrusions and depressions, respectively.

In addition, the area ratios defined as a ratio between the total surface area of the analyzed region to the area of analyzed region in the case of a perfectly flat surface were calculated.

$$S_{ratio} = \frac{S}{S_0}.$$

S_0—area of analyzed region in the case of a perfectly flat surface.

S—the total surface area of the analyzed region.

Research of the electronic structure. X-ray photoelectron spectra of amorphous alloy samples were obtained on JEOL photoelectron spectrometer "XPS-9200" using non-monochromatic Mg K_α (1253.6 eV) X-ray source. Residual pressure was less than 10^{-7} Pa. Accuracy of definition of peak was 0.1 eV. The calibration of spectra was performed taking into account the Au 4*f* line energy (E = 83.8 eV). Ion etching was performed in argon atmosphere under mode of 3 kV and 30 mA. The duration of each etching step was 15 min.

For every studied line the number of scans was at least 200. Analysis of surface element composition was carried out by taking into account the receiving spectra at the same modes and scattering cross sections.

Tunneling spectroscopy. The tunneling spectra of AMA clustered nanostructures were obtained by standard methods. Equation for the tunneling current in the approximation of quasi-continuous spectrum of electrons at some point r_0 on the sample surface, considering density of electronic states of the tip can be represented as follows:

$$I(r_0,\, U) \approx \int_0^{eU} \rho_T(E)\rho_s(r_0,\, E)D(r_0,\, E)dE,$$

where $D(r_0, E)$—barrier transparency, $\rho_T(E)$—tip's electron density of states, $\rho_S(r_0, E)$—sample electron density of states at the point r_0.

Thus, the tunnel current can be considered as a convolution of the tip and the sample density of states. Assuming the sample density of states as dominate in the spectrum, a rectangular barrier at low temperatures and that the density of states are permanently at the Fermi level in the metal tip, the current expression becomes:

$$I(r_0, U) \approx \int_0^{eU} \rho_s(r_0, E)dE,$$

In this case, dependence of the tunnel current on voltage is determined by the energy density spectrum of the sample. In practice $\rho_S(r_0, E)$ values are estimated from the derivative value of the tunneling current on voltage:

$$\rho_s(eU) \approx \frac{\partial I}{\partial U}.$$

Therefore, the tunnel current-voltage characteristics of electronic states reflect the number and distribution energy spectrum of the sample.

The density of electronic states was obtained by recording the tunnel current *I(U)* during changing the voltage between ±3 V and with a fixed position of the tip. If a positive bias voltage is applied to the sample electrons will tunnel into unoccupied state of the sample, while when a negative voltage shift is applied electrons will tunnel from engaged states of the sample. *dI/dU* spectrum was obtained by numerical differentiation of the curves *I(U)*.

EXAFS—spectroscopy (Extended X-ray Absorption Fine Structure). The phenomenon of X-Ray absorption fine structure has been well known since 30th years of the last century. However, the theory has been developed to the beginning of 60th years. The new experimental facilities had been appeared at the beginning of 80th years due to the widely use of synchrotron radiation, which made EXAFS—spectroscopy one of the most rapidly developing methods in a local atomic structure study. The EXAFS begins from energies of 30 ÷ 40 eV to 400 ÷ 1000 eV, since electrons with energy of 10 ÷ 40 eV do not possess enough kinetic energy. The theories for description the distant fine structure edge can be divided into "long-range order" (LRO)—and "short-range order"—theories. The first one was developed by Kronig in the framework of LRO-theory. According to this theory minimums in absorption cross section are caused by electrons under Bragg reflection, i.e. when electron wave vector is at the edge of Brillouin zone. Therefore, this theory of EXAFS modeling is based on the dependency of Bloch waves density of states which are above Fermi level and requires periodical ordering. However, it did not describe EXAFS in unordered materials. The dominant effect of transition matrix element has been neglected in the theory. The modern EXAFS is based on "short-range order"—theory described in [16].

For complete description of χ(k) *K*—edge absorption by 3*d*-metals we used expression [17]:

$$\chi_i(k) = \sum_j \frac{N_j}{kR_j^2} \left| f_j(k, \pi) \right| sin\left(2kR_j + \varphi_j(k)\right) e^{-2\sigma_j^2 k^2} e^{-\frac{2R_j}{\gamma(k)}},$$

where k is the module of photoelectron wave vector,

$$\left|\vec{k}\right| = k = \frac{\sqrt{2mT}}{\hbar} = \frac{\sqrt{2m(h\nu - E_i)}}{\hbar}.$$

R_j—distance to j-th atom; $f_j(k,\pi)$—amplitude of backward scattering by j-th atom of electron with k wave vector.

Within sinus expression is a phase shift. The difference $2kR_j$ is composed by phase shift of in-going and reflected waves on its way to j-th atom and back, phase shift of electron with $l = 1$ during its propagation in own atomic potential $2\delta_1(k)$ and back-scattering phase shift at j-th atom $\varphi_j(k)$. Consequently, the resulting phase difference is defined by expression $2kR_j + 2\delta_1(k) + \varphi_j(k)$. Phase shift $\varphi_j(k)$ is equal to sum of $2\delta_1(k)$ and $\varphi_j(k)$.

Essentially, since k is relatively high at high values of R_j, in the sum the components characterized as fast oscillations arise. Such oscillations cannot be observed in real experiment because they are smoothed. Thus, in the sum over j the closest atomic neighborhood only is taking into account.

Since for EXAFS region (E > 50 eV) for elastic backscattering needs a strong potential the dissipation occurs mainly in the ionic cores of the atoms, while the valence electrons affected by chemical surrounding, do not participate in this process. Hence, $f(k,\pi)$ and $\varphi_j(k)$ does not depend on the nature of the chemical bond and can be easily calculated [18]. For the experimental results processing the Fourier transform technique with the theoretical values of the phase shift and the amplitude of the scattering functions (Fourier transform with a phase) was used. As theoretically calculated amplitude and phase functions the McKale functions were taken [18]. The multiplier $exp(-2\sigma_j^2 k^2)$ is introduced to take into account thermal fluctuations.

The multiplier $exp(-2R_j/\gamma(k))$ describes the process of photoelectron inelastic scattering with surroundings of the absorbing atom while passing distance $2R_j$. Where $\gamma(k)$—the photoelectron mean free path depending on its wave vector module.

Extraction of normalized EXAFS—spectrum $\chi(k)$ from experimental absorption spectrum was carried out by standard methods using the following equation:

$$\chi(\mathrm{k}) = (\mu(\mathrm{k}) - \mu_0(\mathrm{k}))/(\mu_0(\mathrm{k}) - \mu_1(\mathrm{k})),$$

where k—photoelectron wave vector module;

$\mu(k)$ experimental absorption coefficient of the sample;

$\mu_1(k)$ absorption coefficient which arises due to all other processes except investigated photoionization of the atom electron coating (ionization of more high electronic levels, ionization of other chemical elements, scattering);

$\mu_0(k)$ absorption coefficient which could be observed in the absence of neighbor atoms around the absorbing atom.

To determine $\mu_1(h\nu)$ the extrapolation of $\mu(h\nu)$ at $h\nu < E_0$ on region $h\nu > E_0$ was used. For this purpose $\mu_1(h\nu)$ was found in the form of Victorin polynomials $C(h\nu)^{-3} + D(h\nu)^{-4}$. A similar procedure was applied for $\mu_0(h\nu)$.

Additional complicating factor is the fact, that the E_0 is not an ionization potential in the ordinary way; it corresponds to the energy relatively to the inner

level, obtained by electron and allows to reach the neighboring atom with zero kinetic energy. Obviously, this energy cannot be the same as the energy required to remove the electron to infinity, which corresponds to the usual definition of ionization potential. Moreover, this energy can differ for different coordination spheres, as it depends on shape of the interatomic potential in direction to the scattering atom.

Therefore, E_0 may not coincide with the inflection point of the absorption edge and can be either larger or smaller. During the simulation E_0 is taken as a free parameter. However, it can differ for ±30 eV.

Rewriting $\chi(k)$ with consideration of the radial distribution function (RDF) of atoms, then for n—components system the normalized oscillating part of K—absorption of the X-ray spectrum of the i-th atom specie χ(k) is represented as EXAFS integral equation:

$$\chi_i(k) = 4\pi\rho_0 \sum_{j=1}^{n} c_j \frac{f_j(k)}{k} \int_0^{\infty} g_{ij}(R) \sin\left(2kR + \varphi_{ij}(k)\right) e^{-2\sigma_j^2 k^2} e^{-\frac{2R}{\gamma(k)}} dR,$$

where ρ—average atomic density; c_j—concentration of the element.

The radial distribution of the atoms around absorbing atom in this case is determined from the function $g(R)$, obtained by Fourier transform of $\chi(k)$:

$$\mathrm{g}(R) = \int_{k_{min}}^{k_{max}} \chi(k) k^n e^{-2ikR} dk,$$

The values of k_{max} and k_{min} in this formula define an interval in which analysis of experimental data carried out, besides k_{max} is determined by the upper limit of the experimental data, and k_{min} is chosen in the way to achieve a minimal contribution to $\chi(k)$ from the near fine structure of absorption spectrum. Usually, one chooses $k_{min} = 2.0 \div 4.0$ Å^{-} and $k_{max} = 10.0 \div 16.0$ Å^{-}. A multiplier k^n was introduced to compensate the reduction of χ with increasing of k (typically $n = 1 - 3$). It is important to note that the presence of this multiplier does not affect on obtained structural parameters.

$$\mathrm{g}(R) = \int_{-\infty}^{\infty} \chi(k) k^n P(k) e^{-2ikR} dk.$$

An influence of limitation of processing intervals can be described in terms of the window function $P(k)$. With aim to reduce the contribution of false peaks, the window in the form of a Gaussian function was been used [17]. In this case window does not distort the obtained results, at least in the range of 0–5 Å.

Today, there are a lot of EXAFS techniques with use of synchrotron radiation (SR), in particular: the transmission technique, fluorescence spectroscopy EXAFS technique (FEXAFS), surface EXAFS—spectroscopy technique (SEXAFS), optical

luminescence EXAFS—spectroscopy (XEOL), and total external reflection EXAFS—spectroscopy. In this paper, the EXAFS—experiment was carried out according to the transmission method with use of synchrotron radiation [17].

14.3 Electronic Structure of Iron-Based Amorphous Metallic Alloys

14.3.1 Electronic Structure of Amorphous Metallic Alloy $Fe_{77}Si_8B_{15}$

X-ray photoelectron investigations of samples without preliminary ion sputtering of surface showed the presence of significant amount of oxygen, carbon and iron. Spectra of boron have extremely low intensities after longtime (500 scans) accumulation; this demonstrate the presence of significantly low concentrations of boron and its compounds at surfaces (up to ~40 Å) of AMA under application conditions. Due to significant silicon peak intensities at X-ray photoelectron spectra it is obvious that surface segregation of silicon in investigated alloy is quite substantial (Fig. 14.1).

As it is shown in the above picture the main peak of carbon's C 1s is near 284 eV, which is specific for C-C bonds, however, the widening of C 1s line is observed within the region of lower energy. The high energy peak at about 287 eV means the presence of complex carbon compounds with double bonds C = O, this happens probably due to high temperature heating of melt during alloys synthesis because after ion beam sputtering this peak disappeared. Decomposition of C 1s spectra on components shows (Fig. 14.2) that concentration of compounds of bonds C = O, C-O and C-C relates as about 1.0:1.4:8.5 respectively. Therefore, it can be concluded that carbon on a surface of investigated AMA resides in the low oxidized state.

The oxygen peak is characterized by substantial broadening indicating the presence of considerable amount of oxygen atoms in different states. The study of several samples of same film revealed nonstoichiometric distribution of elements over the film, which is probably related to different oxidation state over its length and also the condition of the melt during film synthesis. In terms of chemical self-similarities of alloy its invariance is achieved by number of cases averaging under which the real picture of experiment is observed.

The X-ray spectra after first ion sputtering (5 min at 3 kV, 30 mA) showed that the oxidized layer had the depth higher than the one that was removed by ion sputtering. The substantial intensity of oxygen line still was observed (Fig. 14.3). As for initial surface, the absence of boron was observed. The further surface sputtering revealed considerably decreased amounts of oxygen and carbon.

Notably, after considerably long sputtering duration (over 30 min, and the same conditions) the peaks of low intensities of oxygen and carbon still appeared, which

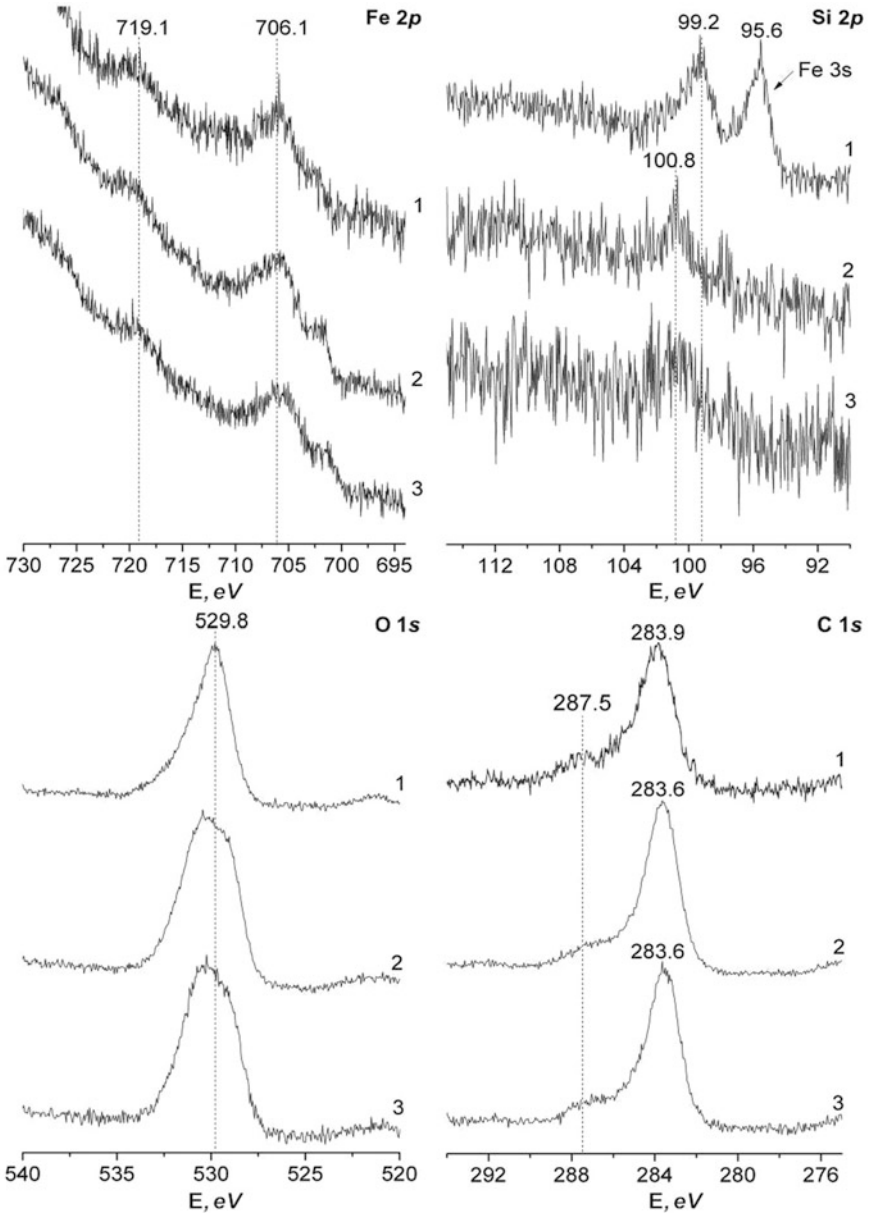

Fig. 14.1 X-ray photoelectron spectra of AMA $Fe_{77}Si_8B_{15}$ (1-3 different partitions of amorphous film)

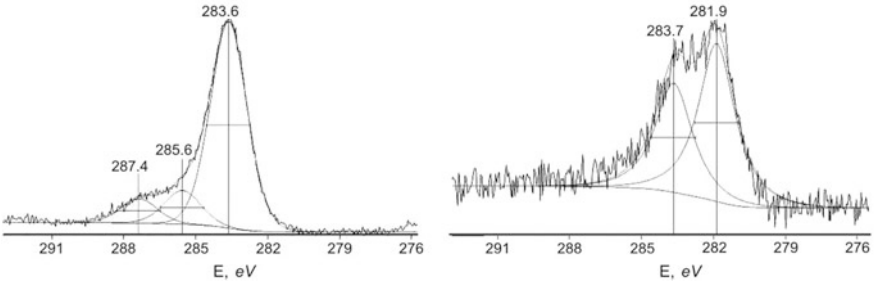

Fig. 14.2 Decomposition of C 1*s* X-ray photoelectron spectra of AMA $Fe_{77}Si_8B_{15}$ (left—before ion beam sputtering; right—after the last ion beam sputtering)

is an evidence that under those technological conditions of amorphous films production the unoxidized states of elements can be hardly achieved.

The intensities of X-ray spectral lines obtained under the same acquire conditions after two steps of ion sputtering (Fig. 14.3) are quite different showing the increase of iron concentration and the decrease of carbon and oxygen concentrations. However, the intensities of Si 2*p* lines retained about the same what is related to preservation of silicon concentration over the film's depth. Formation of morphological peculiarities of amorphous film surface during rapid quenching is accompanied by formation of various phases [19, 20]. As a result, the formation of solid solution α-Fe(Si) and Fe_2B compound takes place. The formation of α-Fe(Si) phase at the amorphous film surface is probably connected with the atomic diffusion at short distances and particular nanoclusters merging. Due to the fact that interatomic distance for Fe-Si is bigger than for Fe-B and it is quite close to Fe-Fe distance, diffusion leads to Si atoms take positions of Fe atoms during crystalline structure formation [21]. Apparently this is one of the possible mechanisms of silicon surface segregation. Therefore, during the process of structural relaxation the redistribution of boron atoms is more intense than the one of Fe and Si.

Such redistribution caused the boron atoms, which were located in energetically unfavorable locations to be moving towards more favorable positions. All this points out to the fact that structure formation which lead to ordering at average distances is one of the ways of local stabilization during rapid quenching [22]. Microstructure of such surface shows close packing arrangement of nanocrystal grains of α-Fe(Si) which are located in amorphous matrix of iron boride.

The presence of characteristic peak at C 1s spectrum in the region about 281.9 eV indicates the presence of Si-C phase. Decomposition of C 1s spectrum onto components showed (Fig. 14.2) that the ratio of silicon carbide amount to other carbon compounds is about 1.4:1.0.

In some cases the tendency to amorphisation is connected to particular electronic concentration in an alloy (Nagel-Tauc theory [23]). The distribution of electronic densities of states near Fermi level was studied by tunnel spectroscopy (Fig. 14.4). In the occupied region three peaks were observed, which characterized *d*-states of

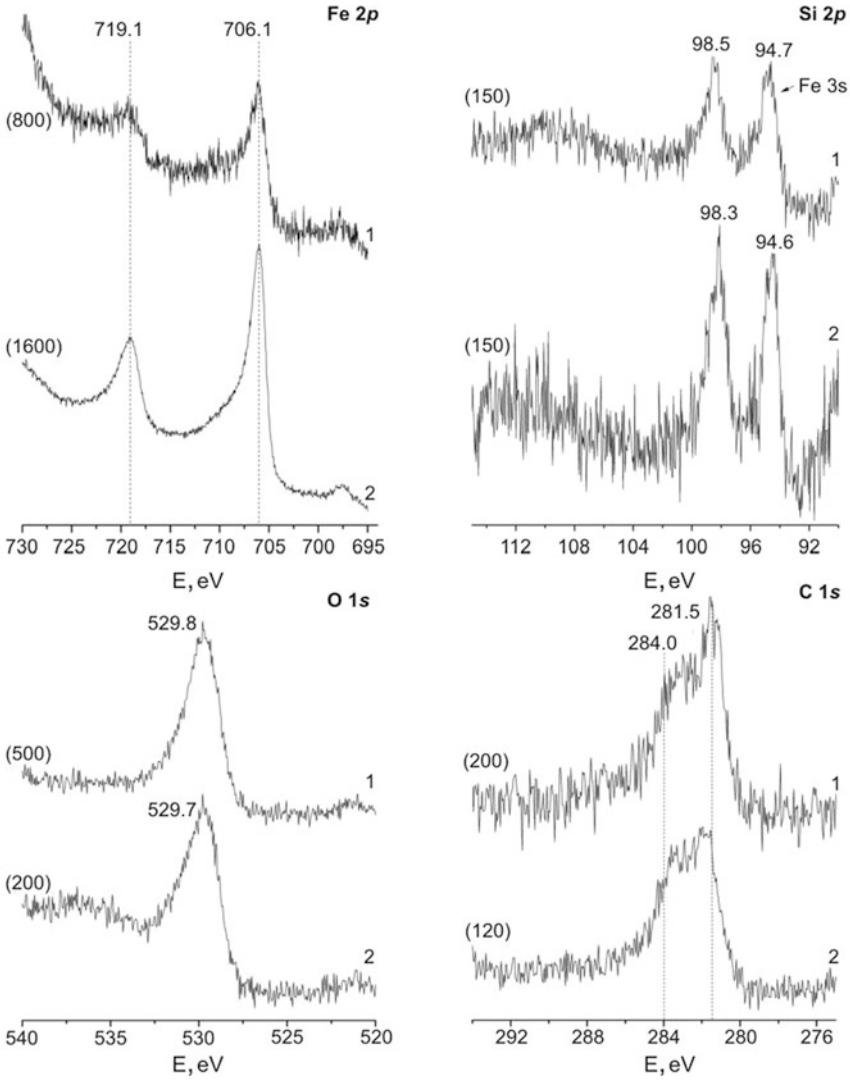

Fig. 14.3 X-ray photoelectron spectra of AMA $Fe_{77}Si_8B_{15}$ after ion beam sputtering. 1—first sputtering—5 min; 2—second sputtering—15 min; the intensities are pointed at left spectra

iron. Those peaks probably correspond to three different iron compounds. The main peak at ~2.5 eV is associated with α-Fe, peaks to the left and to the right from it characterize the compounds of iron with silicon and boron. As can be seen in mentioned above figure the Fermi level corresponds to the minimum of electronic states. In the region of free states the fine band structure is also observed, those can be attributed to formation of various iron complexes.

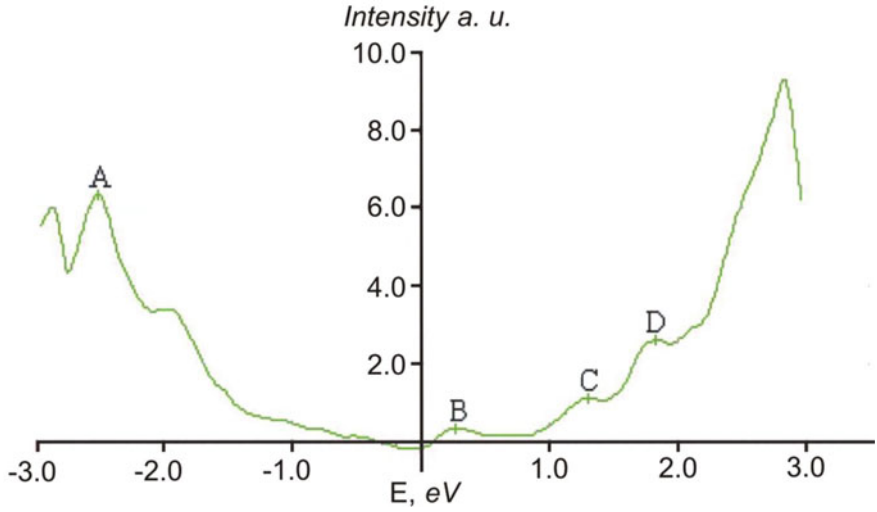

Fig. 14.4 Electronic densities of occupied and free states near Fermi level region (±3 eV) AMA of $Fe_{77}Si_8B_{15}$

It is recognized that the amorphisation is promoted by difference in electronegativity of components. However, the modern theories (e.g. Nagel-Tauc theory [23]) do not provide complete explanation for the number of experimental data. Large amount of system elements can be obtained in amorphous state. A lot of attempts were made by scientists to define the factors causing amorphisation and their results were generalized in works [24–30]. However, so far this issue is still opened. Among the discussed factors, besides electronic factor, the following ones should be mentioned. In the first place there is the size factor, in this framework the ability to amorphisation is suggested to have alloys which components differ in atomic radii on some critical value (about 15%). Although in several amorphised alloys, e.g. Pd-Si, the atomic radii ratio is close to 1. The second factor can be described by peculiarities of components state diagram. Alloys with decreased melt temperature (T_0) and with fairly small interval $T_0 - T_g$ (T_g—glass transition temperature) are inclined to amorphisation at higher extent. For example, eutectic alloys of compositions in the region of "deep" eutectic with big decrease of liquidus temperature in this concentration interval have high ability to amorphisation.

In addition, the crystallographic factor should be mentioned as well. It defines connection between ability to amorphisation and types of phases developed in alloy. It is suggested that the possibility to form amorphous phase depends on the character of topological and chemical SRO in melt providing the ability to amorphisation. A lot of alloys amorphise into constituent regions corresponding to Laves phases, σ-phases and related to them and also Hume-Rothery β—and γ-phases. The structure of all these phases can be represented as a package of "nonreguar"

tetrahedra. It has been known that according to Bernal model the tetrahedral atomic coordination is dominant in structure of amorphous compound.

For the moment the most rational approach to the issue of alloys ability to amorphisation should be the one which takes into account such important characteristic as component mixing energy. As it was mentioned before, the formation of intermediate phase is typical for amorphisating alloys. Even in systems with eutectic (Au–Si, Au-Ge), where under normal crystallization conditions the intermediate phases do not appear, after quenching the formation of Hume-Rothery β- and γ-phases is observed, e.g. Au_4Si phases (with the γ-brass structure). The formation of intermediate phases means the negative sign of components mixing energy. On the basis of the foregoing it can be concluded that investigated alloy obeys the most of mentioned factors.

14.3.2 XPS Investigations of $Fe_{82}Si_4B_{14}$ Alloys

X-ray photoelectron investigation of AMA $Fe_{82}Si_4B_{14}$ before ion sputtering showed the presence of significant amount of oxygen, carbon and iron in different states of oxidation on the surface. Small amount of boron and nitrogen with energies of B 1s about 191.3 eV and N 1s – 399.4 eV was observed, what is, according to [31], the evidence of presence of surface complexes with B-N bonds (Figs. 14.5 and 14.6).

The analysis of silicon peaks intensities in X-ray photoelectron spectra revealed that surface segregation of silicon in investigated alloy is not so strong as for alloy $Fe_{77}Si_8B_{15}$ (Fig. 14.5). C 1s electron spectrum before sputtering has two clear peaks (Fig. 14.7) with energies of 284.4 eV and 288.3 eV, which can be attributed

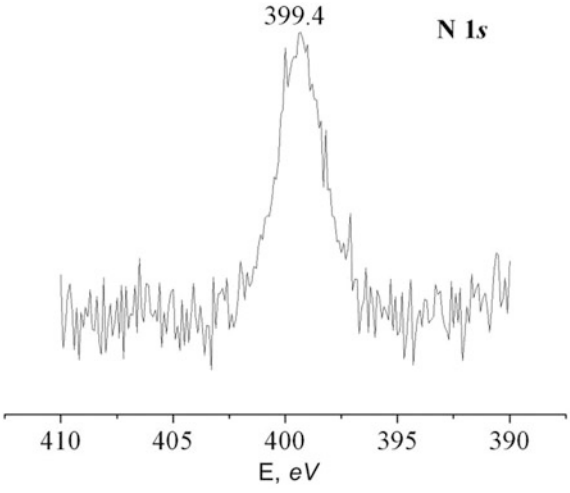

Fig. 14.5 XPS spectrum of AMA $Fe_{82}Si_4B_{14}$, N 1s line (initial sample state)

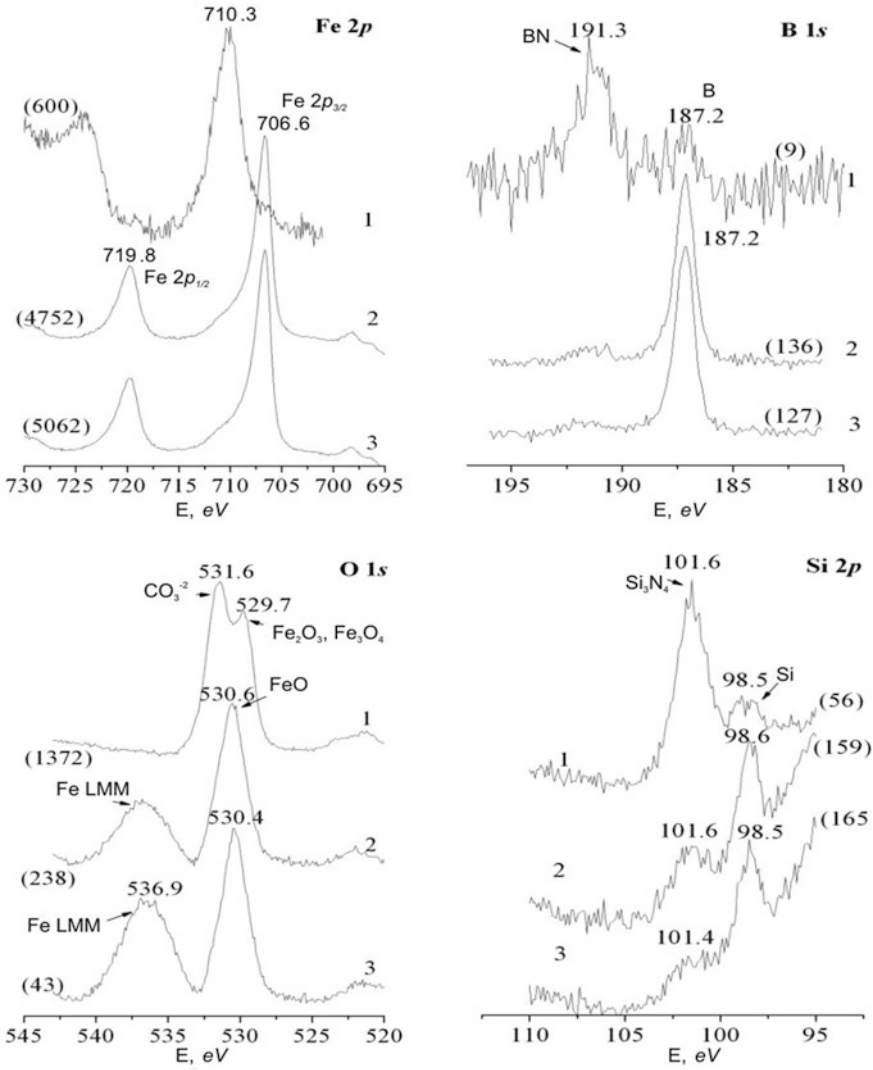

Fig. 14.6 X-ray photoelectron spectra of AMA $Fe_{82}Si_4B_{14}$: 1—initial sample, 2—after first 15 min ion beam sputtering step; 3—after second 15 min ion beam sputtering step; intensities are specified in the brackets

to C-C and O-C = O bonds respectively. Decomposition of this spectrum onto components showed the presence of peaks with energies about 285.7 and 287.4 eV, which correspond to single bond and double bond of oxygen and carbon, C-O and C = O respectively.

On the sample surface before sputtering the presence of iron oxides (Fig. 14.6) and absence of C-Si bonds were observed (Fig. 14.7). Silicon in amorphous alloy

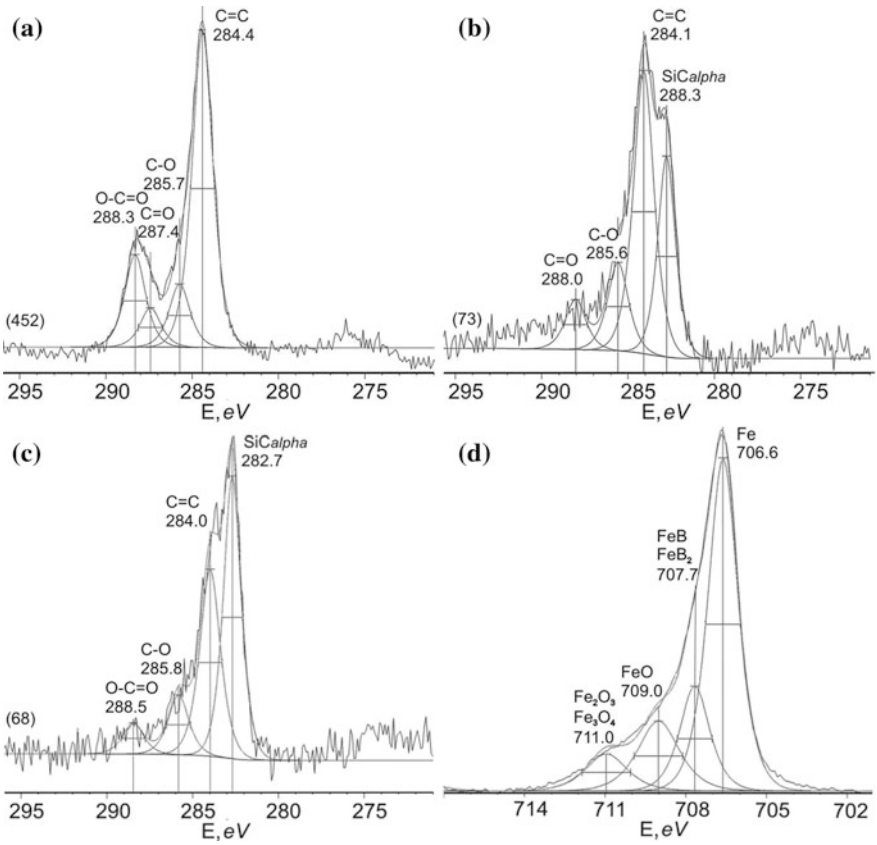

Fig. 14.7 Decomposed X-ray photoelectron spectra of AMA $Fe_{82}Si_4B_{14}$: **a**—C 1s of original sample, **b**—C 1s after first 15 min ion beam sputtering, **c**—C 1s after second 15 min ion beam sputtering, **d**—Fe $2p_{3/2}$ after the second 15 min ion sputtering

with high iron concentration is known to easily oxidize on the surface, which can lead to the concentration decrease of dissolved silicon in the amorphous alloy and, consequently, to changing of alloy properties [32, 33]. Therefore, in this work ion beam sputtering was used with the aim of layer-by-layer analysis of sample surface compound. On the sample surface before sputtering silicon mainly forms Si-N bonds (Fig. 14.6).

The first step of ion beam sputtering (15 min, 3 kV, 30 mA) showed that oxidized layer had considerable depth and cannot be removed during short cycle of ion beam sputtering. Considerable intensity of O 1s peak still was observed (Fig. 14.6), nevertheless, the intensity of this peak decreased six times. Under the same acquire conditions the intensity of Fe 2*p* line increased eight times.

Considerably less amounts of oxygen and carbon were found after the second ion beam sputtering step (Figs. 14.6 and 14.7). The main maximum of C 1s peak

(Fig. 14.7) has typical energy position for Si-C bonds of about 282.7 eV. Silicon carbide possibly is formed by high-temperature heating of components during alloy preparation. The considerable asymmetry of the line with broadening to the high energy direction was observed. The second peculiarity of spectrum at about 284.0 eV indicates the presence of carbon-carbon double bonds. The peak near 285.8 eV points out to the presence of complex carbon-oxygen compounds with C-O bonds; that peak had low intensity after ion beam sputtering, which might be related to high temperature heating of melt during AMA producing. Negligible intensity of component near 288.5 eV indicates the slight amount of compounds with C = O and O-C = O bonds.

Decomposition of C 1s spectrum onto components showed that intensity ratios of lines which characterize different bonds significantly change before and after etching (Table 14.1). The main peak of C 1s spectrum of initial sample corresponds to C = C bonds in contrast to the spectrum after etching, where the main peak corresponds to Si-C bond. Consequently, carbon on the surface of investigated amorphous metallic alloy is mainly in oxidized state, however, in volume it forms the bonds with silicon, probably, as silicon carbide. Generally, the intensity of carbon 1s lines was reduced six times with respect to intensity of before sputtering spectrum.

Table 14.1 Electron binding energies of $Fe_{82}Si_4B_{14}$ core levels and width (HWHM) (in brackets), eV

$Fe_{82}Si_4B_{14}$	Fe $2p_{3/2}$	O 1s	Si $2p$	B 1s	C 1s	N 1s
Initial sample state	710.3 (3.2)	529.7 (1.6) 531.6 (1.8)	98.5 (2.8) 101.6 (1.8)	191.3 (2.0) 187.2 (1.6)	284.4 (1.4) 285.7 (1.4) 287.4 (1.4) 288.3 (1.4)	399.4 (1.2)
After first ion beam sputtering	706.6 (1.3) 707.7 (1.3) 709.0 (1.8) 711.0 (1.8)	530.6 (2.0)	98.6 (1.3) 101.6 (2.0)	187.2 (1.0)	282.8 (1.2) 284.1 (1.4) 285.6 (1.4) 288.0 (1.4)	
After second ion beam sputtering	706.6 (1.3) 707.7 (1.3) 709.0 (1.8) 711.1 (1.8)	530.4 (2.0)	98.5 (1.4) 101.4 (2.8)	187.2 (1.0)	282.7 (1.2) 284.0 (1.4) 285.8 (1.4) 288.5 (1.4)	
Fe [34]	706.9					
FeB [34]	707.4			187.9		
FeB_2 [34]	707.3					
FeO [34]	709.6	529.8				
Fe_3O_4 [34]	710.8					
Fe_2O_3 [34]	710.9	530.1				
Si [34]			99.4			
SiC *alpha* [34]			100.4		282.5	
SiO_2 [34]			103.5			
B [34]				186.5		
B_2O_3 [34]		533.2		193.6		

The analysis of X-ray photoelectron spectra of AMA $Fe_{82}Si_4B_{14}$ showed the presence of silicon oxides on the surface with demonstration of considerable decrease of respective spectra intensities after first ion beam sputtering. At the same time, the intensities of peaks related to unoxidized state of silicon increase (Fig. 14.6). This fact is in good agreement with results of work [34] (where on the surface of $Fe_{83}Si_2B_{15}$ X-ray photoelectron spectroscopy lines of Si 2*p* show the presence of oxides in the region lower than 100 Å, and the presence of unoxidized state was observed below depth of 60 Å). The line Si 2*p* of the sample in the initial state and after sputtering has almost the same energy of about of 98.5 eV, however, line width was significantly larger before sputtering (2.8 eV), which demonstrates the large amount of nonequivalent positions of silicon atoms.

Intensities of X-ray spectra lines of elements acquired under the same conditions after two ion argon sputtering steps are considerably different, demonstrating the increase of iron concentration and decrease of concentrations of carbon and oxygen. However, for intensities of Si 2*p* lines the intensity did not changed both for the first and the second sputtering steps indicating considerable surface segregation of silicon with retaining its concentration over the film depth. One of the possible segregation mechanisms in Fe-Si-B alloys is described above for the case of AMA $Fe_{77}Si_8B_{15}$. The process of fast quenching is accompanied by formation of different phases such as α-Fe(Si) solid solution, Fe_2B compound and growth of amorphous surface layer of α-Fe due to atomic diffusion process. Notably, the Fe-Si distance is larger than the one for Fe-B and close to Fe-Fe. Therefore, diffusion results in atoms substitution of silicon for iron during crystallization.

The oxygen line of initial sample is characterized by two peaks indicating the presence of considerable amount of oxygen in different states. The intensities of X-ray photoelectron lines of oxygen decreased substantially after two subsequent ion beam sputtering (Fig. 14.6 and Table 14.1).

The remarkable thing is that after considerably long-term sputtering (over 30 min) the carbon and oxygen lines with low intensities were still observed, demonstrating that it is hardly to achieve unoxidizability of elements under specified technological conditions of amorphous tapes production.

As it can be seen in Fig. 14.6, on B 1s X-ray photoelectron spectra there is the peak referred to boron nitride, which shows intensity decrease after ion beam sputtering. The presence of boron nitride on the surface is possibly caused by production technology. Boron X-ray photoelectron spectra obtained after ion beam sputtering shows good solubility of boron atoms in the compound structure. The intensities of peaks increase. The process of structural relaxation is characterized by significantly larger atoms redistribution of boron compared to iron and silicon. The nanostructure of sample surface is represented by close packing structure of α-Fe (Si) nanocrystalline grains within amorphous matrix of iron boride.

As it can be seen in Fig. 14.6 the energy position of Fe $2p_{3/2}$ line for the sample in the initial state is of 710.3 eV, whereas after sputtering the peak Fe $2p_{3/2}$ shifts to 3.7 eV and decreases to 706.6 eV. This can be explained by Fe_3O_4 formation at the surface in initial sample state with peak energy of 710.8 eV [34].

The Fe $2p_{3/2}$ line after 1-st and 2-st sample sputtering consists of several components (Fig. 14.7). Decomposition of iron spectrum indicates the presence of the following phases: FeB and FeB_2 (707.7 eV), FeO (709.0 eV), Fe_2O_3 and Fe_3O_4 (711.0 eV). The formation of amorphous α-Fe(Si) layer on the surface occurs as a result of both atomic diffusion at short distances and merging of single nanoclusters.

The distance between Fe $2p_{3/2}$ and Fe $2p_{1/2}$ peaks in studied amorphous metallic alloy is 13.2 eV and for pure iron it is 13.1 eV [34].

14.3.3 The Determination of Quantitative Composition of AMA Alloys Surface According to XPS Data

Using the XPS method the integral quantitative evaluation of surface composition was carried out by method described in [35, 36]. The atomic concentration ratio of investigated elements was calculated according to the formula:

$$\frac{C_1}{C_2} - \frac{I_1}{I_2} / \frac{S_1}{S_2},$$

where C_1—is the atomic concentration, I_1—is the integral intensity of X-ray line, S_1—is the element sensitivity coefficient of 1st element. The S_1/S_2 ratio was obtained according to the formula [35]:

$$\frac{S_1}{S_2} = \frac{T_1 \sigma_1 \lambda_1}{T_2 \sigma_2 \lambda_2}.$$

where T_1—is transmission coefficient of spectrometer, σ_1—is the photoionization cross section, λ_1—is the photoelectron escape depth for particular atomic level of 1-th element. In the calculation σ_1 was taken according to work [37]. It was suggested that $\lambda \sim (E_k)^{1/2}$, since for all analyzed lines $E_k > 150$ eV [35]. For composition analysis widely separated by its energies the lines Fe $2p_{3/2}$ and B 1s were used, therefore one could not neglect T_1/T_2 ratio. It is technically complicated task to obtain in the general form the function $T = f(E_k)$ in the whole range of its definition. The possibly used method for that is described in work [38], which involves a measurement of elastically reflected electrons on the copper sample in the selected ranges of energy and angles using moveable semispherical analyzer with attested transmission dependency on energy. However, it is not easy to implement in practice. Consequently, in this work considerably easier and sufficiently effective method for getting the ratio of function values on two particular energies was used. For determination of first unknown coefficient n in the dependency $T \sim (E_k)^n$ the ratios I(Fe $2p_{3/2}$)/I(Fe $3p$) and I(Co $2p_{3/2}$)/I(Co $3p$) were determined, which were acquired at pure crystalline Fe and Co after ion sputtering of surface by Ar^+ during 30 min.

Table 14.2 Surface composition of crystalline FeB, Fe_2B, and amorphous $Fe_{75}B_{25}$, $Fe_{85}B_{15}$ and $Fe_{82}Si_4B_{14}$ alloys after ion sputtering for 60 min

Composition	C_{Fe}, at.%	C_B, at.%
FeB	48.7	51.3
Fe_2B	67.6	32.4
$Fe_{75}B_{25}$	73.8	26.2
$Fe_{85}B_{15}$	87.0	13.0
$Fe_{82}Si_4B_{14}$	84.0	12.0

The Table 14.2 contains data of surface composition of crystalline FeB, Fe_2B and amorphous $Fe_{75}B_{25}$, $Fe_{85}B_{15}$ and $Fe_{82}Si_4B_{14}$ alloys after ion sputtering for 60 min, obtained by means of found ratio of elements sensibility factor.

According to the submitted table it can be seen that for AMA $Fe_{82}Si_4B_{14}$, as it was mentioned before, the correspondence of silicon concentration to alloy formula is observed.

14.3.4 The Impact of the Second Transition Metal Concentration on Bound Energy of Core Levels in AMA Fe-B

Doping of AMA systems Fe-B with cobalt causes significant shifts of core levels. In amorphous alloys Fe-Co-B systems substitution of Co for Fe leads to decrease of bound energy of B 1s electrons when Co concentration is increased, which attains 0.5 eV for complete substitution of cobalt atoms. Thereby, the increase of Fe $2p_{3/2}$ energy and the decrease of Co $2p_{3/2}$ energy are observed with the lowering of Co proportion. It was noted that Fe $2p_{3/2}$, Co $2p_{3/2}$ bond energies increases in amorphous alloys for all compositions with respect to pure elements.

Comparing Fe $2p_{3/2}$ and Co $2p_{3/2}$ bound energy dependencies for glasses of Fe-Co-B systems and those for Fe $2p_{3/2}$, Ni $2p_{3/2}$ [39], for amorphous alloys of Fe-Ni-Si-B systems shows the similar character of Fe $2p_{3/2}$ and (transition metal $2p_{3/2}$) bound energy changes with respect to concentration of transition metal (TM) = Co, Ni.

As a result, it can be stated that the changes character of bound energies of $2p_{3/2}$ electrons of Fe, Co, Ni and 1s electrons of B in concentration sets of amorphous alloys in Fe-Co-B, Fe-Co-Si-B and Fe-Ni-Si-B systems is analogous. Substitution of part of B atoms for Si in amorphous Fe-Co-B alloy does not influence the B 1s bound energy behavior, which is the evidence of that boron atoms have only atoms of transition metal in their first coordination sphere. The behaviors of Fe $2p_{3/2}$, TM $2p_{3/2}$, B 1s and Si 2s bound energies in amorphous alloys of Fe-TM-B-Si do not depend on the kind of second transition element TM = Co, Ni and increase monotonically on its concentration increase.

It is noteworthy that B 1s electron bound energy is more sensible to the sort of transition metal TM = Fe, Co, Ni in comparison to the energy for Fe $2p_{3/2}$, Co $2p_{3/2}$

and Ni $2p_{3/2}$, which points at the presence of large shift of B 1s bound energy. The energy shift values of B 1s electrons in crystalline Fe-Co-B AMA compared to amorphous alloys are significantly larger than those for Fe $2p_{3/2}$ and Co $2p_{3/2}$ electrons. This is the evidence of that the character of nearest neighborhood of boron atom (coordination number and coordination sphere radius) is more sensitive to the transition of alloy from amorphous to crystalline state than this of iron and cobalt atoms.

14.3.5 Multielectron Effects in Amorphous Alloys

One of the multielectron properties display is asymmetry of core electron levels of metals. Asymmetry parameter contains information about partial electronic density of states of particular atom in alloy near Fermi level [40].

Asymmetry parameters of core Fe $2p_{3/2}$ and Co $2p_{3/2}$ levels are submitted in Table 14.3.

It can be seen in the previously mentioned data that asymmetry of Co $2p_{3/2}$ electron level increases when Fe concentration decreases, whereas asymmetry of Fe $2p_{3/2}$ electronic level increases, which indicates the decrease and the increase of electronic density at Fermi level in the places taken by Co and Fe atoms respectively.

14.3.6 The Peculiarities of Chemical Bounds in the Amorphous Alloys of Fe-Co-B System According to the XPS Data

The observed changes in electronic structure of AMA Fe-Co-B system are apparently connected with changes in the structure of close atomic neighborhood of alloy, primarily of boron atoms, which take place when concentration of Co atoms is changed.

In the investigated amorphous alloys the decrease and the increase of asymmetry parameters of Co $2p_{3/2}$ and Fe $2p_{3/2}$ levels respectively are observed, which is the evidence of the decrease of partial electronic contribution of irons *d*-electrons and of this increase of cobalt's *d*-electrons in total densities of states at Fermi level. Therefore, with the increase of Co atoms concentration in the investigated compounds the "outflow" of *d*-density of Co towards Co-B bond happens, which indicates that B-Co bonds are more preferable than Fe-B ones.

Table 14.3 Asymmetry parameters of core Fe $2p_{3/2}$ and Co $2p_{3/2}$ levels

Composition	Asymmetry Parameters	
	Co $2p_{3/2}$	Fe $2p_{3/2}$
Fe	–	1.9
Co	1.7	–
Fe_{70} $Co_{15}B_{15}$	1.4	2.2
Fe_{60} $Co_{25}B_{15}$	1.3	2.6

Consequently, according to obtained data, it can be asserted that the priority of boron interaction with TM in AMA increases in the row Fe-Co-Ni.

The another separated issue is connected with the state of charge electronic density of the above mentioned compounds. One of the groups of scientists has extreme position: either the model of charge transfer [41–45] or the model of covalent bond [46–51] can be applied. Another way of experiment and calculation results interpretation is to use both of these models [52–54]. Almost all authors have the common vision that there is no significant charge transfer, which is about 1 *electron/atom* from metal atom to TM. Therefore, experimental end theoretical literature data on charge transfer in amorphous systems TM-B are contradictory.

The analysis of the assembly of obtained in this study X-ray electron data confirmed the absence of the direct charge transfer. The observed core levels and valance band shifts in concentration sets can be explained by spatial redistribution of electron density. It is obvious that the decrease of charge density at boron atoms leads to the increase in bound energy of B 1s level. However, after consideration of experimental data of the increase of Fe atoms concentration the increase of boron *s*- and *p*- bound energies is observed, which is the consequence of the increase of *d*-electrons localization in TM bond, which leads to the increase of boron atoms "screening" and as a consequence, to the increase of portion of covalent constituent in TM-B bond.

14.4 Subroughness and Morphological Features of the Surface Amorphous Alloy $Fe_{82}Si_4B_{14}$ by Thermal Treatment

Subroughness can be evaluated by the precise methods and techniques for studying surfaces, such as atomic resolution scanning tunneling and atomic force microscopies. Subroughness is formed by surface inhomogeneities with a characteristic size of nanometer order, with height up to 100 nm and lateral size up to 1000 nm. Subroughness nature is determined by the internal structure of the solid-state, its defects and also by interaction processes of surface with the environment (oxidation, adsorption).

Subroughness relates to a solid body nano-geometry and defines its most important performance properties, particularly, such as friction resistance, strength, joints efficiency and tightness, chemical resistance, etc. The initial subroughness is a consequence of the technological process of producing amorphous alloys.

When heating the original roughness parameters tend to vary. There can be several reasons; first of all the relaxation processes in the amorphous sample is accompanied by cluster growth processes and transformations. Meanwhile, elements segregation processes occurs towards the surface, leading to the chemical composition inhomogeneity, this results in changes in electronic structure and surface properties.

Amorphous metal alloys have been studying thoroughly for a long time, however, the topic is still not fully explored and quite interesting. A variety of articles is written on investigated series of alloys, in particular, [55–58]. Here we discussed the results of studies of roughness, morphological features and electronic structure of AMA $Fe_{82}Si_4B_{14}$ after heat treatment in a wide range of temperatures—from room temperature (RT) to 700 °C. Experiment was carried out by high-vacuum methods of tunneling microscopy and atomic resolution spectroscopy.

In Fig. 14.8 the surface STM images of AMA $Fe_{82}Si_4B_{14}$ at temperatures of 350, 375, 400, 425, 450, 475 °C is depicted.

As seen from Fig. 14.8, the surface image at 400 °C is determined by increased particles size. However, with temperature growth the average particles size decreases, and a significant broadening of spatial parameters is observed. Considering that the disintegration of the particles is unlikely, the particle size reduction can be explained by surface segregation of small clusters up to ~5 nm.

Based on information from Fig. 14.8 and Table 14.4, it can be argued that in the temperature range up to 475 °C a monotonic increase of R_z parameter (the maximum difference between the peaks and valleys at ten points) on retention of the values of R_a (absolute values of deviations from arithmetic average) and R_q (root mean square value of deviation profile) parameters, with some exceptions at temperature about 400 °C, is observed. Apparently, there is a substantial increase of the cluster size with general growth tendency for R_z parameter. The temperature of 400 °C for a given alloy is one of the steps of surface morphological transformations.

STM images for temperatures up to 475 °C show typical uniform field without special features. However, the temperature of 475 °C has a number of features, which is depicted in Fig. 14.9.

There clusters with significant size up to 20 nm are observed, the average cluster size across the field image is about 3 nm. Further detailed investigation showed that large clusters formed by coalescence of small ones with an average size of about 3 nm. The height of large clusters is negligible in comparison with the topographic dimensions and is approximately 3 nm (Fig. 14.10a).

The formation nature of large clusters is still unknown. We can assume that with increasing temperature the behavior of small clusters is similar to liquid drops, which tend to form massive clusters in order to reduce energy of the cluster. Hence, increasing of clusters kinetic energy, which is their mobility, leads to coagulation and coalescence of small to large clusters. This thesis is even further confirmed if we consider the surface snapshot at temperature of 500 °C. Observed massive clusters consist of small separated by the distinct boundary. At that, recesses value is also about 3 nm, which can be seen in Fig. 14.10b.

It should be noted that intense relaxation processes in the amorphous alloy is observed at 500 °C. As it is shown in Table 14.4, there is a significant parameters jump in arithmetic average of the absolute deviation profile, arithmetic average of the absolute deviation, standard deviation, the absolute amount of the average value and the maximum difference between the peaks and valleys. STM image of surface reveals specific morphological features compared with images at lower

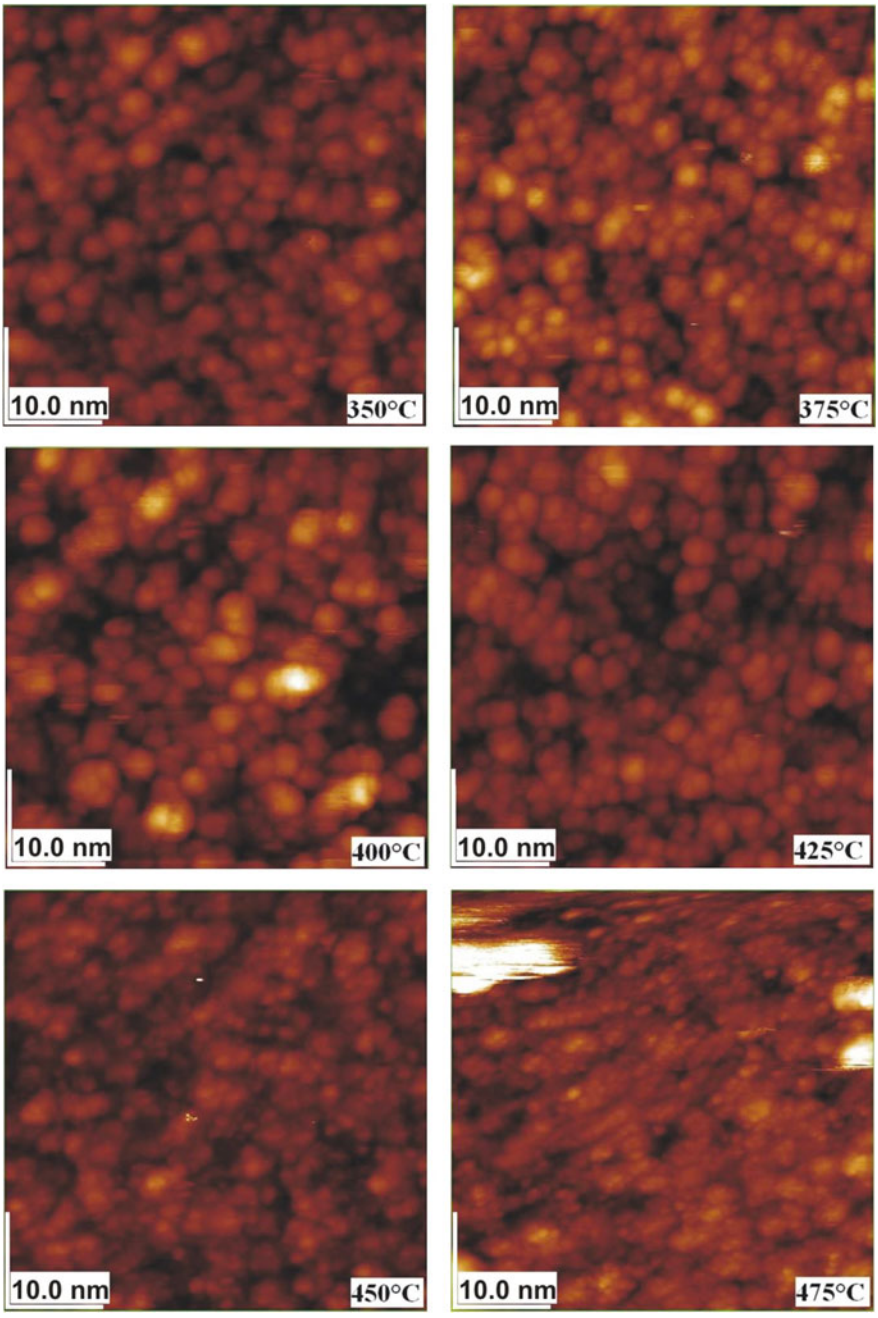

Fig. 14.8 STM—$Fe_{82}Si_4B_{14}$ images at different heating temperatures

Table 14.4 Change of the roughness parameters over heating temperature of $Fe_{82}Si_4B_{14}$ amorphous tape

T, °C	R_a, nm	R_q, nm	R_{zjis}, nm	R_z, nm	S_{ratio}
350	0.208	0.268	2.18	2.88	1.13
375	0.224	0.291	2.65	3.08	1.14
400	0.333	0.423	2.67	3.04	1.14
425	0.222	0.277	2.30	3.15	1.09
450	0.204	0.261	3.20	4.42	1.09
475	0.200	0.252	2.23	4.21	1.09
500	0.544	0.686	4.60	5.27	1.16
550	0.503	0.640	3.94	4.42	1.15
600	0.190	0.242	1.59	1.73	1.05
700	0.532	0.655	3.87	4.40	1.06

temperatures. Formation of regular shaped nanostructures on the amorphous alloy surface is a rather interesting experimental fact, which is quite difficult to predict. Most likely there is a far from equilibrium state, where formation of needle-like nanocrystals is possible. The noteworthy fact is that at 500 °C nanorods formation with lengths of ~90 nm, widths of ~20 nm and heights about 12 nm occurred, which we can see in Figs. 14.2 and 14.5, respectively (Fig. 14.10c).

Further increase of annealing temperature up to 550 °C leads to growth of the cluster average size (Fig. 14.9), and some moderate decrease of parameters R_a, R_q, R_{zjis} and R_z (Table 14.4). However, further temperature increase up to 600 °C leads to a significant reduction of roughness characterizing parameters.

The decrease of roughness parameters values can obviously be explained by influence of crystallization, resulting in the smoothing of crystal grains surface, which takes place at nanoscale level. Roughness parameters R_a, R_q, R_{zjis}, R_z and S_{ratio} are presented in Table 14.4 and those in the form of graphic interpretation are in Fig. 14.11.

Quite interesting feature of nanorelief formation at 700 °C is appearing of the terraced structures (with the following characteristic sizes: lengths of ~200 nm, 120 nm widths and heights of about 20 nm) is shown in Fig. 14.12.

Some terraces steps are flat over a large area. Such formations describe the crystal development process at 700 °C. Extremely large crystals over 200 nm at 700 °C indicates on the state of crystallization process was almost completed.

14.5 STM Spectroscopy of AMA $Fe_{82}Si_4B_{14}$ During Thermal Treatment

STM spectroscopy spectra (*dI/dV* spectra) of the clusters of AMA $Fe_{82}Si_4B_{14}$ surface were obtained for specimens annealed at 350 and 400 °C with a cluster size of about 5.0 nm. Analysis of the electron density of states for clusters in points 1 and 2 shows a significant similarity. The peaks in filled states up to 3.0 eV

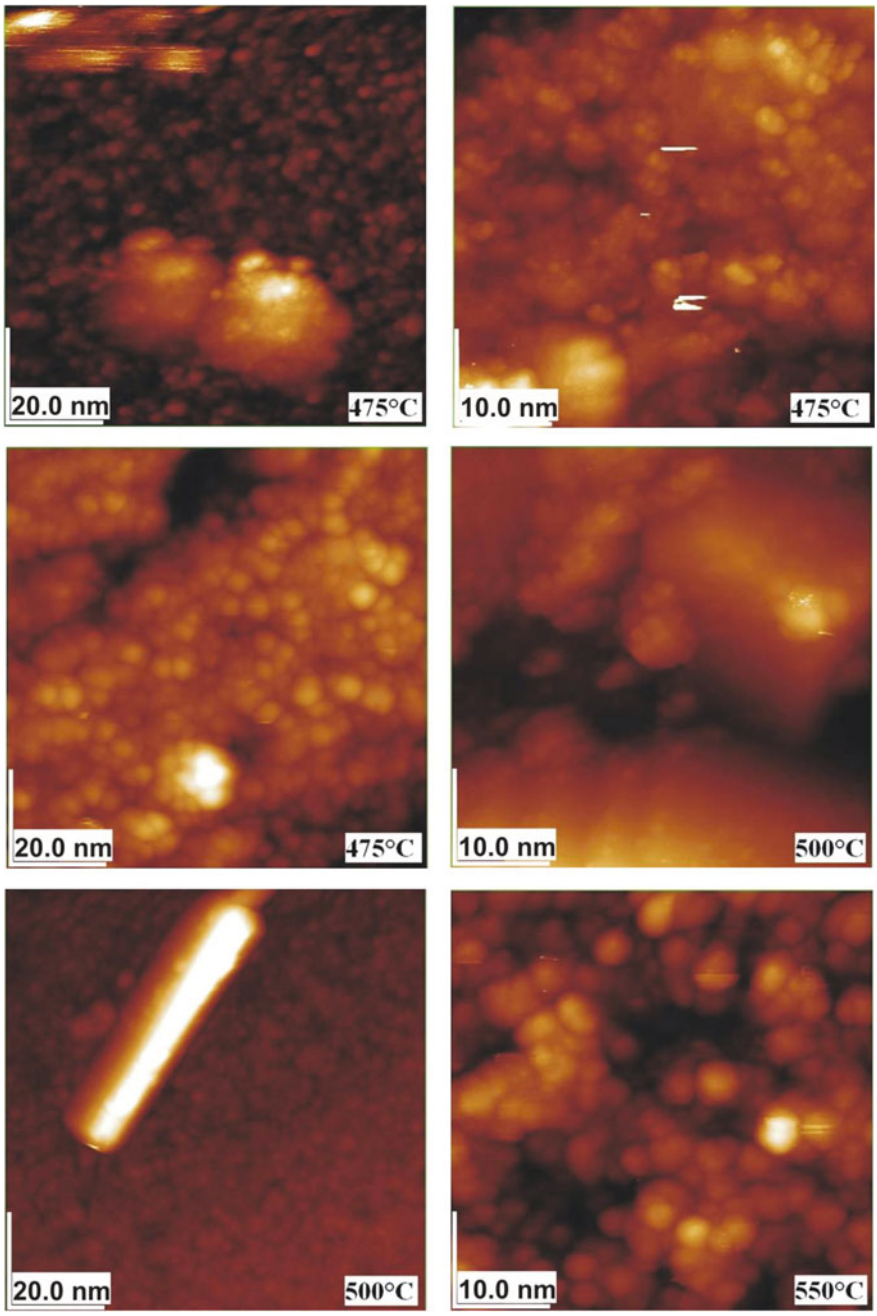

Fig. 14.9 STM images of $Fe_{82}Si_4B_{14}$ annealed at temperatures 475–550 °C

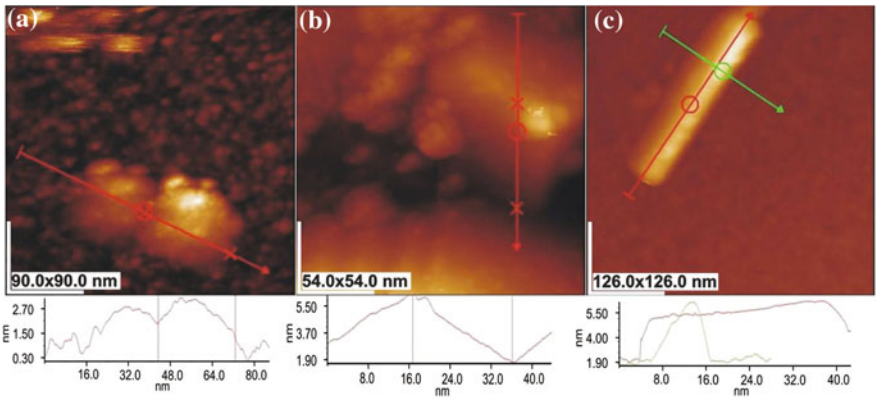

Fig. 14.10 STM images of AMA $Fe_{82}Si_4B_{14}$ surface after annealing at temperatures of (**a**) 475 °C, **b** 500 °C, **c** nanorods at surface annealed at 500 °C

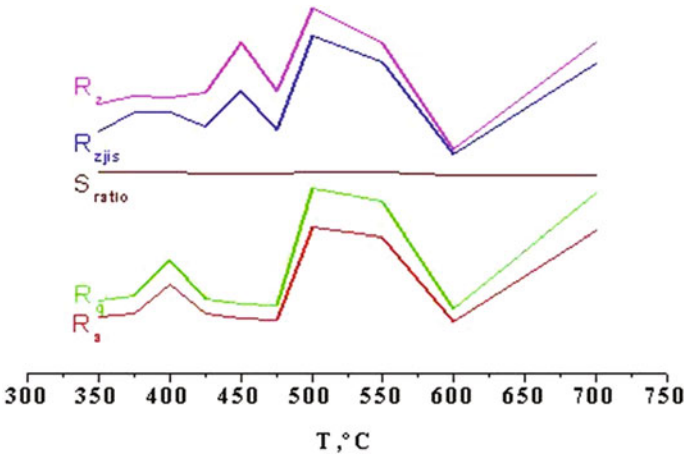

Fig. 14.11 Parameters dependencies of R_a, R_q, R_{zjis} R_z on over the sample annealing temperature

(Fig. 14.13) were determined by the 3*d* states of iron. The presence of two features at approximately 2.5 eV and low-energy peak at ~1.8 eV indicates on splitting and, therefore, on hybridization of 3*d* states of iron with *p*-states of silicon or boron (Fig. 14.13). In the presented spectra valence band local maxima and unfilled state are clearly visible. It is remarkable that major peaks in the regions of unfilled and filled states are localized for different clusters in identical energy areas. The major peak in the unfilled states area is ~2.5 eV for both clusters. Similar shape of the curves of the electron density of states for presented clusters indicates the presence of the same chemical composition. For the studied clusters, the intensities redistribution of the main features of the spectra is observed. While maintaining the

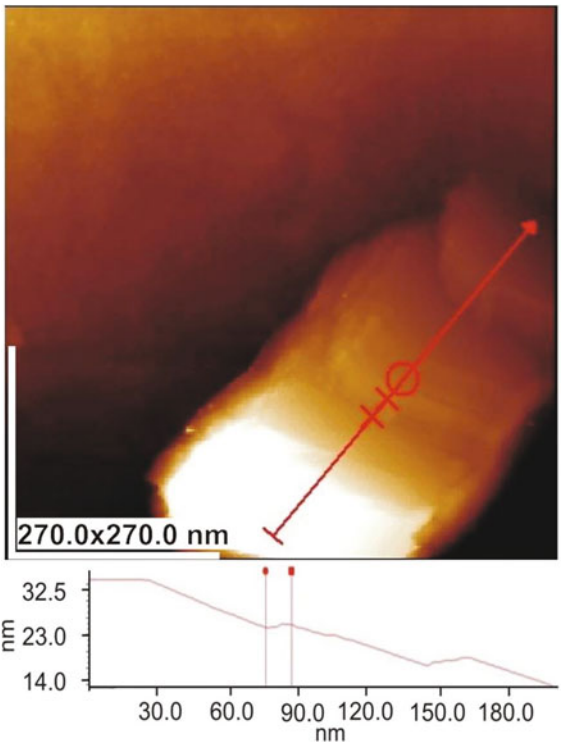

Fig. 14.12 STM image of nanorelief formation at AMA surface of AMA $Fe_{82}Si_4B_{14}$ annealed at temperature 700 °C

energy position of the features the redistribution of the intensities between the filled and unfilled states occurs. This behavior is most likely caused by decrease of the electron density of states in the valence band of 1 cluster. The physical nature of this behavior can be determined by different iron concentration of the clusters.

As it is seen from Table 14.4, the sample annealing to 400 °C leads to significant changes of all roughness parameters. Changes in morphological features of the surface also arise at nanoscale level. Described in Sect. 14.3 the metamorphoses of surface clusters take place. Surface segregation of light elements to the surface of the material leads to revealing of these effects. It should be mentioned that for the composition of AMA $Fe_{82}Si_4B_{14}$ the 400 °C temperature for many hours annealing is the most characteristic for intensive crystallization of amorphous alloy. However, is not observable, clearly formed crystals, and approximately zero electron density of states near Fermi level indicates that the formation of clusters by a mechanism is close to the mechanism of formation of molecular orbitals.

Subsequent annealing of sample up to temperature of 425 °C (Fig. 14.14) does not lead to change of cluster sizes and there are no significant changes in the electron density of states for such clusters. The main peak of electron density of filled states is shifted about 0.5 eV to higher binding energy. The main maximum of unfilled states remains to be localized in the same range. This fact may be attested

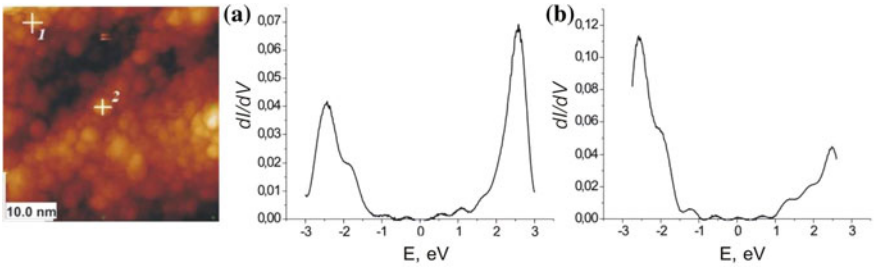

Fig. 14.13 STM image of the surface and tunneling spectra of AMA $Fe_{82}Si_4B_{14}$ annealed at 400 °C, **a** *dI/dV* spectrum acquired at the point 1; **b** *dI/dV* spectrum acquired at the point 2

by extension of formation of crystals process and violation of the molecular mechanism principle of cluster formation.

Taking into account the preservation of the average cluster size after annealing, the increase of number of maxima of the *dI/dV* spectra indicates an intense process of crystallization within clusters and quasicrystals formation.

Interesting case appears for the tunneling spectra acquired in the intercluster region (Fig. 14.15). Based on the analysis these spectra, one can argue that intercluster region has approximately the same local chemical composition as clusters have. Most of the obtained *dI/dV* spectra indicate that intercluster region significantly closer to the alpha iron phase.

The formation of stable spherical clusters based on Fe-Si or Fe-B apparently happens at the step of superfast cooling of the melt by the preference of Fe-Si and Fe-B bound mechanism over Fe-Fe one, however, not of segregation of light elements during the structural relaxation. This conclusion can be confirmed by the presence of similar clusters in the initial amorphous alloy.

Further annealing of sample up to temperature 475 °C does not lead to qualitative changes in the conductivity of individual clusters, as evidenced by recorded spectra for intercluster areas, and for the individual clusters (Fig. 14.16).

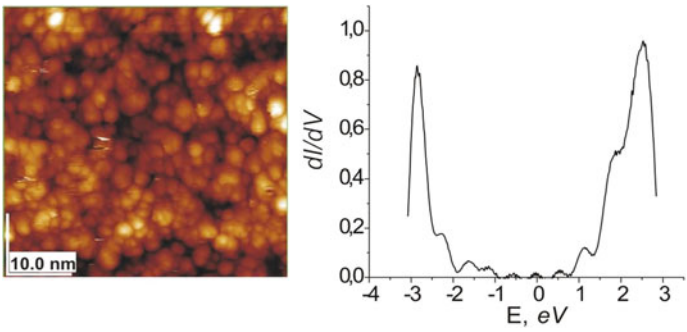

Fig. 14.14 STM image of AMA $Fe_{82}Si_4B_{14}$ surface annealed at 425 °C and *dI/dV* spectrum acquired in the upper left corner of the image

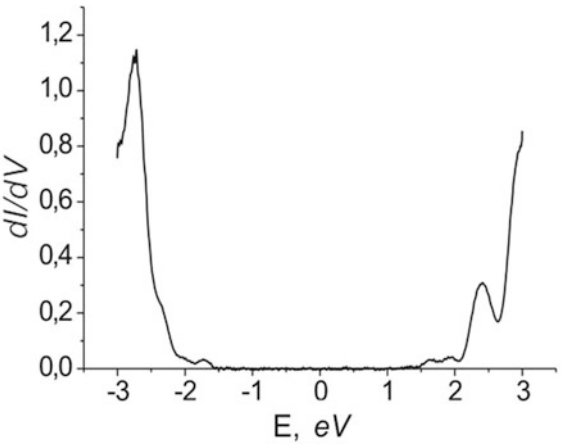

Fig. 14.15 *dI/dV* spectra acquired at intercluster area

Most typical changes were observed after annealing at temperature above 500 °C. At 500 °C surface obtains a completely another look (Fig. 14.16a). As a result, clusters agglomeration of bulk particles is observed. Obtained for the three different points, *dI/dV* spectra have similar nature prompting suggestions about some homogeneity of surface layer with small fluctuations in the phase composition of the sample.

Annealing at 550 °C does not introduce any special changes in the electronic structure of different size clusters, as may be seen in Fig. 14.16b. Therefore, one can see the differential *dI/dV* spectra have a typical for conductors clearly defined. The similar shape of curves for two different clusters (Fig. 14.16a, b) allows to conclude that the sample at a given temperature obtains a surface characteristic mainly for conductors with small concentrations of silicon and boron.

The similar picture can be observed for a samples annealed at temperatures of 600 and 700 °C (Fig. 14.16c, d). Thus, for different acquiring points there are spectra inherent both for metallic conductivity and for low impurities.

Basing on the analysis of the spectra of electronic states, it can be concluded that the crystallization process starts at temperature of 350 °C and continues up to 550 °C. Further temperature increase does not lead to significant changes in curves of the electron density of states.

14.6 EXAFS—Research of AMA Based on Iron

One of the important factors that affects substance properties is its structural state. Consideration of physical models and organization principles of disordered metallic systems allows us to formulate a number of general concepts, the validity of which can be experimentally proved in the research of actually synthesized AMA. At the same time, in terms of the structural self-similarity, invariance for disordered metal

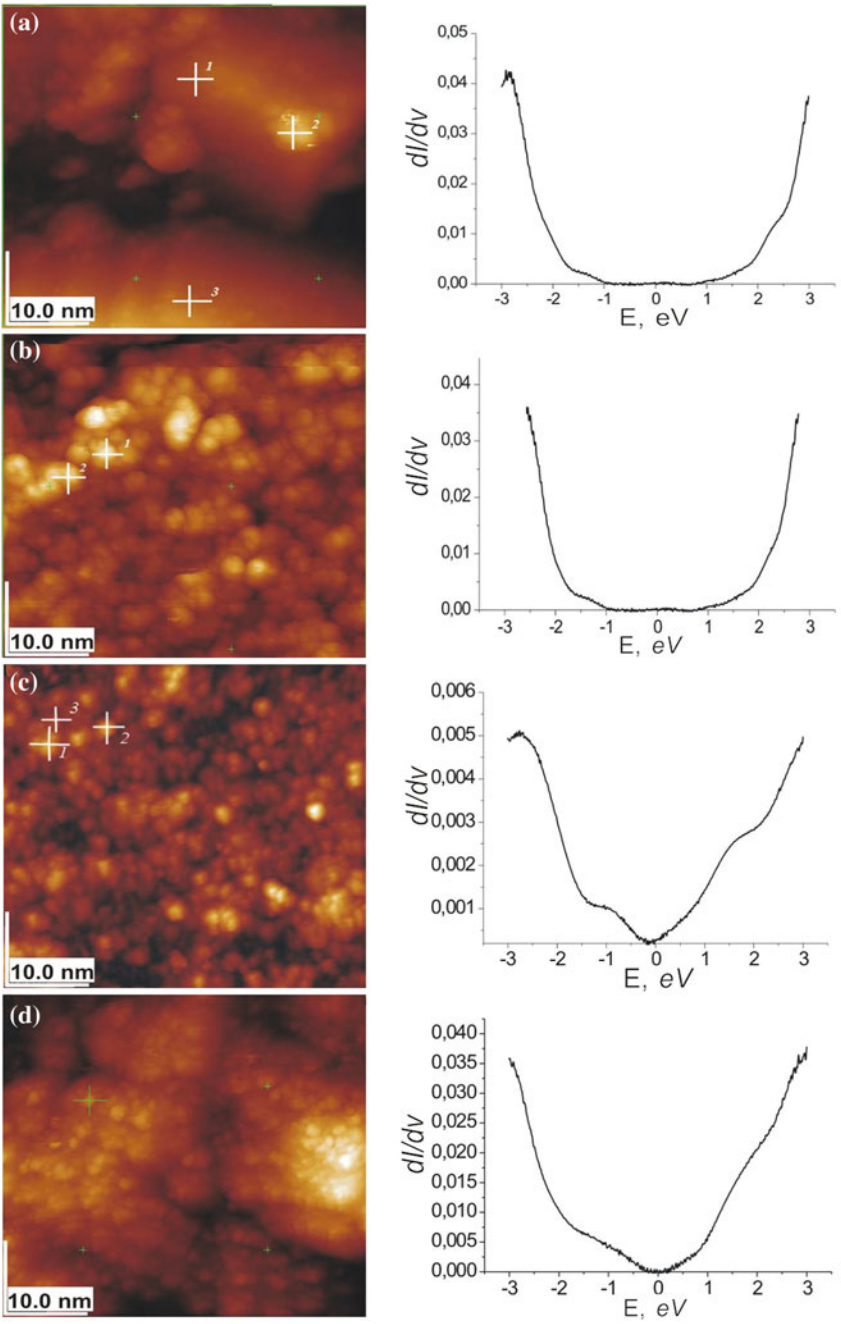

Fig. 14.16 **a** STM image of $Fe_{82}Si_4B_{14}$ surface (annealed at 500 °C) and 3 specific *dI/dV* spectra for different points, **b** STM image surface of $Fe_{82}Si_4B_{14}$ (annealed at 550 °C) and 2 specific *dI/dV* spectra for different points, **c** STM image and 3 specific *dI/dV* spectra characteristic for different points, **d** STM picture surface of $Fe_{82}Si_4B_{14}$ (annealed at 700 °C) and specific *dI/dV* spectra

structures is accomplished by multiple sets of such cases where the real picture of the experiment is realized. Methodology development for studying properties and synthesis of AMA has led to significant progress in the immense field and formation of research interest in physics of disordered metallic systems.

AMAs are complex objects, formation conditions, stability, physical and chemical properties of which are determined by various factors. Therefore, applying methods for an adequate strict description for the real material should take into account the factors diversity that have influences on properties. In this sense, method of Extended X-ray Absorption Fine Structure (EXAFS) spectroscopy is one of the most important instruments for structure research of disordered metallic systems.

Today, EXAFS—spectroscopy method is the most informative in the research of disordered systems and it is based on measurement of modulation of the absorption coefficient of X-rays for energies about 100 − 1000 eV above the *K*- or *L*—absorption edge of the investigated atom. Analysis of EXAFS spectrum provides information about structural parameters, allows to specify interatomic distances and coordination numbers of atoms surrounded by given chemical element. The uniqueness of EXAFS—spectroscopy method is due to it gives the opportunity to explore local atomic environment for atoms independently of each class, which distinguishes it from other methods in structural research of disordered materials and, in particular, amorphous metal alloys.

Among these amorphous metal alloys particularly are highlighted two subgroups that have the widest practical use: Fe-based, characterized by the maximum saturation induction, and Co-based, which have a vanishingly small magnetostriction, resulting in maximum sensitivity and minimum losses.

The aim of presented research was investigation of the changes in SRO in amorphous alloys based on Fe-B with various metals and metalloid doping.

14.6.1 Alloys of Fe-Co-B

For the system Fe-Co-B absorption *K*—edges of iron and cobalt was investigated for the following compositions: $Fe_{73}Co_{12}B_{15}$, $Fe_{68}Co_{17}B_{15}$, $Fe_{64}Co_{21}B_{15}$, $Fe_{60}Co_{25}B_{15}$ and iron absorption *K*—edge for AMA $Fe_{85}B_{15}$.

Within a model of micro inhomogeneous structure of AMA, for all investigated AMA one can assume the presence of at least two types of areas: depleted boron and consisting essentially of metal atoms (solid solution of Co in the α-Fe) and regions enriched with boron and characterized by SRO at orthorhombic type boride $(Fe,Co)_3B$. Therefore, alloying of iron-based AMC by cobalt (in the represented work the concentration range is from 12 to 25 at. %) should not lead to a significant change in the topological SRO.

The Table 14.5 presents the position and intensity of Fourier transforms (FT) obtained from both metal components of AMA. As expected, except for the

Table 14.5 The main peak position of Fourier transforms of iron and cobalt in amorphous alloys

Composition	R_{Fe}, Å	R_{Co}, Å
$Fe_{85}B_{15}$	2.0647	–
$Fe_{73}Co_{12}B_{15}$	2.0757	2.4392
$Fe_{68}Co_{17}B_{15}$	2.0744	2.4076
$Fe_{68}Co_{21}B_{15}$	2.0975	2.4184
$Fe_{60}Co_{25}B_{15}$	2.0805	2.4242

alloy with 21 at. % Co, the cobalt alloying has no significant effect on neither FT peak position nor its intensity.

Figure 14.17 and 14.18 show the FT for *K*—absorption edge of Fe and Co of studied AMA. For all AMA position of the first peak of radial distribution function (RDF) of atoms around Fe atoms is shifted toward longer distances compared to the peak position of RDF around Co ones, so, the probability of the atomic arrangement at shorter distances around Co atoms is higher than around Fe ones.

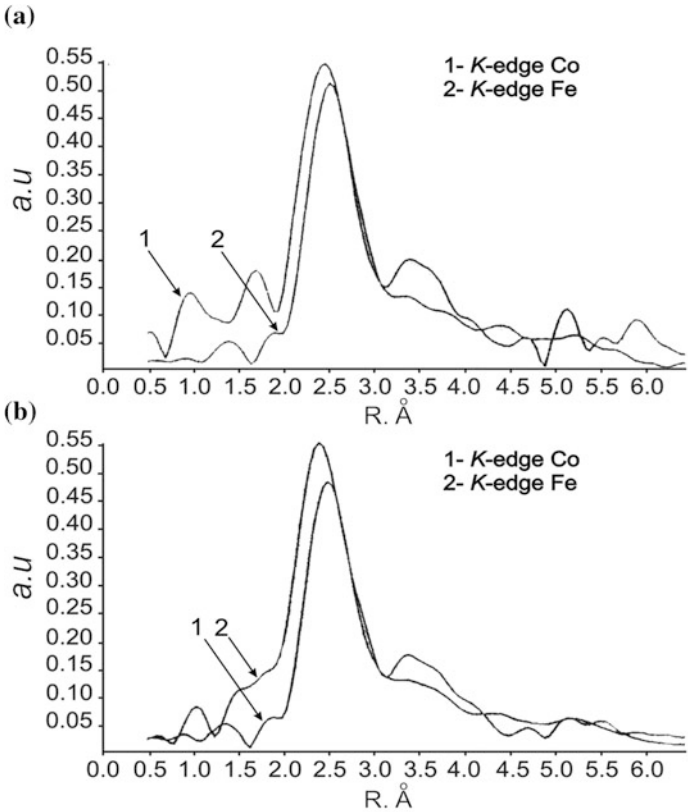

Fig. 14.17 The partial RDF around Fe and Co atoms for $Fe_{73}Co_{12}B_{15}$ AMC (**a**) and AMC $Fe_{68}Co_{17}B_{15}$ (**b**)

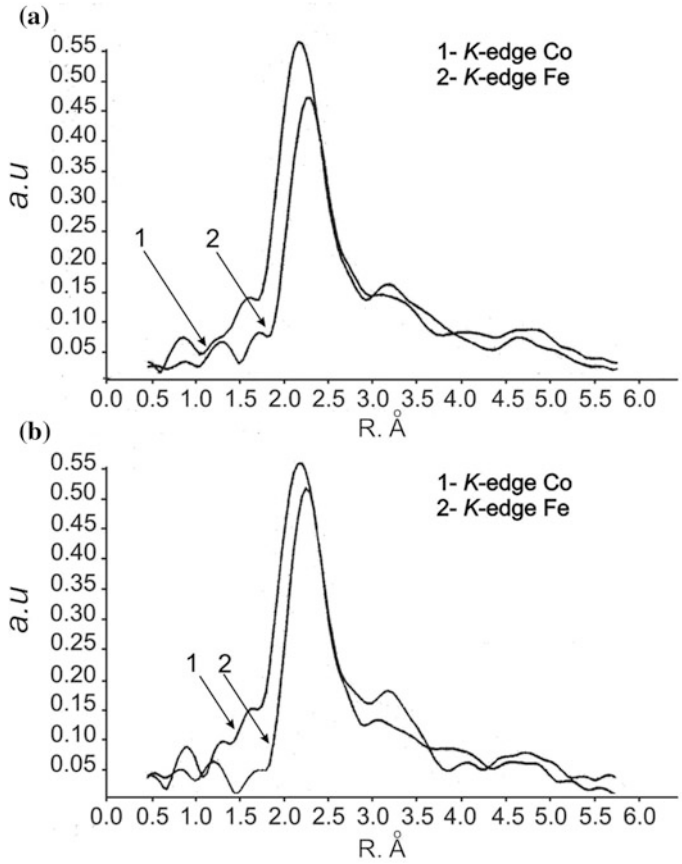

Fig. 14.18 Comparison of the partial RDF around Fe and Co atoms for $Fe_{64}Co_{21}B_{15}$ AMC (**a**) and AMC $Fe_{60}Co_{25}B_{15}$ (**b**)

This result may indicate a greater formation probability of microdomains with SRO according to the type of cobalt borides, compared with SRO according to the type of iron borides (especially since the enthalpy of formation of cobalt boride is lower than iron boride). As the shortest distance between atoms in the orthorhombic boride Co_3B slightly less than in orthorhombic boride Fe_3B, it may lead to the observed effect.

14.6.2 Fe-Cr-B Alloys

In the system Fe-Cr-B of AMA $Fe_{76.5}Cr_{8.5}B_{15}$, $Fe_{75}Cr_{10}B_{15}$, $Fe_{57.8}Cr_{27.2}B_{15}$, $Fe_{53}Cr_{32}B_{15}$ compositions were tested. According to [59], during crystallization of

AMA of Fe-Cr-B system solid solution on the basis of α-Fe and metastable boride $(Fe,Cr)_3B$ is formed. Chromium is randomly located in the α-phase and its concentration in the α-phase for AMC $Fe_{75}Cr_{10}B_{15}$ is 3-5 at. % (i.e., 2.3 times less than original concentration in the AMA). Thus, there is a depletion of α-phase and enrichment of the chromium boride $(Fe,Cr)_3B$.

According to the measurements of the resistance-temperature dependence [59], chromium alloying of Fe-based AMA increases the temperature of crystallization initiation, in other words, improves their thermal stability.

Thus, within microinhomogeneous structure model of AMA it can be assumed that AMA with content of Cr 8.5 at. % possibly have at least two types of microgroups: microregions depleted in boron and consisting essentially from atoms of metal (chromium solid solution in α-Fe or γ-Fe) and microdomains enriched with boron and is characterized by the type of SRO $(Fe,Cr)_3B$ and for AMA of 27.2 at. % chromium, microregions enriched with chromium type structure $(Fe,Cr)_2B$ may also be present.

In Fig. 14.19 the FT *K* absorption edges of Fe and Cr in AMA $Fe_{76.5}Cr_{8.5}B_{15}$ and $Fe_{57.8}Cr_{27.2}B_{15}$ are shown, and in Table 14.6 the positions and intensities of FT

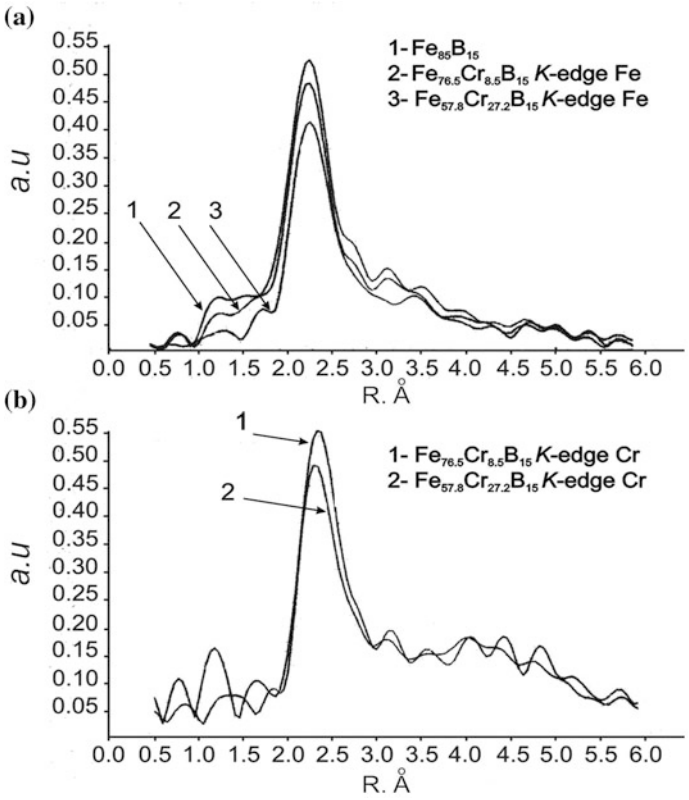

Fig. 14.19 Partial RDF of atoms around Fe (**a**) and Cr (**b**) in the studied AMA Fe-Cr-B system

Table 14.6 FT positions and intensities obtained from the two metal components (Fe and Cr) of amorphous alloys

Composition	$R_{Fe(1)}$, Å	$I_{Fe(1)}$	$R_{Cr(1)}$, Å	$I_{Cr(1)}$	R_{Fe}, Å	R_{Cr}, Å
$Fe_{85}B_{15}$	2.0647	0.2774	–	–	2.4926	–
$Fe_{75}Cr_{10}B_{15}$	2.0464	0.3211	2.0705	0.2383	2.4822	2.5646
$Fe_{53}Cr_{32}B_{15}$	2.0537	0.3371	2.0338	0.2057	2.4905	2.5222

peaks are represented. If to change in position of the first peak of FT of iron absorption *K*—edges than there is no correlation with the change in the concentration of chromium in the studied AMA, increasing the chromium content from 8.5 to 27.2 at. % leads to a significant shift towards lower distances of the first peak of FT of absorption chromium *K*—edges and some decrease in peak intensity. Apparently, this is due to the existence of microscopic regions with a different type of SRO in the AMA with a chromium content of 27.2 at. %.

In Fig. 14.20 at the partial RDF around iron atoms in the studied AMA the presence of the shoulder on the right slope of the first peak in the range of distances $r \sim 3.0 \div 3.1$ Å is clearly visible, wherein there is a clear correlation between intensity of this secondary peak (shoulder) and a change of the content of chromium in the alloy.

For partial RDF around the chromium atoms is also observed the presence of a small extension on the right slope of the first peak of RDF in the same distances, but with a reverse correlation between the intensity of this extension with chromium content in the alloys.

With increasing of annealing temperature lattice type change during crystallization of the metastable AMC boride occurs. Lattice space group $I\bar{4}$ changes into the lattice of the space group $P4_2/n$ and further into primitive lattice.

$$I\bar{4} \Rightarrow P4_2/n \Rightarrow P$$

Among different types of hypothetically possible SRO in this system, only for structure of the boride Fe_3B $P4_2/n$ shortest interatomic distances Metal–Metal exists in the range of values $r \sim 3.0 \div 3.2$ Å, where subordinate maximum is observed at the curves for these partial RDF of AMA.

Thus, it is not excluded that in studied AMA microregions besides the previously listed exists, with topological SRO for these three types.

Taking into account that chromium doping of iron-based AMA increases the temperature of crystallization initiation, it can be assumed that the addition of chromium increases preference of formation of SRO microareas with kind of more "high temperature" modification of boride $(Fe,Cr)_3B$ structure $P4_2/n$ in AMA.

On this assumption correlation between changes in the intensity of this subordinate peak (at $r \sim 3.0 \div 3.1$ Å) with changes in the concentration of chromium in the AMA can be explained. Since for AMA with chromium content of 8.5 at. %, SRO microregions with topological structure type of boride $P4_2/n$, enriched with chromium apparently exist, and where chromium atoms are randomly located, at

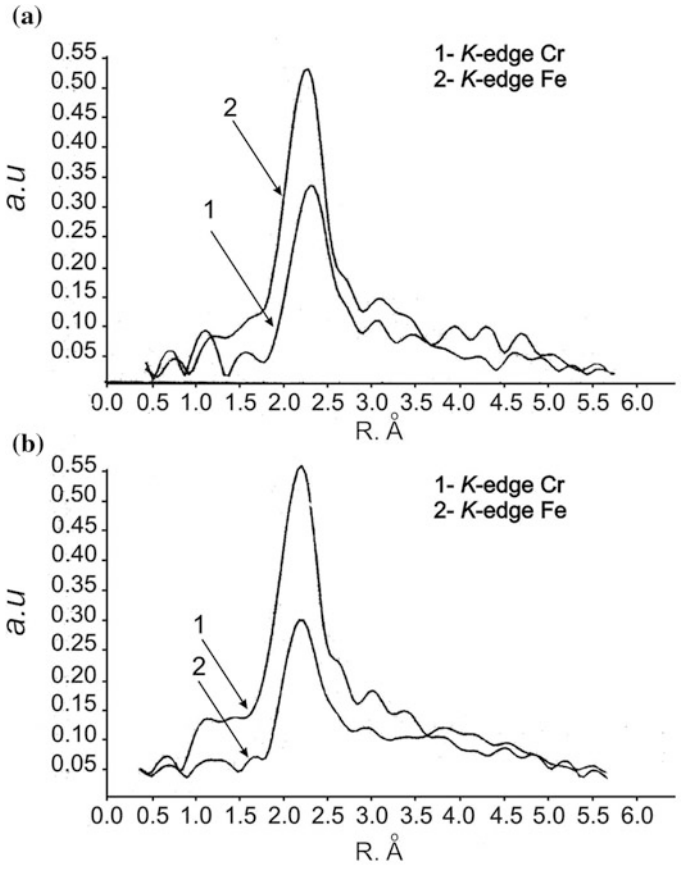

Fig. 14.20 Comparison of the partial RDF around Fe and Cr atoms for AMA $Fe_{75}Cr_{10}B_{15}$ (**a**) and AMA $Fe_{53}Cr_{32}B_{15}$ (**b**)

the partial RDF around the chromium atoms is observed the extension at region of $r \sim 3.0 \div 3.1$ Å, however, its intensity is significantly less than for the partial RDF around the iron atoms. For AMA with chromium content of 27.2 at. % quite another type of topological SRO around the chromium atoms is apparently observed (indicated by reduction of the shoulder intensity and shift of the first peak of the partial RDF toward smaller distances). Based on EXAFS spectra simulation results and the fact that for the Cr_2B structure the shortest Metal—Metal distances are significantly less than for $(Fe,Cr)_3B$, it can be assumed that for AMA with 27.2 at.% Cr enriched microdomains with a topological type of SRO $(Cr,Fe)_2B$ may exist. At the same time, at the partial RDF around the iron atoms in the AMA with 27.2 at. % Cr an increasing shoulder intensity at $r \sim 3.0 \div 3.1$ Å can be seen, which within the above assumptions may be associated with the transition of chromium atoms

from microregions with SRO-type boride $(Fe,Cr)_3B$ structure $P4_2/n$ to microregions characterized by SRO type $(Fe,Cr)_2B$.

Comparison of partial RDF around the atoms of iron and chromium (Fig. 14.20) provides the obvious conclusion about the significant difference of the local environment of Fe atoms and Cr in the studied AMA.

Results obtained by the EXAFS—spectroscopy for AMA Fe-Co-B and Fe-Cr-B systems can be well interpreted in terms of the cluster model of microinhomogeneous AMA structure. In researched AMA the possibility of existence of three types of microregions is shown: microdomains enriched with boron, and characterized by the type of SRO borides, and microregions depleted boron and consisting mainly of metal atoms; microregions characterized by two types of SRO, for different microgroups enriched in TM_1 and microgroups enriched in TM_2.

14.7 Conclusions

Accumulation of the data about atomic and electronic structure of the AMA is the necessary condition for construction of the organization principles for disordered metallic structures. With this background, experimental studies of temperature relaxation processes and their impact on the atomic, electronic structure and morphological properties of the AMA surface during processing is a major task.

The work contains research results of the relaxation processes during heat treatment in temperature range from 250 °C to 700 °C, which occur on the surface of the iron-based AMA. By use of scanning tunneling microscopy with atomic resolution, tunneling spectroscopy, XPS and EXAFS—spectroscopy the influence of processes that appear in the early crystallization stages on the morphological features of the surface and the electronic structure of alloys were studied.

Initial amorphous iron-based alloys, in particular $Fe_{82}Si_4B_{14}$ and $Fe_{77}Si_8B_{15}$, are characterized by the presence of significant surface oxidized layer at a depth up to 150 nm. In addition to the C-C bonds typical for complex carbon compounds C = O bonds is detected at this layer. In oxidized layer and at some distance from it any boron and its compounds were not found. There is a presence of significant surface segregation of Si, the concentration of Si is kept constant both in oxidized layer and in studied depth of the tape. In the tape volume the presence of silicon carbide bond Si-C as well as minor amounts of oxygen and nitrogen was found. Since the interatomic distance of Fe-Si is longer than for Fe-B and close for Fe-Fe, the diffusion leads to substitution of Si atoms for Fe atoms during the process of formation of crystal structure. Apparently, it is one of the possible mechanisms for surface silicon segregation. Accordingly, during the structural relaxation higher redistribution of boron atoms takes place compared to those with Fe and Si atoms. Carbon on the surface of studied AMA is mainly represented in the oxidized state, whereas in the bulk it appears as silicon compounds and, likely, in the form of silicon carbide. A good solubility of boron in the tape volume was observed.

By the tunneling spectroscopy method the areas with low conductivity were detected, what is typical for the formation of nanophases Fe-Si and Fe-B. There is substantial heterogeneity of electronic density of states at intercluster boundaries indicating their complex organization. The Fermi level of the researched alloys occurs in a local minimum of the electronic density of states, and meets the criterion of Nagel-Tauc for the amorphous state formation.

The temperature dependences of roughness parameters R_a, R_q, R_{zjis} and R_z for the alloy $Fe_{82}Si_4B_{14}$ in the annealing temperatures range from RT to 700 °C were established. Nonmonotonic dependence of the subroughness parameters on temperature was observed. At temperatures of about 500 °C the formation of regular shape nanostructures in the form of rods was proved. Apparently, on far from equilibrium conditions the formation of needle-like nanocrystals takes place.

In the case of almost complete crystallization at 700 °C, terraced structures with some reduction of nanoroughness parameters under formation of rather flat planes over 200 nm were observed.

According to EXAFS—research, the increase of the content of Co atoms in the AMA system of Fe-Co-B leads to decrease of the radius of the first coordination sphere of the boron atom, and reduction of unit cell volume in a crystalline alloy $(Co,Fe)_3B$, which indicates strengthening of transition metal-boron bond.

Obtained EXAFS—spectroscopy results for the AMA Fe-Co-B system and Fe-Cr-B are well interpreted in terms of the cluster microinhomogeneous model for AMA structure. It is shown that for researched AMA there is the possibility of existence of three types of microregions: microdomains enriched with boron and characterized by SRO with borides type and microregions depleted with boron and consisting mainly of metal atoms; these microregions are characterized by the presence of two types of SRO, such as microgroups enriched with first transition metal and microgroups enriched with the second transition metal.

Doping with chromium of iron-based AMA leads to pronounced secondary peak at the partial RDF around the iron atoms at distances of $r \sim 3.0 \div 3.2$ Å. The existence of this feature is associated with the formation of AMA microdomains which are characterized by SRO by type borides $(TM_1, TM_2)_3B$ with the structure of $P4_2/n$. At the same time, the appearing of such secondary peak has not been found in the partial RDF around the Fe atoms for the AMA Fe-Co-B system.

Since the boride of the structure of $P4_2/n$ is more "high temperature" boride modification in comparison to the boride of $I\overline{4}$, structure, the possibility of formation of the AMA microregions characterized by SRO type boride of the structure of $P4_2/n$ is associated with influence of various additives the temperature at which the boride phase formation during the amorphous state crystallization begins.

Acknowledgements The authors are grateful for financial support from the Ministry of Education and Science of Ukraine, as well as for the countenance from the National Academy of Sciences of Ukraine.

References

1. T. Osaka, T Asahi, J. Kawaji T. Yokoshima, Electrochim. Acta **23**, 4576 (2005)
2. N.A. Skulkina, O.A. Ivanov, E.A. Stepanova, L.N. Shubina, P.A. Kuznetsov, A.K. Mazeeva, Phys. Procedia. **82**, 69 (2016)
3. A. Boutahar, H. Lassri, E.K. Hlil, D. Fruchart, J. Magn. Magn. Mater. **398**, 26 (2016)
4. X.C. Zhong, H.C. Tian, S.S. Wang, Z.W. Liu, Z.G. Zheng, D.C. Zeng, J. Alloys Compd. **633**, 188 (2015)
5. P. Kwapulinski, Z. Stokosa, J. Rasek, G. Badura, G. Haneczok, L. Pajak, L. Lelatko, J. Magn. Magn. Mater. **320**, e778 (2008)
6. G. Herzer, IEEE Trans. Magn. **25**, 3327 (1989)
7. N. Kobayashi, N. Kataoka, T. Shima, H. Fujimori, J. Magn. Magn. Mater. **129**, 302 (1994)
8. V.A. Blagojevic, D.M. Minic, M.V., Dragica. M. Minic, Mater. Chem. Phys. **142**, 207 (2013)
9. Y. Takahara, N. Narita, Mater. Sci. Eng. A **315**, 153 (2001)
10. T. Nagase, M. Suzuki, T. Tanaka, J. Alloys Compd. **619**, 267 (2015)
11. J.-F. Li, X. Liu, S.-F. Zhao, H.-Y. Dinga, K.-F. Yao, J. Magn. Magn. Mater. **386**, 107 (2015)
12. E.B. Modin, E.V. Pustovalov, A.N. Fedorets, A.V. Dubinets, B.N. Grudin, V.S. Plotnikov, S. S. Grabchikov, J. Alloys Compd. **641**, 139 (2015)
13. Z. Jia, W.C. Zhang, W.M. Wang, D. Habibi, L.C. Zhang, Appl. Catal. B **192**, 46 (2016)
14. M. Ghafari, G. Peng, D. Wang, Y. Imai, S. Kamali, Mater. Lett. **164**, 535 (2016)
15. D.A. Outer, J.F. Kaashoek, H.R.G.K. Hack, Int. J. Rock. Mech. Min. Sci. Geomech. Abstr. **32**, 3 (1995)
16. D.E. Sayers, E.A. Stern, F.W. Lytle, Phys. Rev. Lett. **27**, 1204 (1971)
17. L.N. Mazalov, N.V. Bausk, S.B. Erenburg, S.V. Larionov, Chin. J. Struct. Chem. **42**, 784 (2001)
18. A.G. McKale, B.W. Veal, A.P. Paulikas, S.K. Chan, G.S. Knapp, J. Am. Chem. Soc. **110**, 3763 (1988)
19. I. Kaban, S. Gruner, W. Hoyer, A. Il'inskii, A. Shpak, J. Non-Cryst. Solids **353**, 1979 (2007)
20. J. Madej, Z. Stoklosa, A. Chrobak, Arch. Mater. Sci. Eng. **34**, 1 (2008)
21. Y. Takahara, N. Narita, Mater. Sci. Eng. A **315**, 153 (2001)
22. Y.R. Zhang, R.V. Ramanujan, Thin Solid Films **505**, 97 (2006)
23. S.R. Nagel, J. Tauc, Phys. Rev. Lett. **35**, 380 (1975)
24. I.B. Kekalo, B.A. Samarin, *Physical Metallurgy of Precision Alloys* (Alloys with Special Magnetic Properties (Metallurgiya, Moscow, 1989)
25. I.A. Kuznetsov, G.A. Dorogina, E.S. Gorkunov, Phys. Met. Metallogr. **101**, 247 (2006)
26. I.B. Kekalo, V.P. Menushenkov, *Rapidly hardened system hard-magnetic materials Nd-Fe-B* (MISiS, Moscow, 1989)
27. I.B. Kekalo, V.J. Vvedenski, G.A. Nuzhdin, *The microcrystalline soft Magnetic Materials* (MISiS, Moscow, 1999)
28. I.B. Kekalo, *Amorphous Magnetic Materials. Part I* (MISiS, Moscow, 2001)
29. I.B. Kekalo, *Amorphous magnetic materials. Part II* (MISiS, Moscow, 2002)
30. I.B. Kekalo, O.B. Basargin, V.Y. Tsvetkov, Phys. Met. Metallogr. **57**, 967 (1984)
31. R. Ugo, Catal. Rev. **11**, 225 (1975)
32. M. Fujikura, T. Yamada, T. Sato, J. Magn. Magn. Mater. **133**, 273 (1994)
33. M. Fujikura, T. Yamada, T. Sato, Mater. Sci. Eng. A **A181**, 1351 (1994)
34. N. Ikeo, Y. Iijima, N. Niimura, *Handbook of X-ray Photoelectron Spectroscopy* (Jeol, Japan, 1991)
35. V.T. Cherepin, *Secondary Ion Mass Spectroscopy of Solid Surfaces* (VNU Science Press, Utrecht, 1987)
36. C. Johansson, J. Headman, A. Berndtsson, J. Electron Spectrosc. **2**, 295 (1973)
37. J.H. Scofield, J. Electron Spectrosc. Relat. Phenom. **8**, 129 (1976)
38. D.A. Shirley, Phys. Rev. B. **5**, 4709 (1972)
39. Z.M. Stadnik, G. Stroink, J. Non-Cryst. Solids. **99**, 233 (1988)

40. G.K. Werthelin, P.H. Cltrlri, *Photoemission in Solids I, Topics in Applied Physics* (Springer, Berlin, 1978)
41. T. Honda, F. Itoh, K. Suzuki, in *Proceedings of 4 th International Conference on Rapidly Quenched Metals*, ed. by T. Masumoto, K. Suzuki, vol. 2 (The Japan Institute of Metals, Sendai, Japan, 1982), p. 1303
42. R.C. O'Handly, J. Appl. Phys. **10**, 49 (1987)
43. V.G. Aleshin. T.T. Serebryakova, A.I. Kharlamov, Phys. Status Solidi B. **83**, 537 (1977)
44. S. Falh, P. Lamparter, S. Steeb, Z. Naturforsch. **12**, 1175 (1984)
45. P.A. Mausli, G. Burri, S.G. Steinemann, in *Proceedings 4th International Conference on Rapidly Quenched Metals*, ed. by T. Masumoto, K. Suzuki, vol. 2 (The Japan Institute of Metals, Sendai, Japan, 1982), p. 1275
46. V.F.J. Loo, V.J.A. Beek, Z. Metallk. **4**, 245 (1989)
47. E. Majkova, P. Duhay, Phys. Status Solidi B **146**, K17 (1988)
48. L.J. Joyner, O. Johnson, D.M. Hercules, J. Am. Chem. Soc. **6**, 1910 (1980)
49. K. Tanaka, M. Yoshino, K. Suzuki, J. Phys. Soc. Jpn. **12**, 3882 (1982)
50. D.J. Joyner, R.F. Willis, Phil. Mag. A **3**, 815 (1981)
51. L. Guangwei, W. Dlngsheng, J. Phys. Condens. Matter **1**, 1799 (1989)
52. H. Yasuda, H. Nakayama, H. Fujita, Jap. Y. of Appl. Phys. **11**, 2234 (1989)
53. T. Fujiwara, J. Phys. F. Met. Phys. **2**, 661 (1982)
54. T. Fujiwara, J. Non-Cryst. Solids. **2**, 1039 (1984)
55. N.K. Myshkin, M.I. Petrokovets, S.A. Chizhik, Trib. Int. **32**, 379 (1999)
56. A. Il'inskii, I. Kaban, Yu. Koval, J. Non-Cryst. Solids. **251**, 345 (2004)
57. T. Sato, T. Ozawa, M. Nagumo, in *Proceedings of 4th International Conference on Rapidly Quenched Metals*, ed. by T. Masumoto, K. Suzuki, vol. 2 (The Japan Institute of Metals, Sendai, Japan, 1982), p. 961
58. V.L. Karbivskyy, A.G. Iliinskyi, V.H. Kasyyanenko, O.I. Sluhovskyy, Metallofiz. Noveishie Tekhnol. **36**, 977 (2014)
59. P. Duhai, P. Svac, M. Durcekova, G. Vlasak, Mater. Sci. Eng. **97**, 337 (1988)

Index

L. A. Bulavin and A. V. Chalyi (eds.), *Modern Problems of Molecular Physics*,
Springer Proceedings in Physics 197, https://doi.org/10.1007/978-3-319-61109-9